

---

# Phase Behaviour and Physical Properties of Reservoir Fluids Under Addition of Carbon Dioxide

Saif Zahir Said Al Ghafri

A thesis submitted in partial fulfilment of the requirements for the degree of Doctor of  
Philosophy and the Diploma of Imperial College London

Department of Chemical Engineering  
Imperial College London  
London SW7 2AZ, United Kingdom

October 2013

---

## **Originality Declaration**

I herewith certify that all material in this dissertation which is not my own work has been properly acknowledged.

Saif Zahir Said Al Ghafri

## **Copyright Declaration**

“The copyright of this thesis rests with the author and is made available under a Creative Commons Attribution Non-Commercial No Derivatives licence. Researchers are free to copy, distribute or transmit the thesis on the condition that they attribute it, that they do not use it for commercial purposes and that they do not alter, transform or build upon it. For any reuse or redistribution, researchers must make clear to others the licence terms of this work”

---

## Dedicated to my parents

" وَقَضَىٰ رَبُّكَ أَلَّا تَعْبُدُوا إِلَّا إِيَّاهُ وَبِالْوَالِدَيْنِ إِحْسَانًا ، إِمَّا يَبُلُغَنَّ عِنْدَكَ الْكِبَرَ أَحَدُهُمَا أَوْ كِلَاهُمَا فَلَا تَقُلْ لَهُمَا أَفًّا وَلَا تَنْهَرَهُمَا وَقُلْ لَهُمَا قَوْلًا كَرِيمًا ، وَأَخْفِضْ لَهُمَا جَنَاحَ الذُّلِّ مِنَ الرَّحْمَةِ وَقُلْ رَبِّ ارْحَمْهُمَا كَمَا رَبَّيَانِي صَغِيرًا "

*"And your Lord has decreed that you worship none but **Him**. And that you be dutiful to your parents. If one of them or both of them attain old age in your life, say not to them a word of disrespect, nor shout at them but address them in terms of honour, And lower unto them the wing of submission and humility through mercy, and say: "My Lord! Bestow on them Your Mercy as they did bring me up when I was small."*

*The Nobel Quran, Surah Al-Isra 23-24, (The Journey by Night)*

---

## Acknowledgements

*" الْحَمْدُ لِلَّهِ الَّذِي لَهُ مَا فِي السَّمَاوَاتِ وَمَا فِي الْأَرْضِ وَلَهُ الْحَمْدُ فِي الْآخِرَةِ وَهُوَ الْحَكِيمُ الْخَبِيرُ، يَعْلَمُ مَا يَلِجُ فِي الْأَرْضِ وَمَا يَخْرُجُ مِنْهَا وَمَا يَنْزِلُ مِنَ السَّمَاءِ وَمَا يَعْرُجُ فِيهَا وَهُوَ الرَّحِيمُ الْعَفُورُ "*

"And my success (in my task) can only come from **Allah**. In **Him** I trust, and unto **Him** I look". In the name of **Allah**, the most Gracious and the most Merciful, all devoted praises to **Him** for the strengths and **His** blessing in completing this thesis. "All praise is due to **Allah**, Lord of the universe".

Four years journey at last comes to rest, loaded with intensive memories, immense moments and astonishing experiences. Many people have contributed directly or indirectly towards the thriving achievement of this path; to them I will be always grateful. First and foremost, I offer my sincerest gratitude to my supervisors Martin Trusler and Geoffrey Maitland for the invaluable support, guidance and contributions towards the success of this work. Your broad knowledge, experience and inspiring conversations established a rich environment for me to learn and kept me always enthused and determined to prevail over all obstacles. The close interaction with the thermophysical group on various significant aspects of thermophysical property measurements, and pleasant relationships is sincerely acknowledged, especially Xuesong Li, David Vega, Shuxin Hou, Faheem Ijaz, Mark McBride-Wright, Chih-wei, John Crawshaw, Edo Boek, Tina Secuianu, Shane Cadogan, Cheng Peng, Rayane Hoballah, Eric May and Tay Weparn. To them I owe many interesting discussions and valuable suggestions. Special thanks are owned to David Vega and Shuxin Hou for sharing their knowledge on phase behaviour, which was crucial at the beginning of my PhD. It has been a real privilege for me to work in an interdisciplinary group under the guidance of such passionate and motivated scientists.

Special gratitude goes to MSE group who greatly helped me from modelling prospective, mainly Amparo Galindo, George Jackson, Andrew Haslam, Esther Forte, Apostolos Georgiadis, Simon Dufal, Vasileios Papaioannou and Daniel Erikson. In particular, sincere appreciation goes to Esther Forte and Apostolos Georgiadis for performing the SAFT calculations. I offer my sincerest appreciation to Andrew Haslam for all of the support and interesting discussions in understanding various aspects of the theory. People from the financial department, mechanical and electrical workshops are much acknowledged for their continuous support and collaboration, in particular, Chin Lang and Gavin Barnes. Last but



---

not least at all, Hak Lui and José Rodríguez are most acknowledged for assisting directly in some aspects of experimental measurements.

During my time in Imperial and London, I had the chance of meeting truly wonderful people who have been of great importance and help to me, in all aspects of life. Your valuable friendships during all these years have been priceless and have provided me with some of the most enjoyable discussions and deep conversations. Through your sincere and profound friendships, much evolved throughout periods of intense experiences, I am ever indebted to Abdulaziz Al Balushi, Ahmed Al Yaqoobi, Abdulwahab Al Hinai, Mohammed Al Siyabi, Bader Al Abri and few others. I hope you know that the limited, but so much motivating for life, moments we spent together during the last few years, form the very core of what I perceive to be the only thing one can ever really own. Thank you and I hope life will always keep us in close proximity. Some others, their presence are very special, don't need a quotation; you know I could not have words to express all that you have done for me during this time.

Finally, deep letters with love and appreciation are owned to my family and close relatives for their permanent and intense presence in every distinct step engaged throughout this journey. My parents Zahir and Thuraya, Grandmother, Brothers, Sisters and Nieces, words are so limited. I don't know to which extent all of this would have happened without your love, support and understanding. The best and most beautiful things in the world cannot be seen or even touched but felt with the heart; this is simply you. Throughout your profound admiration, I learned that the power of love is stronger than any hate or anger or stress. Your faithful prayers, and so much your true wishes, have endlessly provided me the strength and carried away all ambiguity that kept disturbing my soul. I will be always indebted to you.

This work was carried out as part of the activities of the Qatar Carbonates & Carbon Storage Research Centre (QCCSRC). We gratefully acknowledge the funding of QCCSRC provided jointly by Qatar Petroleum, Shell, and the Qatar Science and Technology Park.

من وحي حروفك أمير الروح...

Saif Zahir Al Ghafri

2013

---

## Abstract

The phase behaviour of reservoir fluids under the addition of carbon dioxide (CO<sub>2</sub>) were studied at elevated pressures and temperatures similar to those encountered in enhanced oil recovery (EOR) and carbon storage processes. The principal focus of the work presented in this thesis is the experimental investigation of the phase behaviour of these CO<sub>2</sub> mixtures with hydrocarbon reservoir fluids. For this purpose, a new high-pressure high-temperature apparatus was designed and constructed. The apparatus consisted of a thermostated variable-volume view cell driven by a computer-controlled servo motor system. The maximum operating pressure and temperature were 40 MPa and 473.15 K, respectively. Measurements were then made over a wide range of pressure and temperature conditions for two representative CO<sub>2</sub>-hydrocarbon systems: (CO<sub>2</sub> + *n*-heptane + methylbenzene) and (CO<sub>2</sub> + synthetic crude oil). The vapour-liquid phase behaviour of the former system was studied, under CO<sub>2</sub> addition and various molar ratios of *n*-heptane to methylbenzene, along different isotherms at temperatures between (298 and 473) K and at pressures up to approximately 16 MPa. In the latter, the synthetic oil contained a total of 17 components while solution gas (methane, ethane and propane) was added to obtain live synthetic crudes with gas-oil ratios of either 58 or 160. Phase equilibrium and density measurements were then made for the 'dead' oil and the two 'live' oils under the addition of CO<sub>2</sub>. The measurements were carried out at temperatures between (298.15 and 423.15) K and at pressures up to 36 MPa, and included vapour-liquid, liquid-liquid and vapour-liquid-liquid equilibrium conditions.

The phase equilibria of (carbon dioxide + *n*-heptane + water) and (carbon dioxide + methane + water) mixtures were also studied using a high pressure quasi-static analytical apparatus with on-line compositional analysis by gas chromatography. The former system was studied under conditions of three-phase equilibria along five isotherms at temperatures from (323.15 to 413.15) K and at pressures up to the upper critical end point (UCEP). In the latter system, compositions of three coexisting fluid phases have been obtained along eight isotherms at temperatures from (285.15 to 303.5) K and at pressures up to either the UCEP or up to the hydrate formation locus. Compositions of coexisting vapour and liquid phases have been obtained along three isotherms at temperatures from (323.15 to 423.15) K and pressures up to 20 MPa for mixtures containing nearly equal overall mole fractions of CH<sub>4</sub> and CO<sub>2</sub>. The quadruple curve along which hydrate coexists with the three fluid phases was also measured. A detailed study of these ternary mixtures was carried out based on comparison with available ternary data of the type (CO<sub>2</sub> + *n*-alkane + water) and available data for the

---

constituent binary subsystems. In this way, we analyze the observed effects on the solubility when the *n*-alkane component was changed or a third component was added.

The experimental data for the (CO<sub>2</sub> + hydrocarbon) systems have been compared with results calculated with two predictive models, PPR78 and PR<sub>2</sub>SRK, based on Peng-Robinson 78 (PR78) and Soave-Redlich-Kwong (SRK) cubic equations of state (EoS) with group-contribution formula for the binary interaction parameters and with the use of different alpha functions. Careful attention was paid to the critical constants and acentric factor of high molar-mass components. The use of the Boston-Mathias modification of the PR78 and SRK equations was also investigated. The experimental data obtained for the (CO<sub>2</sub> + *n*-heptane + methylbenzene) mixture were also compared with the predictions made using SAFT- $\gamma$ -Mie, a group-contribution version of the Statistical Associating Fluid Theory (SAFT), which was implemented with the generalized Mie potential to represent segment-segment interactions. Detailed assessment of the predictive capability of these models concluded that the agreement between the experimental data and prediction from these methods, while not perfect, is very good, especially on the bubble curve. The results suggest that there is merit in the approach of combining these methods with a group-contribution scheme. Comparison between these approaches concluded that they all have comparable accuracies regarding VLE calculations. The experimental data obtained for the ternary mixtures (CO<sub>2</sub> + *n*-alkane + water) have been compared with the predictions of SAFT for potentials of variable range (SAFT-VR), implemented with the square-well (SW) potential using parameters fitted to experimental pure-component and binary-mixture data. A good performance of the SAFT-VR equation in predicting the phase behaviour at different temperatures was observed even with the use of temperature-independent binary interaction parameters. It was also observed that an accurate prediction of phase behaviour at conditions close to criticality cannot be accomplished by mean-field based theories, such as the models used in this work, that do not incorporate long-range density fluctuations.

Density measurements on a variety of brines (both single-salt and mixed) were studied in the present work within the context of CO<sub>2</sub> storage processes in saline aquifers. Densities of MgCl<sub>2</sub>(aq), CaCl<sub>2</sub>(aq), KI(aq), NaCl(aq), KCl(aq), AlCl<sub>3</sub>(aq), SrCl<sub>2</sub>(aq), Na<sub>2</sub>SO<sub>4</sub>(aq), NaHCO<sub>3</sub>(aq), the mixed salt system [(1 - *x*) NaCl + *x*KCl](aq) and the synthetic reservoir brine system [*x*<sub>1</sub>NaCl + *x*<sub>2</sub>KCl + *x*<sub>3</sub>MgCl<sub>2</sub> + *x*<sub>4</sub>CaCl<sub>2</sub> + *x*<sub>5</sub>SrCl<sub>2</sub> + *x*<sub>6</sub>Na<sub>2</sub>SO<sub>4</sub> + *x*<sub>7</sub>NaHCO<sub>3</sub>](aq), where *x* denotes mole fraction, were studied at temperatures between (283 and 473) K and pressures up to 68.5 MPa. The measurements were performed with a vibrating-tube densimeter calibrated under vacuum and with pure water over the full ranges of pressure

---

and temperature investigated. It was observed that careful attention needs to be paid to the type of calibration method selected.

An empirical correlation is reported that represents the density for each brine system as a function of temperature, pressure and molality with absolute average relative deviations ( $\Delta_{AAD}$ ) of approximately 0.02 %. Comparing the model with a large database of results from the literature suggested that the model is in good agreement with most of the available data. The model can be used to calculate density, apparent molar volume and isothermal compressibility of single component salt solutions over the full ranges of temperature, pressure and molality studied. An ideal mixing rule for the density of a mixed electrolyte solution was tested against our mixed salts data and was found to offer good predictions at all conditions studied with an absolute average relative deviation of 0.05 %.

The present work was carried out as part of the Qatar Carbonates and Carbon Storage Research Centre (QCCSRC) program. It covered a wide range of phase behaviour and density measurements at conditions relevant to oil and gas fields' applications, and explored the predictive capabilities of some available models, in particular predictive cubic EoS, SAFT-VR and SAFT- $\lambda$ -Mie. The research and data collected represents a good step in enabling the direct design and optimisation of CO<sub>2</sub>-EOR and carbon storage processes. An example is the validation of the predictive models and the determination of the miscibility pressure which is essential for effective recovery of the heavy hydrocarbons. Areas in which the research might be extended, both through further experimental studies and improved modelling, have been identified.

---

# Contents

<b>Acknowledgements</b> .....	<b>iv</b>
<b>Abstract</b> .....	<b>vi</b>
<b>List of Figures</b> .....	<b>xiii</b>
<b>List of Tables</b> .....	<b>xviii</b>
<b>Chapter 1: Introduction</b> .....	<b>20</b>
1.1 Energy, Climate Change and Environment.....	20
1.2 Carbon Capture and Storage Processes (CCS) .....	20
1.3 Enhanced Oil Recovery Processes (EOR) .....	22
1.4 Qatar Carbonates and Carbon Storage Research Centre .....	23
1.5 Experimental and Modelling Challenges.....	25
1.6 Project Motivation.....	27
1.7 Scope and Objectives .....	27
1.8 Selection Criteria of the Measured Systems .....	29
1.9 Thesis Outline .....	30
<b>Chapter 2: Fluid Phase Equilibria: Literature and Background</b> .....	<b>31</b>
2.1 Phase Equilibria and Phase Diagrams .....	31
2.1.1 Introduction.....	31
2.1.2 Phase Behaviour of Pure Components .....	32
2.1.3 Phase Behaviour of Binary Mixtures .....	33
2.1.4 Phase Behaviour of Ternary Mixtures .....	37
2.2 Experimental Methods for Fluid Phase Equilibria.....	40
2.2.1 Overview .....	40
2.2.2 Analytical Method .....	40
2.2.3 Synthetic Method.....	42
2.3 Phase Behaviour of Hydrocarbon Mixtures.....	43
2.3.1 Types and Behaviour of Hydrocarbon Fluids .....	43
2.3.2 Characterization of Hydrocarbon Fluids .....	45
2.4 Phase Behaviour of CO <sub>2</sub> + Hydrocarbon Mixtures .....	46
2.5 Phase Behaviour of CO <sub>2</sub> + Hydrocarbon + Water Mixtures.....	47
<b>Chapter 3: Theory and Modelling</b> .....	<b>50</b>
3.1 The Virial Equation of State.....	50
3.2 Cubic Equations of State (EoS).....	51
3.2.1 Introduction.....	51
3.2.2 Cubic Equations of State .....	52
3.2.3 Mixing Rules and Binary Interactions .....	56

3.2.4 Predictive Cubic Equations of State .....	57
3.3 Activity Coefficient Models.....	59
3.4 The Statistical Associating Fluid Theory (SAFT).....	61
3.4.1 Introduction.....	61
3.4.2 SAFT-VR Approach .....	64
3.4.3 SAFT- $\gamma$ -Mie Approach.....	67
3.5 Summary.....	68
<b>Chapter 4: New Synthetic Apparatus for Fluid Phase Equilibrium Measurements .....</b>	<b>69</b>
4.1 Apparatus Design.....	69
4.2 Apparatus Control and Operation .....	74
4.2.1 Servo Control System .....	74
4.2.2 Electrically Actuated Valves Control.....	78
4.2.3 Other Controllers .....	79
4.2.4 Operational Manuals.....	82
4.3 Health, Safety and Environment (HSE) .....	82
4.4 Materials .....	83
4.5 Experimental Procedure and Calculations .....	84
4.6 Calibration and Uncertainty Analysis .....	86
4.7 Apparatus Validation .....	91
4.8 Apparatus Maintenance.....	93
4.9 Summary.....	93
<b>Chapter 5: Analytical Apparatus for Fluid Phase Equilibrium Measurements .....</b>	<b>94</b>
5.1 Apparatus Design.....	94
5.2 Materials .....	96
5.3 Experimental Procedure .....	96
5.4 Apparatus Calibration .....	98
5.5 Uncertainty Analysis.....	100
5.6 Apparatus Validation .....	103
5.7 Summary.....	107
<b>Chapter 6: Phase Behaviour of (CO<sub>2</sub> + <i>n</i>-Heptane + Methylbenzene) Mixtures .....</b>	<b>108</b>
6.1 Overview .....	108
6.2 Introduction .....	109
6.3 Modelling Approaches.....	110
6.4 Discussion and Comparison with Experiment.....	112
6.5 Conclusion .....	121
<b>Chapter 7: Phase Behaviour and Density of (CO<sub>2</sub> + Synthetic Crude Oil) Mixtures ...</b>	<b>122</b>
7.1 Overview .....	122

7.2	Introduction .....	122
7.3	Selection of the Synthetic Crude Oil .....	124
7.4	Experimental Results and Discussion.....	128
7.5	Modelling Approaches .....	134
7.6	Evaluation of the Critical Properties.....	135
7.7	Comparison with Experiment.....	139
7.8	Conclusion .....	145
<b>Chapter 8: Phase Behaviour of (CO<sub>2</sub> + <i>n</i>-Heptane + Water) Mixtures .....</b>		<b>147</b>
8.1	Overview .....	147
8.2	Introduction .....	147
8.3	Experimental Results .....	149
8.4	Modelling Approach.....	150
8.5	Discussion and Comparison with Experiment.....	152
8.6	Conclusion .....	161
<b>Chapter 9: Phase Behaviour of (CO<sub>2</sub> + Methane + Water) Mixtures .....</b>		<b>162</b>
9.1	Overview .....	162
9.2	Introduction .....	163
9.3	Experimental Results .....	167
9.4	Modelling Approach.....	170
9.5	Discussion and Comparison with Experiment.....	171
9.6	Conclusions.....	183
<b>Chapter 10: Density of Aqueous Solutions .....</b>		<b>185</b>
10.1	Overview .....	185
10.2	Introduction .....	186
10.3	Theory of the Vibrating Tube Densimeter .....	188
10.4	Experimental Work .....	191
10.5	Apparatus Calibration .....	194
10.6	Uncertainty Analysis .....	196
10.7	Experimental Results .....	198
10.8	Correlation and Modelling.....	199
10.9	Discussion and Comparison with Experiment.....	205
10.10	Evaluation of the Calibration Method .....	207
10.11	Conclusion .....	211
<b>Chapter 11: Conclusions and Recommendations for Future Work.....</b>		<b>213</b>
11.1	Summary.....	213
11.2	Contribution of This Work .....	218
11.3	Recommendation for Future Work.....	219

---

11.3.1 Further Experimental Investigations.....	219
11.3.2 Further Apparatus Improvement .....	221
11.3.3 Further Modelling Investigation .....	223
Appendixes .....	261
Appendix A. Engineering Drawings and Technical Specifications.....	261
Appendix B. Safety Critical System Analysis (SCSA) .....	272
Appendix C. Experimental Data for Mixtures Studied in this Work.....	275
Appendix D. Experimental Density Data for Aqueous Solutions .....	290
Appendix E. Relative Deviations of Densities from the Correlation Model.....	296
Appendix F. An Analytical Expression for the Determination of Density Error .....	304



---

## List of Figures

<b>Figure 2.1.</b> Plots showing the phase diagrams for pure component. (a), Pressure-Temperature phase envelope; (b), Pressure-Volume phase envelope.....	32
<b>Figure 2.2.</b> Plots showing the phase diagrams for binary components. (a), Pressure-Temperature phase envelope; (b), Pressure-Volume phase envelope.....	34
<b>Figure 2.3.</b> ( $p$ , $T$ ) projections showing the phase behaviour diagrams for binary mixtures according to Van Konynenburg and Scott classification. ....	35
<b>Figure 3.1.</b> Illustration of molecular models underlying EoS showing the non-spherical nature of the molecule.....	63
<b>Figure 4.1.</b> Schematic diagram of the variable-volume cell apparatus.....	70
<b>Figure 4.2.</b> Perspective drawing of the variable-volume cell assembly. ....	71
<b>Figure 4.3.</b> Pictures showing the synthetic apparatus setup located in the chemical engineering department, ACEX building, lab 424.....	73
<b>Figure 4.4.</b> A schematic representing the sequences and items required to control the servo motor, and hence the pressure.....	74
<b>Figure 4.5.</b> Schematics illustrating the front and rear view of the servo controller crate respectively.....	75
<b>Figure 4.6.</b> A schematic showing the connections arrangements for the five and three ways electrical actuated valves. ....	79
<b>Figure 4.7.</b> Schematic of the pressure and temperature control systems connections.....	81
<b>Figure 4.8.</b> Calibration curves for the cell volume against piston position and temperature	89
<b>Figure 4.9.</b> Bubble- and dew-point pressures $p$ for ( $\text{CO}_2 + n$ -heptane) as a function of the mole fraction $x_{\text{CO}_2}$ of $\text{CO}_2$ at $T = 394.15$ K. The figure shows the comparison with the available literature data.....	92
<b>Figure 5.1.</b> Schematic diagram of the analytical apparatus.....	95
<b>Figure 5.2.</b> Amount of component ( $n$ ) versus detector response area ( $A$ ) graph showing the data points measured for different components and the calibration curve obtained for the response of the detectors at 90mA.....	100
<b>Figure 5.3.</b> Isothermal pressure composition ( $p$ , $x$ ) phase diagram for the binary system ( $\text{CO}_2 + n$ -heptane) at different temperatures. The figures shows the compariosn with the published data.....	104
<b>Figure 5.4.</b> Isothermal pressure-composition ( $p$ , $x$ ) phase diagram at temperature $T = 298.15$ K for the binary system (carbon dioxide + water). The figures shows the compariosn with the published data.....	106
<b>Figure 6.1.</b> Isothermal bubble pressure-composition ( $p$ , $x$ ) phase diagram at temperature $T = 373.15$ K for the binary systems (carbon dioxide + $n$ -heptane) and (carbon dioxide +	

---

methylbenzene) and the ternary mixture (carbon dioxide + *n*-heptane + methylbenzene). The figures shows the compariosn with the binary published data Solid and prediction from SAFT- $\gamma$ -Mie for the ternary and binary mixtures. .... 113

**Figure 6.2.** Bubble- and dew-point pressures  $p$  for (CO<sub>2</sub> + *n*-heptane) as a function of the mole fraction  $x$  of CO<sub>2</sub> at  $T = 394.15$  K. The figures shows the compariosn with the published data and predictions of the PPR78 EoS, the PR<sub>2</sub>SRK EoS and SAFT- $\gamma$ -Mie ..... 114

**Figure 6.3.** Bubble curve for the ternary mixture (CO<sub>2</sub> + *n*-heptane + methylbenzene) at temperature  $T = 298.15$  K. The figure represents prediction from SAFT- $\gamma$ -Mie. .... 115

**Figure 6.4.** Bubble and dew curves for the ternary mixture (CO<sub>2</sub> + *n*-heptane + methylbenzene) at temperature  $T = 323.15$  K. The figure represents prediction from SAFT- $\gamma$ -Mie ..... 115

**Figure 6.5.** Bubble and dew curves for the ternary mixture (CO<sub>2</sub> + *n*-heptane + methylbenzene) at temperature  $T = 423.15$  K. The figure represents prediction from SAFT- $\gamma$ -Mie ..... 116

**Figure 6.6.** Bubble and dew curves for the ternary mixture (CO<sub>2</sub> + *n*-heptane + methylbenzene) at temperature  $T = 473.15$  K. The figure represents prediction from SAFT- $\gamma$ -Mie ..... 116

**Figure 6.7.** Bubble and dew curves versus temperature at fixed molar ratio of *n*-heptane to methylbenzene mixture ( $y = 0.3383$ ) and two different CO<sub>2</sub> compositions. The figure represents prediction from SAFT- $\gamma$ -Mie ..... 118

**Figure 6.8.** Triangular diagram for the (carbon dioxide + *n*-heptane + methylbenzene) system at temperature  $T = 423.15$  K and different pressures. The figure represents prediction from SAFT- $\gamma$ -Mie showing the two and one phase regions..... 118

**Figure 6.9.** Triangular diagram for the (carbon dioxide + *n*-heptane + methylbenzene) system at pressure  $p = 3.5$  MPa and different temperatures. The figure represents prediction from SAFT- $\gamma$ -Mie showing the two and one phase regions..... 119

**Figure 6.10.** Bubble and dew curves for the ternary mixture CO<sub>2</sub> (1) + *n*-heptane (2) + methylbenzene (3) at temperature  $T = 373.15$  K. The figure represents prediction from SAFT- $\gamma$ -Mie, PPR78, PR<sub>2</sub>SRK and PSRK. .... 120

**Figure 7.1.** True boiling and density curves respectively: Celsius boiling temperature  $t$  and density  $\rho$  as a function of cumulative volume fraction  $V_r$ . The figure shows the comparison between experimental data and simulated data for the synthetic dead oil. .... 126

**Figure 7.2.** Images of the interior of the variable volume cell showing VLLE, LLE and critical opalescence phenomena observed between the hydrocarbon and carbon dioxide-rich phases. .... 128

**Figure 7.3.** Bubble- and dew-point pressures  $p$  as a function of the mole fraction  $x_{\text{CO}_2}$  of CO<sub>2</sub> for CO<sub>2</sub> with dead and live oils. The figure shows the VLE predictions of the PPR78 EoS with the Soave alpha function..... 129

<b>Figure 7.4.</b> Phase-boundary pressures $p$ as a function of the mole fraction $x_{\text{CO}_2}$ of $\text{CO}_2$ for $\text{CO}_2$ with dead and live oils. The figure shows the VLE, VLLE and LLE predictions of PPR78 EoS with the Soave alpha function.....	131
<b>Figure 7.5.</b> Three-phase VLLE locus for the ( $\text{CO}_2$ + dead oil) mixture .....	133
<b>Figure 7.6.</b> Saturated phase densities $\rho$ as a function of the mole fraction $x_{\text{CO}_2}$ of $\text{CO}_2$ for $\text{CO}_2$ with dead and live oils. The figure shows the predictions of the PPR78 EoS with the Soave alpha function.....	134
<b>Figure 7.7.</b> Absolute average deviation $\Delta_{\text{AAD}}$ of experimental VLE data for ( $\text{CO}_2$ + squalane) and ( $\text{CH}_4$ + squalane) from the PPR78 EoS with different values of the critical temperature $T_c$ and critical pressure $p_c$ for squalane. ....	138
<b>Figure 7.8.</b> Bubble- and dew-point pressures $p$ as a function of the mole fraction $x_{\text{CO}_2}$ of $\text{CO}_2$ for ( $\text{CO}_2$ + dead oil) at $T = 373.15$ K. The figure shows the prediction of the PPR78 EoS with the Soave alpha function and different critical constants for squalane.....	138
<b>Figure 7.9.</b> Bubble- and dew-point pressures $p$ as a function of the mole fraction $x_{\text{CO}_2}$ of $\text{CO}_2$ for $\text{CO}_2$ with dead and live oils. The figure shows the predictions of the the PPR78 EoS with the Boston-Mathias alpha function .....	141
<b>Figure 7.10.</b> Bubble- and dew-point pressures $p$ as a function of the mole fraction $x_{\text{CO}_2}$ of $\text{CO}_2$ for $\text{CO}_2$ with dead and live oils. The figure shows the predictions of the of the PP <sub>2</sub> SRK EoS with the Soave alpha function.....	142
<b>Figure 7.11.</b> Bubble- and dew-point pressures $p$ as a function of the mole fraction $x_{\text{CO}_2}$ of $\text{CO}_2$ for $\text{CO}_2$ with dead and live oils. The figure shows the predictions of the of the PP <sub>2</sub> SRK EoS with the Boston-Mathias alpha function .....	144
<b>Figure 7.12.</b> Binary interaction parameters for $\text{CO}_2$ - $\text{CH}_4$ . The figure shows the comparison between the optimized values and those predicted by the PPR78 model with the Soave alpha function.....	145
<b>Figure 8.1.</b> Images of the interior of the vessel showing the critical opalescence phenomena observed between the $n$ -heptane-rich and carbon dioxide-rich phases (middle and upper, respectively), what is so called upper critical end point, UCEP, at $T = 323.15$ K .....	150
<b>Figure 8.2.</b> Isothermal pressure composition ( $p, x$ ) phase diagram for the binary system ( $\text{CO}_2$ + $n$ -heptane) at different temperatures. The figure shows the comparison with the published data and the prediction fro SAFT-VR. ....	153
<b>Figure 8.3.</b> Experimental ( $p, T$ ) UCEP critical locus showing the critical points between the $\text{CO}_2$ -rich and the $n$ -heptane-rich phases in the presence of a third water-rich phase visually observed in this work .....	154
<b>Figure 8.4.</b> Isothermal composition diagram for the (carbon dioxide + $n$ -heptane + water) system at different temperatures. The figures shows the prediction of SAFT-VR .....	155
<b>Figure 8.5.</b> Isothermal pressure-composition ( $p, x$ ) phase diagram for the (carbon dioxide + $n$ -heptane + water) system in the different phases at different temperatures. The figure shows the prediction of SAFT-VR .....	156

<b>Figure 8.6.</b> Isothermal pressure-composition phase diagram for the (carbon dioxide + <i>n</i> -heptane + water) system at different temperatures. The figure shows the prediction of SAFT-VR for the <i>n</i> -heptane-rich and the carbon dioxide-rich phases in the ternary system at conditions of VLLE equilibria and the temperature of our measurements. It also shows the SAFT-VR predictions for the binary system ( <i>n</i> -heptane + carbon dioxide) at the same temperatures.....	157
<b>Figure 8.7.</b> Isothermal pressure composition phase diagram for the (carbon dioxide + <i>n</i> -heptane + water) system representing the CO <sub>2</sub> <i>K factor</i> in the water-rich phase (a) and water <i>K factor</i> in the CO <sub>2</sub> -rich phase (b) respectively as a function of pressure.....	159
<b>Figure 8.8.</b> Isothermal pressure composition phase diagram for the (carbon dioxide + <i>n</i> -heptane + water) system representing the <i>n</i> -heptane <i>K factor</i> in the water-rich phase as a function of CO <sub>2</sub> mole fraction ratio in the <i>n</i> -heptane-rich phase and equilibrium pressure. ....	160
<b>Figure 9.1.</b> Images of the interior of the vessel showing the formation of hydrate observed in the water-rich phases (bottom phase), at <i>T</i> = 285.15 K.....	168
<b>Figure 9.2.</b> The VLLE region and its boundaries.....	172
<b>Figure 9.3.</b> A plot showing the UCEP curve against temperature and comparison with the critical curve for the binary system CO <sub>2</sub> + CH <sub>4</sub> .....	172
<b>Figure 9.4.</b> Triangular diagram for the (carbon dioxide + methane + water) system at different temperatures. The figure shows the SAFT-VR predictions of the three phase equilibrium region for every pressure and temperature data point.....	173
<b>Figure 9.5.</b> A plot showing the distribution of CO <sub>2</sub> and CH <sub>4</sub> in the water-rich and gas phases as a function of methane or CO <sub>2</sub> mole fraction in the gas phase under VLE conditions.....	175
<b>Figure 9.6.</b> Pressure-composition phase diagram showing the solubility of CO <sub>2</sub> in the water-rich phase under VLE conditions.....	176
<b>Figure 9.7.</b> Isothermal pressure-composition ( <i>p</i> , <i>x</i> ) phase diagram for the (carbon dioxide + methane + water) system in the water-rich phase, CO <sub>2</sub> -rich phase and Gas phase. The figure shows the SAFT-VR predictions of the three phases equilibrium region.....	177
<b>Figure 9.8.</b> Isothermal pressure-composition phase diagram for the (carbon dioxide + methane + water) system at different temperatures. The figure shows the SAFT-VR predictions .....	179
<b>Figure 9.9.</b> Isothermal pressure-composition phase diagram for the (carbon dioxide + methane + water) system at at different temperatures. The figure shows the SAFT-VR predictions .....	179
<b>Figure 9.10.</b> Isothermal pressure composition phase diagram for the (carbon dioxide + methane + water) system representing the CO <sub>2</sub> solubility in the water-rich phase and water content in the gas phase respectively as a function of pressure.....	181
<b>Figure 9.11.</b> A plot showing the solubility of CO <sub>2</sub> in the water-rich phase as a function of <i>n</i> -alkane mole fraction and pressure in the hydrocarbon-rich phase under VLLE conditions. ....	182

---

<b>Figure 9.12.</b> Isothermal pressure composition phase diagram for the (carbon dioxide + methane + water) system representing the CH <sub>4</sub> solubility in the water-rich phase and water content in the gas phase respectively as a function of pressure.....	183
<b>Figure 10.1.</b> Schematic and picture showing the density apparatus setup.....	192
<b>Figure 10.2.</b> Calibration results showing the behaviour of coefficients <i>A</i> and <i>B</i> obtained from the use of the calibration equation with pressure and temperature.....	196
<b>Figure 10.3:</b> Deviations $\Delta\rho$ of experimental densities $\rho$ from the correlation model as a function of molality <i>b</i> . .....	203
<b>Figure 10.4.</b> Deviation $\Delta\rho$ of experimental densities $\rho$ for the synthetic brines from the predictive model as a function of molality <i>b</i> . .....	204
<b>Figure 10.5.</b> Deviation $\Delta\rho_m$ of densities $\rho_m$ for the mixed brine [(1 – <i>x</i> )NaCl + <i>x</i> KCl] from the predictive model as a function of molality <i>b</i> . .....	205
<b>Figure 10.6.</b> Relative deviations $\Delta\rho/\rho$ of densities $\rho$ from the correlation model for NaCl(aq) as a function of molality <i>b</i> . .....	205
<b>Figure 10.7.</b> Relative deviations $\Delta\rho/\rho$ of densities $\rho$ from the correlation model for CaCl <sub>2</sub> (aq) as a function of molality <i>b</i> . .....	206
<b>Figure 10.8.</b> Relative deviations $\Delta\rho/\rho$ of <i>n</i> -nonane calculated densities $\rho$ using different calibration methods as a function of pressure <i>p</i> .....	210
<b>Figure 10.9.</b> Relative deviations $\Delta\rho/\rho$ of <i>n</i> -nonane calculated densities $\rho$ using different calibration methods from NIST data as a function of pressure <i>p</i> .....	211

---

## List of Tables

<b>Table 2.1.</b> Ternary phase diagrams classes in terms of binary subsystems.....	38
<b>Table 2.2.</b> Gas Oil Ratio (GOR) and C7 <sup>+</sup> properties of the different types of hydrocarbon fluid .....	44
<b>Table 2.3.</b> Literature data of ternary mixtures of the type (carbon dioxide + <i>n</i> -alkanes + water).....	48
<b>Table 4.1.</b> Details of the variables allocated to specific functions for servo controller.....	77
<b>Table 4.2.</b> Agilent 34970A channels numbers and descriptions showing the ports connections of the electrical actuated valves .....	80
<b>Table 4.3.</b> Bubble and dew experimental points obtained in this work for the binary mixture (CO <sub>2</sub> + <i>n</i> -heptane) at <i>T</i> = 394.15 K .....	92
<b>Table 5.1.</b> Gas chromatography conditions for the analysis of the studied mixtures. ....	97
<b>Table 5.2.</b> Combined expanded uncertainty, $U(x_i)$ , for the composition measurements of the system (water (1) + carbon dioxide (2) + <i>n</i> -heptane (3)) in mole fraction at different conditions, using a coverage factor $k = 2$ . ....	102
<b>Table 5.3.</b> Combined expanded uncertainty, $U(x_i)$ , for the composition measurements of the system (water (1) + carbon dioxide (2) + methane (3)) in mole fraction at different conditions, using a coverage factor $k = 2$ . ....	103
<b>Table 5.4.</b> Experimental VLE Data for <i>n</i> -Heptane (1) + Carbon Dioxide (2) .....	105
<b>Table 5.5.</b> Experimental VLE Data for Water (1) + Carbon Dioxide (2) .....	106
<b>Table 6.1.</b> Critical pressure $p_c$ and critical temperature $T_c$ (with uncertainties), and acentric factor $\omega$ for the components studied in this work.....	111
<b>Table 6.2.</b> Parameters for the groups used in SAFT- $\gamma$ -Mie.....	112
<b>Table 6.3.</b> Cross interaction energies for the groups used in SAFT- $\gamma$ -Mie .....	112
<b>Table 7.1.</b> Properties of Qatari crude oil sample: density $\rho$ , relative density $\rho_r$ , API gravity, kinematic viscosity $\mu$ , PNA ratios, Asphaltene mass fraction and boiling-range analysis. .	126
<b>Table 7.2.</b> The list of all components used in this work with mole fraction $x$ , normal boiling temperature $T_b$ and molar mass $M_w$ .....	127
<b>Table 7.3.</b> Three phases VLLE locus for the CO <sub>2</sub> + dead oil mixture.....	130
<b>Table 7.4.</b> Critical pressure $p_c$ and critical temperature $T_c$ (with uncertainties), acentric factor $\omega$ and critical compressibility factor $Z_c$ for the components studied in this work.....	136
<b>Table 7.5</b> .Optimized binary interaction values for CO <sub>2</sub> -CH <sub>4</sub> and squalane-CH <sub>4</sub> .....	145

---

<b>Table 8.1.</b> Experimental LLE data for (water (1) + <i>n</i> -heptane (2) + carbon dioxide (3)) at the critical point between the <i>n</i> -heptane-rich phase and CO <sub>2</sub> -rich phase (the combination of both phases is referred here as CO <sub>2</sub> -rich phase). .....	149
<b>Table 8.2.</b> SAFT-VR Parameters used for modeling the behaviour of the pure components .....	151
<b>Table 9.1.</b> Hydrate equilibrium data for the ternary (CO <sub>2</sub> + CH <sub>4</sub> + water) mixture .....	165
<b>Table 9.2.</b> Comparison between quadruple data obtained in this work and other references and predictions from models at same conditions. ....	168
<b>Table 9.3.</b> Experimental LLE Data for (methane (1) + Carbon Dioxide (2) + Water (3)) at the Critical Point between the CO <sub>2</sub> -rich and Water-rich phases.....	169
<b>Table 9.4.</b> SAFT-VR Parameters used for modeling the behaviour of the pure components .....	170
<b>Table 10.1.</b> Composition of the two synthetic brines in terms of ions and salts together with their mole fractions where 1 and 2 refer to the two synthetic brines used in this study .....	194
<b>Table 10.2.</b> The period of oscillation obtained during calibration with vacuum and water at different pressure and temperature conditions. ....	195
<b>Table 10.3.</b> Contributions to the expanded uncertainty $U(\rho)$ of the density of CaCl <sub>2</sub> (aq) at $T = 472.04$ K and $p = 10.2$ MPa and density of SrCl <sub>2</sub> (aq) at $T = 473.02$ K and $p = 10.10$ MPa, with a coverage factor $k = 2$ .....	197
<b>Table 10.4.</b> Coefficients $\alpha_i$ , $\beta_{0j}$ , $\gamma_0$ , and $\sigma_i$ for pure water in Equations 10.11 to 10.14 .....	200
<b>Table 10.5.</b> Coefficients $\alpha_{ij}$ , $\beta_{ij}$ , and $\gamma_1$ and statistical parameters absolute average relative deviation ( $\Delta_{AAD}$ ), average relative deviation ( $\Delta_{Bias}$ ) and maximum absolute relative deviation ( $\Delta_{MAD}$ ) for the brines CaCl <sub>2</sub> (aq), MgCl <sub>2</sub> (aq), KI(aq), NaCl(aq), KCl(aq), [0.864NaCl + 0.136KCl] (aq) and AlCl <sub>3</sub> (aq) in Equations 10.11 to 10.15. ....	201
<b>Table 10.6.</b> Coefficients $\alpha_{ij}$ , $\beta_{ij}$ , and $\gamma_1$ and statistical parameters absolute average relative deviation ( $\Delta_{AAD}$ ), average relative deviation ( $\Delta_{Bias}$ ) and maximum absolute relative deviation ( $\Delta_{MAD}$ ) for the brines: KCl(aq), AlCl <sub>3</sub> (aq), SrCl <sub>2</sub> (aq), Na <sub>2</sub> SO <sub>4</sub> (aq) and NaHCO <sub>3</sub> (aq) in Equations 10.11 to 10.15. ....	202
<b>Table 10.7.</b> The seven VTD apparatus parameters used in Equation 10.19 .....	209

# Chapter 1: Introduction

## 1.1 Energy, Climate Change and Environment

The global economy (and hence energy demand) is expected to grow four fold between now and 2050, according to the International Energy Agency (IEA) baseline scenario [1]. If we continue to meet all the energy needs using fossil fuels without taking steps to reduce carbon emissions, this will lead to unsustainable pressure on the environment and natural resources. It will result in a 130 % rise in CO<sub>2</sub> emissions by 2050 leading to a trajectory corresponding to an average global temperature increase of around 6 °C in the long term [2], resulting in severe consequences. These consequences include a rise in sea levels, causing dislocation of human settlements, as well as extreme weather events, such as higher incidence of heat waves, destructive storms, and changes to rainfall patterns, resulting in droughts and floods affecting food production, human disease and mortality.

Although it has a lower global-warming potential (GWP) than the other major greenhouse gases (GHGs) such as CH<sub>4</sub>, N<sub>2</sub>O and hydrofluorocarbons, carbon dioxide (CO<sub>2</sub>) is the most significant GHG emitted by human activity in terms of both volumes emitted and environmental impact. Therefore, there must be a dramatic reduction in overall CO<sub>2</sub> emissions in the coming decades in order to avoid dangerous climate changes. This will require massive deployment of various clean-energy technologies, including renewable energy, cleaner transport technologies, energy efficiency, and carbon capture and storage (CCS) technology.

Nowadays, CCS is the largest-scale option available to mitigate the CO<sub>2</sub> emissions from the industrial and power-generation sectors. This is despite the fact that implementing CCS will eventually add to the operating costs of the processes that emit CO<sub>2</sub> and thus increase fossil-fuel energy prices, making other energy sources more cost competitive. To offset some of the additional costs associated with CCS, the use of captured CO<sub>2</sub> from large point sources in CO<sub>2</sub>-EOR operations to recover additional oil has been suggested. Since CO<sub>2</sub> is largely used as a process fluid in CO<sub>2</sub>-EOR projects, it provides the possibility for long-term storage of CO<sub>2</sub> by capillary forces (or by absorption) in the pores of the reservoir rock after displacing the *in-situ* oil.

## 1.2 Carbon Capture and Storage Processes (CCS)

CCS involves capturing and compressing CO<sub>2</sub> at fixed point sources (such as oil refineries, fossil-fuel power plants and cement works). The supercritical CO<sub>2</sub> is then transported



through dedicated pipelines, and injected into geological reservoirs (such as depleted oil and gas fields, saline aquifers, or deep-sea sediments) where it should be trapped for thousands of years. For this mitigation option to be successful and widely adopted, it is essential that the technology can be safely demonstrated at well-characterised sites where the long-term fate of the injected CO<sub>2</sub> can be monitored. With this in mind, attempts have been made to develop a best-practice approach to guide site-specific characterisation efforts. Some examples of such approaches are those developed by the IEA, the World Resources Institute (WRI) and the Intergovernmental Panel on Climate Change (IPCC) [2-6].

CO<sub>2</sub> storage underground is controlled by four main trapping mechanisms [7], which are effective on different timescales, ranging from days to thousands of years. The four trapping mechanisms are as follow: **(1)**, structural or stratigraphic trapping, in which CO<sub>2</sub> percolates up through the porous rocks until it reaches the top of the formation where it is sealed by an impermeable layer of cap-rock; **(2)**, residual trapping by capillary forces (capillary trapping), in which interfacial tension causes the non-wetting CO<sub>2</sub> phase to be retained between narrow pore throats; **(3)**, solubility trapping, in which CO<sub>2</sub> dissolves in resident formation fluids forming a non-buoyant fluid; and **(4)**, mineral trapping, a process whereby CO<sub>2</sub> reacts with reservoir minerals to form insoluble carbonate minerals.

A guideline [8] for selection and qualification of sites and projects for geological storage of CO<sub>2</sub> was recently developed by Det Norske Veritas (DNV) in cooperation with the IEA and many industrial partners such as Shell and BP. In this guideline, the geological CO<sub>2</sub> storage life cycle typically involves six stages as follows: screening, assessment and selection, design, construction, operation and closure. Sites that may be suitable for geological CO<sub>2</sub> storage with an adequate level of certainty are identified during the screening stage, while the storage site is characterized in sufficient details during the assessment and selection stage to demonstrate that selected sites have sufficient accessible storage capacity and can provide long-term effective storage containment. The design stage includes the detailed design of the process (such as front end engineering design studies) while the construction stage involves the physical construction of the surface facilities and wells. The operational stage outlines a structured process aiming to verify that a storage site provides, and will continue to provide, safe long-term storage of CO<sub>2</sub> [8].

Throughout these stages, numerical simulations play a key in predicting the flow of CO<sub>2</sub> from the injection wells into the storage formation and determining the long term evolution of the CO<sub>2</sub> plume after the termination of injection. These predictive models feed then into a larger geological/reservoir models which should provide an adequately correct and detailed

representation of the storage site. In this way, proper selection and operation of storage sites can be accomplished with lower uncertainty. These models require detailed thermophysical property data for CO<sub>2</sub> and its mixtures with the reservoir fluids it encounters in the underground storage sites, in particular their phase behaviour. To acquire all the experimental data required over the range of reservoir temperatures, pressures and fluid compositions encountered involves an enormous amount of work. If existing predictive models can be validated with suitable accuracy, or new models developed, then this would greatly enhance the feasibility of this process.

Unfortunately, and notwithstanding the importance of CCS in CO<sub>2</sub> emissions reduction, there remain some barriers to the full-scale deployment of the technology. These include: a lack of financial rewards that are sufficiently large and long term to incentivise carbon abatement using CCS; lack of public understanding and acceptance of the technology; difficulties in ensuring that geological formations can accept the injection of CO<sub>2</sub> at a rate comparable to that of oil and gas extraction from the subsurface today; and legal and regulatory issues for the transport and geological storage of CO<sub>2</sub>. Regardless of these barriers, there are currently some CO<sub>2</sub> capture and storage demonstration projects on-going worldwide. An example is the Otway project, located in south-eastern Australia [9], which was established to demonstrate the secure geological storage of CO<sub>2</sub> in a depleted natural-gas field.

### **1.3 Enhanced Oil Recovery Processes (EOR)**

There are many EOR processes applied worldwide in order to improve the recovery of the remaining oil in place. These technologies are usually applied after the use of water flooding to displace oil; surfactants are sometimes added to the flooding water to lower interfacial tension and hence promote recovery of oil trapped by capillary forces. Other EOR processes include miscible and immiscible gas injections, chemical flooding such as polymer, surfactants and alkali injections, and thermal technologies such as steam injections, hot water injections, electrical heating and *in-situ* combustions. These techniques change certain physical properties of the crude-oil system; mainly interfacial tension, wettability, mobility, viscosity, and phase behaviour. Most miscible and immiscible gas injections in operation today are CO<sub>2</sub> injections [10-14], in which oil displacement by CO<sub>2</sub> injection relies on the phase behaviour of the mixtures of gas and the oil, which is strongly dependent on reservoir temperature, pressure and oil composition. Carbon dioxide is widely used as the gas injected in EOR processes because of its high availability and low cost, and its non-toxic and non-flammable characteristics, making it a favoured solvent for use in recovery process compared to hydrocarbon gases which usually have limited availability and/or high cost.

In miscible CO<sub>2</sub>-EOR (which is the most dominant form of CO<sub>2</sub>-EOR deployed), interactions between the injected CO<sub>2</sub> and the reservoir fluids occur through multiple-contact processes. During such a process, CO<sub>2</sub> vapourizes the lighter oil fractions into the injected CO<sub>2</sub> phase and CO<sub>2</sub> dissolves in the oil phase. This leads to two reservoir fluids that become miscible (mixing in all parts) with favourable properties of low viscosity, enhanced mobility, and low interfacial tension leading to a remobilization and reduction of the residual oil saturation in the reservoir's pore space, hence allowing the recovery of more oil. Immiscible CO<sub>2</sub>-EOR occurs, however, when insufficient reservoir pressure is available or the reservoir's oil composition is less favourable (heavier). The main mechanisms involved in immiscible CO<sub>2</sub>-EOR processes are oil phase swelling, in which the oil becomes saturated with CO<sub>2</sub>, viscosity reduction of the CO<sub>2</sub>-expanded oil phase, and extraction of lighter hydrocarbon into the CO<sub>2</sub>-rich phase. These mechanisms enable a portion of the reservoir's remaining oil to be mobilized and recovered; this is not as efficient as miscible CO<sub>2</sub>-EOR but still commercial in some instances [15]. It worth noting here that in certain crudes, injection of CO<sub>2</sub> has resulted in fouling inside the well due to asphaltenes precipitation; it is then very important to understand when CO<sub>2</sub> should not be used in EOR.

In this context, determining the minimum miscibility pressure<sup>1</sup> (MMP) for the CO<sub>2</sub>-crude oil system at the actual reservoir temperature is required in order to determine whether or not the CO<sub>2</sub>-flooding process will be immiscible or miscible at the actual reservoir pressure. In the petroleum industry, the determination of the MMP between the CO<sub>2</sub> and crude oils is usually accomplished by techniques such as the slim-tube method [16], rising-bubble method [17], and the vanishing-interfacial tension technique [18]. Numerous MMP studies have been published, such as those in references [19-21].

## 1.4 Qatar Carbonates and Carbon Storage Research Centre

Carbonate reservoirs, which exist predominantly in Qatar and the Middle East in general, contain more than 50% of the world's conventional fossil-fuel reserves. These formations are less well understood than the sandstone reservoirs found across Europe and the Americas. Therefore, an essential precursor to optimising recovery from these carbonate reservoirs is to gain a thorough understanding of their evolution, combined with detailed characterisation of each reservoir and the fluids contained within it. Reservoir characterisation procedures, simulators and CO<sub>2</sub> injection processes for EOR or solely for sequestration have been

---

<sup>1</sup> MMP between a crude oil and CO<sub>2</sub> is defined as the minimum pressure under which CO<sub>2</sub> can achieve total miscibility with the crude oil.

intensively studied and applied to good effect for sandstone reservoirs for several decades now, but their development is much less refined for carbonate reservoirs, where the structures and physics and chemistry vary significantly.

The Qatar Carbonates and Carbon Storage Research Centre (QCCSRC) [22] is the embodiment of a long-term collaboration between Imperial College London, Qatar Petroleum, Shell, and the Qatar Science and Technology Park (which is part of the Qatar Foundation). The collaboration aims to revolutionise the current limited knowledge of carbonate reservoir formations. In addition, QCCSRC aims to harness, integrate and optimise existing technology, developing processes currently used within Qatar to extract oil and gas while evolving the practice of storing carbon dioxide in carbonate reservoirs. To achieve these objectives, four specialist carbon storage laboratories were established, enabling scientists and engineers to study in detail carbonate rocks, geology and fluid-rocks interactions. The fundamental results obtained from these laboratories are being used for developing an integrated reservoir simulator using novel numerical methods, in which the complex geology of fractured carbonate reservoirs is captured. Eventually, this project will feed into the design and execution of demonstration projects by exploiting the new reservoir understanding, fluid characterisation methodologies and state-of-the-art reservoir-simulation techniques. The main objectives of the established four laboratories are summarized as follow:

**The Qatar CCS Multiscale Imaging Laboratory:** To be able to study and understand carbon dioxide injection and trapping in carbonate reservoirs, state-of-the-art imaging equipment is employed, including a Medical CT with 0.25 mm resolution, a Micro CT scanner (1  $\mu\text{m}$ ), a Confocal Laser Scanning Microscope (< 1  $\mu\text{m}$ ) and access to a Synchrotron X-ray source (diamond facility) and Scanning Electron Microscopes. This advanced facility allows the study of these processes by recreating the extremely hot and pressurised conditions that exist in subsurface reservoirs, imaging flow and reaction in individual pores all the way up to meter-length rock samples.

**The Qatar Complex Fluid Laboratory:** The Qatar Complex Fluid Laboratory focuses on fluid, pore-space and pore-surface interactions relevant to improving the fundamental understanding of carbon sequestration and CO<sub>2</sub> driven enhanced oil recovery. Micro-fluidic micro-models of realistic pore-space images with varying complexity allow fundamental flow processes to be observed for different reservoir fluids (hydrocarbons, brines and gases such as CO<sub>2</sub>). These flows are modelled using state-of-the-art Lattice Boltzmann simulations developed in-house.

**The Qatar Stable Isotope Laboratory:** This lab operates mass spectrometers dedicated to developing, calibrating and testing clumped isotopes for application to subsurface reservoirs. The clumped-isotopes method is a new technique that allows the determination of the accurate temperature of precipitation of carbonate minerals, which helps in understanding the geological history of the reservoir and thus improving its management. In addition, fieldwork in the Middle East, notably Oman, is conducted; researchers are trying to understand the factors that determine the dimensions of important reservoir features such as (geo)bodies of carbonate formed during deposition of the sediment, or (geo)bodies of dolomite found associated with faults and fractures.

**The Qatar Thermophysical Properties Laboratory:** This laboratory is dedicated to the study of fundamental physics and chemistry to improve the understanding of carbon sequestration and CO<sub>2</sub>-driven enhanced oil recovery. There are significant gaps in the literature concerning the thermophysical properties that are basic input parameters for reservoir simulators and the building blocks of quality predictive simulations of CO<sub>2</sub> storage. The properties studied include phase equilibria, interfacial tension, density, as well as viscosity and diffusion coefficients. Data at a limited number of conditions covering the range of interest are used to calibrate and validate molecular-based EoS and transport models, which are in turn used to predict the thermophysical properties for all conditions in the pore-scale and reservoir models.

Thermodynamic modelling is carried out using the latest Statistical Associated Fluid Theory (SAFT) while transport properties are modelled using the world-leading Vesovic-Wakeham (VW) approach, incorporating on-going developments tailored specifically to overcome the difficulties presented by the complex fluids encountered in CO<sub>2</sub>-EOR and carbon storage. Experiments obtained from the thermophysical properties laboratory and modelling approaches are carried out in close collaboration, ensuring effective exchange of knowledge. Once those models are validated, they feed into the integrated reservoir simulations where the fluid properties are calculated / predicted. The present work lies mainly in the framework of this laboratory and has involved close collaboration with the modelling group; reliable experimental data for representative fluids is an essential step towards validating and optimizing the SAFT and other predictive models.

## 1.5 Experimental and Modelling Challenges

The most precise way to study the thermophysical properties of CO<sub>2</sub>-reservoir mixtures is through experiments. However, because CO<sub>2</sub>-EOR and CCS processes cover a large range of operational conditions from normal atmospheric to supercritical states, and involve multi-

component mixtures; the limited experimental data cannot satisfy the requirements of the engineering applications and therefore predictive models remain essential. Available models still require experimental data to validate the assumptions used and to examine their predictive capabilities. Providing these data is a challenging task from an experimental perspective since performing such measurements is not straightforward. Typically, data relating to pure components and binary mixtures are used in the calibration and optimization of these models, while results for multi-component mixtures are used to validate their predictive capabilities.

Unfortunately, from a review of the literature (see Chapter 2), it is apparent that available experimental phase-equilibrium data relating to ternary and compositionally well-characterised multi-component mixtures involving CO<sub>2</sub> are scarce. The lack of such data (and their inconsistency in some cases) limits the validation and development of the required models. Nevertheless, a wide variety of modelling approaches has been developed, ranging from empirical and semi-empirical correlations, to molecular-based theories. Cubic EoS (EoS), for example, are widely used in the oil and gas industry for the calculation of phase equilibrium and other properties of reservoir fluids over wide ranges of pressure and temperature.

These EoS still rely for the determination of model parameters upon the availability of certain experimental data for each pure component in the mixture and, crucially, for all possible binary pairs, usually over a range of temperatures. However, such reliance upon experimental data is of concern in the case of multi-component mixtures as the amount of information required becomes very large. Hence, for such systems, more predictive approaches are sought. In addition, these equations fail to give good correlation/prediction for complex mixtures. Molecular-based approaches, such as the SAFT, may be useful in this context but cubic EoS remain popular because they are simple, reasonably reliable for systems encountered in the petroleum industry, and provide for fast calculations. Predictive approaches such as SAFT and CPA (Cubic Plus Association), on the other hand, work better for complex mixtures such as those containing water and polymers but are more complex and require more computation time.

In general, the available approaches work well for specific mixtures while they fail for others, hence there is still a need to develop models which can be widely applied to large variety of mixtures. To facilitate this development, the provision of reliable experimental data for representative and complex mixtures is always necessary.

## 1.6 Project Motivation

In view of the complexity of reservoir fluids, an understanding of their phase behaviour is required to design more-economical production, transportation and refining processes. Phase behaviour data are key inputs to reservoir simulations that are used for evaluating reservoir-development plans, interpreting well-test data, and designing surface facilities and processing plants [23]. During water-flooding projects, it is necessary to determine the conditions of temperature and pressure at which the displacement of oil by water is most effective. Furthermore, determining the conditions at which solid deposition may occur (such as formation of hydrates or precipitation of asphaltene) is essential to avoid blockages of pipelines and other process equipments, and to properly design surface facilities such as separators and compressors.

How a specific operating parameter affects the performance and costs of these processes depends strongly upon knowledge of the thermodynamic properties of CO<sub>2</sub> mixtures. For example, the vapour-liquid equilibrium (VLE) of CO<sub>2</sub> mixtures is of fundamental importance in the design of processes for the purification of CO<sub>2</sub> from captured flue-gas mixtures during coal-fired power generation. Meanwhile, for transportation, it is preferable that CO<sub>2</sub> be present in a high-density state to avoid the occurrence of two-phase flow; thereby reducing energy consumption and investment costs, and securing operational safety. In order to guarantee the right operational conditions, accurate prediction of the thermodynamic properties of CO<sub>2</sub> mixtures is of great importance.

In addition, high-pressure phase equilibria of systems containing hydrocarbons and CO<sub>2</sub> are also of interest in a wide range of industrial processes such as hydro-treatment of aqueous waste streams [24], production of coal liquids and petroleum processing [25], separation processes [26], and supercritical fluid extraction [27-28]. In addition, supercritical CO<sub>2</sub> is used as a solvent on both laboratory and industrial scales [29] for reactions such as hydrogenation [30] hydroformylation [31] and polymerization [32-33]. Therefore, phase equilibrium data for mixtures containing carbon dioxide and hydrocarbons are significant in many industrial and scientific fields in addition to CCS and CO<sub>2</sub>-EOR. In view of the foregoing discussion, a prime motivation for this project is the provision of such data, and the understanding, modelling and prediction of the associated phase equilibria.

## 1.7 Scope and Objectives

The scope of the present work was to conduct key experimental measurements of fluid thermophysical properties in a wide range of pressure and temperature conditions that are

relevant to the oil and gas industry, and to employ them to examine the predictive capabilities of the available theoretical approaches in the field of thermophysical properties. In the context of CO<sub>2</sub>-EOR and CO<sub>2</sub>-storage processes, the phase behaviour measurements and modelling of these mixtures was the prime focus of the present study. Other thermophysical properties measurements, in particular the density of CO<sub>2</sub>-hydrocarbon mixtures and the density of brines and mixed brines were also conducted.

The present work focused on experimental investigations at representative reservoir conditions over wide range of pressures and temperature conditions. To accomplish this, the construction and validation of a new apparatus to permit phase-behaviour measurements at conditions similar to reservoir conditions was a key initial. Using this for VLE, LLE and VLLE, studies on two representative systems containing CO<sub>2</sub> with multiple hydrocarbon components constituted the main overall objective. A ternary mixture (CO<sub>2</sub> + *n*-heptane + methylbenzene) and a more representative complex mixture (CO<sub>2</sub> + synthetic oil) were used to model the reservoir fluids. Further investigation of two ternary mixtures of the type (CO<sub>2</sub> + *n*-alkane + water), using a previously built apparatus capable of analysing the composition of different components, was consistent with the overall motivation. In this work, *n*-heptane and methane were used as the *n*-alkane.

The comparison of experimental data with results calculated from predictive Peng Robinson (PPR78 EoS) [34], predictive Soave-Redlich-Kwong (PR<sub>2</sub>SRK EoS) [35-36], SAFT-VR [37-38] and SAFT- $\gamma$ -Mie [39] was also one of the objectives. In this case, the comparison enables one to evaluate and demonstrate the predictive capabilities of these methods, as well as their potential for improvement. Once validated and/or tuned to reliable data, accurate modelling tools can then be used for predicting the phase behaviour (and other thermophysical properties) of relevant systems over a much wider range of conditions and fluid systems.

In addition, the last objective of the current project, in line with the overall motivation, was experimental and modelling studies on the densities of a variety of brines (both single-salt and mixed) over wide ranges of pressures up to 70 MPa and temperatures up to 473 K. The experimental data were represented by precise correlations to enable interpolation within the range of pressure, temperature and molality studied. The comparison of the experimental density data of mixed brines with predictions from a simple predictive approach was carried out to evaluate and demonstrate its predictive capability.



Complementing the studies mentioned above, further complementary objectives include detailed analyses of the data and comparisons with available data for relevant systems. The extent to which these data are linked to CO<sub>2</sub>-EOR, CO<sub>2</sub>-storage and other processes, both through further experimental studies and improved modelling, have been identified.

## 1.8 Selection Criteria of the Measured Systems

The systems studied in the present work were chosen primarily due to the lack of available experimental data especially at reservoir conditions and by the desire of providing novel data for complex mixtures which is required in model development.

The system (CO<sub>2</sub> + *n*-heptane + methylbenzene) was selected to represent a simple model of the type (CO<sub>2</sub> + *n*-alkane + aromatic). Different molar ratios of *n*-heptane to methylbenzene were chosen to study the effect on the phase envelope of changing the alkane-to-aromatic ratio. The synthetic oil was designed to match the physical and chemical properties of a bottom-hole crude-oil sample from a Qatari field. The synthetic 'dead' oil contained 17 components; 'live' oils were also obtained by adding a 3-component solutions gas (0.81 CH<sub>4</sub> + 0.13 C<sub>2</sub>H<sub>6</sub> + 0.06 C<sub>3</sub>H<sub>8</sub>). A more detailed account of the selection of the 20 components of the synthetic live oil is given later (in Chapter 7).

The systems (CO<sub>2</sub> + *n*-heptane + water) and (CO<sub>2</sub> + methane + water) were selected because there are no VLLE data available in the literature for these ternary mixtures. The *n*-heptane was thus chosen to represent the light-oil fraction in the (carbon dioxide + light oil fraction + water) mixtures, while the methane was chosen to represent the natural gas in the (carbon dioxide + natural gas + water) mixtures.

The selection of the above systems was also encouraged by the desire to examine the predictive capabilities of the available predictive models. The conditions of measurements studied were chosen to lie within the category of complex conditions. Such conditions offer a real challenge to modelling and good opportunity to improve their predictive capabilities.

In the study of brines densities, the CaCl<sub>2</sub> and MgCl<sub>2</sub> systems were selected as these salts are significant constituents of carbonate reservoir formation brines and there are significant gaps in the available data. The mixed salt system was chosen as this mixture is often used as a simple model for sandstone reservoir brine in core-flooding experiments and a consistent  $\rho(T, p)$  surface is required for interpreting the data from such experiments. The mole fraction of KCl in this mixture is equivalent to a NaCl:KCl mass ratio of 5:1. Similarly, the KI system was studied as this brine is also used in core-flooding experiments because of

its excellent contrast in x-ray imaging. Although the NaCl system is the most well studied, no single data set covers the full ranges of temperature and pressure considered in this work and it was therefore considered appropriate to measure this system too. Similar considerations apply to the KCl system. The new data for NaCl(aq) and KCl(aq) were helpful in testing a predictive model for the density of the mixed brine system (0.864 NaCl + 0.136 KCl)(aq). SrCl<sub>2</sub>(aq), Na<sub>2</sub>SO<sub>4</sub>(aq), and NaHCO<sub>3</sub>(aq) were chosen due to the significant gap in the available literature for these systems. The synthetic reservoir brines contained Na<sup>+</sup>, K<sup>+</sup>, Mg<sup>2+</sup>, Ca<sup>2+</sup>, Sr<sup>2+</sup>, Cl<sup>-</sup>, SO<sub>4</sub><sup>2-</sup> and HCO<sub>3</sub><sup>-</sup> and their compositions were chosen to be representative of some natural saline aquifer brines existing in carbonate formations. In addition, the experimental data for these mixtures were helpful in further testing a simple predictive model for the density of a mixed brines system. The measured density of these brines is significant in the studies related to carbon storage in saline aquifers.

## 1.9 Thesis Outline

This thesis commences with a discussion of the literature and theoretical background pertaining to phase equilibria and phase behaviour in Chapter 2, followed by a review on the theory and modelling approaches relevant to the present work in Chapter 3. A complete description of the new equipment (synthetic apparatus) is outlined in Chapter 4 while the details of the second equipment (analytical apparatus) are given in Chapter 5. The phase equilibrium results acquired during the course of the project are presented, analysed and discussed in detail in Chapters 6, 7, 8 and 9. This includes detailed analysis and comparison with predictive cubic EoS and SAFT models. The density of brines and mixed brines is presented, analysed and discussed in Chapter 10. This includes the development of correlation models for the density of brines and testing the predictive capability of a simple mixing rule for the density of mixed brines. The main conclusions of the thesis and recommendation for future work are summarised in Chapter 11.

## Chapter 2: Fluid Phase Equilibria: Literature and Background

In this Chapter an introduction to fluid phase equilibria, providing the basis for the complete understanding of phase diagrams is presented. Then a brief discussion of the main experimental methods to measure phase equilibria is given; and in the last section the phase behaviour of pure hydrocarbon fluids and their mixtures with CO<sub>2</sub> and water is reviewed.

### 2.1 Phase Equilibria and Phase Diagrams

#### 2.1.1 Introduction

Phase behaviour describes the way in which a fluid undergoes phase changes (or remains in the same phase) when thermodynamic conditions, such as temperature, pressure and, in the case of mixtures, composition, are altered. It is usually represented graphically by phase diagrams, which show the boundaries between phases and the conditions that occur when the pressure and/or temperature is changed to cross these boundaries. Knowledge of these boundaries is required in simulating reservoirs, evaluating reserves, forecasting production, designing production facilities, designing transportation systems and many other applications. This subject has been covered extensively in numerous text books and reviews such as the book written by Prausnitz et al. [40], which provides a good description of the basic thermodynamic concepts of fluid phase equilibria.

In the oil and gas industry, the phase behaviour of hydrocarbon mixtures at reservoir and surface conditions, which is determined by its chemical composition and the prevailing temperature and pressure, is of a prime consideration in the development and management of reservoirs, affecting all aspects of petroleum exploration and production. Although a reservoir fluid may be composed of many thousands of compounds, the phase behaviour fundamentals can be explained by examining the behaviour of pure and simple multi-component mixtures. The behaviour of all real reservoir fluids basically follows qualitatively the same principles as those found in binary, ternary and other simple multi-component mixtures. Therefore, understanding the phase diagrams of binary and simple mixtures is required to understand the phase behaviour of multi-component complex mixtures.

At equilibrium, a system may form of a number of co-existing phases, with all the fluid constituents present in all the equilibrated phases. The temperature, pressure, and chemical potential of each component throughout all phases should be uniform at equilibrium conditions. The number of independent intensive variables  $F$  required to define the state of a

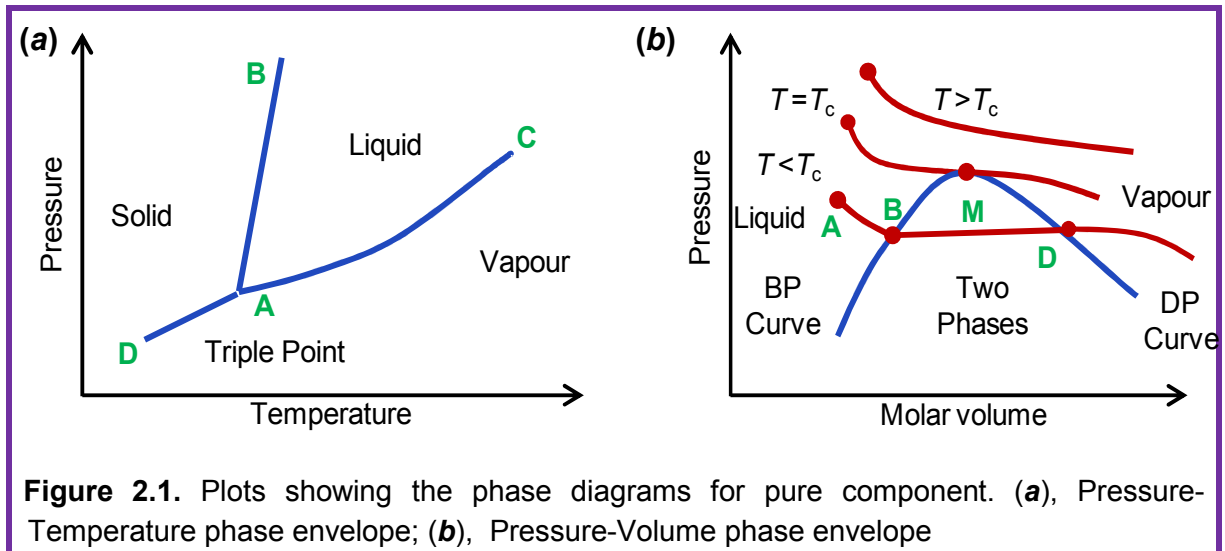
system containing of  $N$  components distributed over  $K$  phases is determined by the Gibbs phase rule:

$$F = N - K + 2, \quad 2.1$$

where  $F$  is also known as the number of degrees of freedom. The state of the equilibrium of, for example, a vapour-liquid mixture of a pure fluid, therefore, is determined by identifying just one variable, either its pressure or its temperature [41].

### 2.1.2 Phase Behaviour of Pure Components

The phase behaviour of a pure component is shown by the pressure-temperature and pressure-volume diagrams in Figure 2.1. In Figure 2.1 a, all the conditions at which the vapour and liquid phases can coexist at equilibrium are shown by the line AC. The line AC is commonly known as the vapour pressure curve, as it shows the pressure exerted by the vapour coexisting with its liquid at any temperature. The line AB is the solid-liquid equilibrium line, which is also known as the melting point curve. The intersection of the vapour-liquid and liquid-solid lines is the triple point. It is the only point where the three phases can coexist at equilibrium for a pure system. The line AD is the solid-vapour equilibrium line or the sublimation curve.



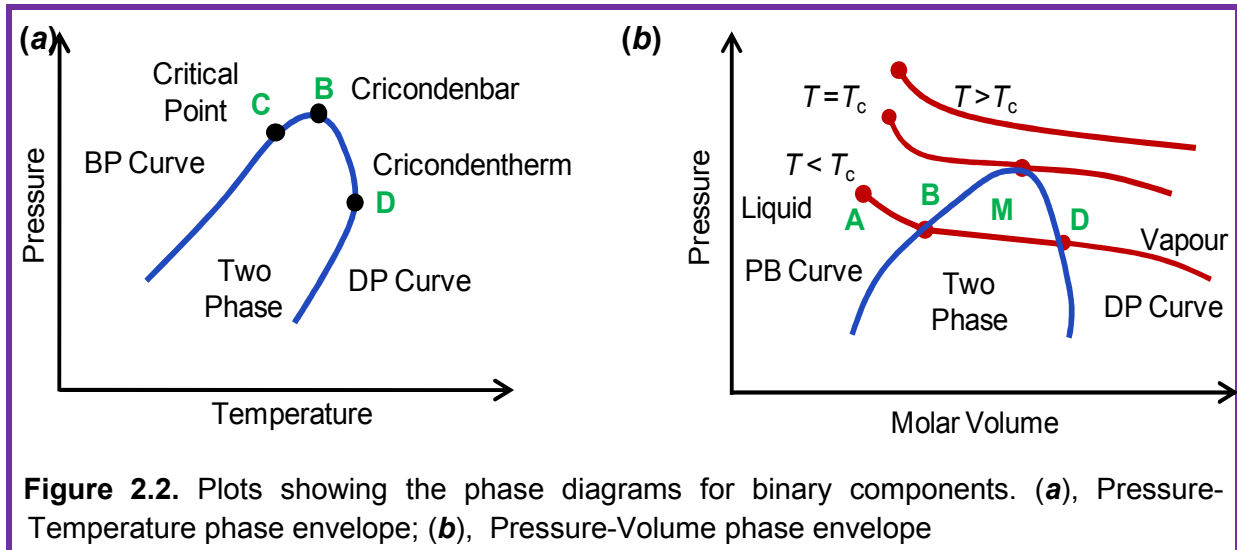
All the differences between the phases are reduced as the system approaches the critical point. At this point, the phases become indistinguishable. The critical temperature and the critical pressure are the maximum temperature and pressure at which a pure compound can form coexisting vapour and liquid phases. The pressure-volume diagram of a pure substance is shown in Figure 2.1.b. Considering the compressed liquid, point A, at a

temperature below the critical temperature, the reduction of fluid pressure at constant temperature increases its volume. As the liquid is relatively incompressible the fluid expansion is small until the vapour pressure is reached, at point B, where the first bubble evolves. Further expansion of the system results in changing the liquid into the vapour phase. The pressure remains constant and equal to the vapour pressure, a consequence of the phase rule, until the last drop of the liquid vapourizes, point D. This point, where the vapour is in equilibrium with an infinitesimal amount of liquid is called the dew point.

The system bubble points at various temperatures form the bubble point curve, whereas the dew points at various temperatures form the dew point curve. The two curves meet at the critical point and together identify the phase envelope. Any state within the phase envelope, e.g. point M, forms two equilibrated phases with the vapour/ liquid molar ratio equal to BM/MD. The change of phase from liquid to vapour is accompanied by a large increase in volume at low temperatures. The expansion reduces as the temperature approaches the critical point. The system changes from all liquid into all vapour, or vice versa, without any change in the mixture volume at the critical point. An isothermal expansion of a fluid at temperature above the critical temperature does not result in any phase change. At this condition, the fluid is called a supercritical fluid.

### 2.1.3 Phase Behaviour of Binary Mixtures

The phase behaviour of a multi-component system is more elaborate than that of a pure compound. The complexity generally increases as the differences in molecular structure and size of the constituent components become large. A complete description of a binary mixture requires three independent variables. For a two-component system, the most convenient experimental variables are pressure, temperature and composition. However, since it is tedious to draw three-dimensional diagrams in perspective, they are more commonly depicted in  $(p, T)$  projections. Other possible diagrams are those representing  $(T, x)$ ,  $(p, v)$  and  $(p, x)$  projections. An example of the phase diagrams of a binary mixture is shown schematically in Figure 2.2. The phase envelope, inside which the two phases coexist, is bounded by the bubble point and dew point curves. The two curves meet at the critical point (C). Note that the two phases can coexist at some conditions above the critical point. The highest pressure (B) and the highest temperature (D) on the phase envelope are called the cricondenbar and the cricondentherm, respectively. For binary or multi-component mixtures, the pressure does not remain constant during expansion moving from point (B) towards point (D) where the last drop of the liquid vapourizes.



According to the classification of van Konynenburg and Scott [42-43], six main types of fluid phase behaviour are found experimentally. These types can be predicted with a simple EoS such as van der Waals equation (apart from type VI). The occurrence of a positive or negative azeotrope leads to subdivision of these six main types. The main six types of fluid phase behaviour systems are shown in Figure 2.3

The simplest case is type I, which is typical for binary systems containing compounds with similar molecular size and/or their critical properties. Only one critical curve is found. This is the liquid-vapour critical curve which runs continuously from the critical point of component one to the critical point of component two. An example of this behaviour is the binary system of methane + CO<sub>2</sub> [44].

As differences between the two components become greater, the phase diagram presents liquid-liquid separation at low temperature as in type II phase behaviour. This also has a continuous liquid-vapour critical curve just as in the case of type I. In addition, there is a liquid-liquid critical curve  $L_2 = L_1$  and a three-phase equilibrium  $L_2L_1V$  line. The curves  $L_2 = L_1$  and  $L_2L_1V$  intersect in a UCEP (Upper Critical End Point). The liquid-liquid critical curve may run to infinite pressure if there is no formation of a solid phase. The mixtures of carbon dioxide + *n*-alkane up to *n*-dodecane exhibit this type of phase behaviour [45-46].

Type IV represents a transition between type II and III. In this case, the vapour-liquid critical line starting at the critical point of the less volatile component ends at a lower critical end point (LCEP). However, in type IV, a region of immiscibility at low temperature is seen, and the locus of the LLV three-phase line exhibit two parts.

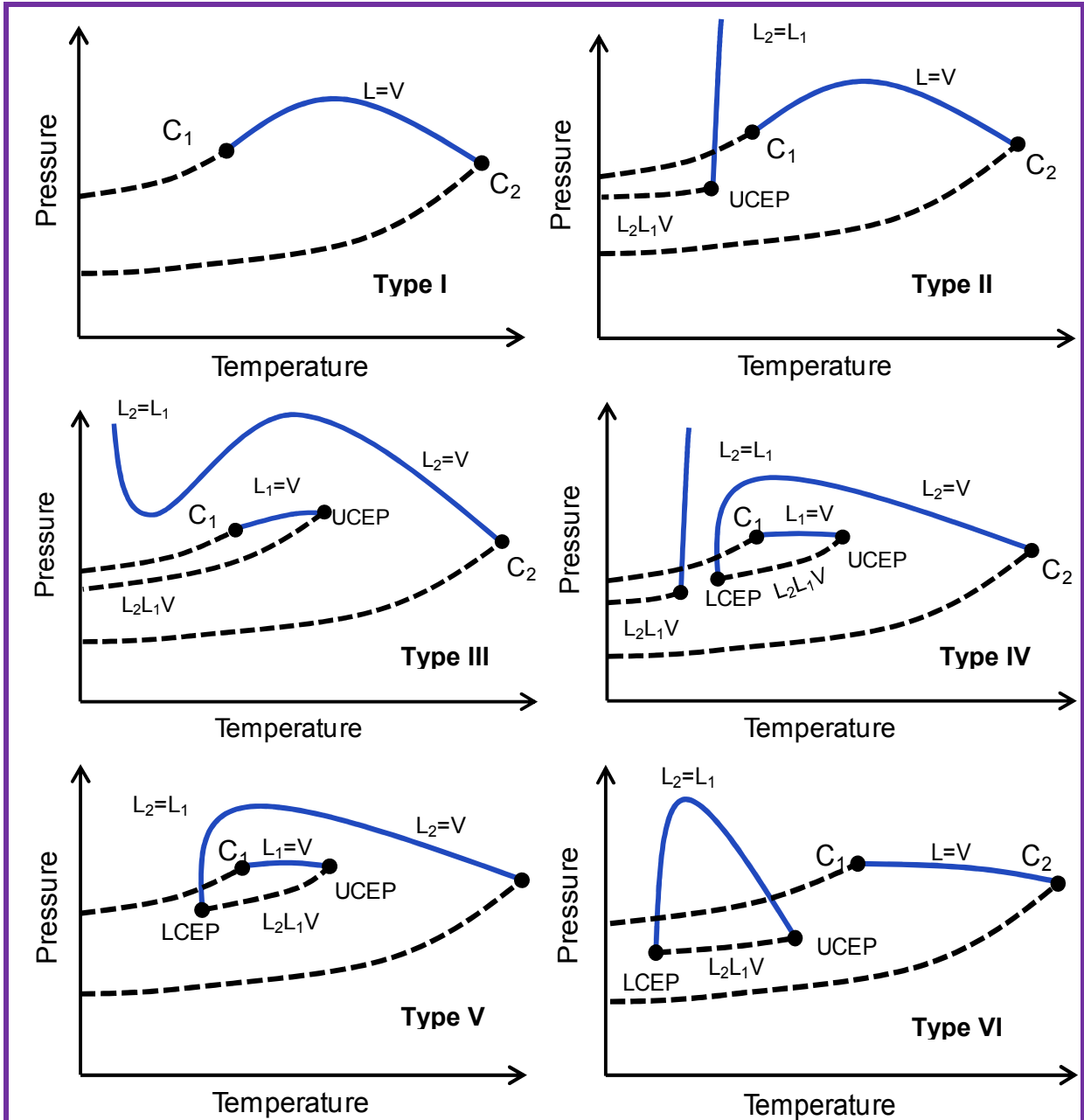


**Figure 2.3.**  $(p, T)$  projections showing the phase behaviour diagrams for binary mixtures according to Van Konynenburg and Scott classification.

In the type III phase behaviour, the two branches of the  $L_2L_1V$  equilibrium of type IV phase behaviour are combined. The liquid-liquid and the vapour-liquid critical lines interfere with each other. As a consequence, the vapour-liquid critical line is not a continuous line connecting the pure components critical points, but it has two branches. One starts at the critical point of the less volatile component and rises with pressure, merging into the liquid-liquid critical line. The second branch goes from the critical point of the more volatile component to the UCEP. Mixtures of carbon dioxide with *n*-tetradecane or with longer *n*-

alkanes exhibit this type of phase behaviour [45-46]. For a binary mixture of CO<sub>2</sub>+*n*-eicosane, type III E diagrams are expected which is as type III global phase equilibrium diagrams but with a LLV equilibrium line interrupted by a quadruple (Q) point, where a solid phase appears. At the Q point, three other three-phase equilibrium lines meet; two SLV curves and a SLL line [47]. The three phase equilibrium L<sub>2</sub>L<sub>1</sub>V consists of two branches. The low temperature branch shows a UCEP and comparable with L<sub>2</sub>L<sub>1</sub>V equilibrium which is found in type II systems. The high temperature branch shows a LCEP and a UCEP which is similar to the L<sub>2</sub>L<sub>1</sub>V equilibrium found in type V systems. An example to this type is the mixture of carbon dioxide + *n*-tridecane [45-46, 48].

In type V behaviour systems, three phase equilibrium L<sub>2</sub>L<sub>1</sub>V with a LCEP and a UCEP, and a discontinuous critical curve is found. The first branch of the critical curve connects the critical point of the more volatile component with the UCEP. The second branch runs from the LCEP to the critical point of the less volatile component. A binary system of ethane + *n*-eicosane shows this behaviour. In type VI, the phase behaviour is found in systems with specific chemical interactions such as water + 2-butoxyethanol. A three phase equilibrium L<sub>2</sub>L<sub>1</sub>V is found with a LECP and a UECP. The LECP and UECP are connected by the liquid-liquid critical curve which shows a pressure maximum.

Raeissi et al. [49] highlighted the role of degree of asymmetry on the nature of the phase behaviour exhibited by quasi binary mixtures of light gases (such as CO<sub>2</sub>) and members of various homologous series (such as *n*-alkanes and alkyl-benzenes). Transition from type II to type IV and from type IV to type III occurs experimentally for *n*-alkanes when the carbon atom number of the *n*-alkanes lies, respectively, between 12 and 13 and between 13 and 14. According to Schneider [46], tridecane (C<sub>13</sub>H<sub>28</sub>) is the smallest normal alkane which shifts the liquid-liquid critical branch to the extent that it merges with the liquid gas critical branch, with a second critical branch extending from the critical point of carbon dioxide to the critical end point where it intersects the liquid-liquid gas equilibrium line [48, 50].

Binary mixtures of carbon dioxide with branched alkanes or aromatics usually show type I, II or III phase behaviour systems. For example, Lansangan [51] studied the mixture of CO<sub>2</sub> + *n*-octyl benzene. This system exhibits type VIII phase behaviour, which is similar to type III but with the addition of liquid-liquid critical curve. The LLV patterns, or thermodynamic phase space topography, of CO<sub>2</sub> with the homologous series of *n*-alkyl benzenes are quite similar to those of the homologous *n*-paraffins. For a binary mixture of CO<sub>2</sub> with the homologous series of *n*-paraffins, the extent of the liquid-liquid vapour immiscibility decreases from a



maximum at carbon number 14 to carbon number 21 and doesn't exist for carbon number 22 and higher [50].

#### 2.1.4 Phase Behaviour of Ternary Mixtures

As required by the phase rule, an extra degree of freedom is needed to describe the ternary system. The additional variable is usually the second mole fraction needed to state the composition of the mixture. The representation of ternary diagrams in three-dimensional space requires the dropping of one variable. One can choose to represent just one composition and continue to represent fluid phase behaviour in  $(p, T, x)$  space. Another option is to discard temperature and depict ternary diagrams in  $(p, x_1, x_2)$  space or the pressure can be dropped and  $(T, x_1, x_2)$  space can be used. The last two representations usually take the familiar form of the triangular prism diagrams of ternary mixtures which are widely used to represent the phase diagrams of ternary mixtures. Such diagrams are presented in Chapters 8 and 9, in which the measurements of the ternary mixtures ( $\text{CO}_2 + n$ -heptane + water) and ( $\text{CO}_2 + \text{methane} + \text{water}$ ) are reported.

Notwithstanding the importance of multi-component mixtures, a classification scheme for ternary mixtures equivalent to that for binaries has not been fully established. However, two ternary classification schemes have been suggested. A significant attempt to establish a global scheme for ternary diagrams was made by Bluma and Deiters [52]. As van Konynenburg and Scott have done in their examination of binary mixtures, Bluma and Deiters used the van der Waals EoS [53] with Lorentz-Berthelot combining rules [54] to describe the phase diagrams and critical states of ternary fluid mixtures assuming equal size molecules. Eight major classes of ternary diagram have been classified as listed in Table 2.1.

The first ternary class (T-I) is characterized by closed liquid-gas critical curves between the three critical points of the pure components. All the binary subsystems are of the binary type I which means that this class is only available for mixtures of similar chemical compounds. The ternary class II has two binary subsystems of type I and one binary subsystem of type II of the Van Konynenburg and Scott classification. There are a liquid-gas critical surface and a liquid-liquid critical plane at low temperatures. A critical endpoint curve exists at low pressure and consists of upper critical endpoints (UCEL). In ternary class III, there is one binary subsystem of type III and two binary subsystems of type I. There is only one continuous critical plane which appears to have a gash in it. The rim of the gash is an UCEL, which ends in a tricritical point. Along the other side of the gash the critical plain runs to infinite

pressures, and a continuous transition from liquid-gas to liquid-liquid phase equilibria takes place.

In ternary class IV, there is one binary subsystem of type I and both other binary subsystems are of type III. Typical examples would be systems containing two similar heavy components plus one very light component, which shows type III behaviour with either of the heavy ones. There is a large critical surface running upwards to infinite pressure at high temperatures, and a smaller one at low temperatures, which is bounded by an UCEL. In Ternary class V; the binary subsystems are of type I, II and III. This class is quite similar to class III, except that there is an additional liquid-liquid critical surface at low temperatures. Ternary class VI: this class is the “opposite of ternary class IV. Again, the binary subsystems are of type I, III, and III, but now we have the case of two similar light compounds mixed with a heavy one. There are two critical surfaces; again the lower one is bounded by an UCEL.

**Table 2.1.** Ternary phase diagrams classes in terms of binary subsystems

Binary Subsystems			Ternary class
I	I	I	T-I
I	I	II	T-II
I	I	III	T-III
I	II	II	-
I	II	III	T-V
I	III	III	T-IV, T-V
II	II	II	T-VIII
II	II	III	-
II	III	III	-
III	III	III	T-VII

In ternary class VII, all binary subsystems are of the binary type III. This ternary phase diagram has three critical planes. The critical surface of the component with the highest critical data shows liquid-liquid critical behaviour, the surface of the component with the lowest critical data liquid-gas-critical behaviour, and the third component has a critical plane showing liquid-liquid critical behaviour with the light component and liquid-gas critical behaviour with the other one. In ternary class VIII, all binary subsystems are of type II. The phase diagram shows a contiguous liquid-gas-critical surface (as for the ternary class I), and in addition there are three liquid-liquid-critical surfaces at lower temperatures. Depending on the temperature range of the liquid-liquid surfaces and binary interaction parameters of the

mixture constituents several subtypes are conceivable; practically, however, these liquid-liquid surfaces will probably be hidden by crystallization [52].

Another approach to classify the ternary mixture is proposed by Lopes [55]. He stated that the classification of fluid phase behaviour in ternary systems can be derived from the corresponding classification implemented for binary mixtures. The first step in such classification would be the naming of the three binary subsystems which establish the boundaries of the ternary system. His approach was to classify the ternary systems based on the topology of the immiscibility windows of each binary subsystem that constitutes the outer shell of the prismatic ternary diagram plus the type of connectivity between those windows in the inner core of the diagram.

Some examples of studies related to ternary mixtures are given below. Benham et al. [56] employed a pseudo-ternary representation for the prediction of the miscibility of hydrocarbons. In their approach, complex mixtures are considered as pseudo-ternary mixtures of methane, intermediates (ethane, propane, butane) and heavy hydrocarbon (pentane and higher). Based on this approach, the mechanism for obtaining miscibility between reservoir fluid and various injected fluids may be shown. Fall and Luks [57] studied the ternary mixture of CO<sub>2</sub> + propane + *n*-nonadecane to determine the effect of additive gases on the liquid-liquid-vapour behaviour seen in the binary mixture CO<sub>2</sub> + *n*-nonadecane. The addition of propane to the binary mixture results in a three phase region developing to the high-temperature side of the binary locus in the pressure-temperature phase diagram projection.

Smith and Wormald [58] measured the solubility of naphthalene in solvent mixtures (0.4 CO<sub>2</sub> + 0.6 ethane) and (0.85 CO<sub>2</sub> + 0.15 propane) at temperatures between (307.9 and 338) K over the pressure range of (6 to 26) MPa. They found that the addition of ethane or propane to the binary mixture CO<sub>2</sub> + naphthalene preserves the minimum in the pressure-temperature projection of the solid-liquid-vapour curve, but reduced the UCEP pressure by nearly 40%. This means that solvent mixtures have a clear advantage of a maximum in the solubility at lower operating pressures. Hottovy et al. [59] studied the ternary mixture of CO<sub>2</sub> + methane + *n*-octane in the region of liquid-liquid-vapour immiscibility. This region is bounded by the presence of K-points (L<sub>1</sub>-L<sub>2</sub>=V), N-points (L<sub>1</sub>=L<sub>2</sub>-V) and Q-points (S-L<sub>1</sub>-L<sub>2</sub>-V). The liquid-liquid-vapour immiscibility region is also studied by Merrill et al. [60] for the ternary mixture of CO<sub>2</sub> + methane + *n*-hexane. This region is bounded by the locus of K-points and N-points, and by the L<sub>1</sub>L<sub>2</sub>V locus of the methane + *n*-hexane binary system. Orr and Jensen [61] stated that for a temperature less than 323 K, mixtures of carbon dioxide with crude oil can form three fluid phases. It has been observed that moderately supercritical carbon

dioxide can form liquid-liquid-vapour occurrence when pressurized with crude oil in porous media [62]. Above the VLLE pressure, LLE behaviour occurs and it is at such elevated pressures that the enhanced recovery process is often conducted.

## 2.2 Experimental Methods for Fluid Phase Equilibria

### 2.2.1 Overview

Various techniques have been employed to determine the phase behaviour of multi-component mixtures under high-pressure and high-temperature conditions. The classification of these techniques depends mainly on how composition is determined. In the analytical method, the compositions of the coexisting bulk phases are determined (often by sampling and chromatographic analysis) whereas, in the synthetic method, only the overall composition is determined experimentally (usually by metering the amounts of each pure substance introduced into the apparatus). Multi-component mixtures, especially those containing heavy components, can be difficult to analyze and so a synthetic method may be preferred in which mixtures of precisely known composition are prepared [63].

Several review articles have been published covering both experimental methods and the available high-pressure high-temperature phase behaviour data in general: Fornari [64] reviewed the data published between 1978 and 1987; Dohrn and Brunne [65] covered the period 1988 to 1993; Christov and Dohrn [66] covered the data published between 1994 and 1999; and recently Dohrn, Peper, and Fonseca reviewed the published data from 2000 to 2004 [67] and from 2005 to 2008 [63]. In these articles, high-pressure experimental data from the 17 most relevant journals in the field were reviewed. The phase equilibria studied included vapour–liquid equilibria, liquid–liquid equilibria, vapour–liquid–liquid equilibria, solid–liquid equilibria, solid–vapour equilibria, solid–vapour–liquid equilibria, critical points, the solubility of high-boiling substances in supercritical fluids, the solubility of gases in liquids, and the solubility (sorption) of volatile components in polymers. The following description of the analytical and synthetic methods draws heavily on these reviews.

### 2.2.2 Analytical Method

In the analytical method, the overall composition of the mixture at the beginning of the experiment is often not known. The compositions of the equilibrated coexisting phases are analyzed either with sampling under the experimental pressure or without sampling by using *in-situ* physicochemical methods of analysis. The sampling methods are divided into isothermal, isobaric and isobaric-isothermal based on the attainment of equilibrium. Pressure drop during large sampling is avoided by using a variable-volume cell or buffer autoclave in

combination with a syringe pump (for sampling) or by blocking of the sampling volume from the remaining content of the equilibrium cell before pressure reduction. Small amounts of sample withdrawn will result in only a small pressure drop and will not affect the phase composition significantly.

Small samples can be withdrawn through capillaries using special sampling valves such as HPLC and ROLSI valves or fast acting pneumatic valves. Sampling with capillaries can lead to differential vapourization (due to pressure drop) especially for mixtures containing light and heavy components. The recirculation of one or more phases through a sample collection loop has the advantage that the sampling volume is filled isobarically but this requires a working pump with little pressure drop and uniform temperature to avoid partial condensation or vapourization in the recirculation line. Hence, recirculation methods are not a proper choice for regions close to critical points where small changes in temperature and pressure have a strong influence on phase behaviour. In the case of recirculation of the vapour phase, samples can be withdrawn by placing a sampling valve in the recirculation loop or by blocking off a volume between two valves in the recirculation loop. The recirculation of liquid phase is usually used to determine the solubility of gases in liquids.

In isobaric-isothermal analytical methods, one or more fluid streams are pumped continuously into a thermostated equilibrium cell. The pressure is kept constant by controlling the effluent stream, usually of the vapour phase. In the continuous flow of all streams, preheated components are fed (using a pump) into a mixer where the desired temperature and phase equilibrium is attained. Then feed streams from the mixer are separated into a vapour and liquid phase where they are withdrawn continuously, depressurized, accumulated and analyzed. Due to the short residence time of the components in the apparatus, measurements at high temperatures are possible without the occurrence of thermal decomposition or polymerization reactions. Such measurements have been done by Haruki et al. [68] for a system of hydrocarbon + water near the critical point of water. In semi-flow methods, the gas stream from a high pressure cylinder is passed through two cells in series containing the liquid, where the first cell serves as a presaturator and the second cell as the equilibrium cell. Upon reaching equilibrium, the effluent of the vapour phase is reduced in pressure and directed to a trap where the condensed liquid is collected.

The compositions of the phases can also be analyzed without the need to take samples. The advantage of avoiding the trouble with samples is often overcompensated by the need of time consuming calibrations at high pressures. Only a few systems have been investigated using this method. The analysis is carried out using spectroscopic methods, gravimetric

methods (it can be done *in-situ*) where the mass of the condensed phase is measured and the phase composition is determined using additional information such as densities. For example, Quartz crystal microbalances may be used to determine the solubility of a gas in a polymer by measuring the mass of the polymer in equilibrium with the gas. A palladium electrical resistance sensor has also been used to determine the hydrogen content in the liquid phase for low gas solubility measurements [63].

### 2.2.3 Synthetic Method

In the synthetic method, mixtures of precisely known composition are prepared and the phase behaviour in an equilibrium cell is either directly observed or inferred from other measurements. No sampling is required and these methods can be applied with or without phase transition, but in both cases a known overall composition of the mixture is required. In multi-component systems, experiments with synthetic methods give less information than with analytical methods because the tie lines cannot be determined without additional experiments. In synthetic methods without phase transition, equilibrium properties such as pressure, temperature, phase volumes and densities are measured and phase compositions are calculated using material balance, often combined with an assumed equation of state for the vapour phase. They are divided into isothermal, isobaric and other synthetic methods. Regarding synthetic methods with a phase transition, values of temperature and pressure are adjusted so that the mixture is homogenous. Then the temperature or pressure is varied until the formation of a second phase is observed. The composition of the bulk phase is taken to be the same as the known overall composition while the composition of the incipient phase is not known.

Synthetic methods with phase transition are divided into visual and non-visual synthetic methods. In visual synthetic methods, the appearance of a new phase is detected by visual observation. This approach can be used for the determination of vapour-liquid equilibria, multiphase equilibria, solid-liquid equilibria, critical curves of mixtures, gas hydrate formation, and cloud point determination. In non-visual synthetic observation, the phase transition is detected by monitoring some other physical properties. For example, Minicucci et al. [69] used transmitted x-rays instead of visible light to detect the phase transition of complex organic fluids and to determine individual phase densities and compositions without sampling. The apparatus developed works up to a pressure of 28 MPa, temperature of 725 K, and volume range of (10 to 175) cm<sup>3</sup>. May et al. [70] used microwave technology to detect the appearance of dew and bubble points in hydrocarbon systems (lean gas condensate fluid). Ngo et al. [71] measured the solubility of organic solids in CO<sub>2</sub> using

spectroscopy techniques including infrared, ultraviolet, and fluorescence spectroscopy. No calibration was required and the diffusion of solute from the solid phase into the fluid phase could be observed *in situ* to assure the equilibrium of the solution mixture. Oag et al. [72] developed a shear mode sensor for monitoring the vapour-liquid phase behaviour and determining the dew point lines, bubble point lines, and coexistence regions of fluid mixtures. This approach has been applied to CO<sub>2</sub>-ethane mixture where the dew and bubble point lines were clearly identified.

In isothermal synthetic methods, the pressure is measured at isothermal conditions and the phase compositions are calculated using material balances. The equilibrium cell is firstly evacuated and charged with a known amount of the first component, and thermostated to a given temperature. Then a known amount of the second component is added whereby the pressure increases. This method is very commonly used at low pressures. In the synthetic isobaric method, the boiling point of a synthesized mixture is measured at isobaric conditions and phase compositions are calculated using material balance and an equation of state for the vapour phase.

An example of synthetic study is given here. Sato et al. [73] developed a compact synthetic variable-volume cell with a free piston, position sensing device for the piston, precise pressure and temperature control, and a window for visual observation. The inner volume of the cell can vary from (2.5 to 8.8) cm<sup>3</sup>. The cell was constructed from titanium so that the composition of the sample can be determined by direct weighing of the cell. The apparatus was designed for temperatures up to 473 K and pressures up to 25 MPa. The apparatus was validated by measuring the vapour-liquid equilibria of the (carbon dioxide + methanol) binary system and good agreement with literature data was found. The apparatus was used to measure bubble-point pressure data for carbon dioxide with acetone, methyl ethyl ketone (MEK), and methyl isobutyl ketone (MIBE) at temperatures ranging from (313 to 353) K.

## **2.3 Phase Behaviour of Hydrocarbon Mixtures**

### **2.3.1 Types and Behaviour of Hydrocarbon Fluids**

Hydrocarbon reservoir rocks are porous and permeable because they have interconnected passageways between microscopic pores or holes that occupy the volumes between the grains of the rock. Oil, water and gas are accumulated under such conditions in these reservoirs rocks where they usually trapped by structural or stratigraphic features such as impermeable cap rock [74]. The flow of petroleum fluids through the reservoir rocks is ultimately dependent on flow through the pores. This is a very complicated process due to

the multi-phase flow and mass-transfer phenomena that occur. Petroleum reservoir fluids are multi-component mixtures which can contain thousands of components, primarily hydrocarbons, some as heavy as C<sub>200</sub><sup>+</sup> with some hetero-atoms such as sulphur, nitrogen, oxygen and metallic elements mostly present in heavy fractions. Water with dissolved salts (brines) is also present in gas and oil reservoirs. As water has limited miscibility with hydrocarbon, it usually exists as a separated water-rich phase zone beneath the oil and gas zones. Hydrocarbon components are mainly classified as paraffins, naphthenes and aromatics (PNA). Paraffins (alkanes) have a saturated straight chain structure composed entirely of carbon and hydrogen with the formula C<sub>n</sub>H<sub>2n+2</sub>. The naphthenes (cyclo alkanes) are cyclic compounds composed of saturated rings (C<sub>n</sub>H<sub>2n</sub>) and aromatics are unsaturated cyclic compounds with the formula C<sub>n</sub>H<sub>m</sub>, with  $m < 2n$ .

In order to facilitate the existing applications of the technology in the oil and gas industries, hydrocarbon fluids are classified into five types as illustrated in Table 2.2, where the phase behaviour of a reservoir fluid is dominated by its composition, mainly the presence of heavy hydrocarbon.

**Table 2.2.** Gas Oil Ratio (GOR) and C<sub>7</sub><sup>+</sup> properties of the different types of hydrocarbon fluid

	Dry gas	Wet gas	Retrograde condensate	Volatile oil	Black oil
<b>GOR</b> , [m <sup>3</sup> /m <sup>3</sup> ]	no liquid	> 2500	600 to 2500	300 to 600	< 300
<b>C<sub>7</sub><sup>+</sup></b> , [mol%]	< 0.7	0.7-4	4-12.5	12.5 to 20	> 20

Dry gases are principally composed of methane and non-hydrocarbons such as nitrogen and carbon dioxide. The phase envelope is relatively tight and typically located below the ambient temperature. The gas remains single phase from the reservoir to the separator conditions. Water, however, may condense at the surface conditions due to the gas cooling. A wet gas is mainly composed of methane and other light hydrocarbon components such as ethane and propane with its phase envelope located entirely over a temperature range below that of the reservoir. A wet gas, therefore, will not drop-out condensate in the reservoir during depletion. The separator conditions lie, however, within the phase envelope, producing some condensate at the surface.

The presence of heavy hydrocarbons expands the area of retrograde condensate relative to a wet gas; hence, the reservoir temperature lies between the critical point and the cricondentherm. The gas will drop-out liquid by retrograde condensation in the reservoir, when the pressure falls below the dew point. Volatile oils have many common features with gas condensates, but as they contain more heavy compounds they are liquid-like at



reservoir conditions. The phase envelope of a volatile oil is wider than that of a gas condensate, with a higher critical temperature due to its larger concentration of heavy compounds. The reservoir temperature is often near the critical temperature so that a small reduction of pressure below the bubble point vapourizes a significant amount of the reservoir oil. Black oils are the most common type of crude-oil reserves. The oil is generally composed of more than about 20 mol% heptanes and heavier compounds (often known collectively as “C<sub>7</sub><sup>+</sup>”). Its phase envelope, therefore, is the widest of all types of reservoir fluids, with its critical temperature well above the reservoir temperature [75-76].

The depletion of the reservoir will result in retrograde condensation in the reservoir if the reservoir temperature lies between the critical temperature and the cricondentherm, whereas no liquid will form if it is above the cricondentherm. The oil in a reservoir with a temperature close to its critical point is more volatile than that at a lower temperature. A small reduction of pressure below the bubble point, in a reservoir with a temperature just below the fluid critical temperature, may vapourize half the oil volume [75].

### 2.3.2 Characterization of Hydrocarbon Fluids

A feed composition representative of the fluid entering the system is critical for any process design. Hydrocarbon reservoir fluids may have a composition varying over the field and over field life so it is fundamental that the description of the feed stream entered into the computer model will provide an accurate representation of the actual behaviour and properties of the fluid. To have reliable, valid and applicable experimental data for particular crude oils, it is important that the selection of simplified mixtures is representative of the real crude oil. Inaccurate representation may result in erroneous design of the processing facilities and a subsequent requirement for costly modifications, or in the case of optimization studies, poor agreement with measured experimental data. A well stream will in general contain some fraction of heavy hydrocarbon components, for which the composition and properties cannot be measured in detail. This fraction must be represented by pseudo-components.

The process of construction of a feed composition for a well fluid together with a thermodynamic model that can be used in process simulation, based on experimental data is called fluid characterization. A single C<sub>7</sub><sup>+</sup> fraction lumps together thousands of compounds with a carbon number higher than six. Those compounds (paraffinic, naphthenic and aromatic) play a dominant role in determining the phase behaviour of the reservoir fluid. For example, in heavy oils, these components dictate the viscosity behaviour and control the asphaltene and wax deposition characteristics. Molecular weight and specific gravity or

density of the  $C_7^+$  fraction may be the only measured data available from  $pVT$  reports. Hence, several techniques are used to lump these components into pseudo-components.

The most widely used method is due to Whitson [77] in which the  $C_7^+$  distribution is represented by a continuous gamma function that is optimally discretized into a few pseudo-components. In the Whitson approach, the three parameter gamma probability function is used to characterize the molar distribution as well as to fit experimental weight and molar distributions and to generate synthetic distributions of heptanes-plus fractions. The approach is used to calculate physical properties such as critical pressure and temperature of single carbon number (SCN) groups. A simple three parameter equation is also presented for calculating the Watson characterization factor<sup>2</sup>, the molecular weight and specific gravity. Finally, a regrouping scheme is developed to reduce the extended analysis to only a few multiple carbon number groups where two sets of mixing rules are considered [23, 77-79].

## 2.4 Phase Behaviour of $CO_2$ + Hydrocarbon Mixtures

Despite the significance of phase diagrams of  $CO_2$  + hydrocarbon mixtures in processes such as  $CO_2$ -EOR, phase equilibrium data for ternary and compositionally-characterized multi-component  $CO_2$ -hydrocarbon mixtures are limited, especially for systems containing heavy hydrocarbons and/or hydrocarbons other than alkanes. Nevertheless, a few such studies have been published. An example is the study of Vitue et al. [79] in which a high-pressure variable-volume cell was used to measure bubble and dew-points of a five-component synthetic oil mixture in the presence of  $CO_2$ . The gravimetrically-prepared mixture contained octane, hexadecane, methylcyclohexane, *cis*-decalin, and methylbenzene (toluene) and bubble- and dew-points were measured at temperatures ranging from (292.95 to 373.35) K and at pressures between (2 and 16.5) MPa. Shariati et al. [80] studied the bubble points of some selected synthetic  $C_6^+$  mixtures in the presence of carbon dioxide. In their study, the mole fraction of  $CO_2$  was kept close to 0.25 and the measurements were carried out in the Cailletet apparatus in a temperature range of (312 to 470) K at pressures up to 6.2 MPa. In addition to these studies, a few experimental data sets pertaining to ( $CO_2$  + crude oils) have been published in the open literature. Examples of phase equilibria studies on ( $CO_2$  + crude oils) can be found in the work of Orr et al. [81], Gardner et al. [82], Rathmell et al. [83], Turek et al. [84], and Simon et al. [85].

---

<sup>2</sup> This parameter is used to denote the “paraffinicity” of hydrocarbon fraction; and can be obtained knowing the boiling point and specific gravity of the crude oil.

Because of the differences between CO<sub>2</sub> and hydrocarbon components in terms of size and volatility, the phase behaviour of these mixtures usually varies widely from type I to type IV according to the classification of Van Konynenburg and Scott [42-43], depending on the hydrocarbon component as described previously. The phase behaviour of CO<sub>2</sub> + real crude oils also lies within this range in most cases; the phase diagrams of these mixtures are usually presented by ( $p$ ,  $T$ ) or ( $p$ ,  $x$ ) diagrams, in which the hydrocarbon is treated as a pseudo-component in a similar way to the phase diagrams of the binary mixtures.

Overall, the data reported in the literature suggests that two distinct types of equilibria usually occur depending on the type/nature of the crude oil and reservoir conditions (temperature and pressure). In one, there are only two phases, liquid and vapour existing at high temperatures. In the other, there is a region of liquid-vapour equilibrium, but in the phase diagram it exists in conjunction with both liquid-liquid and liquid-liquid-vapour regions. The size and shape of the three phase regions depend mainly on the temperature and the amount of light hydrocarbon gases presents in the mixture. Furthermore, the phase behaviour of CO<sub>2</sub> with real crude oils reported in these papers is qualitatively similar to the phase behaviour observed in ternary mixtures of CO<sub>2</sub> with hydrocarbon components such as the one reported by Orr et al. [86] for the ternary mixture of CO<sub>2</sub> + methane + hexadecane. Solid deposition, such as asphaltene precipitation, under CO<sub>2</sub> addition may occur as well at different pressure and temperature conditions (usually at low temperature and high pressures) which may block pipeline and associated fittings and also the reservoir pore system.

## 2.5 Phase Behaviour of CO<sub>2</sub> + Hydrocarbon + Water Mixtures

Water is almost always found in oil-bearing geological formations. Because of the complexity of oil mixtures in which components present are not all known, simpler systems that may represent certain characteristics of the real ones are usually used. Despite their importance as a simple model for reservoir fluids, experimental data for CO<sub>2</sub> + hydrocarbon + water ternary mixtures are still scarce and limited to VLE measurements in most of the cases. Table 2.3 summarizes - as an example - the published data for the type (CO<sub>2</sub> +  $n$ -alkane + water) together with the type of phases studied, pressure ranges and temperature ranges. Here those ternary mixtures studied with the three-phase region are highlighted. Brunner et al. [24] studied the VLLE for the ternary mixture (water +  $n$ -hexadecane + carbon dioxide) at two different temperatures (473.15 and 573.15) K and two different pressures (20.1 and 30.1) MPa using static analytical method. The three phase compositions were all analyzed using gas chromatography.

Forte et al. [87] measured the three phase vapour-liquid-liquid equilibrium (VLLE) data of the ternary system ( $\text{CO}_2 + n\text{-decane} + \text{water}$ ) at temperatures from (323 to 413) K and pressures from (1 to 18) MPa using an analytical apparatus with a modelling approach using statistical associating fluid theory for potentials of variable range (SAFT-VR) [37-38]. Also they studied the VLLE of the ternary system ( $\text{CO}_2 + \text{propane} + \text{water}$ ) at temperatures from (311 to 353) K and pressures from (1.7 to 6.7) MPa using the same apparatus. The experimental data obtained for the ternary mixture have been compared to the predictions of the SAFT-VR [88]. To our knowledge, these systems were the widest systems studied of the type ( $\text{CO}_2 + n\text{-alkane} + \text{water}$ ) covering the three phase region. The rest of the published data covers only the two phase regions and they are given in Table 2.3.

**Table 2.3.** Literature data of ternary mixtures of the type (carbon dioxide +  $n$ -alkanes + water)

Ref	System	Equilibria	$T_{\min}$ (K)	$T_{\max}$ (K)	$p_{\min}$ (MPa)	$p_{\max}$ (MPa)
[89]	$\text{CH}_4 + \text{H}_2\text{O} + \text{CO}_2$	VLE	324.30	375.50	10.5	50.6
[90]	$\text{CH}_4 + \text{H}_2\text{O} + \text{CO}_2$	VLE	344.15	344.15	10	100
[91]	$\text{CH}_4 + \text{H}_2\text{O} + \text{CO}_2$	VLE	298.75	323.15	6.2	13.8
[92]	$\text{CH}_4 + \text{H}_2\text{O} + \text{CO}_2$	VLE	243.1	288.4	0.11	6.05
[92]	$\text{C}_2\text{H}_6 + \text{H}_2\text{O} + \text{CO}_2$	VLE	252.20	288.4	0.11	2.03
[93]	$\text{C}_3\text{H}_8 + \text{H}_2\text{O} + \text{CO}_2$	VLE	247.50	289.00	0.1	2.1
[88]	$\text{C}_3\text{H}_8 + \text{H}_2\text{O} + \text{CO}_2$	VLLE	311.10	353.18	1.67	6.71
[93]	$\text{C}_4\text{H}_{10} + \text{H}_2\text{O} + \text{CO}_2$	VLE	252.90	288.30	0.1	2.1
[87]	$\text{C}_{10}\text{H}_{22} + \text{H}_2\text{O} + \text{CO}_2$	VLLE	323.08	413.16	0.94	18.12
[24]	$\text{C}_{16}\text{H}_{34} + \text{H}_2\text{O} + \text{CO}_2$	VLLE	473.15	573.15	10.1	30.1

The binary systems ( $\text{CO}_2 + \text{water}$ ) exhibit type III phase behaviour while the binary systems ( $\text{CO}_2 + \text{hydrocarbon}$ ) exhibit a variety of types of phase behaviour (usually from type I to type IV) according to the classification of Van Konynenburg and Scott. Because of this, a large LLE immiscibility region would be expected to occur which can extend to high temperatures. Due to this immiscibility, a VLLE region ( $\text{CO}_2$ -rich phase, hydrocarbon-rich phase and water-rich phase) will exist and extend to wide ranges of pressure and temperature conditions depending on the mixture. Usually these mixtures are presented by the ternary diagrams rather than ( $p, T$ ) or ( $p, x$ ) as in the case of  $\text{CO}_2 + \text{hydrocarbon}$  mixtures. The size of the three-phase region depends mainly on the binary behaviour of  $\text{CO}_2$  and hydrocarbon components.  $\text{CO}_2$  with light hydrocarbon components (such as methane) reaches the UCEP

at lower temperature and pressure conditions which limit the size of VLLE region. However, CO<sub>2</sub> with heavier hydrocarbon components have larger LLE immiscibility regions and hence extend the three-phase regions to wider pressure and temperature ranges compared to lighter hydrocarbon components. In addition, solid deposition such as asphaltene precipitation can occur at different pressure and temperature conditions, which may block pipeline and associated fittings.

In the oil and gas industries, the water content of the hydrocarbon phases usually creates problems during transportation and processing, the most severe of which is the formation of gas hydrates<sup>3</sup> which may block pipelines, equipment and instruments. Pipeline conditions are usually in the temperature range of (253.15 to 323.15) K and a pressure range of (5 to 25) MPa. At these conditions, hydrates may form. Carbon dioxide as well is an important hydrate former because of its presence as a contaminant in natural gas [94]. Based on the combination and ratio of the hydrate formers, the crystalline and thermodynamic properties in mixed systems can vary significantly from that of hydrate formed from pure guest. Because of this, a better understanding of the phase equilibria of mixed hydrate systems is required in order to exploit the potential applications of hydrate formation in the presence of gas mixtures.

---

<sup>3</sup> Gas hydrates are ice-like crystalline solids that form from mixtures of water and light natural gases such as methane, carbon dioxide, ethane, propane and butane. In gas hydrates, the gas molecules (such as methane), known in this context as "guests" or "formers", are trapped in water cavities that are composed of hydrogen bonded water molecules

## Chapter 3: Theory and Modelling

Accurate predictions of the phase behaviour and other thermophysical properties of (carbon dioxide + reservoir fluid) mixtures with or without the presence of water play a crucial role in chemical and petroleum engineering for process design and optimization. Experimental measurements made on chosen systems can be used to evaluate modelling capabilities and to adjust associated interaction parameters. A wide variety of approaches have been implemented, ranging from empirical and semi-empirical correlations, such as cubic equations of states (EoS) and activity coefficient models, to molecular-based models such as Statistical Associating Fluid Theory (SAFT). In this Chapter, a brief description of some widely used EoS models and their applications and limitations in the oil and gas industry are given. In addition, other mathematical approaches such as activity coefficient models are described. Finally, SAFT is described with the different available versions. The primary focus is on predictive cubic EoSs and SAFT; properties calculated using these approaches are compared with experimental data. A good comprehensive review regarding available thermodynamic models and their applications is covered extensively in many text books such as in the reference [95].

### 3.1 The Virial Equation of State

The virial equation [96] is expressed as an infinite series of either molar volume (or molar density) or pressure. In terms of the compressibility factor and molar volume, the virial EoS is expressed as

$$z = 1 + \frac{B(T)}{v} + \frac{C(T)}{v^2} + \frac{D(T)}{v^3} + \dots \quad 3.1$$

$B$ ,  $C$ ,  $D$  ... are the second, third, fourth ..., virial coefficients and  $v$  is the molar volume of the mixture. These coefficients depend upon temperature and composition, and they account for the interaction between molecules. For example,  $B$  coefficient accounts for the interaction between two molecules, whereas  $C$  accounts for the interaction between three molecules and so on.

Bendick, Webb, and Rubin (BWR) [97] extended empirically the virial equation and introduced eight numerical parameters. The new modified equation was capable of representing the  $pVT$  properties of the liquid and gas phases, critical properties, vapour pressures and enthalpy of vapourization. The BWR EoS was a modification of the Beattie-Bridgeman equation [98]. A modification of the BWR EoS was proposed by Starling with

eleven parameters, expressed as functions of critical temperature, critical molar density and acentric factor [99-100]. The BWR parameters for the heavy hydrocarbons were developed together with the modification of the mathematical form of the BWR EoS for complex hydrocarbon mixtures. In his modification, phase equilibria were used for the determination of the parameters [99]. Numerous theoretical and experimental studies have been published to determine the virial coefficients, especially the second virial coefficient. However, as it is very hard to determine the higher order coefficients, this equation is used to describe the behavior of the vapour phase only and hence it is of little value in reservoir fluid studies where a single equation is usually required to describe the behavior of both phases [96].

## 3.2 Cubic Equations of State (EoS)

### 3.2.1 Introduction

Amongst many available thermodynamic models, cubic EoSs are the most widely used in the oil and gas industries for the calculation of phase equilibria and other properties over wide ranges of pressure and temperature. Since the introduction of the van der Waals EoS in 1873 [53], great effort has been expended in developing these methods that can be used to describe the phase behaviour of pure fluids and mixtures. In most of cases, an EoS relies on the availability of experimental data for the specific system in order to determine intermolecular parameters in the model; these commonly involve complex interaction parameters that can be temperature-dependent. In terms of mixtures, more advantageous approaches would be those that are able to predict effectively the phase behaviour of the system just by means of information regarding the pure components. Among the cubic EoSs, two equations which have enjoyed widespread acceptance in the refinery and oil and gas-processing industries are the Soave-Redlich-Kwong (SRK) [101] and the Peng-Robinson (PR) [102] EoSs. Both of these descended from the van der Waals EoS [53].

The wide interest in cubic EoSs is because of their simplicity, reliability and their facility for enabling fast calculations; they can be applied to both liquid and vapour phases, are applicable over wide ranges of pressure and temperature, allow for good correlation for non-polar systems encountered in the petroleum industry, and they can be reasonably used to estimate densities if a volume translation is employed [103]. Regardless of the widespread application of cubic EoSs using (for example)  $T$ -dependent parameters and  $V$  or volume translations, in their original form these equations have limited applicability. There are various reasons for this: liquid densities are inaccurate; they are unreliable for fluids composed of large (non-spherical) molecules, or those that are highly polar or hydrogen bond; they are unreliable for electrolytes (except in conjunction with an electrolyte model, as

one would expect); they often provide unsatisfactory predictions of LLE, especially in highly immiscible systems such as water with alkanes. Often,  $T$ -dependent parameters are needed to overcome these shortcomings; these might be impossible to obtain for multi-component mixtures.

However, to overcome some of their limitations and to extend their applicability to more complex mixtures, several modifications to well-known cubic EoS models have been proposed by many authors. Also, many new mixing rules have been developed, including those based on excess free energy models, giving so-called EoS/ $G^E$  models. Some of these models are found to be applicable to complex systems in which the components can be highly polar, differ greatly in size or may have specific association. Some of these modifications are addressed in the following sections.

### 3.2.2 Cubic Equations of State

The van der Waals EoS [53] was the first mathematical model able to represent both the gas-liquid transition and criticality. Van der Waals corrected the pressure and volume terms of the ideal gas equation, taking into account the facts that molecules occupy space and they exert an attraction on each other, and derived his well-known EoS as expressed by

$$p(T, v) = \frac{RT}{v-b} - \frac{a}{v^2}, \quad 3.2$$

where  $p$  and  $v$  are the pressure and molar volume respectively,  $a/v^2$  accounts for the attractive interaction between molecules (and is called the attractive term) and  $b$  (the co-volume) accounts for the volume that occupied by molecules. The parameters  $a$  and  $b$  in the vdW EoS, and in other cubic EoS that are descended from it, are found by applying the critical constraints. In this case, it is possible to obtain these parameters with respect to the experimental critical temperature ( $T_c$ ) and critical pressure ( $p_c$ ) as follows:

$$a = \Omega_a \left( \frac{R^2 T_c^2}{p_c} \right) \text{ and } b = \Omega_b \left( \frac{R T_c}{p_c} \right) \quad 3.3$$

The values of  $\Omega_a$  and  $\Omega_b$  depends on the type of equation used; in the case of the van der Waals EoS,  $\Omega_a = 27/64$  and  $\Omega_b = 1/8$ . Equation 3.2 is an example of an EoS, all of which have the property that a maximum of three real roots exist for the molar volume at given pressure and temperature. Because the phase behavior of dense fluids particularly of those complex fluid mixtures can't be modelled accurately, numerous modifications have been



made to improve the capability of the van der Waals EoS. In fact, the main departure from the original form is the treatment of the attractive term as a parameter dependent upon temperature and a parameter related to the complexity of the molecule. In the middle of the 20<sup>th</sup> century, Redlich and Kwong [104] modified the attractive term (a temperature dependency was introduced in the attractive term) in order to obtain better fluid phase behaviour at low and high densities. Zudkevitch and Joffe [105] assumed that  $\Omega_a$  and  $\Omega_b$  were temperature dependent and not constant as previously assumed by Redlich and Kwong. The approaches of Redlich-Kwong, and Zudkevitch-Joffe, to make the parameters of EoS temperature dependent, have been adopted in all the successful modifications of the van der Waals EoS.

For example, Soave (SRK EoS) [101] replaced the temperature dependency of the attractive term in Redlich-Kwong by a more general function considering the variation in the behaviour of different fluids at the same reduced pressure and reduced temperature. He introduced the acentric factor as a third parameter in the definition of the attractive term. The acentric factor<sup>4</sup> (as defined by Pitzer [106]) is used to take into account molecular size and shape effects. The SRK EoS is given by

$$p(T, v) = \frac{RT}{v - b} - \frac{a(T)}{v(v + b)} \quad 3.4$$

The parameters are calculated for individual components by the following equations

$$\left. \begin{aligned} a_i &= 0.42748(R^2 T_{c,i}^2 / p_{c,i}) \alpha(T) \\ \alpha_i(T) &= \left[ 1 + m_i \left( 1 - \sqrt{T / T_{c,i}} \right) \right]^2 \\ m_i &= 0.480 + 1.574 \omega_i - 0.176 \omega_i^2 \\ b_i &= 0.08664(R T_{c,i} / p_{c,i}) \end{aligned} \right\}, \quad 3.5$$

where subscript  $i$  denotes properties of the  $i^{\text{th}}$  component, subscript  $c$  denotes critical properties and  $\omega_i$  is the acentric factor of component  $i$ . The so-called Soave alpha function  $\alpha(T)$ , which appears in Eq. (3.5) determines the temperature dependency of the parameter  $a$  and usually optimized so as to obtain a good representation of the vapour pressure curves of pure, mainly non-polar, substances. The expression of this parameter was subjected to

<sup>4</sup> The acentric factor is a conceptual number introduced by Pitzer in 1955 to measure the non-sphericity (centricity) of molecules. It measures the amount by which the thermodynamic properties of a particular substance differ from those predicted by the Principle of Corresponding States.

many modifications in order to improve the accuracy of the van der Waals EoS [107]. The SRK EoS is quite good in predicting the vapour-liquid equilibria but it does not provide very reliable liquid densities. Peng and Robinson (PR EoS) [102] modified the attractive term to improve the prediction of liquid density in comparison with SRK EoS. They attributed the poor liquid densities of SRK to its unrealistically large critical compressibility factor  $Z_c$ , and sought an EoS with a lower value of  $Z_c$  to correct for this. The PR78<sup>5</sup> equation is given by

$$p(T, v) = \frac{RT}{v-b} - \frac{a(T)}{v(v+b) + b(v-b)} \quad 3.6$$

The parameters are calculated for individual components by the following equations

$$\left. \begin{aligned} a_i &= 0.457236(R^2 T_{c,i}^2 / p_{c,i}) \alpha(T) \\ \alpha_i(T) &= \left[ 1 + m_i \left( 1 - \sqrt{T/T_{c,i}} \right) \right]^2 \\ m_i &= 0.37464 + 1.54226 \omega_i - 0.26992 \omega_i^2 & (\omega_i \leq 0.491) \\ &= 0.379642 + 1.48503 \omega_i - 0.164423 \omega_i^2 + 0.016666 \omega_i^3 & (\omega_i > 0.491) \\ b_i &= 0.077796(R T_{c,i} / p_{c,i}) \end{aligned} \right\} \quad 3.7$$

The SRK EoS together with that of PR EoS are today the two most widely used EoSs in the oil and gas industry. One of the drawbacks of these two equations is that the critical compressibility is always constant regardless of the component. Their wide success is, however, not their accuracies but rather their simplicity and development of many ways to tune the parameters for specific applications. A comprehensive study of the predictive capabilities of different EoSs concluded that both SRK and PR equations were of roughly equal reliability for VLE calculations [107]. To apply the equations above to mixtures, a mixing rule is required to calculate the values of the parameters  $a$  and  $b$  of the mixtures. An overview of the work done using these two EoSs with their VLE predictions of some interesting systems such as water/hydrocarbon mixtures was discussed by Ghosh [108].

The Soave alpha function does not necessarily work well for polar substances or for very light components with  $T_{c,i} \ll T$  and/or very heavy components with  $T_{c,i} \gg T$ . In order to deal with some such cases, alternative alpha functions have been proposed such as the Mathias and Copeman alpha function developed to extend the range of PR EoS to highly polar

<sup>5</sup> Note that in 1978, Peng and Robinson slightly modify the expression of  $m$  function in their original equation (PR76), in order to improve the representation of heavy molecules ( $\omega > 0.491$ ). This model is named PR78.

components [109], the Stryjek and Vera alpha function proposed for improving the modelling capacity of the PR EoS at low reduced temperatures [110] and the Boston-Mathias alpha function [111], which was developed to improve the prediction in light gases at high reduced temperatures. The latter is identical to the Soave alpha function at  $T \leq T_{c,i}$  but, for higher reduced temperatures, asserts that

$$\left. \begin{aligned} \alpha(T) &= \left[ \exp(C_i \{1 - T_r^d\}) \right]^2 \quad (T_r > 1) \\ d &= 1 + m_i / 2 \\ C &= 1 - d^{-1} \end{aligned} \right\}, \quad 3.8$$

where  $T_r = T/T_{c,i}$ . In addition, Twu et al. [112-114] proposed two different alpha functions. The first one requires experimental VLE data in order to obtain (by fitting) the model parameters while the second one is a predictive function requiring only the knowledge of acentric factor. A good review and analysis of the different alpha functions has been reported by Neau et al. [111, 115], in which a theoretical analysis of the strengths and weaknesses of the Soave, Twu and Boston–Mathias alpha functions was performed with the RK EoS. Special attention was paid to the variations of the alpha functions and their first and second derivatives with respect to temperature.

The previously described cubic EoSs predicts the same critical compressibility factor,  $Z_c$  for all substances, i.e. 0.307 and 0.333 by PR and SRK respectively, whereas  $Z_c$  varies within a range of 0.2 to 0.3 for typical hydrocarbons. Although the inaccuracy of the predicted molar volume at the critical point does not necessarily lead to unreliable volumetric data at other conditions, it demonstrates the inflexibility of these EoSs for matching both the vapour pressure and molar volume. To improve the density calculated by these equations, it can be calculated using the volume translation method introduced by Peneloux [116] to minimize the deviation between the predicted liquid molar volume and the experimental data. In his approach, the translated molar volume  $v'$  is calculated from the following relations

$$\left. \begin{aligned} v' &= v - c \\ c &= \sum_{i=1}^N x_i c_i \\ c_i &= 0.50033(RT_{c,i} / p_{c,i})(0.25969 - Z_{c,i}) \end{aligned} \right\} \quad 3.9$$

Here,  $v$  is the mixture molar volume calculated from the EoS,  $c$  is the volume translation parameter,  $x_i$  is the mole fraction of component  $i$ , and  $Z_{c,i}$  is the compressibility factor for component  $i$  at its critical point.

### 3.2.3 Mixing Rules and Binary Interactions

The values of  $p_c$ ,  $T_c$  and  $\omega$  are the only required parameters in the cubic EoSs mentioned previously for pure component. These parameters are experimentally measured but can be estimated in the case of heavy components. To apply the equations to mixtures, a mixing rule is required to calculate the values of the parameters  $a$  and  $b$  of the mixtures. Usually, the van der Waals one-fluid mixing rules (vdW1) are applied

$$\left. \begin{aligned} a &= \sum_{i=1}^N \sum_{j=1}^N x_i x_j \sqrt{a_i a_j} [1 - k_{ij}(T)] \\ b &= \sum_{i=1}^N x_i b_i \end{aligned} \right\} \quad 3.10$$

Here  $x_i$  denotes the mole fraction of component  $i$ ,  $N$  is the total number of components and  $k_{ij}(T)$  is a temperature-dependent binary interaction parameter pertaining to components  $i$  and  $j$  with the properties that  $k_{ii} = 1$  and  $k_{ij} = k_{ji}$ . The above mixing rules work well at low and high pressures for hydrocarbon and simple mixtures but fail when applied to polar and other complex mixtures. Ghosh [108] has reviewed alternative different mixing rules which have been widely studied to improve the prediction of these cubic EoSs.

For hydrocarbon reservoir fluids the random mixing rule, in which one consider only the interaction between pairs of molecules and neglects interactions between three or more molecules, are found to be adequate [117]. They cannot, however, represent the interaction between hydrocarbons and asymmetric compounds such as water, or methanol which is often added to reservoir fluids as a hydrates inhibitor. Although additional flexibility that is achieved by increasing the number of coefficients in binary interaction parameters may provide acceptable results for binary mixtures containing these compounds, the model can fail completely for multi-component systems. Generally speaking, when used in conjunction with cubic EoS, conventional mixing rules such as vdW1 is not sufficient to provide accurately the properties of mixtures that contain strongly associating substances and highly polar compounds. This can be overcome by the adoption of more suitable mixing rules for the parameters in the EoS.

One approach is to incorporate an activity-coefficient model in the mixing rules used with a cubic EoS, giving rise to EoS/ $G^E$  methods. The objective of this method is to determine one or both of the parameters  $a$  and  $b$  in the EoS by equating at a given pressure the predicted excess Gibbs free energy with that given by an activity-coefficient model [107]. In this case, the strengths of EoS (accurate results at low and high pressures for simple mixtures) and

activity-coefficient models (ability to handle polar mixtures at low pressures) are combined. However, even though the combination of them gives good correlation or prediction for polar mixtures, but this is only true at low pressures in most cases.

Because activity-coefficients models are pressure independent while EoS models are pressure dependent, a reference pressure needs to be selected before equating the two quantities. Based on this, two types of EoS/ $G^E$  models are distinguished depending on whether the link is made at infinite pressures (such as in the Huron-Vidal [118] and Wong-Sandler [119] methods) or at zero pressure (such as in the modified Huron-Vidal, MHV-1, [120] method, the PSRK [121] and MHV-2 [122] mixing rules).

In most of these approaches, the binary interaction parameter ( $k_{ij}$ ) between two components is assigned an appropriate value to describe the behaviour of these mixtures (usually by a regression procedure to have the best fit between experimental data and those calculated by the EoS). This binary interaction parameter is usually, by observation, a function of temperature and depends on the considered EoS and alpha function involved in the mathematical expression of the energy parameter  $a$  appearing in the EoS. Many authors have proposed some correlation to estimate the binary interaction values [103].

The inclusion of binary interaction parameters in EoS mixing rules will provide more flexibility, and in most cases reliability, at least within a limited working range. Additional flexibility can also be obtained by making the binary interaction parameter temperature, pressure, and composition dependent. However, these correlations are only applicable to specific mixtures, or specific EoS, and they are often empirical and hence unsuitable for extrapolation; additionally they may need other properties beside those required by the EoS itself. These temperature-dependent interaction parameters required may be impossible to find for multi-component systems and hence a group-contribution approach to predict these values is suggested.

### 3.2.4 Predictive Cubic Equations of State

#### PPR78 and PR<sub>2</sub>SRK

Recently Jaubert and co-workers [34-36, 79, 123-126] proposed a group-contribution scheme in which the binary interaction parameter between two components can be calculated from the following equation based on a group-contribution method.

$$k_{ij}(T) = \left[ \left\{ -\frac{1}{2} \sum_{k=1}^{N_g} \sum_{l=1}^{N_g} (\alpha_{ik} - \alpha_{jk})(\alpha_{il} - \alpha_{jl}) A_{kl} (T_0/T)^{(B_{kl}/A_{kl}-1)} \right\} - \left\{ \frac{\sqrt{a_i(T)}}{b_i} - \frac{\sqrt{a_j(T)}}{b_j} \right\}^2 \right] \times \left[ \frac{2\sqrt{a_i(T)a_j(T)}}{b_i b_j} \right]^{-1} \quad 3.11$$

Here,  $N_g$  is the number of distinct functional groups present in the molecule,  $\alpha_{ik}$  is the occurrence of group  $k$  in component  $i$  divided by the total number of groups present in that component, and  $A_{kl}$  and  $B_{kl}$  are group parameters. Jaubert and co-workers defined 21 functional groups and determined the group parameters  $A_{kl}$  and  $B_{kl}$  by fitting a very large database of experimental binary VLE using the PR78 EoS with the Soave alpha function. The result is the PPR78 EoS. Using this approach, the properties of arbitrary mixture containing any number of components may be computed knowing only the critical temperature, critical pressure and acentric factor of each component, provided that the components may be represented in terms of the 21 elementary groups.

The parameters appearing in Eq. (3.11) cannot be applied directly to other EoS or other alpha functions. However, Jaubert and co-workers proposed a method to transform the binary interaction parameters calculated using the PPR78 EoS model for use with other EoS (such as SRK EoS) or alternative different alpha functions. The proposed relationship is given by the following equations [35]

$$\left. \begin{aligned} k_{ij}^{EoS2} &= \frac{2\xi_{1 \rightarrow 2} k_{ij}^{EoS1} \delta_i^{EoS1} \delta_j^{EoS1} + \xi_{1 \rightarrow 2} (\delta_i^{EoS1} - \delta_j^{EoS1})^2 - (\delta_i^{EoS2} - \delta_j^{EoS2})^2}{2(\delta_i^{EoS2} \delta_j^{EoS2})} \\ \delta_i^{EoS} &= \frac{\sqrt{a_i^{EoS}}}{b_i^{EoS}} \end{aligned} \right\} \quad 3.12$$

In these equations, superscripts EoS1 and EoS2 refer to the two EoS models, and  $\xi_{1 \rightarrow 2}$  is a parameter linking the two. The binary parameter is assumed to be known for EoS1;  $\xi_{1 \rightarrow 2}$  is unity when EoS1 and EoS2 differ only in their alpha functions, but generally takes a constant value other than unity when the EoS model differ in other respects. The parameter value linking the PPR78 EoS (EoS1) with the SRK EoS (EoS2) is  $\xi_{1 \rightarrow 2} = 0.807341$ . When applied in this way to the SRK Equation, the result is the PR<sub>2</sub>SRK EoS [35-36]. This approach has been already tested in the work of Jaubert and co-workers [35-36] against some binary mixtures using the PR<sub>2</sub>SRK EoS which shows similar accuracies to the PPR78 EoS. For example, the binary system (H<sub>2</sub> + butane) was modelled with this approach where due to the presence of hydrogen the  $k_{ij}$  can vary largely by only changing the alpha function. In this case, the Mathias and Copeman alpha function [109] was used instead of the Soave one.

However, additional measurements and testing of these approaches are still required to examine these models especially against multi-component mixtures and mixtures containing heavy components for which there are scarce or no experimental VLE data available. Data collected in the present work provide a great opportunity to examine the proposed group-contribution method. We, therefore, examined the predictive capability of both the PPR78 EoS and PR<sub>2</sub>SRK EoS with the applications of two different alpha functions. Details of comparison with experimental results are given in Chapters 6 and 7.

### Modelling Procedure

Phase equilibrium calculations were performed in this work using the PPR78 EoS, with binary parameters from Eq. (3.11), using the Aspen Properties software package [127]. The model was applied first to the binary mixture (CO<sub>2</sub> + *n*-heptane) at  $T = 394.15$  K and the predicted bubble- and dew-curves are compared with our experimental data<sup>6</sup>. The binary interaction value found at this temperature for the PPR78 EoS was then transformed with Eq. (3.12) for use with the SRK EoS.

The same procedure was applied to calculate the phase equilibria of (CO<sub>2</sub> + *n*-heptane + methylbenzene) and (CO<sub>2</sub> + synthetic oils) mixtures. In these calculations, the mole ratios of all hydrocarbon components were fixed at the relevant experimental values while the mole fraction of CO<sub>2</sub> was adjusted to find the bubble- or dew points at given temperature and pressure. Overall, 210 binary interaction parameters were required to describe the (CO<sub>2</sub> + live oil) systems while only 3 binary interaction parameters were required to describe the (CO<sub>2</sub> + *n*-heptane + methylbenzene).

### 3.3 Activity Coefficient Models

Cubic EoS models are only applicable to mixtures without strong specific interactions and they generally fail to give reliable results for the liquid phase of associating mixtures. Better results can be obtained when the fugacity of components in the liquid phase are estimated from an activity-coefficient model. Hence, the combination of an EoS for the vapour phase and an activity-coefficient model for the liquid phase offers a practical method for phase equilibrium calculations in systems containing associating molecules. Two general approaches are used to determine the parameters of the activity-coefficient model.

---

<sup>6</sup> This binary mixture was studied at  $T = 394.15$  K and used to validate the synthetic apparatus by means of comparison with available literature data

In one of the approaches, the parameters are determined by fitting to experimental VLE data on binary mixtures, usually at a single temperature. The model may then be used to predict the activity coefficients in multi-component mixtures. The modern development of this approach began with the work of Wilson in which he introduced the local composition model [128]. Later developments include the Non-Random Two-Liquid (NRTL) model of Renon [129] and Universal Quasi-Chemical Model (UNIQUAC) [130] introduced by Abrams and Prausnitz. In the second approach, the parameters are estimated by a group-contribution method. Examples of this approach are Analytical Solution of Groups (ASOG Model) which was proposed by Deal and Wilson [131] and UNIQUAC Functional Group Activity Coefficients (UNIFAC) Model which was developed by Fredenslund et al. [132].

Wilson [128] recognized that the distribution of molecules is not purely random in a mixture with specific interactions. His approach has the ability of treating multi-component systems with only binary parameters. However, it is unable to handle either liquid-liquid equilibria or vapour liquid-liquid equilibria. This limitation has been overcome in the NRTL approach. The ASOG model is based on a treatment of the excess Gibbs free energy, similar to that of the UNIQUAC model. The UNIFAC model based on the UNIQUAC equations with all pure-substance and binary parameters determined by empirical group-contribution methods. Because the UNIFAC has the predictive capability, it has gained wide popularity and has undergone several modifications to incorporate new groups of compounds as well as to extend its applicability to wider range of temperature and pressure. The UNIFAC group parameters and group interactions can be obtained from the Dortmund Databank<sup>7</sup> [133].

A limitation of these models is found when approaching the critical region. The critical point cannot be predicted due to the use of a different physical model for each phase. Moreover, difficulties related to the definition of the standard state are also found when the conditions of interest are above the critical temperature of one or more components. This limitation comes from the fact that the activity coefficients are defined based on the mixing of liquid components at conditions of temperature equal to that of the mixture, and so the pure components must be liquid at those conditions. Finally, because they are not written as explicit functions of temperature, pressure and composition they do not have the flexibility of EoS to calculate densities or derivative properties.

---

<sup>7</sup> The Dortmund Data Bank (DDB) was started in 1973 with the intention to employ the vast store of vapour-liquid equilibrium (VLE) data from the literature for the development of models for the prediction of VLE and other properties. [www.ddbst.com](http://www.ddbst.com)



Therefore, these methods are not of practical use over the whole fluid range or for very large molecules and are not widely implemented in oil and gas industry.

## 3.4 The Statistical Associating Fluid Theory (SAFT)

### 3.4.1 Introduction

Cubic EoS described previously works well for fluids composed of simple molecules. Simple molecules are those in which the most important intermolecular forces are repulsion and dispersion (van der Waals attractions), together with weak electrostatic forces. Most of the hydrocarbon fluids fall within this category, making for the wide successful use of cubic EoS. However, mixtures containing complex electrolytes, polar solvents, hydrogen-bonded fluids, polymers and liquid crystals are characterized by stronger and more specific intermolecular forces which cannot be described by cubic EoS; therefore more appropriate approaches are required to describe the non-ideality of these mixtures.

The non-ideality of associating systems was firstly described by the quasi-chemical theory, in which the association is treated as a chemical reaction forming distinct chemical species. However, the fact that the equilibrium constant for this theory must be obtained empirically and varies with temperature, limits the use of this theory as a predictive tool. More modern theories have been established to model complex associations. Amongst them are the integral-equation and perturbation theories. The possibility of molecular association are introduced into integral theories by considering a strong, spherically symmetric and attraction forces. In the case of perturbation theories, a reference fluid whose properties are well known is considered where the thermodynamic properties of the fluids of interest are obtained through a perturbation expansion [134].

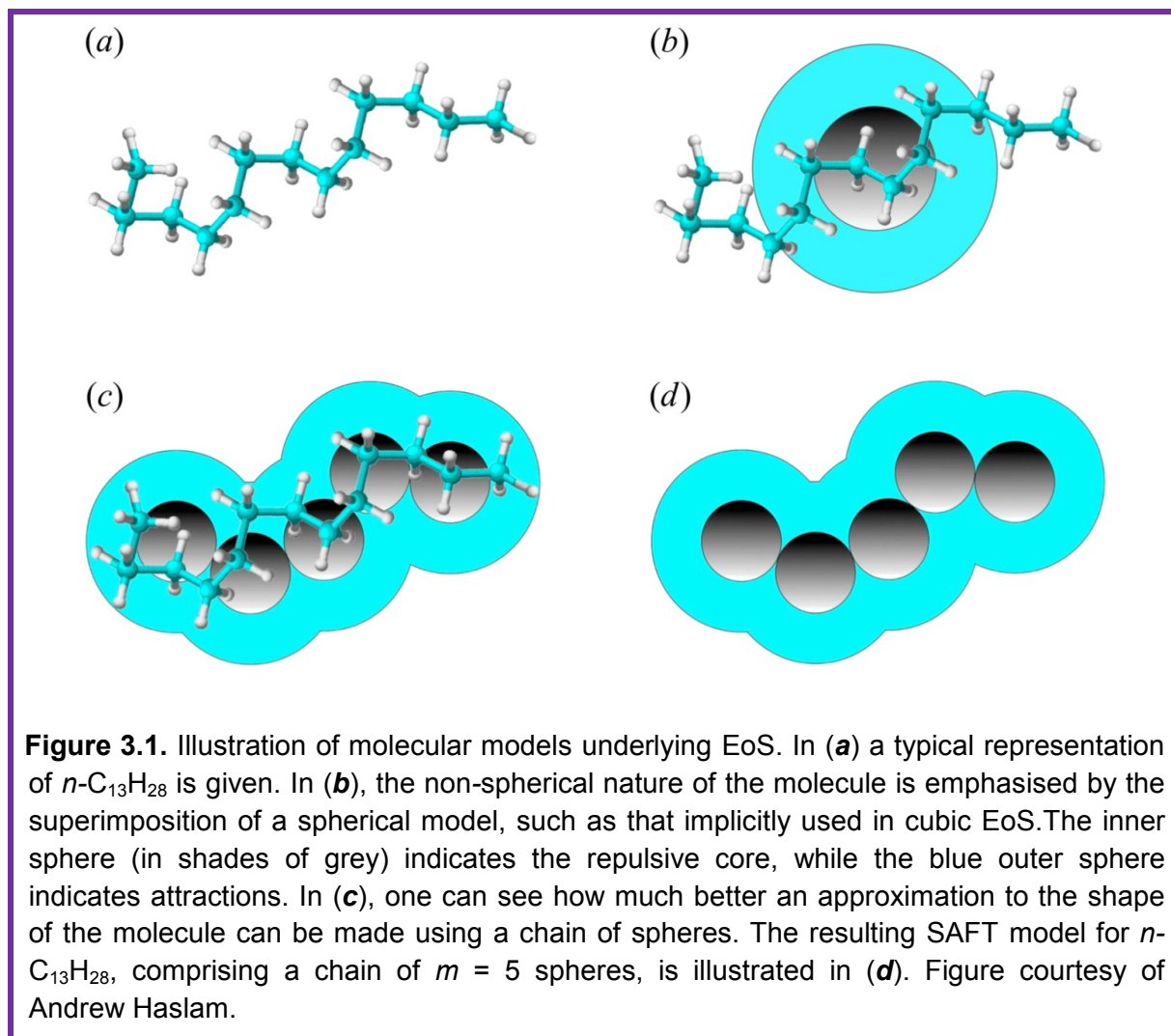
Perturbation theory provides a means by which the free energy of a system with complicated intermolecular interactions can be represented as a perturbation on a system that is well known (termed the reference system). The most-frequently adopted reference is the hard-sphere system. However, the hard sphere reference is inappropriate for fluids containing molecules which are highly nonspherical and associating. A more appropriate reference is one that incorporates both the chain length and molecular association, since both effects have a dramatic effect on the fluid structure. Wertheim [135-140] has proposed a statistical-mechanical theory of associating fluids in which molecules are treated as different species according to the number of bonded associating sites. Other interactions such as dispersion and long-range dipolar forces can then be treated via a perturbation or approximate mean-field terms. Such an approach has been proposed by Chapman et al. [141-142] and termed

the Statistical Associating Fluid Theory (SAFT). As part of his work with Gubbins, Chapman et al. [143] extended Wertheim's theory of hydrogen bonding spheres to mixtures and then to mixtures of associating polymer molecules. In the SAFT approach, molecules are modelled as chains of spherical monomeric segments that interact through isotropic repulsive and dispersive forces. In this case, the EoS is expressed in terms of Helmholtz free energy  $A$  as following

$$\frac{A}{Nk_B T} = \frac{A^{ideal}}{Nk_B T} + \frac{A^{mono}}{Nk_B T} + \frac{A^{chain}}{Nk_B T} + \frac{A^{assoc}}{Nk_B T}, \quad 3.13$$

where  $N$  is the number of molecules and  $k_B$  is Boltzmann's constant. The term  $A^{ideal}$  is the ideal free energy of the fluid, to which three residual contributions are added: the monomeric contribution ( $A^{mono}$ ) due to the repulsion-dispersion segment-segment interactions represented by models such as the Lennard-Jones (LJ), square-well (SW) or Mie potential; the contribution due to the chain formation ( $A^{chain}$ ) and the contribution that takes into account short-range intermolecular association ( $A^{assoc}$ ). The flexibility of the equation together with the different possible choices for the reference fluid has given rise to numerous SAFT versions. The nature and expression of the different terms corresponding to these contributions are specific to each particular version of SAFT.

Among the more popular versions of SAFT are the original SAFT [141-142], Huang-Radosz (HR) SAFT [144], (sometimes referred to as CK-SAFT), simplified SAFT [145], SAFT-LJ (Lennard-Jones) [146-149], SAFT-VR (Variable Range) [37-38], Soft SAFT [150-151], PC-SAFT (Perturbed Chain) [152-153] and simplified PC-SAFT [154]. In the original SAFT, molecules are modelled as associating chains of Lennard-Jones segments, while in the simpler SAFT-HS theory associating chain molecules of hard-sphere segments are considered. SAFT-VR describes the fluid as associating chains of segments interacting through an attractive potential of variable range, for example, the square well potential. In this version, the properties of the monomeric segments are obtained through a Barker and Henderson high-temperature perturbation expansion from a reference hard-sphere fluid [155-156]. A version that has become very popular for chain fluids is the perturbed-chain SAFT (PC-SAFT) in which the usual monomer reference system is replaced by a hard-chain reference fluid. More recently, heteronuclear versions (where different sizes of spheres are used, allowing them to be fused rather than tangent) of the SAFT equation have been developed such as the SAFT- $\gamma$  approach where the equation is coupled with group-contribution formalism [157-159]. Comprehensive review about SAFT and its different versions can be found in the references [160-162].



In SAFT calculations, the number of parameters required to be determined for pure components depends mainly on the expression of the different terms (mainly the monomeric contribution term) and the interaction potential used (such as Lennard-Jones (LJ), square-well (SW) or Mie potential). In general, SAFT requires a minimum of two parameters, the characteristic energy  $\epsilon$  and the characteristic size of a monomeric segment  $\sigma$  to describe simple conformal fluids. A third parameter representing the number of segments per molecule,  $m$ , is required to describe the nonsphericity for fluids. For associating fluids, one must also assign two additional parameters to characterize both the association energy and the volume available for bonding. For each species, one must additionally define the associating sites and their bonding correspondence (which site bonds to which). All of these parameters are usually regressed from experimental properties, mainly vapour pressure and saturated-liquid density data. The parameters estimated follow well-defined trends in most cases with the molecular weight which can be used for extrapolating to higher molecular

weight compounds. Parameters for new systems can then be estimated from those of previously modelled systems. In the case of a fluid mixture, where interactions between molecules from different fluids are also present, unlike or cross parameters will also be required for a complete description. Mixing rules are needed in the dispersion term for SAFT versions. Moreover, combining rules are needed for the segment energy and volume parameters where a correcting interaction parameter  $k_{ij}$  is often used, in a similar way to cubic EoS. This parameter can be obtained by fitting to experimental data or estimated in some cases.

In the present study, the experimental data of phase equilibrium were coupled to the state-of-the-art modelling approaches SAFT-VR and SAFT- $\gamma$ -Mie which enable for extending predictions over the entire  $pTxy$  space. This is validated by the good agreement between experimental results and theoretical predictions presented in this thesis in Chapters 8 and 9.

### 3.4.2 SAFT-VR Approach

The SAFT-VR formulation has been implemented for the square-well, Sutherland, Lennard-Jones, Yukawa and Mie potentials. In this work we use the SAFT-VR approach [37-38] with square-well attractive potential of variable range. Including the range of the potential in the description of the molecular interactions allows the nature of non-conformal changes to be accounted for in the theory, which is advantageous to deal effectively with polar interactions. Here, only a brief description of the approach will be provided; for a more detailed description the reader is referred to the original papers.

The following description draws heavily on those of references [37-38]. Within the SAFT-VR formalism, molecules are modelled as chains of  $m$  attractive spherical monomeric segments of equal core diameter  $\sigma$  which are tangentially bonded to form a chain. The monomeric segments interact through a square-well intermolecular potential. In the case of non-associating fluids  $m$ ,  $\sigma$ ,  $\varepsilon$  and  $\lambda$  are the four necessary intermolecular model parameters for describing a pure component. For associating fluids, short-range directional interactions such as hydrogen bonding are mediated by adding associating sites of different types in the model. Two additional parameters are required to characterize the site-site interactions; the volume available for bonding and the well depth. To study the behaviour of mixtures, a number of unlike interactions, or cross parameters, need to be determined. In the simplest analysis, arithmetic and geometric-mean rules using the pure component parameters can be applied. Unfortunately, the application of simple combining rules for the unlike depth  $\varepsilon_{ij}$  and the range  $\lambda_{ij}$  of the square-well potential rarely leads to accurate predictions of mixture phase

behaviour and hence adjustable parameters (such as  $k_{ij}$ ) are usually included. These parameters are obtained by comparison with experimental mixture data. The strong non-ideality of the systems studied here, together with differences in molecular size, makes it necessary to go beyond the simple geometric-mean for  $\varepsilon_{ij}$ .

For details on expressions regarding the different terms appear in Eq. (3.13), the reader is referred to references [37-38]. Here only a summary is given for completeness. In the SAFT-VR approach, the interactions in the SW potential between segments  $i$  and  $j$  separated by a distance ( $r_{ij}$ ) are given by

$$u_{ij}(r_{ij}) = \begin{cases} +\infty & \text{if } r_{ij} < \sigma_{ij} \\ -\varepsilon_{ij} & \text{if } \sigma_{ij} \leq r_{ij} \leq \lambda_{ij}\sigma_{ij} \\ 0 & \text{if } r_{ij} > \sigma_{ij} \end{cases} \quad 3.14$$

Here  $\sigma_{ij}$  defines the contact distance between spheres,  $\lambda_{ij}$  and  $\varepsilon_{ij}$  define the range and depth of the potential square well for  $i$ - $j$  interactions. The Helmholtz free energy of an ideal mixture of  $n$  components is given by [163]

$$\frac{A^{ideal}}{Nk_B T} = \sum_{i=1}^n x_i \ln \rho_i \Lambda_i^3 - 1, \quad 3.15$$

where  $\rho_i$  is the molecular density of component  $i$ ,  $N_i$ ,  $x_i$  and  $\Lambda_i$  are the number of molecules, the molar fraction and the thermal de Broglie wavelength of species  $i$  respectively. The monomer free energy is given by a second order high temperature expansion of the Barker and Henderson perturbation theory for mixtures [156] as following

$$\frac{A^{mono}}{Nk_B T} = \frac{A^{HS}}{Nk_B T} + \frac{A_1}{Nk_B T} + \frac{A_2}{Nk_B T} \quad 3.16$$

The first term is the free energy of a reference hard-sphere mixture which is obtained from the expression of Boublik [164]. The second and third terms are the first and second order perturbation terms associated with the attractive interactions  $u_{ij}(r_{ij})$  where the former is treated in the context of the M1Xb mixing rule [37-38] and the latter is obtained using the local compressibility expansion. The contribution to the free energy as a result of the chain formation of SW segments for a mixture of chains is given by [146]

$$\frac{A^{chain}}{Nk_B T} = -\sum_{i=1}^n x_i (m_i - 1) \ln y_{ii}^{SW}(\sigma_{ii}), \quad 3.17$$

where  $m_i$  is the number of segments of component  $i$ , and  $y_{ii}^{SW}(\sigma_{ii})$  is the background correlation function ( $y_{ii}^{SW}(\sigma_{ii}) = g_{ii}^{SW}(\sigma_{ii}) \exp(-\beta \varepsilon_{ii})$ ). The function  $g_{ii}^{SW}(\sigma_{ii})$  is obtained from a first order high temperature expansion [156]. Finally the contribution to the free energy as a result of the association of  $s_i$  sites on a molecule of species  $i$  can be obtained from the theory of Wertheim [136-140] as

$$\frac{A^{assoc}}{Nk_B T} = \sum_{i=1}^n x_i \left[ \sum_{a=1}^{s_i} \left( \ln X_{a,i} - \frac{X_{a,i}}{2} \right) + \frac{s_i}{2} \right], \quad 3.18$$

where the first sum is over component  $i$  while the second sum is over all  $s_i$  sites of type  $a$  on a molecule  $i$ . The function  $X_{a,i}$  of molecule  $i$  not bonded at site  $a$  is given by the mass action equation [141, 165]

$$X_{a,i} = \frac{1}{1 + \rho \sum_{j=1}^n x_j \sum_{b=1}^{s_j} X_{b,j} \Delta_{a,b,i,j}}, \quad 3.19$$

where  $\Delta$  is the characterize the association between site  $a$  on molecule  $i$  and site  $b$  on molecule  $j$ .

For mixtures, the determination of a number of cross interaction parameters is required which account for the interaction between unlike components in the mixture. Usually, the Lorentz-arithmetic mean is used for the unlike hard-core diameter as following

$$\sigma_{ij} = \frac{\sigma_{ii} + \sigma_{jj}}{2}, \quad 3.20$$

and the unlike square-well potential range parameter is given by

$$\lambda_{ij} = \frac{\lambda_{ii} \sigma_{ii} + \lambda_{jj} \sigma_{jj}}{\sigma_{ii} + \sigma_{jj}} \quad 3.21$$

The unlike square-well dispersive energy parameter is given by

$$\varepsilon_{ij} = (1 - k_{ij}) \sqrt{\varepsilon_{ii} \varepsilon_{jj}}, \quad 3.22$$

and  $k_{ij}$  can be obtained by direct fitting to experimental data or using a predictive approach such as the modification of the Hudson and McCoubrey combining rules for square-well

intermolecular potentials [166]. Once the Helmholtz free energy is defined, other thermodynamic properties (such as chemical potential) can be obtained using standard relations. The phase equilibria problem can then be solved by considering the necessary conditions for equilibrium. The  $(p, T)$  flash algorithm of Pereira et al. [167-168] was used here for the SAFT-VR calculations.

### 3.4.3 SAFT- $\gamma$ -Mie Approach

The SAFT- $\gamma$  method is a generalisation of the SAFT-VR EoS to treat molecules formed of fused heteronuclear segments where each segment, or group of segments, represents a functional group. In SAFT- $\gamma$  approach, group-contribution methodology has been combined with SAFT to couple the predictive capabilities of GC methods with the accuracy of SAFT description of complex fluid mixtures [169]. This approach is combined with Mie potential where the Mie potential has long been recognized to allow for an improved description of different properties, when the Lennard-Jones, SW or other potential is found to fail [170]. In their study, Lafitte and co-workers [171] showed that the versatility of the Mie (generalised Lennard-Jones) potential allows for a significant improvement in the description of derivative properties when compared to the other SAFT variants and popular cubic EoSs. Derivative properties used in the comparison were saturated liquid density, heat capacity, heat of vapourization, speed of sound, compressibility and thermal expansivity. Within Mie approach, the pair interaction energy between segment  $k$  and  $l$  is given by

$$\Phi_{kl}^{Mie}(r_{kl}) = C_{kl} \varepsilon_{kl} \left[ \left( \frac{\sigma_{kl}}{r_{kl}} \right)^{\lambda_r} - \left( \frac{\sigma_{kl}}{r} \right)^{\lambda_a} \right], \quad 3.23$$

where  $\sigma_{kl}$  is the segment diameter,  $\varepsilon_{kl}$  is the depth of the potential well, and  $\lambda_r$  and  $\lambda_a$  are the repulsive and attractive exponents of the unlike interactions. Within the SAFT- $\gamma$ -Mie group-contribution approach molecular properties are obtained by subdividing the molecules into distinct functional groups chosen to represent the chemical structure of a molecule, with appropriate summations over the contributions of all of the functional groups. A functional group can comprise one or multiple identical Mie segments described by the same set of group parameters. The parameters that fully describe a functional group  $k$  are the number of identical segments that the group comprises, the segment diameter  $\sigma_{kk}$  of the segments of the group, the energy of interaction  $\varepsilon_{kk}$  between the segments of the group, and the values  $\lambda_r$  and  $\lambda_a$  of the repulsive and attractive exponents, respectively, that determine the form of the

interaction potential. The extent to which the segments of a given group contribute to the overall molecular properties is characterised by the shape factor  $S_k$ . In the case of associating groups, the number of the different site types, the number of sites of each type together with the position of the site, and the energy and range of the association between different sites has to be determined [39]. The interactions between groups of different kind which contribute to the description of pure components are described by means of combining rules similar to the ones mentioned previously. The value of the unlike dispersion energy,  $\epsilon_{kl}$ , is typically treated as an adjustable parameter and is therefore obtained by regression to experimental data. These group parameters are usually obtained by fitting to liquid-vapour experimental data of pure components and binary mixtures.

In this work, predictions from SAFT- $\gamma$ -Mie were compared with our experimental data for the ternary mixture ( $\text{CO}_2$  + *n*-heptane + methylbenzene). A key feature of the implementation adopted here is that all interactions, both like and unlike, were determined from experimental data, which are necessarily for systems comprising the relevant constituent groups, but not necessarily the same molecules. Thus, when applied to the current system, the method is regarded as predictive. However, this is not true in the case of aqueous mixtures where because water has to be treated as a single functional group, the unlike interaction parameters between water and other functional groups have to be determined based on available experimental data for the appropriate mixture; same is applicable to the  $\text{CO}_2$  functional group. The expression of the different terms of Eq. (3.13) differs from those for SAFT-VR but they are usually similar. A full description of the SAFT- $\gamma$ -Mie model can be found in the work of Vasileios Papaioannou [39]. The ( $p$ ,  $T$ ) flash algorithm of Pereira et al. [167-168] was used here for the VLE calculations

### 3.5 Summary

In view of the previous discussions, the predictive cubic EoS PPR78 and  $\text{PR}_2\text{SRK}$ , SAFT-VR and SAFT- $\gamma$ -Mie are used to compare with the experimental data reported in this thesis. Except the case of SAFT-VR, these models are based on group-contribution schemes. Cubic EoS models are widely used in the oil and gas industry. SAFT has already been shown to provide an excellent description of complex mixtures, where cubic EoS fails, such as in modelling associating fluids. It is thus interesting to examine the predictive capabilities of such equations against data obtained for complex mixtures, such as those studied in the present work.



## Chapter 4: New Synthetic Apparatus for Fluid Phase Equilibrium Measurements

In applications where phase behaviour measurements for multi-component mixtures are required, synthetic technique is desired. In this Chapter, the details of a new experimental synthetic apparatus designed and constructed to measure the phase equilibria of systems containing CO<sub>2</sub> and multi-component hydrocarbons at reservoir temperatures and pressures are presented. The synthetic apparatus was used to measure the phase equilibrium and density of (CO<sub>2</sub> + *n*-heptane + methylbenzene) and (CO<sub>2</sub> + synthetic crude oil) mixtures. The measurements included LLE, VLE, VLLE and critical conditions. The experimental results are presented in Chapters 6 and 7. Details of the apparatus control and operation, experimental procedure and calculations, experimental calibration and uncertainty analysis, apparatus validation, health, safety and environmental (HSE) considerations and maintenance are presented.

### 4.1 Apparatus Design

Phase behaviour and phase boundaries of CO<sub>2</sub>-reservoir fluid mixtures are typically observed in a variable-volume view cell employing visible light. Additionally, transmission and/or scattering of visible or infra red light may be used depending on how opaque is the real crudes. The technique presented in this work permits the determination of various types of phase boundary including vapour-liquid, liquid-liquid and vapour-liquid-liquid equilibria, critical curves of mixtures, solid-fluid equilibria, and cloud curves. The apparatus, shown schematically in Figure 4.1, was designed for a maximum working pressure and temperature of 40 MPa and 473.15 K respectively. The main parts are the variable-volume cell, high pressure syringe pumps, electrically actuated valves, servo-control system, and heating system. Wetted metallic parts were made from either Hastelloy C276 or titanium, both of which are resistant to corrosion. The technical drawings/specifications of the main parts of the apparatus are given in Appendix A.

The core of the apparatus was the variable-volume equilibrium cell (Sitec-Sieber, model 759.1061) in which one end of the equilibrium cell was fitted with a movable piston while the other end was closed by a sapphire window allowing visual observation of the interior of the cell. Figure 4.2 is an isometric view of the variable-volume cell assembly. The cell was a horizontally-orientated cylindrical vessel of 26.5 mm internal diameter, 85 mm external diameter, and volume variable from (11 to 67) cm<sup>3</sup>. A blind axial hole in the vessel wall (5 mm diameter x 80 mm long) accommodated a Pt100 sensor for temperature measurements.

The cell and piston were made of Hastelloy C-276. The end of the hollow piston was closed with an 8.2 mm diameter sapphire window that permitted back illumination of the cell contents, while a CCD camera fitted with a LED ring was used for visual observation with front illumination.

A brushed DC servomotor (Hardmeier control, model MT30U4-36), connected through a 66:1 right-angled reduction gearbox to a 6 mm-pitch ball screw, was used to drive the piston. The piston speed and position were determined by means of a rotary encoder (Hardmeier control, model E 260-6-1000 HV) and the servo motor was also fitted with a tacho-generator for speed/acceleration control. Limit switches (Burgess, model V3S) were used to detect the ends of travel. The control system consisted of a Trio MC302X motion controller and a Parker RTS DC servo drive, programmed to allow simple operation of the machine via a host PC. Using software running on the host PC, the drive system could easily be instructed to find its home position, to move an incremental distance, or move to an absolute distance from the home position. The software was also used to implement constant-pressure and volume-ramping modes of operations.

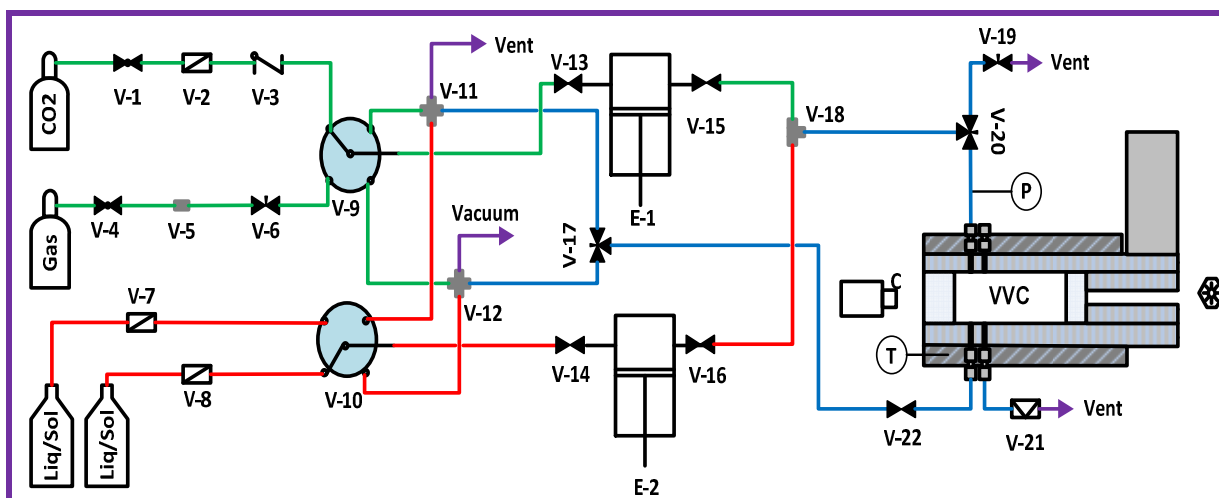


**Figure 4.1.** Schematic diagram of the variable volume cell apparatus: V-1, on/off valve; V-2, filter; V-3, check valve; V-4, on/off valve; V-5, reducer; V-6 valve; V-7 and V-8, filter; V-9 and V-10, 5 way electrically actuated valves; V-11 and V-12, union crosses; V13 to V16, check valves; V17, three way electrically actuated valve; V-18, tee; V-19, two way manual valve; V-20, three way manual valve; V-21 safety head; V-22, two way air operated normally closed valve; VVC, variable volume cell; E-1 and E-2, high pressure syringe pumps; notation P and T indicates pressure transducer and temperature sensors respectively. Green colour indicates gas paths, red colour indicates liquid paths, and blue colour indicates mixture paths

The cell was equipped with four high pressure ports: two, fitted with reducing unions, were used for the fluid inlet and outlet; a third was closed by a rupture-disc safety device (Sitec-Sieber, model 728.0500-HC276, 500 bar); and the fourth was plugged. The main sapphire window assembly was sealed to the cell body by means of a solid PTFE o-ring. The piston was sealed by means of a proprietary gland fitted an annular PTFE sealing ring between two PEEK guide rings that served both to avoid seal extrusion and to protect the polished surface of the piston. The axial compression on the seal was adjustable by means of a threaded ring. The gland itself was sealed to the body of the cell by means of two additional PTFE o-rings.

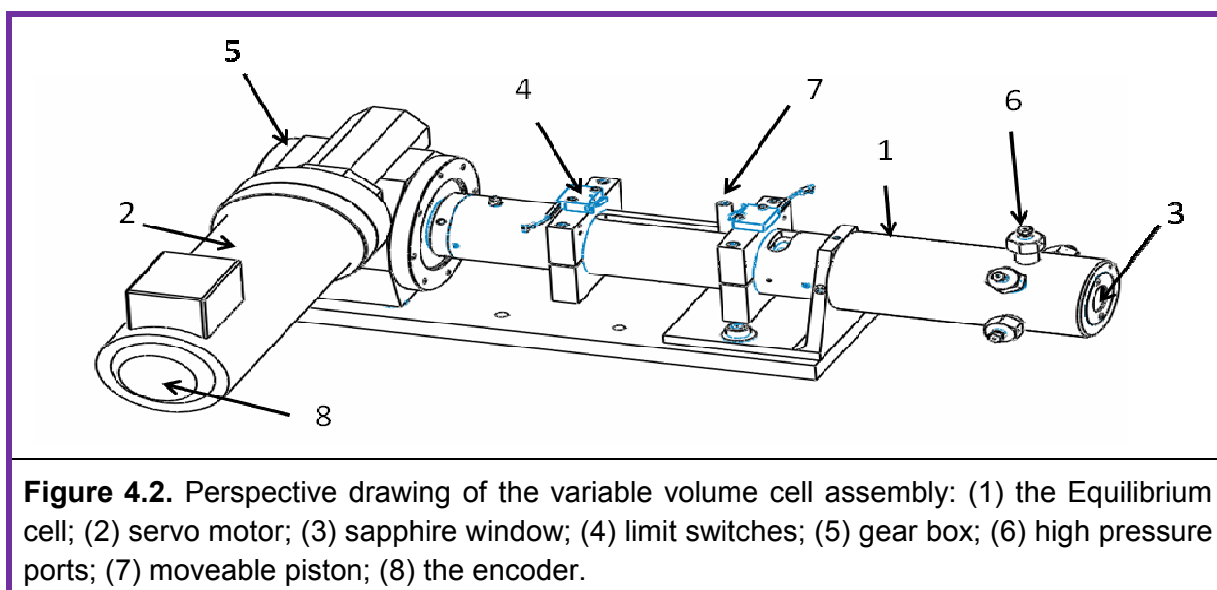


**Figure 4.2.** Perspective drawing of the variable volume cell assembly: (1) the Equilibrium cell; (2) servo motor; (3) sapphire window; (4) limit switches; (5) gear box; (6) high pressure ports; (7) moveable piston; (8) the encoder.

Mixing of the cell contents was accomplished by means of an PTFE-coated magnetic follower of ellipsoidal shape (10 mm long x 6 mm diameter) placed inside the cell. An external magnet driven by a variable-speed motor was used to rotate the follower, typically at a rotational speed of about  $30 \text{ s}^{-1}$ . An optical rail located below the cell was used to mount the CCD camera, front and back illumination devices and also the stirrer motor. It was therefore possible to adjust the position of the stirrer back or forth after movement of the piston by sliding the motor along the rail.

A pair of high-pressure syringe pumps (Chandler Engineering, Quizix model Q5210) were used to inject the components of interest into the equilibrium cell. One pump was used for liquid injections while the other for both  $\text{CO}_2$  and gas injections. These pumps provided precise pressure control, flow rate and volume displacements. The wetted parts were made of Hastelloy C-276. The pumps were thermostated by means of cooling jackets through which water from a chiller (Huber, model HB3006.0015.99) was passed at  $T = 283.15 \text{ K}$ . The

temperature and pressure of the fluid in each pump cylinder were monitored for purposes of determining the density of the fluid from an EoS and hence determining the mass of fluid injected from the calibrated volumetric displacement. Flexible surface-mounted Pt100 temperature sensors affixed to the wall of the cylinders were used to measure the temperature, while a calibrated pressure transducer attached to each pump was used to obtain the pressure. The pumps were connected to the cell through Hastelloy C276 or titanium tubing of 1.6 mm o.d. and 0.5 mm i.d., chosen to minimize dead volumes in the injection line.

The pressure transducer (DJ Instruments, model DF2) was inserted in this line between valve V-20 and the equilibrium cell. This two-port transducer had titanium wetted parts, an internal volume of only 12  $\mu\text{L}$ , and a full-scale range of 40 MPa. Its position was such that it was always in communication with the interior of the cell. The cell temperature was measured using a calibrated 4-wire Pt100 sensor (Sensing Device Ltd, model SD01168, 4.8 mm o.d. x 75 mm length) inserted into an axial hole in the cell body. This was connected to a data acquisition unit fitted with a high-precision multimeter for four-wire resistance measurements.

Two five-way electrically-actuated valves (Swagelok, model SS-43ZFS2-049-42DCZ, V-9 and V-10 in Figure 1) were installed in the inlet streams of the syringe pumps. The main port was connected to the syringe pump inlet valves (V-13 and V-14) through a 3.2 mm o.d. stainless steel tubes. The other ports were connected with 3.2 mm o.d tubing to the CO<sub>2</sub> and gas systems (through valves V-1 and V-6 respectively), liquid/solvent system, vent system (through the union cross V-11) and vacuum system (through the union cross V-12). A normally-closed air operated valve (Sitec-Sieber, model 610.3224-HC276, V-22) could be used to discharge fluid from the cell. The air supplied to this valve was controlled by a solenoid valve which was actuated electrically. Fluid could also be vented slowly from the cell through the three-port valve V-20 (Sitec-Sieber, model 610.3240-HC276), via a small-bore restrictor tube and valve V-19 (Sitec-Sieber, model 610.3220-HC276) to waste.

The equilibrium cell was encased in a 10 mm-thick aluminium heating jacket which was used to control the temperature. The jacket was fitted with axial holes to accommodate four cartridge heaters and two Pt100 temperature sensors. A PID process controller (Eurotherm, model 2216E) was used to regulate the temperature within  $\pm 0.01$  K, while a second supervisory controller was used for over-temperature protection.



**Figure 4.3.** Pictures showing the synthetic apparatus setup located in the chemical engineering department, ACEX building, lab 424. The top picture represents the entire apparatus including the variable volume cell assembly, a rack holding the servo controller and other instruments, the Quizix pumps, the chiller and fluid system. The bottom left picture shows the CCD camera used and the front of the equilibrium cell. The bottom right picture represents the variable volume equilibrium cell (top view) combined with the servo motor, gear box, limit switches and the encoder.



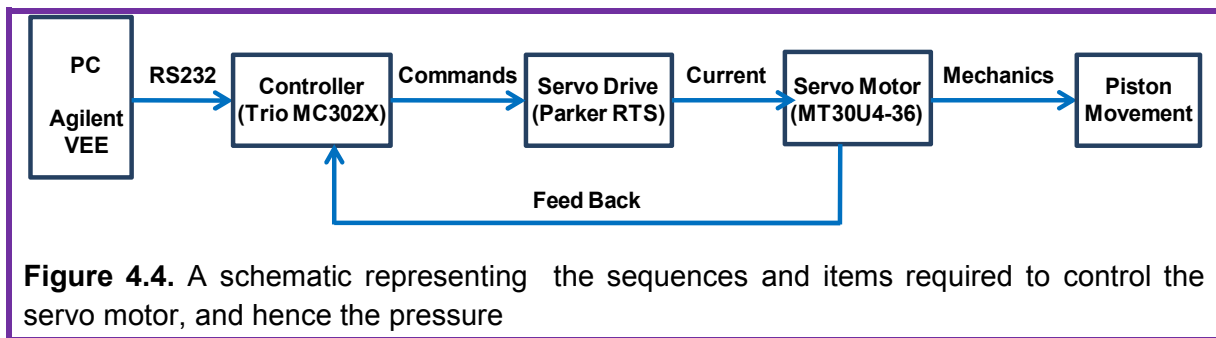
All aspects of experiment control, except for fluid injection, and data acquisition were computer controlled using software written in Agilent VEE. The controller system included over-temperature and over-pressure cut-out functions interlocked to the servomotor and heating systems.

Prior to use, the system was thoroughly leak tested in the whole pressure range with both helium and water; it exhibited a high-level of integrity. The system was also checked for leakage during the course of measurements. The piston sealing system required periodic adjustments, and eventually seals replacement, to maintain leak-free performance. The details of the main parts of the apparatus are listed in Appendix A, including supplier details and specifications. Figure 4.3 shows some pictures of the apparatus.

## 4.2 Apparatus Control and Operation

### 4.2.1 Servo Control System

**Controller Overview:** The servo drive is controlled using an (-10 VDC to + 10 VDC) command reference from the Trio controller with + 10 VDC represent the full motor speed applied (3000 rpm). A schematic is shown in Figure 4.4, where the items required to control the servo motor are presented. The controller uses a simple table to exchange data with a host computer over an RS232 serial communication link.



The table has an array of values that are allocated to specific functions and this allows the computer to control the machine easily. Schematic drawings for the front and rear view of the servo controller crate is shown in Figure 4.5. The front view contains the indicators, the emergency stop, switch on/off and the RS232 connection to the host PC. The rear side contains the cables connections to the servo motor, tacho generator, the encoder, and the limit switches. It also holds the main three phase power supply and the pressure safety switch connections.

The front of the control system crate has a serial port that is used to connect the controller to a computer with a standard RS232 port. Communications to the controller is simplified by the use of a free ActiveX control that can be incorporated into a high level windows programming environment such as Labview, Visual Basic or Agilent VEE. The Trio controller is programmed using Motion Perfect 2 software [172]. Before full operation is allowed, the actuator must be homed. This is started by the Host PC initiating the homing routine. The actuator is driven to the negative travel limit switch and then driven forward until the switch is no longer activated and the home position is set. After homing, the actuator can be jogged manually by using the hand held pendant or can be moved by a distance from the current position or can be moved to an absolute position.

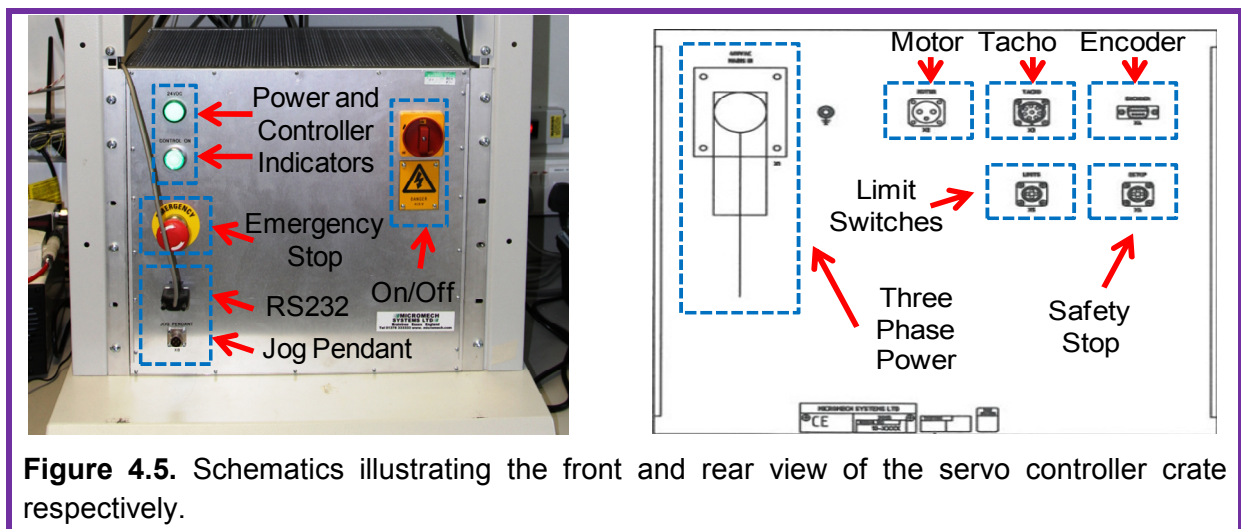


**Figure 4.5.** Schematics illustrating the front and rear view of the servo controller crate respectively.

**Controller Details:** There are two power supplies that are required for operation of the control system. The 24VDC power supply has a corresponding indicator on the front of the main cabinet and required for operation of most of the control system components such as the Trio motion controller, safety relay and logic circuit supply. The second power supply is the 100VAC three phase transformer which has a 415VAC 3 phase input and steps down to an output voltage of 100VAC three phase. This supply is required to power the Parker RTS DC brushed servo drive. The machine safety circuit uses a safety relay to ensure complete isolation of all hazardous movement when the safety circuit is interrupted. Once the safety circuit is interrupted and the cause is resolved, the safety circuit must be reset by pressing the control on push button. The machine safety circuit is checked upon the control on operation and will only reset if all hazardous devices are at a safe state. As well as the control cabinet emergency stop push button, the machine pressure switch is also integrated into the safety circuit for monitoring.

A simple hand-held pendant is used to manually jog the actuator forwards and reverse. This pendant can be plugged into the front of the control system panel and only consists of two buttons that must be pressed and held to jog the actuator. Jogging continues until the button is released or a fault occurs such as an over travel limit switch being hit. The jogging operation cannot be initiated until the machine has been homed after powering up of the system. The control on illuminated push button is required to reset the machine safety circuit. This is necessary after the machine is powered on and also after the machine safety circuit is interrupted. The button is illuminated when the machine safety circuit is successfully reset. The emergency stop push button is used to stop all motion immediately and to isolate the machine to a safe state. The emergency stop push button will latch when pushed and will require a twist or pull action to release once the hazard has been resolved.

The pressure safety switch is located on the machine assembly and is connected as part of the machine safety circuit. If the pressure becomes higher than the desired set value, this will isolate the machine so that no further movement can occur and potentially cause damage to the machine. If the pressure switch is activated, the pressure will have to be reduced manually as the motor cannot be driven in reverse with the safety circuit interrupted. The machine should be powered on by operating the main isolator on the front of the control cabinet. When power is on, the 24VDC indicator should be illuminated. Upon power up, the safety circuit will not be operational. The control on push button should be pressed to reset the safety circuit. If the control on button does not illuminate, then the emergency stop push button should be checked that it is not depressed and that the pressure switch is healthy before attempting to reset the safety circuit again. With the control on button illuminated, the machine is ready to begin the homing routine.

**Controller Operation:** The program in the controller is written such that it uses a variable table shared between the controller and the PC to provide the required functionality. The variable table (VR) has many cells that are allocated to a specific function and must be considered carefully during operation. Details of these table allocations are given in Table 4.1. The operation of the servo motor entirely depends on the variables given in this Table. The PC can instruct the system to find its home position by writing a value of '1' to the 'command' variable. The motor will run in reverse at a fixed speed of 0.2 mm/second until the reverse limit switch is hit (this value can be adjusted). The motor will then creep forwards at  $1/10^{\text{th}}$  of this speed until the switch turns off. The controller will then set its current position to the value stored in homing position variable, VR (14).



**Table 4.1.** Details of the variables allocated to specific functions for servo controller

VR	Function	Values	PC Read/Write
1	Fault Status	0 = No Fault 1 = Emergency Stop 2 = Drive Fault 3 = Motor Thermostat Fault 4 = Positive Limit Hit 5 = Negative Limit Hit 6 = Motor Stalled	Read
2	I/O Status	Individual bits represent the status of each digital I/O signal (0=off, 1=on).	Read
3	Axis Status	0 = Idle 1 = Homing 2 = Moving incremental distance 3 = Moving to abs. Position 4 = Jogging Positive 5 = Jogging Negative	Read
4	Spare		Read
5	Spare		Read
6	Command	1 = Home position 2 = Move incremental distance 3 = Move to absolute position	Write
7	Target Distance	Units = millimetres, Distance to travel incrementally, or absolute position to move to in absolute mode.	Write
8	Move Speed	Speed when moving in incremental or absolute modes, units = mm/sec	Write
9	Move Acceleration	Acceleration rate in incremental or absolute modes, units = mm/sec <sup>2</sup>	Write
10	Move Deceleration	Deceleration rate in incremental or absolute modes, units = mm/sec <sup>2</sup>	Write
11	Jog Speed	Speed when jogging, Units = mm/sec	Write
12	Jog Acceleration	Acceleration rate when jogging, units = mm/sec <sup>2</sup>	Write
13	Jog Deceleration	Deceleration rate when jogging, units = mm/sec <sup>2</sup>	Write
14	Spare		Write
15	Spare		Write

The PC can then instruct the motor to move an incremental distance (in mm) from its current position. A positive value will move forwards, and a negative value will move in reverse. The speed, acceleration, and deceleration values can also be set via the PC interface using variables 8 to 10. The axis status value will indicate a value of 2 (moving incremental distance) whilst the motor is moving, and then a value of 0 (idle) when the motor has

stopped. The PC can also instruct the motor to move to an absolute position (in mm) from the home position. Only positive values are valid. The axis status value will indicate a value of 3 (moving to absolute position) whilst the motor is moving, and then a value of 0 (idle) when the motor has stopped. When a jog push button is pressed, the motor will run in the specified direction until the input turns off or a limit switch is hit. The speed, acceleration, and deceleration values can be set via the PC interface using variables 11 to 13. In the event of a fault, operation of the machine will stop. The faults are indication in variable 1 as a value.

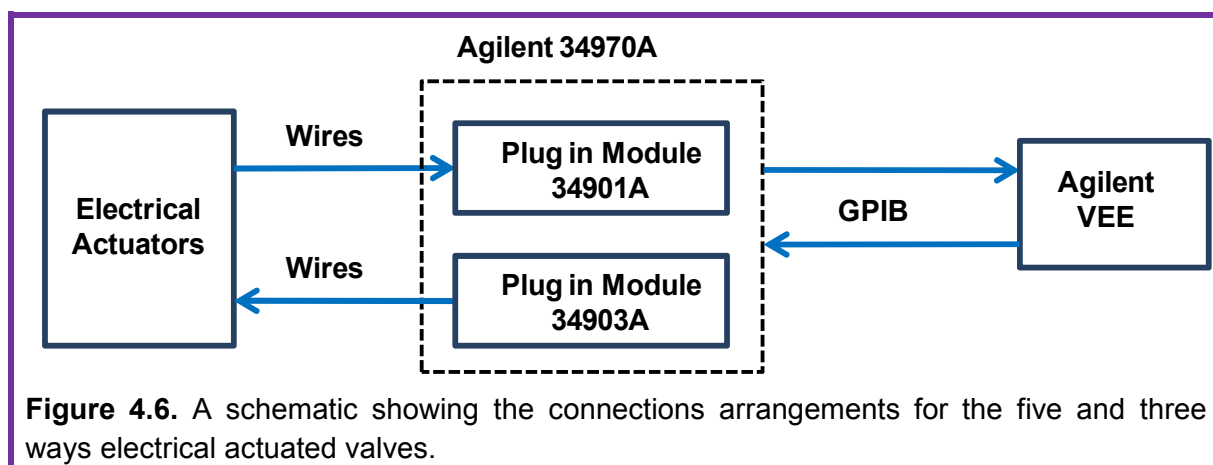
With the exception of the emergency stop/pressure fault, all other faults must be acknowledged by the host computer to allow the control system to be reset. The host computer can acknowledge the fault by writing a value of 1 to variable 5. Once the fault is reset, then a value of 0 must be written to variable 5. If a limit switch has been triggered, then after the fault has been reset, the homing routine must be completed before any other motion can occur. For reliable movement of the piston, the speed should be set up as low as possible. In this way, a smooth movement can be ensured and any possible damages to the sealing system can be prevented.

In the present study, Agilent VEE program [173] was used to communicate with the servo trio motion controller through the RS232 connection. The written program in Agilent allows for the use of the same variables previously described. A PID controller is used in the program to operate the servomotor based on pressure input readings from the pressure transducer. This allows operating the cell at constant pressure mode by instantaneously driving the piston forward and backward to maintain the desired pressure. This also allows operating the cell in volume or pressure ramping mode by driving the piston to move in one direction until a desired volume or pressure is reached. The two flexible modes of operation have given some advantages in the way the synthetic measurements were performed. The pressure reading values are continuously monitored and recorded in the Agilent VEE program as a function of time and cell volume. The latter is important where the generated  $p$ - $v$  curve is sometimes used as a mean of detecting phase transitions.

#### **4.2.2 Electrically Actuated Valves Control**

The wiring arrangements of the five and three ways Swagelok electrically actuated valves allow for the detection of the ports connections (open or closed) and the control of the opening/closing of these connections at any time. The arrangements are schematically shown in Figure 4.6. Two sets of wires are connected. The first set is connected to acquisition plug in module (34901A) which gives the ports connections status

(opened/closed). A 24 Vdc will be detected if there is a connection between the ports while zero voltage will be detected when the ports are not connected. A second set of wires are connected to a relay card (Plug in Module 34903A) which allow the opening and closing of the connections between these ports. Agilent VEE can be programmed so that it sends/receive the commands and status to Agilent 34970A through GPIB interface connector.



Agilent 34970A is used to open or close the different ports of these valves. Table 4.2 summarizes the relay and input cards channels arrangements for these valves. The valves 1, 2, 3 and 4 refer to the five way valve (V-10) used in the liquid side connections, five way valve (V-9) used in the gas side connections, three ways valve (V-17) connected to the vent and vacuum systems (in the equilibrium cell outlet side), and the solenoid valve used to supply air to the normally closed air operated valve (V-22) respectively. The channels numbers should be carefully considered during operation so that correct ports can be opened or closed. Mistakes in opening or closing the correct ports can lead to potential risks if no risk recovery measures are in place. In valves one and two, port one is the main port which is always connected to the inlet of the Quizix pumps while the other remaining four ports can be connected to port one as desired. In valve three, port one is always connected to the cell outlet while ports two and three connects the cell outlet to vacuum and vent respectively. Valve four supplies air to the air operated valve by opening port two.

### 4.2.3 Other Controllers

In the present study, PumpWorks software is used to control and operate the Quizix pumps [174]. This software allows complete and automated control of the Quizix pumps and runs on window based computers. The pump cylinder can be operated in constant flow rate or constant pressure.

**Table 4.2.** Agilent 34970A channels numbers and descriptions showing the ports connections of the electrical actuated valves

<b>Relay card (used for opening or closing the ports)</b>			
<b>Channel</b>	<b>Valve</b>	<b>Port</b>	<b>Comments</b>
1	1	2	To connect to the liquid/solvent system
2	1	3	To connect to the liquid/solvent system
3	1	4	To connect to vacuum system
4	1	5	To connect to vent system
5	2	2	To connect to the vacuum system
6	2	3	To connect to the CO <sub>2</sub> system
7	2	4	To connect to the gases system
8	2	5	To connect to the vent system
9	3	2	To connect to the vacuum system
10	3	close	Closed (no connections)
11	3	3	To connect to the vent system
12	3	N/A	
13	4	2	To open the valve (supply air)
14	4	close	
15	4	3	To discharge the air
16	4	N/A	
<b>Input card (used for reading the ports status)</b>			
<b>Channel</b>	<b>Valve</b>	<b>Port</b>	<b>Comments</b>
3	1	2	24 Vdc if open, otherwise 0 Vdc
4	1	3	24 Vdc if open, otherwise 0 Vdc
5	1	4	24 Vdc if open, otherwise 0 Vdc
6	1	5	24 Vdc if open, otherwise 0 Vdc
7	2	2	24 Vdc if open, otherwise 0 Vdc
8	2	3	24 Vdc if open, otherwise 0 Vdc
9	2	4	24 Vdc if open, otherwise 0 Vdc
10	2	5	24 Vdc if open, otherwise 0 Vdc
13	3	2	24 Vdc if open, otherwise 0 Vdc
14	3	close	
15	3	3	24 Vdc if open, otherwise 0 Vdc
16	3	N/A	
17	4	2	24 Vdc if open, otherwise 0 Vdc
18	4	close	
19	4	3	24 Vdc if open, otherwise 0 Vdc
20	4	N/A	

The pump cylinder can also be operated in automated volume or time operation. This causes the pump cylinder to stop pumping automatically after a set amount of fluid has been pumped or a set amount of time has been elapsed. Agilent VEE can also be used to communicate with the PumpWorks software through the Dynamic Data Exchange (DDE) server which allows data to be sent or received between any two applications with DDE capability in them. The Agilent VEE can be then easily programmed to have different mode of operations of the pumps.

A PID process controller (Eurotherm, model 2216E) was used to regulate the temperature of the heating jacket within  $\pm 0.01$  K, while a second supervisory controller (CAREL) was used for over-temperature protection. Both of these controller modules are mounted in a small box which contains the sensors communication ports, RS232 port and outputs a current of 230 V Ac at 4 Amp max. Eurotherm iTools software [175] can be used to communicate with the controller. The software allows for defining temperature set point and configuring the controller if required. Agilent VEE is linked to the iTools software through ActiveX which enabled both software to share information and functionality. Agilent VEE is used in the present study to adjust the temperature set point and to configure the PID controller.

The two supervisory CAREL controllers used for over-temperature and over-pressure protections are connected with each other as schematically shown in Figure 4.7

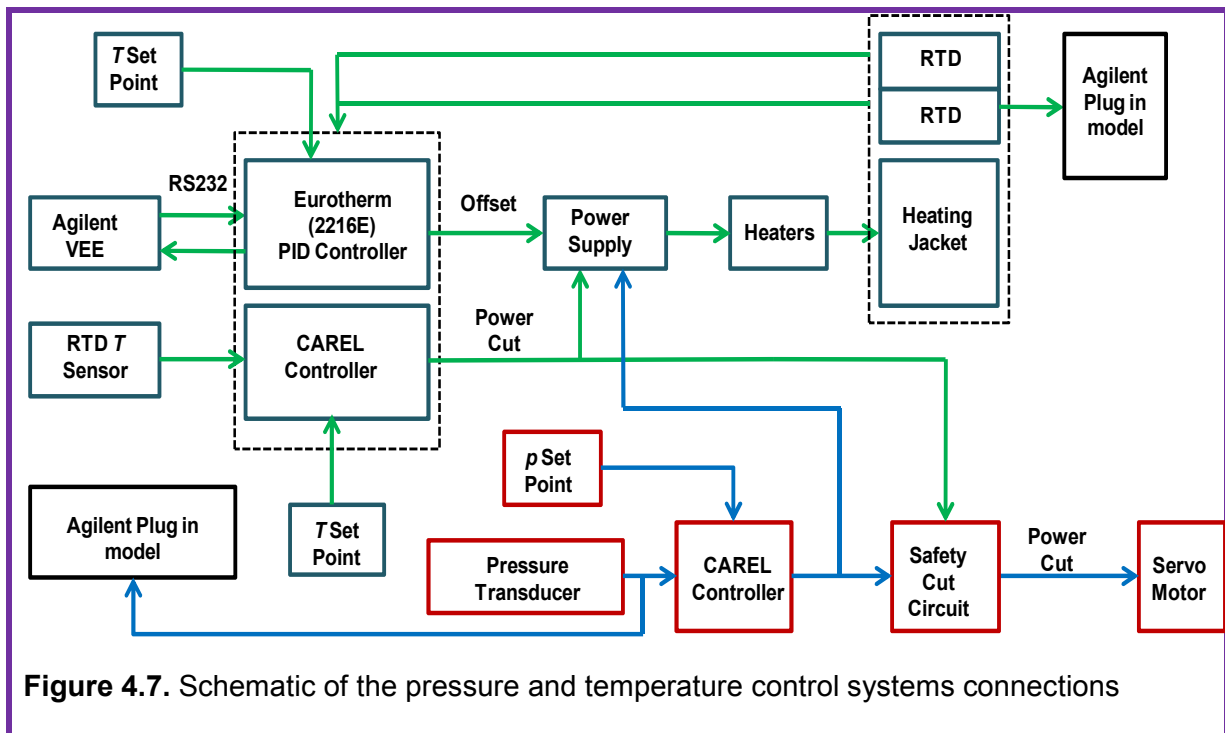


Figure 4.7. Schematic of the pressure and temperature control systems connections

If the pressure exceeds the defined limit, the CAREL supervisory controller will trigger the pressure safety switch and immediately stop the servo movement. It will also cut the power supplied to the cartridge heaters. Vice versa, if the temperature exceeds the defined set point, the controller will cut off the heat supplied to the cartridge heaters and will trigger the pressure safety switch which will stop the servo movement. This gives additional precautions to ensure that neither pressure nor temperature will exceed the maximum limits.

#### **4.2.4 Operational Manuals**

Operational manuals with technical details are available for most of the main parts of the apparatus. This include operation and maintenance manuals for the Quizix pumps, user manual for the PumpWorks software, operational manual for the servo control system, operation and configuration manuals for the Eurotherm and Carel controllers, configuration manual for the Agilent acquisition and switch unit 34901A, and instruction manuals for the chiller, magnet motor, electrical actuator valves, and the CCD camera. In addition, electronic manuals exist as well regarding the use of the motion perfect 2 software, the use of the Agilent VEE programming and so on. These manuals should be carefully considered prior the operation of this apparatus. In line with the present study, a general manual will be developed in the future for the entire apparatus to enable users of this apparatus to operate it easily. This, together with safety considerations and maintenance records will be carefully documented [176].

### **4.3 Health, Safety and Environment (HSE)**

A detailed risk assessment has been carried out following the college safety procedure to ensure safe operation of the entire apparatus. The major hazard is that of over pressurization of the system which might lead to very serious issues such as damage of the vessel, breakage of the sapphire windows and possible personnel injuries. Careful attention is required in dealing with incompressible liquids as a small change of volume will rapidly increase the pressure to very high values. A safety head is attached to the cell with a rupture disk rupturing at 50 MPa to protect the cell from over pressurization. In addition, the pressure transducer is connected to a controller module (CAREL) which will cut the power and immediately stop the servo motor whenever the predefined pressure set point is exceeded. Limit switches are used to ensure that the piston will not reach the static sapphire window. A poly carbonate sheets are placed around the high pressure system to prevent injuries to personnel in case of blow up of one or more of the parts as a result of over pressurization. The safety head is also connected to a 1/8" SS tube to dispose the mixture to a safe area whenever the rupture disk brakes.

Another major possible hazard is the over-heating where the maximum working temperature of the cell is 473 K. Over-temperature may damage the vessel, the sapphire window, the sealing system and may cause fire or personnel injuries. Two temperature controller modules are used to ensure the cut of the power supplied to the heaters used whenever it exceeds the predefined set point.

A check valve is used downstream of the CO<sub>2</sub> cylinder to prevent any back pressure from the high pressure system. The line connecting the high pressure outlet vessel stream and vacuum pump is also protected by over pressure relief valve. This is to prevent over-pressurization of the vacuum pump inlet which, if over pressurized, might lead to dangerous consequences. Other possible hazards (minor) are the exposure to hot surfaces, escape of hot and flammable fluids, gas bottle falling and electrical shocks. These hazards are prevented by using continuously audible warning and signage. A discharge lines to suitable containers are used to dispose the mixtures. Gas cylinders are restrained with clamps and all socket/plugs are off the floor and clear of water with complete testing of all electrical connections.

In Appendix B, a summary of the hazards and the precaution implanted is described, with referring to the experimental general procedure steps listed in that Appendix. The hazards and risks are identified following a safety critical system analysis (SCSA) which is based on hazards analysis, where the system is examined for potential to cause harm, and risk analysis, where the system is examined for potential damage which may occur because of the presence of the hazards. Recommended control measures are described and implemented in the present work.

#### 4.4 Materials

Pure deionised and degassed water (electrical resistivity > 18 MΩ·cm at  $T = 298.15$  K) was used. Carbon dioxide was supplied by BOC with a mole fraction purity higher than 0.99995, and was used as supplied. All liquid hydrocarbon components were supplied by Sigma-Aldrich and were used as supplied. The mole fraction purity of *n*-heptane, methylbenzene and *n*-hexane were  $x = 0.990$ ,  $x = 0.998$  and  $x = 0.950$ , respectively. The mole fraction purity  $x$  of the components used in preparing the synthetic oil were as follows: 2,2-dimethylbutane > 0.99, ethylcyclohexane > 0.99, 1,2,3,4-tetrahydronaphthalene > 0.99, 1,3,5-triethylbenzene > 0.97, hexadecylbenzene > 0.97, 1-phenyloctane > 0.98, *n*-hexadecane > 0.99, 1-phenylhexane > 0.97, *n*-nonadecane > 0.99, *n*-nonane > 0.99, *n*-octadecane > 0.99, *n*-pentadecane > 0.99, propylcyclohexane > 0.99, tetracosane > 0.99, *n*-tridecane > 0.99, and

squalane > 0.99. The hydrocarbon gas mixture (0.813 CH<sub>4</sub> + 0.126 C<sub>2</sub>H<sub>6</sub> + 0.061 C<sub>3</sub>H<sub>8</sub>) was supplied by BOC who prepared it to our specification from gases having a minimum mole-fraction purity of 0.99. No analysis or purification was attempted.

#### 4.5 Experimental Procedure and Calculations

The hydrocarbon liquid mixtures were prepared gravimetrically at ambient pressure and temperature and in a sufficient quantity for the entire study. In the case of synthetic dead oil, some heavy components, such as hexadecylbenzene, were solid at ambient temperature but the entire mixture formed a stable homogenous liquid after mixing at ambient temperature. Starting from a clean and evacuated system, gases and liquids were introduced into the syringe pumps through valves V-9 and V-10 respectively. The pump cylinders were maintained at constant temperature, usually  $T = 283.15$  K. The liquid or gas inside each pump was pressurized to a reference pressure, the value of which depended upon the experimental conditions, both before and after the injection of fluid into the equilibrium cell. In this way, the mass of fluid introduced in each injection step could be obtained from the syringe displacement and knowledge of the density at the pump temperature and pressure. For the synthetic dead oil and the binary liquid mixture (*n*-heptane + methylbenzene) reference pressure was always 1 MPa. The reference pressure for the solution gas was 10 MPa, while the reference pressure for CO<sub>2</sub> was adjusted as needed to match the experimental conditions.

Initially, a measured amount of liquid was injected into the cell through valve V-20. For the studies of live synthetic oil, this was followed by: (a) injection of the desired amount of solution gas; and (b) replacement of solution gas in the relevant syringe pump by pure CO<sub>2</sub>. Next, measured amounts of CO<sub>2</sub> was introduced into the cell and, after each injection of CO<sub>2</sub>, valve V-20 was closed. Each injection had the effect of pushing the fluid previously in the connecting tubing into the cell. In order to achieve high mole fractions of CO<sub>2</sub>, it was sometimes necessary to expel some of the mixture and to replace it by additional CO<sub>2</sub>. In these cases, the mixture was first brought into a measured homogeneous state and the desired amount pushed out by driving the piston forward while allowing sample to flow out through V-20 and V-19. The amount expelled in this way was calculated from the swept volume. The overall composition of the system could be calculated at every stage of the experiment from the cumulative amounts of liquid, solution gas and CO<sub>2</sub> introduced from the pumps, the amounts and composition of homogenous mixture expelled from the system, and the amount and composition of the fluid remaining in the connecting tubing. Same procedure was applied for the studies of CO<sub>2</sub> with dead synthetic oil and (*n*-heptane + methylbenzene)



liquid mixture. In this case, no solution gas was added and the CO<sub>2</sub> was introduced into the cell after desired amount of liquid was injected.

The dead volumes considered were those in the tubing between syringe pumps and the cell, and between the cell and valve V-22, as well as the volumes within V-19, V-20, V-22, and the pressure transducer. The safety head (V-21) was considered as part of the cell volume as it communicated reasonably freely with the interior of the cylinder. The amounts  $n_{\text{CO}_2}$  of CO<sub>2</sub> and  $n_{\text{HC}}$  of total hydrocarbons prior to expulsion of any material were determined from the following relations:

$$n_{\text{CO}_2} = M_{\text{CO}_2}^{-1} \left[ \sum_{k=1}^{N_k} \rho_{\text{CO}_2}(T_{\text{inj}}, p_{\text{inj}}) V_k - \sum_{l=1}^{N_l} \rho_{\text{CO}_2}(T_{\text{dead}}, p_{\text{dead}}) V_l \right] \quad 4.1$$

$$n_{\text{HC}} = M_{\text{L}}^{-1} \left[ \sum_{k=1}^{N_k} \rho_{\text{L}}(T_{\text{inj}}, p_{\text{inj}}) V_k - \sum_{l=1}^{N_l} \rho_{\text{L}}(T_{\text{dead}}, p_{\text{dead}}) V_l \right] + M_{\text{G}}^{-1} \left[ \sum_{k=1}^{N_k} \rho_{\text{G}}(T_{\text{inj}}, p_{\text{inj}}) V_k - \sum_{l=1}^{N_l} \rho_{\text{G}}(T_{\text{dead}}, p_{\text{dead}}) V_l \right] \quad 4.2$$

Here, the summations over  $k$  refer to  $N_k$  sequential injections from the syringe pumps and the summations over  $l$  refer to the  $N_l$  sections into which the dead volume was divided; these sections may contain different fluids at different times depending upon the sequence of injections. Additionally, subscripts “inj” and “dead” refers to the conditions in the syringe pumps and the dead volumes respectively, and subscripts L and G refer to the hydrocarbon liquid and gas mixtures, respectively, that were injected into the cell. Following the expulsion of volume  $\Delta V$ , starting from an initial cell volume of  $V_0$ , the amounts of CO<sub>2</sub> and hydrocarbon present in the cell were both modified by the factor  $(1 - \Delta V / V_0)$  and the above equations were used to obtain the additional amounts of CO<sub>2</sub> and hydrocarbon (if any) following subsequent injections.

Following the injection of components, V-20 was closed and the pressure inside the cell was adjusted by moving the piston until one homogenous phase was obtained. The system was then left to equilibrate under stirring. The time required to achieve thermodynamic equilibrium, as determined from pressure measurements at constant temperature and volume, was typically about one hour under continuous stirring. The pressure was then decreased in small decrements, each followed by a further equilibration period, while simultaneously recording temperature, pressure and volume, and observing the state of the system. This process continued until the appearance of a second phase. If necessary, the pressure was raised again and the phase boundary approached in smaller decrements. In some cases, the disappearance of a phase was measured during isothermal compression

steps. It was found that bubble- or dew-points determined with increasing or decreasing pressure agreed to within 0.1 to 0.2 MPa, which is within the uncertainty of the measurements. Usually, after observing a bubble- or dew-point, additional CO<sub>2</sub> was injected and a new measurement initiated.

Visual observation through the CCD camera was the primary means of detecting phase changes. At low pressures, there was also an abrupt change in slope of pressure versus volume when passing through a bubble point and this coincided closely with the results of visual observations. The sensitivity of the pressure-volume plot became unfavourable at high pressures and, especially, close to a critical point.

## **4.6 Calibration and Uncertainty Analysis**

The Pt100 thermometer used to measure the cell temperature was calibrated at temperatures in the range (273 to 473) K by comparison in a constant-temperature bath with a standard platinum resistance thermometer having an expanded uncertainty of 2 mK in the present temperature range. The extent of axial temperature gradients in the phase-equilibrium cell was checked by locating the sensor at different depths inside the thermowell: the differences were within  $\pm 0.03$  K. Taking calibration uncertainty, sensor drift, fluctuations and temperature gradients across the equilibrium cell into account, we estimate that the overall standard uncertainty of the cell temperature measurements was 0.04 K. The Pt100 sensors used to measure the temperature of the fluid in the syringe pumps was not calibrated. Based on the manufacturing tolerance, the standard uncertainty of the pump temperature was taken to be 0.25 K.

The pressure transducers fitted to the syringe pumps were calibrated at pressures in the range (1 to 70) MPa by comparison with a quartz pressure sensor in a pneumatic calibrator (Fluke-DHI model PPCH-G-70M). It is estimated that the standard uncertainty of the pressure transducer after calibration was 17.5 kPa (0.025 % of the full scale reading). The pressure transducer used to measure the sample pressure was calibrated against a hydraulic pressure balance (DH-Budenberg model 580EHX) having standard relative uncertainty of 0.004 %. In the calibration, the transducer exhibited good linearity and a lack of hysteresis, leading to a standard uncertainty of 6 kPa. However, this sensor did drift over time and corrections were required. For this purpose, the reading was checked at ambient pressure prior to each experiment and any difference was applied as a constant offset to correct subsequent readings in that run. Taking all factors into account, the standard uncertainty of the experimental pressure was estimated to be 35 kPa.

Since the syringe pumps were used for quantitative injections of the components, they were carefully calibrated using deionised and degassed water. The water displaced by the syringe at a referenced pressure and temperature was collected and weighed on an analytical balance with a resolution of 0.001 g. The mass collected in this way was compared with that calculated from the displaced volume recorded by the syringe pump using water densities  $\rho_w$  computed from the IAPWS-95 EoS developed by Pruss and Wagner [177]. The calibration was broken down into several steps for a full cycle of each syringe and the whole process was repeated two or more times. A linear relationship between volume displaced and actual volume was established for the liquid and gas syringes, respectively, as follows:

$$V_{\text{inj}} = 0.9982 \cdot V_{\text{dis}} \quad 4.3$$

$$V_{\text{inj}} = 0.9977 \cdot V_{\text{dis}} \quad 4.4$$

Here, subscripts “inj” and “dis” refers to the actual volume injected into the cell and the displaced volume indicated by the pump respectively.

Throughout this article, standard uncertainties for experimental quantities are determined using the *Guide to the Expression of Uncertainty in Measurements* (GUM) [178], according to which the standard uncertainty  $u(f)$  of a quantity  $f(x_1, x_2, \dots, x_n)$  is obtained from

$$u^2(f) = \sum_{i=1}^n \sum_{j=1}^n \frac{\partial f}{\partial x_i} \frac{\partial f}{\partial x_j} u^2(x_i, x_j) \quad 4.5$$

Here,  $x_i$  and  $x_j$  represent pairs of input variables from which  $f$  is to be evaluated,  $(\partial f / \partial x_i)$  is the sensitivity coefficient of  $f$  with respect to  $x_i$ , and  $u^2(x_i, x_j)$  is the covariance ( $i \neq j$ ) or the variance ( $i = j$ ) for variables  $x_i, x_j$ . Usually, only the diagonal terms in Eq. (4.5) are ( $i = j$ ) retained and we abbreviate  $u^2(x_i, x_i)$  as  $u^2(x_i)$ . Where appropriate, expanded uncertainties are obtained by multiplying the standard uncertainty  $u(f)$  by a coverage factor  $k$ .

In the case of the calibrated volume injected from a syringe pump, the combined standard uncertainty  $u(V_{\text{inj}})$  is given by

$$u^2(V_{\text{inj}}) = \left[ \left( \frac{1}{\rho_w(T_{\text{inj}}, p_{\text{inj}})} \right)^2 u^2(m) + \left( \frac{-\Delta m}{\rho_w^2(T_{\text{inj}}, p_{\text{inj}})} \right)^2 u^2(\rho_w(T_{\text{inj}}, p_{\text{inj}})) \right], \quad 4.6$$

where

$$u^2(\rho_w(T_{inj}, p_{inj})) = \left[ \left( \frac{\partial \rho}{\partial T} \right)^2 u^2(T_{inj}) + \left( \frac{\partial \rho}{\partial p} \right)^2 u^2(p_{inj}) + u^2(\text{EoS}) \right] \quad 4.7$$

The uncertainty of the water density is determined by the uncertainties of the syringe temperature and pressure (given above) and, in principle, by the uncertainty  $u(\text{EoS})$  associated with the EoS of water; however, the latter is negligible under the conditions of our calibration. From Equation 4.7, the standard relative uncertainty of  $\rho_w$  was found to be 0.01 %. The uncertainty of the weighing itself was very small ( $< 1$  mg) but the true uncertainty of the mass  $m$  of collected water is larger because of the drop-wise nature of the flow. The uncertainty in the mass was therefore taken to be the mass of one collected drop (estimated as 5 mg) and, from Equation 4.6, the final standard relative uncertainty of the volumes was found to be 0.1% for both cylinders.

The volume of the equilibrium cell was also calibrated, as shown in Figure 4.8, using deionised and degassed water, in this case making use of one of the calibrated syringe pumps to inject known amounts. The lines from the syringe pumps were first filled up to the closed valve V-20, and the branch to V-19 was plugged at this time. Thus the dead volumes associated with the calibration were those in the filling line beyond V-20, including the pressure transducer, and in the discharge line as far as V-22. These volumes combined amounted to  $V_{\text{dead}} = (0.18 \pm 0.01) \text{ cm}^3$ . The cell was calibrated at different temperatures and positions of the piston to establish a relationship between piston position and total cell volume. At each calibration point, the cell was filled with water injected from a syringe pump held at a reference pressure of 1 MPa and a reference temperature of 283.15 K and the cell volume was calculated as follows:

$$V_{\text{cell}} = \frac{\rho_w(T_{inj}, p_{inj})V_{inj} - \rho_w(T_{\text{dead}}, p_{\text{dead}})V_{\text{dead}}}{\rho_w(T_{\text{cell}}, p_{\text{cell}})} \quad 4.8$$

From these calibration measurements, a linear relationship was established between cell volume and the piston displacement  $L$  measured from the home position (maximum retraction) at each temperature. The effect of temperature was also found to be linear the calibration data were fitted by the following simple Equation

$$V_{\text{cell}} = V_0(1 - cL)[1 + \alpha_v(T - T_0)], \quad 4.9$$

in which  $T_0 = 323.15$  K and  $\alpha_v = 36 \cdot 10^{-6} \text{ K}^{-1}$  was assumed equal the mean volumetric expansivity of Hastelloy HC-276 [179]. The fitted parameters were  $V_0 = 67.19 \text{ cm}^3$  and

$c = 0.007414 \text{ mm}^{-1}$ , and the standard deviation of Eq. (4.9) was  $0.029 \text{ cm}^3$  or 0.13 % of the minimum cell volume. The extent of mechanical backlash was also considered by repeating calibration measurements at the same temperature and theoretical volume with the piston extending and retracting; the volumes were found to be repeatable to within  $\pm 0.02 \text{ cm}^3$ , which is within the standard deviation of Eq. (4.9).

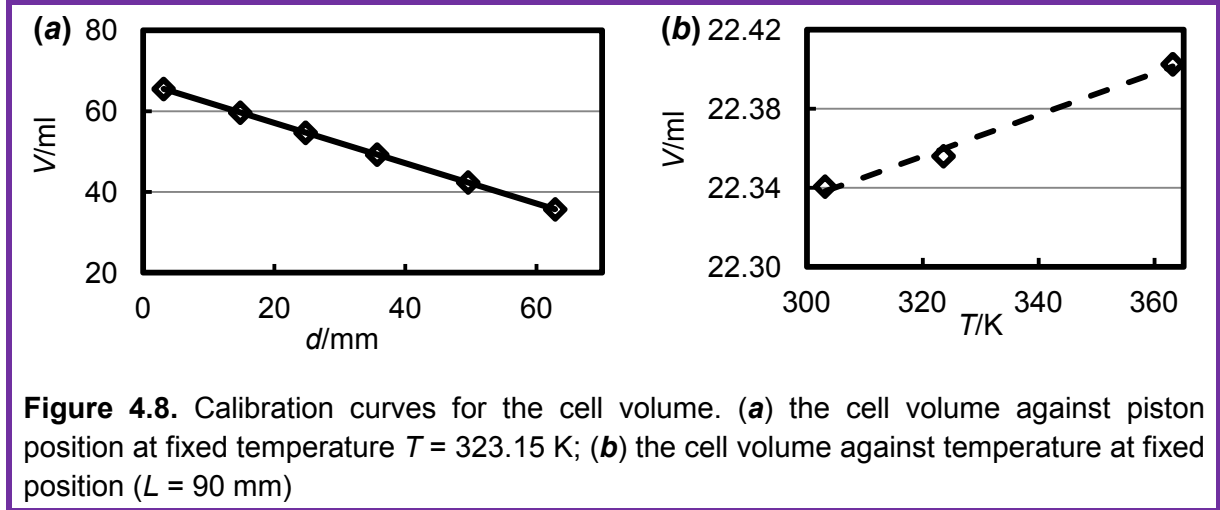


**Figure 4.8.** Calibration curves for the cell volume. (a) the cell volume against piston position at fixed temperature  $T = 323.15 \text{ K}$ ; (b) the cell volume against temperature at fixed position ( $L = 90 \text{ mm}$ )

To estimate the uncertainty of the calibrated cell volume at constant temperature, the contribution associated with each input quantity appearing in Equations (4.8) was determined as follows:

$$u^2(V_{\text{cell}}) = \left[ \left( \frac{1}{\rho_w(T_{\text{cell}}, p_{\text{cell}})} \right)^2 u^2(m_{\text{total}}) + \left( \frac{-m_{\text{total}}}{\rho_w^2(T_{\text{cell}}, p_{\text{cell}})} \right)^2 u^2(\rho_w(T_{\text{cell}}, p_{\text{cell}})) \right], \quad 4.10$$

where the standard uncertainty of the total mass of water inside the cell was given by

$$u^2(m_{\text{total}}) = V_{\text{inj}}^2 \cdot u^2(\rho_w(T_{\text{inj}}, p_{\text{inj}})) + [\rho_w(T_{\text{inj}}, p_{\text{inj}})]^2 u^2(V_{\text{inj}}) + V_{\text{dead}}^2 \cdot u^2(\rho_w(T_{\text{dead}}, p_{\text{dead}})) + [\rho_w(T_{\text{dead}}, p_{\text{dead}})]^2 u^2(V_{\text{dead}}) \quad 4.11$$

The standard relative uncertainty of  $m_{\text{total}}$  was found from Eq. (4.11) to be 0.15 % and the standard relative uncertainty of the cell volume was then determined to be 0.18 % from Eq. (4.10). Taking into account also an estimated 20 % relative uncertainty in the volumetric expansivity, we obtain an overall relative standard uncertainty in the cell volume, of 0.2 %.

The uncertainty of the mass of fluid injected into the cell from syringe  $i$  depends on the uncertainty of the mass expelled from the syringe pump and the uncertainty of any dead volume correction required. The calculation of the dead volume correction for each fluid

depends on the mode of operation, the order in which fluids were injected, and the pressure and temperature conditions. The following Equation was used to calculate the combined standard uncertainty of the calculated mass  $m_i$  of the fluid injected from syringe  $i$ :

$$u^2(m_i) = V_{i,inj}^2 \cdot u^2(\rho_{i,inj}(T_{i,inj}, p_{i,inj})) + [\rho_{i,inj}(T_{i,inj}, p_{i,inj})]^2 u^2(V_{i,inj}) + V_{i,dead}^2 \cdot u^2(\rho_{i,dead}(T_{i,dead}, p_{i,dead})) + [\rho_{i,dead}(T_{i,dead}, p_{i,dead})]^2 u^2(V_{i,dead}) \quad 4.12$$

The uncertainty of the density varies widely depending on the fluid and the available data at the pump conditions. For CO<sub>2</sub>, the density was obtained from the EoS of Span and Wagner [180] with an estimated relative uncertainty of between 0.03 % to 0.05 % (which we interpret as an expanded uncertainty with coverage factor  $k = 2$ ). For the sake of simplicity, we ascribe the value 0.025 % to the standard relative uncertainty of the CO<sub>2</sub> density. The density of the gas mixture was obtained from the GERG-2008 model of Kunz and Wagner [181] with an estimated standard relative uncertainty of 0.05 %. The densities of the synthetic dead oil liquid was measured at ambient pressure and different temperatures using an Anton Paar DMA 5000 densimeter calibrated at that temperature with ambient air and pure water. The relative estimated uncertainty was estimated to be 0.001 %. This measured density was applied, without correction for pressure changes, in the calculation of the amount of liquid injected. The syringe pump was operated at a reference pressure of 1 MPa and so the effect of compressibility would have been small. For example, if the liquid were *n*-heptane then the density change between pressures of 0.1 MPa and 1.0 MPa would be 0.8 kg·m<sup>-3</sup> [182]. Since the dead volume filled by the synthetic oil was very small, we also applied the same density there with a negligible effect on the final mole fraction uncertainty. The liquid hydrocarbon mixture (*n*-heptane + methylbenzene) density was obtained from the experimental data reported in the reference [183] where vibrating tube densimeter (DMA 60 Fa, Anton Paar) was used. The estimated relative uncertainty in the density ranges from 0.023 % to 0.057 % (which we interpret as an expanded uncertainty with coverage factor  $k = 2$ ) and for the sake of simplicity; we ascribe the value 0.029 % to the standard relative uncertainty of the liquid hydrocarbon density.

Considering all factors, the standard relative uncertainty of the mass injected from each syringe varied from 0.11 % to 0.15 % depending on the fluid injected. For the sake of simplicity, we ascribe the larger value of 0.15 % to all cases. The mole fraction  $x_{CO_2}$  of CO<sub>2</sub> in the system was calculated from the simple expression:

$$x_{CO_2} = \frac{n_{CO_2}}{n_{CO_2} + n_{HC}}, \quad 4.13$$

where  $n$  denotes amount of substance and subscripts CO<sub>2</sub> and HC denote CO<sub>2</sub> and total hydrocarbons. The standard uncertainty of  $x_{\text{CO}_2}$  which follows from this expression is

$$u^2(x_{\text{CO}_2}) = [x_{\text{CO}_2}(1 - x_{\text{CO}_2})]^2 [u_r^2(n_{\text{CO}_2}) + u_r^2(n_{\text{HC}})], \quad 4.14$$

where  $u_r$  denotes relative standard uncertainty. With  $u_r(x_{\text{CO}_2}) = u_r(x_{\text{HC}}) = 0.0015$ , identical with the standard relative uncertainty of the masses, the standard uncertainty of the mole fraction turns out to be  $0.0021x_{\text{CO}_2}(1 - x_{\text{CO}_2})$ .

The uncertainty of the bubble- and dew-pressures depends on both the subjective uncertainty in observing the bubble- or dew-point condition and the uncertainty of the pressure measurement itself. Except in the critical region, bubble points were easily observed visually during isothermal compression and these observations also coincided closely with an abrupt change in slope of pressure against volume. Dew points were generally more difficult to observe by this method and were only measured at high pressures. Close to the critical point, it became more difficult to detect bubble- or dew-point conditions. Nevertheless, the repeatability of the bubble- and dew-pressures was found to be (0.1 to 0.2) MPa. Considering both this and the uncertainty of the pressure measurements, the standard uncertainty of the bubble pressures  $p_b$  were estimated to be 0.1 MPa for  $p_b \leq 25$  MPa and 0.15 MPa for  $p_b > 25$  MPa at all temperatures, while the standard uncertainties of the critical pressure and of dew pressures  $p_d$  were estimated to be 0.15 MPa at  $T \leq 373.15$  K and 0.2 MPa at  $T > 373.15$  K.

Finally, the standard relative uncertainty of the homogeneous phase density was found to be 0.4 %., deduced from the relation

$$u^2(\rho_m) = \left(\frac{1}{V_{\text{cell}}}\right)^2 u^2(m_{\text{total}}) + \left(\frac{-m_{\text{total}}}{V_{\text{cell}}^2}\right)^2 u^2(V_{\text{cell}}) \quad 4.15,$$

## 4.7 Apparatus Validation

Several validation experiments were conducted to test the apparatus. The vapour pressure of CO<sub>2</sub> was measured at  $T = 298.15$  K and found to be 6.394 MPa, which is 0.04 MPa below the value obtained from the EoS of Span and Wagner. The phase behaviour of the binary mixture (CO<sub>2</sub> + *n*-heptane) was measured at  $T = 394.15$  K. The density of CO<sub>2</sub> was obtained as described above while the density of *n*-heptane was obtained using the EoS of by Span and Wagner [182] which is associated with a relative uncertainty of 0.2% at the injection

conditions. The results obtained are presented in Table 4.3 and Figure 4.9. The results were compared with the available literature data reported by Mutelet et al. [184], Kalra et al. [185], and Inomata et al. [186] at this temperature and they are in good agreement with all available data. The CO<sub>2</sub> density was also measured at different conditions and compared with the EoS of Span and Wagner [180]; the absolute relative deviations were less than 1 % except close to the critical point.

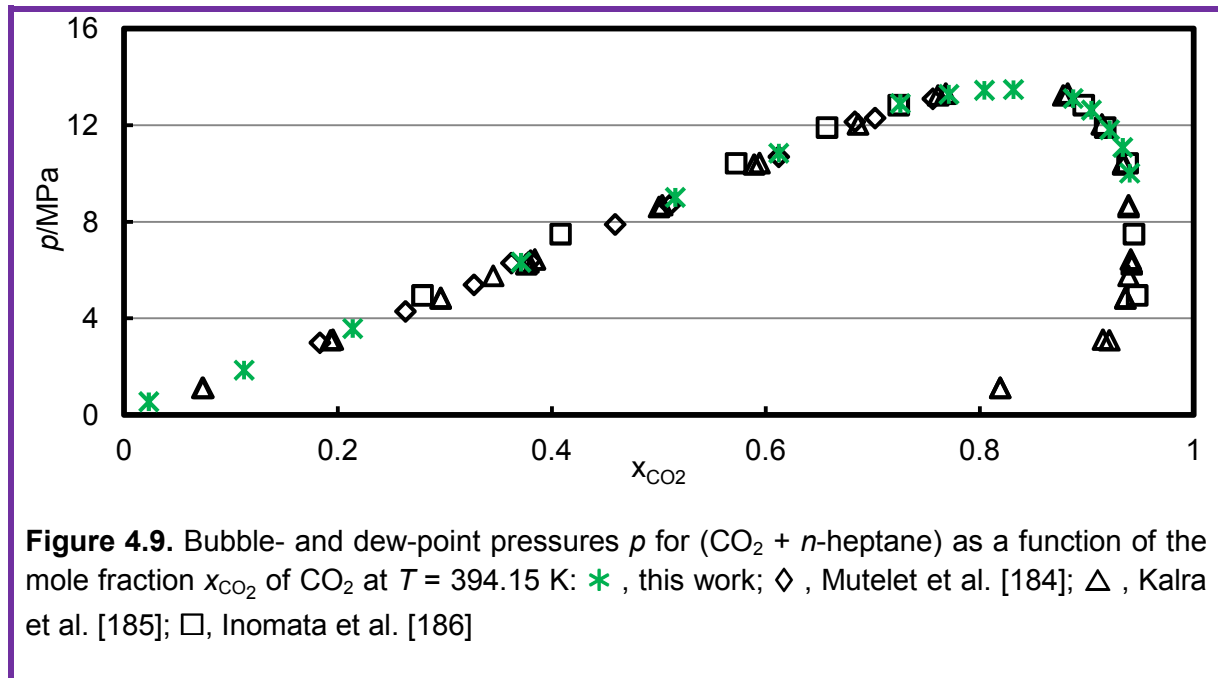


**Table 4.3.** Bubble and dew experimental points obtained in this work for the binary mixture (CO<sub>2</sub> +  $n$ -heptane) at  $T = 394.15$  K.<sup>a</sup>

$p/\text{MPa}$	$x_{\text{CO}_2}$	Status	$p/\text{MPa}$	$x_{\text{CO}_2}$	Status
0.56	0.0230	bubble	13.45	0.8042	bubble
1.87	0.1121	bubble	13.48	0.8314	bubble
3.59	0.2136	bubble	13.11	0.8873	dew
6.34	0.3711	bubble	12.63	0.9043	dew
9.02	0.5153	bubble	11.82	0.9213	dew
10.85	0.6120	bubble	11.09	0.9336	dew
12.90	0.7256	bubble	10.02	0.9400	dew
13.29	0.7710	bubble			

<sup>a</sup> Expanded uncertainties are  $U(T) = 0.08$  K,  $U(p) = 0.2$  MPa and  $U(x_{\text{CO}_2}) = 0.0042x_{\text{CO}_2}(1 - x_{\text{CO}_2})$ , with coverage factor  $k = 2$ .



## 4.8 Apparatus Maintenance

The apparatus should be periodically checked. This should include, for example, testing the safety cuts of the pressure and temperature controllers, limit switches and possible leakage from different items such as Quizix pumps, sapphire window and the cell sealing system. The relieve valve before the vacuum pump and the software limits implemented in the Agilent VEE written programs should be regularly checked. A regular inspection for any sign of corrosion or electrical failure should be always considered.

Regular inspection of the servo control system should be considered. This should be carried out by visual inspection of the control panel, clean out any dust and debris inside the control panel, check that all LED bulbs work, and replace any that have blown, functional testing of all emergency stop buttons and pressure switch to ensure they are operating correctly, and are not stuck. Should any component fail in this circuit, the equipment must be taken out of service until it has been replaced, Inspection of all cables and electrical equipment to ensure there is no damage, and that the screen and earth wire are securely fitted. Damaged parts should be replaced to avoid risk of electric shock and incorrect operation, all covers and gland-plates should also be inspected to ensure they are securely fitted, and there are no open holes in the control cabinet.

## 4.9 Summary

The details of a new experimental synthetic apparatus designed and constructed have been presented in this Chapter. The apparatus was designed to measure phase equilibria at high pressure and high temperature conditions. The apparatus was almost fully controlled to ensure a user-friendly and smooth operation. The apparatus was calibrated and validated by comparison with published isothermal vapour-liquid equilibrium data for the binary system ( $\text{CO}_2 + n$ -heptane). The apparatus was used to measure the phase equilibrium of ( $\text{CO}_2 + n$ -heptane + methylbenzene) and ( $\text{CO}_2 + \text{synthetic crude oil}$ ) mixtures. Results of these systems are provided in Chapters 6 and 7.

## Chapter 5: Analytical Apparatus for Fluid Phase Equilibrium Measurements

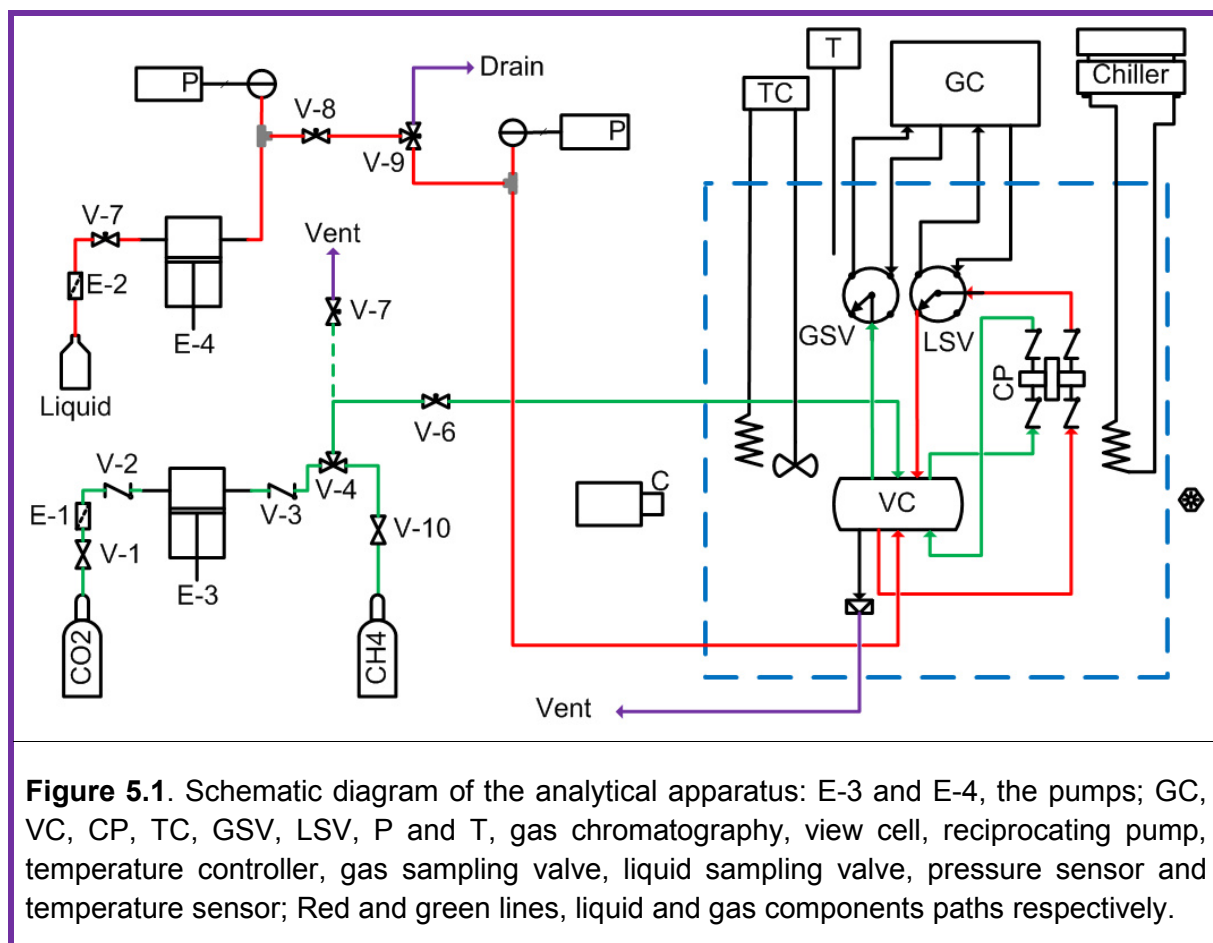
In applications where the formation of more than two phases is expected, an analytical technique is desired. While synthetic apparatus can only measure pressure and temperature conditions at which more than two phases region occur, the analytical apparatus measures the composition of each component present in these phases. In the present work, a quasi-static-analytical apparatus to measure phase equilibria of ( $\text{CO}_2 + n\text{-heptane} + \text{water}$ ) and ( $\text{CO}_2 + \text{methane} + \text{water}$ ) is presented. The measurements included VLE, VLLE, UCEP and quadruple curve along which hydrates coexists with the three fluid phases. The equipment design, setup, control and operation was previously described in detail by Esther Forte [87, 187], who designed and constructed the original system. In this Chapter, a summary of the experimental setup is only given. The calibration of the apparatus together with the experimental procedure, validation measurements and uncertainty analysis is presented.

### 5.1 Apparatus Design

Here only a summary is given and the reader is referred to the references mentioned above for the detailed description of this apparatus. The analytical technique used in the present study was slightly modified by installing a timed events board (PRG-2010 Aux for GC model GC-2014, Shimadzu, Shimadzu Scientific Instruments, Inc) which allowed for the automation and program control of the sampling valves. The main components, as schematically shown in Figure 5.1, are a high pressure equilibrium cell, a magnetically coupled reciprocating pump, electronically-actuated sampling valves (Cheminert, model C2-2206EH3Y, and Valco, model DCI4UWT1Y, VICI AG International), a gas chromatograph (Shimadzu, model GC-2014, Shimadzu Scientific Instruments, Inc.), and a temperature controller system.

The reciprocating pump was used to provide representative samples in the sampling loop. The equilibrium cell was made from type 17-4PH martensitic stainless steel with a nominal internal volume of  $35 \text{ cm}^3$  and equipped with two diametrically-opposite sapphire windows that enabled visual observation of the interior. The gas chromatograph (GC) was equipped with three detectors in series, a dual thermal conductivity detector (TCD) connecting both analytical lines and two flame ionisation detectors (FID). The TCD was used for the detection of  $\text{CO}_2$  and  $\text{H}_2\text{O}$ , while FID detectors were used for the detection of the hydrocarbons. A HayeSep Q column with 80/100 mesh was used for the separation and analysis of all components. During sampling, the components are vapourised in the injector, transported to the column by the carrier gas, where they experience a certain retention based on their

volatility and polarity, and then eluted to the detectors where their quantities are finally analysed.



The tubes connecting the samples to the GC was heated by means of low voltage mineral insulated heater cables coupled with k type thermocouple temperature sensors and temperature PID controllers. A manual syringe pump (Sitec model 750.110, SITEC-Sieber Engineering AG) was used for the injection of liquid components while an automatic syringe pump (Teledyne Isco, model 100DM, Teledyne Technologies Inc.) was used for the injection of carbon dioxide. The methane was injected using the pressure regulator attached to the cylinder. The valves V-4, V-7 and V-9 shown in Figure 5.1 were used for the purposes of flushing, draining and venting of the system. The temperature was controlled using oil bath filled with silicon, controller unit and stirrer. The bath was equipped with two double-glazed windows, at the front and back, which were aligned with the sapphire windows of the cell. A coil connected to an additional external circulating bath (Huber model CC1, Huber Kältemaschinenbau GmbH) was used to provide refrigeration when working at temperatures near or below ambient.

Back illumination with an LED light source fitted with and a camera in front mounted on an optical rail facilitated the observation of the inside of the cell. The temperature was measured by means of a platinum resistance thermometer (PRT) located in the bath close to the equilibrium cell. The pressure was measured using a pressure transducer (Digiquartz model 410KR-HT-101, Paroscientific Inc.) connected to the liquid inlet line through valve V-9. Prior to use, the system was thoroughly leak tested in the whole pressure range; it exhibited a high-level of integrity. The system was also checked for leakage during the course of measurements.

## 5.2 Materials

The carbon dioxide used in this work was CP graded supplied by BOC with a mole fraction purity  $x$  higher than 0.9999. The carrier gas used was CP graded helium from BOC with purity higher than 0.9999. The water used was deionised to an electrical resistivity greater than 18 M $\Omega$ -cm at 298 K. The methane was supplied by BOC and was of low ethylene grade with mole fraction purity higher than 0.9999. The air and hydrogen was also supplied by BOC with mole fraction purities higher than 0.950 and 0.999 respectively. The *n*-heptane, *n*-hexane and tetrahydrofuran were supplied by Sigma Aldrich with mole fraction purities of 0.970, 0.970 and 0.999 respectively. No further purification was attempted.

## 5.3 Experimental Procedure

The apparatus was initially cleaned with solvents, flushed with CO<sub>2</sub> and subjected to vacuum. Then hydrocarbon liquid (*n*-heptane) was initially loaded into the cell through the manual pump E-4 and valve V-9 until it covers roughly third of the total volume of the cell. Then water was introduced slowly until two phases (water-rich phase and hydrocarbon-rich phases) occupying approximately the two third of the cell formed. Then CO<sub>2</sub> was introduced slowly to the cell using the Isco pump E-3 and valve V-4 until the existence of three phases (Water-rich phase, hydrocarbon-rich liquid phase and CO<sub>2</sub>-rich gas phase). When hydrocarbon gas (methane) is used, water was initially loaded until it occupied approximately one third of the cell volume. Then CO<sub>2</sub> was introduced slowly to the cell until the existence of three phases. Then, methane was introduced slowly through valve V-4 until the pressure was slightly above the saturated vapour pressure of CO<sub>2</sub> at the given temperature.

The system was then left for at least two hours to equilibrate using the circulation pump. After that, the vapour phase was firstly sampled using the gas sampling valve (GSV). The water-rich phase was sampled next by means of the liquid sampling valve (LSV), and finally the cell was tilted to allow sampling of the middle-rich phase with the same valve (LSV).

Then more CO<sub>2</sub> or methane was added to increase the pressure for another measurement. For each phase sampled, at least five or six samples were taken to ensure reproducibility<sup>8</sup> when there was no evidence of cross contamination or entrainment of one phase in the other during sampling or any sign of leakage. The upper critical end point (UCEP) was measured at a pressure around 0.01 to 0.02 MPa above the UCEP pressure by injecting water. The operating conditions of the GC used in the measurements of (CO<sub>2</sub> + *n*-heptane + water) and (CO<sub>2</sub> + methane + water) are listed in Table 5.1

**Table 5.1.** Gas chromatography conditions for the analysis of the studied mixtures.<sup>a</sup>

System	Injector		Column		TCD		FID	
	$\dot{V}/\text{cm}^3\text{s}^{-1}$	<i>T</i> /K	<i>T</i> /K	<i>T</i> /K	<i>I</i> /mA	<i>T</i> /K	$\phi$	
CO <sub>2</sub> + methane + water	40	423.15	343.15	523.15	90	523.15	1:10	
CO <sub>2</sub> + heptane + water	40	423.15	383.15	523.15	90	523.15	1:10	

<sup>a</sup> TCD = thermal conductivity detector, FID = flame ionization detector,  $\dot{V}$  = He flow rate, *I* = current,  $\phi$  = H<sub>2</sub>/air flow ratio.

During VLE measurements, same procedure was used. In this case, the molar ratio between CO<sub>2</sub> and CH<sub>4</sub> in the gas phase was kept roughly fixed at around  $y = 0.5$  in the (CO<sub>2</sub> + methane + water) measurements. This ratio was monitored by sampling the vapour phase until correct ratio was achieved.

Pressure and temperature conditions at which hydrates coexist with the three fluid phases were measured for (CO<sub>2</sub> + methane + water) system. In these measurements, the system was initially in the three phase region. Then temperature was cooled until the formation of hydrates which was observed visually. The system was then left for at least 24 hours to overcome the metastable period and allow complete hydrate formation. Temperature was then slowly increased in steps and a pressure-temperature curve was continuously monitored. The point at which the slope of pressure-temperature data plots changes sharply was considered to be the point at which the hydrate crystals have dissociated and, hence, it is reported as the hydrate dissociation condition. Same procedure was implemented in the references [188-189].

<sup>8</sup> At lower temperatures, it was harder to obtain reproducible data due to condensation of heavier components (water); additional purges were required.

## 5.4 Apparatus Calibration

The pressure transducer was calibrated previously [87] by regulating it at a fixed temperature of 313.15 K and was calibrated against a pressure balance (Desgranges et Huot, model 26000) fitted with a piston-cylinder unit having a full-scale range of 50 MPa and expanded relative uncertainty of 0.01%. The calibration was done in a range of pressures from (0.1 to 50) MPa and the final uncertainty of the pressure measurements was estimated to be 10 kPa. No additional calibration was done for this work and in order to account for any sensor drift over time, the pressure readings of the transducer were periodically compared at ambient pressure against a digital barometer located in the same laboratory, and small additive corrections were made to account for the observed differences. Taking this into account, the standard uncertainty was estimated to be 10 KPa.

The PRT was as well calibrated previously [87] on ITS-90 at the temperature of the triple-point of water and by comparison with a standard platinum resistance thermometer in a constant temperature bath at temperatures up to 473 K. The uncertainty of the PRT was 0.02 K, but fluctuations of the bath temperature could be as much as  $\pm 0.05$  K. Consequently the overall standard uncertainty of the cell temperature was estimated to be 0.025 K.

The TCD and FID detectors response area against the amount of each component present was calibrated by an absolute method using one of the sampling valves (liquid sampling valve) for all components. The calibration was carried out at fixed column temperature at which measurements were performed and covered the range beyond experimental measurements so that no extrapolation was performed beyond the calibration curves of all components.

The amount of carbon dioxide was calibrated against the TCD response area by varying the amount loaded into the cell. The equilibrium vessel was filled with the pure substance and the conditions of pressure and temperature were varied with the aid of temperature controller and Isco pump. The CO<sub>2</sub> density was obtained from the EoS developed by Span and Wagner [180] with an estimated relative uncertainty of between 0.03 % to 0.05 % (which we interpret as an expanded uncertainty with coverage factor  $k = 2$ ). For the sake of simplicity, we ascribe the value 0.025 % to the standard relative uncertainty of the CO<sub>2</sub> density. Hence, taking all of this into account and considering the reproducibility in the response peak area, the standard uncertainty in the peak area response for CO<sub>2</sub> was estimated to be 0.01 while the standard uncertainty in the calculated amount of CO<sub>2</sub> at each given pressure and temperature was estimated to be 0.005.

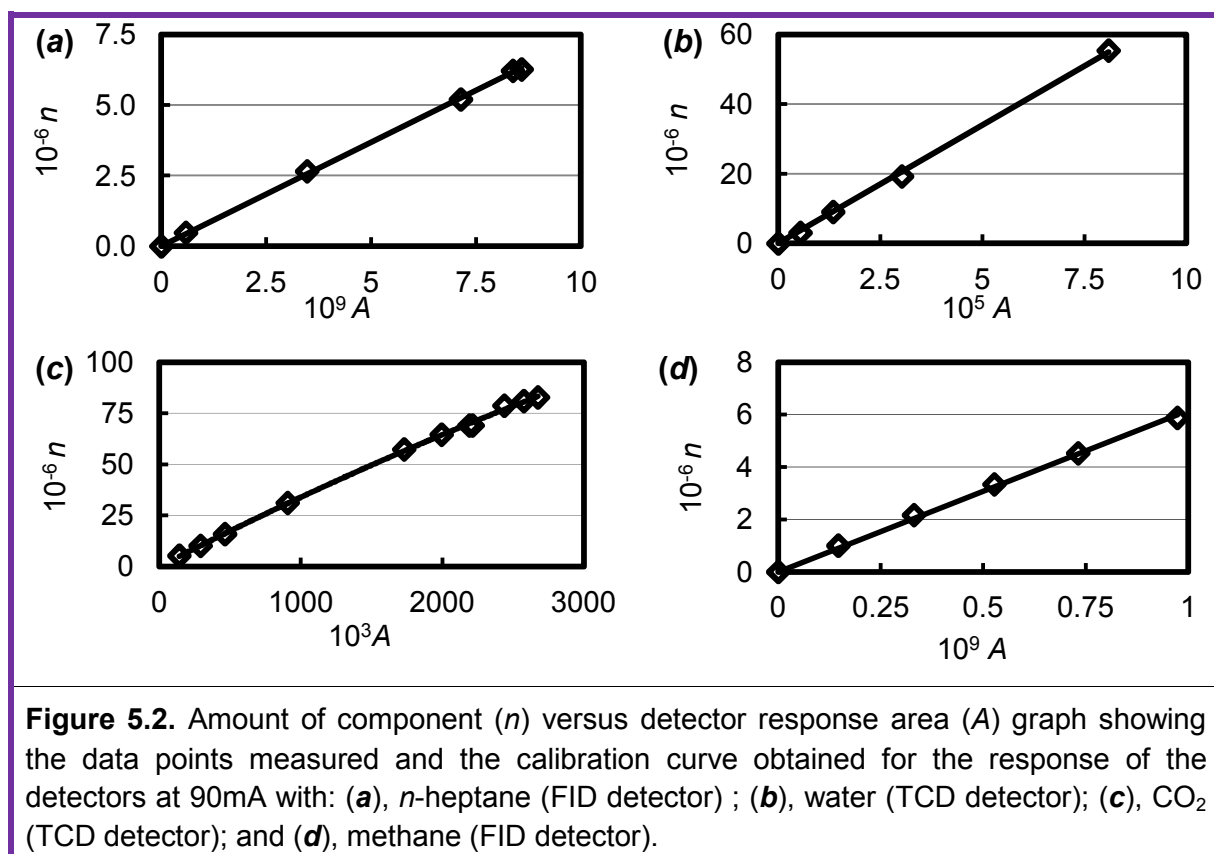
The amount of methane was calibrated against FID response area by varying the amount loaded into the cell. The density of methane was obtained from the EoS developed by Setzmann and Wagner [190] with an estimated uncertainty ranges from 0.03 % to 0.07 %. Hence, taking all of this into account and considering the reproducibility in the response peak area, the standard uncertainty in the peak area response for CH<sub>4</sub> was estimated to be 0.01 while the standard uncertainty in the calculated amount of CH<sub>4</sub> at each given pressure and temperature was estimated to be 0.005.

The amount of water was calibrated against TCD response peak area by filling the equilibrium cell with a solution of the water diluted with tetrahydrofuran. The calibration was carried out at ambient pressure and different temperatures and at different mole fraction of water in which the desired amount was measured and prepared gravimetrically. The density and mixture volume was obtained from the work of Schedemann et al. [191] using a vibrating tube densimeter with estimated standard uncertainty of 0.02 % in the mole composition. Hence, taking all of this into account and considering the reproducibility in the response peak area, the standard uncertainty in the peak area response for water was estimated to be 0.01 while the standard uncertainty in the calculated amount of water at each given pressure and temperature was estimated to be 0.01.

The amount of *n*-heptane was calibrated against FID response peak area by filling the equilibrium cell with a solution of the *n*-heptane diluted with hexane. The calibration was carried out at ambient pressure and different temperatures and at different mole fraction of *n*-heptane in which the desired amount was measured and prepared gravimetrically. The density and mixture volume was obtained from the work of Ramos-Estrada et al. [192] using a vibrating tube densimeter (Anton Paar, model DMA 5000) with overall standard uncertainty of 0.03 kg.m<sup>-3</sup> in the density measurements. Hence, taking all of this into account and considering the reproducibility in the response peak area the standard uncertainty in the peak area response for *n*-heptane was estimated to be 0.005 while the standard uncertainty in the calculated amount of *n*-heptane at each given pressure and temperature was estimated to be 0.005.

As previously mentioned, TCD was used for both water and CO<sub>2</sub>. A linear relationship between the amount of water present and TCD response area was observed. However, in the case of CO<sub>2</sub>, nonlinear behaviour was observed at conditions where a large amount of CO<sub>2</sub> was present and a quadratic polynomial was considered in this case. The FID detector shows a very linear behaviour for *n*-heptane and methane. During the course of measurements, the calibration was checked from time to time to ensure no drift will occur by

filling the equilibrium vessel with CO<sub>2</sub> or other components following the same procedure as described above and using direct injections from gas-tight syringes and a precision digital syringe for the liquid components. The calibration was also repeated for some of the measurements by the end of the experimental production of results to ensure that there was no considerable drift in the calibration curve has occurred. The calibration curves used in the present work are shown in Figure 5.2.



## 5.5 Uncertainty Analysis

The combined standard uncertainty of the mole fraction of each component in a given phase  $u(x_i)$  is obtained using the *Guide to the Expression of Uncertainty in Measurements* (GUM) [178]

$$u^2(f) = \sum_{i=1}^n \sum_{j=1}^n \frac{\partial f}{\partial x_i} \frac{\partial f}{\partial x_j} u^2(x_i, x_j) \quad 5.1$$

Here,  $x_i$  and  $x_j$  represent pairs of input variables from which  $f$  is to be evaluated,  $(\partial f/\partial x_i)$  is the sensitivity coefficient of  $f$  with respect to  $x_i$ , and  $u^2(x_i, x_j)$  is the covariance ( $i \neq j$ ) or the variance ( $i = j$ ) for variables  $x_i, x_j$ . Usually, only the diagonal terms in Eq. (5.1) are ( $i = j$ )



retained and we abbreviate  $u^2(x_i, x_i)$  as  $u^2(x_i)$ . Where appropriate, expanded uncertainties are obtained by multiplying the standard uncertainty  $u(f)$  by a coverage factor  $k$ .

In this work, the absolute area method was used for composition calculations in which the method assumes that the peak area  $A_i$  in the chromatogram measured for component  $i$  in the mixture is proportional to the amount  $n_i$  of that substance in the sample. It is necessary to quantify all components present to obtain the mole fraction of each component. The response factors  $f_i$  and mole fractions  $x_i$  of each component are given by

$$\left. \begin{aligned} n_i &= f_i A \\ x_i &= n_i / \left( \sum_{k=1}^{N_c} n_k \right) \end{aligned} \right\} \quad 5.2$$

Hence, the mole fraction may be obtained from the chromatographic peak areas and response factors as follows:

$$x_i = A_i f_i / \left( \sum_{k=1}^{N_c} A_k f_k \right) \quad 5.3$$

Then considering this and Equation (5.1), the overall combined standard uncertainty of the mole fraction arising from temperature, pressure, response factor and chromatographic peak area uncertainties can be determined as follows:

$$u^2(x_i) = (\partial x_i / \partial T)^2 u^2(T) + (\partial x_i / \partial p)^2 u^2(p) + \sum_{j=1}^{N_c} \left( \frac{\partial x_i}{\partial n_j} \frac{\partial n_j}{\partial f_j} \right)^2 u^2(f_j) + \sum_{j=1}^{N_c} \left( \frac{\partial x_i}{\partial n_j} \frac{\partial n_j}{\partial A_j} \right)^2 u^2(A_j) \quad 5.4$$

The partial derivatives, sensitivity coefficients,  $(\partial x_i / \partial n_j)$  are given by:

$$\left. \begin{aligned} (\partial x_i / \partial n_j) &= -x_i x_j / n_j & (j \neq i) \\ &= (1 - x_i) x_i / n_i & (j = i) \end{aligned} \right\} \quad 5.5$$

The partial derivatives, sensitivity coefficients,  $(\partial n_i / \partial f_j)$  and  $(\partial n_i / \partial A_j)$  are given by:

$$\left. \begin{aligned} (\partial n_j / \partial f_j) &= A_j \\ (\partial n_j / \partial A_j) &= f_j \end{aligned} \right\} \quad 5.6$$

Taking all of this into account, it follows that the overall standard uncertainty of  $x_i$  is given by

$$u^2(x_i) = (\partial x_i / \partial T)^2 u^2(T) + (\partial x_i / \partial p)^2 u^2(p) + \sum_{j \neq i} (x_i x_j)^2 [u_r^2(f_j) + u_r^2(A_j)] + [x_i(1 - x_i)]^2 [u_r^2(f_i) + u_r^2(A_i)], \quad 5.7$$

where  $u_r(X)$  denotes the standard *relative* uncertainty of variable  $X$ . The standard relative uncertainties in the response factors are given by

$$u_r^2(f_j) = f_j^2 [u_r^2(n_j) + u_r^2(A_j)]_{\text{cal}} \quad 5.8$$

where subscript 'cal' denotes the calibration measurement for component  $j$ , finally, Equation (5.7) reduces to the following simpler form in the case of a binary mixture

$$u^2(x_1) = (\partial x_1 / \partial T)^2 u^2(T) + (\partial x_1 / \partial p)^2 u^2(p) + [x_1(1 - x_1)]^2 \sum_{j=1}^2 [u_r^2(f_j) + u_r^2(A_j)] \quad 5.9.$$

**Table 5.2.** Combined expanded uncertainty,  $U(x_i)$ , for the composition measurements of the system (water (1) + carbon dioxide (2) + *n*-heptane (3)) in mole fraction at different conditions, using a coverage factor  $k = 2$ .

	Water-rich phase			CO <sub>2</sub> -rich phase			<i>n</i> -Heptane-rich phase		
	$x_1$	$x_2$	$x_3$	$x_1$	$x_2$	$x_3$	$x_1$	$x_2$	$x_3$
	<b><math>p = 2.07 \text{ MPa}, T = 323.15 \text{ K}</math></b>								
<b><math>U(x)</math></b>	0.0004	0.0004	0.0004	0.0006	0.0006	0.0020	0.0042	0.0045	0.0045
	<b><math>p = 6.94 \text{ MPa}, T = 323.15 \text{ K}</math></b>								
<b><math>U(x)</math></b>	0.0010	0.0010	0.0010	0.0003	0.0020	0.0003	0.0060	0.0064	0.0064
	<b><math>p = 1.88 \text{ MPa}, T = 413.15 \text{ K}</math></b>								
<b><math>U(x)</math></b>	0.0001	0.0001	0.0001	0.0082	0.0083	0.0085	0.0028	0.0033	0.0033
	<b><math>p = 13.00 \text{ MPa}, T = 413.15 \text{ K}</math></b>								
<b><math>U(x)</math></b>	0.0008	0.0008	0.0008	0.0043	0.0043	0.0049	0.0065	0.0072	0.0071

Considering the above equations, the quantities considered are the pressure, temperature, response area and response factor. The uncertainty of the response factor is obtained from the uncertainties of the response area and the calculated amount of component during calibration. The latter depends on the uncertainties of pressure, temperature, and density values. The standard uncertainty values of all of these variables were discussed and given in the calibration section. Hence, taking all of this into account and considering the reproducibility of measurements and using Equation (5.7), the overall combined expanded

uncertainty in the mole fraction of each component varies from 0.0001 to 0.009 depending on temperature, pressure, phase in question and component analysed, with coverage factor  $k = 2$ . Examples of the various contributions to the uncertainty for the two ternary mixtures are given in Tables 5.2 and 5.3.

In summary, detailed uncertainty analysis concluded that the combined standard uncertainty in the mole fractions varies from (0.0001 to 0.004) for the ternary mixture (carbon dioxide + *n*-heptane + water) and from (0.0002 to 0.005) for the ternary mixture (carbon dioxide + methane + water), depending on the phase in question and component analyzed.

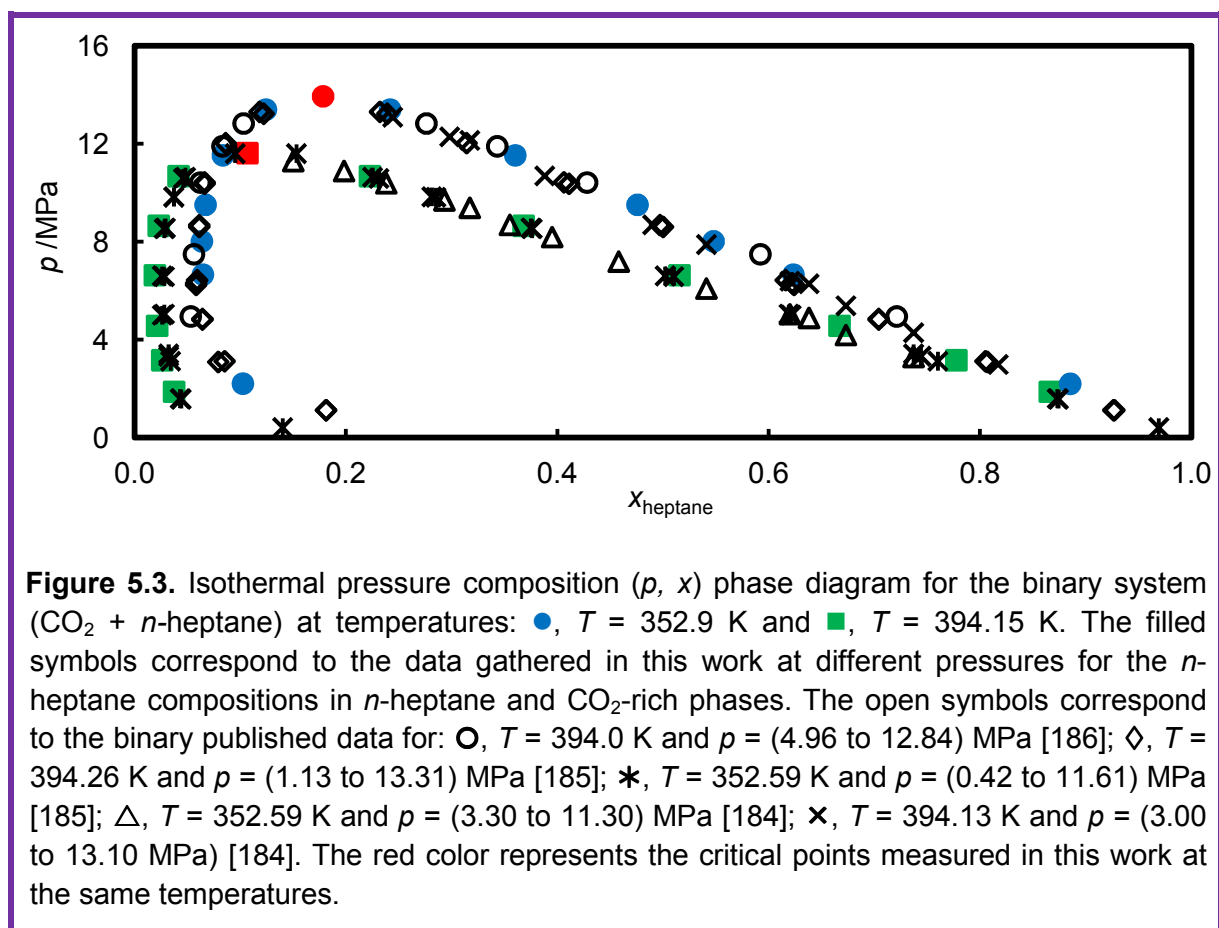
**Table 5.3.** Combined expanded uncertainty,  $U(x_i)$ , for the composition measurements of the system (water (1) + carbon dioxide (2) + methane (3)) in mole fraction at different conditions, using a coverage factor  $k = 2$ .

	Water-rich phase			CO <sub>2</sub> -rich liquid phase			Gas-phase		
	$x_1$	$x_2$	$x_3$	$x_1$	$x_2$	$x_3$	$x_1$	$x_2$	$x_3$
	<b>(5.82 MPa) , (287.65 K)</b>			<b>(7.09 MPa) , (287.65 K)</b>			<b>(7.92 MPa) , (287.65 K)</b>		
<b><math>U(x)</math></b>	0.0039	0.0039	0.0039	0.0043	0.0045	0.0045	0.0096	0.0097	0.0097
	<b>(7.92 MPa) , (287.65 K)</b>			<b>(7.92 MPa) , (287.65 K)</b>			<b>(5.29 MPa) , (287.65 K)</b>		
<b><math>U(x)</math></b>	0.0037	0.0037	0.0037	0.0065	0.0066	0.0066	0.0013	0.0029	0.0029
	<b>(6.66 MPa) , (297.65 K)</b>			<b>(7.70 MPa) , (297.65 K)</b>			<b>(7.70 MPa) , (297.65 K)</b>		
<b><math>U(x)</math></b>	0.0036	0.0036	0.0036	0.0031	0.0034	0.0034	0.0044	0.0047	0.0047

## 5.6 Apparatus Validation

The mixture (carbon dioxide + *n*-heptane) was chosen to validate the apparatus through comparison with published experimental data. The first experimental study on the system (carbon dioxide + *n*-heptane) was that of Kalra et al. [185] who reported VLE composition at  $T = (310.65, 352.59, 394.26 \text{ and } 477.21) \text{ K}$  and at several pressures between the vapour pressures of *n*-heptane and the critical point of the system. Inomata et al. [186] studied VLE composition using static method at temperatures of (394 to 502) K and pressures up to 12.84 MPa, where a new modified flow-type apparatus was developed and used to overcome the thermal decomposition problem in high temperature range by minimizing the residence time of the sample in this study. In the study of Sako et al. [193] the VLE for this system was measured at  $T = 343 \text{ K}$  to check the reliability of the apparatus and procedure.

King and Al-Najjar [194] measured the solubility of carbon dioxide as function of temperature in *n*-heptane at normal pressure. It has been reported that the solubility for carbon dioxide, hydrogen sulphide and propane were found to increase with increasing *n*-alkane chain length. Choi and Yeo [195] presented composition and critical point data of this binary mixture using a variable-volume view cell. The dew point and bubble point of the mixture were also measured by visual observation.



Fenghour et al. [196] reported phase behaviour and density of the binary mixture at  $T = (301.76, 321.08 \text{ and } 362.90)$  K. The measurements were carried out in an automated isochoric instrument which gives accuracy to be better than  $\pm 0.1\%$ . In the study of Mutelet et al. [184] phase equilibria and bubble point pressures of the binary mixture were measured on 12 isotherms at temperatures between  $(310.65 \text{ to } 413.15)$  K using synthetic method. A  $12.4 \text{ cm}^3$  equilibrium cell with a window in sapphire was used. The phase transitions resulting from pressure variation were observed by direct visualization through the sapphire window using a cine camera which was connected to a television. Recently, Lay et al. [197] studied the bubble point pressures and the phase behaviour of the binary mixture at different

CO<sub>2</sub> mole fractions ranging from (0.502 to 0.91) and at temperatures in the range from (293.15 to 313.15) K.

Based on the available literature, the apparatus was validated by measuring the vapour liquid equilibria (VLE) of the binary system (CO<sub>2</sub> + *n*-heptane) at  $T = 252.9$  K and  $T = 394.15$  K, and pressures up to 14 MPa. The results obtained are presented in Table 5.4 and Figure 5.3. In Figure 5.3, the composition of *n*-heptane in the *n*-heptane-rich phase and CO<sub>2</sub>-rich phase was plotted at different pressures together with available literature data. A good agreement (within the estimated combined uncertainty) was observed between our measurements and available data reported at  $T = 394.0$  K and  $p = (4.96$  to  $12.84)$  MPa [186];  $T = 394.26$  K and  $p = (1.13$  to  $13.31)$  MPa [185];  $T = 352.59$  K and  $p = (0.42$  to  $11.61)$  MPa [185];  $T = 352.59$  K and  $p = (3.30$  to  $11.30)$  MPa [184];  $T = 394.13$  K and  $p = (3.00$  to  $13.10)$  MPa [184].

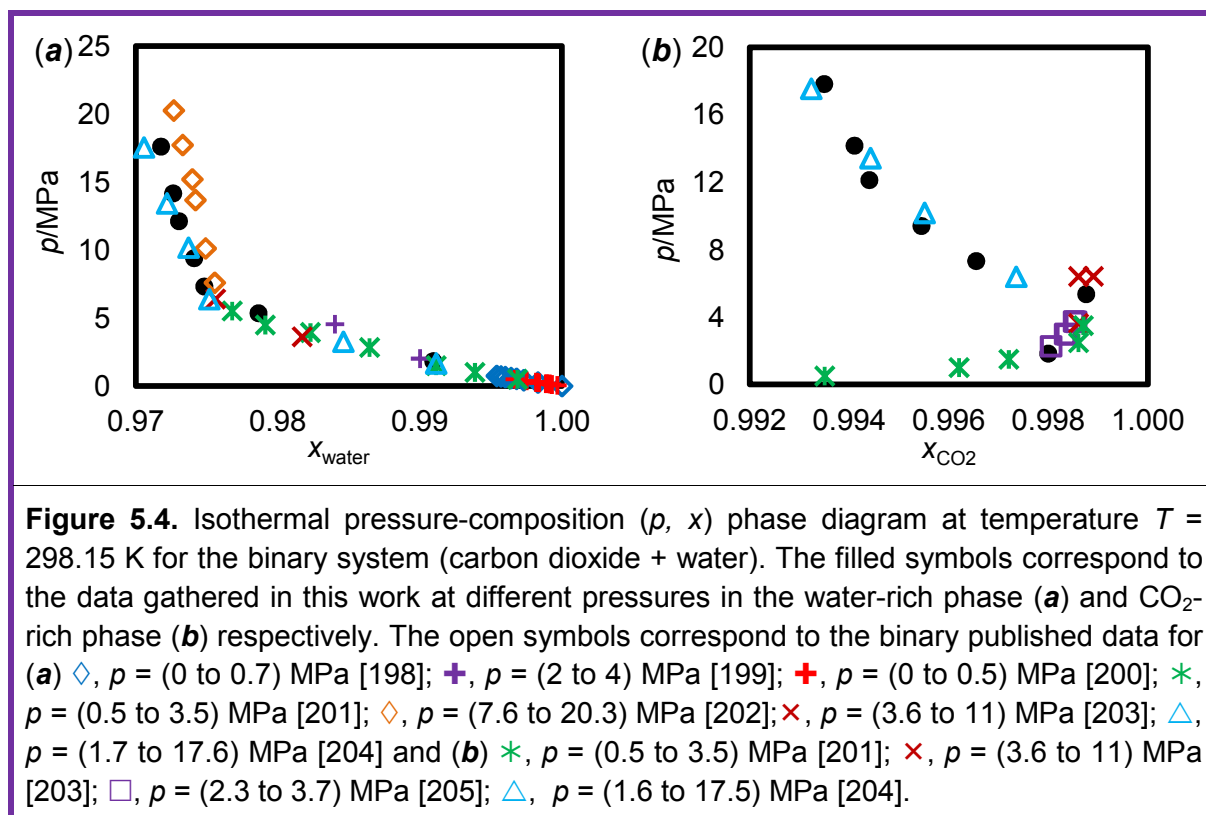
**Table 5.4.** Experimental VLE Data for *n*-Heptane (1) + Carbon Dioxide (2) <sup>a</sup>

$p/\text{MPa}$	phase II	phase III	phase II	phase II	phase III
	$x_1^{\text{exp}}$	$y_1^{\text{exp}}$	$p/\text{MPa}$	$x_1^{\text{exp}}$	$y_1^{\text{exp}}$
<b><math>T = 352.9</math> K</b>					
1.89	0.8660	0.0371	6.64	0.5155	0.0190
3.17	0.7774	0.0260	8.67	0.3680	0.0227
4.58	0.6669	0.0212	10.69	0.2226	0.0414
11.63	0.1066 (critical)				
<b><math>T = 394.15</math> K</b>					
2.21	0.8852	0.1023	9.52	0.4757	0.0670
6.67	0.6232	0.0645	11.54	0.3601	0.0834
8.03	0.5477	0.0635	13.41	0.2416	0.1241
13.95	0.1782 (critical)				

<sup>a</sup> The phases are labelled as II and III for the *n*-heptane-rich liquid phase and CO<sub>2</sub>-rich gas phase respectively.

The apparatus was additionally validated by measuring the vapour liquid equilibria of the binary system (CO<sub>2</sub> + water) at  $T = 298.15$  K and pressures up to 18 MPa, and compare it with the available literature data. The results obtained are presented in Table 5.5 and Figure 5.4. In Figure 5.4 a, the composition of water in the water-rich phase at different pressures was plotted together with available literature data. The composition decreases as pressure

increases. There was a good agreement between our measurements and available data at low pressures up to around the critical pressure of CO<sub>2</sub>.



However, at higher pressures, there was some slight deviation observed between our measurements and the measurements reported by Shuxin et al. [204] and King et al. [202]. The deviation lies within the overall uncertainty of the measurements. The CO<sub>2</sub> mole fraction in the CO<sub>2</sub>-rich phase at different pressures was plotted in Figure 5.4 b.

**Table 5.5.** Experimental VLE Data for Water (1) + Carbon Dioxide (2) <sup>a</sup>

$p/\text{MPa}$	phase II	phase III	phase II	phase II	phase III
	$x_1^{\text{exp}}$	$y_1^{\text{exp}}$	$p/\text{MPa}$	$x_1^{\text{exp}}$	$y_1^{\text{exp}}$
<b><math>T = 298.15</math> K</b>					
1.838	0.9909	0.0020	9.484	0.9741	0.0046
5.369	0.9786	0.0012	12.260	0.9730	0.0056
7.362	0.9748	0.0035	14.198	0.9726	0.0059
17.726	0.9718	0.0065			

<sup>a</sup> The phases are labelled as II and III for the water-rich phase and CO<sub>2</sub>-rich gas phase respectively.

The amount of CO<sub>2</sub> in this phase increases as pressure increases up to approximately the saturation pressure of CO<sub>2</sub> at the given temperature. Above this pressure, the amount of CO<sub>2</sub> presents decreases as pressure increases. The Figure shows good agreement with the available literature data, mainly with those reported by Shuxin et al. [204].

## 5.7 Summary

In this Chapter, details of a quasi-static-analytical apparatus calibration and validation have been given. The apparatus relies on recirculation of two coexisting phases with sampling and on-line compositional analysis by gas chromatograph. The equipment was used to measure the phase equilibria of (CO<sub>2</sub> + *n*-heptane + water) and (CO<sub>2</sub> + methane + water). The measurements included VLE, VLLE, UCEP and quadruple curve along which hydrates coexists with the three fluid phases. The apparatus was calibrated and validated by means of comparison with the published available literature data of the binary systems (*n*-heptane + carbon dioxide) and (water + carbon dioxide). Detailed uncertainty analysis concluded that the combined standard uncertainty in the mole fractions varies from 0.0001 to 0.005 depending on the phase in question and component analyzed. The results for the ternary mixtures are presented in Chapters 8 and 9.

## Chapter 6: Phase Behaviour of (CO<sub>2</sub> + *n*-Heptane + Methylbenzene) Mixtures

### 6.1 Overview

In order to model CO<sub>2</sub>-EOR and CO<sub>2</sub> storage processes quantitatively, compositional thermodynamic models are required. Traditional EoS models rely upon adjustable binary parameters between molecules for the determination of thermophysical properties. These may be determined by fitting to available experimental data for the constituent binary subsystems, which effectively constrains the applicability of the model to within the available data range. Group-contribution methods offer the possibility of employing transferable interaction parameters that may be adjusted from a wider range of experimental data. In this work, the synthetic apparatus was used to measure the vapour-liquid phase behaviour of the mixture (CO<sub>2</sub> + *n*-heptane + methylbenzene) over the temperature range (298 to 473) K and pressures up to 16 MPa. In the experiments, the molar ratio between *n*-heptane and methylbenzene in the ternary system was fixed at different values, and the bubble-curve and part of the dew-curve was measured under carbon dioxide addition along five isotherms.

In this work, in collaboration with a colleague, Apostolos Georgiadis, who performed the SAFT- $\gamma$ -Mie calculations, we explore<sup>9</sup> the capabilities of the Statistical Associating Fluid Theory with a generalized group-contribution approach for the Mie potential parameters to model the phase behaviour of the (carbon dioxide + *n*-heptane + methylbenzene) system. A key feature of the implementation adopted here is that all interactions both like and unlike, were determined from pure-component and binary mixtures data. Thus, when applied to mixtures, the method is entirely predictive. The results suggested that there is merit in the approach of combining, within a SAFT approach, the Mie potential with a group-contribution scheme for the interaction parameters based on pure-component data alone. Finally the capabilities of the predictive cubic EoS (PPR78 EoS and PR<sub>2</sub>SRK EoS) were tested against our experimental data. In these methods, the binary parameters are obtained from a group-contribution scheme and no regression was done. The results showed that these models can predict the vapour-liquid equilibria of this mixture with very good accuracy without the need to regress binary parameters against experimental data. It was observed that both SAFT- $\gamma$ -Mie and predictive cubic EoSs give similar accuracies in VLE calculations.

---

<sup>9</sup> The main focus of this Chapter in terms of modelling is the comparison of experimental data with SAFT- $\gamma$ -Mie. SAFT- $\gamma$ -Mie calculations were performed by Apostolos Georgiadis, with the help of Vasileios Papaioannou.



## 6.2 Introduction

The ternary mixture (CO<sub>2</sub> + *n*-heptane + methylbenzene) was chosen to represent (CO<sub>2</sub> + *n*-alkane + aromatic) mixtures in general and was studied as a first step towards accurately determining the conditions of phase separation of multi-component (CO<sub>2</sub> + hydrocarbon) systems. New data on phase equilibrium were obtained, covering a wide range of conditions and compositions at different fixed molar ratios between *n*-heptane and methylbenzene in the ternary system. This work permitted a state-of-the-art modelling approach (SAFT- $\gamma$ -Mie) to be tested in predictions over an extended  $pTxy$  space. The approach was validated by the excellent agreement found between experimental results and theoretical predictions presented in the current study.

There appear to be no phase equilibria data reported in the literature for the ternary mixture. However, the constituent binary systems have been studied extensively. The (CO<sub>2</sub> + methylbenzene) system has been studied recently by Lay and co-workers [197, 206] at pressures up to 7.5 MPa, temperatures up to 313 K and CO<sub>2</sub> composition over the range (0.215 to 0.955) using a  $pVT$  apparatus with a variable-volume cell. Tochigi et al. [207] also studied the system at pressures up to 6.0 MPa, temperatures up to 333 K and CO<sub>2</sub> composition over the range (0.080 to 0.889) using a static-type apparatus composed of equilibrium cell, sampling and analyzing system. Wu et al. [208] extended the studied range of phase-equilibrium conditions using a dynamic synthetic method based on a fiber-optic reflectometer, reaching pressures up to 16.6 MPa and temperatures up to 572 K over CO<sub>2</sub> composition range of (0.01 to 0.78); this is the widest range studied for this mixture. These authors also used the Peng Robinson EoS [102] as a modelling tool. Naidoo et al. [209] studied this mixture at pressures up to 12.1 MPa, temperatures up to 391 K and CO<sub>2</sub> compositions of (0.0578 to 0.8871) using a static analytical apparatus equipped with sapphire window for visual observation, liquid sampling techniques and gas chromatography for composition analysis. Other studies reporting the phase equilibria of the (CO<sub>2</sub> + methylbenzene) system can be found in references [210-216].

The (CO<sub>2</sub> + *n*-heptane) system has also been studied by Lay [197] at pressures up to 7.4 MPa, temperatures up to 313 K and CO<sub>2</sub> composition over the range (0.503 to 0.904) using the same apparatus mentioned above. Choi and Yeo [195] studied the system at pressures up to 12.2 MPa, temperatures up to 370 K and CO<sub>2</sub> compositions of (0.885 to 0.958) using a high pressure variable-volume cell. Kalra et al. [185] studied the system at pressures up to 3.3 MPa and temperatures up to 477 K over the range  $x_{\text{CO}_2}$  = (0.022 to 0.949); the temperature range was the widest range for this system. Fenghour et al. [196] measured

bubble points for this system at pressures up to 55.5 MPa, temperatures up to 459 K, and CO<sub>2</sub> composition of (0.2918 to 0.4270); the pressure range was the widest measured. Mutelet et al. [184] used a high-pressure variable-volume cell to perform static phase equilibria measurements at pressures up to 13.40 MPa, temperatures up to 413 K and compositions range of (0.183 to 0.914). The data were compared against the predictive EoS recently developed by Jaubert and co-workers [34-36, 79, 123-126], which was based on the use of a developed group-contribution approach to estimate the temperature-dependent binary interaction parameters  $k_{ij}(T)$  for the PR EoS. Other studies reporting the phase equilibria of this system can be found in references [186, 193, 217].

Available experimental data for binary systems of the type (CO<sub>2</sub> + *n*-alkane) and (CO<sub>2</sub> + aromatic) have been coupled with predictions from different predictive equations. For example, (CO<sub>2</sub> + *n*-heptane) and (CO<sub>2</sub> + methylbenzene) have been already compared with the prediction from PPR78 EoS [45]. The comparison proved the predictive capability of this method. Different molecular SAFT versions (SAFT-VR [218], PC-SAFT [219-222], Soft-SAFT [223], and a group-contribution approach GC-SAFT [224]) have also been used to model these binaries, mainly (CO<sub>2</sub> + *n*-alkane) systems. PSRK [225] was also used to predict the phase equilibria of different (CO<sub>2</sub> + *n*-alkane) binary mixtures. As to our knowledge, predictions from PR<sub>2</sub>SRK and SAFT- $\gamma$ -Mie have not been used to compare with the available data for the (CO<sub>2</sub> + *n*-heptane) and (CO<sub>2</sub> + methylbenzene) binary systems. There are no modelling approaches reported for the ternary mixture.

### 6.3 Modelling Approaches

Both predictive PPR78 and PR<sub>2</sub>SRK EoSs were described previously (Chapter 3, section 3.2.4). The PPR78 and PR<sub>2</sub>SRK EoS were applied directly without any fitting to experimental data. The temperature-dependent binary interaction between each pair of components was calculated by the group-contribution scheme (Equation 3.11); they were found to be similar to those available in the literature at similar temperatures. The critical temperature, critical pressure and acentric factor of each substance are required in these models. The latter was defined by Pitzer [106] as

$$\omega = \log_{10} \left[ \frac{p_c}{p_s(T = 0.7T_c)} \right] - 1, \quad 6.1$$

where  $p_s$  denotes the saturated-vapour pressure. For the components present in our mixture, the critical constants and acentric factor are readily available, and the uncertainties associated with their values are small. The values were taken from available data as listed in

Table 6.1. The acentric values obtained are the same as, or similar, to those available from the NIST Thermodata Engine (TDE) software [226-227].

**Table 6.1.** Critical pressure  $p_c$  and critical temperature  $T_c$  (with uncertainties), and acentric factor  $\omega$  for the components studied in this work.

Component	Ref	$\omega$	$p_c$ (MPa)	$u(p_c)$ (MPa)	$T_c$ (K)	$u(T_c)$ (K)
<i>n</i> -heptane	[228]	0.3481 <sup>a</sup>	2.734	0.02	540.30	0.6
methylbenzene	[229]	0.2640 <sup>a</sup>	4.108 <sup>b</sup>	0.01	591.75 <sup>b</sup>	0.15
carbon dioxide	[230]	0.2310 <sup>a</sup>	7.378	0.007	304.16	0.082

<sup>a</sup> calculated from the available vapour-pressure data with the use of Equation 6.1 for the acentric factor; <sup>b</sup> recommended values by Tsonopoulos and Ambrose [229].

SAFT- $\gamma$ -Mie has been described previously (Chapter 3, section 3.4.3). A brief reference is made here for the particular compounds of the (carbon dioxide + *n*-heptane + methylbenzene) system, and their interactions. The compounds are modelled by means of transferable groups; each described by a set of parameters that determine the shape factor  $S_k$ , and size  $\sigma$  of the segments, and depth of the interaction potential  $\epsilon/k_B$ . The Mie potential used here is a general case of the Lennard-Jones potential [231] with adjustable exponents for both the attractive  $\lambda_r$ , and repulsive  $\lambda_a$ , parts of the interaction. All interactions, both like and unlike, as implemented in this work were determined from experimental data of systems comprising the constituent groups, but not necessarily the constituent compounds or sub-systems of the (carbon dioxide + *n*-heptane + methylbenzene) mixture. Thus, when applied to the current system, the method is regarded as predictive.<sup>10</sup>

The parameters used for the different groups are given in Table 6.2. These have been obtained in previous work [170]. The cross interaction energies between the groups were obtained by fitting to experimental vapour pressure data over a range of binary systems of families of compounds composed of the groups in question; these are given in Tables 6.3. The CO<sub>2</sub>-aCCH<sub>3</sub> cross interaction parameters were determined by fitting on binary (carbon dioxide + methylbenzene) vapour-liquid equilibrium data of Naidoo et al. [209] up to 391 K

<sup>10</sup> Note that CO<sub>2</sub> is a group on its own. Correspondingly, its cross interaction with other molecules has to be fitted to mixture data - though binary data is used. The interaction is known from previous works. For this reason, and because the system is a ternary (to which no adjustments made), this is predictive.

and 10 MPa. All other cross interactions parameters are calculated in the usual manner. (Combining rules, Chapter 3, section 3.4.2)

**Table 6.2.** Parameters for the groups used in SAFT- $\gamma$ -Mie

	$S_k$	$(\epsilon/k_B) / K$	$\sigma \cdot 10^{10} / m$	$\lambda_r$	$\lambda_a$
CH <sub>3</sub>	0.5725	256.7662	4.077	15.050	6.00
CH <sub>2</sub>	0.2293	473.3893	4.880	19.871	6.00
aCH	0.3113	377.2721	4.091	14.762	6.00
aCCH <sub>3</sub>	0.3878	531.9750	5.105	22.839	6.00
CO <sub>2</sub>	0.8470	207.8910	3.050	26.408	5.06

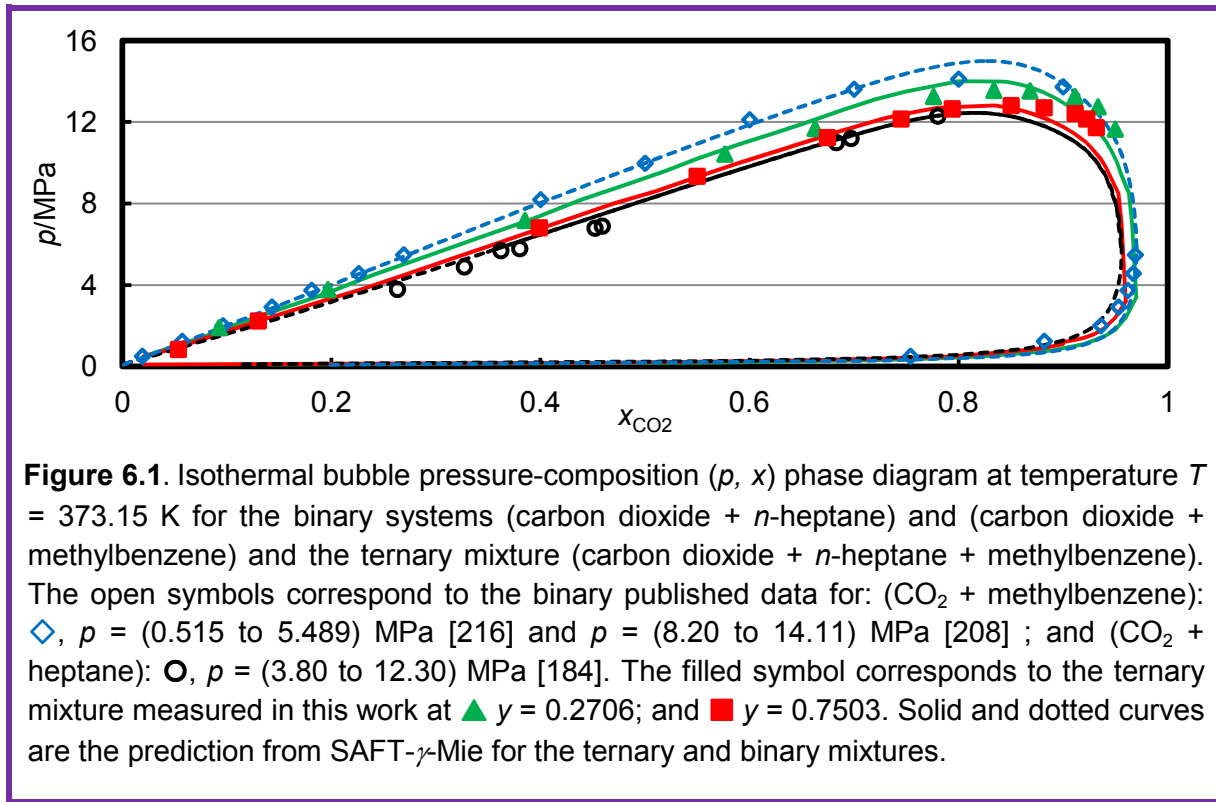
**Table 6.3.** Cross interaction energies for the groups used in SAFT- $\gamma$ -Mie

	CH <sub>3</sub>	CH <sub>2</sub>	aCH	aCCH <sub>3</sub>	CO <sub>2</sub>
CH <sub>3</sub>	256.766				
CH <sub>2</sub>	350.772	473.389			
aCH	309.156	419.960	377.273		
aCCH <sub>3</sub>	368.113	517.981	461.212	531.975	
CO <sub>2</sub>	187.976	275.149	213.332	284.657	207.891

## 6.4 Discussion and Comparison with Experiment

The experimental bubble and dew pressures of (carbon dioxide + *n*-heptane + methylbenzene) system are given in Appendix C for all isotherms measured over the whole composition range of carbon dioxide at different *n*-heptane-to-methylbenzene molar ratios. The measurements were carried out at  $T = (298.15, 323.15, 373.15, 423.15, \text{ and } 473.15) \text{ K}$ , over a range of pressures up to 16 MPa. Four different molar ratios  $y$  of *n*-heptane-to-methylbenzene were selected: 0.1214, 0.2706, 0.4819, and 0.7503. For each of these fixed ratios, the VLE of the ternary system was studied over the entire composition range of carbon dioxide for all isotherms. Also given in Appendix C are the absolute relative deviation

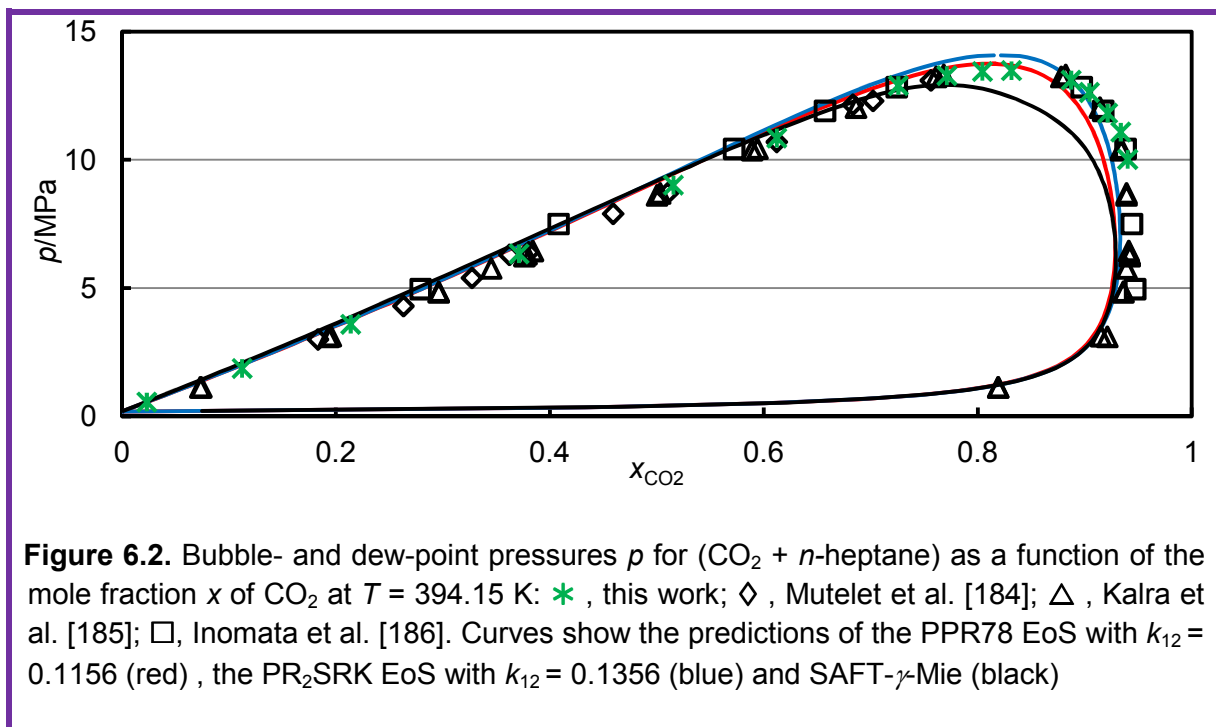
between the experimental data and obtained phase equilibria as described for the SAFT- $\gamma$ -Mie theory.



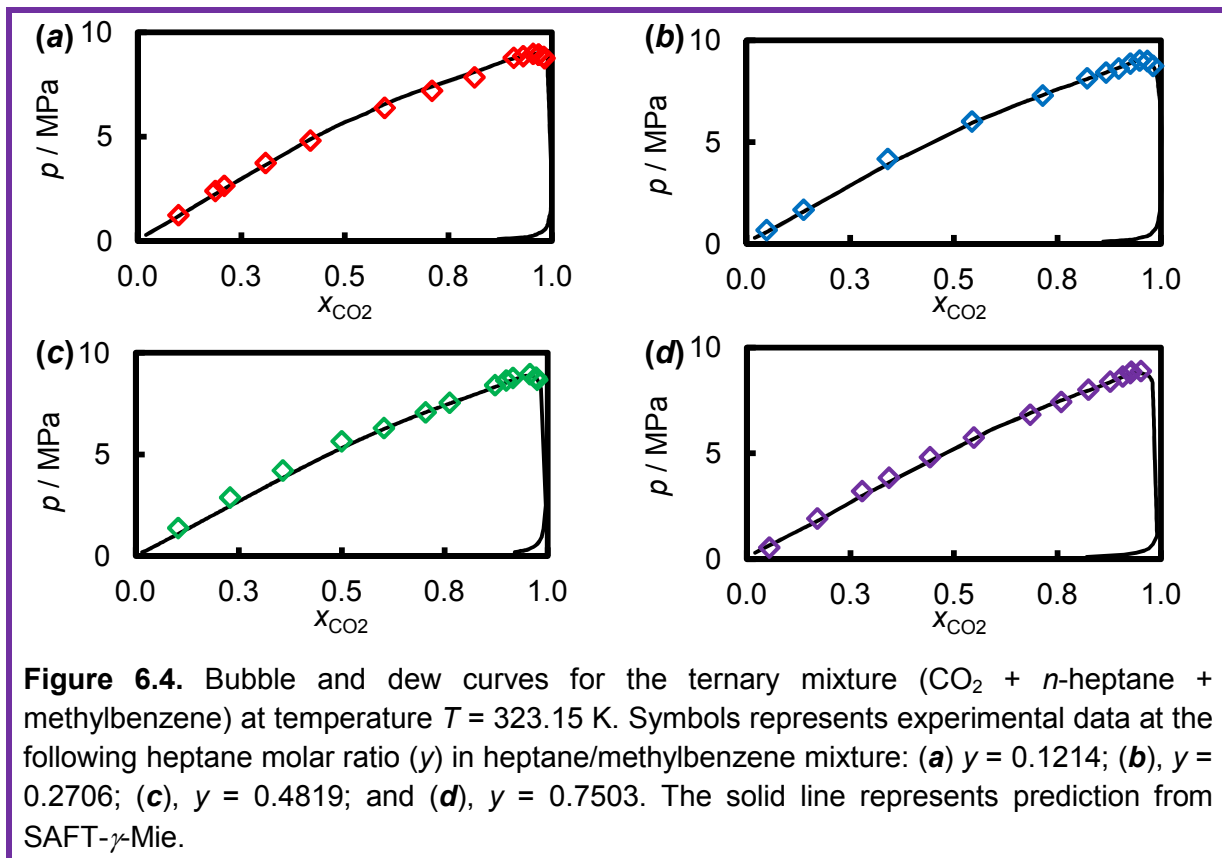
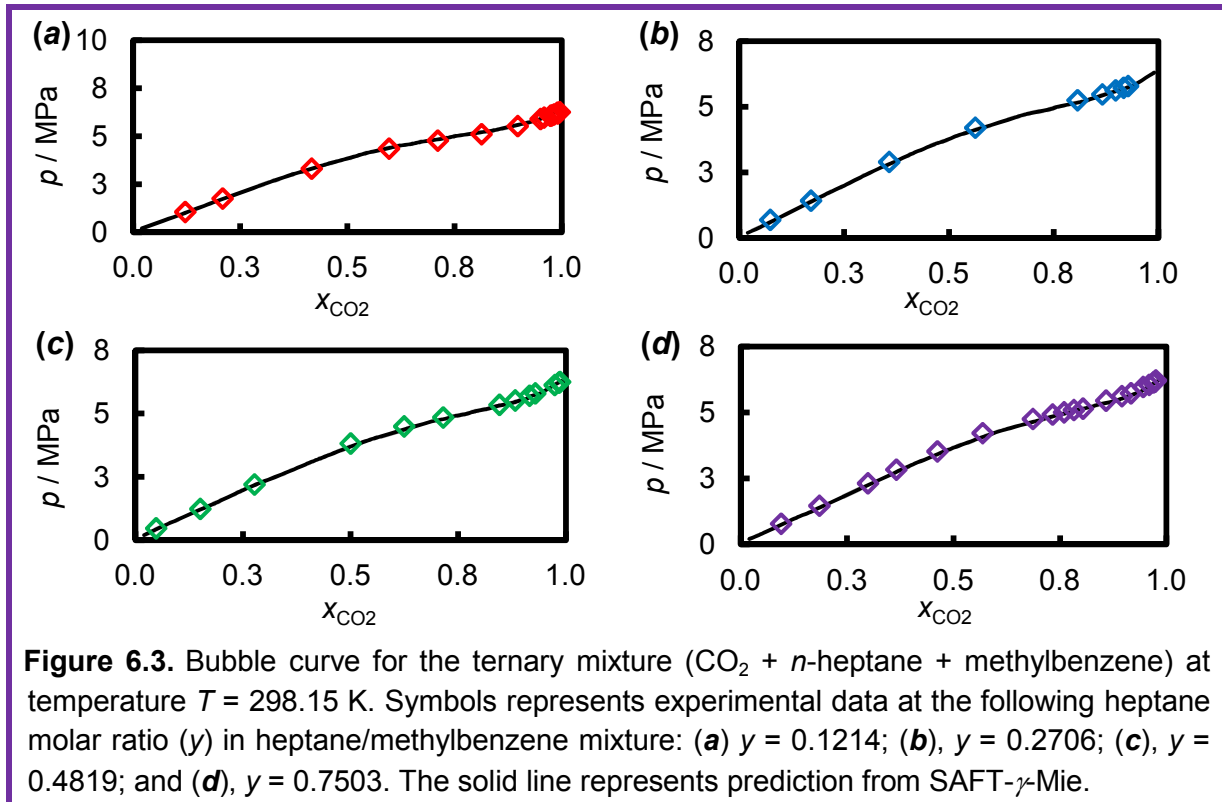
The binary mixture (carbon dioxide +  $n$ -heptane) exhibits type II phase behaviour [45-46] based on the classification of van Konynenburg and Scott [42-43]. The binary mixture (carbon dioxide + methylbenzene) exhibits type I [208] phase behaviour. In type II phase behaviour, due to differences between the two components, the phase diagram presents liquid-liquid separation at low temperature. The ternary mixture exhibits ternary class II phase behaviour according to the global ternary diagrams proposed by Bluma and Deiters [52]. A liquid-gas critical surface and liquid-liquid critical plane exist at low temperatures. A critical endpoint curve exists at low pressure and consists of upper critical endpoints. The phase envelope of the ternary mixture lies between the phase envelopes of the binary mixtures as shown in Figure 6.1. In this Figure, we plot the experimental bubble and dew curves against  $\text{CO}_2$  mole fraction at  $T = 373.15$  K, for the ternary mixture studied in this work at two different molar ratios and the binaries ( $\text{CO}_2 + \text{methylbenzene}$ ) [208, 216] and ( $\text{CO}_2 + n\text{-heptane}$ ) [184]. It can be observed that, for example, increasing the heptane molar ratio shifts the curve towards the binary system ( $\text{CO}_2 + n\text{-heptane}$ ). In this figure, predictions from SAFT- $\gamma$ -Mie are also shown for ternary (solid curve) and binary mixtures (dotted curves). The theory is in very good agreement with experiment. Qualitatively, the theory was able to

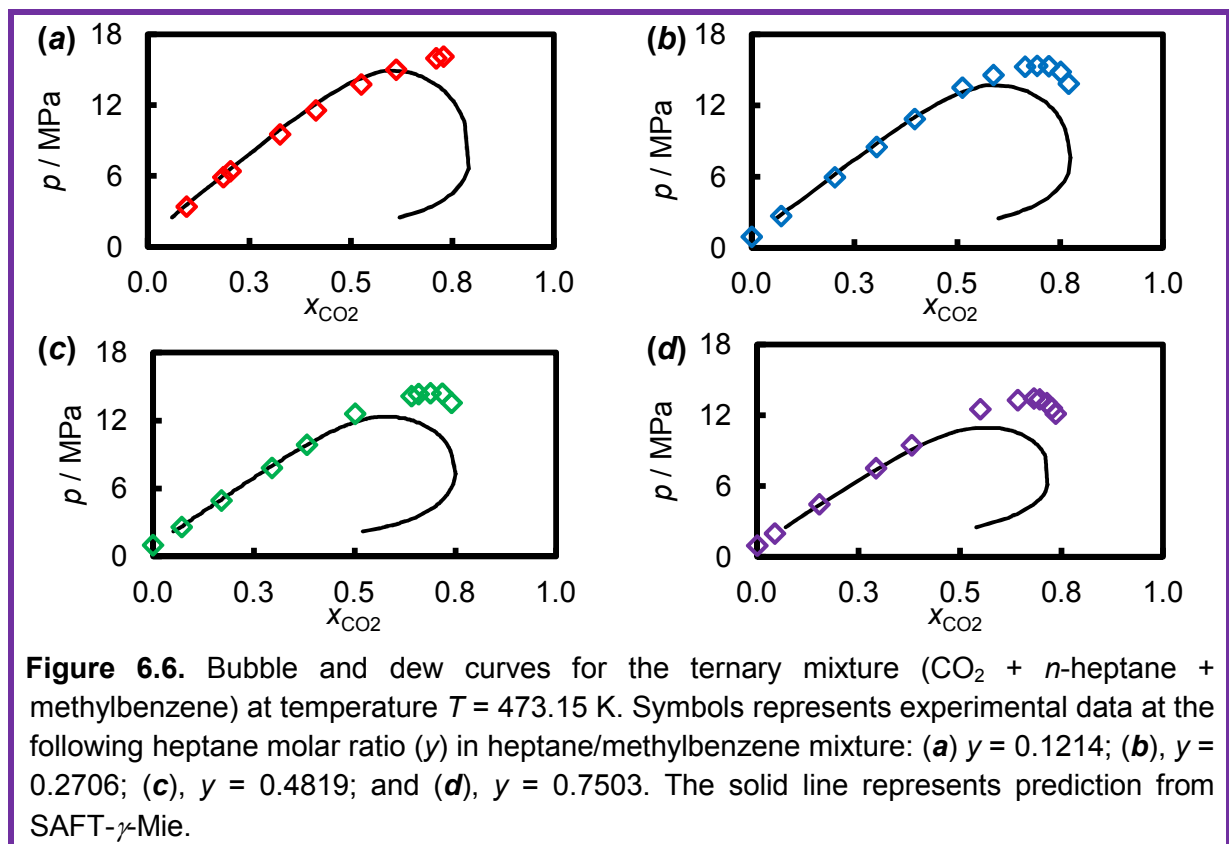
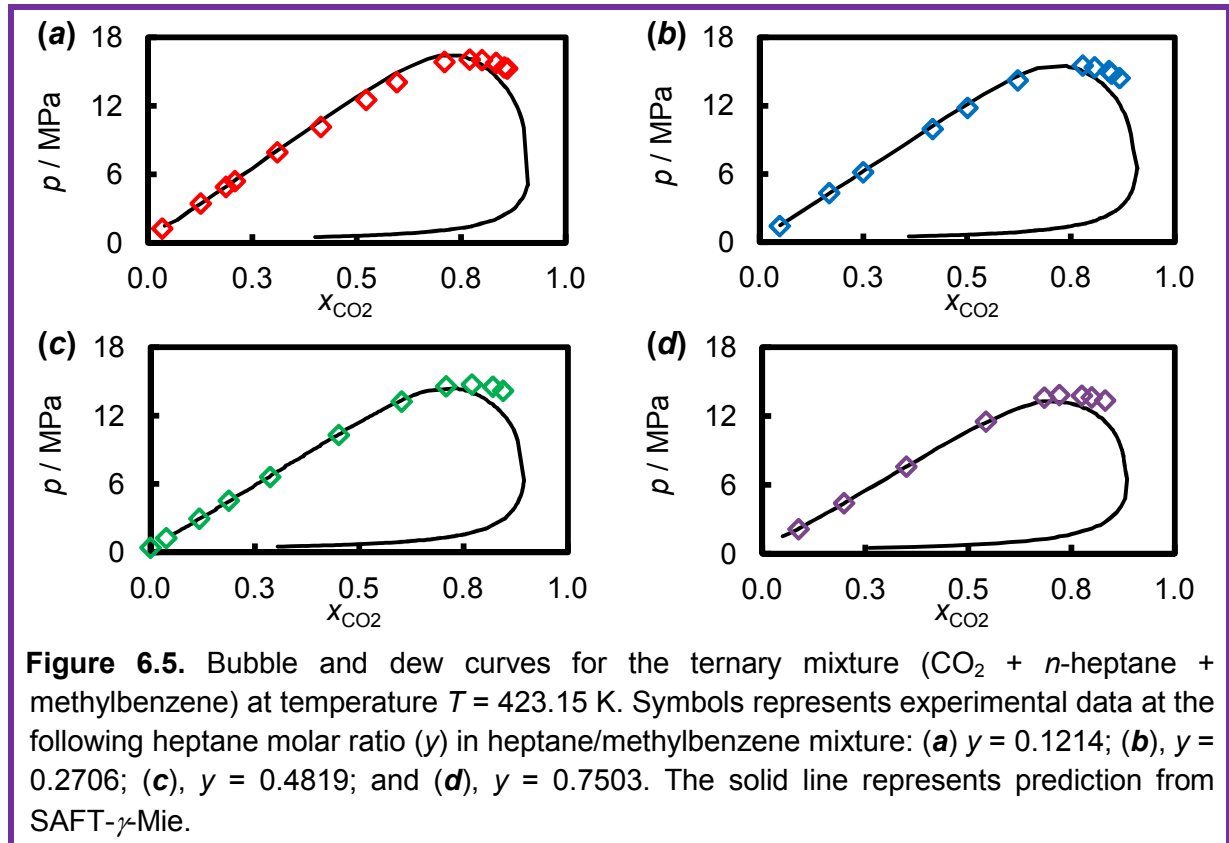
pick up the change in phase envelope when the molar ratios of *n*-heptane-to-methylbenzene are changed. This is true for all temperatures and other molar ratios.

Initially, PPR78, PR<sub>2</sub>SRK and SAFT- $\gamma$ -Mie EoSs were applied to the binary mixture (CO<sub>2</sub> + *n*-heptane) at  $T = 394.15$  K and the predicted bubble- and dew-curves were compared with our experimental data, as shown in Figure 6.2. The comparison shows small differences between these methods; overall they are in quite good agreement with the experimental data. The comparison proves the predictive capabilities of these approaches.



It can be seen that these equations over-predict or under-predict at conditions close to critical. This is a common difficulty of classical EoS as an accurate prediction of phase behaviour at conditions both far from and close to criticality cannot be accomplished by mean-field based theories that do not incorporate long-range density fluctuations. There is a noticeable difference between predictions from SAFT- $\gamma$ -Mie and predictions from predictive cubic EoSs in the critical region; predictive cubic EoS is shown to give better agreement. In cubic EoSs, critical points for pure components are fixed; hence this may explain why their prediction in the critical region is better. In addition, the CO<sub>2</sub>-hydrocarbon functional groups interaction parameters in SAFT- $\gamma$ -Mie still require additional tuning against wider conditions of pressures and temperatures.







However, it worth noting here that in predictive cubic EoS, compound and binary mixture specific adjustable parameters are required to describe the phase behaviour of the system, while SAFT- $\gamma$ -Mie has group-dependent, and compound- and mixture-independent parameters, which are derived fundamentally, and do not require available data of necessarily constituent mixtures, or compounds for that matter.

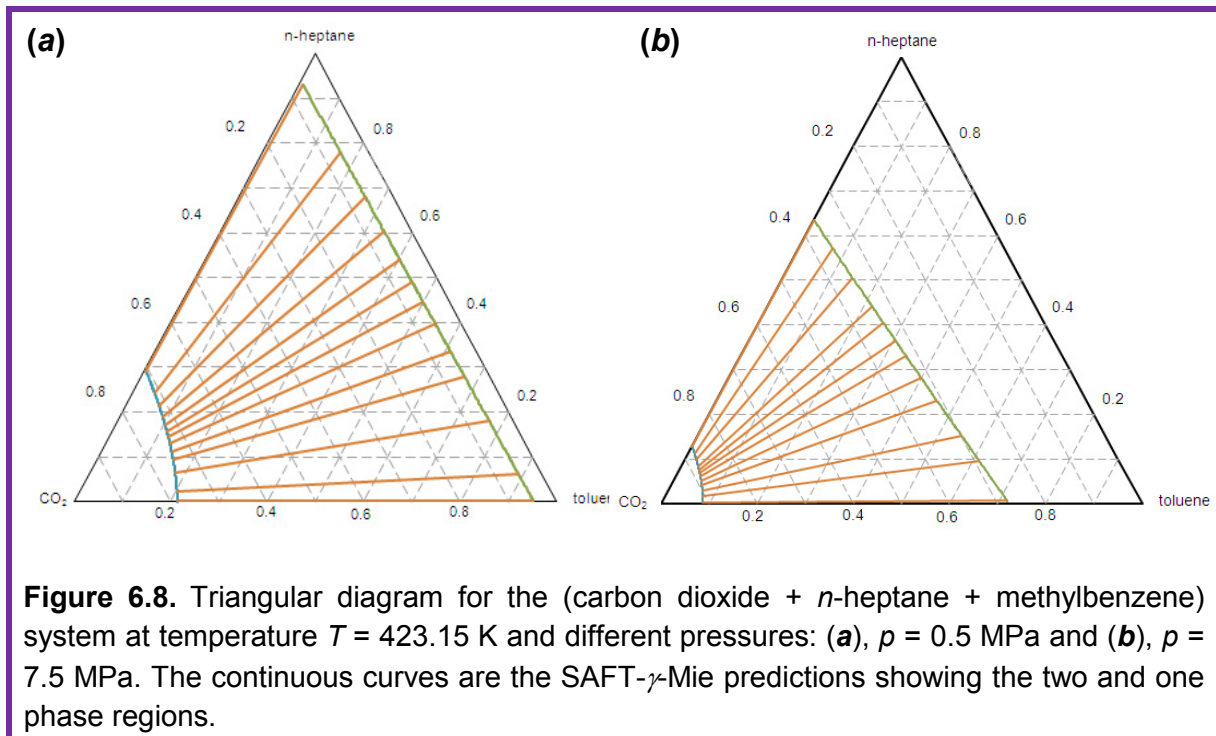
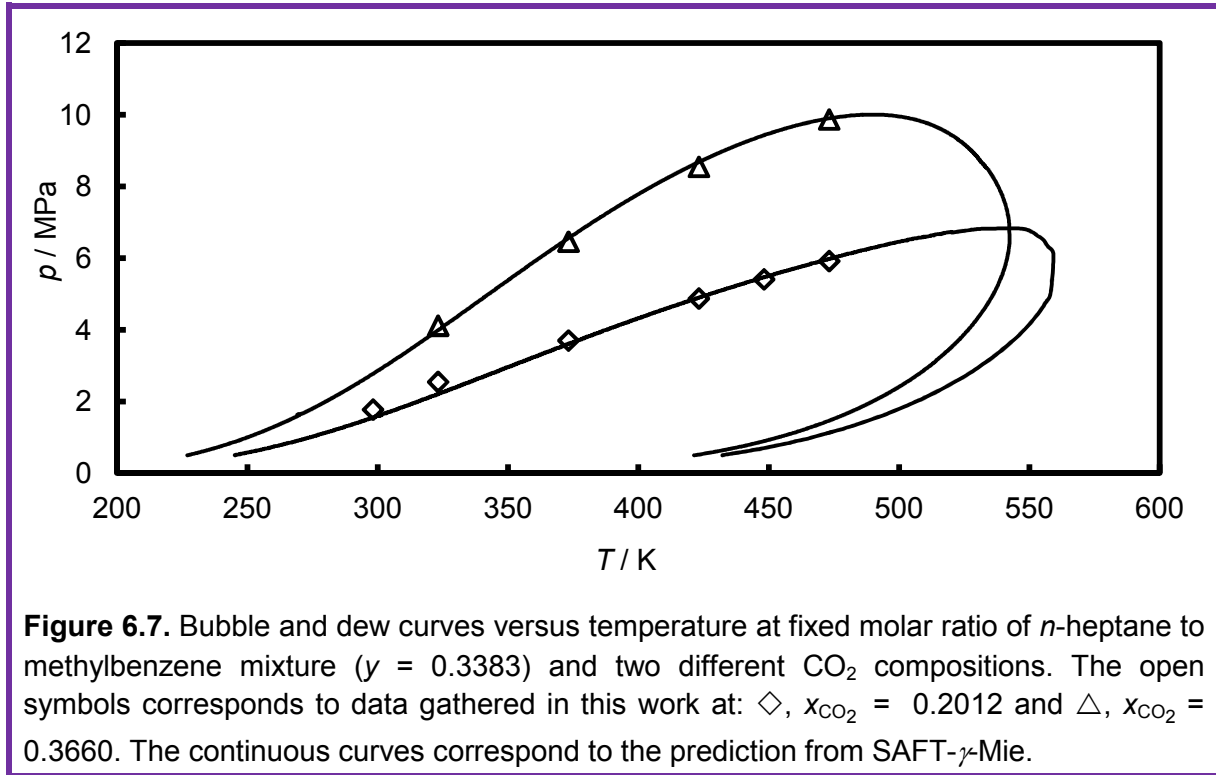
The results are also presented at constant temperature in ( $p, x_{\text{CO}_2}$ ) diagrams by considering the  $\text{CO}_2$  and the liquid mixture as a pseudo binary mixture as shown in Figures 6.3, 6.4, 6.5 and 6.6. In these Figures, the comparison between experimental data and predicted data from SAFT- $\gamma$ -Mie are shown. The solid lines correspond to SAFT- $\gamma$ -Mie predictions at  $T = (298.15, 323.15, 423.15 \text{ and } 473.15)$  K respectively. In Figure 6.7 we plot the experimental and predicted bubble and dew pressure curves against temperature at two fixed mole fractions of  $\text{CO}_2$ .

The comparison between experimental data and SAFT- $\gamma$ -Mie theory for the ternary mixture gives an absolute average deviation  $\Delta_{\text{AAD}} = 4.4\%$  for all isotherms, with the best agreement shown for  $T = 373.15$  K, with  $\Delta_{\text{AAD}} = 1.9\%$ , and biggest deviation for  $T = 473.15$  K, with  $\Delta_{\text{AAD}} = 10.5\%$ . This indicates an increased deviation with increasing temperature, particularly above  $T = 423.15$  K, which require further investigation. Overall, the agreement, while not perfect, is good, especially on the bubble curve. The results suggest that there is merit in the approach of combining, within a SAFT approach, the Mie potential with a group-contribution scheme for the interaction parameters based on pure-component data alone. The comparison, as shown in these figures, illustrates the strong agreement between experimental data (open symbols) and theory (continuous curves) over the entire composition range of carbon dioxide for all  $n$ -heptane-to-methylbenzene molar ratios, given the aforementioned deviation at higher temperatures.

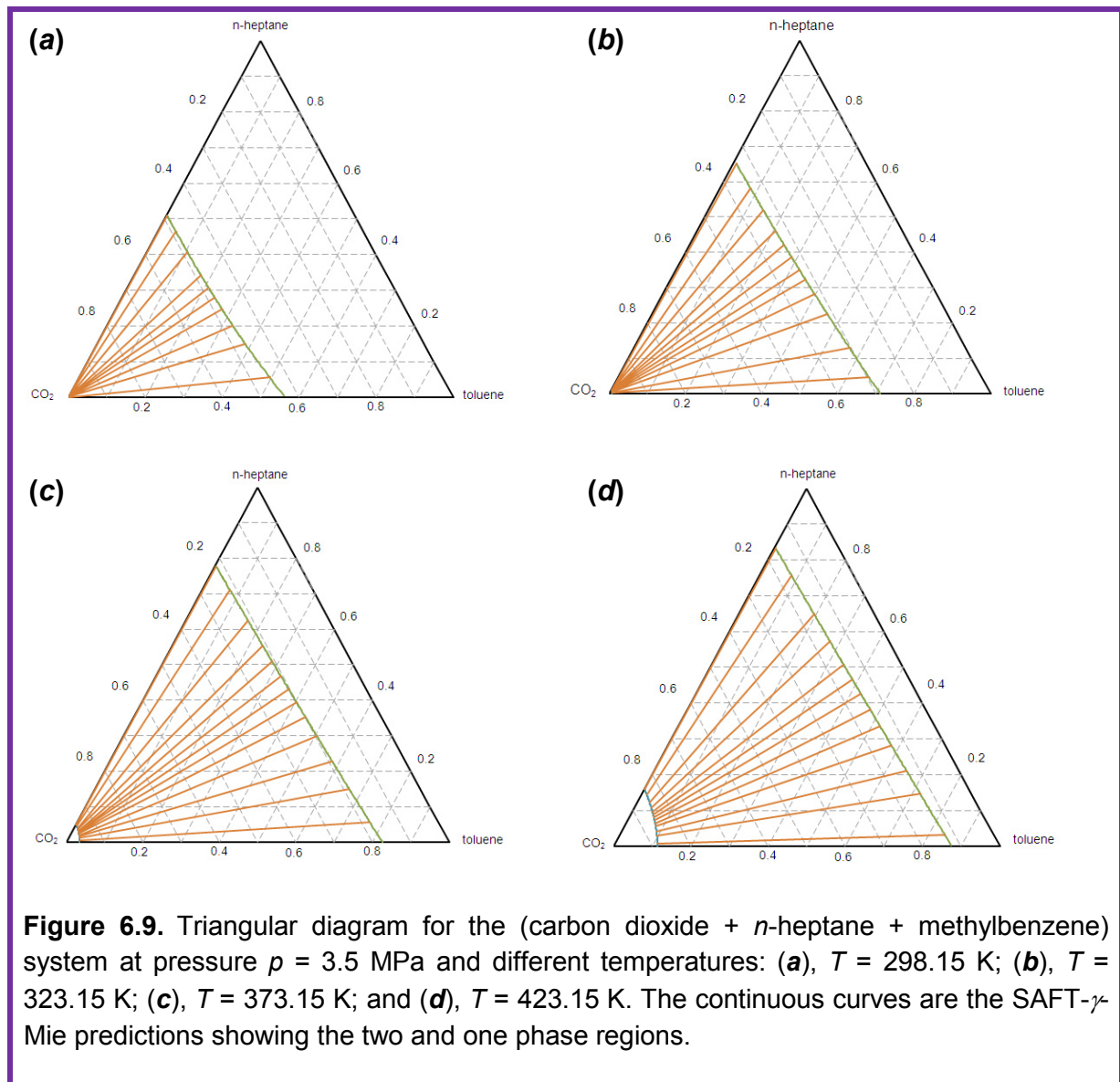
In addition, in Figures 6.8 and 6.9, some examples of the calculated ternary diagrams for this mixture are shown. Figure 6.8 shows the effect of changing pressure on ternary diagrams at fixed temperature while Figure 6.9 represents ternary diagrams at fixed pressure but different temperatures. These figures serve to illustrate what other phase behaviour calculations can be performed once the model is proved to be predictable.

Finally, comparison between SAFT- $\gamma$ -Mie, PPR78 and  $\text{PR}_2\text{SRK}$  EoSs at  $T = 373.15$  K is shown in Figure 6.10. The comparison is made against two different molar ratios of  $n$ -heptane-to-methylbenzene. We also make use of the predictive PSRK approach [121] in this comparison for completeness, which is a combination of the SRK EoS and the predictive

UNIFAC approach for calculating the mixture parameters  $a$  and  $b$ . The UNIFAC group parameters and group interactions (which are obtained from parametric fits to experimental vapour-liquid equilibria for mixtures) were obtained from the Dortmund Databank [133].



Different alpha functions can be used for better description of the phase equilibria but this is not applied in the current work. It can be observed that these predictive methods give similar accuracies regarding VLE prediction, with, as expected, some deviation in the critical region as previously described. It worth noting here that the PSRK method usually fails in the description of highly asymmetric systems [232]. Overall, the agreement is excellent for all approaches, illustrating the predictive capability of these methods. It was observed that at higher temperatures, PPR78 and  $\text{PR}_2\text{SRK}$  EoSs show better agreement close to the critical region than  $\text{SAFT-}\gamma\text{-Mie}$ .



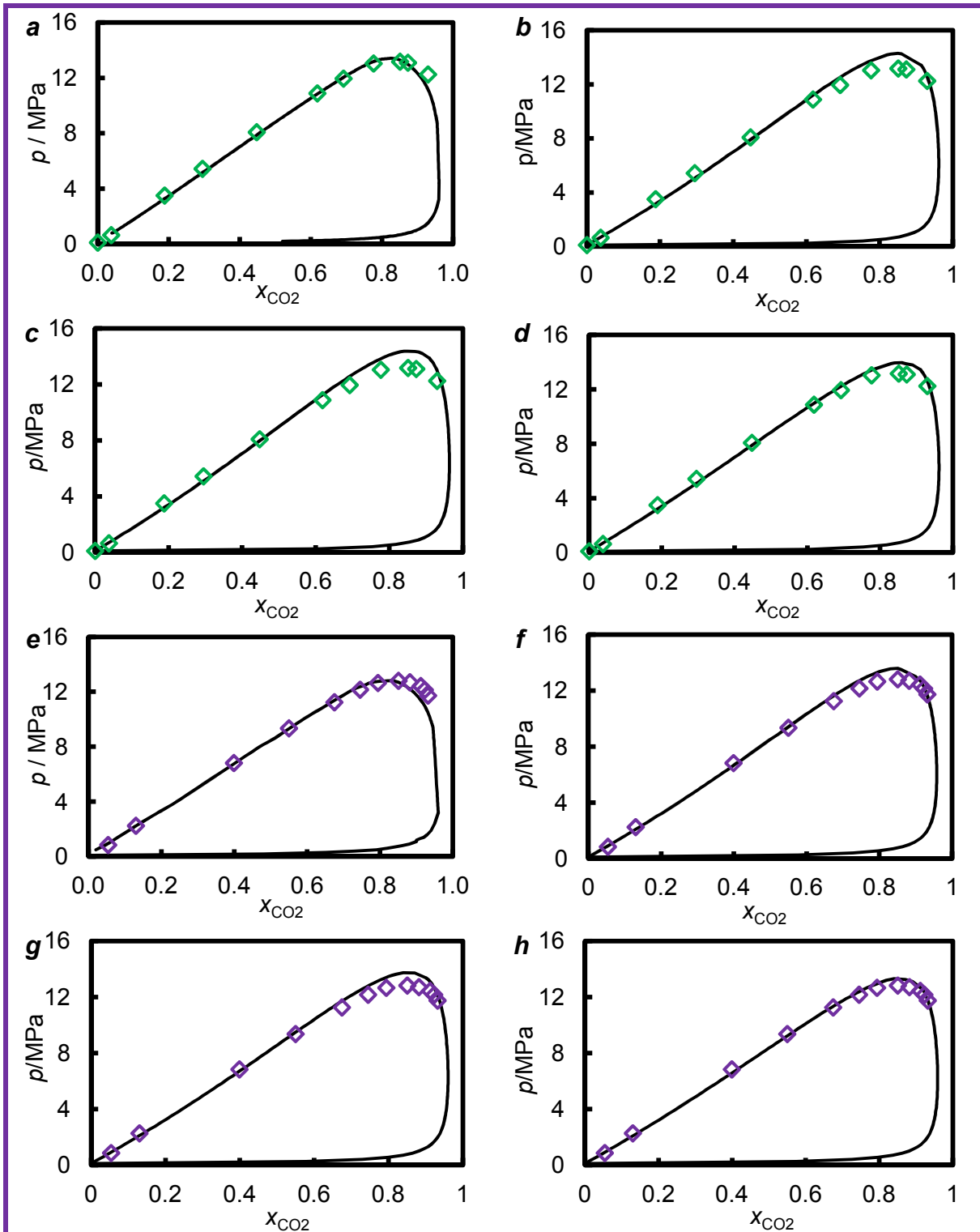


**Figure 6.10.** Bubble and dew curves for the ternary mixture  $\text{CO}_2$  (1) +  $n$ -heptane (2) + methylbenzene (3) at temperature  $T = 373.15$  K. Symbols represents experimental data at the following heptane molar ratio ( $y$ ) in heptane/methylbenzene mixture: (a), (b), (c), (d)  $y = 0.4819$ ; and (e), (f), (g), (h)  $y = 0.7503$ . The solid line represents prediction from: (a) and (e) SAFT- $\gamma$ -Mie; (b) and (f), PPR78 with  $k_{12} = 0.1134$ ,  $k_{13} = 0.0913$  and  $k_{23} = 0.0049$ ; (c) and (g), PR<sub>2</sub>SRK with  $k_{12} = 0.1322$ ,  $k_{13} = 0.0990$  and  $k_{23} = 0.0050$ ; and (d) and (h), PSRK.

Again, this might be because in PPR78 and PR<sub>2</sub>SRK approach, group interaction parameters were optimised using much wider range of literature data and conditions [45], while the group interactions between  $\text{CO}_2$  and hydrocarbon functional groups were only optimised using available data up to around  $T = 400$  K [39]. This may explain the observed deviation at temperatures higher than this value. However, it was proved that SAFT versions work better than cubic EoSs for derivative properties. An example is the work reported by Lafitte and co-workers [171], in which an improved description of derivative properties (such as heat capacity and speed of sound) when compared to popular cubic EoSs was shown. It is well known that cubic EoSs cannot predict these properties really well.

## 6.5 Conclusion

Reliable new experimental vapour-liquid phase behaviour data of mixtures containing (carbon dioxide + *n*-heptane + methylbenzene) at temperature between (298 and 473) K and at pressures up to approximately 16 MPa are provided. The results contain four different fixed molar ratio of *n*-heptane to methylbenzene and for each fixed ratio, five isotherms was studied.

The results were compared with predictions from SAFT- $\gamma$ -Mie, PPR78 and PR<sub>2</sub>SRK EoS. Overall, good agreement between theory and experiment was observed. The comparison proves the advantages of using a group-contribution scheme in these methods. It was observed that these methods give similar accuracies for VLE calculations. It was also observed that PPR78 and PR<sub>2</sub>SRK EoSs work better than SAFT- $\gamma$ -Mie in the critical region. However, it is well known that cubic EoSs predict poorly the derivative properties of pure components and mixtures while SAFT predicts better in this regard. Further examination and comparison (hence more reliable experimental data) between these predictive methods is still required against more complex mixtures and for other thermophysical properties such as density. This is a good scope for further work.

## Chapter 7: Phase Behaviour and Density of (CO<sub>2</sub> + Synthetic Crude Oil) Mixtures

### 7.1 Overview

In this work, the phase behaviour and density of (CO<sub>2</sub> + synthetic crude oil) mixtures was studied. The 'dead' oil contained a total of 17 components including alkanes, branched-alkanes, cyclo-alkanes, and aromatics. Solution gas (0.81 methane + 0.13 ethane + 0.06 propane) was added to obtain live synthetic crudes with gas-oil ratios of either 58 or 160. Phase equilibrium and density measurements are reported for the 'dead' oil and the two 'live' oils under the addition of CO<sub>2</sub>. The measurements were carried out at temperatures of (298.15, 323.15, 373.15 and 423.15) K and at pressures up to 36 MPa, and included vapour-liquid, liquid-liquid and vapour-liquid-liquid equilibrium conditions. The results are qualitatively similar to published data for mixtures of CO<sub>2</sub> with both real crude oils and simple hydrocarbon mixtures containing both light and heavy components.

The present experimental data have been compared with results calculated with the two predictive models, PPR78 and PR<sub>2</sub>SRK. Careful attention was paid to the critical constants and acentric factor of high molar-mass components. Since the mixture also contained several light substances with critical temperatures below some or all experimental temperatures, the use of the Boston-Mathias modification of the PR78 and SRK equations was investigated. The results showed that these models can predict with reasonable accuracy the vapour-liquid equilibria of systems containing CO<sub>2</sub> and complex hydrocarbon mixtures without the need to regress multiple binary parameters against experimental data.

### 7.2 Introduction

An underlying database of experimental phase equilibrium results is essential for the optimization and/or validation of thermodynamic models. Typically, data for multi-component mixtures are used to validate the predictive capabilities of these models. Unfortunately, few experimental data sets pertaining to (CO<sub>2</sub> + crude oils) have been published in the open literature. The crude oils investigated range from black oil, through volatile oils, to gas condensates. Even though modern analysis methods can resolve much information about the composition of the crude oil, it is still extremely difficult to characterize the composition of the oil in a fully-satisfactory way. In the published studies, the reported oil composition was usually given up to C<sub>7</sub> with the components heavier than heptane typically lumped into as single pseudo-component, the properties of which were not well known. From a modelling perspective, this limited composition analysis restricts the usefulness of the data. Examples

of phase equilibria studies on (CO<sub>2</sub> + crude oils) can be found in the work of Orr et al. [81], Gardner et al. [82], Rathmell et al. [83], Turek et al. [84], and Simon et al. [85].

In summary, the available phase-equilibrium data for mixtures of CO<sub>2</sub> with compositionally-characterized multi-component hydrocarbons is limited in terms of the diversity of the hydrocarbons, and the ranges of temperature and pressure investigated. Meanwhile, the few available data for CO<sub>2</sub> with crude oils are of restricted generic value because of the imperfect compositional analysis of the oil. Thus, the present work aimed to provide new experimental data suitable for testing thermodynamic models rigorously under representative conditions of temperature, pressure and composition. In the present study, the experimental data have been compared with results calculated with the two predictive models, PPR78 and PR<sub>2</sub>SRK. Since these predictive EoS models have not yet been extensively tested against multi-component mixture data, one of the objectives of the present study was to facilitate such comparisons for the case of (CO<sub>2</sub> + hydrocarbon) systems.

We remark in passing that, in addition to the phase equilibrium conditions, it is also very useful to know the coexisting phase densities. In the case of CO<sub>2</sub> + crude oil mixtures, the saturated phase densities are necessary for calculating the crude-oil swelling during CO<sub>2</sub> reservoir flooding and for other reservoir and process engineering calculations associated with fluids having an appreciable CO<sub>2</sub> content. Thus, a second objective of the present work was to provide experimental data for saturated phase densities, albeit with modest accuracy.

The present work called for the study of a synthetic hydrocarbon mixture with properties similar to a crude oil. Based on this, a synthetic oil was designed to match the physical and chemical properties of a bottom-hole crude oil sample from a Qatari field. The synthetic 'dead' oil contained 17 components; 'live' oils were also obtained by adding a 3-component solutions gas (0.81 CH<sub>4</sub> + 0.13 C<sub>2</sub>H<sub>6</sub> + 0.06 C<sub>3</sub>H<sub>8</sub>).

For the light substances considered in this study, the pure-component properties (critical temperature, critical pressure and acentric factor) needed for modelling with e.g. the PPR78 EoS are readily available in the literature. There also exists abundant binary vapour-liquid equilibrium data for their mixtures with CO<sub>2</sub> that can be used to validate such predictive models for particular pairs of components. However, such data for the three heaviest components (squalane, tetracosane and phenylhexadecane) are scarce. Thus, the estimation of the critical temperature, critical pressure and acentric factor for these components, and the validation of the model for binary (hydrocarbon + CO<sub>2</sub>) systems, was an important precursor to the modelling aspects of the present study.

Regarding the binary system (CO<sub>2</sub> + squalane), three authors have reported VLE data. Brunner et al. [233] used a static-analytical method for the measurements at  $T = (313.15 \text{ to } 426.0) \text{ K}$ ,  $p = (3.50 \text{ to } 35.0) \text{ MPa}$ , and  $x_{\text{CO}_2} = (0.122 \text{ to } 0.884)$ . They also correlated the data with SRK EoS with Mathias-Klotz-Prausnitz (MKP) mixing rule. Liphard and Schneider [234] used a high-pressure view cell at  $T = (273 \text{ to } 423) \text{ K}$ ,  $p = (5 \text{ to } 100) \text{ MPa}$  and  $w_{\text{CO}_2} = (0.070 \text{ to } 0.931)$ , where  $w$  denotes mass fraction. Sovova et al. [235] measured the solubility of squalane in CO<sub>2</sub> using a flow type apparatus at temperatures  $T = (303 \text{ to } 328) \text{ K}$  and  $p = (7.9 \text{ to } 27.5) \text{ MPa}$ . For the binary system (CO<sub>2</sub> + tetracosane), there are also three reported VLE data sets. Tsai and Yau [236] measured the solubility of CO<sub>2</sub> in *n*-tetracosane at  $T = (373.15 \text{ to } 573.15) \text{ K}$ ,  $p = (1 \text{ to } 5) \text{ MPa}$  and  $x_{\text{CO}_2} = (0.0819 \text{ to } 0.3531)$  using a semi-flow apparatus. Kordikowski and Schneider [237] measured the VLE of this system at  $T = (353.15 \text{ and } 393.15) \text{ K}$  and  $p \leq 47.5 \text{ MPa}$  using an analytical apparatus. Sato et al. [238] measured the solubility of CO<sub>2</sub> in tetracosane at  $T = (373.15 \text{ to } 473.15) \text{ K}$  and  $p \leq 40 \text{ MPa}$  using a synthetic method with a variable-volume view cell. Unfortunately, there appear to be no available experimental data for the binary system (CO<sub>2</sub> + phenylhexadecane).

The phase behaviour studied in this work included vapour-liquid, liquid-liquid and vapour-liquid-liquid equilibrium conditions observed at temperatures of (298.15, 323.15, 373.15 and 423.15) K and at pressures up to 36 MPa. We also report the experimental and modelling of mixture density at each measured bubble- or dew-point, and measurements of the vapour-liquid critical points.

### 7.3 Selection of the Synthetic Crude Oil

The synthetic liquid oil was identified and selected based on available literature data to match the physical and chemical properties of a crude oil sample from a Qatari field [239]. The properties of the oil sample used in this analysis are given in Table 7.1. These include properties of the whole sample, such as density and kinematic viscosity, and properties of different cuts obtained by fractional distillation. Overall, 8 cuts were reported and for each cut, certain properties such as boiling temperature range, cumulative volume, density, and ratios of paraffins, naphthenes, and aromatics (PNA) were given.

In order to find a representative synthetic mixture, the properties of the whole dead oil and of the 8 cuts were analyzed with the aid of the *Oil Manager* function in *Aspen Hysys* simulation software [240]. This resulted in the identification of a mixture of hypothetical components that best represented the known physical properties of each cut. The hypothetical components were identified by molar mass, density and normal boiling temperature. We then selected



real components with properties chosen to approximate those of the hypothetical components. In making this match we considered also the availability and cost of potential real components and the desired PNA ratios that we also wished to match.

Once real components were selected, the simulation software was run again with a fixed component slate and the composition optimized to best match the boiling curve and densities of the fractions. Initially, polycyclic components (such as chrysene and anthracene) and long-chain normal alkanes (such as *n*-C<sub>30</sub>H<sub>62</sub>) were considered but these were found not to be soluble in the rest of the mixture. Consequently, polycyclic were abandoned, and normal alkanes longer than C<sub>24</sub> were replaced with the C<sub>30</sub> isomer 2,6,10,15,19,23-hexamethyltetracosane (squalane).

Finally, 17 components were selected to represent the dead oil, including alkanes, branched- and cyclo-alkanes, and aromatics as detailed in Table 7.2. The PNA ratio of the synthetic dead oil was 72.7 %, 4.9 % and 22.4 % respectively. These values lie within the ranges found in the literature. A comparison between the experimental true boiling and density curves of the original dead crude oil and that simulated for the synthetic mixture is shown in Figure 7.1. Good agreement was achieved for approximately 80 % of the boiling range but deviations are observed at the heavy end due to the elimination of heavy polycyclic components.

In order to generate so-called live oils, a three-component solution gas (0.813 CH<sub>4</sub> + 0.126 C<sub>2</sub>H<sub>6</sub> + 0.061 C<sub>3</sub>H<sub>8</sub>) mixture was added to obtain two different gas-oil ratios (GOR),<sup>11</sup> leading to a live oil containing 20 components in total. The solution gas composition was identified and characterized based on the properties of gas from a Qatari field [241].

Table 7.2 list all components and gives their mole fractions in the dead oil and in the live oil with both low and high GOR. Also given are the values of the normal boiling temperatures (*T<sub>b</sub>*) and molar mass (*M*) obtained from the National Institute of Standard and Technology (NIST) Thermodata Engine (TDE) software [226-227].

---

<sup>11</sup> The GOR is defined as the ratio of the volumes of gas and liquid obtained when the mixtures is flashed at standard conditions of *T* = 288.15 K and *p* = 0.1013 MPa.

**Table 7.1.** Properties of Qatari crude oil sample: density  $\rho$ , relative density  $\rho_r$ , API gravity, kinematic viscosity  $\mu$ , PNA ratios, Asphaltene mass fraction and boiling-range analysis.

$\rho(T = 283.15 \text{ K}) \text{ (kg}\cdot\text{m}^{-3}\text{)}$	886.5	Paraffins volume fraction <sup>c</sup>	69.19 %		
$\rho_r(T = 288.7 \text{ K})$ <sup>a</sup>	0.8873	Naphthenes volume fraction <sup>c</sup>	23.41 %		
API gravity <sup>b</sup>	27.97	Aromatics volume fraction <sup>c</sup>	7.40 %		
$\mu(T = 293.15 \text{ K}) \text{ (mm}^2\cdot\text{s}^{-1}\text{)}$	44.06	Asphaltene mass fraction	1.7 %		
$\mu(T = 313.15 \text{ K}) \text{ (mm}^2\cdot\text{s}^{-1}\text{)}$	13.32				
Boiling range (°C)	Cumulative volume fraction	$\rho$ (T = 283.15 K) (kg·m <sup>-3</sup> )	Boiling range (°C)	Cumulative volume fraction	$\rho$ (T = 283.15 K) (kg·m <sup>-3</sup> )
5-65	5.7 %	646.4	250-300	39.48 %	857.8
65-150	14.47 %	731.6	300-350	48.92 %	880.3
150-200	21.66 %	789.7	350-420	60.69 %	905.2
200-250	29.89 %	825.5	420-560	80.5 %	944.9

<sup>a</sup> Relative density  $\rho_r = \rho/\rho(\text{H}_2\text{O})$   
<sup>b</sup> API (American Petroleum Institute) gravity =  $(141.5/\rho_r) - 131.5$  at  $T = 288.7 \text{ K}$   
<sup>c</sup> PNA ratios refer to the boiling range up to 200 °C only.

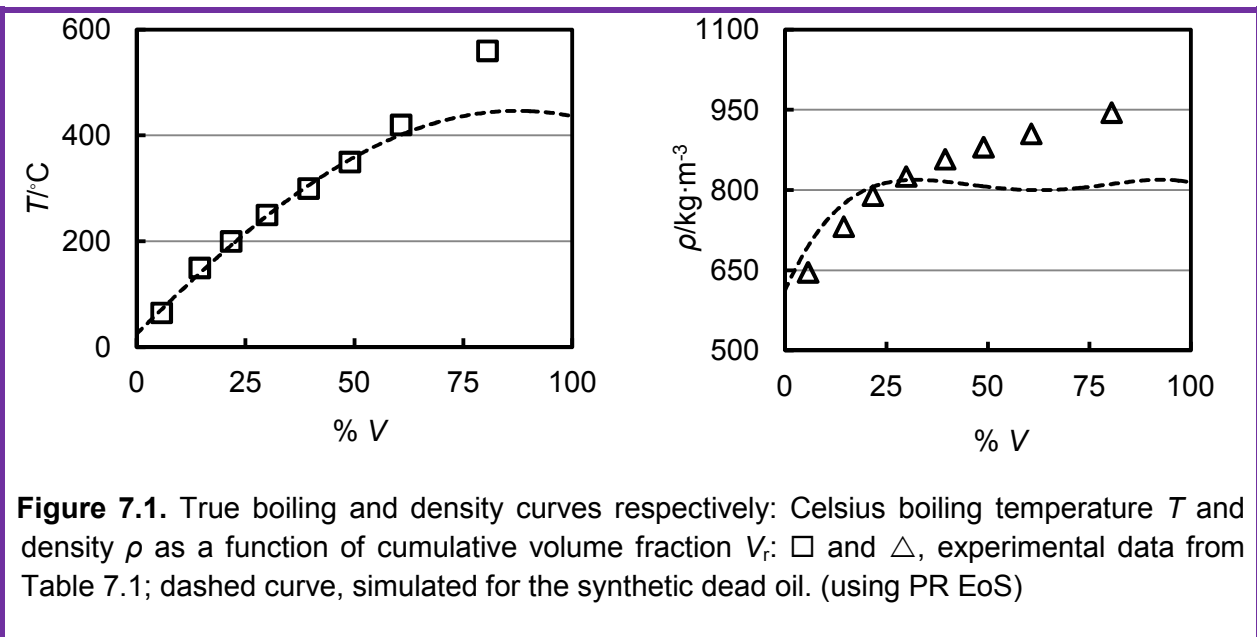


**Table 7.2.** The list of all components used in this work with mole fraction  $x$ , normal boiling temperature  $T_b$  and molar mass  $M_w$ <sup>a</sup>

Component	$x_1$	$x_2$	$x_3$	$T_b$ K	$M_w$ g·mole <sup>-1</sup>
2,2-Dimethylbutane	0.1192	0.0715	0.0417	322.88	86.18
<i>n</i> -Heptane	0.1047	0.0628	0.0366	371.58	100.21
Ethylcyclohexane	0.0621	0.0373	0.0217	404.94	112.21
<i>n</i> -Nonane	0.0503	0.0302	0.0176	423.97	128.26
propylcyclohexane	0.0301	0.0181	0.0105	429.89	126.24
1,2,3,4-Tetrahydronaphthalene	0.0454	0.0272	0.0159	480.77	132.21
1,3,5-Triethylbenzene	0.0666	0.0400	0.0233	489.20	162.27
1-Phenylhexane	0.0379	0.0227	0.0133	499.30	162.27
<i>n</i> -Tridecane	0.0127	0.0076	0.0044	508.58	184.37
1-phenyloctane	0.0638	0.0383	0.0223	537.54	190.32
<i>n</i> -Pentadecane	0.0310	0.0186	0.0109	543.77	212.41
<i>n</i> -Hexadecane	0.0131	0.0079	0.0046	559.94	226.43
Octadecane	0.0420	0.0252	0.0147	589.86	254.48
Nonadecane	0.0365	0.0219	0.0128	603.80	268.51
Hexadecylbenzene	0.0449	0.0269	0.0157	662.15	316.57
Tetracosane	0.0066	0.0040	0.0023	664.43	338.64
Squalane	0.2331	0.1399	0.0816	720.00	422.82
Methane	0.0000	0.3252	0.5285	111.63	16.04
Ethane	0.0000	0.0504	0.0819	184.55	30.07
Propane	0.0000	0.0244	0.0397	231.05	44.10

<sup>a</sup>  $x_1$  is the mole fraction of the components present in the synthetic dead oil mixture,  $x_2$  is the mole fraction of the components present in the synthetic live oil mixture with low gas oil ratio,  $x_3$  is the mole fraction of the components present in the synthetic live oil mixture with high gas oil ratio. The boiling point temperatures  $T_b$ , molar mass  $M_w$ , and standard density  $\rho_{std}$  were obtained from the NIST Thermodata Engine (TDE) software.

## 7.4 Experimental Results and Discussion

Phase equilibrium measurements are reported for the ‘dead’ synthetic oil, and for two ‘live’ synthetic oils with GORs of 58 and 160, and under the addition of CO<sub>2</sub>. The measurements were carried out at temperatures of (298.15 K, 323.15 K, 373.15 K and 423.15 K) and at pressures up to 36 MPa and include vapour-liquid equilibrium (VLE), vapour-liquid-liquid equilibrium (VLLE) and liquid-liquid equilibrium (LLE) conditions. The results, in the form of isothermal ( $p$ ,  $x_{\text{CO}_2}$ ) data, are given in Appendix C for the measurements of (CO<sub>2</sub> + dead oil), (CO<sub>2</sub> + live oil 1), and (CO<sub>2</sub> + live oil 2). In the Appendix, some experimentally determined critical points are also given. Typically, when approaching the critical point, the sample appeared as a white cloud, with color changes and darkening. At this condition, retracting the piston yielded two phases of equal volume. Generally speaking, at high pressures, phase separation was harder to spot because the two phases had only slightly different densities and therefore separated more slowly. Because of this, and as indicated in the uncertainty calculations, the high pressure portions of the phase boundaries are known less precisely than the portions at low pressures. Images of the interior of the variable-volume cell showing VLLE, LLE and critical conditions are given in Figure 7.2.

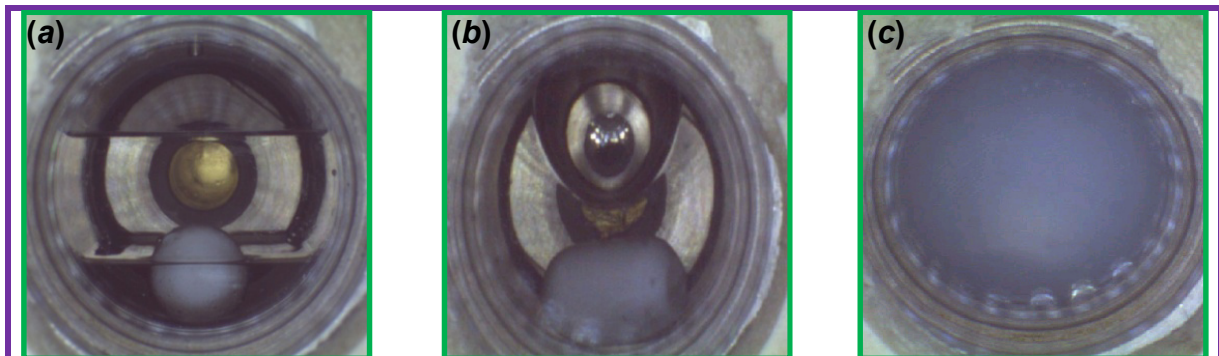
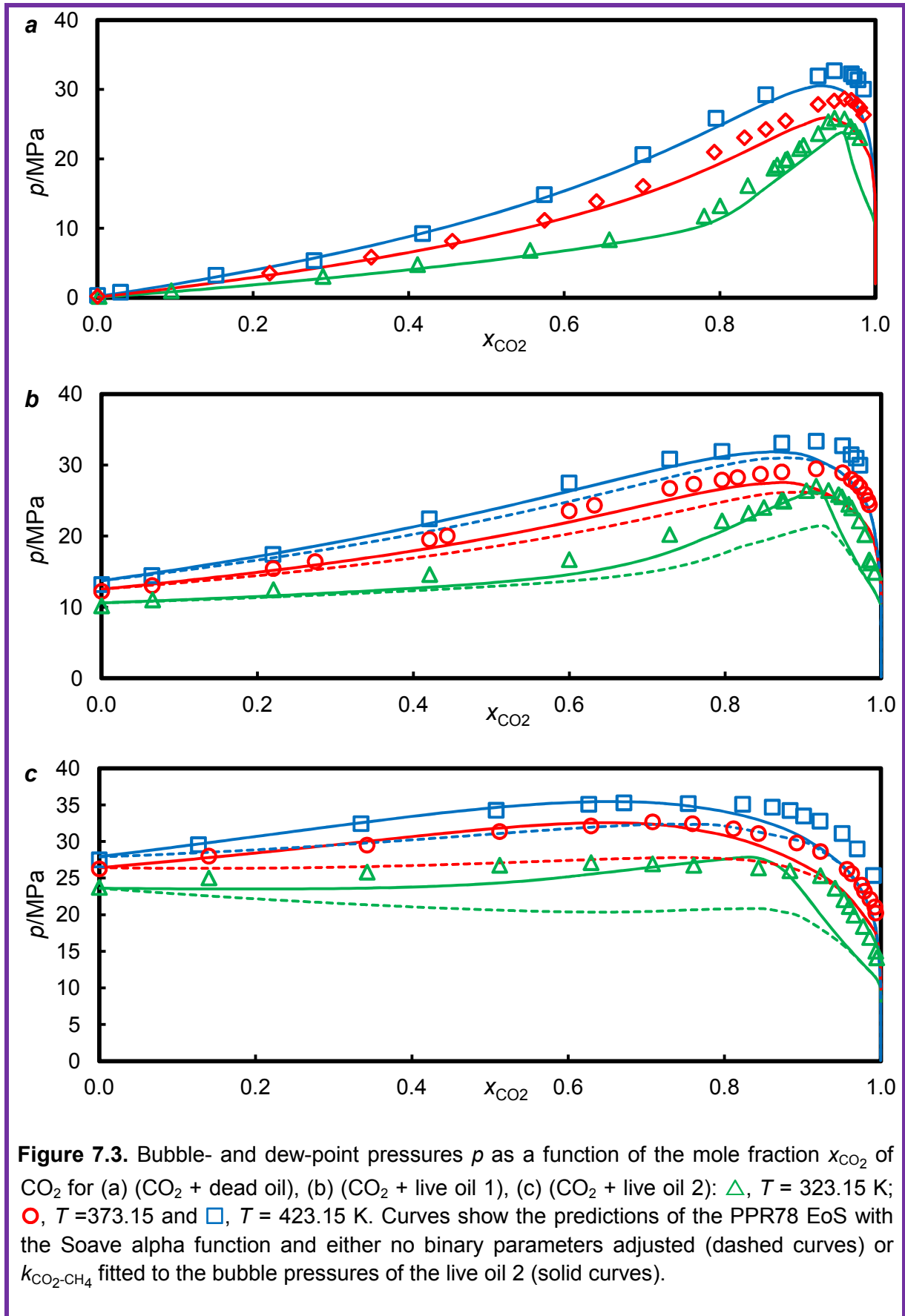


**Figure 7.2.** Images of the interior of the variable volume cell showing: (a), VLLE (hydrocarbon-rich, CO<sub>2</sub>-rich liquid and CO<sub>2</sub>-rich gas phases); (b), LLE (hydrocarbon rich and CO<sub>2</sub> liquid rich phases where the CO<sub>2</sub> liquid rich phase is getting denser and start to sink into the bottom, this is one of the trapping mechanism for CO<sub>2</sub>); (c), critical opalescence phenomena observed between the hydrocarbon and carbon dioxide-rich phases.

The ( $p$ ,  $x_{\text{CO}_2}$ ) data at  $T = (323.15, 373.15, \text{ and } 423.15)$  K are plotted in Figures 7.3a, 7.3b, and 7.3c for the dead oil, live oil 1, and live oil 2 respectively. Under these conditions, only vapour-liquid equilibria were found. The ( $p$ ,  $x_{\text{CO}_2}$ ) data are plotted for the same systems in Figures 7.4a, 7.4b, and 7.4c at  $T = 298.15$  K, at which temperature vapour-liquid, vapour-liquid-liquid and liquid-liquid equilibria were observed.



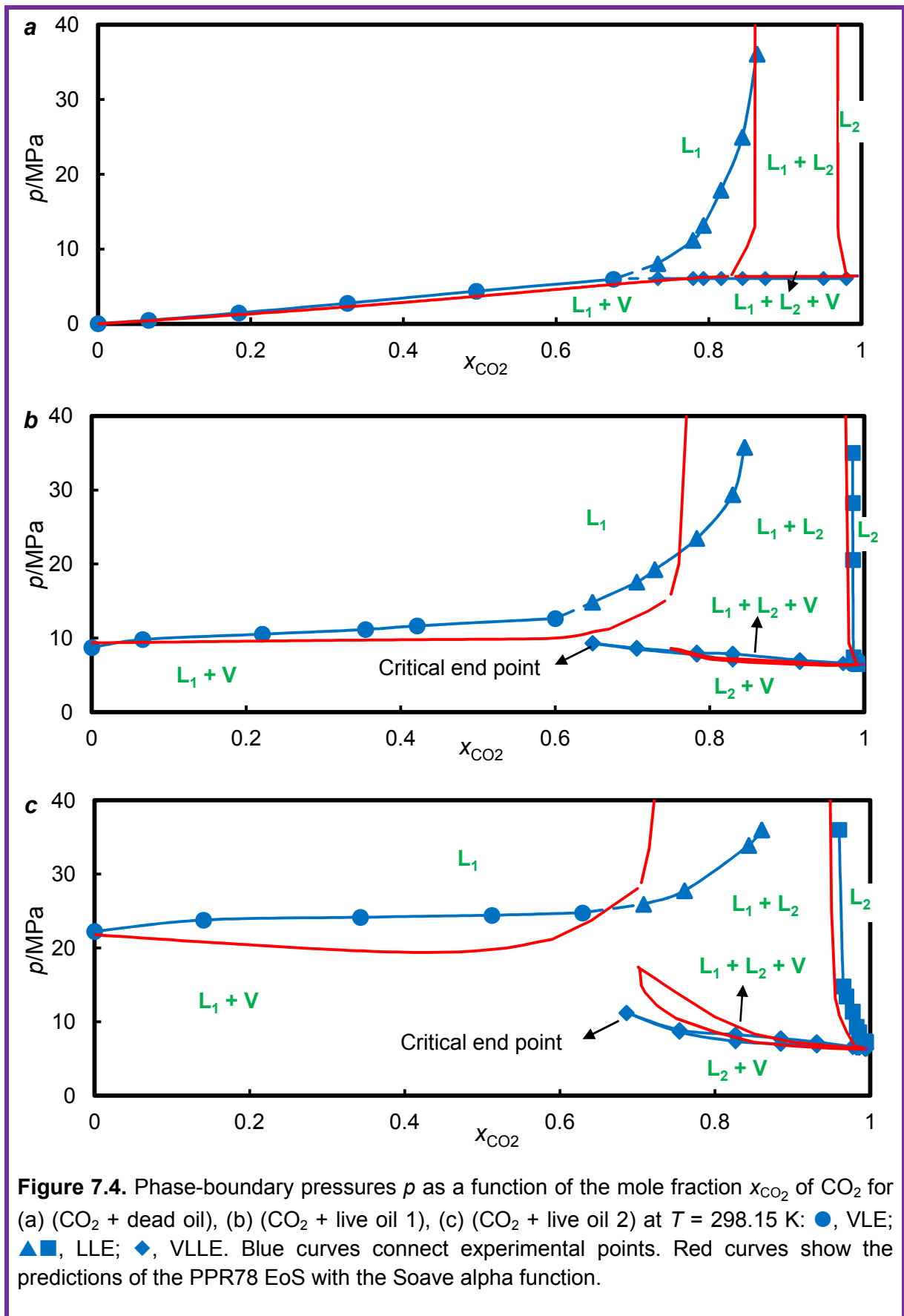
We first discuss the system (CO<sub>2</sub> + dead oil). At low temperatures, this system behaves as a pseudo-binary mixture of (CO<sub>2</sub> + hydrocarbon). The VLLE observed at the lowest temperature is typical of type III phase behaviour in the classifications of Van Konynenburg and Scott for a binary system [42]. This is expected due to the presence of heavy components which exhibit only partial miscibility with CO<sub>2</sub>-rich liquid due to the large differences in molecular size and volatility. The three-phase VLLE region at fixed temperature in a multi-component system is, in principle, delimited by lower and upper pressure loci that vary with composition. However, for (CO<sub>2</sub> + dead oil), the upper and lower bounds were almost indistinguishable and we found the horizontal three-phase line at  $p = 6.06$  MPa, as shown in Figure 7.4a. The  $T$ - $p$  projection of this three-phase line was measured from  $T = 298.15$  K to the upper critical end point, which was found to be at  $T = 316.3$  K, and the data are given in Table 7.3 and plotted in Figure 7.5 in comparison with the vapour-pressure curve of CO<sub>2</sub>.

**Table 7.3.** Three phases VLLE locus for the CO<sub>2</sub> + dead oil mixture. <sup>a</sup>

$T$ (K)	$p$ (MPa)	$T$ (K)	$p$ (MPa)	$T$ (K)	$p$ (MPa)
298.15	6.04	308.62	7.39	313.9	8.173
300.5	6.28	310.16	7.636	314.27	8.211
303.02	6.62	311.2	7.749	315.28	8.311
306.06	7.02	312.92	8.026	316.3	8.443

<sup>a</sup> Expanded uncertainties are  $U(T) = 0.08$  K and  $U(p) = 0.2$  MPa with coverage factor  $k = 2$ .

Thus, the three-phase behaviour in the (CO<sub>2</sub> + dead oil) system is essentially that of a type III binary system in the classification of Van Konynenburg and Scott. The same behaviour is observed in binary (CO<sub>2</sub> + alkane) systems when the alkane contains more than 13 carbon atoms. For example, in the system (CO<sub>2</sub> + hexadecane) at temperatures of 294.15 K and 305.15 K, the three-phase line has been measured at  $p = 5.5$  MPa and  $p = 5.8$  MPa respectively with  $x_{\text{CO}_2} \geq 0.75$  [242-243]. It was also observed in the same binary system that the LLE region separated from the VLE region as temperature increased. Similar VLLE behaviour has also been observed for CO<sub>2</sub> with either multi-component hydrocarbon mixtures or real crude oils, as in the studies reported by Orr et al. [81], Gardner et al. [82], Rathmell et al. [83], Turek et al. [84], and Simon et al. [85]. Although limited to  $T \leq 316.3$  K in the present work, it is likely that the three phase region can extend into the temperature range of CO<sub>2</sub> reservoir-flooding processes because of multiple contacts between CO<sub>2</sub> and hydrocarbons during CO<sub>2</sub> injection [244].



Returning to Figure 7.4a, we see that there is a change in slope where the bubble-curve meets the three-phase line at  $x_{\text{CO}_2} = 0.68$ , above which the system is characterized by LLE. While mapping the boundary between the  $L_1$  and  $L_1 + L_2$  regions, where  $L_1$  is hydrocarbon-rich liquid and  $L_2$  is CO<sub>2</sub>-rich liquid, it was observed that there was a density inversion at a pressure of approximately 12 MPa above which  $L_2$  was the more dense phase.

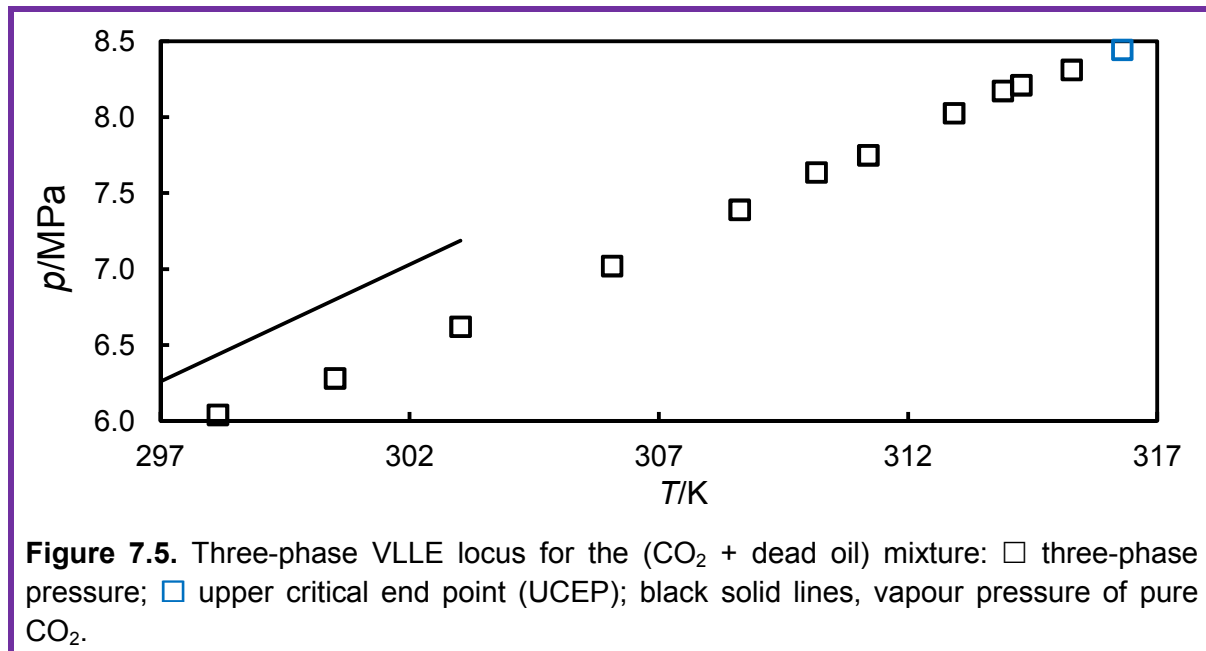
Experimentally, we were not able to reach a sufficiently high mole fraction of CO<sub>2</sub> to observe the boundary between the ( $L_1 + L_2$ ) and the  $L_2$  regions in the (CO<sub>2</sub> + dead oil) system. This boundary is predicted in our modelling, as discussed below, to occur at around  $x_{\text{CO}_2} = 0.98$  and to be bounded at low pressures by a small VLE region that terminates at the vapour pressure of CO<sub>2</sub>. The dew curve, expected at very high CO<sub>2</sub> concentrations and at pressures below the three-phase pressure, was also not observed in our experiments on (CO<sub>2</sub> + dead oil). Figure 7.3a shows that, at the higher temperatures investigated, only VLE conditions were observed for (CO<sub>2</sub> + dead oil) with the bubble- and dew-curves meeting at a vapour-liquid critical point. At  $T = 323.15$  K, the ( $p, x_{\text{CO}_2}$ ) loci are steeper to either side of the critical point than at higher temperatures, and this behaviour may be identified as a precursor of the appearance of LLE at lower temperatures.

We now consider the systems (CO<sub>2</sub> + live oil 1) and (CO<sub>2</sub> + live oil 2), where live oil 1 contained 40 mol% solution gas (GOR of 58) and live oil 2 contained 65 mol% solution gas (GOR of 160). The addition of solution gas raises the pressure of the VLE loci relative to that observed for (CO<sub>2</sub> + dead oil). For  $T = 323.15$  K and higher temperatures, Figures 7.3b and 7.3c show that only VLE conditions were observed while, as shown in Figures 7.4b and 7.4c, VLE, VLLE and LLE were all observed at  $T = 298.15$  K. Due to the presence of the light components in the solution gas, the VLLE region is observed at increasing pressures as the GOR is increased and we also observe a narrow loop in the ( $p, x_{\text{CO}_2}$ ) diagram instead of the horizontal three-phase line found in the absence of solution gas. It can also be seen that the VLLE region does not intersect the VLE/LLE locus. This is because the hydrocarbon mixture is rich in methane (33 mol% in live oil 1). If the oil had lower methane content then the three phase region could extend to the intersection of the VLE and LLE curves. Such behaviour was observed in (CO<sub>2</sub> + crude oil) systems and in simple ternary mixtures containing (CO<sub>2</sub> + CH<sub>4</sub> + heavy alkanes) such as the ternary mixture (CO<sub>2</sub> + CH<sub>4</sub> + C<sub>16</sub>H<sub>34</sub>) reported by Orr et al. [86] in which the methane represents the solution gas and hexadecane represents the synthetic dead oil.



It is worth mentioning here that knowing the pressure at which LLE behaviour occurs provides an indication of the pressure required to make the CO<sub>2</sub>-rich phase behave as a dense, relatively incompressible liquid that could offer better displacement of oil during EOR processes. Turek et al. [84] studied mixtures of CO<sub>2</sub> with crude oils. For the crude oils containing 27 mol% and 69 mol% C<sub>7+</sub> components, the VLLE region at  $T = 313.7$  K occurred for  $x_{\text{CO}_2} \geq 0.60$  with an envelope that was qualitatively similar to that observed for our (CO<sub>2</sub> + live oil) systems, while for an oil with 95 mol% C<sub>7+</sub> components the behaviour was similar to our (CO<sub>2</sub> + dead oil) system.

The two liquid-liquid curves usually meet at a critical point, the position of which is mainly determined by whether the light components partition strongly into the lower or upper phase. This point will lie to the right of the maximum pressure if the light hydrocarbons partition more strongly into the lower phase while it will lie to the left of the maximum pressure if they partition more strongly into the upper phase. This was not experimentally determined as this critical pressure is much higher than the maximum working pressure of our apparatus ( $p = 40$  MPa).



Finally, in Figures 7.6a and 7.6b, we show the saturated phase densities measured in the (CO<sub>2</sub> + dead oil) and (CO<sub>2</sub> + live oil 2) systems at  $T = (323.15, 373.15, \text{ and } 423.15)$  K. In each case, the density increased slightly with increasing CO<sub>2</sub> content along the bubble curve but then fell sharply along the dew curve. As expected, the saturated phase densities declined with increase of either temperature or GOR.

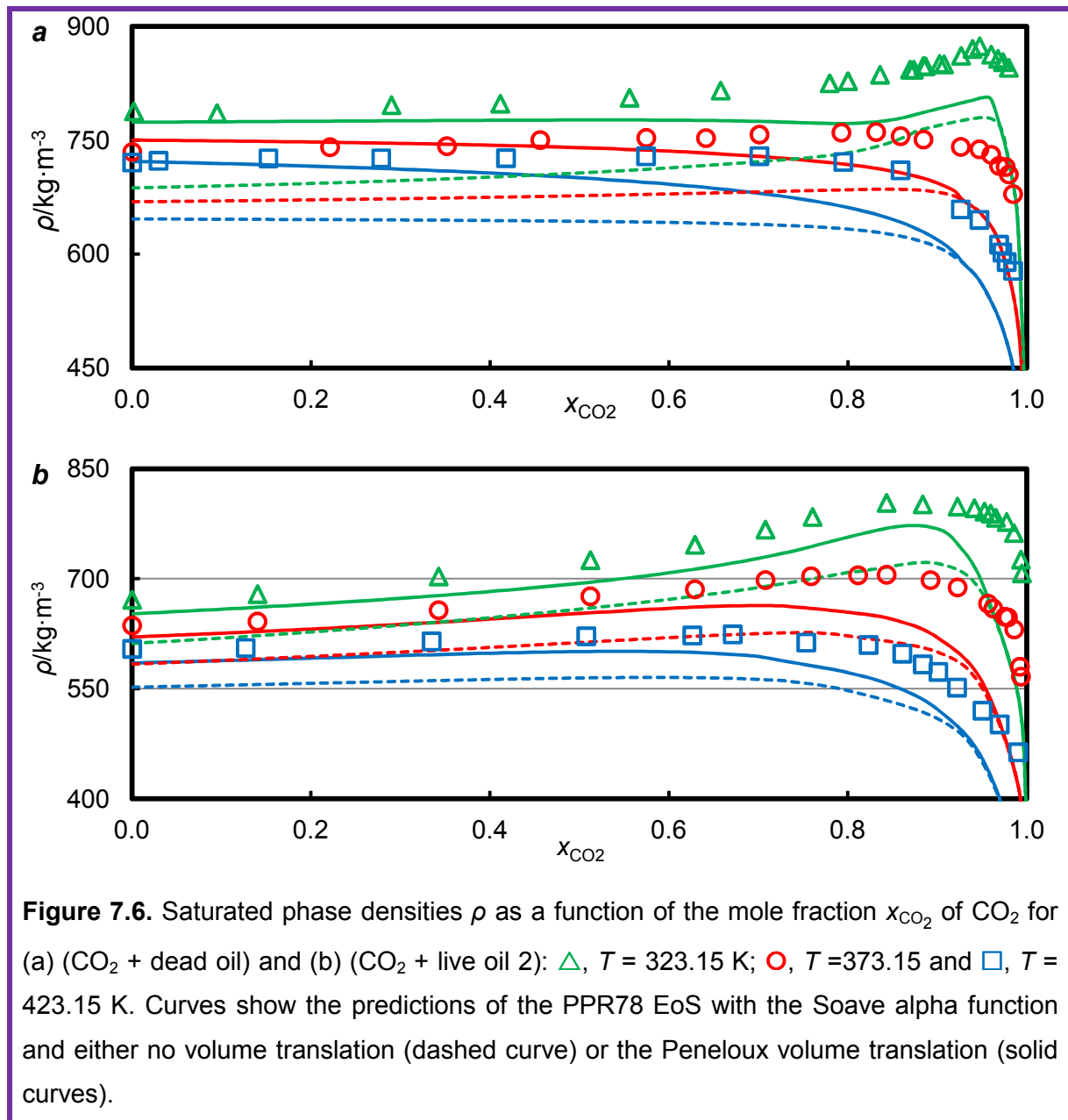


**Figure 7.6.** Saturated phase densities  $\rho$  as a function of the mole fraction  $x_{\text{CO}_2}$  of CO<sub>2</sub> for (a) (CO<sub>2</sub> + dead oil) and (b) (CO<sub>2</sub> + live oil 2):  $\triangle$ ,  $T = 323.15$  K;  $\circ$ ,  $T = 373.15$  and  $\square$ ,  $T = 423.15$  K. Curves show the predictions of the PPR78 EoS with the Soave alpha function and either no volume translation (dashed curve) or the Peneloux volume translation (solid curves).

## 7.5 Modelling Approaches

Two predictive cubic equations of state were considered in this work: the PPR78 [34-36, 79, 123-126] and PR<sub>2</sub>SRK models [35-36]. They were applied to mixtures by means of conventional van der Waals one-fluid mixing rules. Beside the standard alpha function (Soave), Boston-Mathias alpha function [111] was also used. The saturated density was calculated using PPR78 EoS with the Soave alpha function and predicted binary interactions from the group-contribution scheme. The saturated density was also calculated using the volume translation method introduced by Peneloux [116]. The above methods are described in Chapter 3, section 3.2.4.

## 7.6 Evaluation of the Critical Properties

In order to apply the predictive PPR78 and PR<sub>2</sub>SRK models, it is necessary to know the critical temperature, critical pressure and acentric factor of each substance. For most of the components present in our mixtures, the critical constants and acentric factor are readily available and are associated with small uncertainties. However, some of the heavier components are not chemically stable at their critical points and there exists uncertainty about the correct values of  $T_c$  and  $p_c$ , and consequently about  $\omega$ .

We have carefully reviewed the available pure-component data in order to arrive at the critical constants and acentric factors listed in Table 7.4. For light components, the values were taken from available experimental data. Generally speaking, experimental vapour pressure data exists for all components of interest, with the light components having the largest and most-reliable amount data. The acentric values obtained are the same as or similar to with those available from the NIST Thermodata Engine (TDE) software [226-227]. The heavier components required more-careful consideration. In the case of the *n*-alkanes up to octadecane, we used the critical constants measured by Rosenthal and Teja [228] using a low-residence-time flow method. The critical temperature and pressure of nonadecane were obtained from the study of Nikitin et al. [245], who used the method of pulse heating to measure the critical properties of *n*-alkanes with  $n = 5, 6, 7, 17$  and  $19$  to  $24$ . The critical temperature of tetracosane was also obtained from this work but, to reduce the uncertainty, the critical pressure was adjusted to fit the available binary VLE data for (CO<sub>2</sub> + tetracosane) at  $T = 353.15$  K [237] and (ethane + tetracosane) at  $T = 352.7$  K [246]. To accomplish this, a trial value of the critical pressure for tetracosane was adopted, the acentric factor was evaluated from Eq. (6.1) and the available vapour-pressure data, and binary VLE data were simulated with the PPR78 EoS model. The value of the critical pressure was adjusted to minimize the combined absolute average pressure deviations from the two experimental data sets.

Nikitin et al. [247] measured the critical temperature and critical pressure of ten phenylalkanes, C<sub>6</sub>H<sub>5</sub>C<sub>n</sub>H<sub>2n+1</sub> with  $n = 1$  to  $11$ , and  $13$ , using the method of pulse heating. We took  $T_c$  and  $p_c$  for 1-phenylhexane and 1-phenyloctane from this study. Nikitin et al. also reported correlations for the critical constants of phenylalkanes as functions of  $n$  and compared their values with those calculated by the group-contribution methods of Lydersen [248], Joback and Reid [249], and Constantinou and Gani [250]. We used these to obtain  $T_c$  and  $p_c$  for 1-phenylhexadecane.

**Table 7.4.** Critical pressure  $p_c$  and critical temperature  $T_c$  (with uncertainties), acentric factor  $\omega$  and critical compressibility factor  $Z_c$  for the components studied in this work.

Component	Ref	$\omega$	$p_c$ (MPa)	$u(p_c)$ (MPa)	$T_c$ (K)	$u(T_c)$ (K)	$Z_c$
2,2-dimethylbutane	[251]	0.2251 <sup>f</sup>	3.102	0.01	489.21	0.11	0.27415
<i>n</i> -heptane	[228]	0.3481 <sup>f</sup>	2.734	0.02	540.30	0.6	0.26078
ethylcyclohexane	[252-253]	0.3180 <sup>f</sup>	3.250 <sup>a</sup>	0.1	606.9 <sup>a</sup>	0.4	0.26046
<i>n</i> -nonane	[228]	0.4409 <sup>f</sup>	2.280	0.02	594.70	0.6	0.25451
propylcyclohexane	[252-253]	0.3149 <sup>f</sup>	2.860 <sup>a</sup>	0.09	630.80 <sup>a</sup>	0.9	0.26011
1,2,3,4 tetrahydronaphthalene	[254]	0.3318 <sup>f</sup>	3.630	0.1	719.50	2	0.26194
1,3,5-triethylbenzene	[255]	0.5070 <sup>f</sup>	2.330 <sup>b</sup>	0.115	679.00 <sup>b</sup>	2	0.24980
1-phenylhexane	[247]	0.4498 <sup>f</sup>	2.350	0.07	695.00	7	0.25217
<i>n</i> -tridecane	[228]	0.6099 <sup>f</sup>	1.679	0.02	676.00	0.6	0.24324
1-phenyloctane	[247]	0.5845 <sup>f</sup>	1.98	0.06	725.00	7	0.24749
<i>n</i> -pentadecane	[228]	0.7192 <sup>f</sup>	1.479	0.02	707.50	0.7	0.23836
<i>n</i> -hexadecane	[228]	0.7442 <sup>f</sup>	1.401	0.05	722.40	1.1	0.23659
octadecane	[228]	0.8020 <sup>f</sup>	1.292	0.11	747.70	1	0.23473
nonadecane	[245]	0.8722 <sup>f</sup>	1.160	0.023	755.30	7.6	0.23337
1-phenylhexadecane	[247]	0.9055 <sup>f</sup>	1.279 <sup>d</sup>	0.06	827.35 <sup>d</sup>	7	0.23682
tetracosane	[245]	1.1840 <sup>f</sup>	1.075	0.2	799.8 <sup>c</sup>	8	0.22839
squalane		1.2436 <sup>f</sup>	0.900 <sup>e</sup>	0.2	820.00 <sup>e</sup>	15	0.23296
methane	[256]	0.0100 <sup>f</sup>	4.599	0.017	190.56	0.01	0.28927
ethane	[257]	0.0990 <sup>f</sup>	4.885	0.0002	305.36	0.01	0.28085
propane	[258]	0.1520 <sup>f</sup>	4.260	0.005	370.01	0.03	0.27657
carbon Dioxide	[230]	0.2310 <sup>f</sup>	7.378	0.007	304.16	0.082	0.27256

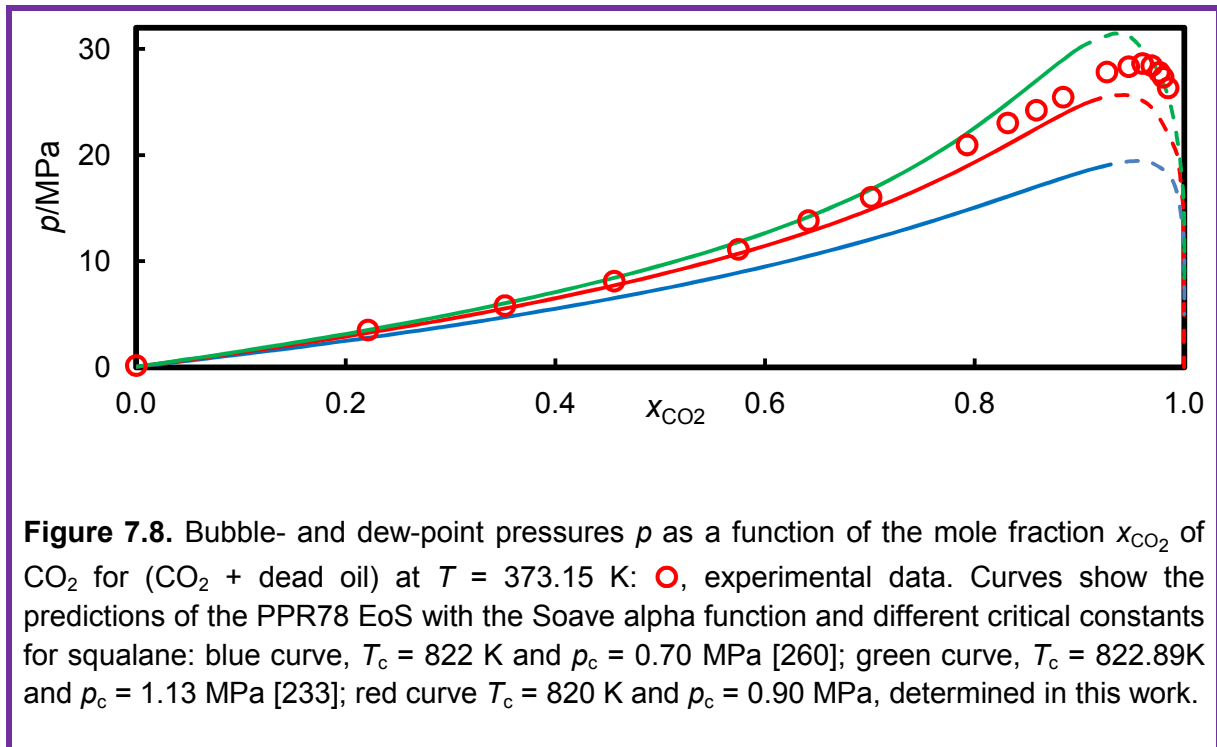
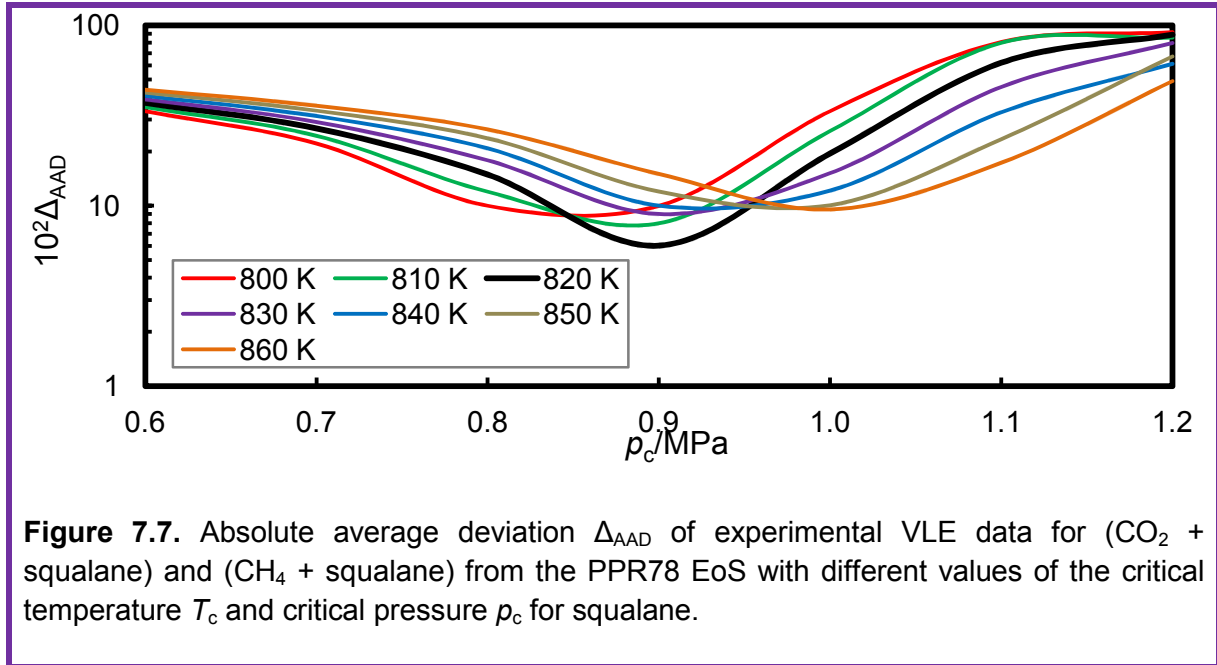
<sup>a</sup> reference [253] was used for the experimental critical temperature while reference [252] was used for the experimental critical pressure; <sup>b</sup> reference [255] was used for the critical temperature while the critical pressure was calculated using the Ambrose-Walton method; <sup>c</sup> reference [245] was only used to obtain the critical temperature while the critical pressure was obtained by fitting to match the available binary data of tetracosane + CO<sub>2</sub> and tetracosane + ethane; <sup>d</sup> calculated using the correlation function given in reference [247]; <sup>e</sup> fitted against available binary data of squalane + CO<sub>2</sub> and squalane + methane; <sup>f</sup> calculated from the available vapour pressure data with the use of Equation 6.1 for the acentric factor.

The critical pressures of ethylcyclohexane and propylcyclohexane were obtained from the work of Nikitin et al. [253] which is associated with an uncertainty of 0.1 MPa. However, the critical temperatures reported in that study have an uncertainty of 6 K and we preferred instead the values of Morton et al. [252], who used a conventional sealed-ampoule method with an uncertainty in  $T_c$  of 1 K. The case of squalane, which is a major component in this work, was considered in some detail. To our knowledge, only two studies of the critical constants of squalane have been published. Von Niederhausen et al. [259] employed a flow method and reported  $T_c = (795.9 \pm 2.0)$  K and  $p_c = (0.59 \pm 0.02)$  MPa. Nikitin and Popov [260] used the pulse heating method and obtained  $T_c = (822 \pm 12)$  K and  $p_c = (0.70 \pm 0.03)$  MPa. They compared their measurements with the results obtained by Von Niederhausen et al. [259], computer-simulation data [261-264], and the values predicted by group-contribution methods [249-250, 265]. Clearly, these experimental determinations are not in mutual agreement. Zhuravlev et al. [264] used Monte Carlo simulations to estimate the critical properties of squalane and concluded that a critical temperature of between 820 K and 830 K was most likely. They observed that a value in this range would also yield a relative difference in the critical temperatures between *n*-triacontane and squalane in good agreement with experimental data for low-molecular-weight analogues (e.g. *n*-octane versus 2,5-dimethylhexane or *n*-nonane versus 2,6-dimethylheptane) in which the critical temperatures of the dimethyl-branched isomers are about 3% lower than those of the linear isomers.

In view of the lack of agreement, we again resorted to binary VLE data to arrive at optimized critical constants. In this case, both  $T_c$  and  $p_c$  were adjusted, starting from trial values in the range of the reported experimental data. For every trial pair,  $T_c$  and  $p_c$ , the corresponding value of  $\omega$  was determined from vapour pressure data of Mokbel et al. [266] and Von Niederhausen et al. [259] together with Eq. (24). Binary VLE data were then simulated using the PPR78 EoS and compared with experiment. The experimental values considered were bubble-curve data for both (CO<sub>2</sub> + squalane) at  $T = 343.15$  K, from the study of Brunner et al. [233], and (CH<sub>4</sub> + squalane) at  $T = 370$  K, from the study of Marteau et al. [267]. Figure 7.7 shows the combined absolute average relative deviations,  $\Delta_{AAD}$ , between the simulated and experimental data for the two binary systems considered. The optimal critical constants determined from this were  $T_c = 820$  K and  $p_c = 0.90$  MPa; the corresponding acentric factor was found to be  $\omega = 1.2436$ .

Figure 7.8 illustrates the important role of the critical constants and acentric factor of squalane in the context of the present study. Here we compare our experimental VLE data for (CO<sub>2</sub> + dead oil) at  $T = 373.15$  K with simulations based on the PPR78 EoS with different

values of  $T_c$ ,  $p_c$  and  $\omega$  for squalane. The values considered are those fitted in this work ( $T_c = 820$  K,  $p_c = 0.90$  MPa,  $\omega = 1.2436$ ), those measured experimentally by Nikitin and Popov [260] ( $T_c = 822$  K,  $p_c = 0.70$  MPa with  $\omega = 1.075$ ), and those fitted to VLE data using the SRK EoS by Brunner and co-workers [233] ( $T_c = 822.89$  K,  $p_c = 1.13$  MPa and  $\omega = 1.1515$ ).



The calculated binary interaction parameters between CO<sub>2</sub> and squalane in the PPR78 model corresponding to these choices are 0.0409, -0.0234, and 0.0680. We observe that, of the three cases plotted, our fitted critical constants and acentric factor provide the best predictions when using PPR78 for the (CO<sub>2</sub> + dead oil) system.

## 7.7 Comparison with Experiment

Figure 7.3a compares our experimental results for (CO<sub>2</sub> + dead oil) at  $T = (323.15, 373.15, \text{ and } 423.15)$  K with the predictions of the PPR78 EoS with the 'standard' Soave alpha function. The bubble curves are generally in reasonably good agreement with experiment, especially considering the fact that no parameters were tuned to fit these data. The deviations increase in the critical regions and are more pronounced for the dew curves. When considering the two live oils, we found that the PPR78 EoS provided an excellent prediction of the bubble pressure in the absence of CO<sub>2</sub> as shown by the dotted lines in Figure 7.3b and 7.3c. However, the model was much less successful when CO<sub>2</sub> was introduced, mainly at high pressures in the critical and dew regions. This is not surprising; it has been already shown that poor results are obtained at low temperature for systems containing CO<sub>2</sub> and *n*-alkane longer than Undecane [45].

This suggests that at least some of the binary parameters involving CO<sub>2</sub> are not well predicted by the model of Jaubert and co-workers [34-36, 79, 123-126] for  $T \geq 323.15$  K. In our opinion, this problem is most significant for the (CO<sub>2</sub> + CH<sub>4</sub>) system because no binary VLE data exist for that mixture at temperatures above the critical temperature of CO<sub>2</sub> and hence the group parameters between these components were not constrained by experimental data at higher temperatures. The good agreement shown previously (Chapter 6, Figure 6.2) for the (CO<sub>2</sub> + *n*-heptane) system lends weight to the idea that it is the interactions between CO<sub>2</sub> and the lightest components that need to be adjusted. Consequently, it was decided to proceed by fitting the binary interaction parameter between CO<sub>2</sub> and CH<sub>4</sub> at each temperature. The results obtained after this one-parameter optimization at each temperature are shown in Figures 7.3b and 7.3c as solid lines for the two (CO<sub>2</sub> + live oil) systems. The agreement, after fitting, with the experimental data is reasonably good along the bubble curves but less good on the dew curves, especially at  $T = 323.15$  K where the predicted dew pressures drop too rapidly with increasing  $x_{\text{CO}_2}$ .

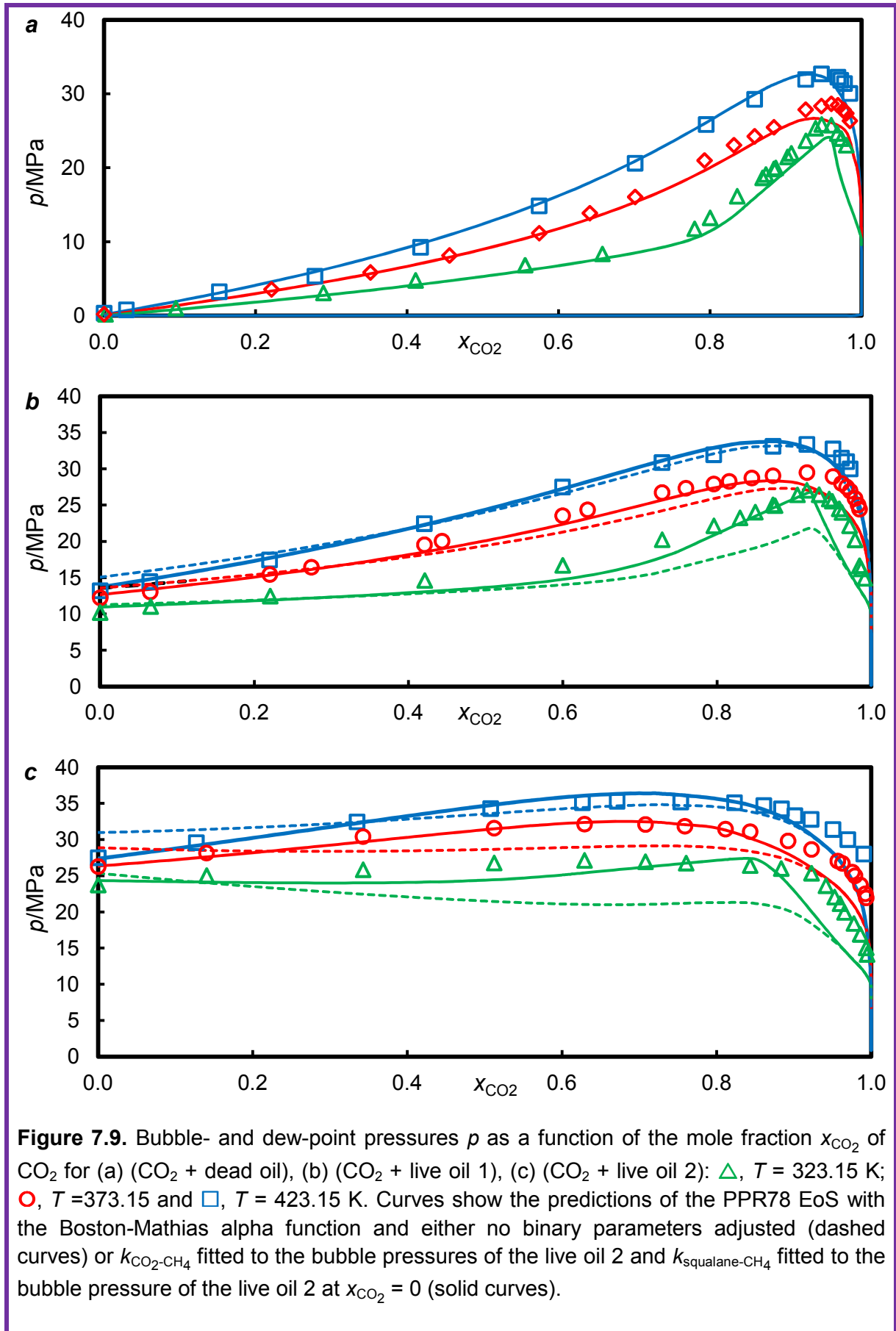
Figure 7.4 compares the experimental data with the predictions of the PPR78 EoS with the Soave alpha function at  $T = 298.15$  K. Again, the binary parameter between CO<sub>2</sub> and CH<sub>4</sub> was adjusted (based on the bubble-curve data). It is interesting to note that the model is in

qualitative agreement with experiment in respect of the appearance of VLE, VLLE and LLE regions. The bubble pressures and three-phase pressure of the (CO<sub>2</sub> + dead oil) system are well predicted, although the predicted LLE region is too narrow. For the (CO<sub>2</sub> + live oil) systems, the predictions of the PPR78 EoS are good for the bubble pressure at  $x_{\text{CO}_2} = 0$ , but less good for the VLE, VLLE and LLE data at finite  $x_{\text{CO}_2}$ . At this temperature, the model also predicts for the (CO<sub>2</sub> + live oil) systems a second small VLE region in the region  $0.995 \leq x_{\text{CO}_2} \leq 1$  joining the VLLE region to the vapour pressure of pure CO<sub>2</sub>.

In view of the fact that several components, especially CH<sub>4</sub>, are supercritical under the conditions investigated here, we explored the effect of replacing the Soave alpha function with the Boston-Mathias alpha function. All predicted binary parameters in the PPR78 EoS were transformed using Eq. (3.13) and, initially, no terms were fitted. We found good agreement for the (CO<sub>2</sub> + dead oil) system at all mole fractions of CO<sub>2</sub>, as can be seen in Figure 7.9a. However, for the live oils, significant deviations from experiment of up to 3.6 MPa were observed for the bubble pressures at  $x_{\text{CO}_2} = 0$  as shown by the dotted lines in Figure 7.9b and 7.9c. These discrepancies suggested that the transformed binary interaction parameters between CH<sub>4</sub> and some of the heavy components, especially squalane, might be inaccurate. To explore this, we compared the predictions of the PPR78 EoS model using both the Soave and the Boston-Mathias alpha functions, the latter with transformed  $k_{ij}$ , with the experimental data of Marteau et al. [267] at  $T = 370$  K.

With the Soave alpha function, the average absolute relative deviation of bubble pressure was 5.5 %, while for the Boston-Mathias function it was 17 %. We note that the former was the model used in the tuning of the squalane critical constants, and so it might be that better results could be obtained with the Boston-Mathias alpha function if the critical constants of squalane were re-optimized. However, we decided to address the problem instead by adjusting the binary interaction parameter between CH<sub>4</sub> and squalane at each temperature. Figure 7.9 compares the results obtained in this way with experiment at  $T \geq 323.15$  K. We see for all three systems a noticeable improvement in agreement with experiment compared with the results seen in Figure 7.3 for the case of the Soave alpha function. The improvement is more marked at high temperatures, as expected, because the Soave and Boston-Mathias functions differ increasingly as the temperature increases above the critical. However, it worth mentioning that in this case two parameters were fitted while only one parameter was adjusted with the Soave alpha function.





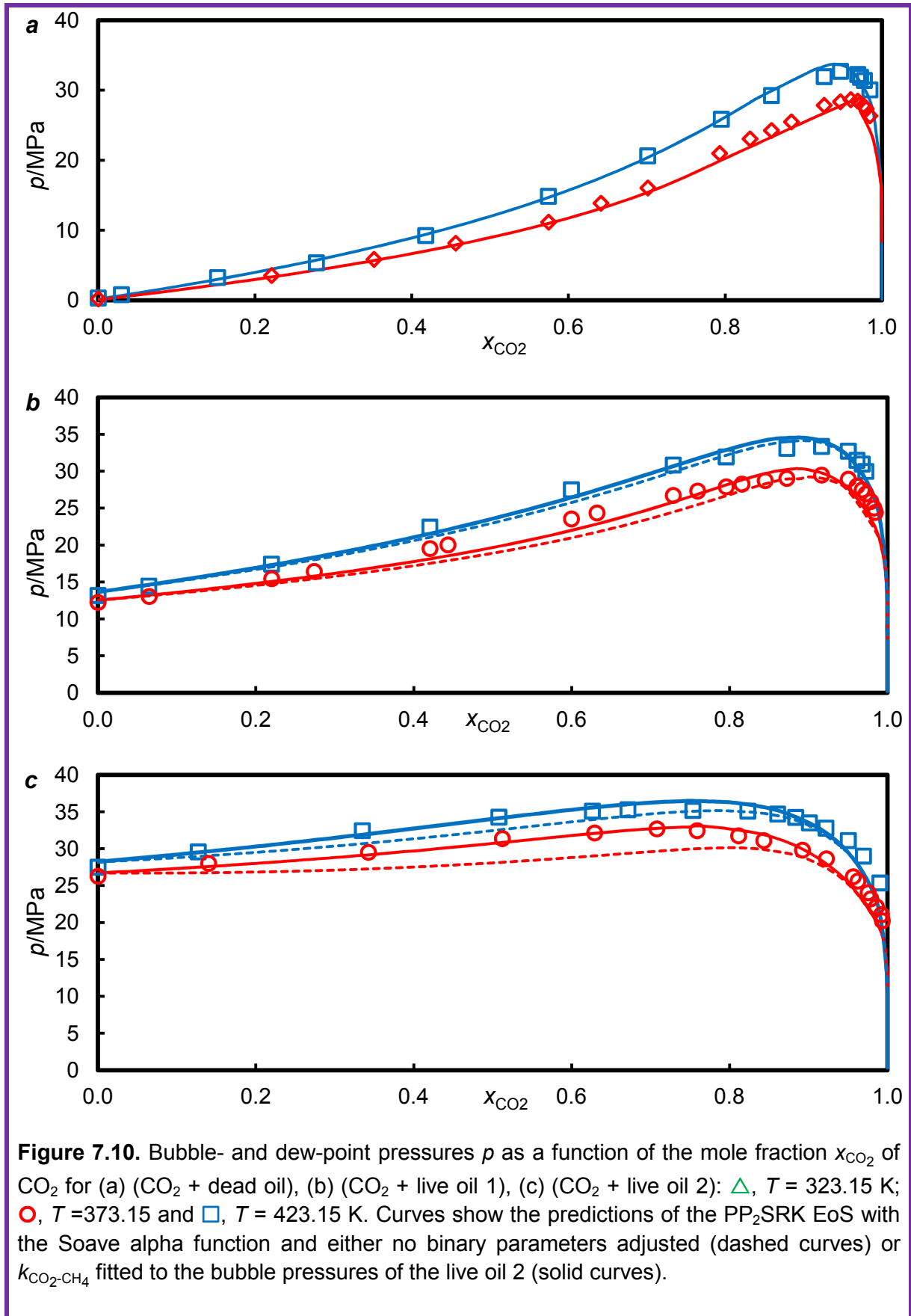
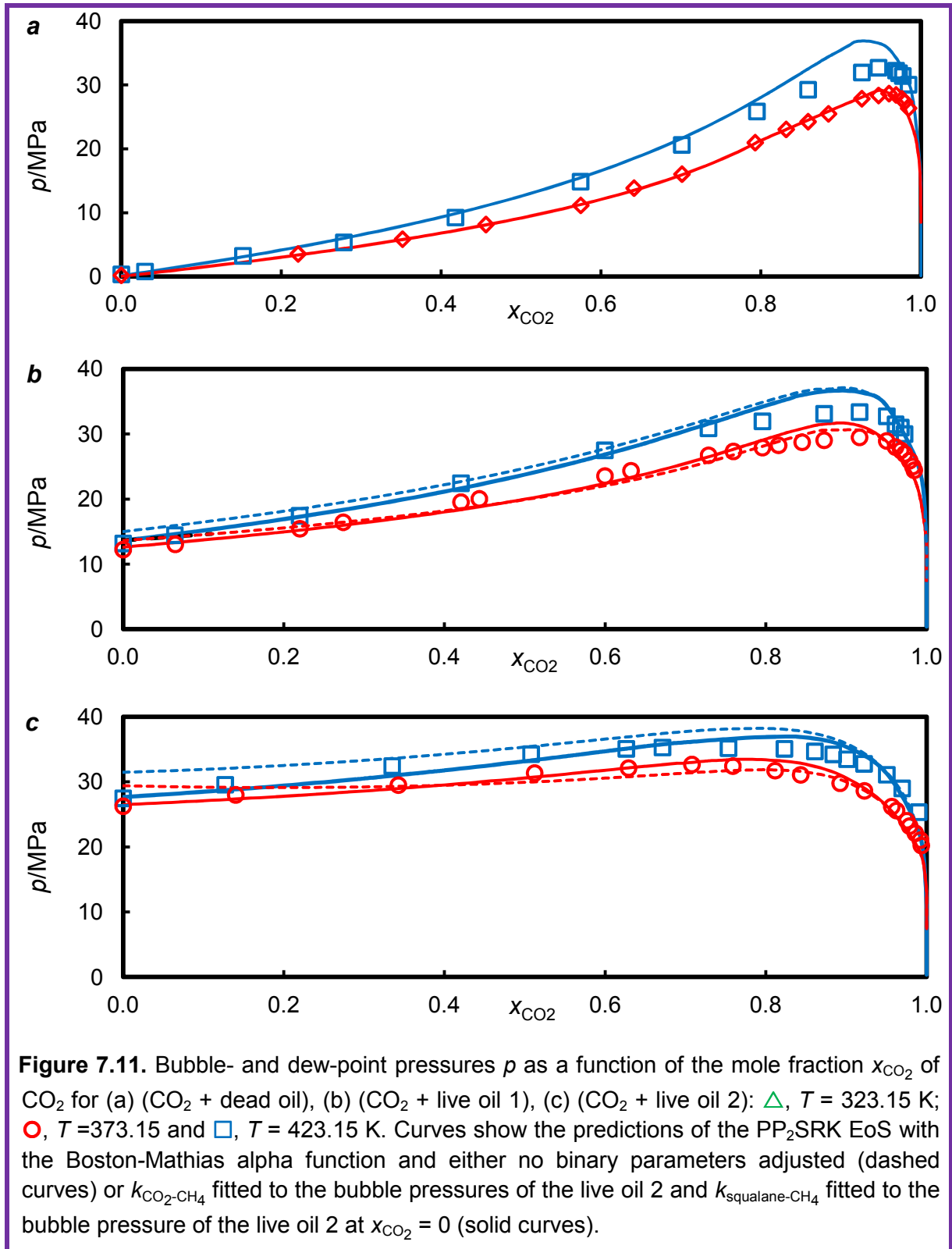


Figure 7.10 shows the VLE predictions of the PR<sub>2</sub>SRK EoS model with the Soave alpha function. Better agreement was observed in the critical and dew region (Figure 7.10a) for the (CO<sub>2</sub> + dead oil) compared with PPR78 EoS prediction (Figure 7.3a). For the (CO<sub>2</sub> + live oil) systems, less deviation, as shown by the dotted lines, was observed in comparison with PPR78 EoS. However, the model is still less successful when CO<sub>2</sub> was introduced. Hence, again the CO<sub>2</sub>-CH<sub>4</sub> binary interaction parameters were subjected to optimization. The results for  $T = (373.15 \text{ and } 423.15) \text{ K}$  provide an excellent representation of both the bubble- and dew-curve experimental data.

Unfortunately, the PR<sub>2</sub>SRK model predicts three-phase equilibria extending up to at least  $T = 323.15 \text{ K}$ , at which temperature the model fails qualitatively for all three systems investigated. For this reason, the PR<sub>2</sub>SRK predictions are not compared with experiment in Figures 7.10. Finally, in Figure 7.11 we compare the PR<sub>2</sub>SRK EoS with the Boston-Mathias model with experiment at  $T = (373.15 \text{ and } 423.15) \text{ K}$ . As with the PPR78-Boston-Mathias combination, significant discrepancies were found in the bubble pressures of the live oils at  $x_{\text{CO}_2} = 0$  and these were addressed by adjusting the CO<sub>2</sub>-squalane binary interaction parameter at each temperature. The results are slightly less good than those obtained with PR<sub>2</sub>SRK and the Soave alpha function.

Finally, in Figures 7.6a and 7.6b, we show the experimental and predicted saturated phase densities measured in the (CO<sub>2</sub> + dead oil) and (CO<sub>2</sub> + live oil 2) systems at  $T = (323.15, 373.15, \text{ and } 423.15) \text{ K}$ . The solid lines corresponds to the values obtained using the volume translation correction while the dotted lines corresponds to values obtained without the use of this correction. The agreement, while not perfect, is good for the liquid densities with noticeable deviation in the critical and dew regions. Without the use of volume translation, the density values are under predicted by an average of approximately 10 % in most of the cases. Better agreements were observed with the use of volume correction.

The density values are under predicted by amount varying from less than 1 % at around zero CO<sub>2</sub> to around 10 % in the critical and dew regions. The use of volume correction is only effective for the saturated liquid densities. The predicted saturated vapour densities are almost the same in both cases. The binary parameters for CO<sub>2</sub>-CH<sub>4</sub> according to the prediction from PPR78 with the Soave alpha function and our optimized values are presented in Figure 7.12. It seems that the two curves intersect at lower temperatures, where large amount of CO<sub>2</sub>-CH<sub>4</sub> VLE data exists. This suggests that extrapolating at high temperatures using equation (3.12) does not give good predictions.

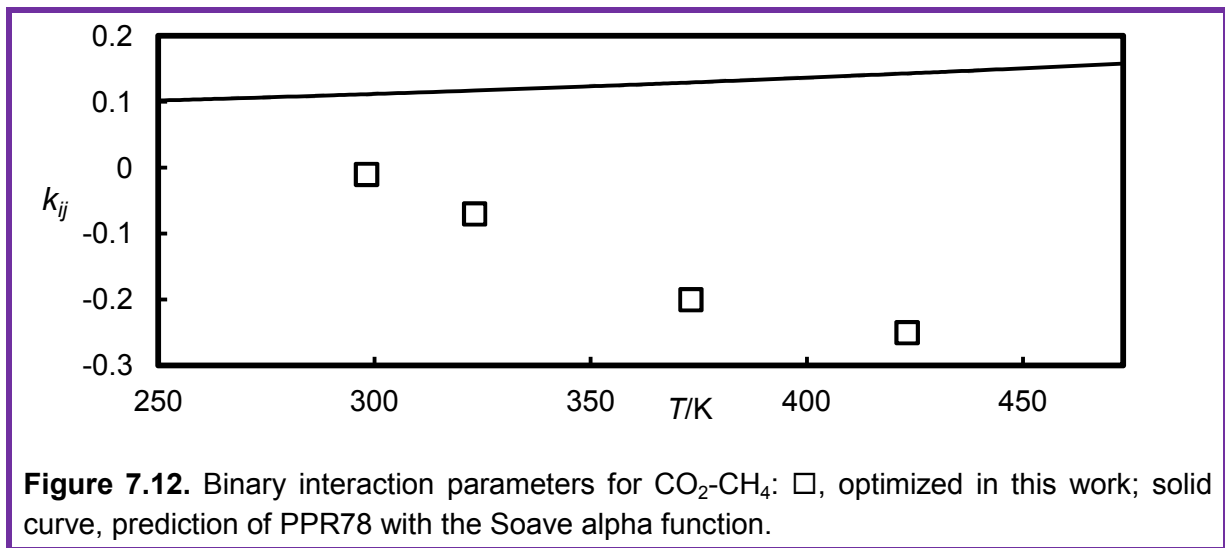


The optimized binary interactions for CO<sub>2</sub>-CH<sub>4</sub> and squalane-CH<sub>4</sub> are summarized in Table 7.5. It was found that the optimized CO<sub>2</sub>-CH<sub>4</sub> binary interactions for a given temperature did not change much when the Soave and Boston-Mathias alpha functions were interchanged.

**Table 7.5** .Optimized binary interaction values for CO<sub>2</sub>-CH<sub>4</sub> and squalane-CH<sub>4</sub>

T (K)	PPR78 EoS			PR <sub>2</sub> SRK EoS		
	Soave alpha	B-M alpha		Soave alpha	B-M alpha	
	CO <sub>2</sub> -CH <sub>4</sub>	CO <sub>2</sub> -CH <sub>4</sub>	Squ-CH <sub>4</sub>	CO <sub>2</sub> -CH <sub>4</sub>	CO <sub>2</sub> -CH <sub>4</sub>	Squ-CH <sub>4</sub>
298.15	-0.01	N/A	N/A	N/A	N/A	N/A
323.15	-0.07	-0.07	0.03	N/A	N/A	N/A
373.15	-0.2	-0.2	-0.01	-0.08	-0.08	-0.01
423.15	-0.25	-0.25	-0.05	-0.05	0.1613 <sup>a</sup>	-0.05

<sup>a</sup> The fitting of this parameter yielded a value which is almost same as the value predicted by the group-contribution method, and hence we used the predicted value



## 7.8 Conclusion

Experimental measurements of the phase behaviour of (CO<sub>2</sub> + synthetic crude oil) mixtures were completed. The composition of the synthetic oil was chosen to match the physical and chemical properties of a bottom-hole crude oil sample from a Qatari field. The ‘dead’ oil contained a total of 17 components and live oils were created by adding a three-component solution gas. Experimental results are reported for the dead oil and for two live oils under the addition of CO<sub>2</sub> at temperatures of (298.15, 323.15, 373.15 and 423.15) K and at pressures up to 36 MPa. VLE conditions were observed at all temperatures; additionally, VLLE and LLE conditions were measured at the lowest temperature.

The experimental results are compared with two predictive EoS: the PPR78 and PR2SRK models. In making this comparison, careful attention was paid to the critical constants and acentric factors of the heavy components in the mixture. The two EoS models were considered in combination with either the ‘standard’ Soave alpha function or the Boston-Mathias alpha function. It was found that the PPR78, in combination with either alpha function and with no parameters adjusted, generally provided a good description of the

bubble pressures for the (CO<sub>2</sub> + dead oil) system. The same model predicted well the pressure at which VLLE occurred at  $T = 298.15$  K. The PPR78 with the Soave alpha function also predicted well the bubble pressures of the live oils in the absence of CO<sub>2</sub>. However, discrepancies were found at finite  $x_{\text{CO}_2}$  which suggested that the binary parameter between CO<sub>2</sub> and CH<sub>4</sub> should be adjusted. After optimizing that single parameter at each temperature, quite good agreement was observed with the experimental bubble points, while some discrepancies remained with the dew points. When the Boston-Mathias alpha function was used, it was necessary to adjust the CO<sub>2</sub>-CH<sub>4</sub> and the CH<sub>4</sub>-squalane parameters. The agreement, after adjusting these two parameters, is better than the previous agreement using the Soave alpha function but this comes with the cost of an additional adjustable parameter.

The PR<sub>2</sub>SRK model was found to predict qualitatively incorrect phase behaviour at  $T = 323.15$  K but, in combination with the standard Soave alpha function, it gave a superior account of the experimental VLE data, including dew points, at  $T = (373.15 \text{ and } 423.15)$  K when the CO<sub>2</sub>-CH<sub>4</sub> binary parameter was optimized. Use of the Boston-Mathias alpha function resulted in some deterioration in comparison with experiment.

Overall, the PPR78 model with the Boston-Mathias alpha function performed best in qualitative and quantitative predictions of the phase behaviour observed experimentally. However, this model requires the adjustment of two binary interaction parameters and hence, on a purely predictive basis, it seems that the PPR78 EoS with the Soave alpha function performed best compared to the other options investigated.

We can draw several conclusions in relation to modelling the phase behaviour of CO<sub>2</sub> + multi-component hydrocarbon mixtures with predictive cubic EoS. First, very careful attention must be paid to the critical constants and acentric factors of heavy components. We suggest that comparisons of experimental and simulated binary VLE data for such substances with light components, such as CO<sub>2</sub> and/or CH<sub>4</sub>, may be a good way of discriminating between discrepant critical-point data. Second, we note that the binary interaction parameters between two supercritical components may not be predicted well by group-contribution methods that were developed by fitting binary phase-equilibrium data only. Such binary parameters may require adjustment. Finally, the transformation of binary parameters to account for different alpha functions may result in erroneous results for pairs of components that differ greatly in volatility. It seems that there is scope for further improvement in the performance of predictive cubic EoS in relation to the class of mixtures considered in this work.

## Chapter 8: Phase Behaviour of (CO<sub>2</sub> + *n*-Heptane + Water) Mixtures

### 8.1 Overview

Due to the complexity of oil mixtures, simpler systems that may represent certain characteristics of the real ones are often studied. In this work the phase equilibria of (carbon dioxide + *n*-heptane + water) was studied. The *n*-heptane system was chosen as being a representative model for (carbon dioxide + light oil fraction + water) mixtures. This work adds to the previously reported studies of two systems made on the mixtures of CO<sub>2</sub> and water with propane [88] or decane [87]. The measurements were carried out under conditions of three-phase equilibria. Compositions of the three coexisting phases have been obtained along five isotherms at temperatures from (323.15 to 413.15) K and at pressures up to an upper critical end point at which the *n*-heptane-rich liquid and the carbon dioxide-rich gas phases become critical.

In this work, in collaboration with a colleague, Esther Forte, who performed the SAFT-VR calculations, the experimental data obtained for the ternary mixture have been compared with the predictions of the statistical associating fluid theory for potentials of variable range (SAFT-VR). The unlike binary interaction parameters used here are consistent with a previous study for a ternary mixture of a different *n*-alkane (*n*-decane). The *n*-alkane-water binary interaction parameter is found to be transferable and the *n*-alkane-carbon dioxide one is predicted using a modified Hudson-McCoubrey combining rule. Furthermore, comparison with available data for the constituent binary subsystems is carried out. In this way, we analyze the observed effects on the solubility of each pair of compounds when the third component is added.

### 8.2 Introduction

Water and hydrocarbons mixtures are frequently encountered in oil refining and reservoir operations, where knowledge of the phase equilibria for (hydrocarbon + water) mixtures at high temperatures and pressures is vital for designing such chemical processes. However, the hydrocarbon + water mixtures are very immiscible with water in oil being orders of magnitude larger than that of oil in water. Few, or no, thermodynamically-consistent models in the literature exist which can capture accurately these two extreme phases (even when experimental data are used to fit model parameters). A thermodynamic model required for the mutual solubility of water and hydrocarbons are not easy to handle because of the association of water molecules by means of hydrogen bonding, which restricts the

application of traditional cubic EoS, and in most cases experimental data on mutual solubility is still required to validate the models. As a result, the mutual solubility of water and hydrocarbon fluids is often neglected in reservoir and pipeline simulation studies and the two fluids are normally treated as pure (pure water phase or pure oil phase) which may lead to improper design. Hence, it is vital to provide reliable experimental data on mutual solubility of hydrocarbons and water mixtures so that accurate thermodynamic models for these mixtures can be developed.

Treatment of crude-oil mixtures is challenging, both experimentally and computationally, because of the vast number of components that they contain and the extreme difficulty of obtaining a very detailed characterisation. The most rational approach to understand the phase behaviour of mixtures of oil with carbon dioxide and water may be to tackle first the study of simpler systems that represent certain characteristics of the real ones. Despite their importance as simple models for reservoir fluids, experimental data for hydrocarbon-CO<sub>2</sub>-water ternary mixtures are scarce and limited to VLE measurements in most of the cases as described previously (Chapter 2). In this work, the three-phase VLLE region for the system (CO<sub>2</sub> + *n*-heptane + water) is considered. Regarding the constituting binaries: the VLE and LLE for the binary system (CO<sub>2</sub> + water) have been extensively studied both in terms of experimental and modelling approaches [90, 198-205, 268-295]; the binary system (CO<sub>2</sub> + *n*-heptane) has also been studied broadly in the literature [184-186, 193, 195-197, 217]; the binary system (*n*-heptane + water) has been studied only in a few works, with limited VLE and LLE data available in the literature [296-301].

In order to model the mixture of interest, an approach able to capture the nature of each of the molecules and their interactions is desirable. In this work we use the SAFT-VR EoS [37-38] with square well (SW) potential to account for the possibility of chain formation and directional interactions. These descriptions are especially useful to treat the non-sphericity of alkanes and the hydrogen-bonding interactions of water. The description of aqueous systems with EoS is not a simple task, particularly in mixtures with a non-polar compound such as *n*-alkane, which is characterised by large regions of extreme immiscibility. The alkane in the aqueous phase is highly diluted and polarised inside a hydrogen-bonding network of water molecules; the environment of water in the alkane phase is completely different. It has been shown that binary interaction parameters can be expressed as a function of the nature of the interactions between the unlike molecules and the characteristics of the media [166]. One can then imagine that modelling the extreme nature of two these phases with a single binary interaction parameter that describes the unlike interaction between the molecules in both phases may not likely provide the best description



of the phase behaviour of the mixture. The application of associating modelling approaches to describe the phase behaviour of alkane aqueous systems has been a matter of considerable amount of work [149, 169, 302-313] and remains a challenge. Regarding mixtures of carbon dioxide with water, although in some cases cross-association models (models in which effective hydrogen-bonding between CO<sub>2</sub> and water is incorporated to enhance solvation) have been suggested [201, 314-315] here we do not make use of this approach, as SAFT-VR has shown able to capture the features of the phase diagram without the need to include cross-association [316-318]. The SAFT-VR formalism has been shown to be successful in the application to a wide variety of systems. Here we extend the application of the equation to the system (carbon dioxide + *n*-heptane + water) and avoid re-adjustment of parameters from previous work: the unlike interaction parameter for (*n*-heptane + carbon dioxide) system is re-calculated based on a modification of the Hudson and McCoubrey combining rules [166] and that for (*n*-heptane + water) is seen to transfer well from (*n*-decane + water) [87], based on the availability of experimental data for the system.

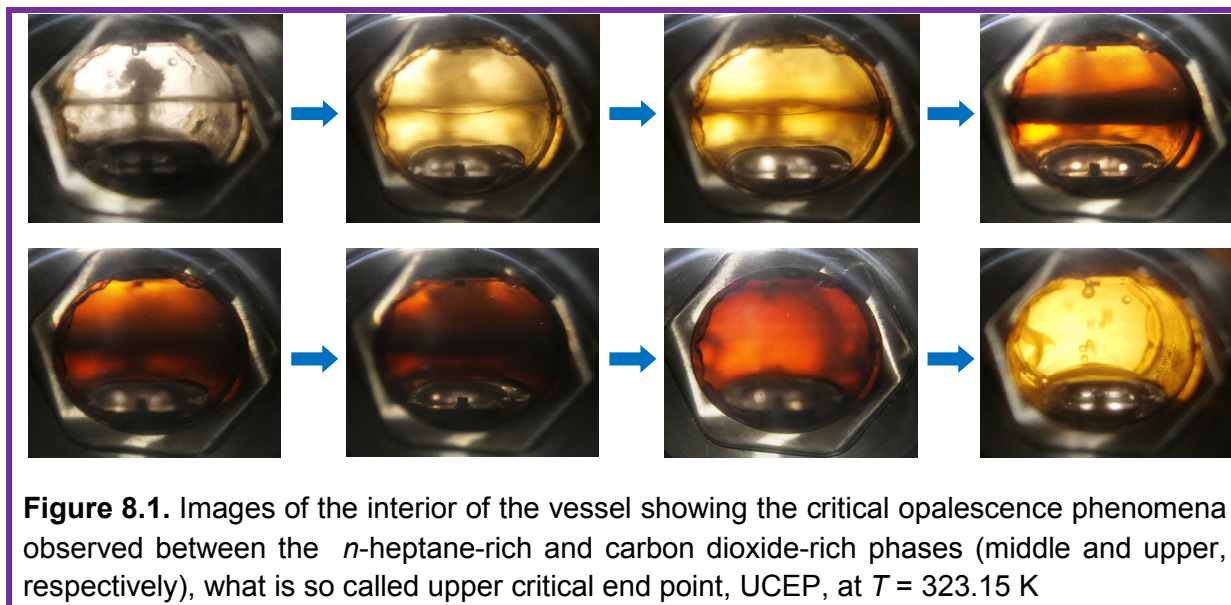
### 8.3 Experimental Results

The VLLE results for the ternary mixture (carbon dioxide + *n*-heptane + water) are given in Appendix C. In these Tables, the mole fraction of each component in each phase is given together with pressure and temperature values; the prediction from SAFT-VR is given as well. The measurements were carried out at temperatures of (323.15, 343.15, 363.15, 388.15 and 413.15) K and at pressures up to the UCEP. The UCEP results are given in Table 8.1 and images showing the UCEP opalescence phenomena are shown in Figure 8.1.

**Table 8.1.** Experimental LLE data for (water (1) + *n*-heptane (2) + carbon dioxide (3)) at the critical point between the *n*-heptane-rich phase and CO<sub>2</sub>-rich phase (the combination of both phases is referred here as CO<sub>2</sub>-rich phase).

<i>T</i> /K	<i>p</i> /MPa	Water-rich phase			CO <sub>2</sub> -rich phase		
		<i>x</i> <sub>1</sub> <sup>exp</sup>	<i>x</i> <sub>2</sub> <sup>exp</sup>	<i>x</i> <sub>3</sub> <sup>exp</sup>	<i>x</i> <sub>1</sub> <sup>exp</sup>	<i>x</i> <sub>2</sub> <sup>exp</sup>	<i>x</i> <sub>3</sub> <sup>exp</sup>
323.15	9.06	0.9798	3.58E-05	0.0201	0.0027	4.16E-02	0.9558
343.15	10.82	0.9811	1.06E-04	0.0188	0.0060	9.94E-02	0.8946
363.15	12.20	0.9833	3.58E-05	0.0166	0.0112	1.34E-01	0.8550
388.15	13.21	0.9842	6.31E-05	0.0158	0.0214	1.62E-01	0.8164
413.15	13.33	0.9850	2.84E-04	0.0147	0.0389	2.22E-01	0.7391

The experimental results are plotted in comparison with the theory in the next section. The results are shown in Figures 8.3 to 8.8 and comparison with SAFT-VR predictions are shown in some of these Figures. In some of these plots, the effect of adding a third component on the binary system is shown together with comparison with some available literature binary data. Details are addressed in the next section.



## 8.4 Modelling Approach

The models used in this study have been kept as consistent as possible with the previous work on related mixtures [87-88]. In SAFT-VR, association by means of specific interactions such as hydrogen bonds is mediated through the addition of short-range association sites. The model intermolecular parameters for each pure component are collected in Table 8.2; these were obtained from fits to vapour pressure and saturated liquid density data. A standard four-association-site model is used for water, with two sites of type H and two of type e. All the parameters have been presented in previous work [218, 319-321].

In order to describe binary mixtures, only the unlike (dispersion) energies have been modified by means of adjustable binary interaction parameters  $k_{ij}$  in the usual manner (Eq. 3.23). These are treated as temperature-independent, and therefore a single binary interaction parameter is used per pair of compounds. The binary interaction parameter for the system (carbon dioxide + *n*-heptane) was predicted using a modification of the Hudson and McCoubrey combining rules for square-well intermolecular potentials [166]. The method asserts that the unlike interaction dispersion energy can be obtained equating the expression for the attractive part of the intermolecular potential to the sum of all possible

attractive interaction energies between the pair of molecules (i.e., London dispersion, Keesom, Debye and quadrupole interactions, among others). For this mixture where there are no dipole-dipole or hydrogen-bonding interactions, the modification of Hudson and McCoubrey combining rules can be shown to lead to the following expression for the  $k_{ij}$  unlike interaction parameter [166]:

$$k_{ij} = 1 - \left[ \frac{\frac{3}{m_i m_j \sigma_{ij}^3 (\lambda_{ij}^3 - 1)} \frac{1}{\sqrt{(\varepsilon_{ii} \varepsilon_{jj})}}}{\left( \frac{1}{2 \sigma_{ij}^3 (4 \pi \varepsilon_r \varepsilon_0)^2} \frac{I_i I_j}{(I_i + I_j)} \alpha_{0,i}^* \alpha_{0,j}^* + \frac{1}{5 \sigma_{ij}^5 (4 \pi \varepsilon_r \varepsilon_0)^2} \frac{3}{2} (Q_i^2 \alpha_{0,j}^* + Q_j^2 \alpha_{0,i}^*) \right)} \right] \quad 8.1$$

Here,  $\varepsilon_0$  is the permittivity of vacuum,  $\varepsilon_r$  is the relative permittivity (or dielectric constant) of the media,  $I_i$  and  $I_j$  are the ionization potentials of the molecules,  $\alpha_{0,i}^*$  and  $\alpha_{0,j}^*$  are the electronic polarisabilities and  $Q_i$  and  $Q_j$  are the total quadrupole moments. The electronic polarisabilities  $\alpha_{0,i}^*$  and  $\alpha_{0,j}^*$  are obtained using an equivalent expression for the like-like interactions.

**Table 8.2.** SAFT-VR Parameters<sup>a</sup> used for modeling the behaviour of the pure components

Compound	Ref.	$m$	$\sigma_{ii}/\text{\AA}$	$(\varepsilon_{ii}/k_B)/\text{K}$	$\lambda_i$	$(\varepsilon_{ii}^{\text{HB}}/k_B)/\text{K}$	$r_{c,ii}/\text{\AA}$
CO <sub>2</sub>	[218, 320]	2.0	2.7864	179.27	1.5157		
H <sub>2</sub> O	[319]	1.0	3.0342	250.00	1.7889	1400.0	2.10822
<i>n</i> -heptane	[321]	3.0	1.5574	253.28	3.9567		

<sup>a</sup>  $m_i$  is the number of square-well segments in the molecule,  $\sigma_{ii}$  is the hard-core diameter,  $\lambda_{ii}$  and  $\varepsilon_{ii}$  are the range and the depth of the square-well potential, and  $\varepsilon_{ii}^{\text{HB}}$  and  $r_{c,ii}$  are those of the hydrogen-bonding interaction.

For the mixture of CO<sub>2</sub> + *n*-heptane, the dependence of the dielectric constant with temperature and density is neglected by approximating the values of both liquid *n*-heptane and liquid CO<sub>2</sub> to be unity. This is a good approximation at the temperatures of this study [322]. A value [323] of  $Q = -1.4 \times 10^{-39} \text{ C} \cdot \text{m}^2$  is used for the quadrupole moment of CO<sub>2</sub>, and values of  $I = 1.6 \times 10^{-18} \text{ J}$  and  $I = 2.2 \times 10^{-18} \text{ J}$  for the ionisation potentials [323] of *n*-heptane and CO<sub>2</sub>, respectively, so that the determined binary interaction parameter from Equation (8.1) is  $k_{ij} = 0.1162$ .

In the case of aqueous solutions, differences between the dielectric constant of each equilibrium liquid phase are not negligible, due to the high value of the dielectric constant of liquid water. According to the modified Hudson and McCoubrey combining rules for polar molecules [166], different binary interaction parameters are therefore predicted for each equilibrium phase. This justifies the general difficulty that is found in the literature to describe both liquid phases of aqueous mixtures with a single binary interaction parameter, as it was commented in the introduction of this Chapter. (See also discussion in Ref.[87])

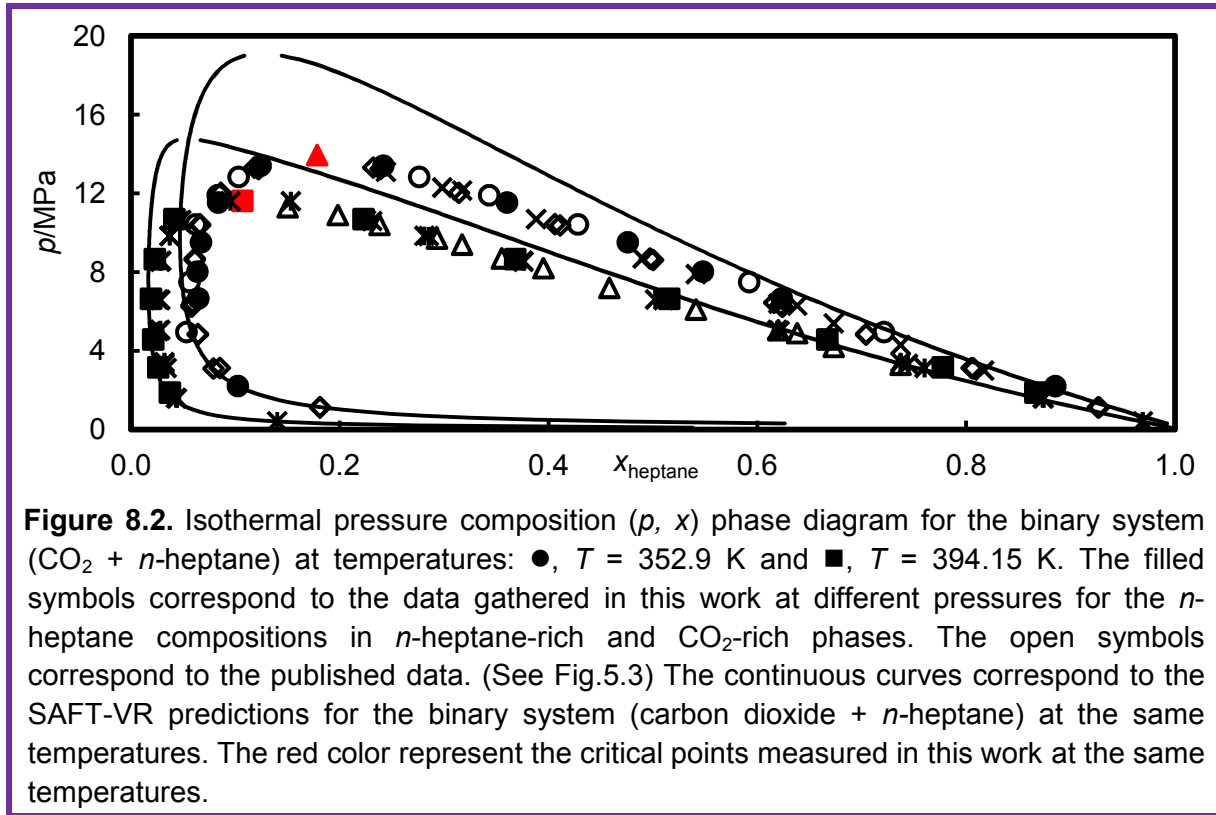
Here we opt for a single  $k_{ij}$  value; instead, for each pair of compounds and the Hudson and McCoubrey combining rule is not applied to the binaries including water. Appropriate values for the  $k_{ij}$  of each pair are instead obtained through fitting to experimental data. The binary interaction parameter for (*n*-heptane + water) has been kept to the value of  $k_{ij}= 0.2725$  that was optimised fitting to VLE and saturated decane-rich phase LLE data for (decane + water) at temperatures of (473 to 523) K and pressures of (0.1 to 75) MPa on the basis of available data [87]. This leads to good agreement with the available experimental data for the system, although the measured composition of the aqueous-rich phase is under predicted, as was the case in the (*n*-decane + water) mixture [87]; in absolute terms these deviations are negligible. A binary interaction parameter value of  $k_{ij}= -0.06$  is used for the (carbon dioxide + water) system, obtained [316] by regression against experimental data over a temperature range of (273 to 373) K and pressures of (0.007 to 10) MPa.

## 8.5 Discussion and Comparison with Experiment

The binary system (*n*-heptane + CO<sub>2</sub>) exhibits type II phase behaviour [45] while the binary systems of (CO<sub>2</sub> + water) [201] and (*n*-heptane + water) [324] exhibit types III phase behaviour according to the classification of Van Konynenburg and Scott [42-43]. In general, mixtures of (*n*-alkane + carbon dioxide) up to *n*-dodecane exhibit type II phase behaviour [45-46]. The differences between type II and type III is that type III corresponds to a more marked immiscibility than type II, and that aqueous mixtures of non-polar systems usually present this type of phase diagram.

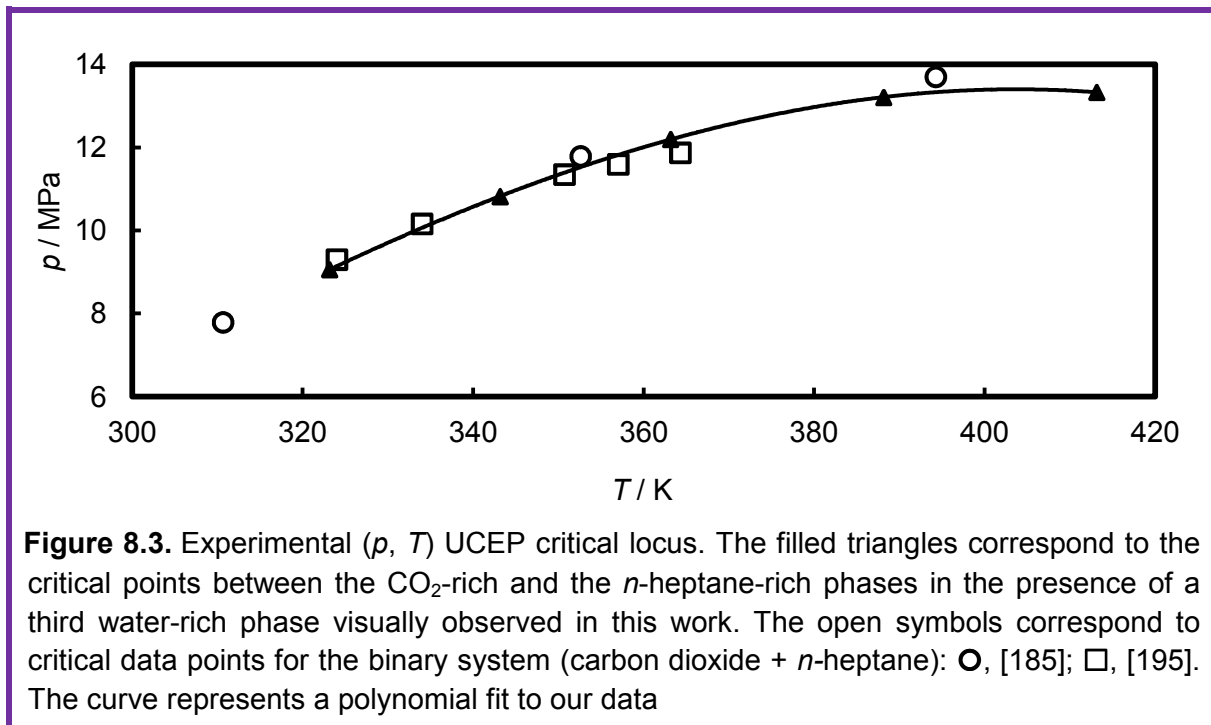
The VLLE equilibrium curves of binary mixtures appear as regions in ternary systems, which can extend to wide range of pressures and temperatures depending on the mixture. In the case of (CO<sub>2</sub> + *n*-heptane + water), this region occurs within a wide range because of the differences in volatility and size between *n*-heptane and carbon dioxide molecules and because of the very large immiscible regions of the aqueous binaries leading to wide immiscible range conditions.

SAFT-VR was initially used to model liquid equilibria (VLE) of the binary system (CO<sub>2</sub> + *n*-heptane) at  $T = 252.9$  K and  $T = 394.15$  K as shown in Figure 8.2.



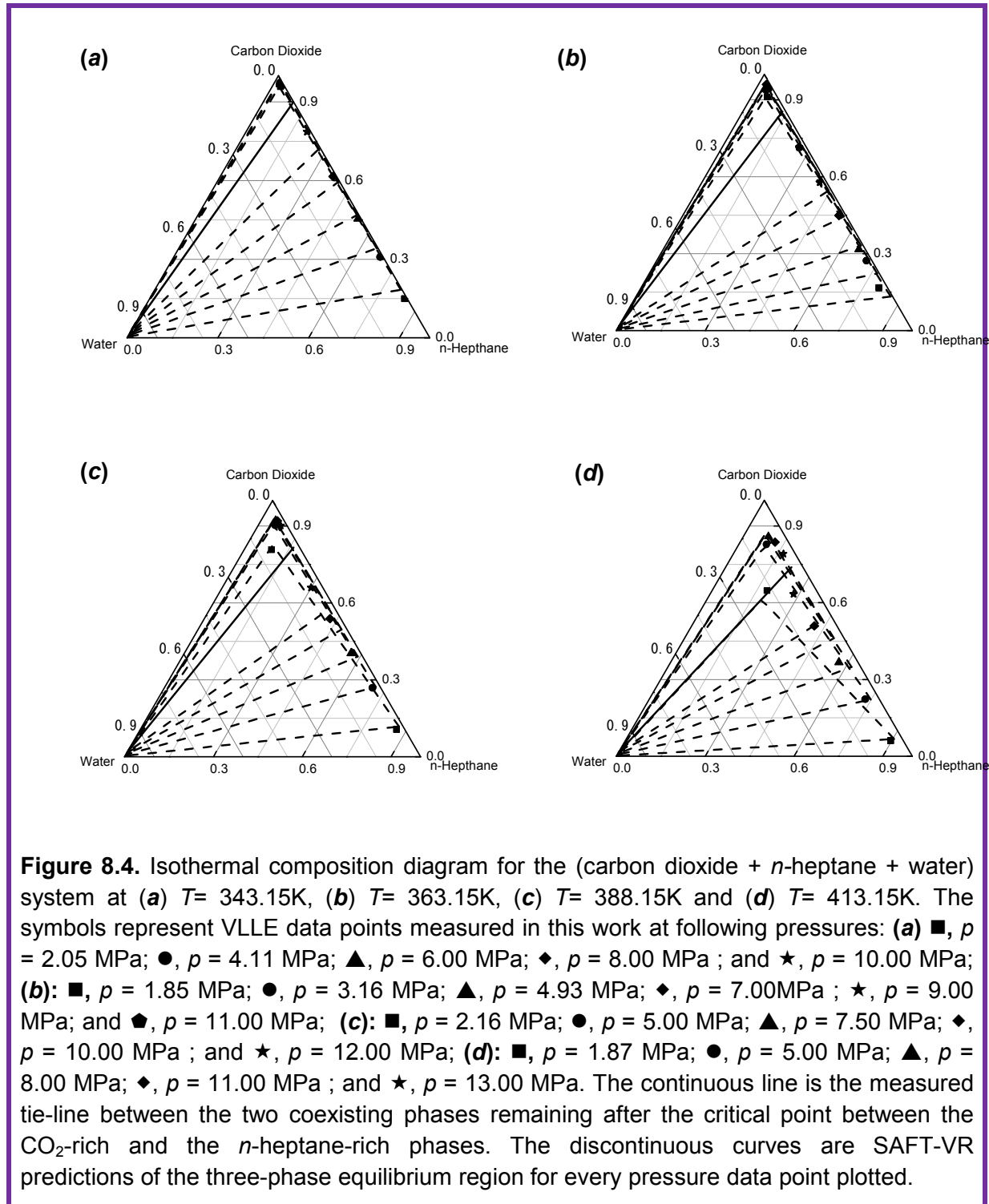
This system was used to validate the analytical apparatus. In this Figure, it can be seen that the SAFT-VR prediction is in good agreement with the data at low pressures only. Overall, the agreement is not really that good in an absolute sense. At high pressures, close to the critical region, the equation considerably over-predicts the pressure for given compositions at these temperatures. As discussed previously, this is a known difficulty of classical EoS, which is based in a mean-field approximation and therefore, in practice, treats the density as homogenous. Density fluctuations are however not negligible close to the critical region, where the magnitude of these fluctuations may span from microscopic to macroscopic lengths. Appropriate treatments to incorporate a description of the contribution of such density fluctuations in EoS have been developed, and applied to SAFT-VR [325-329]. Such improved versions of the theory are however not used here. It can also be seen that the deviation is considerable even far from the mixture critical region. This is in fact a general limitation of the old SAFT-VR versions (with SW potential); more recent version with Mie potential with the 3<sup>rd</sup> order perturbation expansion is proved to give better agreement [170] but this is not applied in the current work.

The *n*-heptane-CO<sub>2</sub> binary mixture exhibits a single homogeneous fluid phase at pressures above the UCEP of the ternary mixture and hence only VLE exist for the ternary mixture. Figure 8.3 shows a plot of the UCEP curve as a function of temperature. In this plot, the comparison with the experimental critical data points [185, 195] for the binary system (*n*-heptane + CO<sub>2</sub>) is shown as well so that the effect of adding a third component (water) on the critical curve of the binary system can be observed. It can be seen that the presence of water has negligible effect on the critical curve of the binary *n*-heptane+CO<sub>2</sub> system. This is because the amount of water dissolved in the *n*-heptane-rich phase and CO<sub>2</sub>-rich phase is very small. The calculations performed with SAFT-VR are not shown here as SAFT-VR is a classical EoS and it tends to over predict the critical pressures and temperatures. This has already been discussed above.

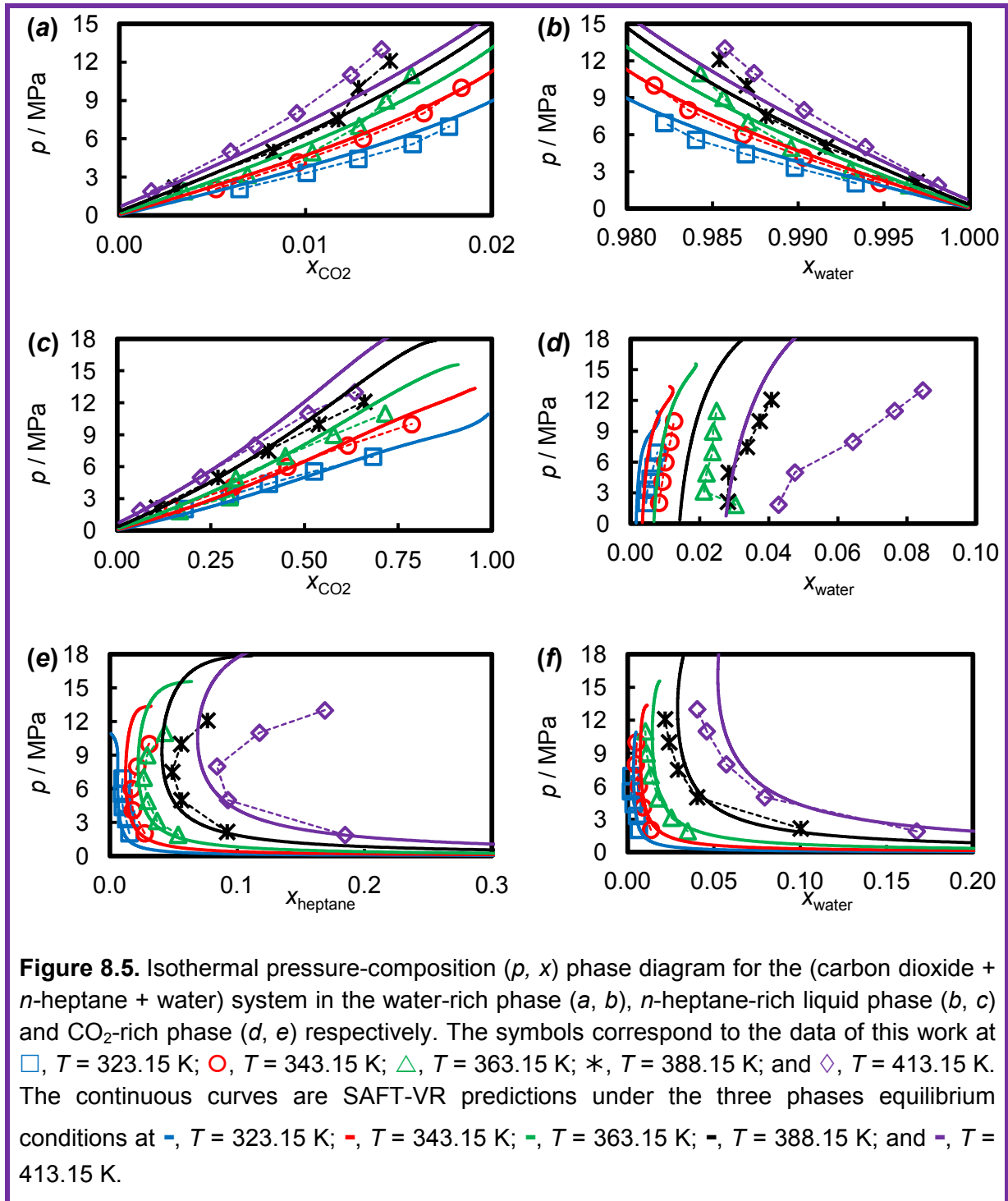


The experimental results are also plotted in the form of triangular diagrams, which show the composition of the different components in the different phases at given temperature and pressure, in Figures 8.4. The pressure dependence is not quantitatively represented in the plots, these are just mere projections of  $p,x$  prismatic diagrams. It can be seen that the three-phase region for a given pressure diminishes as the critical point between the CO<sub>2</sub>-rich and *n*-heptane-rich phases is approached. Comparing the subfigures it can also be observed that the three-phase region gets smaller as temperature increases. In general a good agreement between experimental data and theory is observed, where it is worth noting the good performance of the equation in predicting the phase behaviour at different

temperatures even with the use of temperature-independent binary interaction parameters. Expected deviations are seen at higher pressures, in the near-critical region. In addition, Figure 8.5 is a set of isothermal pressure-composition phase diagrams for the ternary system showing the solubility of the components in different phases compared with the calculations from SAFT-VR.







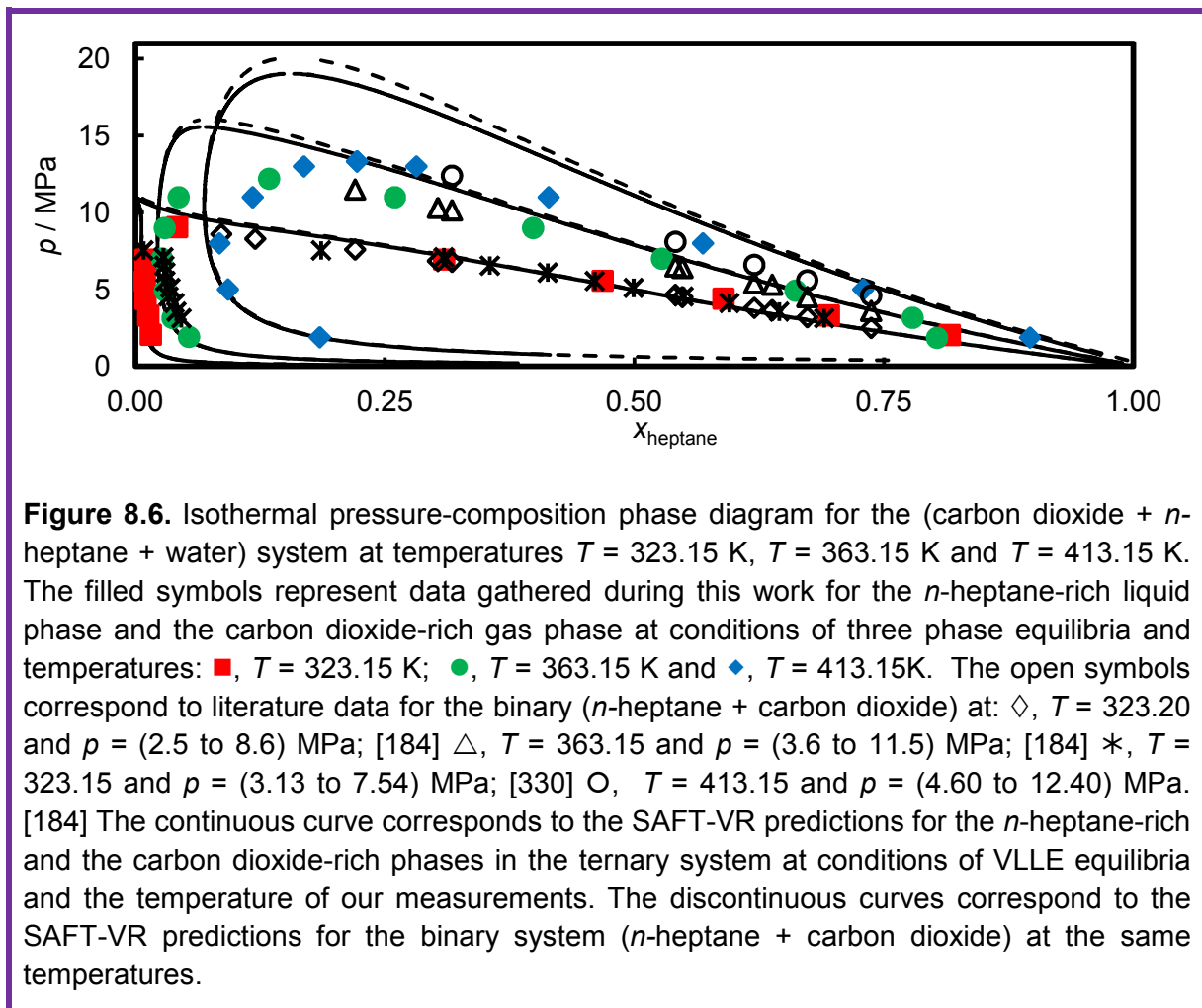
The CO<sub>2</sub> solubility and water content predicted by SAFT-VR agree reasonably well with the experimental values both in the water-rich (Figures 8.5a and 8.5b) and *n*-heptane-rich phases (Figures 8.5c and 8.5d), with slight deviation regarding water content in the *n*-heptane-rich phase. The last two Figures (Figures 8.5e and 8.5f) show the amount of *n*-heptane and water in the CO<sub>2</sub>-rich gas phase. The water content dissolved in the CO<sub>2</sub>-rich gas phase predicted by SAFT-VR agrees well with the experimental values.



The *n*-heptane content predicted by SAFT-VR agrees well with the measured data in the low pressure region, where deviations in the proximity of the UCEP are here more obvious. Generally speaking, from these Figures it can be seen that the SAFT-VR prediction is in good agreement with our experimental data. In the following section, the binaries systems are compared with the VLLE experimental data of the ternary mixture. We use such a comparison to draw conclusions regarding the effect of adding a component on the phase behaviour of the other two. The effect of changing *n*-alkane components on CO<sub>2</sub> solubility in the water-rich phase is also studied.

### Influence of water on the phase behaviour of (*n*-heptane + carbon dioxide) binary mixture

The amount of water presents in the *n*-heptane and CO<sub>2</sub>-rich phases is very small and should have small affect on the mutual solubility between *n*-heptane and CO<sub>2</sub> as shown in Figure 8.6.



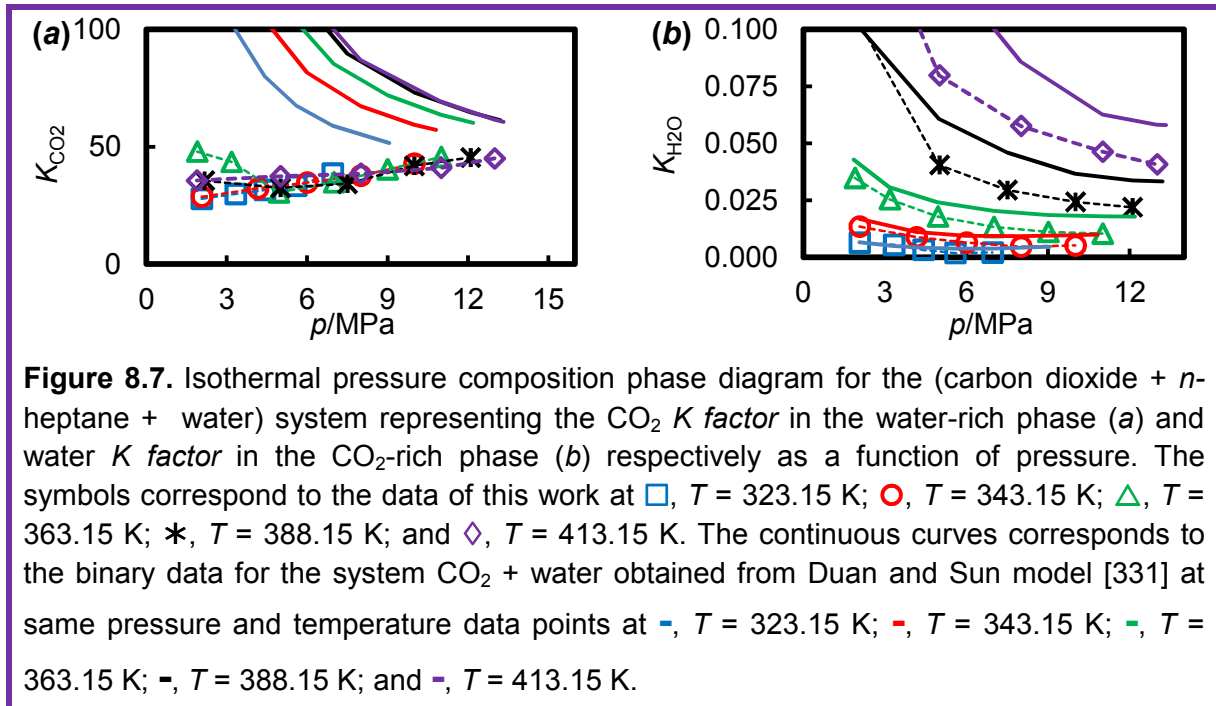
The water content present in the *n*-heptane-rich and CO<sub>2</sub>-rich phases increases as temperature increases while it rapidly decreases as pressure increases in the CO<sub>2</sub>-rich phase. However, in the *n*-heptane-rich phase, it slightly increases as pressure increases. In this Figure, the amount of *n*-heptane presents in the *n*-heptane-rich liquid phase and CO<sub>2</sub>-rich gas phase are plotted against equilibrium pressures at  $T = 323.15$  K,  $T = 363.15$  K and  $T = 413.15$  K. These experimental data are compared with the binary CO<sub>2</sub>-*n*-heptane data published by Mutelet et al. [184] at  $T = 323.20$  and  $p = (2.5 \text{ to } 8.6)$  MPa; Mutelet et al. [184] at  $T = 363.15$  and  $p = (3.6 \text{ to } 11.5)$  MPa; Y. He [330] at  $T = 323.15$  and  $p = (3.13 \text{ to } 7.54)$  MPa; and Mutelet et al. [184] at  $T = 413.15$  and  $p = (4.60 \text{ to } 12.40)$  MPa. It can be clearly seen that as temperature increases, the saturated region shifts towards less *n*-heptane concentration and become larger in size. It can be seen as well that the effect of the presence of water is small in both the low and high-pressure region. Comparisons between the SAFT-VR calculations for the ternary mixture against the binary lead to the same conclusion. It can be observed that the theory prediction agrees well at low pressures. At pressures close to critical region, deviations between theory and experiment are expected, as commented in earlier sections.

It is perhaps useful to compare the influence of water on the phase behaviour of this system with that on the phase behaviour of (*n*-decane + carbon dioxide) [87], (propane + carbon dioxide) [88] and (methane + carbon dioxide) binary mixtures. It can be concluded that generally water has small effect on the phase behaviour of (*n*-alkane + CO<sub>2</sub>) mixtures where moving towards lighter *n*-alkane such as methane does not increase the amount of water dissolved in the CO<sub>2</sub>-rich phase and *n*-alkane-rich phase. In fact the water content dissolved decreases in the case of methane compared to heavier *n*-alkane mixtures, which suggests that lighter hydrocarbons have higher anti solvents effects against water than heavier hydrocarbons. This will be addressed further in the next Chapter. Finally, the amount of water dissolved in *n*-alkane-rich or gas phase increases as the temperature increases. This is because as temperature increases, the association due to hydrogen bonding between water molecules decreases and as a consequence of this, the mutual solubility of water with hydrocarbon and carbon dioxide increases.

#### **Influence of *n*-heptane on the phase behaviour of (CO<sub>2</sub> + water)**

The influence of the presence of *n*-heptane on the mutual solubility of (CO<sub>2</sub> + water) is studied by comparison to the available binary data for (CO<sub>2</sub> + water) mixtures at similar pressure and temperature ranges as shown in Figure 8.7. For the sake of comparison, the available binary data were obtained from the models developed by Duan and Sun [331] for

the binary mixture CO<sub>2</sub> + water as this model agrees well with the available experimental values in the literature. In Figure 8.7a, the  $K$  factor value  $K_{\text{CO}_2} = y_{\text{CO}_2}/x_{\text{CO}_2}$  is plotted against the pressure where  $y$  is the CO<sub>2</sub> mole fraction in the *n*-heptane-rich phase and  $x$  is the CO<sub>2</sub> solubility in the water-rich phase. The  $K$  factor represents the distribution of a component in the gas and liquid phases where higher value means higher volatility and lower solubility in the liquid phase. The dotted lines connect our experimental data while the solid lines represent the binary data obtained from the Duan and Sun model [331].



It can be observed that CO<sub>2</sub> solubility in the case of ternary is higher than that of the binary mixture and decreases as pressure increases. As pressure increases, the amount of *n*-heptane dissolved in the *n*-heptane-rich phase decreases. As a consequence, CO<sub>2</sub> solubility increases because of the presence of *n*-heptane as compared to the binary mixtures. This suggests that *n*-heptane works as a cosolvent since its presence (in the *n*-heptane-rich phase) increases the CO<sub>2</sub> solubility in the water-rich phase. The same observation was observed for the ternary mixture (CO<sub>2</sub> + methane + water) in VLE and VLLE regions (Chapter 9), (CO<sub>2</sub> + propane + water) in VLLE regions [88] and (CO<sub>2</sub> + *n*-decane + water) in VLLE regions [87]. In Figure 8.7b, we plotted the  $K$  factor  $K_{\text{H}_2\text{O}} = y_{\text{H}_2\text{O}}/x_{\text{H}_2\text{O}}$  in the CO<sub>2</sub>-rich phase against equilibrium pressure. It can be clearly seen that because of the presence of *n*-heptane, the water content in the CO<sub>2</sub>-rich phase is less than the content in the CO<sub>2</sub>-water binary mixtures.

The water content decreases as pressure increases which depends on the trend at which the amount of *n*-heptane in the CO<sub>2</sub>-rich phase changes with pressure and temperature conditions. In addition, comparing the CO<sub>2</sub> solubility in the water-rich phase in VLLE measurements of the type (CO<sub>2</sub> + *n*-alkane + water), it was observed that the presence of hydrocarbon component in general increases the solubility of CO<sub>2</sub> in the water-rich phase, as observed in this work. This means that in general hydrocarbons act as cosolvents in which they increase the tendency towards dissolving more CO<sub>2</sub> in the water. Also it was observed as well that water content in the CO<sub>2</sub>-rich gas phase decreases because of the presence of the hydrocarbon components compared to the binary system CO<sub>2</sub> + water and the water content decreases as more hydrocarbons was dissolved. The effect of pressure on CO<sub>2</sub> solubility depends mainly on the presence of the third component in the *n*-alkane-rich phase. If increasing the pressure means that, for example, the *n*-alkane ratio increases hence the solubility would be expected to increase and vice versa. The CO<sub>2</sub> solubility in the water-rich phase decreases as temperature increases. It was also observed that the *n*-alkane solubility in the water-rich phase increases because of the presence of CO<sub>2</sub> as compared to the pure *n*-alkanes.

#### Influence of carbon dioxide on the phase behaviour of (*n*-heptane + water)

The effect of the presence of CO<sub>2</sub> on the phase equilibria of the binary system of *n*-heptane + water was analyzed as shown in Figure 8.8. Unfortunately, there are no binary data available for the system *n*-heptane + water to compare with the VLLE measurements of the ternary mixture.

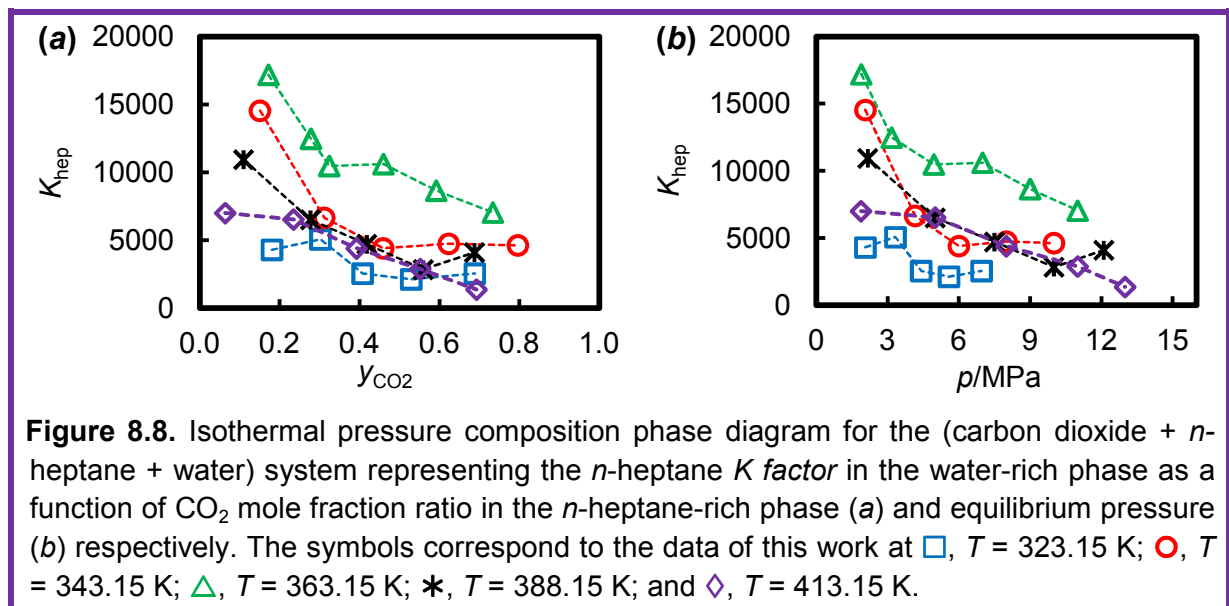


**Figure 8.8.** Isothermal pressure composition phase diagram for the (carbon dioxide + *n*-heptane + water) system representing the *n*-heptane  $K$  factor in the water-rich phase as a function of CO<sub>2</sub> mole fraction ratio in the *n*-heptane-rich phase (a) and equilibrium pressure (b) respectively. The symbols correspond to the data of this work at  $\square$ ,  $T = 323.15$  K;  $\circ$ ,  $T = 343.15$  K;  $\triangle$ ,  $T = 363.15$  K;  $*$ ,  $T = 388.15$  K; and  $\diamond$ ,  $T = 413.15$  K.

In Figures 8.8a and 8.8b, we plot the value  $K_{\text{hep}} = y_{\text{hep}}/x_{\text{hep}}$  against the CO<sub>2</sub> molar ratio in the *n*-heptane-rich phase and equilibrium pressure respectively where  $y_{\text{hep}}$  represents the *n*-heptane mole fraction in the *n*-heptane-rich liquid phase and  $x_{\text{hep}}$  is the *n*-heptane solubility in the water-rich liquid phase. As can be seen that *n*-heptane solubility increases as pressure increases. The increase in pressure leads to an increase in the CO<sub>2</sub> content in the *n*-heptane-rich phase. As a consequence, *n*-heptane solubility increases as more CO<sub>2</sub> presents in the *n*-heptane-rich phase. This means that CO<sub>2</sub> as well works as a cosolvent dissolving more *n*-heptane in the water. The same observation was noticed with the other ternary mixtures of the type (CO<sub>2</sub> + *n*-alkane + water) [87-88]. It can therefore be concluded that, in general, the presence of CO<sub>2</sub> increases the solubility of *n*-alkanes in water. The effect of pressure or temperature on *n*-heptane solubility in water follows the trend at which the CO<sub>2</sub> ratio changes with pressure and temperature.

## 8.6 Conclusion

Compositions for the system (carbon dioxide + *n*-heptane + water) have been obtained along five isotherms at temperatures from (323.15 to 413.5) K and at pressures up to the UCEP. The experimental data obtained for this mixture have been compared with SAFT-VR. In our application of the SAFT equation we keep the models used as consistent as possible with previous studies. Only the unlike dispersion energies between each pair of compounds are modified through binary interaction parameters. These are all temperature-independent. The *n*-alkane-water binary interaction parameter is found to be transferable from a previous study (CO<sub>2</sub> + *n*-decane + water) with a different *n*-alkane (*n*-decane) and the *n*-alkane-carbon dioxide one is predicted using a modified Hudson-McCoubrey combining rule. The binary interaction parameter relative to the carbon dioxide-water interaction is taken from a previous work. Detailed comparison concluded that SAFT-VR predicts reasonably well our experimental data, which proves the predictive capabilities of the approach applied to this ternary mixture.

Furthermore, a detailed study of the ternary mixtures was carried out based on comparison with available data for the constituent binary subsystems. It was concluded that the presence of CO<sub>2</sub> increases the *n*-alkane solubility in water as compared to the binary mixture *n*-alkane + water. In addition, the presence of *n*-alkane increases the CO<sub>2</sub> solubility in the water-rich phase compared to the binary mixture CO<sub>2</sub> + water. The effect of pressure and temperature depends mainly on the trend at which the *n*-alkane to CO<sub>2</sub> ratio changes in the *n*-alkane-rich phase with pressure and temperature.

## Chapter 9: Phase Behaviour of (CO<sub>2</sub> + Methane + Water) Mixtures

### 9.1 Overview

The ternary mixture (carbon dioxide + methane + water) was considered representative of (carbon dioxide + natural gas + water), being a model system which should mimic most of the characteristics of the real one. Surprisingly, despite its importance as a simple model mixture, there are no VLLE in the literature for this mixture. This work is a continuation to the previous system studied (Chapter 8) and adds to the previously reported studies of the two systems made on the mixtures of CO<sub>2</sub> and water with propane [88] or decane [87]. In this work, new experimental data have been measured under conditions of two-phase vapour-liquid equilibrium, three-phase vapour-liquid-liquid equilibrium, and four-phase vapour-liquid-liquid-hydrate equilibrium. The compositions of three coexisting fluid phases<sup>12</sup> have been obtained along eight isotherms at temperatures from (285.15 to 303.5) K and at pressures up to either the UCEP or up to the hydrate formation locus. Compositions of coexisting vapour and liquid phases have been obtained along three isotherms at temperatures from (323.15 to 423.15) K and pressures up to 20 MPa. The quadruple curve along which hydrates coexists with the three fluid phases was also measured. Only determining the unlike binary interaction parameter for the system CO<sub>2</sub>-H<sub>2</sub>O was found necessary to describe the phase equilibria of this mixture

The VLLE experimental data obtained for this mixture have been compared with the predictions of the statistical associating fluid theory for potentials of variable range (SAFT-VR)<sup>13</sup> in a similar manner to the previous system discussed in Chapter 8. In this work, we used the SAFT-VR parameters reported previously in the work of Míguez and co-workers [332]. The pressure along the quadruple curve was predicted using two different thermodynamic models and compared with our experimental data. Furthermore, a detailed study of the ternary mixtures was carried out based on comparison with available ternary data of the type (CO<sub>2</sub> + *n*-alkane + water) and available data for the constituent binary subsystems. In this way, we analyze the observed effects on the solubility when the *n*-alkane component was changed or a third component was added.

---

<sup>12</sup> The majority of the three phase VLLE measurements were obtained with the help of Hak Lui and José Rodríguez

<sup>13</sup> SAFT-VR calculations were performed by Esther Forte, using the parameters reported previously in the work of Míguez and co-workers

## 9.2 Introduction

High pressure mutual solubility data of water and hydrocarbons gases are still scarce. As emphasised previously, thermodynamic models required for the mutual solubility of water and hydrocarbons are not easy to handle because of the association of water molecules by means of hydrogen bonding, which restricts the application of traditional cubic EoS, and in most cases experimental data on mutual solubility is still required to validate the models. Large quantities of CH<sub>4</sub> are most likely to exist in reservoir production processes and CO<sub>2</sub> flooding projects, hence investigation of the impact of the presence of CH<sub>4</sub> on the mutual solubility of water and methane and on the CO<sub>2</sub> MMP are of both technical and economical significance.

Considerable research has been devoted in the last decades to examine potential industrial applications of gas hydrate technology. Examples are natural gas processing, storage and transportation, carbon dioxide (CO<sub>2</sub>) capture from industrial or flue gases, CO<sub>2</sub> sequestration where trapping carbon dioxide as a hydrate in the bottom of the ocean has been proposed as an alternative to reduce increasing atmospheric CO<sub>2</sub> concentration [333], steam reforming processes, hydrogen storage, and water desalination [273, 334-337].

The ternary mixture (CO<sub>2</sub> + methane + water) was the most widely studied system of the type (CO<sub>2</sub> + *n*-alkane + water) both in the region of fluid phase equilibria [89-92] and fluid-hydrates equilibria [188, 338-342]. However, fluid phase equilibria measurements (as already shown in Table 2.3) for this mixture were restricted to the vapour-liquid region only and no VLLE measurements for this system exist to our knowledge. The most recent study on this ternary mixture was those published by Qin et al. [89] where the vapour-liquid equilibrium was studied at different ratios of CO<sub>2</sub> to CH<sub>4</sub> at  $T = (324.3 \text{ and } 375.7) \text{ K}$  and  $p = (10 \text{ to } 50) \text{ MPa}$ . In their study, it was observed that carbon dioxide solubility in water increased due to the presence of methane and also methane solubility in water increased due to the presence of carbon dioxide compared to the binary mixtures. In addition, the solubility of CO<sub>2</sub> or methane in the water-rich phase depends on the ratio of these two components and increased as the amount of the other component in the gas phase increased.

Jerne et al. [343] measured the dew points in the temperature range of (243.1 to 288.1) K and pressure range of (0.11 to 6.05) MPa. The experimental results obtained were analysed in terms of a predictive excess function-EoS (EF-EoS). It was observed that when the water concentration of the ternary system increased, the dew point temperature of the ternary system also increased; the increase was also greater for systems at higher pressure. In

addition, the dew point temperature and pressure were highly dependent on the water concentration of the mixture, but not on the composition of the (hydrocarbon + carbon dioxide) mixtures. Dhima et al. [90] have studied the solubility of methane, carbon dioxide and their binary mixtures in water at  $T = 344.25$  K and pressures of (10 to 100) MPa with a modelling approach using a combination of the PR EoS and Henry 's Law. In their study, it was observed that CO<sub>2</sub> solubility increased in the case of the ternary mixture compared to that of the binary mixture. Similarly in a previous study [89], it was also observed that the solubility of CO<sub>2</sub> increased as more methane was present in the gas mixture. The study published by Ren et al. [344] reported the interfacial tension measurements of this system in the temperature range (298 to 373) K and pressure range (1 to 30) MPa. It was observed that the pressure effect on interfacial tension was significant; the higher the pressure, the lower the interfacial tension. Also at fixed temperature and pressure conditions, the interfacial tension for the mixture decreased as the concentration of carbon dioxide increased while an increase in the temperature resulted in the lowering of interfacial tension of the mixture.

Generally speaking, fluid-phase equilibrium studies for this mixture were reported for vapour-liquid equilibrium only with one phase typically measured in most of the cases. Only in the work of Song and Kobayashi [91] was the three phase equilibrium VLLE measured but only one phase was analysed (the gas phase). In their work, the water content in the carbon dioxide-rich phase was analyzed and it was concluded that the presence of the methane lowered the water content in the gas phase by 20 % to 30 % from that of pure CO<sub>2</sub>.

Methane in the form of hydrates is considered a potential source of energy, with conservative estimates suggesting that the energy stored in the form of hydrates exceeds all other hydrocarbon sources combined [341]. In addition, the enormous quantities of methane stored as thermally unstable hydrates also cause an environmental concern due to the high global warming potential of methane [345]. Hydrates have also been suggested as an economically-advantageous alternative to liquefied natural gas (LNG) for transportation and storage of gas [346]. Furthermore, the use of hydrate technology to sequester CO<sub>2</sub> from mixed streams is currently being explored [347]. In this process, for effective CH<sub>4</sub>-CO<sub>2</sub> hydrate replacement for CO<sub>2</sub> sequestration and CH<sub>4</sub> recovery from natural gas hydrates, the phase equilibrium properties of the mixed gas hydrates and quadruple equilibria are essential. An extensive review on the potential energy resource of methane hydrates is covered by Demirbas [348-349].



**Table 9.1.** Hydrate equilibrium data for the ternary (CO<sub>2</sub> + CH<sub>4</sub> + water) mixture

Ref	Equilibria	$T_{\min}$ K	$T_{\max}$ K	$p_{\min}$ MPa	$p_{\max}$ MPa
[339]	H-V	273.06	280.46	2.0	3.5
[188]	H-L <sub>w</sub> -V	273.6	284.2	1.51	7.19
[338]	H-L <sub>w</sub> -V	275.14	285.34	1.92	7.47
[350]	H-L <sub>w</sub> -V	273.56	283.26	1.5	5.0
[340]	H-L <sub>w</sub> -V	280.3	280.3	3.04	5.46
[341]	H-L <sub>w</sub> -V	274.02	280.1	1.66	4.03
[342]	H-L <sub>w</sub> -V	258	274.1	0.5	3
[351]	H-L <sub>w</sub> -L <sub>CO<sub>2</sub></sub> -V	283.09	286.51	4.46	7.93
[339, 350]	H-L <sub>w</sub> -L <sub>CO<sub>2</sub></sub> -V	283.32	285.56	4.53	6.72

Although a significant amount of research has been carried out for mixed hydrates of carbon dioxide and methane, the compositions of the gas, hydrate, and fluid phases reported in the literature are still limited. Table 9.1 summarizes the hydrate studies reported in the literature for the mixture of interest. Belandria et al. [188] used a cylindrical equilibrium cell for gas hydrate-rich phase equilibrium measurements with two sapphire windows located in the front and rear end sides of the cell enabling the visual observation of the gas hydrate formation and phase behaviour combined with an electromagnetic online micro-sampler (ROLSI) which was connected to a gas chromatograph for phase composition analyses. However, only the gas phase was analysed experimentally while the compositions of the hydrate and aqueous phases were determined using a material balance approach in combination with the experimental data and the volumetric properties evaluated from the EoS for gas mixtures. In addition, the hydrate dissociation pressures were predicted (at the corresponding equilibrium temperature, CO<sub>2</sub> mole fraction in the gas feed, and water mole fraction introduced to the system) using two hydrate thermodynamic models: CSMGem [352] (which is based on the Gibbs energy minimization) and HWHYD [353] (which is based on fugacity equality of each component throughout all phases present). The absolute average relative deviation (% AAD) of the predicted hydrate dissociation conditions by HWHYD and CSMGem models were 9.7% and 5.1%, respectively, which are considered to be in acceptable agreement with the experimental values measured.

Beltrán and Servio [338] also used a high-pressure  $pVT$  cell consisting of a very narrow glass tube for full visualisation of the entire contents of the cell. They measured the hydrate,

liquid and vapour phases (H-L<sub>w</sub>-V) at temperatures of (275.15 to 285.34) K and pressures of (1.92 to 7.47) MPa. However, they only measured the gas composition at these conditions. Seo et al. [339, 350] measured the three-phase - hydrate, water-rich phase, and vapour phase - (H-L<sub>w</sub>-V) equilibrium conditions at different gas feed compositions. They also measured the quadruple points at which the four phases (H-L<sub>w</sub>-L<sub>CO<sub>2</sub></sub>-V) coexisted. In addition, the two phase equilibrium of hydrate and vapour were measured and the concentration of carbon dioxide in the hydrate-phase was also analyzed. Recently, Bi et al. [351] measured the upper-quadruple phase equilibrium properties of CO<sub>2</sub>-CH<sub>4</sub> mixed hydrates by using a visual experimental apparatus in the temperature range of (273.16 to 297.15) K and pressure up to 10 MPa and verified by calculation with thermodynamic models. In their study, it was found that an upper quadruple phase region existed in the range of (4.46 to 8.4) MPa, (283.09 to 287.9) K and (0 to 0.225) methane mole fractions in the gas phase.

Thermodynamic models based on accurate experimental equilibrium data are needed to predict phase equilibria and hydrate thermodynamic properties for potential industrial applications. To be able to treat the non-sphericity of alkanes and the hydrogen-bonding interactions of water, SAFT-VR was used in the present study with SW potential for VLLE calculations. SAFT-VR intermolecular parameters were obtained from the work of Míguez et al. [332]. In their work, they used the SAFT-VR to estimate the global phase equilibria diagram of the ternary mixture over a wide pressure and temperature range. Regarding hydrates, recently, Dufal et al. [354] integrated the SAFT-VR into a traditional van der Waals and Platteeuw [355-356] (vdWP) framework for modelling clathrate hydrates where SAFT-VR are used to describe the fluid phases while vdWP method used to model the hydrates themselves. In the present work, we make use of such model to compare with experimental data. Additionally, a hydrate model (CSMHYD) developed by Colorado School of Mines [357] was also used. A number of experimental devices, methods and mathematical models implemented for the measurements and predictions of hydrate-rich phase equilibrium of various systems have been extensively reviewed by Sloan and Koh in their recent book [352].

The binary systems (CO<sub>2</sub> + CH<sub>4</sub>) [358-365], (CH<sub>4</sub> + H<sub>2</sub>O) [89, 273, 277, 282, 334-337, 366-379] , and (CO<sub>2</sub> + H<sub>2</sub>O) [90, 198-205, 268-295] have been covered extensively in the literature, both in terms of phase equilibria and hydrate experimental data and modelling approaches, especially for solubility. A thermodynamic model based on specific particle interaction theory developed by Duan and Sun [331] for the solubility of CO<sub>2</sub> in water at temperatures of (273 to 533) K and pressures of (0 to 200) MPa was able to predict the CO<sub>2</sub>

solubility to within the uncertainty of available experimental data. However, it worth noting here that Shuxin et al. [204], in their VLE measurements of CO<sub>2</sub> + water, showed that this model gives large deviations above about  $T = 400$  K. In addition, Duan and Mao [380] developed a thermodynamic model for the binary mixture methane + water at temperatures of (273 to 523) K and pressures of (0 to 200) MPa which was also able to predict the methane solubility to within the uncertainty of the available experimental data. We make use of these two models for our analysis.

In the binary system (CO<sub>2</sub> + water) the water content in the gas phase decreases as pressure increases in the subcritical region. However, in the supercritical region, it decreases as pressure increases up to a pressure around (8 to 10) MPa, and then it increases as pressure increases further. In all cases, the water content in the gas phase increases as temperature increases. The CO<sub>2</sub> solubility in the water-rich phase increases as pressure increases but decreases as temperature increases. For the binary system of (methane + water), the water content in the gas phase decreases as pressure increases and increases as temperature increases while the methane solubility in the water-rich phase increases as pressure increases and decreases as temperature increases, similar to the behaviour observed in the (CO<sub>2</sub> + water) binary system. In this work, the effect of adding a third component on the behaviour of these binaries is studied both experimentally and by modelling.

### 9.3 Experimental Results

The compositions of the three coexisting phases have been obtained along eight isotherms at temperatures (285.15, 287.65, 290.15, 292.65, 295.15, 297.65, 300.15 and 303.15) K and at pressures up to the UCEP or the quadruple curve. The compositions of the coexisting vapour and liquid phases have been also obtained along three isotherms at temperatures (323.15, 373.15 and 423.15) K and pressures up to 20 MPa. For each measurement, the ratio  $y$  of CH<sub>4</sub> to CO<sub>2</sub> in the gas phase was kept roughly constant around  $y = 0.5$ . The VLE and VLLE results are given in Appendix C. In these Tables, the mole fraction of each component in all phases is given, together with the pressure and temperature values. The SAFT-VR prediction is given as well for the VLLE measurements.

The quadruple curve along which hydrate coexists with the three fluid phases was also measured and is presented in Table 9.2, while the UCEP results are given in Table 9.3.

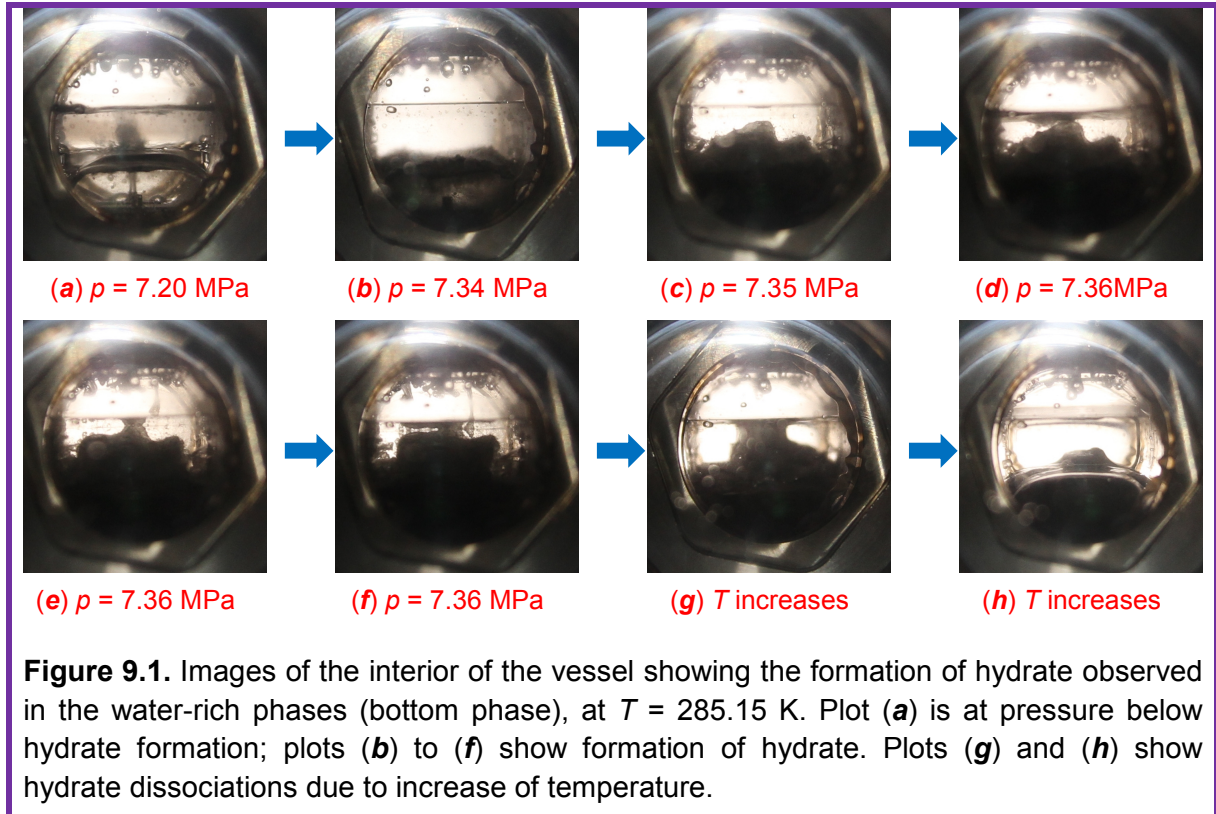


**Table 9.2.** Comparison between quadruple data obtained in this work and other references and predictions from models at same conditions.

$T/K$	$p/MPa$	$y_{CH_4}$	$y_{CO_2}$	$p/MPa$	Phases	$p/MPa$	Phases
<b>Data obtained in this work</b>				CSMHYD		SAFT-VR + vdWP	
285.60	6.81	0.189	0.811	6.52	L <sub>w</sub> -H-L <sub>hyd</sub>	6.47	L <sub>w</sub> -H-L <sub>hyd</sub>
285.15	6.17	0.144	0.856	6.03	L <sub>w</sub> -H-L <sub>hyd</sub>	6.04	L <sub>w</sub> -H-L <sub>hyd</sub>
284.37	5.352	0.072	0.928	5.26	L <sub>w</sub> -H-L <sub>hyd</sub>	5.37	L <sub>w</sub> -H-L <sub>hyd</sub>
283.90	4.925	0.028	0.972	4.86	L <sub>w</sub> -H-L <sub>hyd</sub>	5.08	L <sub>w</sub> -H-L <sub>hyd</sub>
286.19	7.62	0.228	0.772	7.23	L <sub>w</sub> -H-L <sub>hyd</sub>	7.06	L <sub>w</sub> -H-L <sub>hyd</sub>
<b>Data obtained from reference [351]</b>							
283.51	4.74	0.032	0.968	4.56	L <sub>w</sub> -H-L <sub>hyd</sub>	4.77	L <sub>w</sub> -H-L <sub>hyd</sub>
284.41	5.51	0.108	0.892	5.31	L <sub>w</sub> -H-L <sub>hyd</sub>	5.44	L <sub>w</sub> -H-L <sub>hyd</sub>
285.10	6.23	0.161	0.839	5.97	L <sub>w</sub> -H-L <sub>hyd</sub>	6.02	L <sub>w</sub> -H-L <sub>hyd</sub>
285.77	6.96	0.198	0.802	6.72	L <sub>w</sub> -H-L <sub>hyd</sub>	6.63	L <sub>w</sub> -H-L <sub>hyd</sub>
285.99	7.28	0.210	0.790	6.98	L <sub>w</sub> -H-L <sub>hyd</sub>	6.85	L <sub>w</sub> -H-L <sub>hyd</sub>
<b>Data obtained from reference [339, 350]</b>							
283.32	4.53	0.000	1.000	4.41	L <sub>w</sub> -H-L <sub>hyd</sub>	4.47	L <sub>w</sub> -H-L <sub>hyd</sub>
283.86	4.93	0.060	0.940	4.83	L <sub>w</sub> -H-L <sub>hyd</sub>	5.01	L <sub>w</sub> -H-L <sub>hyd</sub>

Images showing the formation of hydrate observed at  $T = 285.15$  K are shown in Figure 9.1. The phase equilibrium results are shown in Figures 9.2 to 9.12 together, in some figures, with comparison with the predictions of SAFT-VR. In addition, in some of these plots, the effect of adding a third component to the binary system is shown, together with comparison with some available literature binary data. Additional comparison with other ternary mixtures of the type (CO<sub>2</sub> + *n*-alkane + water) is also given. In this case, the effect of changing the *n*-alkane component on the mutual solubility of the binary systems can be observed. Details are addressed in the discussion section below.

**Table 9.3.** Experimental LLE Data for (methane (1) + Carbon Dioxide (2) + Water (3)) at the Critical Point between the CO<sub>2</sub>-rich and Water-rich phases <sup>a</sup>

<i>T</i> /K	<i>p</i> /MPa	phase II			phase III		
		<i>x</i> <sub>1</sub>	<i>x</i> <sub>2</sub>	<i>x</i> <sub>3</sub>	<i>x</i> <sub>1</sub>	<i>x</i> <sub>2</sub>	<i>x</i> <sub>3</sub>
287.65	8.629	0.1979	0.8021	0.0001	8.52E-04	0.0256	0.9736
290.15	8.186	0.1716	0.8283	0.0001	7.04E-04	0.0249	0.9744
292.65	8.084	0.1403	0.8596	0.0001	5.69E-04	0.0247	0.9747
295.15	7.964	0.1109	0.8889	0.0001	4.28E-04	0.0245	0.9751
297.65	7.861	0.0826	0.9173	0.0002	3.14E-04	0.0243	0.9754
300.15	7.751	0.0542	0.9456	0.0002	1.93E-04	0.0242	0.9756
303.50	7.615	0.0162	0.9835	0.0003	5.56E-05	0.0241	0.9758

<sup>a</sup> The phases are labelled as II and III for the CO<sub>2</sub>-rich and water-rich phases respectively.

In hydrate measurements, there is a fundamental difference between hydrate formation and dissociation conditions. This is because the gas and aqueous phases are initially disordered on a molecular level which means that the initial hydrate formation is affected by a metastability (nucleation) period, while hydrate crystals are ordered structures in nature and they are quickly dissociated when taken out of their pressure-temperature stability region. This is why hydrate equilibria were measured through dissociation rather than formation. In addition, Bi et al. [351] measured the quadruple states where the start and end melting points were identified. It was observed that the temperature difference was small between the start and end points but the pressure differences were considerable, which was similar to our observation.

## 9.4 Modelling Approach

In this work, we used the SAFT-VR parameters reported previously in the work of Míguez and co-workers [332] to predict the VLLE. The intermolecular model parameters for each pure component are collected in Table 9.4; these were obtained from fits to vapour pressure and saturated liquid density data. The parameters used in the work of Míguez and co-workers [332] are those previously reported by Clark et al. [319] for H<sub>2</sub>O, Patel et al. for CH<sub>4</sub> [304] and Galindo and Blas for CO<sub>2</sub> [218, 320]. The parameters used for water in the present study are different from those used in the calculations for the system (CO<sub>2</sub> + *n*-heptane + water) in Chapter 8.

This is because Clark et al. [319] presented different site models for water depending on the number of association sites selected. In both systems, the water molecule is modelled as a hard sphere with four off centre short-range sites that mediate the hydrogen bonding interactions. Within this structure, four different sets of intermolecular parameters for water were reported by Clark et al. [319]; these were examined and optimized along minimal surface from low dispersion to high dispersion regions. We previously selected the one which gave best agreement with the experimental data; the same is true for this system as well. For the unlike (dispersion) energies, only the binary interaction for the system CO<sub>2</sub>-H<sub>2</sub>O were considered; it was fitted to improve the description of the phase equilibrium of the CO<sub>2</sub>-H<sub>2</sub>O binary system [332].

**Table 9.4.** SAFT-VR Parameters<sup>a</sup> used for modeling the behaviour of the pure components

Compound	Ref.	$m$	$\sigma_{ii}/\text{Å}$	$(\epsilon_{ii}/k_B)/\text{K}$	$\lambda_i$	$(\epsilon_{ii}^{\text{HB}}/k_B)/\text{K}$	$K^{\text{HB}}/\text{Å}^3$
CO <sub>2</sub>	[218, 320]	2.0	2.786	179.27	1.515		
H <sub>2</sub> O	[319]	1.0	3.033	300.43	1.718	1336.9	0.8937
methane	[304]	2	3.685	167.30	1.448		

<sup>a</sup>  $m_i$  is the number of square-well segments in the molecule,  $\sigma_{ii}$  is the hard-core diameter,  $\lambda_{ii}$  and  $\epsilon_{ii}$  are the range and the depth of the square-well potential, and  $\epsilon_{ii}^{\text{HB}}$  and  $K^{\text{HB}}$  are those of the hydrogen-bonding interaction.

All other cross interactions parameters were obtained in the usual manner (using the combining rules detailed in Chapter 3, section 3.4.2). This set of parameters has been shown to provide an excellent description of the phase behaviour of this system over a wide range of temperatures, except in the area near the critical point. A more satisfactory description of the critical region could be obtained using the new version of SAFT-VR

proposed by Forte et al. [87] in combination with renormalization group theory. Such improved version of the theory is however not used here. The model approach in the work of Dufal et al. [354] and the CSMHYD model [357] were both used for hydrate calculations.

## 9.5 Discussion and Comparison with Experiment

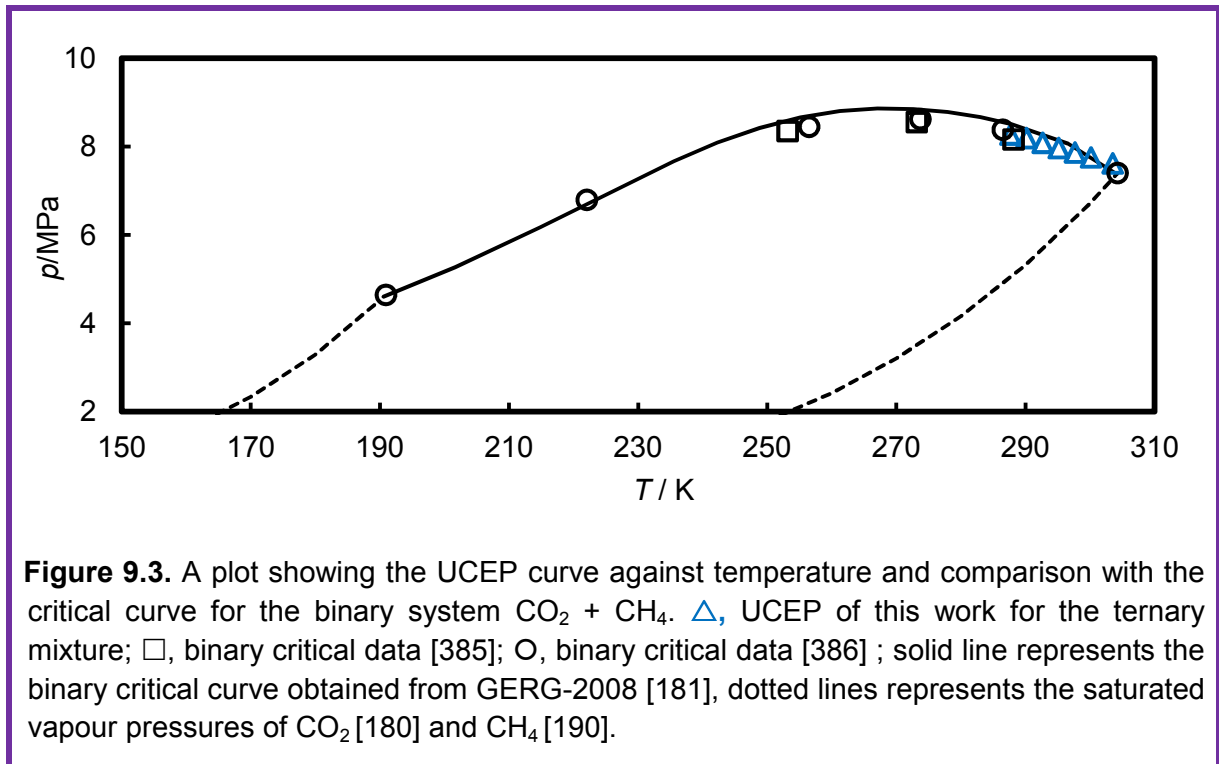
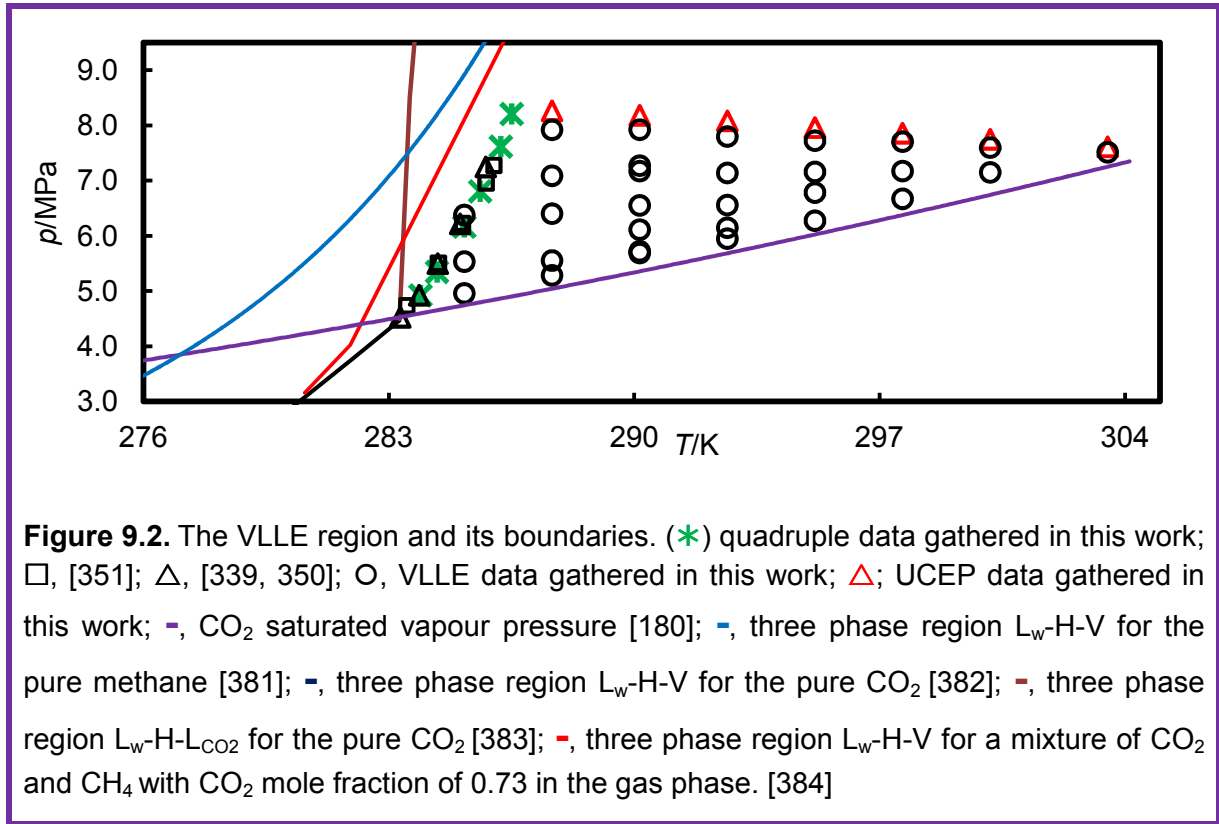
The binary system (CH<sub>4</sub> + CO<sub>2</sub>) [44] exhibits type I phase behaviour while the binary systems of (CO<sub>2</sub> + water) [201] and (methane + water) [324] exhibit type III phase behaviour according to the classification of Van Konynenburg and Scott [42-43]. As a consequence, the ternary mixture exhibits class IV according to the global ternary diagram classification proposed by Bluma and Deiters [52]. Mixtures of this type possess a LLE immiscibility region and hence, a VLLE region would be expected.

The VLLE equilibrium regions of binary mixtures appear as distinct areas in ternary systems, and can extend to wide range of pressures and temperatures depending on the mixture. In the case of (CO<sub>2</sub> + methane + water), at temperatures above ambient this region occurs within a small range because of the very large miscible regions of the CH<sub>4</sub>-CO<sub>2</sub> binaries leading to wide miscible range conditions. At lower temperatures, hydrates are formed which limit the existence of the VLLE region. Effectively, the VLLE region, as shown in Figure 9.2, is bounded by the CO<sub>2</sub> saturated vapour pressure, the UCCP curve where the CO<sub>2</sub>-rich liquid and gas phases becomes identical and merge into one phase, and the quadruple curve where hydrates form and exist in equilibrium with the three phases.

In Figure 9.2, the quadruple curve obtained in the present study agrees well with the data reported by Bi et al. [351] and Seo et al. [339, 350]. This curve is the upper limit for the existence of the three phase regions where at lower temperatures hydrate occurs and coexists with other phases in equilibrium. It intersects the CO<sub>2</sub> saturated vapour pressure, L<sub>w</sub>-H-V<sub>CO<sub>2</sub></sub>, L<sub>w</sub>-H-L<sub>CO<sub>2</sub></sub> and the quadruple point L<sub>w</sub>-H-L<sub>CO<sub>2</sub></sub>-V<sub>CO<sub>2</sub></sub> of pure CO<sub>2</sub>. The CO<sub>2</sub> saturated vapour pressure curve [180], L<sub>w</sub>-H-V for pure methane [381], L<sub>w</sub>-H-V for pure CO<sub>2</sub> [382], L<sub>w</sub>-H-L<sub>CO<sub>2</sub></sub> [383] for pure CO<sub>2</sub> and L<sub>w</sub>-H-V for a mixture of CO<sub>2</sub> and CH<sub>4</sub> [384] are all plotted in this figure to show the connections among these phase regions.

The CH<sub>4</sub>-CO<sub>2</sub> binary mixture exhibits a single homogeneous fluid phase at pressures above the UCEP of the ternary mixture and hence only VLE exists for the ternary mixture. The composition at this point was measured at a very slightly higher pressure by injecting some water. Figure 9.3 shows a plot of the UCEP curve as a function of temperature. In this plot, the comparison with the experimental critical data points [385-386] for the binary system

(CO<sub>2</sub> + CH<sub>4</sub>) is shown as well so that the effect of adding a third component (water) on the critical curve of the binary system can be observed.





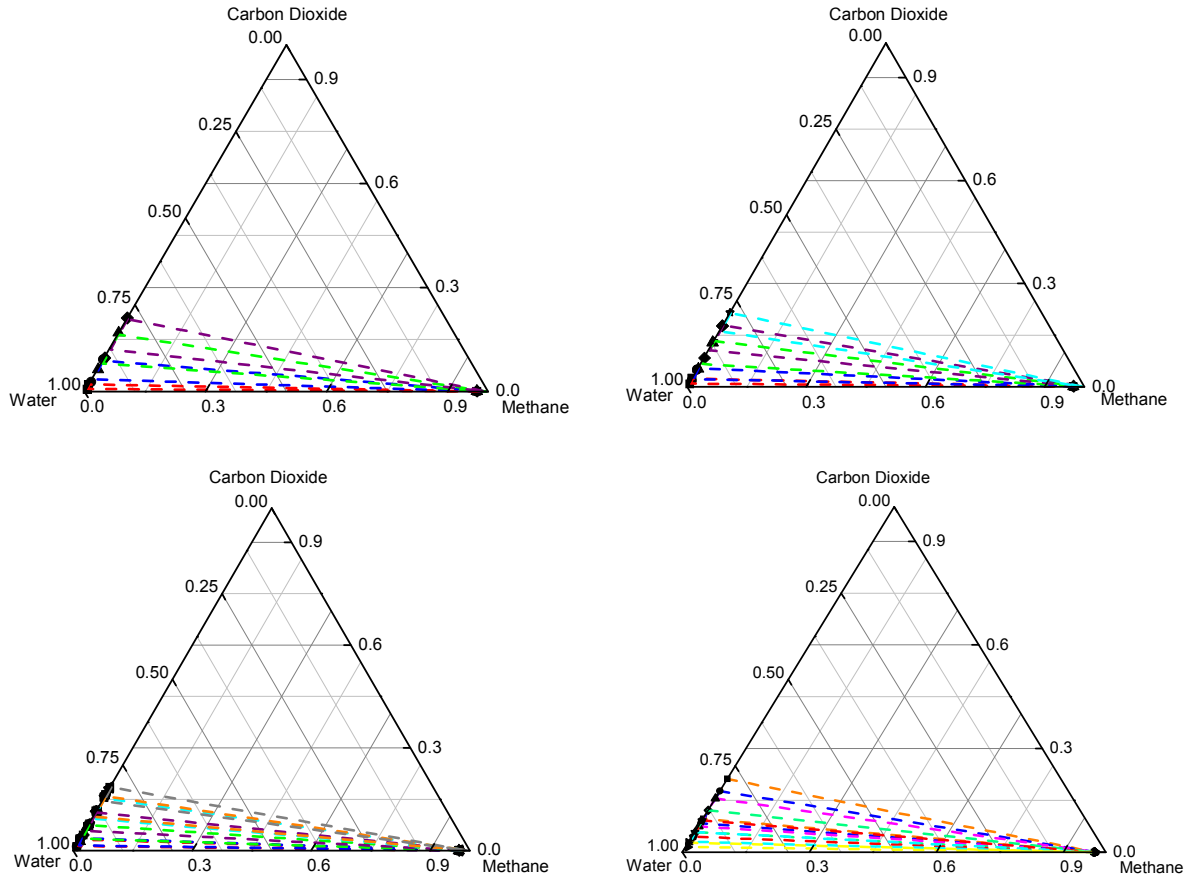


**Figure 9.4.** Triangular diagram for the (carbon dioxide + methane + water) system at (a) 285.15 K, (b) 287.65K, (c) 290.15K, and (d) isobaric diagram at fixed pressure  $p = 7.1$  MPa. The filled symbols represent VLE data measured in this work at average pressure: (a) ■,  $p = 4.96$ MPa; ●,  $p = 5.52$ MPa; ▲,  $p = 6.28$ MPa; and ◆,  $p = 7.07$ MPa; (b) ■,  $p = 5.28$ MPa; ●,  $p = 5.55$ MPa; ▲,  $p = 6.40$ MPa; ◆,  $p = 7.08$ MPa; and ★,  $p = 7.91$ MPa; (c) ■,  $p = 5.69$ MPa; ●,  $p = 5.72$ MPa; ▲,  $p = 6.11$ MPa; ◆,  $p = 6.55$ MPa; ★,  $p = 7.17$ MPa; ◆,  $p = 7.27$  MPa; and ◀,  $p = 7.92$ MPa; (d) ■,  $T = 285.15$ K; ●,  $T = 287.65$ K; ▲,  $T = 290.15$ K; ◆,  $T = 292.65$ K; ◆,  $T = 295.15$ K; ★,  $T = 297.65$ K; and ►,  $T = 300.15$ K. The discontinuous curves are SAFT-VR predictions of the three phase equilibrium region for every pressure and temperature data point

The solid line is the predicted critical curve of the binary system CO<sub>2</sub> + methane obtained from the GERG-2008 model developed by Kunz and Wagner [181], which is in good agreement with the literature data. The dotted lines represent the saturated CO<sub>2</sub> [180] and CH<sub>4</sub> [190] vapour pressures. It can be clearly observed that the presence of water has a negligible effect on the critical curve of the binary CH<sub>4</sub>+CO<sub>2</sub> system. This is because the amount of water dissolved in the gas phase and CO<sub>2</sub>-rich liquid phase is very small. The calculations performed with SAFT-VR are not shown here as SAFT-VR is a classical EoS

and it tends to over predict the critical pressures and temperatures. This has already been discussed previously in Chapter 8.

The experimental results are also plotted in the form of triangular diagrams, which show the composition of the different components in the different phases at given temperature and pressure, in Figures 9.4. Figures 9.4(a) to (c) are isothermal projections of  $p,x$  prismatic diagrams. However, Figure 9.4d is an isobaric projection of the VLLE region at  $p = 7.1$  MPa. It can be seen that the three-phase region for a given pressure diminishes as the critical point between the CO<sub>2</sub> and gas-rich phases is approached. Comparing the subfigures it can also be observed that the three-phase region gets smaller as temperature increases.

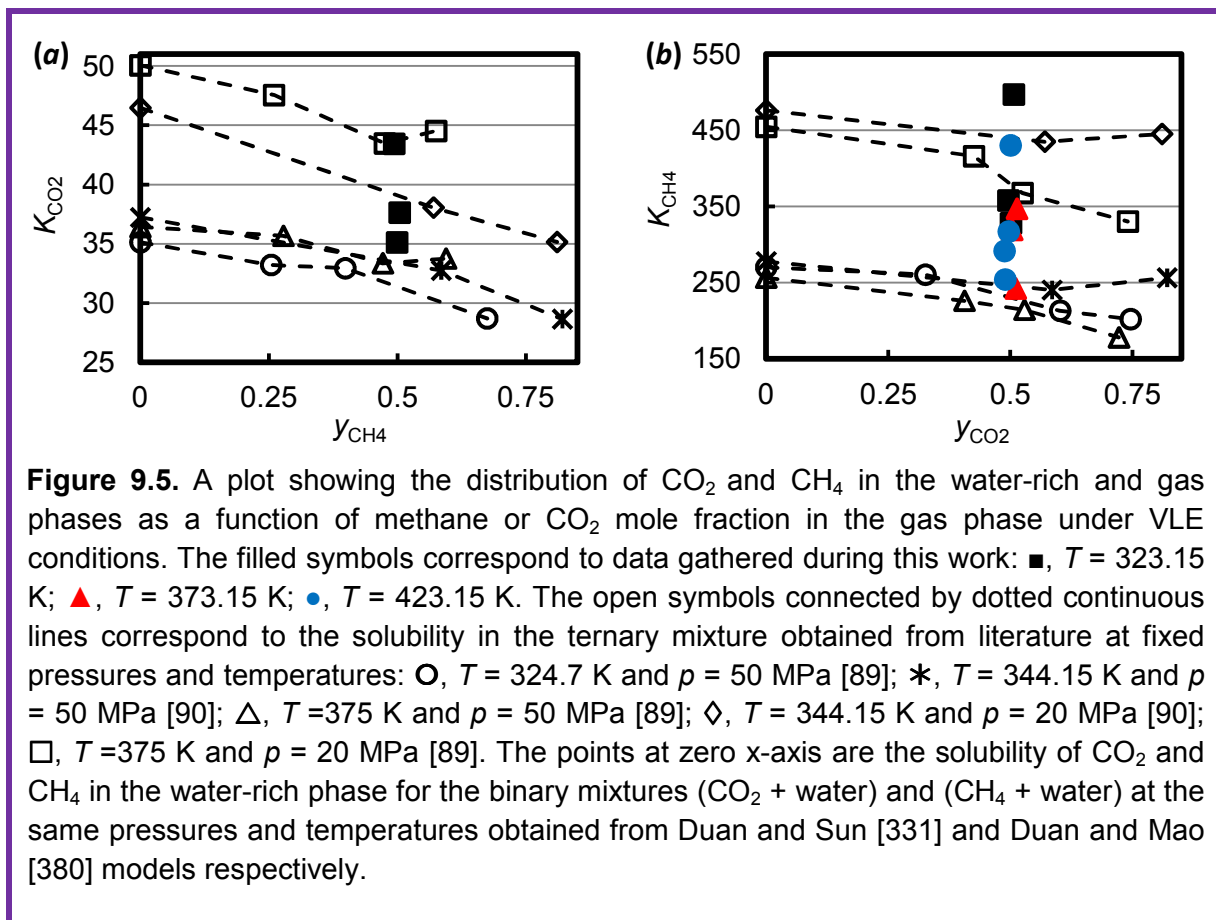
SAFT-VR predictions are shown in Figure 9.4 as discontinuous lines. In general good agreement between experimental data and theory is observed. It is worth noting the good performance of the equation in predicting the phase behaviour at different temperatures even with the use of only one temperature-independent binary interaction parameter (for CO<sub>2</sub>-H<sub>2</sub>O only). For example, it was reported in the work of Míguez and co-workers [332] that the pressure at which the VLLE region vanishes at  $T = 295$  K is below 8 MPa which agrees well with our observation. Expected deviations are seen at higher pressures, in the near-critical region. The agreements are a proof of the ability of the SAFT-VR EoS to describe remarkably complex phase equilibria using only a small number of molecular based characteristic parameters; for example here the CO<sub>2</sub> + H<sub>2</sub>O set demanded only the determination of an unlike interaction energy parameter in addition to the pure component parameters.

The experimental data for the quadruple curve are given in Table 9.2 together with the experimental results obtained by Bi et al. [351] and Seo et al. [339, 350]. In this Table, the vapour composition is also given and compared with the available literature data. The vapour composition values at hydrate conditions were obtained by fitting the three phase region data with a quadratic polynomial function of pressure and temperature and extrapolating to the quadruple line. It can be clearly seen that there is good agreement between our values and literature data both in terms of equilibrium conditions and vapour compositions. In addition, comparison with the models reported by Dufal et al. [354]<sup>14</sup> and the CSMHYD model [357] are shown. In these models, vapour composition and temperature are fixed while the pressure was calculated.

---

<sup>14</sup> Model calculations are courtesy of Andrew Haslam and Simon Dufal

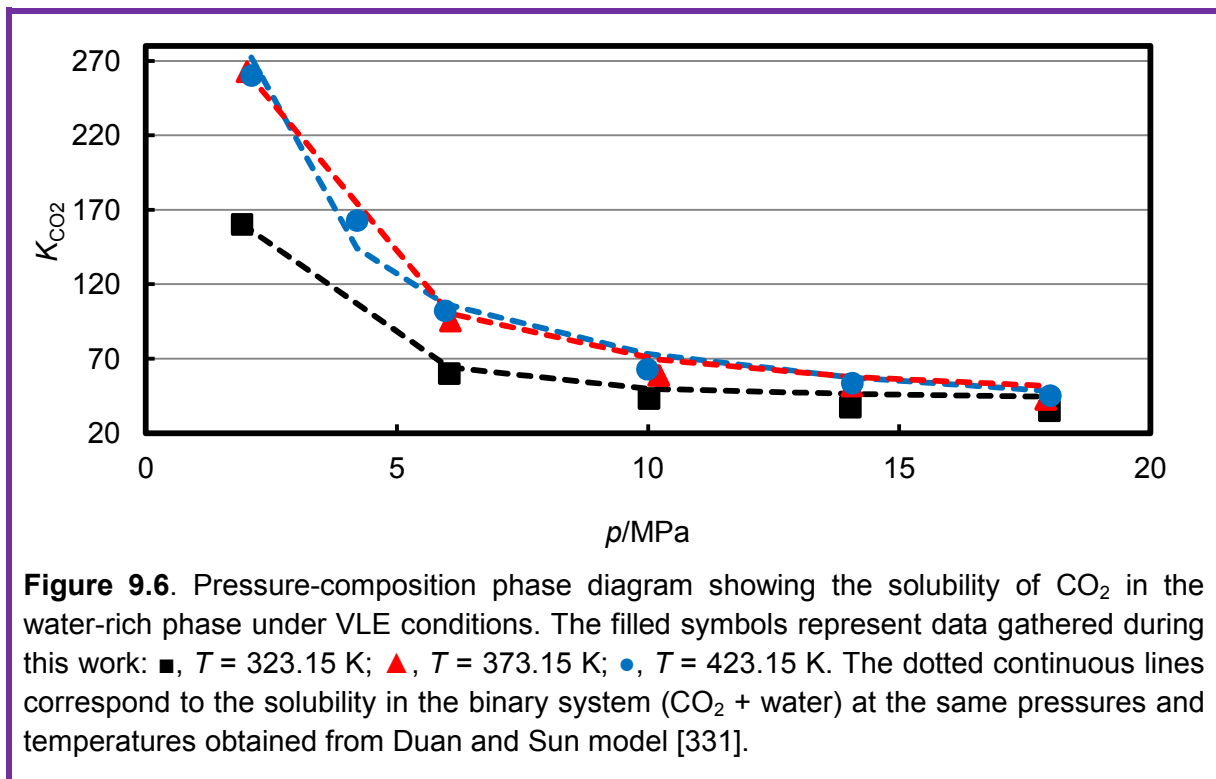
The predictions from both models agree reasonably well with the experimental data, with some observable deviation at higher pressures. The differences between the two models are small. However, both of these models predict that only three phase equilibria exist rather than four phases, which is different from what is observed experimentally. In both of these models, the hydrate forms structure I where CO<sub>2</sub> composition in the larger cavities is much higher than methane. It was observed that for CSMHYD to predict the presence of four phases, the methane mole fraction in the gas phase should be roughly higher than  $y = 0.5$  which does not agree with our observation and the available literature data.



In the VLE measurements, the CO<sub>2</sub> and CH<sub>4</sub> solubility in the water-rich phase is compared in Figure 9.5 with the VLE data reported by Qin et al. [89] at temperatures of (324.7 and 375.4) K and pressures of (20 and 50) MPa, and Dhima et al. [90] at temperature of 344.15 K and pressures of (20 and 50) MPa. In this figure, the  $K$  factor of either CO<sub>2</sub> or methane is plotted against the mole fraction of the other component in the CO<sub>2</sub>-rich phase in order to study the effect of adding a third component on the solubility. The binary values at corresponding pressures and temperatures were also obtained from the model developed by Duan and Sun [331] and Duan and Mao [380].

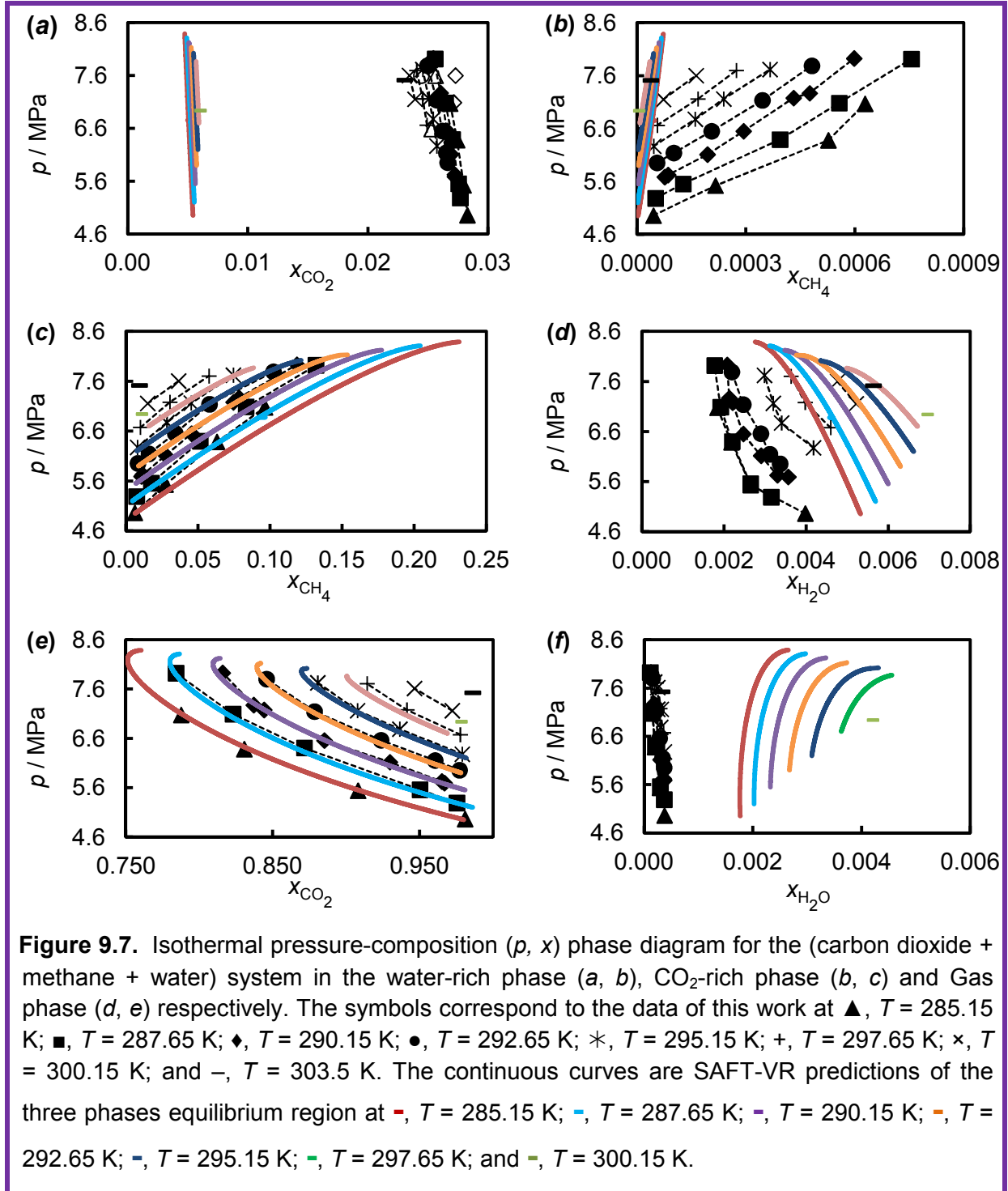
In addition, CO<sub>2</sub> solubility at  $T = (323.15, 373.15 \text{ and } 423.15) \text{ K}$  are plotted as a function of pressure in figure 9.6 together with the binary data obtained from the model developed by Duan and Sun [331].

From figures 9.5 and 9.6, it can be observed that as pressure increases, CO<sub>2</sub> solubility in the water-rich phase slightly increases. This indicates that the presence of methane increases the solubility of CO<sub>2</sub> in the water-rich phase compared to the binary system. It can also be seen that the solubility decreases as temperature increases which agrees with the behaviour of the binary mixture. In figure 9.5b, it can be observed that methane solubility increases because of the presence of CO<sub>2</sub> as compared to the binary mixtures. The effect of pressure on CO<sub>2</sub> or methane solubility in water-rich phase depends on the trend at which the ratio between methane and CO<sub>2</sub> changes with pressure in the gas phase. The above observations agree well with the observations in the work reported by Qin et al. [89] and Dhima et al. [90].



The amount of water dissolved in the CO<sub>2</sub>-rich or gas phase depends on the compositions of carbon dioxide and methane in that phase. It was observed that as more methane is present in the gas phase, the amount of water dissolved decreases. This was also observed in the work reported by Song and Kobayashi [91] where it was concluded that the presence of the methane lowered the water content in the gas phase by 20 % to 30 % from that of pure CO<sub>2</sub>.

Isothermal pressure-composition phase diagrams for the ternary system showing the solubility of the components in different phases are shown in Figure 9.7 and compared with the calculations from SAFT-VR.



The CO<sub>2</sub> and methane solubility predicted by SAFT-VR (Figures 9.7a and 9.7b) deviates slightly from the experimental values in the water-rich phase. The methane solubility and water content predicted by SAFT-VR agrees reasonably well with the experimental values in the CO<sub>2</sub>-rich liquid phase (Figures 9.7c and 9.7d), with a slight deviation regarding water content. The CO<sub>2</sub> content predicted by SAFT-VR agrees well with the experimental values in the gas phase, again with slight deviation regarding water content (Figures 9.7e and 9.7f). Generally speaking, from these figures it can be seen that the SAFT prediction is overall in good agreement with our experimental data.

In the following section, the binary systems are compared with the VLLE experimental data of the ternary mixture. We use such a comparison to draw conclusions regarding the effect of adding a component on the phase behaviour of the other two. Additional comparison with other ternary mixtures of the type (CO<sub>2</sub> + *n*-alkane + water) is also given.

#### **Influence of water on the phase behaviour of (methane + carbon dioxide) binary mixture**

The amount of water present in the CO<sub>2</sub>-rich liquid and CO<sub>2</sub>-rich gas phases is very small and has only a small effect on the mutual solubility between CO<sub>2</sub> and CH<sub>4</sub> as shown in Figures 9.8 and 9.9. The water content present in the gas and CO<sub>2</sub>-rich phases increases as temperature increases while it decreases as pressure increases, with more water dissolved in the CO<sub>2</sub>-rich phase than in the gas phase. In these figures, the amount of CO<sub>2</sub> present in the CO<sub>2</sub>-rich liquid phase and CO<sub>2</sub>-rich gas phase are plotted against equilibrium pressures at  $T = 287.65$  K and  $T = 295.15$  K (Figure 9.8) and  $T = 292.65$  K and  $T = 295.15$  K (Figure 9.9). These experimental data are compared with the binary CO<sub>2</sub>-CH<sub>4</sub> data published by Xu et al. [364] at  $T = 288.5$  K and  $T = 293.4$  K and Arai et al. [385] at  $T = 288.15$  K. These two sets of literature data exist at the temperature range of our interests. Most of the available binary data for the CO<sub>2</sub> + CH<sub>4</sub> were reported at temperatures less than 273.15 K.

It can be clearly seen that as temperature increases, the saturated region shifts towards higher CO<sub>2</sub> concentration and becomes smaller in size until it vanishes at the CO<sub>2</sub> critical temperature. It can be seen as well that the effect of the presence of water is small in the low pressure region. However, there is a noticeable deviation in the high pressure region close to the critical point, which is surprising considering the fact that water content in both CO<sub>2</sub>-rich phase and gas phase is small.

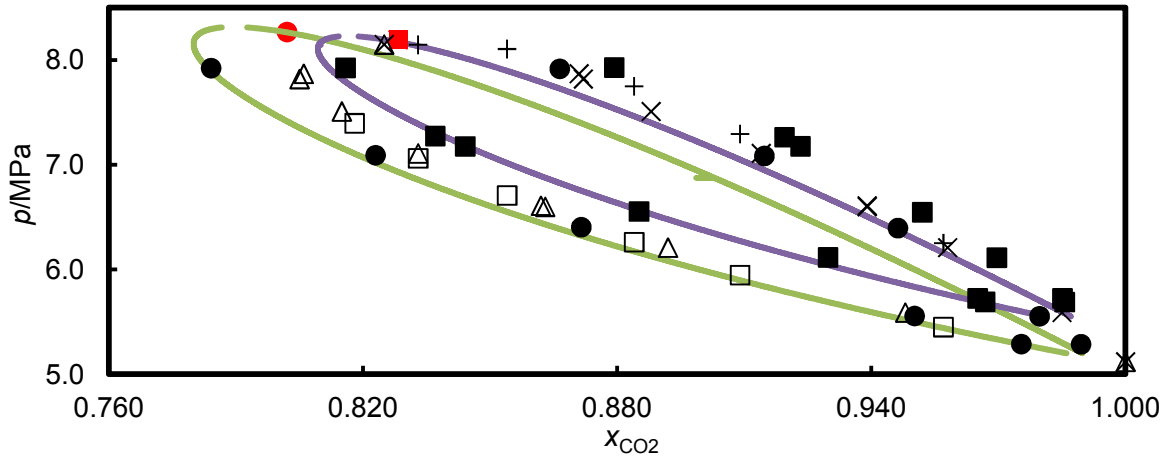


**Figure 9.8.** Isothermal pressure-composition phase diagram for the (carbon dioxide + methane + water) system at  $T = 287.65$  and  $T = 290.15$  K. The fill symbol correspond to the data of this work (with red colour representing critical points) at:  $\blacksquare$ ,  $T = 290.15$ K and  $\bullet$ ,  $T = 287.65$ K. The continuous curves correspond to SAFT-VR predictions at:  $-$ ,  $T = 287.65$ K and  $-$ ,  $T = 290.15$ K. The open symbols correspond to published data for the binary system (CO<sub>2</sub> + CH<sub>4</sub>):  $\times, \triangle$ ,  $T = 288.55$ K; [364] and  $+, \square$ ,  $T = 288.15$ K. [385]

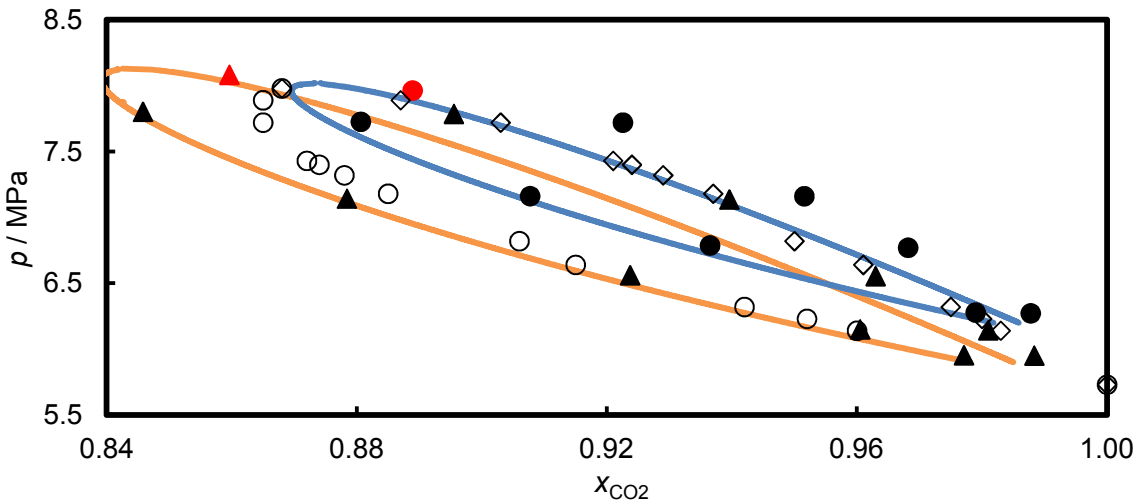


**Figure 9.9.** Isothermal pressure-composition phase diagram for the (carbon dioxide + methane + water) system at  $T = 292.65$  and  $T = 295.15$  K. The fill symbol corresponds to the data of this work (with red colour representing critical points) at:  $\blacktriangle$ ,  $T = 292.65$ K and  $\bullet$ ,  $T = 295.15$ K. The continuous curves correspond to SAFT-VR predictions at:  $-$ ,  $T = 292.65$ K and  $-$ ,  $T = 295.15$ K. The open symbols correspond to published data for the binary system (CO<sub>2</sub> + CH<sub>4</sub>):  $\diamond, \circ$ ,  $T = 293.4$ K. [364]

It seems that the presence of water (even a small quantity) modifies slightly the diagram in the high pressure region. It can be observed that the theory prediction agrees well at low pressures. At pressures in the critical region, deviations between theory and experiment are expected, as commented on previously. The UCEP locus is plotted in figure 9.3 with good agreement with the VL critical curve for the binary mixture CO<sub>2</sub> + CH<sub>4</sub>. This suggests that in general the presence of water has negligible effect on the VL critical curve of the binary system. In addition, comparing the influence of water on the phase behaviour of this system with that on the phase behaviour of the binaries (carbon dioxide + propane) [88], (carbon dioxide + *n*-decane) [87] and our previous system (carbon dioxide + *n*-heptane) leads to the conclusion that generally water has a small effect on the phase behaviour of (CO<sub>2</sub> + *n*-alkane) mixtures. Moving towards lighter *n*-alkanes such as methane doesn't actually increase the amount of water dissolved in the CO<sub>2</sub> gas rich and the *n*-alkane-rich phases. In fact the dissolved water content decreases in the case of methane compared to heavier *n*-alkane mixtures, which suggests that lighter hydrocarbons have higher anti-solvent effects against water than heavier hydrocarbons.

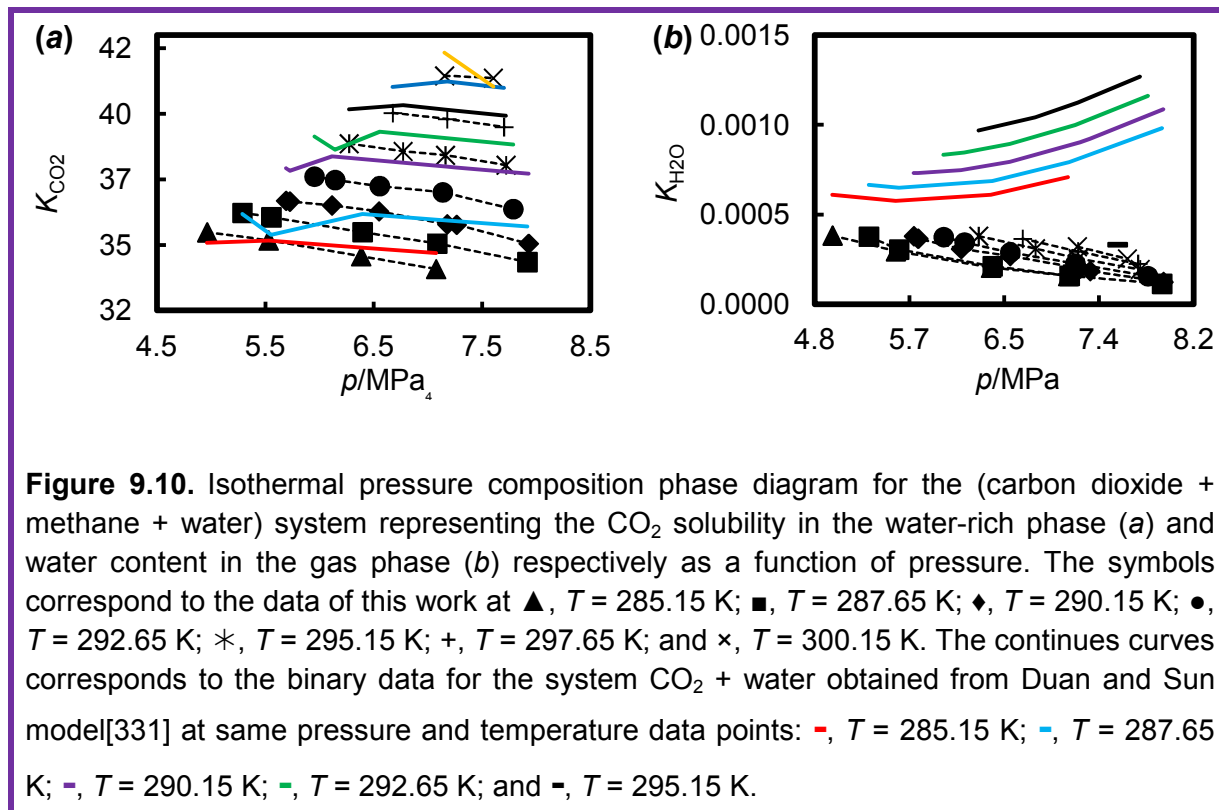
#### **Influence of methane on the phase behaviour of (CO<sub>2</sub> + water)**

The influence of the presence of methane on the mutual solubility of (CO<sub>2</sub> + water) is studied by comparison with the available binary data for (CO<sub>2</sub> + water) mixtures at similar pressure and temperature ranges, as shown in Figure 9.10. For the sake of comparison, the available binary data were obtained from the models developed by Duan and Sun [331] for (CO<sub>2</sub> + water) binary mixture and Duan and Mao [380] for the (methane + water) binary mixture. In Figure 9.10a, we plotted the  $K_{\text{CO}_2}$  values against the pressure. The dotted lines connect our experimental data while the solid lines represent the binary data. It can be observed that CO<sub>2</sub> solubility in the case of the ternary system is higher than that for the binary mixture and increases as pressure increases, similar to the behaviour of the binary system.

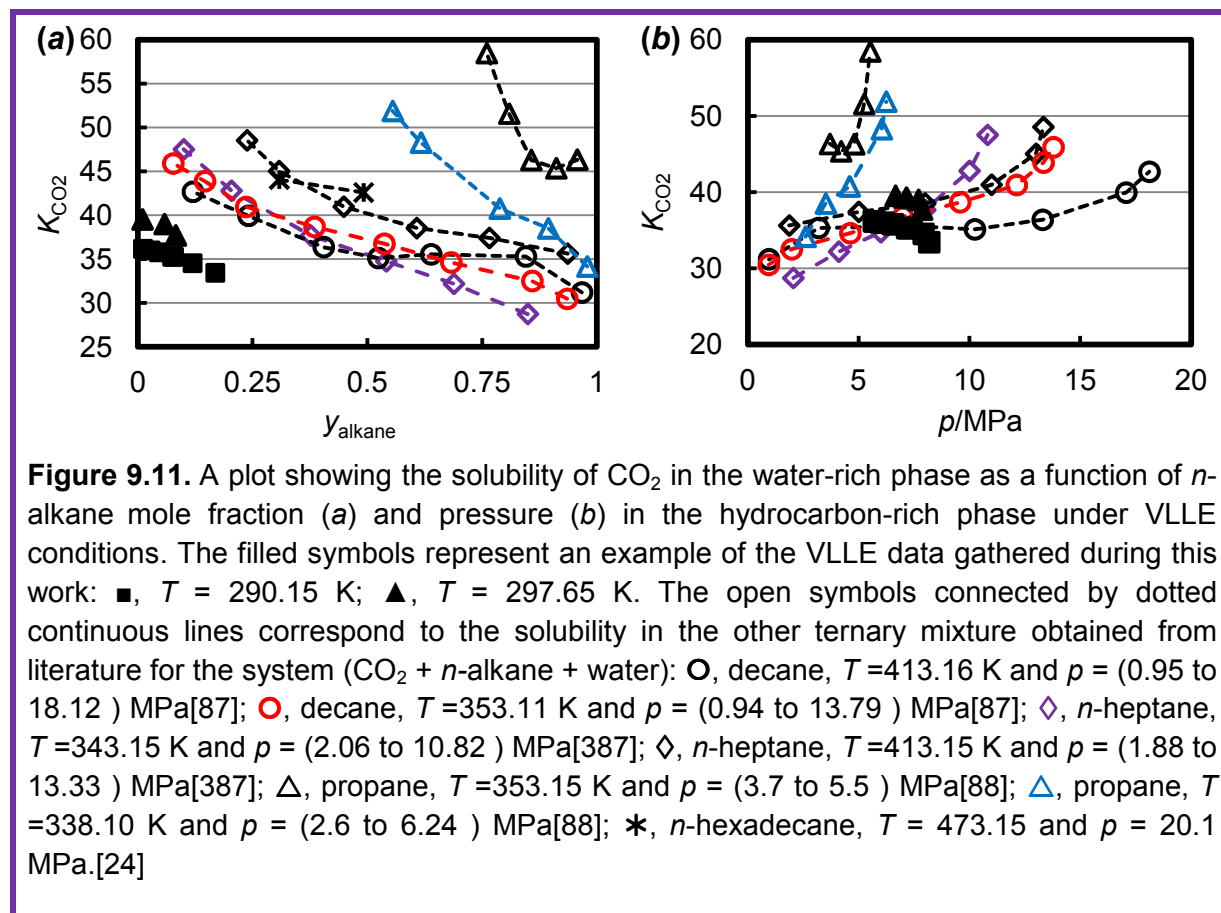
The pressure increase is also accompanied by an increase in the methane ratio in the CO<sub>2</sub>-rich phase. Hence this means as well that the CO<sub>2</sub> solubility increases because of the presence of methane, when compared to the binary mixtures. We therefore conclude that methane works as a cosolvent whereby its presence in the CO<sub>2</sub>-rich phase increases the CO<sub>2</sub> solubility in the water-rich phase. In Figure 9.10b, we plotted the  $K_{\text{H}_2\text{O}}$  values against the pressure. It can be clearly seen that because of the presence of methane, the water content in the CO<sub>2</sub>-rich phase is much less than in the CO<sub>2</sub>-water binary mixtures. In addition, the water content decreases as pressure increases. This is because as we increase the



pressure, we increase the methane content in the CO<sub>2</sub>-rich phase, hence dissolving less water.



The CO<sub>2</sub> solubility in the water-rich phase for (CO<sub>2</sub> + methane + water) is compared in Figure 9.11 with the measurements reported by Forte et al. [88] for the ternary mixture (CO<sub>2</sub> + propane + water), by Forte et al. [87] for the ternary mixture (CO<sub>2</sub> + *n*-decane + water), by Brunner et al. [24] for the ternary mixture (CO<sub>2</sub> + *n*-hexadecane + water) and also our previous ternary mixture (CO<sub>2</sub> + *n*-heptane + water) (Chapter 8), in the context of VLLE measurements. It can be observed that for all these systems the presence of a hydrocarbon component in general increases the solubility of CO<sub>2</sub> in the water-rich phase as observed in the current study. The differences in CO<sub>2</sub> solubility because of the presence of *n*-heptane or *n*-decane are not large. However, larger effect can be observed with the presence of lighter hydrocarbons. The presence of methane, for example, increases CO<sub>2</sub> solubility compared to the other hydrocarbons. Also it was observed that the water content in the CO<sub>2</sub>-rich phase decreases because of the presence of the hydrocarbon components compared to the binary system (CO<sub>2</sub> + water) and the water content decreases as more hydrocarbons is present in the hydrocarbon-rich phase.

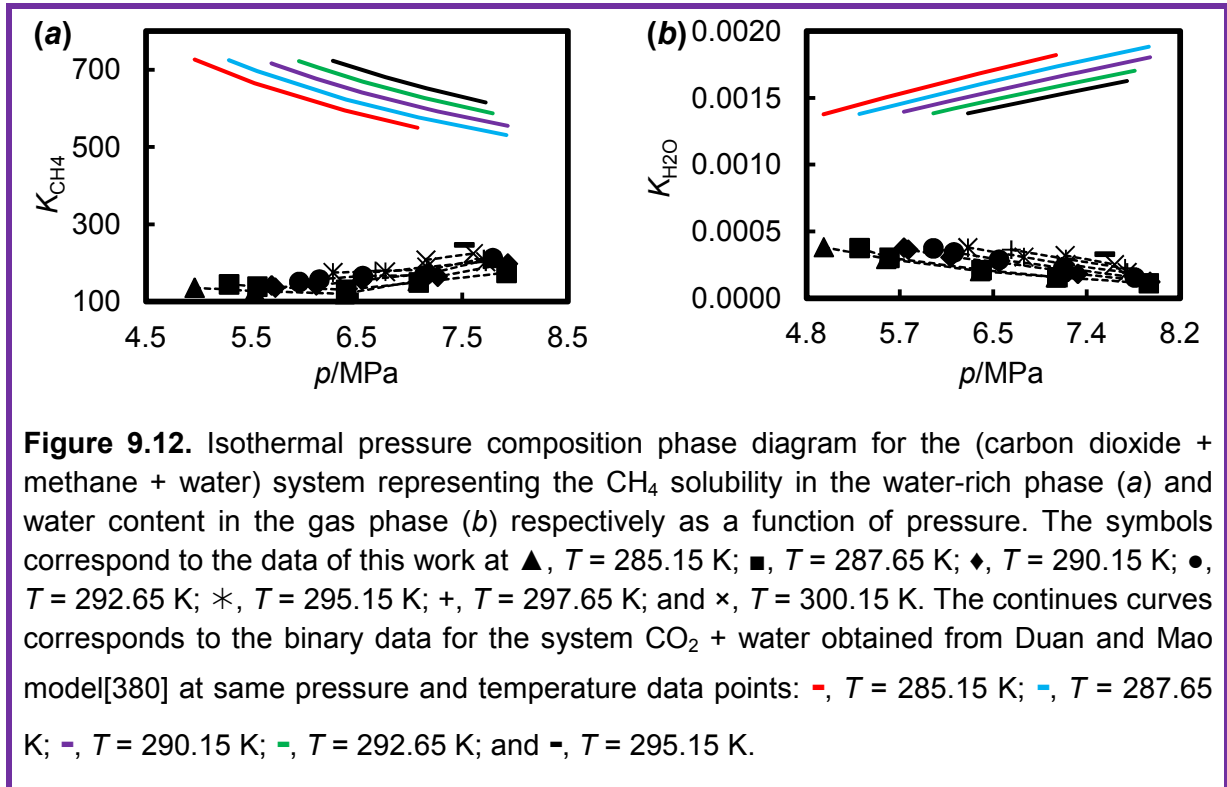


The effect of pressure on CO<sub>2</sub> solubility in this case depends on the presence of the third component in the CO<sub>2</sub>-rich phase. If increasing the pressure means that, for example, the methane ratio increases hence the CO<sub>2</sub> solubility would be expected to increase and vice versa. The CO<sub>2</sub> solubility in the water-rich phase decreases as temperature increases. It was also observed that the *n*-alkane solubility in the water-rich phase increases because of the presence of CO<sub>2</sub> as compared to the pure *n*-alkanes. All of the above observations agree well with our previous observations regarding VLE measurements of the ternary mixture (CO<sub>2</sub> + CH<sub>4</sub> + water).

#### Influence of carbon dioxide on the phase behaviour of (methane + water)

The effect of the presence of CO<sub>2</sub> on the phase equilibria of the binary system of methane + water was analyzed by comparing the solubility of methane in the water-rich phase and the solubility of water in the methane-rich phase in the ternary system with that in the binary system as shown in figure 9.12. It can be observed that the solubility of methane in the water-rich phase increases compared to that of the binary mixture and decreases as

pressure increases (figure 9.12 a). The increase in pressure corresponds to a decrease of the CO<sub>2</sub> ratio in the CO<sub>2</sub>-rich phase.



Hence we conclude that methane solubility in the water increases as more CO<sub>2</sub> is present in the CO<sub>2</sub>-rich phase. The same observation was noticed with the other ternary mixtures of the type (CO<sub>2</sub> + *n*-alkane + water). This means that in general, the presence of CO<sub>2</sub> increases the solubility of *n*-alkanes in water. The solubility decreases as temperature increases which is similar to what is observed in the case of the binary mixtures. Similar observations were noticed in the case of the VLE measurements. In Figure 9.12 b, the water content in the gas phase is plotted against pressure and compared with the water content in the binary mixture (methane + water) at the same pressures and temperatures. It can be observed that the amount of water dissolved in the CO<sub>2</sub>-rich phase is less than that for the binary mixture. This means that the presence of CO<sub>2</sub> lowered the water content compared to the binary mixture.

## 9.6 Conclusions

Compositions of three coexisting fluid phases for the system (carbon dioxide + methane + water) have been obtained along eight isotherms at temperatures from (285.15 to 303.5) K and at pressures up to either the upper critical end point (UCEP) or up to the hydrate formation locus. Compositions of coexisting vapour and liquid phases have been also obtained along three isotherms at temperatures from (323.15 to 423.15) K and pressures up

to 20 MPa. The quadruple curve along which hydrates coexists with the three fluid phases was also measured.

The experimental data obtained for this mixture have been compared with the predictions of the statistical associating fluid theory for potentials of variable range (SAFT-VR). In this work, we used the SAFT-VR parameters reported previously in the work of Míguez and co-workers. For the unlike (dispersion) energies, only the binary interaction for the system CO<sub>2</sub>-H<sub>2</sub>O was considered while all other cross interactions parameters were obtained in the usual manner using combining rules. A detailed comparison concluded that SAFT-VR predicts reasonably well our experimental data both quantitatively and qualitatively which demonstrates the predictive power of this model.

Furthermore, a detailed study of the ternary mixtures was carried out based on comparison with available data for the constituent binary subsystems and other ternary mixtures. It was concluded that the presence of CO<sub>2</sub> increases the *n*-alkane (such as methane) solubility in the water under both VLE and VLLE as compared to the binary mixture of (*n*-alkane + water). In addition, the presence of *n*-alkane (such as methane) increases the CO<sub>2</sub> solubility in the water-rich phase compared to the binary mixture of (CO<sub>2</sub> + water) for both VLE and VLLE measurements. The effect of pressure and temperature depends mainly on the trend at which the *n*-alkane to CO<sub>2</sub> ratio changes in the other phases. It was also concluded that the water content in the CO<sub>2</sub>-rich phase decreases because of the presence of *n*-alkane as compared to the binary system of (CO<sub>2</sub> + water) and because of the presence of CO<sub>2</sub> as compared to the binary system of (*n*-alkane + water). It was found that the effect of water content on the behaviour of the binary system (CO<sub>2</sub> + *n*-alkane) was small because of the small amount of water present in the gas phase. Finally, it was observed that predictions from hydrate models agree reasonably well with the experimental data. However, these models predict only three phases in equilibrium which does not agree with the experimental observations. Clearly the models require more refinement to be able to describe the full range of phase behaviour observed for the (carbon dioxide + methane + water) system.

## Chapter 10: Density of Aqueous Solutions

### 10.1 Overview

The densities of  $\text{MgCl}_2(\text{aq})$ ,  $\text{CaCl}_2(\text{aq})$ ,  $\text{KI}(\text{aq})$ ,  $\text{NaCl}(\text{aq})$ ,  $\text{KCl}(\text{aq})$ ,  $\text{AlCl}_3(\text{aq})$ ,  $\text{SrCl}_2(\text{aq})$ ,  $\text{Na}_2\text{SO}_4(\text{aq})$ ,  $\text{NaHCO}_3(\text{aq})$ , the mixed salt system  $[(1 - x)\text{NaCl} + x\text{KCl}](\text{aq})$  and the synthetic reservoir brine system  $[x_1\text{NaCl} + x_2\text{KCl} + x_3\text{MgCl}_2 + x_4\text{CaCl}_2 + x_5\text{SrCl}_2 + x_6\text{Na}_2\text{SO}_4 + x_7\text{NaHCO}_3](\text{aq})$ , where  $x$  denotes mole fraction, were studied at temperatures between (283 and 473) K and pressures up to 68.5 MPa. The molalities at which the solutions were studied were (1.00, 3.00 and 5.00)  $\text{mol}\cdot\text{kg}^{-1}$  for  $\text{MgCl}_2(\text{aq})$ , (1.00, 3.00 and 6.00)  $\text{mol}\cdot\text{kg}^{-1}$  for  $\text{CaCl}_2(\text{aq})$ , (0.67, 0.90 and 1.06)  $\text{mol}\cdot\text{kg}^{-1}$  for  $\text{KI}(\text{aq})$ , (1.06, 3.16 and 6.00)  $\text{mol}\cdot\text{kg}^{-1}$  for  $\text{NaCl}(\text{aq})$ , (1.06, 3.15 and 4.49)  $\text{mol}\cdot\text{kg}^{-1}$  for  $\text{KCl}(\text{aq})$ , (1.00 and 2.00)  $\text{mol}\cdot\text{kg}^{-1}$  for  $\text{AlCl}_3(\text{aq})$ , (1.022, 2.024 and 3.031)  $\text{mol}\cdot\text{kg}^{-1}$  for  $\text{SrCl}_2(\text{aq})$ , (0.783 and 1.502)  $\text{mol}\cdot\text{kg}^{-1}$  for  $\text{Na}_2\text{SO}_4(\text{aq})$ , and (0.507 and 1.000)  $\text{mol}\cdot\text{kg}^{-1}$  for  $\text{NaHCO}_3(\text{aq})$  and (1.05, 1.98, 3.15 and 4.95)  $\text{mol}\cdot\text{kg}^{-1}$  for  $[(1 - x)\text{NaCl} + x\text{KCl}](\text{aq})$ , with  $x = 0.136$ . The compositions of the synthetic reservoir brines studied were, first,  $x_1 = 0.770$ ,  $x_2 = 0.022$ ,  $x_3 = 0.040$ ,  $x_4 = 0.105$ ,  $x_5 = 0.002$ ,  $x_6 = 0.044$ , and  $x_7 = 0.018$  with molality  $0.359 \text{ mol}\cdot\text{kg}^{-1}$  and, second,  $x_1 = 0.797$ ,  $x_2 = 0.006$ ,  $x_3 = 0.042$ ,  $x_4 = 0.145$ ,  $x_5 = 0.002$ ,  $x_6 = 0.006$ , and  $x_7 = 0.002$  with molality  $1.900 \text{ mol}\cdot\text{kg}^{-1}$ .

The measurements were performed with a vibrating-tube densimeter calibrated under vacuum and with pure water over the full ranges of pressure and temperature investigated. An analysis of uncertainties shows that the relative uncertainty of density varies from 0.03 % to 0.06 % depending upon the salt and the molality of the solution and can be expressed as linear function of molality. An empirical correlation is reported that represents the density for each brine system as a function of temperature, pressure and molality with absolute average relative deviations (% AAD) of approximately 0.02 %. Comparing the model with a large database of results from the literature, we find absolute average relative deviations of 0.03 %, 0.06 %, 0.04 %, 0.02 %, 0.02 %, 0.10 %, 0.03 %, and 0.01 % for the systems  $\text{MgCl}_2(\text{aq})$ ,  $\text{CaCl}_2(\text{aq})$ ,  $\text{KI}(\text{aq})$ ,  $\text{NaCl}(\text{aq})$ ,  $\text{KCl}(\text{aq})$ ,  $\text{SrCl}_2(\text{aq})$ ,  $\text{Na}_2\text{SO}_4(\text{aq})$ , and  $\text{NaHCO}_3(\text{aq})$  respectively. The model can be used to calculate density, apparent molar volume and isothermal compressibility over the full ranges of temperature, pressure and molality studied in this work. An ideal mixing rule for the density of a mixed electrolyte solution was tested against our mixed salt data and was found to offer good predictions at all conditions studied with an absolute average relative deviation of 0.05 %. It was observed that careful attention needs to be paid to the type of calibration method selected.

## 10.2 Introduction

Brines play a significant role in numerous physical, chemical, geothermal and geochemical processes, often involving high temperatures and/or high pressures, and knowledge of their thermophysical properties, including density, is required to understand fully these diverse applications. Examples in which brine density is important include fluid inclusion studies [388-389], fluid flow simulation [390], studies of fluid-rock interactions [391], CO<sub>2</sub> sequestration [392-393] and enhanced oil recovery (EOR). In both geological CO<sub>2</sub> storage and CO<sub>2</sub>-EOR, the compressibility of brines plays a role in determining the injection rate; consequently this derivative property is also significant. Brines are also used in absorption refrigeration machines and absorption heat pumps, and the thermodynamic properties of aqueous solutions of calcium chloride in particular play a major role in the analysis of such cycles [394]. NaCl and KCl are the major solutes present in natural brines from various geological environments, and accurate density formulations for these saline fluids are a fundamental prerequisite for reliable simulations of fluid flow in geological processes. [395] Density data are also essential in establishing reliable EoSs and calculations of other properties such as isothermal compressibility, isobaric expansibility, dynamic viscosity, interfacial tension, and conversion from molarity to molality.

A critical survey of the available density data for single- and multi-components brines has been carried out in this work [396-397]. Many data are available at ambient pressure and temperature over wide ranges of molality. However, there are few published data at elevated pressure and at temperatures above 373.15 K. Here we highlight some of the studies related to the brines measured in this work that do extend to high pressures or temperatures. For CaCl<sub>2</sub>(aq), Safarov et al. [394] studied the range (0.1 to 60) MPa at  $T = (298.15 \text{ to } 398.15) \text{ K}$  and molality  $b = (0.184 \text{ to } 6.007) \text{ mol}\cdot\text{kg}^{-1}$  using a constant volume piezometer. Gates [398] studied a wider range of temperature (up to 600 K) with  $b$  up to  $6.4 \text{ mol}\cdot\text{kg}^{-1}$  for  $p \leq 40 \text{ MPa}$ . For MgCl<sub>2</sub>(aq), Obsil [399] reported densities at  $T = (298.15 \text{ to } 623.15) \text{ K}$  and  $b = (0.005 \text{ to } 3) \text{ mol}\cdot\text{kg}^{-1}$  at pressures up to 30 MPa. This study covers the widest range of conditions for this system in the literature but the molality was still restricted to values well below saturation. For the KI(aq) system, the available data are restricted to ambient and near ambient pressures. Swenson [400] has covered temperatures of (278.15 to 368.15) K with molality of (0.02 to 7.50) mol·kg<sup>-1</sup> at a constant pressure of 0.35 MPa. For the NaCl(aq) system, wider ranges of conditions are covered in the literature [401-406] with  $T = (298.15 \text{ to } 716.73) \text{ K}$ ,  $b = (0.003 \text{ to } 5.97) \text{ mol}\cdot\text{kg}^{-1}$  and pressures up to 40.16 MPa. For the KCl(aq) system, few data are reported at high pressures and/or high temperatures. Gates and Wood [407] reported the densities at  $p = (0.1 \text{ to } 40.64) \text{ MPa}$  and  $b = (0.059 \text{ to } 3.012) \text{ mol}\cdot\text{kg}^{-1}$ .

However, this range was studied only at  $T = 298.15$  K. Clearly, there is a gap in the literature for this system. There are no data available at pressure  $p \neq 0.1$  MPa and/or  $T \neq 298.15$  K for  $\text{AlCl}_3(\text{aq})$ . For  $\text{SrCl}_2(\text{aq})$ , Kumar [408] studied the range (323.20 to 473.20) K at  $p = 2.03$  MPa and molality  $b = (0.303 \text{ to } 2.718) \text{ mol}\cdot\text{kg}^{-1}$  using a dilatometer. Ellis [409] reported densities at the same pressure but at  $T = (348.20 \text{ to } 473.20)$  K and  $b = (0.100 \text{ to } 1.000) \text{ mol}\cdot\text{kg}^{-1}$ . To our knowledge, the pressure reported in these two studies was the highest studied for this system. For the  $\text{Na}_2\text{SO}_4(\text{aq})$  system, Obšil [410] reported densities at  $T = (298.20 \text{ to } 572.67)$  K and  $b = (0.005 \text{ to } 1.003) \text{ mol}\cdot\text{kg}^{-1}$  at pressures up to 30.7 MPa. This study covers wide ranges of pressure and temperature but the molality was restricted to values well below saturation. Phutela and Pitzer [411] studied the  $\text{Na}_2\text{SO}_4(\text{aq})$  system at  $T = (294.52 \text{ to } 475.78)$  K,  $b = (0.058 \text{ to } 0.330) \text{ mol}\cdot\text{kg}^{-1}$  and pressures between (9.59 and 10.24) MPa. Rogers and Pitzer [412] covered a wider range of molality with  $b = (0.050 \text{ to } 2.629) \text{ mol}\cdot\text{kg}^{-1}$ ,  $T = (304.62 \text{ to } 474.68)$  K, and  $p = (0.10 \text{ to } 20)$  MPa. Few data exist for the  $\text{NaHCO}_3(\text{aq})$  system. Sharygin and Wood [413] covered the ranges  $b = (0.100 \text{ to } 0.998) \text{ mol}\cdot\text{kg}^{-1}$ ,  $T = (298.13 \text{ to } 448.50)$  K, and  $p = (9.80 \text{ to } 28.20)$  MPa. These are the only data available for this system at a pressure higher than 0.1 MPa. Few measurements have been made on ternary or multi-component brines. The aim of the present study was to expand the available brine density database to wider ranges of  $p$ ,  $T$ , and  $b$  and to provide reliable data with precise measurements.

Due to the gaps in the available data, extensive work has been devoted to modelling the volumetric properties of these aqueous solutions so as to interpolate between the available data and to extrapolate beyond the ranges studied experimentally. Mao and Duan [414] have reviewed the available models and developed a new model for aqueous chloride solutions of the type  $\text{MCl}$  and  $\text{MCl}_2$  where  $\text{M} = (\text{Li}, \text{Na}, \text{K}, \text{Mg}, \text{Ca}, \text{Sr} \text{ and } \text{Ba})$ . Their model was parameterised separately for each system and covers wide ranges of conditions. For example for the  $\text{MgCl}_2(\text{aq})$  system, the ranges are (273 to 543) K, (0.1 to 40) MPa, and (0 to 3)  $\text{mol}\cdot\text{kg}^{-1}$  while for the  $\text{CaCl}_2(\text{aq})$  system the ranges are (273 to 523) K, (0.1 to 60) MPa, and (0 to 6)  $\text{mol}\cdot\text{kg}^{-1}$ . For the  $\text{NaCl}(\text{aq})$  system the ranges are (273 to 573) K, (0.1 to 100) MPa, and (0 to 6)  $\text{mol}\cdot\text{kg}^{-1}$  while for the  $\text{KCl}(\text{aq})$  system the ranges are (273 to 543) K, (0.1 to 50) MPa, and (0 to 4.5)  $\text{mol}\cdot\text{kg}^{-1}$ . For the  $\text{SrCl}_2(\text{aq})$  system, the ranges are (298 to 473) K, (0.1 to 2) MPa, and (0 to 2)  $\text{mol}\cdot\text{kg}^{-1}$ . The absolute average relative deviations  $\Delta_{\text{AAD}}$  over the entire range were between 0.020 % and 0.066 %, depending on the system. Safarov et al. [394] used an EoS [415] to correlate the experimental values for  $\text{CaCl}_2(\text{aq})$  for  $T = (298.15 \text{ to } 398.15)$  K,  $p = (0.1 \text{ to } 60)$  MPa, and  $b = (0.18 \text{ to } 6.01) \text{ mol}\cdot\text{kg}^{-1}$ . The equation was able to reproduce the experimental values with  $\Delta_{\text{AAD}} = 0.02$  %. Other models have also been

reported. [416-427] In addition numerous empirical correlations have been published for particular brines. For example, Kiepe [428] has developed an empirical correlation method incorporating two adjustable parameters. When applied to the  $\text{CaCl}_2(\text{aq})$  system, the average absolute deviation was  $1.1 \text{ kg}\cdot\text{m}^{-3}$ . However, the correlation covers small ranges of temperature and molality at ambient pressure only. Apelblat [429] fitted density data for  $\text{KI}(\text{aq})$  to a polynomial function for each given molality at ambient pressure. Most of the available correlation functions [407, 430-447] have been fitted only at ambient pressure and/or ambient temperature and cover small ranges of molality. Isono [430] fitted the temperature dependence of the density of  $\text{SrCl}_2(\text{aq})$  and other brines measured at atmospheric pressure using an empirical Equation of a polynomial type. Kumar [448] also used a polynomial function to fit the measured density data for the  $\text{SrCl}_2(\text{aq})$ . This fit covers wide ranges of conditions with temperatures up to 473 K and molalities up to  $b = 2.718 \text{ mol}\cdot\text{kg}^{-1}$  but is restricted to a pressure of 2.03 MPa only. Hervello and Sánchez [449] used a polynomial function to fit the density data for  $\text{Na}_2\text{SO}_4(\text{aq})$ . This correlation covers small ranges of temperature and molality at ambient pressure only. Kiepe [428] developed an empirical correlation method incorporating two adjustable parameters. When applied to the  $\text{Na}_2\text{SO}_4(\text{aq})$  system, the correlation covers small ranges of temperature and molality at ambient pressure only. Hershey et al. [450] fitted the data for  $\text{NaHCO}_3(\text{aq})$  with an empirical Equation of polynomial type covering the ranges  $T = (278.15 \text{ to } 318.15) \text{ K}$ ,  $b = (0.003 \text{ to } 1.008) \text{ mol}\cdot\text{kg}^{-1}$ . However, this was fitted also at ambient pressure only. From this survey of the available literature, we conclude that there are significant gaps in the available experimental data in terms of both the salts and the thermodynamic states that have been investigated, especially in respect of high temperatures, pressures and molalities. The available models are similarly restricted either by their form or simply by a lack of experimental validation. Hence, there is a need for new experimental data covering wider ranges of pressure, temperature and molality, so that improved wide-range correlating functions or predictive models can be developed.

### 10.3 Theory of the Vibrating Tube Densimeter

Different absolute and relative methods for the experimental determination of density at elevated pressures and temperatures, based on diverse physical principles, have been used by various authors aiming to improve the accuracy of the measured data. Among relative methods the vibrating tube densimeter (VTD) [451] has been most used both in research and industry due to its precision and easiness of operation. The VTD relies on the measurement of the resonance frequency of a tube filled with fluid and excited electronically. Its accuracy is, however, very much dependent on the calibration procedure employed.



Despite its widespread use, the main limitation of the vibrating tube densimeter relies on the fact that it has not been feasible so far to transform it in an absolute instrument, due to the lack of a correct modelling of its working equation.

The oscillator consists usually of a U-shaped tube fused into a dual-wall cylinder. The space between the U-shaped tube and the inner wall of the dual-wall cylinder is filled with a gas of high thermal conductivity, to aid a rapid temperature equilibration of the sample inside the oscillator, and of low density, to avoid additional damping in the vibrating move. Through the dual-wall cylinder a thermostatic liquid flows. The U-shaped tube is forced to oscillate by two magnetic dynamic converters in connection with an electronic control and amplifier circuit which guarantees constant amplitude of the oscillator tube. The direction of the oscillation is normal to the plane of the U-shaped tube. Under this type of geometry the system executes a simple harmonic oscillation, if the time duration of an oscillation can be made short. The primary variable is the period of oscillation, which is measured by a system coupled to the cell and driven by a quartz oscillator. The density  $\rho$  is related to the period of oscillation  $\tau$  of the tube through a linear relationship given by the following equation

$$\rho(p, T) = A(p, T)\tau^2 - B(p, T), \quad 10.1$$

where  $A$  and  $B$  are characteristic parameters of the apparatus that are determined by calibration with fluids of known density. Equation (10.1) can be derived considering a system represented by a hollow body of mass  $M_0$  and volume  $V(p, T)$ , filled with a sample of density  $\rho(p, T)$  and suspended on a spring of stiffness  $K(p, T)$ . The natural frequency and the period of oscillation of this system is thus given by

$$f = \frac{1}{2\pi} \left( \frac{K}{M_0 + \rho V} \right)^{\frac{1}{2}}, \tau = 2\pi \left( \frac{M_0 + \rho V}{K} \right)^{\frac{1}{2}} \quad 10.2$$

Hence using Equations 10.1 and 10.2, the coefficients  $A$  and  $B$  can be expressed by

$$A(p, T) = \frac{K}{4\pi^2 V}, B(p, T) = \frac{M_0}{V} \quad 10.3$$

These coefficients depend on pressure and temperature and once  $A$  and  $B$  are known, by measuring the periodic oscillation  $\tau$ , the density of the sample is readily obtained from equation 10.1. The temperature and pressure affect the resonant frequency of the vibrating tube (and hence the coefficients  $A$  and  $B$ ) in three ways: **(1)**, the tube expands with increasing temperature, lowering the resonant frequency; **(2)**, the tube becomes less stiff

with increasing temperature, lowering the resonant frequency; and (3), the tube radius expands and the tube length decreases with increasing pressure, increasing the resonant frequency. Hence, the accuracy of density measurements depends mainly on the way  $A$  and  $B$  coefficients are determined.

These parameters are usually determined by calibration with at least two fluids with well known accurate density values. For calibration at atmospheric pressure, it is possible to get calibration fluids with accurate density values. However, the situation at higher pressures is completely different where it is not really possible to obtain calibration fluids with accurate density values. Therefore, and in order to overcome this limitation, Lagourette et al. [452] and Sousa et al. [453] proposed eliminating one of the calibration fluids in favour of determining the period of oscillation of the vibrating tube under vacuum,  $\tau_0$ . The hypothesis of Lagourette et al. [452] is that the stiffness parameter  $K$  does not depend on pressure  $p$ . As a consequence of this assumption,  $A(p, T)$  and  $B(p, T)$  would vary with pressure in the same way and hence  $A/B$  would be independent of pressure. Hence based on this assumption, knowledge of the volumetric behaviour with  $p$  and  $T$  of a reference substance is sufficient where in most cases water is selected because of its well known density values at wide range of pressure and temperature conditions. However, it is nonetheless necessary to measure the period of oscillation for a second substance with known density, but only as a function of temperature. In most cases, vacuum is used as a second fluid. This hypothesis leads to the following expression

$$\rho(p, T) = \rho_{\text{ref}}(p, T) \left[ \frac{\tau^2(p, T) - \tau_0^2(T)}{\tau_{\text{ref}}^2(p, T) - \tau_0^2(T)} \right], \quad 10.4$$

where  $\tau_{\text{ref}}(p, T)$  and  $\rho_{\text{ref}}(p, T)$  are the period of oscillation and the density for calibration with the well known fluid at given pressure and temperature, and  $\tau_0(T)$  is the period of oscillation under vacuum at given temperature. Therefore, in this case the variables required to be determined during calibration are the period of oscillation under vacuum as a function of temperature, the period of oscillation when filled with a reference fluid as a function of temperature and pressure, and obviously the density of the reference fluid as a function of temperature and pressure. In addition, Lagourette et al. [452] and Sousa et al. [453] also proposed an alternative assumption in which the stiffness and tube volume vary with pressure in the same way. As a consequence, the parameter  $A$  is only temperature dependent while parameter  $B$  is both pressure and temperature dependent. This assumption leads eventually to the following expression

$$\rho(p, T) = \rho_{\text{ref}}(p_o, T) \left[ \frac{\tau^2(p, T) - \tau_{\text{ref}}^2(p, T)}{\tau_{\text{ref}}^2(p_o, T) - \tau_0^2(T)} \right] + \rho_{\text{ref}}(p, T), \quad 10.5$$

where  $\tau_{\text{ref}}(p, T)$  and  $\rho_{\text{ref}}(p, T)$  are the period of oscillation and the density for calibration with the well known fluid at given pressure and temperature,  $\tau_0(T)$  is the period of oscillation under vacuum at given temperature,  $p_o$  is the reference pressure (usually 0.1 MPa) at which the density for a reference fluid as a function of temperature and at this fixed pressure is obtained. Therefore, the variables required in this case are the same as before.

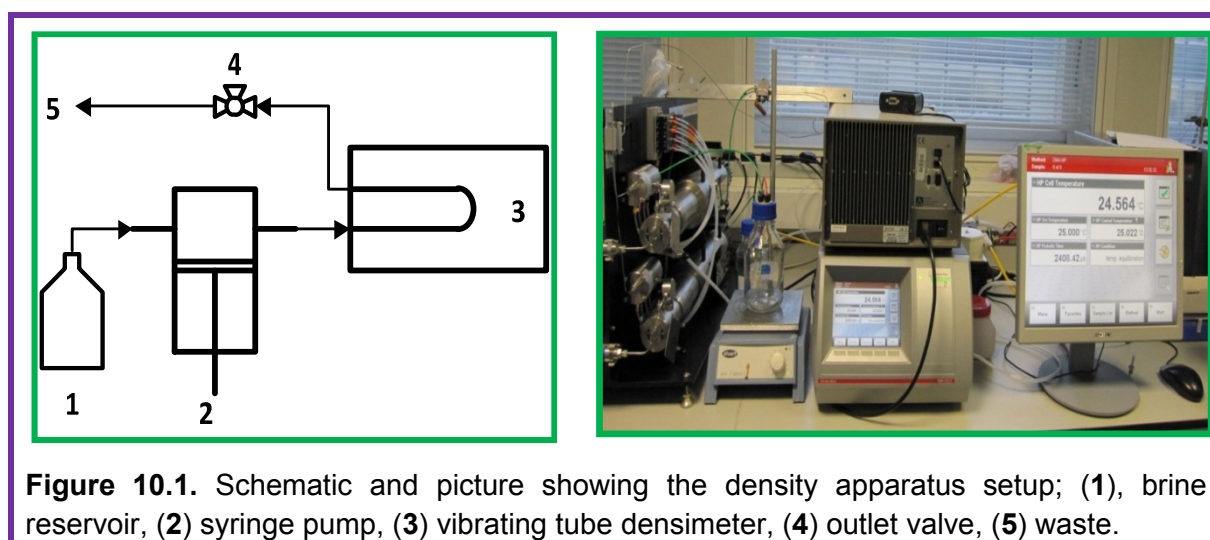
These two equations are widely used in literature. However, the use of different hypothesis leads to different values in the density measurements. This difference becomes higher when the sample density is much higher than the density of the reference fluid used in the calibration. This is because the assumptions made in the above two equations do not necessarily provide a full description of the coefficients  $A$  and  $B$  for the entire range of the measurements. It is then difficult to tell which working equation is more accurate for the density measurements and further investigation is still required. In addition, little information is provided about the ability of vibrating tube densimeter to provide accurate results at intermediate densities between the vacuum limit and the reference liquid. This point is important because if the calibration model is set to represent the real behaviour of the instrument, then it should work on the whole reachable density range within stated accuracy. However, it has been shown [454] that equation 10.1 is obeyed accurately over very wide density range at fixed ambient pressure. The issue is then not the linearity of the device but the determination of the correct dependence of  $A$  and  $B$  upon pressure and temperature. This is discussed further in section 10.10.

## 10.4 Experimental Work

**Materials:** NaCl ( $x \geq 0.999$ ), KCl ( $x \geq 0.99$ ), KI ( $x \geq 0.995$ ), CaCl<sub>2</sub> ( $x \geq 0.99$ ), MgCl<sub>2</sub> ( $x \geq 0.99$ ), AlCl<sub>3</sub> ( $x \geq 0.99$ ), Na<sub>2</sub>SO<sub>4</sub> ( $x \geq 0.99$ ), SrCl<sub>2</sub> ( $x \geq 0.99$ ), and NaHCO<sub>3</sub> ( $x \geq 0.995$ ), where  $x$  denotes mole fraction purity, were supplied by Sigma Aldrich (UK). The magnesium chloride, aluminium chloride calcium chloride, strontium chloride were supplied as hexahydrates (MgCl<sub>2</sub>·6H<sub>2</sub>O, AlCl<sub>3</sub>·6H<sub>2</sub>O, CaCl<sub>2</sub>·6H<sub>2</sub>O and SrCl<sub>2</sub>·6H<sub>2</sub>O). Anhydrous calcium chloride ( $x \geq 0.9999$ ) and magnesium chloride ( $x \geq 0.9999$ ) were supplied by Sigma Aldrich. The magnesium chloride hexahydrated used to prepare the solution with  $b = 5 \text{ mol}\cdot\text{kg}^{-1}$  was supplied by VWR (UK) with  $x \geq 0.99$ . Deionised water was used for all solutions (Millipore, 18 M $\Omega$ ·cm at  $T = 298.15 \text{ K}$ ).

**Apparatus Setup:** The vibrating tube densimeter was the technique adopted in this work and the experimental setup is illustrated in Figure 10.1.

A syringe pump (Quizix, model Q5210) with a maximum service pressure of 70 MPa, and with wetted parts fabricated from brine-resistant Hastelloy C-276, was used to inject the brines and raise the pressure. The pressure was measured using the pressure transducer installed in the syringe pump. The pump was connected to the vibrating tube densimeter through 1.6 mm o.d. Hastelloy C-276 tubing. The densimeter (Anton Paar, DMA HP) is designed to measure the density of liquids and gases at pressures up to 70 MPa and temperatures between (283 and 473) K using a U-shaped vibrating tube of 2 mL total volume. The temperature of the vibrating tube was controlled by an integrated Peltier thermostat to within  $\pm 0.01$  K. The temperature was measured by means of a Pt100 sensor located in a thermowell in the cellblock. A second calibrated Pt100 temperature sensor (Sensing Device Ltd) was used to verify the temperature readings. The DMA HP was connected to a master instrument (Anton Paar, DMA 5000 M) which displayed the measured parameters including the period of oscillation with a resolution of  $0.01 \mu\text{s}$ . The outlet of the densimeter was connected via a two-way valve (also fabricated from Hastelloy C-276) to the waste outlet.



**TGA analysis:** Attempting to ensure that the hexahydrated salts are fully hydrated (6 molecules of water), Thermogravimetric analysis (TGA) were performed to examine this. TGA is a technique in which the mass of a substance is monitored as a function of temperature or time as the sample is subjected to a controlled temperature program in a controlled atmosphere. Hexahydrated magnesium chloride was dehydrated using TGA with the assumption that all water should be evaporated during this process. The mass of the

salt before and after TGA analysis was recorded. It was observed that the loss in mass due to the dehydration process was higher than expected based on the theoretical six water molecules per salt unit. Initially the additional mass loss was interpreted as being due to the absorption of moisture.

However, in the work reported by Hou et al. [455] regarding magnesium chloride dehydration, it was concluded that magnesium chloride hydrates can be dehydrated to only some extent by heating. It is not possible to fully dehydrate magnesium chloride by heating in air because of hydrolytic decomposition. Accordingly, the dehydration should be carried out in hydrogen chloride gas atmosphere. Thus in the TGA experiment, there was some conversion of chloride to hydroxide and other compounds, giving increased mass loss which is an alternative explanation to supposing that there is excess water present based on the TGA analysis. This was considered to be the cause behind such increase in mass loss due to the following reasons: **(1)**, Sigma Aldrich determined the purity of hexahydrated magnesium chloride (and other hexahydrated salts) by titration against EDTA, which forms a complex with calcium and magnesium ions and is a precise and reliable method; **(2)**, It was observed experimentally that a mixture of the magnesium chloride salt and water that should (assuming number of water molecules  $n$  is not equal to 6) produce a  $5 \text{ mol}\cdot\text{kg}^{-1}$  solution does not fully dissolve; whereas if we assume  $n = 6$  then the amounts mixed would be beyond the solubility limit of this salt which is in agreement with the experimental observation; and finally **(3)**, comparison of density obtained with a large database of available literature concluded that the number is actually 6.

**Experimental Procedure:** The solutions were prepared gravimetrically on an analytical balance (Mettler Toledo, model PR5003) with 0.001 g resolution. Prior to loading each sample, the solution was stirred to ensure homogeneity and degassed under vacuum. The densimeter was flushed many times with deionised water and dried with air. Then the system was flushed with the degassed brine and the period of oscillation was recorded after equilibration at  $T = 298.15 \text{ K}$  and  $p = 1 \text{ MPa}$ . Next, the system was flushed again with the brine and the measurement of the period of oscillation at  $T = 298.15 \text{ K}$  and  $p = 1 \text{ MPa}$  was repeated. If the two values matched, the measurements were continued. If not, another sample was injected until consistent values were found. Typically, the temperature was raised in steps of 25 K from  $T = 298.15$  to  $T = 473.15 \text{ K}$  and then returned to the initial temperature for a check measurement. The temperature  $T = 283.15 \text{ K}$  was also studied for some of the brines. For each isotherm, the pressure values studied were 1 MPa, (10 to 60) MPa in steps of 10 MPa, 68.5 MPa and a final check measurement at  $p = 1 \text{ MPa}$ . No

hysteresis was observed going up and down in temperature or in pressure. It was found that the system was very reliable and the period measurements were reproducible within 0.01  $\mu\text{s}$ , which was taken to be the uncertainty of the period of oscillation.

**Table 10.1.** Composition of the two synthetic brines in terms of ions and salts together with their mole fractions where 1 and 2 refer to the two synthetic brines used in this study

Ions	$b_1$ $\text{mol}\cdot\text{kg}^{-1}$	$b_2$ $\text{mol}\cdot\text{kg}^{-1}$	Salts	$b_1$ $\text{mol}\cdot\text{kg}^{-1}$	$b_2$ $\text{mol}\cdot\text{kg}^{-1}$	$x_1$	$x_2$
$\text{Na}^+$	0.315	1.539	$\text{NaHCO}_3$	0.006	0.003	0.018	0.002
$\text{K}^+$	0.008	0.012	$\text{Na}_2\text{SO}_4$	0.016	0.011	0.044	0.006
$\text{Ca}^{2+}$	0.038	0.276	$\text{SrCl}_2$	0.001	0.004	0.002	0.002
$\text{Mg}^{2+}$	0.014	0.080	$\text{MgCl}_2$	0.014	0.080	0.040	0.042
$\text{Sr}^{2+}$	0.001	0.004	$\text{CaCl}_2$	0.038	0.276	0.105	0.145
$\text{Cl}^-$	0.389	2.245	$\text{KCl}$	0.008	0.012	0.022	0.006
$(\text{HCO}_3)^-$	0.006	0.003	$\text{NaCl}$	0.276	1.514	0.770	0.797
$(\text{SO}_4)^{2-}$	0.016	0.011	Total	0.359	1.900	1.000	1.000

The synthetic reservoir brines were prepared based on real geological brines composition data. Seven individual salts were used to make up these brines. Table 10.1 summarizes the full list of cations and anions and their molalities together with a list of the individual salts used to make up these brines and their molalities and mole fractions in the synthetic brines. Initially, it was difficult to get the second synthetic brine (with  $b = 1.9 \text{ mol}\cdot\text{kg}^{-1}$ ) to dissolve completely. This was found to depend on the order of mixing (which salt to add first). The procedure to get full dissolution was to dissolve all the other salts first and then add the sodium bicarbonate ( $\text{NaHCO}_3$ ) and sodium sulphate ( $\text{NaSO}_4$ ).

## 10.5 Apparatus Calibration

The pressure transducer was calibrated at pressures in the range (1 to 70) MPa by comparison with a quartz pressure sensor in a pneumatic calibrator (Fluke-DHI model PPCH-G-70M). It is estimated that the expanded uncertainty of the pressure transducer after calibration was 35 kPa (0.05 % of the full scale reading) with a coverage factor  $k = 2$ . The platinum resistance thermometer was calibrated at temperatures in the range (273 to 473) K by comparison in a constant-temperature bath with a standard platinum resistance thermometer having an expanded uncertainty of 2 mK in the present temperature range. It is estimated that the expanded uncertainty of the temperature measurements after calibration was 0.05 K with a coverage factor  $k = 2$ . Densimeter calibration was carried out under

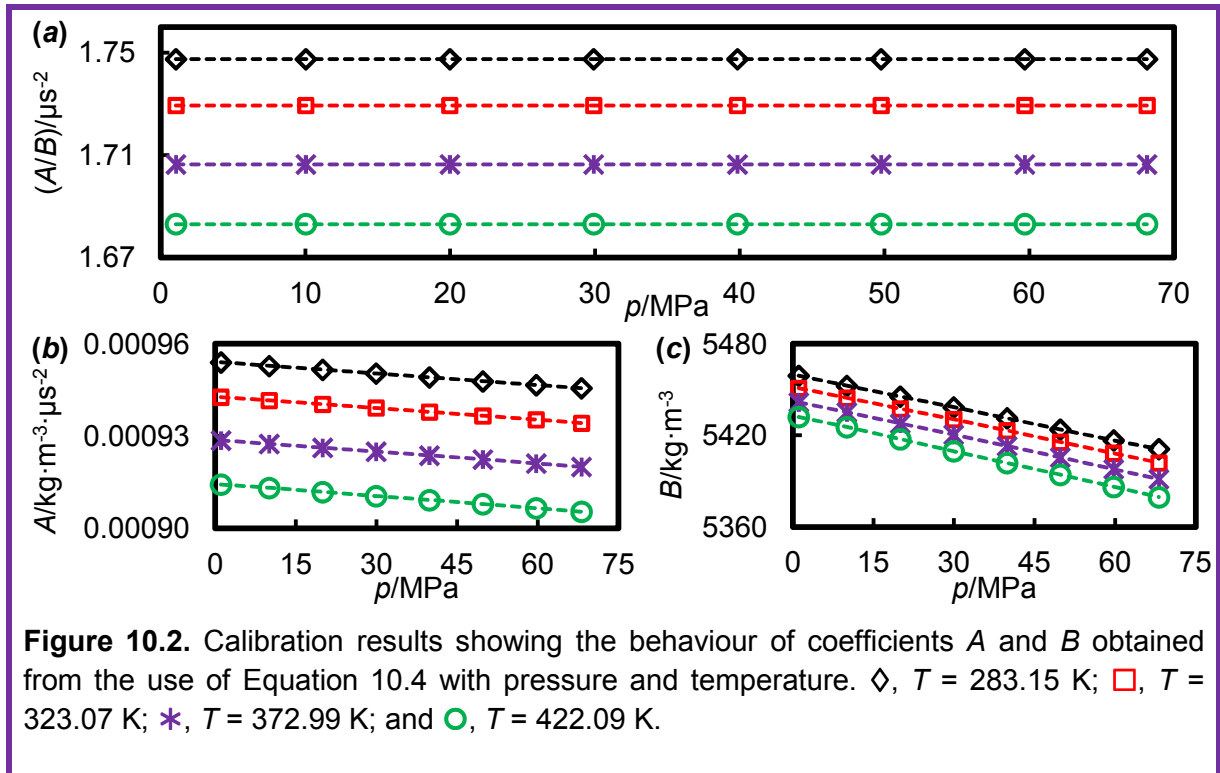
vacuum at all experimental temperatures and in pure water at every temperature and pressure to be studied using Equation 10.4. The parameters  $A$  and  $B$  were thus given by:

$$A(p, T) = \frac{\rho_w(p, T)}{\tau_w^2(p, T) - \tau_0^2(T)}, B(p, T) = \frac{\rho_w(p, T)\tau_0^2(T)}{\tau_w^2(T, p) - \tau_0^2(T)}, \quad 10.6$$

where  $\tau_w(p, T)$  and  $\rho_w(p, T)$  are the period of oscillation and the density for calibration with water at given pressure and temperature, and  $\tau_0(T)$  is the period of oscillation under vacuum at given temperature. In the present case,  $\rho_w$  was obtained from the IAPWS-95 EoS developed by Pruss and Wagner [456] which is associated with a relative standard uncertainty of 0.01 % or less at the pressures and temperatures of this study. At  $T = 298.15$  K and  $p = 0.1$  MPa, an alternative calibration was performed using ambient air and water as the reference fluids. When tested in measurements for NaCl(aq) with  $b = 4.95$  mol·kg<sup>-1</sup>, the densities obtained were 1168.11 kg·m<sup>-3</sup> with the calibration in air and water, and 1168.10 kg·m<sup>-3</sup> with the calibration in vacuum and water. This was taken as evidence that the vacuum calibration was reliable. However, as previously discussed, the hypothesis used with the calibration method will change the density measurements and hence careful attention should be paid to the different calibration methods implemented. An example of the calibration results is presented in Table 10.2 and Figure 10.2. It can be seen, for example, the non-dependency of  $A/B$  with pressure. Also both  $A$  and  $B$  decreases with increasing pressure or temperature. This is because the tube volume increases and stiffness decreases with increasing temperature while the tube radius expands with increasing pressure.

**Table 10.2.** The period of oscillation obtained during calibration with vacuum and water at different pressure and temperature conditions.

$p/\text{MPa}$	<b>283.15</b>	<b>298.12</b>	<b>323.07</b>	<b>348.04</b>	<b>372.99</b>	<b>397.97</b>	<b>422.94</b>	<b>447.94</b>
0.00	2392.23	2396.85	2404.70	2412.71	2420.84	2429.12	2437.55	2446.11
1.05	2602.17	2606.77	2613.66	2619.85	2625.48	2630.65	2635.38	2639.63
10.02	2603.26	2607.81	2614.68	2620.89	2626.57	2631.82	2636.65	2641.07
19.97	2604.45	2608.96	2615.80	2622.03	2627.76	2633.09	2638.04	2642.60
29.90	2605.62	2610.09	2616.90	2623.15	2628.92	2634.34	2639.39	2644.09
39.83	2606.78	2611.20	2617.99	2624.25	2630.07	2635.55	2640.70	2645.53
49.76	2607.93	2612.30	2619.07	2625.35	2631.20	2636.74	2641.98	2646.93
59.68	2609.05	2613.39	2620.14	2626.42	2632.32	2637.92	2643.24	2648.29
68.12	2610.00	2614.30	2621.04	2627.33	2633.26	2638.91	2644.29	2649.43



## 10.6 Uncertainty Analysis

Based on the calibration Equation 10.4 given in the above section and using the guide to the expression of uncertainty in measurements (GUM) [178] the combined standard uncertainty of the density  $U(\rho)$  is obtained from the following Equation

$$U^2(\rho) = \sum_{i=1}^n \sum_{j=1}^n \frac{\partial f}{\partial x_i} \frac{\partial f}{\partial x_j} u(x_i, x_j) \quad 10.7$$

By neglecting the covariance effects and combining Equations 10.4 and 10.7, the expanded uncertainty is obtained as

$$U^2(\rho) = k^2 \left[ \left( \frac{\tau^2 - \tau_0^2}{\tau_w^2 - \tau_0^2} \right)^2 u^2(\rho_w) + \left( \frac{2\rho_w \tau}{\tau_w^2 - \tau_0^2} \right)^2 u^2(\tau) + \left( \frac{2\rho_w \tau_0}{(\tau_w^2 - \tau_0^2)^2} (\tau_w^2 - \tau_0^2) \right)^2 u^2(\tau_0) + \right. \\ \left. + \left( \frac{-2\rho_w \tau_w}{(\tau_w^2 - \tau_0^2)^2} (\tau^2 - \tau_0^2) \right)^2 u^2(\tau_w) + \left( \frac{\partial \rho}{\partial T} \right)_{p,b}^2 u^2(T) + \left( \frac{\partial \rho}{\partial p} \right)_{T,b}^2 u^2(p) + \left( \frac{\partial \rho}{\partial b} \right)_{T,p}^2 u^2(b) \right] \quad 10.8$$

where  $k$  is a coverage factor, which is the multiplier of the combined standard uncertainty in order to obtain the expanded uncertainty.



The quantities considered are  $\rho_w$ ,  $\tau_w$ ,  $\tau_0$ ,  $\tau$ ,  $T$ ,  $p$  and  $b$ . Examples of the various contributions to the uncertainty are given in Table 10.3 for  $\text{CaCl}_2(\text{aq})$  at  $T = 472.04$  K,  $p = 10.2$  MPa and three different molalities and for  $\text{SrCl}_2(\text{aq})$  at  $T = 473.02$  K,  $p = 10.1$  MPa and three different molalities. The results are very similar for all brines. The uncertainty increases as temperature and molality increase, but decreases as pressure increases hence the largest uncertainty occurs at the highest temperature, highest molality and lowest pressure. The uncertainties in temperature, pressure and oscillation period have been discussed above. The remaining experimental uncertainty is that associated with the molality of the brine which is influenced by weighing errors, salt purity and, especially, the water content of the salt. The relative uncertainty in  $b$  associated with weighing was always below 0.01 %. In the case of the hexahydrated salts, we assumed that there were exactly six water molecules per salt unit. In order to test for the effects of any impurities and possible variations in the water content of these hexahydrates, further solutions of  $\text{CaCl}_2$  and  $\text{MgCl}_2$  were prepared from anhydrous salts with specified mole-fraction purity  $x \geq 0.9999$ . These salts were provided in sealed glass ampoules and the solutions were prepared gravimetrically immediately after opening them. The densities of these solutions were measured at ambient pressure and  $T = 298.15$  K using an Anton Paar DMA 5000 densimeter calibrated at that temperature in air and pure water.

**Table 10.3.** Contributions to the expanded uncertainty  $U(\rho)$  of the density of  $\text{CaCl}_2(\text{aq})$  at  $T = 472.04$  K and  $p = 10.2$  MPa and density of  $\text{SrCl}_2(\text{aq})$  at  $T = 473.02$  K and  $p = 10.10$  MPa, with a coverage factor  $k = 2$

	CaCl <sub>2</sub> (aq)			SrCl <sub>2</sub> (aq)		
	1.00	3.00	6.00	1.022	2.024	3.031
$b/(\text{mol}\cdot\text{kg}^{-1})$						
$u(\tau)/\mu\text{s}$	0.01	0.01	0.01	0.01	0.01	0.01
$u(\tau_0)/\mu\text{s}$	0.01	0.01	0.01	0.01	0.01	0.01
$u(\rho_w)/(\text{kg}\cdot\text{m}^{-3})$	0.09	0.09	0.09	0.09	0.09	0.09
$u(T)/\text{K}$	0.025	0.025	0.025	0.025	0.025	0.025
$u(p)/\text{MPa}$	0.018	0.018	0.018	0.018	0.018	0.018
$u(b)/(\text{mol}\cdot\text{kg}^{-1})$	0.001	0.003	0.006	0.001	0.002	0.003
$(\partial\rho/\partial\tau)/(\text{kg}\cdot\text{m}^{-3}\cdot\mu\text{s}^{-1})$	4.79	4.84	4.90	4.93	4.98	5.01
$(\partial\rho/\partial\tau_0)/(\text{kg}\cdot\text{m}^{-3}\cdot\mu\text{s}^{-1})$	0.48	1.24	2.05	0.71	1.33	1.89
$(\partial\rho/\partial\tau_w)/(\text{kg}\cdot\text{m}^{-3}\cdot\mu\text{s}^{-1})$	-5.27	-6.09	-6.96	-5.65	-6.31	-6.91
$(\partial\rho/\partial T)/(\text{kg}\cdot\text{m}^{-3}\cdot\text{K}^{-1})$	-0.98	-0.81	-0.69	-1.01	-0.93	-0.89
$(\partial\rho/\partial p)/(\text{kg}\cdot\text{m}^{-3}\cdot\text{MPa}^{-1})$	0.57	0.44	0.35	0.59	0.52	0.46
$(\partial\rho/\partial b)/(\text{kg}^2\cdot\text{m}^{-3}\cdot\text{mol}^{-1})$	83.54	66.19	40.15	122.94	112.04	101.09
$U(\rho)/(\text{kg}\cdot\text{m}^{-3})$	0.30	0.49	0.58	0.36	0.54	0.69

The results were  $\rho = 1380.20 \text{ kg}\cdot\text{m}^{-3}$  for  $\text{CaCl}_2(\text{aq})$  at  $b = 5.81 \text{ mol}\cdot\text{kg}^{-1}$  and  $\rho = 1296.41 \text{ kg}\cdot\text{m}^{-3}$  for  $\text{MgCl}_2(\text{aq})$  at  $b = 4.98 \text{ mol}\cdot\text{kg}^{-1}$ . In order to compare these data with the values obtained in our measurements on solutions prepared from  $\text{CaCl}_2\cdot 6(\text{H}_2\text{O})$  and  $\text{MgCl}_2\cdot 6(\text{H}_2\text{O})$ , we made use of the corresponding correlations of our experimental  $\rho(T, p, b)$  results discussed below. The values obtained were  $1380.06 \text{ kg}\cdot\text{m}^{-3}$  for the  $\text{CaCl}_2$  solution and  $1296.59 \text{ kg}\cdot\text{m}^{-3}$  for the  $\text{MgCl}_2$  solution.

Thus the relative differences were 0.010 % and 0.014 %, which are smaller than the uncertainties of the correlations involved in these comparisons. Based on this comparison, we estimate the relative standard uncertainty of molality to be 0.05 % which for  $\text{CaCl}_2(\text{aq})$  at  $T = 298.15 \text{ K}$ ,  $p = 0.1 \text{ MPa}$  and  $b = 6 \text{ mol}\cdot\text{kg}^{-1}$  corresponds to a relative uncertainty in  $\rho$  of 0.015 %. Taking all factors into account, the final expanded relative uncertainty of the density varies from 0.03 % to 0.06 %. The expanded relative uncertainty of the density was found to be bounded by the following a linear function of molality

$$U_r(\rho) \leq 0.01 \left[ b / (\text{mol}\cdot\text{kg}^{-1}) \right] + 0.03 \quad 10.9$$

## 10.7 Experimental Results

The densities of  $\text{MgCl}_2(\text{aq})$ ,  $\text{CaCl}_2(\text{aq})$ ,  $\text{KI}(\text{aq})$ ,  $\text{NaCl}(\text{aq})$ ,  $\text{KCl}(\text{aq})$ ,  $\text{AlCl}_3(\text{aq})$ ,  $\text{SrCl}_2(\text{aq})$ ,  $\text{Na}_2\text{SO}_4(\text{aq})$ ,  $\text{NaHCO}_3(\text{aq})$ , the mixed salt system  $[(1 - x) \text{NaCl} + x\text{KCl}](\text{aq})$  and the synthetic reservoir brine system  $[x_1\text{NaCl} + x_2\text{KCl} + x_3\text{MgCl}_2 + x_4\text{CaCl}_2 + x_5\text{SrCl}_2 + x_6\text{Na}_2\text{SO}_4 + x_7\text{NaHCO}_3](\text{aq})$ , where  $x$  denotes mole fraction, at temperatures between (283 and 473) K and pressures up to 68.5 MPa were measured. The molalities at which the solutions were studied were (1.00, 3.00 and 5.00)  $\text{mol}\cdot\text{kg}^{-1}$  for  $\text{MgCl}_2(\text{aq})$ , (1.00, 3.00 and 6.00)  $\text{mol}\cdot\text{kg}^{-1}$  for  $\text{CaCl}_2(\text{aq})$ , (0.67, 0.90 and 1.06)  $\text{mol}\cdot\text{kg}^{-1}$  for  $\text{KI}(\text{aq})$ , (1.06, 3.16 and 6.00)  $\text{mol}\cdot\text{kg}^{-1}$  for  $\text{NaCl}(\text{aq})$ , (1.06, 3.15 and 4.49)  $\text{mol}\cdot\text{kg}^{-1}$  for  $\text{KCl}(\text{aq})$ , (1.00 and 2.00)  $\text{mol}\cdot\text{kg}^{-1}$  for  $\text{AlCl}_3(\text{aq})$ , (1.022, 2.024 and 3.031)  $\text{mol}\cdot\text{kg}^{-1}$  for  $\text{SrCl}_2(\text{aq})$ , (0.783 and 1.502)  $\text{mol}\cdot\text{kg}^{-1}$  for  $\text{Na}_2\text{SO}_4(\text{aq})$ , and (0.507 and 1.000)  $\text{mol}\cdot\text{kg}^{-1}$  for  $\text{NaHCO}_3(\text{aq})$  and (1.05, 1.98, 3.15 and 4.95)  $\text{mol}\cdot\text{kg}^{-1}$  for  $[(1 - x)\text{NaCl} + x\text{KCl}](\text{aq})$ , with  $x = 0.136$ . The compositions of the synthetic reservoir brines studied were, first,  $x_1 = 0.770$ ,  $x_2 = 0.022$ ,  $x_3 = 0.040$ ,  $x_4 = 0.105$ ,  $x_5 = 0.002$ ,  $x_6 = 0.044$ , and  $x_7 = 0.018$  with molality  $0.359 \text{ mol}\cdot\text{kg}^{-1}$  and, second,  $x_1 = 0.797$ ,  $x_2 = 0.006$ ,  $x_3 = 0.042$ ,  $x_4 = 0.145$ ,  $x_5 = 0.002$ ,  $x_6 = 0.006$ , and  $x_7 = 0.002$  with molality  $1.900 \text{ mol}\cdot\text{kg}^{-1}$ . The  $\text{AlCl}_3(\text{aq})$  solution was only measured at  $T = (298.15 \text{ to } 373.15) \text{ K}$ .

This is because, at higher temperatures, the solutions were found to be reactive, possibly undergoing hydrolysis- precipitation of aluminium as discussed by Bottero et al. [457-458] and the results obtained became erratic within one or two hours in the cell; severe corrosion was later discovered necessitating replacement of the vibrating tube. The results are presented in Appendix D.

## 10.8 Correlation and Modelling

For each salt system investigated, we have parameterised the well-known Tammann-Tait equation [459] so as to fit precisely the density over the entire ( $p$ ,  $T$ ,  $b$ ) ranges investigated. The Tammann-Tait equation is widely used to fit the liquid density data over wide range of pressures. This is a modification to the known Tait equation which was published more than 100 years ago to fit the compressibility of fresh water and sea water at different pressures. Tammann-Tait equation is given by the following expression

$$\rho(T, p, b) = \rho_{\text{ref}}(T, b) \left[ 1 - C(b) \ln \left\{ \frac{B(T, b) + p}{B(T, b) + p_{\text{ref}}(T)} \right\} \right]^{-1} \quad 10.10$$

Here,  $\rho_{\text{ref}}$  is the density at a reference pressure  $p_{\text{ref}}(T)$ , which we take to be the vapour pressure of pure water at the given temperature, and  $B$  and  $C$  are parameters. The vapour pressure of water was obtained from the auxiliary equation given by Wagner and Pruss: [456]

$$\ln p_{\text{ref}}(T) / p_c = (T_c / T) \left[ \sigma_1 \varphi + \sigma_2 \varphi^{1.5} + \sigma_3 \varphi^3 + \sigma_4 \varphi^{3.5} + \sigma_5 \varphi^4 + \sigma_6 \varphi^{7.5} \right], \quad 10.11$$

where  $T_c = 647.10$  K is the critical temperature,  $p_c = 22.064$  MPa is the critical pressure, and  $\varphi = (1 - T/T_c)$ . Initially, optimal values of  $\rho_{\text{ref}}$ ,  $B$  and  $C$  were found by minimizing the sum square of the differences between the experimental and calculated values of density for each isotherm and molality. It was found that the parameters obtained ( $\rho_{\text{ref}}$ ,  $B$  and  $C$ ) could be represented over the full ranges of pressure, temperature and molality for each brine system by means of the relations given below.

In Equation (10.12),  $\rho_0(T)$  is the density of saturated liquid water given by the auxiliary equation of Wagner and Pruss [456] which is presented in Equation (10.15). The coefficients in Equations (10.13) and (10.14) pertaining to pure water were optimised in a fit of Equation (10.10) to densities computed from the IAPWS-95 EoS [456] at all temperatures and pressures considered experimentally. Thus these coefficients were the same for every brine considered. The relative deviations of the density of pure water from this fit were all

within  $\pm 0.02\%$ . In Table 10.4 we give the parameters  $\sigma_i$ ,  $c_i$ ,  $\beta_{0i}$  and  $\gamma_0$  required for pure water.

$$\begin{aligned} [\rho_{\text{ref}}(T, b) - \rho_0(T)] / (\text{kg} \cdot \text{m}^{-3}) &= \sum_{i=1}^{i=3} \alpha_{i0} [b / (\text{mol} \cdot \text{kg}^{-1})]^{i+1/2} + \\ &+ \sum_{i=1}^{i=3} \sum_{j=1}^{j=3} \alpha_{ij} [b / (\text{mol} \cdot \text{kg}^{-1})]^{i+1/2} (T / T_c)^{(j+1)/2}, \end{aligned} \quad 10.12$$

$$B(T, b) / \text{MPa} = \sum_{i=0}^{i=1} \sum_{j=0}^{j=3} \beta_{ij} [b / (\text{mol} \cdot \text{kg}^{-1})]^i (T / T_c)^j \quad 10.13$$

$$C(b) = \gamma_0 + \gamma_1 [b / (\text{mol} \cdot \text{kg}^{-1})] + \gamma_2 [b / (\text{mol} \cdot \text{kg}^{-1})]^{3/2} \quad 10.14$$

$$\rho_0(T) / \rho_c = 1 + c_1 \varphi^{1/3} + c_2 \varphi^{2/3} + c_3 \varphi^{5/3} + c_4 \varphi^{16/3} + c_5 \varphi^{43/3} + c_6 \varphi^{110/3} \quad 10.15$$

**Table 10.4.** Coefficients  $\alpha_i$ ,  $\beta_{0j}$ ,  $\gamma_0$ , and  $\sigma_i$  for pure water in Equations 10.11 to 10.14

<b>c<sub>1</sub></b>	<b>c<sub>2</sub></b>	<b>c<sub>3</sub></b>	<b>c<sub>4</sub></b>	<b>c<sub>5</sub></b>	<b>c<sub>6</sub></b>
1.992741	1.099653	-0.510839	-1.754935	-45.517035	674694.45000
<b>β<sub>00</sub></b>	<b>β<sub>01</sub></b>	<b>β<sub>02</sub></b>	<b>β<sub>03</sub></b>	<b>γ<sub>0</sub></b>	<b>σ<sub>1</sub></b>
-1622.40	9383.80	-14893.80	7309.10	0.11725	-7.859518
<b>σ<sub>2</sub></b>	<b>σ<sub>3</sub></b>	<b>σ<sub>4</sub></b>	<b>σ<sub>5</sub></b>	<b>σ<sub>6</sub></b>	
1.844083	-11.786650	22.680741	-15.961872	1.801225	

The remaining parameters in Equations (10.11 to 10.15) were optimised in a surface fit with Equation (10.10) for each system, considering simultaneously all temperatures and pressures. The coefficients  $\alpha_{ij}$ ,  $\beta_{ij}$  and  $\gamma_i$  obtained are given in Tables 10.5 and 10.6. For each system, we computed the absolute average relative deviation ( $\Delta_{\text{AAD}}$ ), average relative deviation ( $\Delta_{\text{Bias}}$ ) and maximum absolute relative deviation ( $\Delta_{\text{MAD}}$ ) from Equation (10.10). These statistical measures are defined as follows:

$$\Delta_{\text{AAD}} = \frac{1}{N} \sum_i \left| \frac{\rho_i^{\text{exp}} - \rho_i^{\text{cal}}}{\rho_i^{\text{exp}}} \right|, \Delta_{\text{Bias}} = \frac{1}{N} \sum_i \frac{\rho_i^{\text{exp}} - \rho_i^{\text{cal}}}{\rho_i^{\text{exp}}}, \Delta_{\text{MAD}} = \text{Max} \left( \sum_i \left| \frac{\rho_i^{\text{exp}} - \rho_i^{\text{cal}}}{\rho_i^{\text{exp}}} \right| \right) \quad 10.16$$

The values  $\Delta_{\text{AAD}}$ ,  $\Delta_{\text{Bias}}$  and  $\Delta_{\text{MAD}}$  are given in Tables 10.5 and 10.6; they compare favourably with the relative uncertainty of the data. In Figure 10.3, we plot the relative deviations of the experimental densities from Eq. (10.10). Regarding the density of mixed brines, A simple

model for predicting the density of a mixed brine may be obtained with the assumption that the excess volume of mixing single salt solutions at specified ( $p$ ,  $T$ ,  $b$ ) is zero [422].

**Table 10.5.** Coefficients  $\alpha_{ij}$ ,  $\beta_{ij}$ , and  $\gamma_i$  and statistical parameters absolute average relative deviation ( $\Delta_{AAD}$ ), average relative deviation ( $\Delta_{Bias}$ ) and maximum absolute relative deviation ( $\Delta_{MAD}$ ) for the brines  $\text{CaCl}_2(\text{aq})$ ,  $\text{MgCl}_2(\text{aq})$ ,  $\text{KI}(\text{aq})$ ,  $\text{NaCl}(\text{aq})$ ,  $\text{KCl}(\text{aq})$ ,  $[0.864\text{NaCl} + 0.136\text{KCl}] (\text{aq})$  and  $\text{AlCl}_3(\text{aq})$  in Equations 10.11 to 10.15.

	NaCl(aq)	CaCl <sub>2</sub> (aq)	MgCl <sub>2</sub> (aq)	KI (aq)	(0.864NaCl + 0.136KCl) (aq)
$\alpha_{10}$	2863.158	2546.760	2385.823	8657.149	3452.312
$\alpha_{11}$	-46844.356	-39884.946	-38428.112	-94956.477	-58732.356
$\alpha_{12}$	120760.118	102056.957	99526.269	167497.772	154450.565
$\alpha_{13}$	-116867.722	-98403.334	-97041.399	-74952.063	-152574.650
$\alpha_{14}$	40285.426	33976.048	33841.139	-8734.207	53700.479
$\alpha_{20}$	-2000.028	-1362.157	-1254.938	-14420.621	-2900.592
$\alpha_{21}$	34013.518	22785.572	21606.295	137360.624	51539.478
$\alpha_{22}$	-88557.123	-59216.108	-56988.274	-184940.639	-137384.642
$\alpha_{23}$	86351.784	57894.824	56465.943	-11953.289	137291.425
$\alpha_{24}$	-29910.216	-20222.898	-19934.064	79847.960	-48772.381
$\alpha_{30}$	413.046	217.778	192.534	7340.083	712.600
$\alpha_{31}$	-7125.857	-3770.645	-3480.374	-66939.345	-12852.805
$\alpha_{32}$	18640.780	9908.135	9345.908	81446.737	34456.168
$\alpha_{33}$	-18244.074	-9793.484	-9408.904	23983.386	-34603.469
$\alpha_{34}$	6335.275	3455.587	3364.018	-49031.473	12343.593
$\beta_{10}$	241.57	307.24	358.00	241.84	188.98
$\beta_{11}$	-980.97	-1259.10	-1597.10	-1030.61	-722.33
$\beta_{12}$	1482.31	2034.03	2609.47	1548.15	1063.85
$\beta_{13}$	-750.98	-1084.94	-1383.91	-754.36	-525.66
$\gamma_1$	-0.00134	-0.00493	-0.00789	-0.01026	-0.00123
$\gamma_2$	0.00056	0.00231	0.00142	0.00842	0.00059
$10^2\Delta_{AAD}$	0.005	0.004	0.004	0.005	0.005
$10^2\Delta_{Bias}$	-0.0001	-0.0002	-0.0002	-0.0002	0.0000

$10^2\Delta_{\text{MAD}}$	0.016	0.016	0.016	0.019	0.020
---------------------------	-------	-------	-------	-------	-------

**Table 10.6.** Coefficients  $\alpha_{ij}$ ,  $\beta_{ij}$ , and  $\gamma_i$  and statistical parameters absolute average relative deviation ( $\Delta_{\text{AAD}}$ ), average relative deviation ( $\Delta_{\text{Bias}}$ ) and maximum absolute relative deviation ( $\Delta_{\text{MAD}}$ ) for the brines: KCl(aq), AlCl<sub>3</sub>(aq), SrCl<sub>2</sub>(aq), Na<sub>2</sub>SO<sub>4</sub>(aq) and NaHCO<sub>3</sub>(aq) in Equations 10.11 to 10.15.

	KCl(aq)	AlCl <sub>3</sub> (aq)	SrCl <sub>2</sub> (aq)	Na <sub>2</sub> SO <sub>4</sub> (aq)	NaHCO <sub>3</sub> (aq)
$\alpha_{10}$	2332.802	1326.366	7363.500	5138.958	6261.979
$\alpha_{11}$	-39637.418	-310263.216	-122146.701	-80991.943	-101634.157
$\alpha_{12}$	104801.288	443804.244	317462.993	206290.527	259572.354
$\alpha_{13}$	-104266.828	0.000	-309467.167	-197393.310	-248320.723
$\alpha_{14}$	37030.556	0.000	107327.560	67312.440	84396.551
$\alpha_{20}$	-1287.572	-1804.785	-7752.424	-2886.393	-4141.700
$\alpha_{21}$	23543.994	527875.006	133779.423	46971.471	67265.842
$\alpha_{22}$	-63846.097	-755878.487	-350572.554	-120140.799	-170644.806
$\alpha_{23}$	65023.561	0.000	343927.186	115260.015	161809.563
$\alpha_{24}$	-23586.370	0.000	-119803.664	-39341.248	-54388.795
$\alpha_{30}$	206.032	727.779	2420.865	0.000	0.000
$\alpha_{31}$	-4003.757	-218520.857	-42207.475	0.000	0.000
$\alpha_{32}$	11128.162	312961.409	110943.211	0.000	0.000
$\alpha_{33}$	-11595.475	0	-109091.508	0.000	0.000
$\alpha_{34}$	4295.498	0	38058.388	0.000	0.000
$\beta_{10}$	211.49	0	275.72	357.75	-45.76
$\beta_{11}$	-888.16	0	-896.41	-1170.23	640.25
$\beta_{12}$	1400.09	0	1288.98	1502.51	-1256.68
$\beta_{13}$	-732.79	0	-651.97	-676.66	724.74
$\gamma_1$	-0.00170	-0.04236	-0.00139	-0.01078	0.00270
$\gamma_2$	0.00083	0.01319	0.00038	0.00339	0.00074
$10^2\Delta_{\text{AAD}}$	0.005	0.008	0.006	0.005	0.006
$10^2\Delta_{\text{Bias}}$	-0.0002	-0.0003	-0.0003	-0.0003	-0.0003
$10^2\Delta_{\text{MAD}}$	0.016	0.033	0.019	0.016	0.016

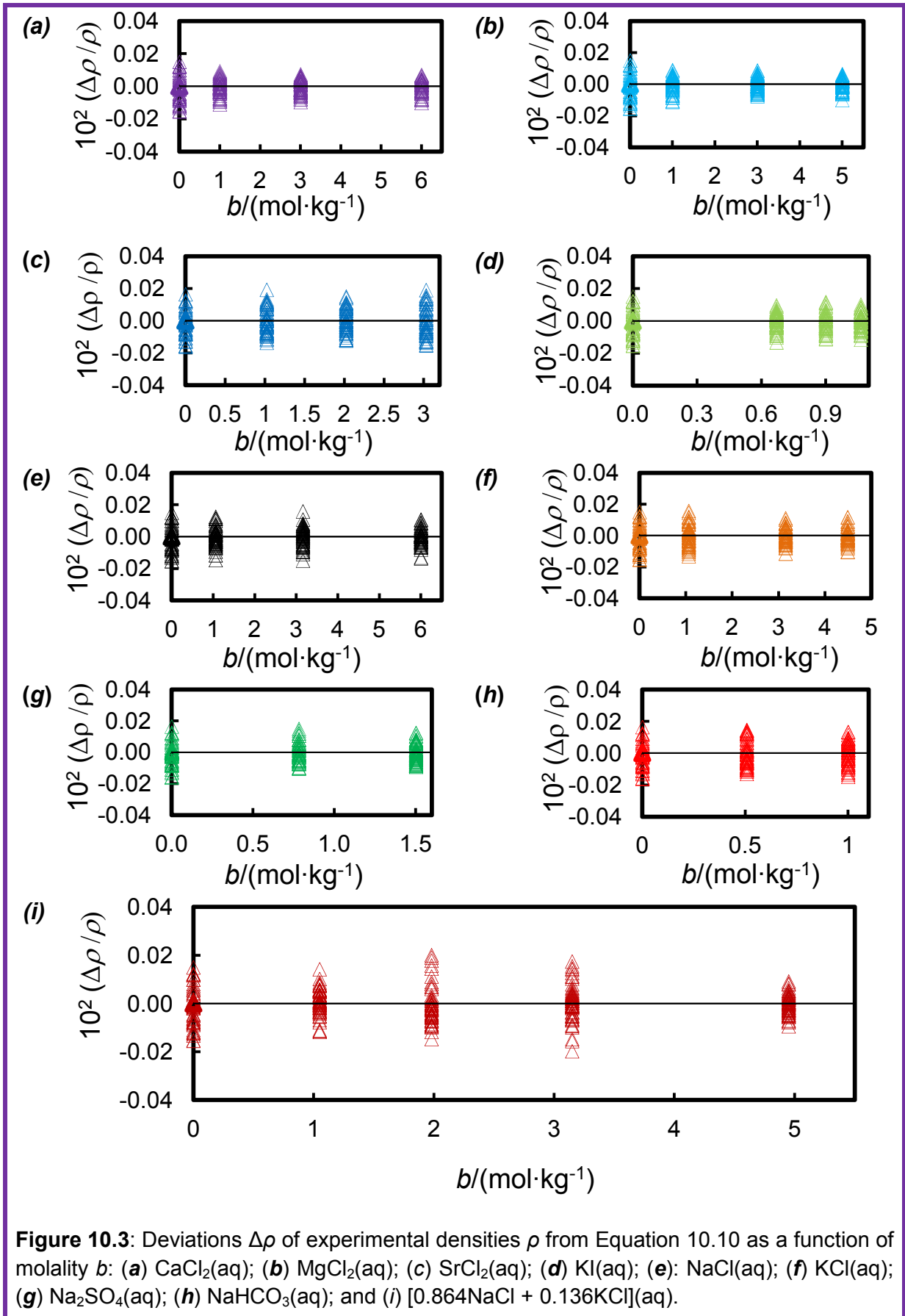
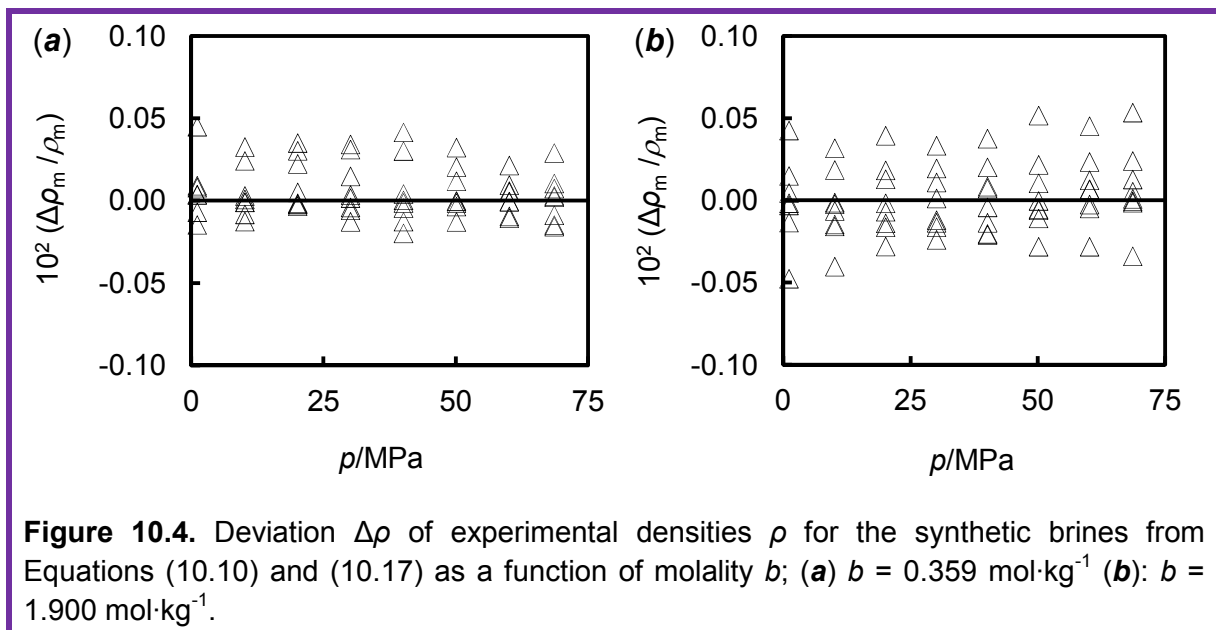


**Figure 10.3:** Deviations  $\Delta\rho$  of experimental densities  $\rho$  from Equation 10.10 as a function of molality  $b$ : (a)  $\text{CaCl}_2(\text{aq})$ ; (b)  $\text{MgCl}_2(\text{aq})$ ; (c)  $\text{SrCl}_2(\text{aq})$ ; (d)  $\text{KI}(\text{aq})$ ; (e)  $\text{NaCl}(\text{aq})$ ; (f)  $\text{KCl}(\text{aq})$ ; (g)  $\text{Na}_2\text{SO}_4(\text{aq})$ ; (h)  $\text{NaHCO}_3(\text{aq})$ ; and (i)  $[0.864\text{NaCl} + 0.136\text{KCl}](\text{aq})$ .

With this approach, the density  $\rho_m$  of a mixed electrolyte solution at given  $(p, T, b)$  is related to the densities of single electrolyte solutions from which it may be formed as follows:

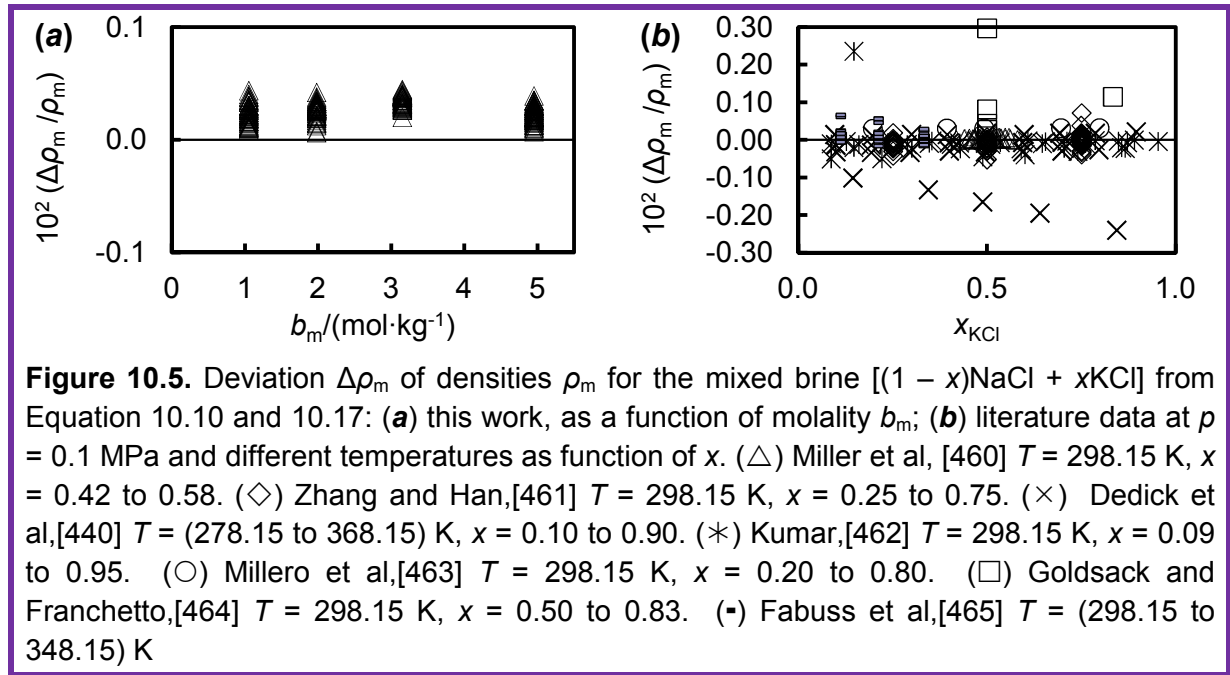
$$\rho_m(p, T, b) = \left[ \sum_i x_i (1 + bM_i) \right] \left[ \sum_i \{x_i (1 + bM_i) / \rho_i(p, T, b)\} \right]^{-1} \quad 10.17$$

Here,  $x_i$  is the mole fraction of electrolyte  $i$  in the mixed salt,  $M_i$  is the molar mass of salt  $i$  and  $\rho_i$  is the density of the single electrolyte solution at the pressure, temperature and molality of the mixed electrolyte solution. This Equation was applied to predict the density of the mixed electrolyte solution (0.864 NaCl + 0.136 KCl)(aq) at temperatures (283.15 to 473.15) K, pressures up to 68.5MPa, and total molalities of (1.05, 1.98, 3.15 and 4.95) mol·kg<sup>-1</sup> and the density of the synthetic reservoir brines [ $x_1$ NaCl +  $x_2$ KCl +  $x_3$ MgCl<sub>2</sub> +  $x_4$ CaCl<sub>2</sub> +  $x_5$ SrCl<sub>2</sub> +  $x_6$ Na<sub>2</sub>SO<sub>4</sub> +  $x_7$ NaHCO<sub>3</sub>](aq), at temperatures (298.15 to 473.15) K, pressures up to 68.5MPa, different compositions, and total molalities of (0.359 and 1.900) mol·kg<sup>-1</sup>.



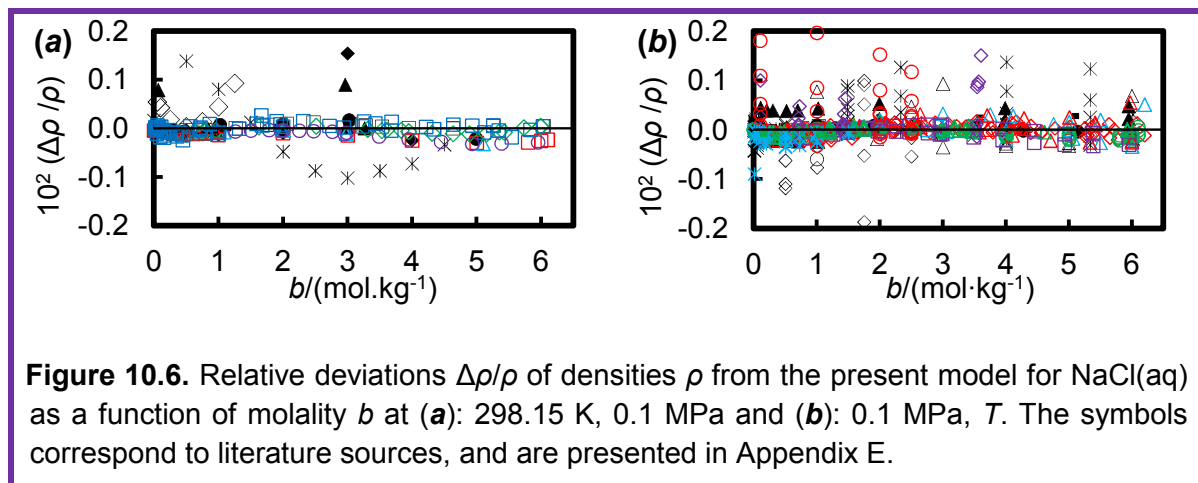
The densities of the single solutions, NaCl(aq), KCl(aq), MgCl<sub>2</sub>(aq), CaCl<sub>2</sub>(aq), SrCl<sub>2</sub>(aq), Na<sub>2</sub>SO<sub>4</sub>(aq) and NaHCO<sub>3</sub>(aq), were obtained from the correlations developed in this work for those brines. The predicted densities were then compared with the experimental values and the relative deviations are plotted in Figures 10.4 and 10.5. The agreement is within  $\pm 0.05\%$  and this suggests that Equation 10.17 is indeed very reliable over extended ranges of temperature, pressure and molality.



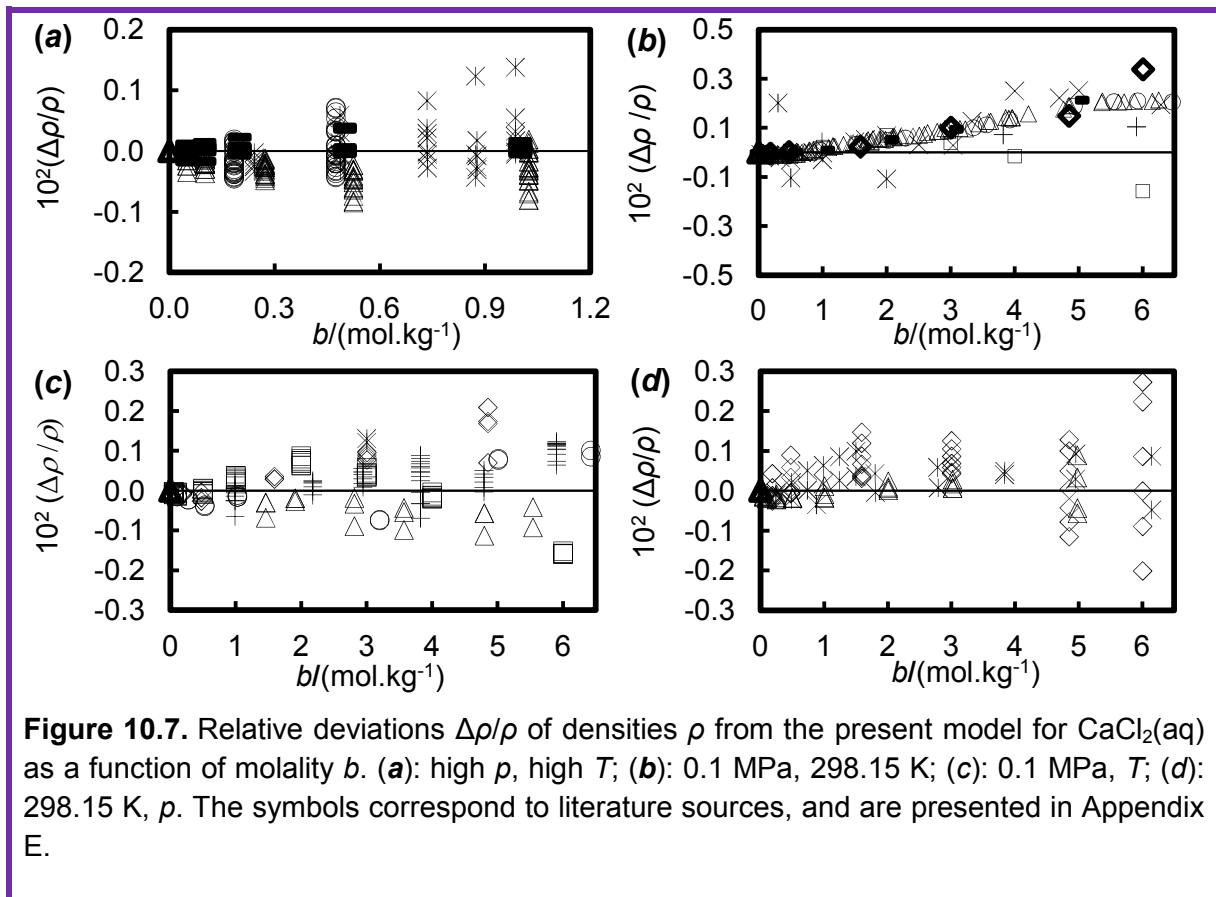


### 10.9 Discussion and Comparison with Experiment

In order to further test the correlations developed in this study, comparisons have been made with the available literature data for the salt systems investigated. There are a large number of literature sources. As discussed above, many of the available data pertain to near ambient conditions of temperature and pressure but wide ranges of molality are covered. For example, the total number of the density data points considered was 1668 for NaCl(aq), 899 for CaCl<sub>2</sub>(aq), 693 for KCl(aq), 506 for MgCl<sub>2</sub>(aq) and 334 for KI(aq). The deviations  $\Delta_{\text{AAD}}$ ,  $\Delta_{\text{Bias}}$  and  $\Delta_{\text{MAD}}$  from Equation 10.10 for each literature source are detailed in the Appendix E together with the number of data points and the temperature, pressure and molality ranges for each.



The average absolute deviation from all literature sources considered are 0.03 %, 0.06 %, 0.04 %, 0.02 %, 0.02 %, 0.10 %, 0.03 %, and 0.01 % for the systems  $\text{MgCl}_2(\text{aq})$ ,  $\text{CaCl}_2(\text{aq})$ ,  $\text{KI}(\text{aq})$ ,  $\text{NaCl}(\text{aq})$ ,  $\text{KCl}(\text{aq})$ ,  $\text{SrCl}_2(\text{aq})$ ,  $\text{Na}_2\text{SO}_4(\text{aq})$ , and  $\text{NaHCO}_3(\text{aq})$  respectively. These values indicate generally good agreement between our results and those available in the literature except for the case of  $\text{SrCl}_2(\text{aq})$ . For this system, the agreement was good with all literature data at ambient pressure and  $T = 298.15 \text{ K}$  but there is a large deviation between our data and those reported by Kumar [408] and Isono [430] at higher temperatures. However, we note that these two literature sources differ considerably. For example, at molalities of around  $2 \text{ mol}\cdot\text{kg}^{-1}$ , the relative deviations between the results reported by Kumar [408] and Isono [430] is around 2%, while our correlation model for this system falls between those literature data.



Generally speaking, the correlation model developed in this work seems to agree reasonably with large available literature data resources. An example showing the relative deviation of literature densities from the correlation model for  $\text{NaCl}(\text{aq})$  as a function of molality is presented in Figures 10.6 (for  $\text{NaCl}$ ) and 10.7 (for  $\text{CaCl}_2$ ). The symbols correspond to the available literature sources for this system. The details of the literature

sources are given in Appendix E. Also in Appendix E, the deviation between the correlation model and experimental data of all other brines studied in this work is given. It can be clearly seen that our model agrees really well with the most of the available data in the literature.

There are a few literature data available for  $[(1-x)\text{NaCl} + x\text{KCl}](\text{aq})$  solution at  $p = 0.1$  MPa,  $T = (298.15 \text{ to } 368.15)$  K and various molalities and mole fractions  $x$ . Figure 10.5b compares the densities obtained from Equation (10.17), with Equation (10.10) for each single-electrolyte solution, with those reported in the literature [440, 460-462, 464-466] for different mole fractions of KCl at  $p = 0.1$  MPa and  $T = (298.15 \text{ to } 368.15)$  K. Most of the data fall well within  $\pm 0.1\%$ .

### 10.10 Evaluation of the Calibration Method

According to Sanmamed et al. [467], in order to implement the assumptions used in equations 10.4 and 10.5 accurately, *(i)* the density uncertainty for the calibration fluid should be as low as possible, *(ii)* the sample density should be bounded by the density values of the two standards, and *(iii)* standards must not present highly different densities in order to maintain the linear response of the equipment. Generally speaking, there is a concern that at wide range of density values, higher than that of the reference fluid, the response of the densimeter is not totally linear. This in fact will lead to large uncertainty at higher density values if only vacuum and a reference fluid is used in the calibration. However, high pressure densimeter was proved to present a linear relationship between measured density and the square value of the period of oscillation. Hence, we believe that extrapolating beyond the reference density should not lead to large error. The actual concern is, as described previously, whether the use of vacuum and one fluid reference is sufficient to give an accurate description of  $A$  and  $B$  coefficients throughout the entire range of measurements.

This is currently being investigated within the group of thermophysical properties. Initial results suggest that the pressure coefficients of  $A$  and  $B$  are actually quite similar but slightly different. However, the simplified calibration strategy followed in our work (Equation 10.4) may fail to give the true values of  $A$  and  $B$  at high pressures. The error arises from an incorrect assumption about the pressure dependence of  $A$  and  $B$ , and can be evaluated. The evaluation, as shown in Appendix F, is based on the assumption that both  $A$  and  $B$  are a linear function of pressure. The error, which arise from the use of Eq(10.4), is found to be proportional to the product of pressure and  $(\rho - \rho_w)$ , where  $\rho$  and  $\rho_w$  are the brine and water

densities at the given pressure and temperature. The density error can be expressed as following:

$$\Delta\rho = B_0(r - r')\beta' p \left( \frac{\tau^2 - \tau_w^2}{r\tau_w^2 - \tau_0^2} \right) \quad 10.18$$

Here, the values of  $B_0$ ,  $\beta$  are obtained from the original calibration data (with water and vacuum) as described in Appendix F. The parameter  $r$  is a measure of the ratio of the pressure dependence of the spring constant to the tube volume. It can be obtained using the following equation, which is based on the expression given in Eq. (19) of Holcomb and Outcalt [468] work.

$$\rho_F = \rho_{0,0}^{(\text{scale})} (1 + \alpha_V t)(1 + \beta_V p) \left[ \frac{\tau^2 (1 + \beta_K p)}{\tau_{0,0}^2 (1 + \alpha_{K,1} t + \alpha_{K,2} t^2)} - 1 \right] \quad 10.19$$

Here  $t$  is the temperature in degrees Celsius or, alternatively, relative to some reference temperature. The model contains seven parameters to describe reliably the wide-ranges of temperature and pressure covered, which can be classified as being associated with either the tube's spring constant, denoted by the subscript  $K$ , or the tube's volume, denoted by the subscript  $V$ . The subscript "0,0" denotes the value of the quantity at  $p = 0 = t$  and the symbols  $\alpha$  and  $\beta$  denote temperature response coefficients and pressure response coefficients, respectively.

The seven parameters are listed in Table 10.7<sup>15</sup>, together with their likely means of estimation, which includes measurements under vacuum, measurements with a reference fluid over a wide range of temperature and pressure and/or, potentially, from literature sources for the tube's material properties. All of the parameters might be determined simultaneously via non-linear least squares regression to calibration data measured under vacuum and with a reference fluid. However, the number of parameters and the likely correlations between them might make the use of only vacuum and water insufficient. A potentially more robust approach is to use two reference fluid with well know densities to find these parameters.

<sup>15</sup> This was suggested by Eric May. He carried the analysis with many different VTD and calibration fluids. Initial results suggest that  $r$  values lie between 1.1 and 1.25 for all VTD used in the analysis.

**Table 10.7.** The seven VTD apparatus parameters used in Equation 10.19

Symbol	Parameter	Determined from
$\rho_{0,0}^{(\text{scale})}$	Density scale factor of evacuated tube at reference temperature	Reference fluid measurements (= mass of empty tube / tube's internal volume)
$\tau_{0,0}$	Resonance period of evacuated tube at reference temperature	Vacuum measurements
$\alpha_{K,1}$	Linear temperature response coefficient of spring constant	Vacuum measurements or material properties estimates
$\alpha_{K,2}$	Quadratic temperature response coefficient of spring constant	High temperature vacuum measurements or material properties estimates
$\beta_K$	Pressure response coefficient of spring constant	High pressure reference fluid measurements
$\alpha_V$	Linear temperature response coefficient of tube volume	Reference fluid measurements or material properties estimates
$\beta_V$	Pressure response coefficient of tube volume	High pressure reference fluid measurements

The parameter  $r$  appears in Eq (10.18) can be then obtained from Eq (10.19) as follows:

$$r = \frac{\beta_V + \beta_K}{\beta_V} \quad 10.20$$

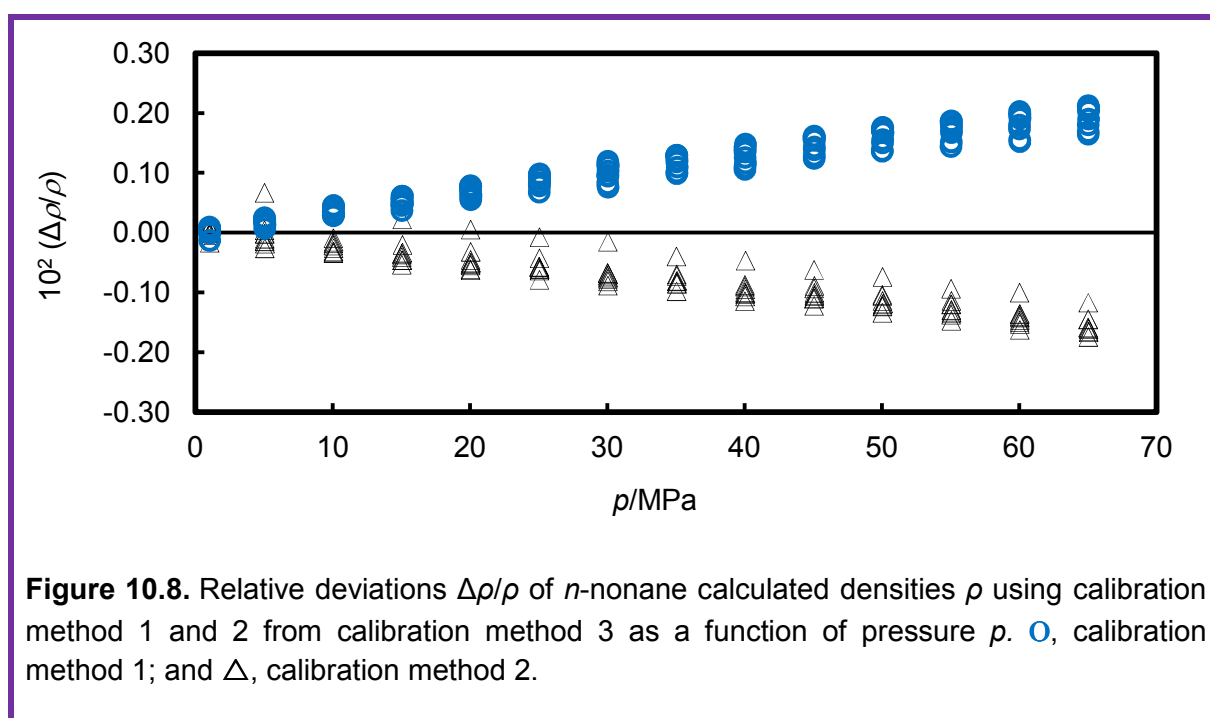
This parameter can be obtained as well by regression (see Appendix F) to the calibration data made with two (or more) reference fluids such as helium and water. The hypothesis of Lagourette et al. [452] (which is used in our density measurements) is that the stiffness parameter  $K$  does not depend on pressure  $p$ . As a result, the value of  $r$  used is actually 1, which we denote as  $r'$  (the original value). Therefore, knowing the real value  $r$ , we should be able to have a rough estimate on the density error which arises from using water and vacuum only during calibration.

To find this, an alternative approach to express the dependence of  $A$  and  $B$  upon pressure was used<sup>16</sup>. In this approach, we make use of two fluids during calibration: water and helium. Both water and helium were calibrated at different pressure and temperature points. The parameters appear in Equation 10.19 were then obtained by regression to the calibration data. The real value of  $r$  was found to be approximately  $r = 1.25$ . Applying this value to

<sup>16</sup> The calibration of these fluids was performed by Tay Weparn

Equation 10.18, and using the heaviest brine we studied ( $\text{SrCl}_2$ ), we found that the density error varies from 0% (at ambient pressures) to around 0.3% at high pressure values.

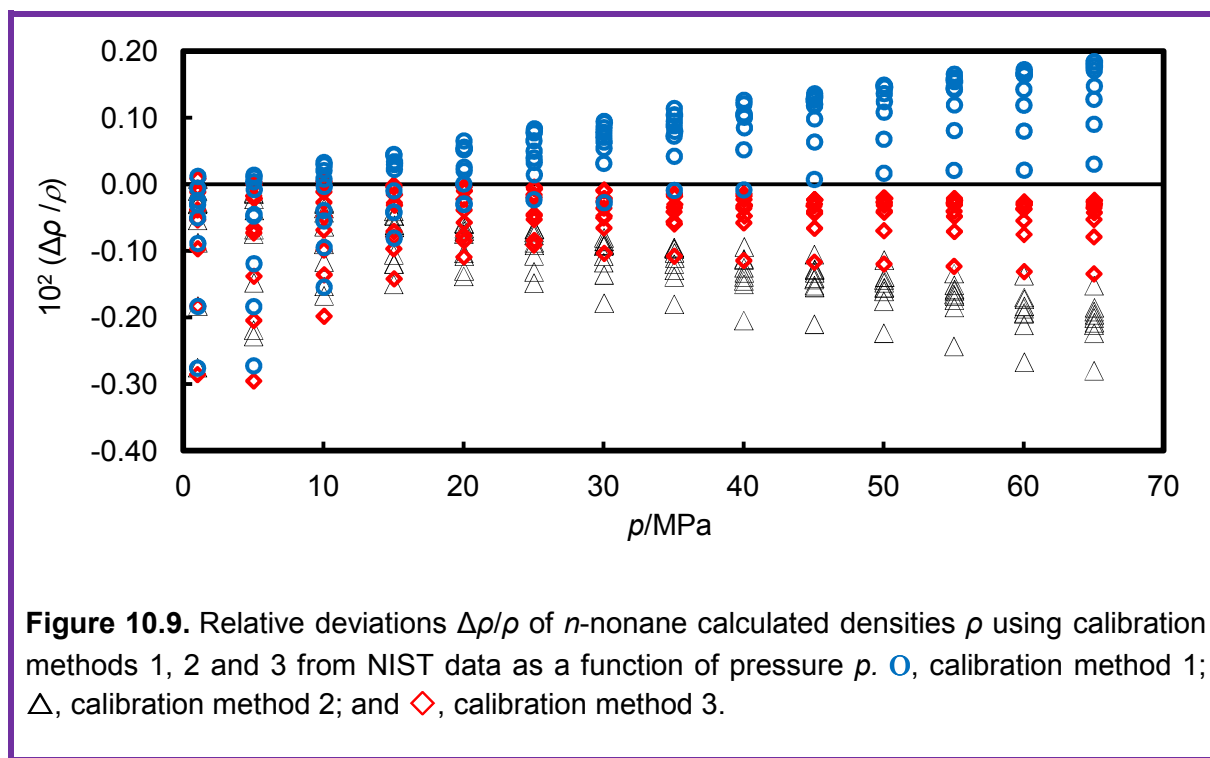
Further investigation regarding the effect of using different calibration methods was conducted. Here we refer to **method 1** ( $A/B$  is independent of pressure, this method is what we used for brines density), **method 2** ( $A$  is only temperature dependent) and **method 3**<sup>17</sup> ( $A$  and  $B$  are pressure and temperature dependent; here we make use of helium and water). The  $n$ -nonane was measured at temperatures range of (283 to 473) K and pressures range up to 70 MPa. The calculated density of  $n$ -nonane from method 1 and 2 were compared with method 3, as shown in Figure 10.8.



It can be clearly seen that there is an observable difference when different calibration approaches are used. The difference is larger at high pressures, as expected. We also compare the calculated densities values from the above three methods with those values reported by NIST, as shown in Figure 10.9. The density values for  $n$ -nonane were obtained from the equation of state developed by Lemmon and Span [469]. The uncertainties in the equation are 0.2% in density in the liquid phase below 430 K and 10 MPa. The uncertainty

<sup>17</sup> Because method 3 relies on the use of two reference fluid during calibration, we consider it more exact (no assumption is used) in determining the pressure dependency of  $A$  and  $B$ ; while other methods are approximate.

below 430 K increases to 0.3% up to 100 MPa while it increases to 0.5% at temperatures higher than 430 K; making such comparison really hard. Nevertheless, from the figure, one can clearly see the difference which arises from using approximate calibration methods.



In summary, the use of water and vacuum seems not to be sufficient to correctly represent the dependency of  $A$  and  $B$  upon pressure. At least, two fluids (such as helium and water) with well known density should be used. This is currently being investigated within the group of thermophysical properties using a wide range of calibration data collected with different types of vibrating tube densimeter. This doesn't only include the error which may arise from incorrect dependence of  $A$  and  $B$  upon pressure, but also the error which may arise when extrapolated beyond the range of the reference fluids used during calibration. A small correction to the reported density values of brines may be applied when this is eventually finalized.

## 10.11 Conclusion

The densities of  $\text{MgCl}_2(\text{aq})$ ,  $\text{CaCl}_2(\text{aq})$ ,  $\text{KI}(\text{aq})$ ,  $\text{NaCl}(\text{aq})$ ,  $\text{KCl}(\text{aq})$ ,  $\text{AlCl}_3(\text{aq})$ ,  $\text{SrCl}_2(\text{aq})$ ,  $\text{Na}_2\text{SO}_4(\text{aq})$ ,  $\text{NaHCO}_3(\text{aq})$ , the mixed salt system  $[(1-x)\text{NaCl} + x\text{KCl}](\text{aq})$  and the synthetic reservoir brine system  $[x_1\text{NaCl} + x_2\text{KCl} + x_3\text{MgCl}_2 + x_4\text{CaCl}_2 + x_5\text{SrCl}_2 + x_6\text{Na}_2\text{SO}_4 + x_7\text{NaHCO}_3](\text{aq})$ , where  $x$  denotes mole fraction, were studied at temperatures between (283

and 473) K and pressures up to 68.5 MPa. The molalities at which the solutions were studied were (1.00, 3.00 and 5.00) mol·kg<sup>-1</sup> for MgCl<sub>2</sub>(aq), (1.00, 3.00 and 6.00) mol·kg<sup>-1</sup> for CaCl<sub>2</sub>(aq), (0.67, 0.90 and 1.06) mol·kg<sup>-1</sup> for KI(aq), (1.06, 3.16 and 6.00) mol·kg<sup>-1</sup> for NaCl(aq), (1.06, 3.15 and 4.49) mol·kg<sup>-1</sup> for KCl(aq), (1.00 and 2.00) mol·kg<sup>-1</sup> for AlCl<sub>3</sub>(aq), (1.022, 2.024 and 3.031) mol·kg<sup>-1</sup> for SrCl<sub>2</sub>(aq), (0.783 and 1.502) mol·kg<sup>-1</sup> for Na<sub>2</sub>SO<sub>4</sub>(aq), and (0.507 and 1.000) mol·kg<sup>-1</sup> for NaHCO<sub>3</sub>(aq) and (1.05, 1.98, 3.15 and 4.95) mol·kg<sup>-1</sup> for [(1 - x)NaCl + xKCl](aq), with x = 0.136. The compositions of the synthetic reservoir brines studied were, first, x<sub>1</sub> = 0.770, x<sub>2</sub> = 0.022, x<sub>3</sub> = 0.040, x<sub>4</sub> = 0.105, x<sub>5</sub> = 0.002, x<sub>6</sub> = 0.044, and x<sub>7</sub> = 0.018 with molality 0.359 mol·kg<sup>-1</sup> and, second, x<sub>1</sub> = 0.797, x<sub>2</sub> = 0.006, x<sub>3</sub> = 0.042, x<sub>4</sub> = 0.145, x<sub>5</sub> = 0.002, x<sub>6</sub> = 0.006, and x<sub>7</sub> = 0.002 with molality 1.900 mol·kg<sup>-1</sup>. The expanded relative uncertainties at 95% confidence are approximately 0.06 % for all the brines studied.

Correlation models were developed for the density of each brine system with relative uncertainties of 0.05 % at 95 % confidence. These are valid in the temperature range (298.15 to 473.15) K and at pressures up to 68.5 MPa for all brines studied except in the case of AlCl<sub>3</sub>(aq) where the temperature is restricted to the range (298.15 to 373.15) K. The correlations are valid for all molalities studied in this work. The correlations were shown to be in good agreement with the available literature data for the brines studied.

A model based on the assumption of zero excess volume of mixing at any given (*T*, *p*, *b*) was tested on predictions of the density of (0.864 NaCl + 0.136 KCl)(aq) and [x<sub>1</sub>NaCl + x<sub>2</sub>KCl + x<sub>3</sub>MgCl<sub>2</sub> + x<sub>4</sub>CaCl<sub>2</sub> + x<sub>5</sub>SrCl<sub>2</sub> + x<sub>6</sub>Na<sub>2</sub>SO<sub>4</sub> + x<sub>7</sub>NaHCO<sub>3</sub>](aq) solutions and was found to agree with the experimental data to within ± 0.05 %. We suggest that the same model may be useful for the density of other mixed brine systems. The data and models presented in this work may be used to obtain derivative properties such as apparent molar volume and compressibility over the (*T*, *p*, *b*) ranges investigated.

Careful attention needs to be paid to the type of calibration method selected. It was observed that the use of water and vacuum is not sufficient to correctly represent the dependency of *A* and *B* coefficients upon pressure. Instead, two fluids with well known density should be used.



# Chapter 11: Conclusions and Recommendations for Future Work

## 11.1 Summary

In this work, the phase behaviour of a number of reservoir fluids has been studied under the addition of carbon dioxide at elevated pressures and temperatures within the context of the data requirements for the design and optimisation of CO<sub>2</sub>-EOR and CO<sub>2</sub>-storage processes. The data gathered in the present study were extensively compared with several predictive equations of state: SAFT-VR, SAFT- $\gamma$ -Mie, PPR78 and PR<sub>2</sub>SRK. These comparisons provide a step forward towards more realistic modelling of reservoir fluids and processes. Two sets of apparatus were used to perform the experimental measurements: a new high-pressure high-temperature synthetic apparatus designed and constructed in this work, and an analytical apparatus with fluid sampling and composition measurements. The synthetic apparatus consisted of a high-pressure high-temperature variable-volume view cell and was used for the measurements on (CO<sub>2</sub> + hydrocarbon) mixtures, while the analytical apparatus was used for the measurements on (CO<sub>2</sub> + hydrocarbon + water) mixtures. The synthetic apparatus was validated by comparison with published isothermal vapour-liquid equilibrium data for the binary system (CO<sub>2</sub> + *n*-heptane) while the analytical apparatus was validated by means of comparison with the published literature data on the binary mixtures (CO<sub>2</sub> + *n*-heptane) and (CO<sub>2</sub> + water). The use of an equation of state that accounts for the asymmetry as well as the possibility of hydrogen bonding (SAFT-VR) was considered suitable for modelling the (CO<sub>2</sub> + hydrocarbon + water) systems, while group contribution approaches (SAFT- $\gamma$ -Mie, PPR78 and PR<sub>2</sub>SRK) were used to model the (CO<sub>2</sub> + hydrocarbon) systems.

Measurements were made over wide ranges of pressure and temperature, including conditions not previously explored in the literature. The vapour-liquid phase behaviour of mixtures containing (CO<sub>2</sub> + *n*-heptane + methylbenzene) was studied at temperature between (298 and 473) K and at pressures up to approximately 16 MPa. The molar ratio of *n*-heptane to methylbenzene in the mixtures was fixed at various values and the bubble-curve and part of the dew-curve was measured under CO<sub>2</sub> addition along different isotherms. The experimental data were then compared with the predictions from SAFT- $\gamma$ -Mie, PPR78 and PR<sub>2</sub>SRK EoSs. It was observed that these approaches predict the VLE with comparable accuracy. The agreement between prediction from SAFT- $\gamma$ -Mie and experimental data, while not perfect, was good, especially on the bubble curve. The results show that the approach of combining, within a SAFT approach, the Mie potential with a

group-contribution scheme for the interaction parameters based on pure- and binary-component data is successful. The agreement between prediction from both PPR78 and PR<sub>2</sub>SRK and the experimental data was also very good. The results show that the approach of combining cubic equation of states with the group-contribution scheme is successful.

Experimental measurements of the phase behaviour of (CO<sub>2</sub> + synthetic crude oil) mixtures were also carried out. The composition of the synthetic oil was chosen to match the physical and chemical properties of a bottom-hole crude oil sample from a Qatari field. The 'dead' oil contained a total of 17 components and live oils were created by adding a three-component solution gas. Experimental results are reported for the dead oil and for two live oils under the addition of CO<sub>2</sub> at temperatures of (298.15, 323.15, 373.15 and 423.15) K and at pressures up to 36 MPa. VLE states were observed at all temperatures; additionally, VLLE and LLE states were measured at the lowest temperature. From the comparison of the experimental results with the published data of CO<sub>2</sub> with real crude oils or ternary hydrocarbon mixtures including CO<sub>2</sub>, one can conclude that the behaviour of the CO<sub>2</sub>-multi-component synthetic oil mixtures is qualitatively similar to the behaviour found in CO<sub>2</sub>-real crude oils or in ternary mixtures containing CO<sub>2</sub> and heavy hydrocarbons such as the CO<sub>2</sub>-CH<sub>4</sub>-C<sub>16</sub>H<sub>34</sub> ternary mixture, both at temperatures below and above those at which the LLE and VLLE regions occur.

The experimental results were compared with the predictions of the PPR78 and PR<sub>2</sub>SRK EoSs. In making this comparison, careful attention was paid to the critical constants and acentric factors of the heavy components in the mixture. The two EoS models were considered in combination with either the 'standard' Soave alpha function or the Boston-Mathias alpha function. It was found that the PPR78, in combination with either alpha function and with no parameters adjusted, generally provided a good description of the bubble pressures for the (CO<sub>2</sub> + dead oil) system. The same model predicted well the pressure at which the VLLE region occurred at  $T = 298.15$  K. The PPR78 with the Soave alpha function also predicted well the bubble pressures of the live oils in the absence of CO<sub>2</sub>. However, discrepancies were found at finite  $x_{\text{CO}_2}$  which suggested that the binary parameter between CO<sub>2</sub> and CH<sub>4</sub> should be adjusted. After optimizing that single parameter at each temperature, quite good agreement was observed with the experimental bubble points, while some discrepancies remained with the dew points. When the Boston-Mathias alpha function was used, it was necessary to adjust the CO<sub>2</sub>-CH<sub>4</sub> and the CH<sub>4</sub>-squalane parameters. The agreement, after adjusting these two parameters, is better than the agreement with the Soave alpha function but this comes at the cost of adjusting an additional parameter.

The PR<sub>2</sub>SRK model was found to predict qualitatively incorrect phase behaviour at  $T = 323.15$  K but, in combination with the standard Soave alpha function, it gave a superior account of the experimental VLE data, including dew points, at  $T = (373.15 \text{ and } 423.15)$  K when the CO<sub>2</sub>-CH<sub>4</sub> binary parameter was optimized. Use of the Boston-Mathias alpha function resulted in some deterioration in comparison with experiment. Overall, the PPR78 model with the Boston-Mathias alpha function performed best in qualitative and quantitative predictions of the phase behaviour observed experimentally. However, this model requires the adjustment of two binary interaction parameters and hence it seems that, on balance, the PPR78 EoS with the Soave alpha function performed best compared to the other options considered.

Several remarks can be made in relation to modelling the phase behaviour of CO<sub>2</sub> + multi-component hydrocarbon mixtures with predictive cubic equation of state. First, very careful attention must be paid to the critical constants and acentric factors of the heavy components. We suggest that comparisons of experimental and calculated binary VLE data for such substances with light components, such as CO<sub>2</sub> and/or CH<sub>4</sub>, may be a good way of discriminating between discrepant critical-point data. Second, we note that the binary interaction parameters between two supercritical components may not be predicted well by group-contribution methods that were developed by fitting binary phase-equilibrium data only. Such binary parameters may require further adjustment. Finally, the transformation of binary parameters to account for different alpha functions may result in erroneous results for pairs of components that differ greatly in volatility. It seems that there is scope for further improvement in the performance of predictive cubic equations of state with respect to the class of mixtures considered in this work.

New experimental data have been measured for the system (carbon dioxide + *n*-heptane + water) under conditions of three-phase vapour-liquid-liquid equilibrium. Compositions of the three coexisting fluid phases have been obtained along five isotherms at temperatures from (323.15 to 413.5) K and at pressures up to the upper critical end point (at which the *n*-heptane-rich and the CO<sub>2</sub>-rich gas phases become critical). The experimental data obtained for this mixture have been compared with the predictions of SAFT-VR with SW potential. In this application of the equation, the models used were kept as consistent as possible with previous studies on (CO<sub>2</sub> + *n*-alkane + H<sub>2</sub>O) systems [87]. Only the unlike dispersion energies between each pair of compounds were modified through binary interaction parameters and these were all temperature independent. The *n*-alkane-water binary interaction parameter was found to be transferable from a previous study with a different *n*-alkane (*n*-decane) and the *n*-alkane-carbon dioxide parameter is predicted using a modified

Hudson-McCoubrey combining rule. The binary interaction parameter for the carbon dioxide-water interaction is taken from previous work [316].

New experimental data have also been measured for the system (carbon dioxide + methane + water) under conditions of two-phase vapour-liquid equilibrium, three-phase vapour-liquid-liquid equilibrium, and four-phase vapour-liquid-liquid-hydrate equilibrium. Compositions of three coexisting fluid phases have been obtained along eight isotherms at temperatures from (285.15 to 303.5) K and at pressures up to either the upper critical end point (UCEP) or up to the hydrate formation locus. Compositions of coexisting vapour and liquid phases have also been obtained along three isotherms at temperatures from (323.15 to 423.15) K and pressures up to 20 MPa. The quadruple curve along which hydrate coexists with the three fluid phases was also measured. The experimental data obtained for this mixture have been compared with the predictions of SAFT-VR with the parameters reported previously by Míguez and co-workers [332]. Only determining the binary interaction parameter for the system CO<sub>2</sub>-H<sub>2</sub>O was found necessary to describe the phase equilibria of this mixture.

From detailed comparison with these two systems, it was concluded that SAFT-VR can predict the observed behaviour reasonably well, which again demonstrates the predictive capabilities of this approach applied to ternary mixtures of alkanes with CO<sub>2</sub> and water. Good agreement between experimental data and theory was observed, and it is worth noting the good performance of the equation in predicting the phase behaviour at different temperatures was achieved even with the use of temperature-independent binary interaction parameters. However, at high pressures, close to the critical region, the equation over-predicts the pressure; this is a known difficulty of classical EoS, which is based in a mean-field approximation and therefore, in practice, treats the density as homogenous. Density fluctuations are however not negligible close to the critical region, where the magnitude of these fluctuations may span from microscopic to macroscopic lengths. Appropriate treatments to incorporate a description of the contribution of such density fluctuations in EoS are thus required. It was also observed that the deviation is considerable even far from the mixture critical region. This is in fact a general limitation of the old SAFT-VR versions (with SW potential); more recent version with Mie potential with the 3<sup>rd</sup> order perturbation expansion will be required to give better agreement.

Furthermore, a detailed study of the ternary mixtures was carried out based on comparison with available data for the constituent binary subsystems. It was concluded that the presence of CO<sub>2</sub> increases slightly the *n*-alkane solubility in the water compared to the binary mixture (*n*-alkane + water). In addition, the presence of *n*-alkane increases slightly the CO<sub>2</sub> solubility

in the water-rich phase compared to the binary mixture (CO<sub>2</sub> + water). The effect of pressure and temperature depends mainly on the trend at which the *n*-alkane to CO<sub>2</sub> ratio changes in the *n*-alkane-rich phase with pressure and temperature. It was also concluded that water content in the CO<sub>2</sub>-rich gas phase decreases because of the presence of *n*-alkane as compared to the binary system CO<sub>2</sub> + water. It was also concluded that the effect of water content on the behaviour of the binary system CO<sub>2</sub> + *n*-alkane was small because of the small amount of water present in the CO<sub>2</sub>-rich gas phase.

The densities of MgCl<sub>2</sub>(aq), CaCl<sub>2</sub>(aq), KI(aq), NaCl(aq), KCl(aq), AlCl<sub>3</sub>(aq), SrCl<sub>2</sub>(aq), Na<sub>2</sub>SO<sub>4</sub>(aq), NaHCO<sub>3</sub>(aq), the mixed salt system [(1 - *x*) NaCl + *x*KCl](aq) and the synthetic reservoir brine system [*x*<sub>1</sub>NaCl + *x*<sub>2</sub>KCl + *x*<sub>3</sub>MgCl<sub>2</sub> + *x*<sub>4</sub>CaCl<sub>2</sub> + *x*<sub>5</sub>SrCl<sub>2</sub> + *x*<sub>6</sub>Na<sub>2</sub>SO<sub>4</sub> + *x*<sub>7</sub>NaHCO<sub>3</sub>](aq), where *x* denotes mole fraction, were studied at temperatures between (283 and 473) K, pressures up to 68.5 MPa and different molalities. Correlations were developed for the density of each brine system with relative uncertainties of 0.05 % at 95 % confidence. These are valid in the temperature range (298.15 to 473.15) K and at pressures up to 68.5 MPa for all brines studied except AlCl<sub>3</sub>(aq) where the temperature is restricted to the range (298.15 to 373.15) K. The correlations are valid for all molalities studied in this work and were shown to be in good agreement with the available literature data. A model based on the assumption of zero excess volume of mixing at any given (*T*, *p*, *b*) was tested in predictions of the density of (0.864 NaCl + 0.136 KCl)(aq) and [*x*<sub>1</sub>NaCl + *x*<sub>2</sub>KCl + *x*<sub>3</sub>MgCl<sub>2</sub> + *x*<sub>4</sub>CaCl<sub>2</sub> + *x*<sub>5</sub>SrCl<sub>2</sub> + *x*<sub>6</sub>Na<sub>2</sub>SO<sub>4</sub> + *x*<sub>7</sub>NaHCO<sub>3</sub>](aq) solutions and was found to agree with the experimental data to within ±0.05 %. We suggest that the same model may be useful for the density of other mixed brine systems. The data and models presented in this work may be used to obtain derivative properties such as apparent molar volume and compressibility over the (*T*, *p*, *b*) ranges investigated. It was observed that careful attention needs to be paid to the type of calibration method selected. Detailed assessment suggests that the use of water and vacuum may not be sufficient to determine the pressure dependency of *A* and *B*. Instead, the use of two fluids with well-known density during calibration is recommended.

Finally, detailed uncertainty analyses were performed for all measurements following the *Guide to the Expression of Uncertainty in Measurements*, GUM [178]. In summary, the combined standard uncertainty of the mole fraction for the systems (CO<sub>2</sub> + *n*-heptane + methylbenzene) and (CO<sub>2</sub> + synthetic oil) was expressed as a function of CO<sub>2</sub> mole fraction, which once applied to these systems, gives uncertainty values in the mole fraction of CO<sub>2</sub> up to 0.00053. The combined standard uncertainty in the mole fractions varies from (0.0001 to 0.004) for the ternary mixture (carbon dioxide + *n*-heptane + water) and from (0.0002 to

0.005) for the ternary mixture (carbon dioxide + methane + water), depending on the phase in question and component analyzed. Finally, the combined standard uncertainty in the density of brines was found to be bounded by a linear function of molality, which once applied to our measured systems, gives uncertainty values in densities varying from (0.2 to 0.3)  $\text{kg}\cdot\text{m}^{-3}$

## 11.2 Contribution of This Work

The current research provided an accurate experimental data for increasingly complex fluid mixtures, including a synthetic live crude oil, integrated with state-of-the-art predictive thermodynamic models. This work is an important stepping stone towards being able to develop predictive equations of state for real reservoir fluids and their mixtures with added fluids such as super-critical  $\text{CO}_2$  with a minimal amount of experimental calibration data. In particular the main contributions of the present work are

- I. The construction and validation of a new apparatus for the measurements of phase behaviour, density and compressibility over wide ranges of pressure and temperature, and involving complex conditions such as VLLE and solid deposition.
- II. The production of a large set of experimental phase-behaviour data for the mixtures ( $\text{CO}_2$  + *n*-heptane + methylbenzene), ( $\text{CO}_2$  + synthetic crude oil), ( $\text{CO}_2$  + *n*-heptane + water) and ( $\text{CO}_2$  + methane + water) over wide range of pressures and temperatures conditions covering VLE, VLLE and LLE together with the measurements of critical points such as UCEPs.
- III. The production of reliable experimental phase-behaviour and saturated liquid density data at reservoir conditions, which can be used in the design and management of different oil and gas applications such as in  $\text{CO}_2$ -EOR and  $\text{CO}_2$  storage processes. This includes, for example,  $\text{CO}_2$ -hydrocarbon miscibility pressures which are required for  $\text{CO}_2$ -EOR applications. Also in  $\text{CO}_2$ -storage process where supercritical  $\text{CO}_2$  is used in these processes, therefore the portions of the phase diagrams involving this region are particularly important as far as this application is concerned.
- IV. The production of a large set of experimental density data for wide range of brines within the context of  $\text{CO}_2$ -storage in saline aquifers, and the development of a correlation approach, as well as the validation of a simple predictive model for the density of mixed brines. In addition, data collected in this work played a key role which enabled further attention to be paid to the type of calibration method selected.

- V. The comparison of the experimental data obtained for the ternary mixtures of the type (CO<sub>2</sub> + *n*-alkane + water) to published binary mixture data to analyse the effects of changing the *n*-alkane component or the addition of a third component in each binary equilibrium, with some conclusions of interest for reservoir processing, mainly in water flooding projects.
- VI. The evaluation and assessment of different predictive models (PPR78, PR<sub>2</sub>SRK, SAFT-VR and SAFT- $\gamma$ -Mie) by means of detailed comparison with our experimental data, with some conclusions of interest for models developments. In most cases, parameters from those obtained from just pure components and binary systems did not need any further adjustment. This shows the remarkable power of SAFT and the group-contribution cubic EoS; this represents a major contribution of this work.
- VII. Providing new experimental data for multi-component mixtures at wide ranges of conditions, coupled with detailed uncertainty analyses, which will be of great importance in the context of data available in the open literature, both in terms of filling the existing gap and in model developments.

## 11.3 Recommendation for Future Work

### 11.3.1 Further Experimental Investigations

Current CO<sub>2</sub> storage implies high purity CO<sub>2</sub> which obviously comes with an energy penalty as both captured CO<sub>2</sub> and naturally available CO<sub>2</sub> contain impurities and a lot of energy is consumed in processes to purify the CO<sub>2</sub>. To reduce such cost, a lower purity specification might be considered. However, the presence of impurities may manipulate the thermophysical properties of CO<sub>2</sub> and its mixtures with reservoir fluids, and may have an impact on reservoir storage integrity; hence there is a need to investigate experimentally their impact on the thermophysical properties of (CO<sub>2</sub> + reservoir fluid) mixtures. These impurities are diluents gases such as O<sub>2</sub>, N<sub>2</sub>, H<sub>2</sub> and other acid gases such as H<sub>2</sub>S and SO<sub>2</sub> which can be extremely corrosive in a wet environment. Unfortunately, a literature review concludes that the available data are scarce, especially for the acid gases. Therefore, there is a need to carry measurements on systems of the type (impurities + hydrocarbon) in a similar manner to the way the (CO<sub>2</sub> + hydrocarbon) mixtures were studied. Such measurements are, however, not easy due to the corrosive nature of these impurities which may damage the integrity of sealing systems and cause corrosion problems. This, however,

can be avoided by selecting compatible materials to these impurities. In addition, measurements of the type (impurities + brines), (impurities + water) and (impurities + hydrocarbon + water) would be interesting as well.

The chemical composition of hydrocarbon reservoir fluids varies widely from field to field and, over time, even from a single production well. Therefore, the study of “synthetic crude oils” with different constituents would be valuable. In these measurements, the effect of changing the synthetic crude oil components and compositions on the phase envelope and miscibility pressures would be studied and analyzed. The selection and identification of different synthetic crude oils could be accomplished following the same steps used for selecting the synthetic crude oil studied in the present work. Another alternative approach would be to fix the components (same synthetic crude oil components as used in the present work) but to change their properties. In this case, the impact of changing the crude oil compositions on phase behaviour and miscibility pressure would be captured. In line with this, another approach would be to study the phase behaviour of CO<sub>2</sub> with real crude oils. The limitation of this is that the crude oil composition is not known in full detail, making it not very useful in terms of being able to predict the properties of other crudes. However, detailed comparison between the phase behaviour of CO<sub>2</sub> with real crude oils and CO<sub>2</sub> with synthetic crude oil will be interesting to study the similarity proximity of the two. If sufficient studies could be accomplished, this could become a useful tool in assaying crudes.

The solubility of carbon dioxide (or impurities) in aqueous solutions plays a key role in numerous processes including CO<sub>2</sub>-EOR, the formation of gas hydrates, seawater desalination and geological carbon storage. Models for the solubility of CO<sub>2</sub> in brines over wide ranges of temperature and pressure are required in many applications. In respect of CO<sub>2</sub>-storage, deep saline aquifers are thought to be the most promising sinks for CO<sub>2</sub> and modelling the long-term fate of CO<sub>2</sub> in such formations depends greatly upon knowledge of the dissolution equilibria. Examination of the literature shows that data relating to the solubility of CO<sub>2</sub> in aqueous solutions at reservoir conditions are scarce. As a consequence, the available models for CO<sub>2</sub> solubility in formation brines are not well validated. Thus there is a need for new measurements which can be used in model validation and improvements. Such measurements can be carried with the current synthetic apparatus setup. The wetting materials are made of HC-276 which makes it compatible with the brines. However, this might not be possible because of the internal dead volume, which -for low solubility- leads to very large uncertainty.



Asphaltene<sup>18</sup> precipitation from reservoir fluids during oil production is a serious problem which can result in plugging of the formation, wellbore and production facilities. Asphaltene precipitation can occur during primary depletion of highly under-saturated reservoirs or during hydrocarbon gas or CO<sub>2</sub> injections in EOR processes or during solvent injection [470]. Many thermodynamic models that describe the phase behaviour of asphaltene precipitation have been reported in the literature. These include, for example, the use of a liquid solubility model, a thermodynamic colloidal model, a colloidal activity-coefficient model, the incorporation of the pure solid model into an EoS [470], and recently PC-SAFT [471] and SAFT-VR [472]. Unfortunately, there are relatively few data in the literature for asphaltene precipitation, in particular the effect of pressure on solid-liquid equilibria. Such data are, however, required to validate and examine these models. Therefore, and as a first approach, providing experimental data for a simple model of asphaltene would be appropriate. A simple model such as polystyrene would be a good approximation [472]. In this case, a certain fraction of alkane to aromatic would be required to solubilise the polystyrene and make a homogenous mixture. Then the asphaltene precipitation under CO<sub>2</sub> addition can be studied for different isotherms. Such measurements can be obtained with the current synthetic apparatus.

In the same line of (carbon dioxide + hydrocarbon + water) experiments, mixtures with other characteristic compounds found in oil, such as branched alkanes, cycloalkanes or aromatics could be studied using the analytical apparatus. In addition, this apparatus can be used to map the ( $p$ ,  $T$ ) envelope at which hydrates form. In this case, different hydrocarbon gases with CO<sub>2</sub> in the presence of water can be studied.

### 11.3.2 Further Apparatus Improvement

The current synthetic apparatus setup can be used for the observation of complex conditions such as asphaltene precipitation and for the study of CO<sub>2</sub> solubility in brines. The measurements of mixtures containing impurities will require the examination of the performance of the sealing system and wetting materials against these impurities, in particular acid gases. Another limitation of the current synthetic apparatus is in obtaining the dew measurements at very high CO<sub>2</sub> concentration and low pressures. At these conditions,

---

<sup>18</sup> Asphaltene are the heaviest, most polar, and non-volatile components of crude oil, defined as the fraction of petroleum insoluble in light hydrocarbons (pentane, hexane, and heptane) but soluble in benzene and toluene. This fraction is usually composed of condensed polyaromatic rings containing aliphatic and naphthenic side chains and sulphur, oxygen, and nitrogen as heteroelements or functional groups.

the amount of liquid present in the mixture is very small, making it impossible to detect the phase transition visually. Therefore, and to expand the measurements range of the apparatus, a light scattering or transmission technique should be implemented. In this approach, the light intensity is continuously measured as a function of time. The dew pressure can then be detected when a sharp drop (or increase) in light intensity occurs during phase transition. This will require the incorporation of light emitting source with adjustable intensity and a receiver, which can be easily incorporated to the current setup. Such a technique can be used as well to detect asphaltene precipitation.

If the system of interest is opaque to visible light (such as heavy crude oil), the determination of bubble or dew points is not possible with the current visualization system. In this case, a near infrared (NIR) technique would be required. This includes, as an example, a halogen light source with visible and NIR output, and a NIR camera system with image-acquisition software. Such a packages can be provided by many suppliers (e.g. Lot-Oriel group), and can be incorporated in the current setup. The lack of phase-sampling techniques limits the capability of the current apparatus. However, the use of phase sampling techniques limits the variety of components which can be studied. For example, heavy crude oil components cannot be studied with the current analytical apparatus. A sampling technique for the gas phase only can be implemented to make the current synthetic apparatus into a semi-analytical apparatus. In this case, a GC system (suitable for the mixtures of interest), a sampling valve for the gas phase (with very small sampling volume) and connecting tubes will be required. Providing a sample valve which can withstand the maximum working pressure (40 MPa) is not easy; this will limit the working pressure of the apparatus. However, ROLSI sampling valves, for example, can stand such pressure but only for non-aqueous systems.

Regarding the analytical apparatus, special care and extra developments would be required to achieve the temperatures needed to avoid condensation of the heavy components in their transfer to the chromatograph; the performance of o-rings and the adequacy of the existing chromatographic separation columns should be examined as well. One of the limitations of this apparatus would be the analysis of the solubility of heavier hydrocarbons in water due to the extremely low values that it can reach. To detect such small amounts, samples of higher volumes would be required with the disadvantage of deteriorating the analysis of water in the chromatograph due to large volumes and consequent overload of the column. Such an analysis of the alkane content in the water-rich phase would thus not be practical to carry out using this approach. The apparatus should be mainly used for light and medium hydrocarbon components.

### 11.3.3 Further Modelling Investigation

In the present study, the experimental data for the (CO<sub>2</sub> + synthetic crude oil) mixtures were only compared with the predictions from predictive cubic EoS. The use of SAFT- $\gamma$ -Mie as a predictive approach for these mixtures would be a good step forwards to examine its predictive capability against phase behaviour and saturated liquid density data collected in this work. This will enable a good comparison between the different predictive models. Further experimental investigations discussed previously should be used to test the predictive capability of these models. For example, such measurements can be used to examine further the group-contribution scheme in the predictive cubic EoS and in SAFT- $\gamma$ -Mie. Different SAFT versions and other predictive approaches (such as PSRK) can be used in these comparisons as well.

As with every group-contribution method, the predictive power of the predictive cubic EoS and SAFT- $\gamma$ -Mie approach depends primarily on the extent of the group parameters available. In order to enhance the predictive power of the methodology presented, the current parameter table has to be extended to include other functional groups that will allow one to model other chemical families. In addition, the introduction of key molecules modeled as single groups, such as water (H<sub>2</sub>O), carbon dioxide (CO<sub>2</sub>) and methane (CH<sub>4</sub>), as well as the binary interaction parameters of these groups with other functional groups will also expand the range of applicability of these methods. Experimental investigations in this context can help expanding the range and type of functional groups.

Finally, the overall target of the approach presented in this work aims for the prediction of the phase behaviour and density of real crude oil-GHG mixtures using predictive equations of state calibrated with minimal amounts of experimental data obtained under as 'mild' conditions as possible – so that this becomes a routine process capable of being carried out in commercial oilfield *pVT* laboratories.

---

## Bibliography

1. IEA, *Energy Technology Perspectives, Scenarios and Strategies to 2050*. 2008.
2. IEA, *Technology Roadmap for Carbon Capture and Storage*. International Energy Agency, 2013. **available online:** [www.iea.org](http://www.iea.org).
3. IEA, *CO<sub>2</sub> capture, storage offer emissions solution*. Oil Gas J., 2005. **103.2**: p. 29-30.
4. IEA, *CO<sub>2</sub> Capture and Storage: a key carbon abatement option*. OECD/IEA, Paris, 2008.
5. In: Metz, B., Davidson, O., de Coninck, H.C., Loos, M. and Mayer, L.A. (Eds.), *Special Report on Carbon Dioxide Capture and Storage*. Intergovernmental Panel on Climate Change (IPCC), 2005. **Cambridge University Press**: p. 195-276.
6. WRI, *CCS Guidelines: Guidelines for carbon dioxide capture, transport, and storage*. Washington, DC, World Resources Institute,, 2008: p. 144.
7. Han, W.S., et al., *Evaluation of trapping mechanisms in geologic CO<sub>2</sub> sequestration: Case study of SACROC northern platform, a 35-year CO<sub>2</sub> injection site*. American Journal of Science, 2010. **310**(4): p. 282-324.
8. Aarnes, J., Carpenter, M., Flach, T., Solomon, S., Sollie, O. K., and K. Johnsen, and Rsnos, O., *Guideline for Selection and Qualication of Sites and Projects for Geological Storage of CO<sub>2</sub>*. Technical Report, Det Norske Veritas, 2009.
9. Dance, T., *Assessment and Geological characterisation of the CO<sub>2</sub>CRC Otway Project CO<sub>2</sub> storage demonstration site: from prefeasibility to injection*. Marine and Petroleum Geology, 2013(0).
10. Manrique, E.J., et al., *EOR: Current Status and Opportunities*, in *SPE Improved Oil Recovery Symposium*. 2010, SPE: Tulsa, Oklahoma, USA.
11. Surguchev, D.L., D.E. Manrique, and P.V. Alvarado, *Improved Oil Recovery: Status And Opportunities*. 2005, World Petroleum Congress.
12. Holstein, E.D., *Status And Outlook For Enhanced Oil Recovery By Chemical Injection*. 1982, API.
13. Henry, J.D., *Status And Outlook For Oil Recovery Using Carbon Dioxide Injection Operations*. 1981, API.
14. Brashear, J.P. and V.A. Kuuskraa, *The Potential and Economics of Enhanced Oil Recovery*. J Petrol Technol, 1978. **30**(9): p. 1231-1239.
15. Ghedan, S.G., *Global Laboratory Experience of CO<sub>2</sub>-EOR Flooding*, in *SPE/EAGE Reservoir Characterization and Simulation Conference*. 2009, SPE: Abu Dhabi, UAE.
16. Elsharkawy, A.M., F.H. Poettmann, and R.L. Christiansen, *Measuring Minimum Miscibility Pressure: Slim-Tube or Rising-Bubble Method?*, in *SPE/DOE Enhanced Oil Recovery Symposium*. 1992, 1992 Copyright 1992, Soc Petrol Eng Inc.: Tulsa, Oklahoma.

17. Christiansen, R.L. and H.K. Haines, *Rapid Measurement of Minimum Miscibility Pressure With the Rising-Bubble Apparatus*. SPE Resev Eng, 1987. **2**(4): p. 523-527.
18. Rao, D.N., *A New Technique of Vanishing Interfacial Tension for Miscibility Determination*. Fluid Phase Equilib., 1997. **139**: p. 311.
19. Nobakht, M., S. Moghadam, and Y. Gu, *Determination of CO<sub>2</sub> Minimum Miscibility Pressure from Measured and Predicted Equilibrium Interfacial Tensions*. Ind. Eng. Chem. Res., 2008. **47**(22): p. 8918-8925.
20. Shokir, E.M.E.-M., *CO<sub>2</sub>-Oil Minimum Miscibility Pressure Model For Impure And Pure CO<sub>2</sub> Streams*. 2007, Offshore Mediterranean Conference.
21. Dong, M., S. Huang, and R. Srivastava, *Effect of Solution Gas in Oil on CO<sub>2</sub> Minimum Miscibility Pressure*. J. Can. Pet. Technol., 2000. **39**(11).
22. *Qatar Carbonates and Carbon Storage Research Centre (QCCSRC)*  
<http://www3.imperial.ac.uk/qatarcarbonatesandcarbonstorage>.
23. Nagarajan, N.R., M.M. Honarpour, and K. Sampath, *Reservoir-Fluid Sampling and Characterization-Key to Efficient Reservoir Management*. J. Pet. Tech, 2007. **59**(8): p. 80-91.
24. Brunner, G., J. Teich, and R. Dohrn, *Phase equilibria in systems containing hydrogen, carbon dioxide, water and hydrocarbons*. Fluid Phase Equilib., 1994. **100**(0): p. 253-268.
25. Neau, E., J.N. Jaubert, and M. Rogalski, *Characterization of heavy oils*. Ind. Eng. Chem. Res., 1993. **32**(6): p. 1196-1203.
26. Jaubert, J.-N., et al., *Phase equilibria measurements and modeling of EPA and DHA ethyl esters in supercritical carbon dioxide*. J. Supercrit. Fluids, 2001. **20**(2): p. 145-155.
27. Chiu, H.-Y., et al., *Vapor-liquid phase equilibrium behavior of mixtures containing supercritical carbon dioxide near critical region*. J. Supercrit. Fluids, 2008. **44**(3): p. 273-278.
28. Eustaquio-Rincón, R. and A. Trejo, *Solubility of n-octadecane in supercritical carbon dioxide at 310, 313, 333, and 353 K, in the range 10-20 MPa*. Fluid Phase Equilib., 2001. **185**(1-2): p. 231-239.
29. Beckman, E.J., *Supercritical and near-critical CO<sub>2</sub> in green chemical synthesis and processing*. J. Supercrit. Fluids, 2004. **28**(2-3): p. 121-191.
30. Jessop, P.G., et al., *Homogeneous Catalysis in Supercritical Fluids: Hydrogenation of Supercritical Carbon Dioxide to Formic Acid, Alkyl Formates, and Formamides*. J. Am. Chem. Soc., 1996. **118**(2): p. 344-355.
31. Bach, I., *Hydroformylation of hex-1-ene in supercritical carbon dioxide catalysed by rhodium trialkylphosphine complexes*. Chem. Commun., 1998. **0**(14): p. 1463-1464.

32. Romack, T.J., E.E. Maury, and J.M. DeSimone, *Precipitation Polymerization of Acrylic Acid in Supercritical Carbon Dioxide*. *Macromolecules*, 1995. **28**(4): p. 912-915.
33. Haruki, M., et al., *High pressure phase behavior for the supercritical ethylene + cyclohexane + hexane + polyethylene systems*. *J. Supercrit. Fluids*, 2009. **49**(2): p. 125-134.
34. Jaubert, J.-N. and F. Mutelet, *VLE predictions with the Peng–Robinson equation of state and temperature dependent  $k_{ij}$  calculated through a group contribution method*. *Fluid Phase Equilib.*, 2004. **224**(2): p. 285-304.
35. Jaubert, J.-N. and R. Privat, *Relationship between the binary interaction parameters ( $k_{ij}$ ) of the Peng–Robinson and those of the Soave–Redlich–Kwong equations of state: Application to the definition of the PR<sub>2</sub>SRK model*. *Fluid Phase Equilib.*, 2010. **295**(1): p. 26-37.
36. Jaubert, J.-N., et al., *Reliability of the correlation allowing the  $k_{ij}$  to switch from an alpha function to another one in hydrogen-containing systems*. *Fluid Phase Equilib.*, 2013. **338**(0): p. 23-29.
37. Galindo, A.D., L. A.; Gil-Villegas, A.; Jackson, G. , *The thermodynamics of mixtures and the corresponding mixing rules in the SAFT-VR approach for potentials of variable range*. *Mol. Phys*, 1998. **93**(2): p. 241-252.
38. Gil-Villegas, A., et al., *Statistical associating fluid theory for chain molecules with attractive potentials of variable range*. *J. Chem. Phys.*, 1997. **106**(10): p. 4168-4186.
39. Papaioannou, V., *A molecular-based group contribution equation of state for the description of fluid phase behaviour and thermodynamic derivative properties of mixtures (SAFT- $\gamma$  Mie)*, in *Chemical Engineering*. 2012, Imperial College London: London.
40. Prausnitz, J., Lichtenthaler, R., and de Azevedo, E. G., *Molecular Thermodynamics of Fluid-Phase Equilibria*. 1999.
41. Loos, T.W.D., *Understanding phase diagrams, Supercritical Fluids, Fundamentals for Application*. *J Appl. Sci*, 1994. **273**: p. 65-89.
42. Scott, P.H.V.K.a.R.L., *Critical Lines and Phase Equilibria in Binary Van Der Waals Mixtures* *Philos. Trans. R. Soc. A*, 1980. **298**: p. 495-540.
43. Scott, R.L. and P.H. van Konynenburg, *Static properties of solutions. Van der Waals and related models for hydrocarbon mixtures*. *Discuss. Faraday Soc*, 1970. **49**(0): p. 87-97.
44. Webster, L.A., *Vapor-liquid equilibria for the methane-propane-carbon dioxide systems at 230 K and 270 K*. *J. Chem. Eng. Data*, 2001. **46**(3): p. 759.
45. Vitu, S., et al., *Predicting the phase equilibria of CO<sub>2</sub> + hydrocarbon systems with the PPR78 model (PR EOS and  $k_{ij}$  calculated through a group contribution method)*. *J. Supercrit. Fluids*, 2008. **45**(1): p. 1-26.

46. Schneider, G.M., *High-pressure investigations on fluid systems--a challenge to experiment, theory, and application*. J. Chem. Thermodyn., 1991. **23**(4): p. 301-326.
47. Rodriguez-Reartes, S.B., et al., *High-pressure phase equilibria of systems carbon dioxide + n-eicosane and propane + n-eicosane*. J. Supercrit. Fluids, 2009. **50**(3): p. 193-202.
48. Enick, R., G.D. Holder, and B.I. Morsi, *Critical and three phase behavior in the carbon dioxide/tridecane system*. Fluid Phase Equilib., 1985. **22**(2): p. 209-224.
49. Raeissi, S., K. Gauter, and C.J. Peters, *Fluid multiphase behavior in quasi-binary mixtures of carbon dioxide and certain 1-alkanols*. Fluid Phase Equilib., 1998. **147**(1-2): p. 239-249.
50. Fall, D.J., J.L. Fall, and K.D. Luks, *Liquid-liquid-vapor immiscibility limits in carbon dioxide + n-paraffin mixtures*. J. Chem. Eng. Data, 1985. **30**(1): p. 82-88.
51. Lansangan, R.M., A. Jangkamolkulchai, and K.D. Luks, *Binary vapor-liquid equilibria behavior in the vicinity of liquid-liquid-vapor loci*. Fluid Phase Equilib., 1987. **36**: p. 49-66.
52. Bluma, M. and U.K. Deiters, *A classification of phase diagrams of ternary fluid systems*. Physical Chemistry Chemical Physics, 1999. **1**(18): p. 4307-4313.
53. Waals, J.D.v.d., *Ph. D. Thesis*. 1873, University of Leiden: Leiden.
54. Lorentz, H.A., *Ueber die Anwendung des Satzes vom Virial in der kinetischen Theorie der Gase*. Annalen der Physik, 1881. **248**(1): p. 127-136.
55. Lopes, J.N.C., *On the classification and representation of ternary phase diagrams: The yin and yang of a T-x approach*. PCCP, 2004. **6**(9): p. 2314-2319.
56. Benham, A.L., W.E. Dowden, and W.J. Kunzman, *Miscible Fluid Displacement - Prediction of Miscibility*. 1960.
57. Fall, J.L. and K.D. Luks, *Effect of additive gases on the liquid-liquid-vapor immiscibility of the carbon dioxide + n-nonadecane mixtures*. J. Chem. Eng. Data, 1986. **31**(3): p. 332-336.
58. Smith, G.R. and C.J. Wormald, *Solubilities of naphthalene in (CO<sub>2</sub> + C<sub>2</sub>H<sub>6</sub>) and (CO<sub>2</sub> + C<sub>3</sub>H<sub>8</sub>) up to 333 K and 17.7 MPa*. Fluid Phase Equilib., 1990. **57**(1-2): p. 205-222.
59. Hottovy, J.D., J.P. Kohn, and K.D. Luks, *Partial miscibility behavior of the ternary systems methane-propane-n-octane, methane-n-butane-n-octane, and methane-carbon dioxide-n-octane*. J. Chem. Eng. Data, 1982. **27**(3): p. 298-302.
60. Merrill, R.C., K.D. Luks, and J.P. Kohn, *Three-phase liquid-liquid-vapor equilibriums in the methane + n-pentane + n-octane, methane + n-hexane + n-octane, and methane + n-hexane + carbon dioxide systems*. J. Chem. Eng. Data, 1983. **28**(2): p. 210-215.
61. Orr, F.M. and C.M. Jensen, *Interpretation of Pressure-Composition Phase-Diagrams for CO<sub>2</sub> Crude-Oil Systems*. Soc Petrol Eng J, 1984. **24**(5): p. 485-497.

62. Henry, R.L. and R.S. Metcalfe, *Multiple-Phase Generation during Carbon-Dioxide Flooding*. Soc Petrol Eng J, 1983. **23**(4): p. 595-601.
63. Fonseca, J.M.S., R. Dohrn, and S. Peper, *High-pressure fluid-phase equilibria: Experimental methods and systems investigated (2005–2008)*. Fluid Phase Equilib., 2011. **300**(1–2): p. 1-69.
64. Fornari, R.E., P. Alessi, and I. Kikic, *High pressure fluid phase equilibria: experimental methods and systems investigated (1978-1987)*. Fluid Phase Equilib., 1990. **57**(1-2): p. 1-33.
65. Dohrn, R., *High-pressure fluid-phase equilibria: Experimental methods and systems investigated (1988–1993)*. Fluid Phase Equilib., 1995. **106**(1): p. 213-282.
66. Christov, M. and R. Dohrn, *High-pressure fluid phase equilibria: Experimental methods and systems investigated (1994-1999)*. Fluid Phase Equilib., 2002. **202**(1): p. 153-218.
67. Dohrn, R., *High-pressure fluid-phase equilibria: Experimental methods and systems investigated (2000–2004)*. Fluid Phase Equilib., 2010. **288**(1): p. 1-54.
68. Haruki, M., et al., *Measurement and Correlation of Phase Equilibria for Water + Hydrocarbon Systems near the Critical Temperature and Pressure of Water*. Ind. Eng. Chem. Res., 2000. **39**(12): p. 4516-4520.
69. Minicucci, D., X.Y. Zou, and J.M. Shaw, *The impact of liquid-liquid-vapour phase behaviour on coke formation from model coke precursors*. Fluid Phase Equilib., 2002. **194-197**: p. 353-360.
70. May, E.F., et al., *An improved microwave apparatus for phase behaviour measurements in lean gas condensate fluids*. Fluid Phase Equilib., 2004. **215**(2): p. 245-252.
71. Ngo, T.T., et al., *Spectroscopic measurement of solid solubility in supercritical fluids*. AIChE Journal, 2001. **47**(11): p. 2566-2572.
72. Oag, R.M., et al., *Probing the Vapor–Liquid Phase Behaviors of Near-Critical and Supercritical Fluids Using a Shear Mode Piezoelectric Sensor*. Anal. Chem., 2003. **75**(3): p. 479-485.
73. Sato, Y., et al., *Compact apparatus for rapid measurement of high-pressure phase equilibria of carbon dioxide expanded liquids*. Fluid Phase Equilib., 2010. **296**(1): p. 25-29.
74. Smith, C.R. Tracy, and G.W.F.R. Lance, *Applied reservoir engineering*. 1992, Tulsa, Okla.: OGCI Publications, Oil & Gas Consultants International.
75. Corbett, P.W.M., *PVT and Phase Behaviour of Petroleum Reservoir Fluids*. Marine and Petroleum Geology. Vol. 17. 2000. 558-559.
76. Moses, P.L., *Engineering Applications of Phase Behavior of Crude Oil and Condensate Systems (includes associated papers 16046, 16177, 16390, 16440, 19214 and 19893)*. SPE Journal of Petroleum Technology, 1986. **38**(7): p. 715-723.



77. Shariati, A., C.J. Peters, and M. Moshfeghian, *Further evaluation of the Shariati-Peters-Moshfeghian  $C_7^+$  characterization method*. Fluid Phase Equilib., 2001. **179**(1-2): p. 23-41.
78. Hosein, R., W.D. McCain, and T. Jagai, *How to Extend the Heptanes plus Fraction for Gas Condensate Systems for Use in Compositional Simulation*, in *Europec/EAGE Conference and Exhibition*. 2008, SPE: Rome, Italy.
79. Vitu, S., et al., *Bubble and Dew Points of Carbon Dioxide + a Five-Component Synthetic Mixture: Experimental Data and Modeling with the PPR78 Model*. J. Chem. Eng. Data, 2007. **52**(5): p. 1851-1855.
80. Shariati, A., C.J. Peters, and M. Moshfeghian, *Bubble Point Pressures of Some Selected Carbon Dioxide + Synthetic  $C_6^+$  Mixtures*. J. Chem. Eng. Data, 1998. **43**(5): p. 785-788.
81. Orr Jr., F.M., A.D. Yu, and C.L. Lien, *Phase Behavior of  $CO_2$  and Crude Oil in Low-Temperature Reservoirs*. Soc Petrol Eng J, 1981. **21**(4): p. 480-492.
82. Gardner, J.W., F.M. Orr, and P.D. Patel, *The Effect of Phase Behavior on  $CO_2$ -Flood Displacement Efficiency*. J Petrol Technol, 1981. **33**(11): p. 2067-2081.
83. Rathmell, J.J., F.I. Stalkup, and R.C. Hassinger, *A Laboratory Investigation of Miscible Displacement by Carbon Dioxide*, in *Fall Meeting of the Society of Petroleum Engineers of AIME*. 1971, 1971 Copyright 1971: New Orleans, Louisiana.
84. Turek, E.A., R.S. Metcalfe, and R.E. Fishback, *Phase Behavior of Several  $CO_2$ / West Texas-Reservoir-Oil Systems*. SPE Reserv Eng, 1988. **3**(2): p. 505-516.
85. Simon, R., A. Rosman, and E. Zana, *Phase-Behavior Properties of  $CO_2$  - Reservoir Oil Systems*. Soc Petrol Eng J, 1978. **18**(1): p. 20-26.
86. Orr Jr., F.M. and C.M. Jensen, *Interpretation of Pressure-Composition Phase Diagrams for  $CO_2$ /Crude-Oil Systems*. Soc Petrol Eng J, 1984. **24**(5): p. 485-497.
87. Forte, E., A. Galindo, and J.P.M. Trusler, *Experimental and Molecular Modeling Study of the Three-Phase Behavior of (*n*-Decane + Carbon Dioxide + Water) at Reservoir Conditions*. J. Phys. Chem. B, 2011. **115**(49): p. 14591-14609.
88. Forte, E., A. Galindo, and J.P.M. Trusler, *Experimental and molecular modelling study of the three-phase behaviour of (propane + carbon dioxide + water) at reservoir conditions*. J. Supercrit. Fluids, 2013. **75**(0): p. 30-42.
89. Qin, J.F., *Experimental measurements of vapor-liquid equilibria of the  $H_2O + CO_2 + CH_4$  ternary system*. J. Chem. Eng. Data, 2008. **53**(6): p. 4-4.
90. Dhima, A., J.-C. de Hemptinne, and J. Jose, *Solubility of Hydrocarbons and  $CO_2$  Mixtures in Water under High Pressure*. Ind. Eng. Chem. Res., 1999. **38**(8): p. 3144-3161.
91. Song, K.Y. and R. Kobayashi, *The water content of a carbon dioxide-rich gas mixture containing 5.31 Mol % methane along the three-phase and supercritical conditions*. J. Chem. Eng. Data, 1990. **35**(3): p. 320-322.

92. Jarne, C., et al., *Dew Points of Ternary Methane (or Ethane) + Carbon Dioxide + Water Mixtures: Measurement and Correlation*. Energy Fuels, 2004. **18**(2): p. 396-404.
93. Gil, L., et al., *Dew Points of Binary Propane or n-butane + Carbon Dioxide, Ternary Propane or n-butane + Carbon Dioxide + Water, and Quaternary Propane or n-butane + Carbon Dioxide + Water + Methanol Mixtures: Measurement and Modeling*. Ind. Eng. Chem. Res., 2006. **45**(11): p. 3974-3980.
94. Golombok, M., et al., *Resolving CO<sub>2</sub> and methane hydrate formation kinetics*. Environ Chem Lett, 2009. **7**(4): p. 325-330.
95. Georgios M. Kontogeorgis, G.K.F., *Thermodynamic Models for Industrial Applications: From Classical and Advanced Mixing Rules to Association Theories*. 2010.
96. Mason, E.A. and T.H. Spurling, *The virial equation of state, by E. A. Mason and T. H. Spurling*. [1st ed.] ed. 1969, Oxford, New York,: Pergamon Press. xi, 297 p.
97. Benedict, M., G.B. Webb, and L.C. Rubin, *An Empirical Equation for Thermodynamic Properties of Light Hydrocarbons and Their Mixtures I. Methane, Ethane, Propane and n-Butane*. The Journal of Chemical Physics, 1940. **8**(4): p. 334-345.
98. Beattie, J.A. and O.C. Bridgeman, *A new Equation of state for Fluids.I. Application to Gaseous Ethyl Ether and Carbon Dioxide*. J. Am. Chem. Soc., 1927. **49**(7): p. 1665-1667.
99. Starling, K.E., *A New Approach for Determining Equation-of-State Parameters Using Phase Equilibria Data*. 1966. **6**(4): p. 363 - 371.
100. Starling, K.E., *Fluid thermodynamic properties for light petroleum systems*. 1973, Houston: Gulf Pub. Co.
101. Soave, G., *Equilibrium constants from a modified Redlich-Kwong equation of state*. Chem. Eng. Sci., 1972. **27**(6): p. 1197-1203.
102. Peng, D.-Y. and D.B. Robinson, *A New Two-Constant Equation of State*. Ind. Eng. Chem. Fun, 1976. **15**(1): p. 59-64.
103. Romain, P. and J. Jean-Noël, *Thermodynamic Models for the Prediction of Petroleum-Fluid Phase Behaviour*. Crude Oil Emulsions-Composition Stability and Charecterization. Vol. Chapter 5. 2012.
104. Redlich, O. and J.N.S. Kwong, *On the Thermodynamics of Solutions. V. An Equation of State. Fugacities of Gaseous Solutions*. Chem. Rev., 1949. **44**(1): p. 233-244.
105. Zudkevitch, D. and J. Joffe, *Correlation and prediction of vapor-liquid equilibria with the redlich-kwong equation of state*. AIChE Journal, 1970. **16**(1): p. 112-119.
106. Pitzer, K.S., et al., *The Volumetric and Thermodynamic Properties of Fluids. II. Compressibility Factor, Vapor Pressure and Entropy of Vaporization1*. J. Am. Chem. Soc., 1955. **77**(13): p. 3433-3440.

107. Marc J. Assael, J.P.M.T., Thomas F.Tsolakis, *THERMOPHYSICAL PROPERTIES OF FLUIDS. An Introduction to their Prediction*. 1996: Imperial College London
108. Ghosh, P., *Prediction of Vapor-Liquid Equilibria Using Peng-Robinson and Soave-Redlich-Kwong Equations of State*. Chemical Engineering & Technology, 1999. **22**(5): p. 379-399.
109. Mathias, P.M. and T.W. Copeman, *Extension of the Peng-Robinson equation of state to complex mixtures: Evaluation of the various forms of the local composition concept*. Fluid Phase Equilib., 1983. **13**(0): p. 91-108.
110. Stryjek, R. and J.H. Vera, *PRSV: An improved Peng-Robinson equation of state for pure compounds and mixtures*. Can. J. Chem. Eng., 1986. **64**(2): p. 323-333.
111. Neau, E., et al., *The Soave, Twu and Boston–Mathias alpha functions in cubic equations of state: Part I. Theoretical analysis of their variations according to temperature*. Fluid Phase Equilib., 2009. **276**(2): p. 87-93.
112. Twu, C.H., et al., *A cubic equation of state with a new alpha function and a new mixing rule*. Fluid Phase Equilib., 1991. **69**(0): p. 33-50.
113. Twu, C.H., J.E. Coon, and J.R. Cunningham, *A new generalized alpha function for a cubic equation of state Part 1. Peng-Robinson equation*. Fluid Phase Equilib., 1995. **105**(1): p. 49-59.
114. Twu, C.H., J.E. Coon, and J.R. Cunningham, *A new generalized alpha function for a cubic equation of state Part 2. Redlich-Kwong equation*. Fluid Phase Equilib., 1995. **105**(1): p. 61-69.
115. Neau, E., et al., *The Soave, Twu and Boston–Mathias alpha functions in cubic equations of state. Part II. Modeling of thermodynamic properties of pure compounds*. Fluid Phase Equilib., 2009. **276**(2): p. 156-164.
116. Péneloux, A., E. Rauzy, and R. Fréze, *A consistent correction for Redlich-Kwong-Soave volumes*. Fluid Phase Equilib., 1982. **8**(1): p. 7-23.
117. Corbett, P.W.M., *PVT and Phase Behaviour of Petroleum Reservoir Fluids: Ali Danesh, Elsevier, 1998, ISBN 0 444 82196 1, 220 NLG (approx. £83)*. Marine and Petroleum Geology. Vol. 17. 2000. 558-559.
118. Huron, M.-J. and J. Vidal, *New mixing rules in simple equations of state for representing vapour-liquid equilibria of strongly non-ideal mixtures*. Fluid Phase Equilib., 1979. **3**(4): p. 255-271.
119. Wong, D.S.H. and S.I. Sandler, *A theoretically correct mixing rule for cubic equations of state*. AIChE J., 1992. **38**(5): p. 671-680.
120. Michelsen, M.L., *A modified Huron-Vidal mixing rule for cubic equations of state*. Fluid Phase Equilib., 1990. **60**(1–2): p. 213-219.
121. Holderbaum, T. and J. Gmehling, *PSRK: A Group Contribution Equation of State Based on UNIFAC*. Fluid Phase Equilib., 1991. **70**(2–3): p. 251-265.

122. Dahl, S. and M.L. Michelsen, *High-pressure vapor-liquid equilibrium with a UNIFAC-based equation of state*. AIChE J., 1990. **36**(12): p. 1829-1836.
123. Vitu, S., et al., *Phase equilibria measurements of CO<sub>2</sub> + methyl cyclopentane and CO<sub>2</sub> + isopropyl cyclohexane binary mixtures at elevated pressures*. J. Supercrit. Fluids, 2008. **44**(2): p. 155-163.
124. Vitu, S., et al., *High-pressure phase behaviour of the binary system CO<sub>2</sub> + cis-decalin from (292.75 to 373.75) K*. J. Chem. Thermodyn., 2008. **40**(9): p. 1358-1363.
125. Vitu, S., J.-N. Jaubert, and F. Mutelet, *Extension of the PPR78 model (Predictive 1978, Peng–Robinson EOS with temperature dependent  $k_{ij}$  calculated through a group contribution method) to systems containing naphthenic compounds*. Fluid Phase Equilib., 2006. **243**(1–2): p. 9-28.
126. Jaubert, J.-N., et al., *Extension of the PPR78 model (predictive 1978, Peng–Robinson EOS with temperature dependent  $k_{ij}$  calculated through a group contribution method) to systems containing aromatic compounds*. Fluid Phase Equilib., 2005. **237**(1–2): p. 193-211.
127. Aspen Technology, *Aspen Properties, version 7.3*. 2011.
128. Wilson, G.M., *Vapor-Liquid Equilibrium. XI. A New Expression for the Excess Free Energy of Mixing*. J. Am. Chem. Soc., 1964. **86**(2): p. 127-130.
129. Renon, H. and J.M. Prausnitz, *Local compositions in thermodynamic excess functions for liquid mixtures*. AIChE Journal, 1968. **14**(1): p. 135-144.
130. Abrams, D.S. and J.M. Prausnitz, *Statistical thermodynamics of liquid mixtures: A new expression for the excess Gibbs energy of partly or completely miscible systems*. AIChE Journal, 1975. **21**(1): p. 116-128.
131. Wilson, G.M. and C.H. Deal, *Activity Coefficients and Molecular Structure. Activity Coefficients in Changing Environments-Solutions of Groups*. Ind. Eng. Chem. Fundam., 1962. **1**(1): p. 20-23.
132. Fredenslund, A., et al., *Computerized Design of Multicomponent Distillation Columns Using the UNIFAC Group Contribution Method for Calculation of Activity Coefficients*. Ind Eng Chem, Process Des Dev, 1977. **16**(4): p. 450-462.
133. Onken, U., J. Rarey-Nies, and J. Gmehling, *The Dortmund Data Bank: A computerized system for retrieval, correlation, and prediction of thermodynamic properties of mixtures*. Int. J. Thermophys., 1989. **10**(3): p. 739-747.
134. J.V. SENGHER, R.F.K., C.J. PETERS and H.J. WHITE, Jr., *Equations of State for Fluids and Fluid Mixtures*. 2000.
135. Wertheim, M.S., *Thermodynamic perturbation theory of polymerization*. J. Chem. Phys., 1987. **87**(12): p. 7323-7331.
136. Wertheim, M.S., *Fluids of dimerizing hard spheres, and fluid mixtures of hard spheres and dispheres*. J. Chem. Phys., 1986. **85**(5): p. 2929-2936.

137. Wertheim, M.S., *Fluids with highly directional attractive forces. IV. Equilibrium polymerization*. J. Stat. Phys, 1986. **42**(3): p. 477-492.
138. Wertheim, M.S., *Fluids with highly directional attractive forces. III. Multiple attraction sites*. J. Stat. Phys, 1986. **42**(3): p. 459-476.
139. Wertheim, M.S., *Fluids with highly directional attractive forces. II. Thermodynamic perturbation theory and integral equations*. J. Stat. Phys, 1984. **35**(1): p. 35-47.
140. Wertheim, M.S., *Fluids with highly directional attractive forces. I. Statistical thermodynamics*. J. Stat. Phys, 1984. **35**(1): p. 19-34.
141. Chapman, W.G., et al., *New reference equation of state for associating liquids*. Ind. Eng. Chem. Res., 1990. **29**(8): p. 1709-1721.
142. Chapman, W.G., et al., *SAFT: Equation-of-state solution model for associating fluids*. Fluid Phase Equilib., 1989. **52**: p. 31-38.
143. Jog, P.K., A. Garcia-Cuellar, and W.G. Chapman, *Extensions and applications of the SAFT equation of state to solvents, monomers, and polymers*. Fluid Phase Equilibria, 1999. **158-160**: p. 321-326.
144. Huang, S.H. and M. Radosz, *Equation of state for small, large, polydisperse, and associating molecules*. Ind. Eng. Chem. Res., 1990. **29**(11): p. 2284-2294.
145. Fu, Y.-H. and S.I. Sandler, *A Simplified SAFT Equation of State for Associating Compounds and Mixtures*. Ind. Eng. Chem. Res., 1995. **34**(5): p. 1897-1909.
146. Chapman, W.G., *Prediction of the thermodynamic properties of associating Lennard-Jones fluids: Theory and simulation*. J. Chem. Phys., 1990. **93**(6): p. 4299-4304.
147. Muller, E.A. and K.E. Gubbins, *An equation of state for water from a simplified intermolecular potential*. Ind. Eng. Chem. Res., 1995. **34**(10): p. 3662-3673.
148. Kraska, T. and K.E. Gubbins, *Phase Equilibria Calculations with a Modified SAFT Equation of State. 1. Pure Alkanes, Alkanols, and Water*. Ind. Eng. Chem. Res., 1996. **35**(12): p. 4727-4737.
149. Kraska, T. and K.E. Gubbins, *Phase Equilibria Calculations with a Modified SAFT Equation of State. 2. Binary Mixtures of n-Alkanes, 1-Alkanols, and Water*. Ind. Eng. Chem. Res., 1996. **35**(12): p. 4738-4746.
150. Blas, F.J. and L.F. Vega, *Prediction of Binary and Ternary Diagrams Using the Statistical Associating Fluid Theory (SAFT) Equation of State*. Ind. Eng. Chem. Res., 1998. **37**(2): p. 660-674.
151. Blas, F.J. and L.F. Vega, *Critical behavior and partial miscibility phenomena in binary mixtures of hydrocarbons by the statistical associating fluid theory*. J. Chem. Phys., 1998. **109**(17): p. 7405-7413.
152. Gross, J. and G. Sadowski, *Perturbed-Chain SAFT: An Equation of State Based on a Perturbation Theory for Chain Molecules*. Ind. Eng. Chem. Res., 2001. **40**(4): p. 1244-1260.

153. Gross, J. and G. Sadowski, *Modeling Polymer Systems Using the Perturbed-Chain Statistical Associating Fluid Theory Equation of State*. Ind. Eng. Chem. Res., 2001. **41**(5): p. 1084-1093.
154. von Solms, N., M.L. Michelsen, and G.M. Kontogeorgis, *Computational and Physical Performance of a Modified PC-SAFT Equation of State for Highly Asymmetric and Associating Mixtures*. Ind. Eng. Chem. Res., 2003. **42**(5): p. 1098-1105.
155. Barker, J.A. and D. Henderson, *Perturbation Theory and Equation of State for Fluids. II. A Successful Theory of Liquids*. J. Chem. Phys., 1967. **47**(11): p. 4714-4721.
156. Barker, J.A. and D. Henderson, *Perturbation Theory and Equation of State for Fluids: The Square-Well Potential*. J. Chem. Phys., 1967. **47**(8): p. 2856-2861.
157. Lymperiadis, A., et al., *A generalisation of the SAFT-gamma group contribution method for groups comprising multiple spherical segments*. Fluid Phase Equilib., 2008. **274**(1-2): p. 85-104.
158. Lymperiadis, A., et al., *A heteronuclear group contribution method for associating chain molecules (SAFT-gamma)*, in *18th European Symposium on Computer Aided Process Engineering*, B. Braunschweig and X. Joulia, Editors. 2008, Elsevier Science Bv: Amsterdam. p. 871-876.
159. Lymperiadis, A., et al., *A group contribution method for associating chain molecules based on the statistical associating fluid theory (SAFT-gamma)*. J. Chem. Phys., 2007. **127**(23): p. 234903.
160. McCabe, C. and A. Galindo., *SAFT: Associating Fluids and Fluids Mixtures*. Applied Thermodynamics of Fluids, ed. A.R.H.G.a.J.V. Sengers. 2010: Royal Society of Chemistry, London.
161. Müller, E.A. and K.E. Gubbins, *Molecular-Based Equations of State for Associating Fluids: A Review of SAFT and Related Approaches*. Ind. Eng. Chem. Res., 2001. **40**(10): p. 2193-2211.
162. Economou, I.G., *Statistical Associating Fluid Theory: A Successful Model for the Calculation of Thermodynamic and Phase Equilibrium Properties of Complex Fluid Mixtures*. Ind. Eng. Chem. Res., 2001. **41**(5): p. 953-962.
163. Hansen, J.-P. and I.R. McDonald, *Theory of Simple Liquids*. 1990.
164. Boublik, T., *Hard-Sphere Equation of State*. J. Chem. Phys., 1970. **53**(1): p. 471-472.
165. Jackson, G., W.G. Chapman, and K.E. Gubbins, *Phase equilibria of associating fluids*. Mol. Phys., 1988. **65**(1): p. 1-31.
166. Haslam, A.J., A. Galindo, and G. Jackson, *Prediction of binary intermolecular potential parameters for use in modelling fluid mixtures*. Fluid Phase Equilib., 2008. **266**(1-2): p. 105-128.
167. Pereira, F.E., et al., *The HELD algorithm for multicomponent, multiphase equilibrium calculations with generic equations of state*. Comput. Chem. Eng., 2012. **36**(0): p. 99-118.

168. Pereira, F.E., et al., *A duality-based optimisation approach for the reliable solution of (p, T) phase equilibrium in volume-composition space*. Fluid Phase Equilib., 2010. **299**(1): p. 1-23.
169. Papaioannou, V., et al., *Simultaneous prediction of vapour-liquid and liquid-liquid equilibria (VLE and LLE) of aqueous mixtures with the SAFT-gamma group contribution approach*. Fluid Phase Equilib., 2011. **306**(1): p. 82-96.
170. Avendaño, C., et al., *SAFT- $\gamma$  Force Field for the Simulation of Molecular Fluids. 1. A Single-Site Coarse Grained Model of Carbon Dioxide*. J. Phys. Chem. B, 2011. **115**(38): p. 11154-11169.
171. Lafitte, T., et al., *A Comprehensive Description of Chemical Association Effects on Second Derivative Properties of Alcohols through a SAFT-VR Approach*. J. Phys. Chem. B, 2007. **111**(13): p. 3447-3461.
172. Trio Motion Technology, *Motion Perfect 2*. 2010: Tewkesbury.
173. Agilent Technologies, *Agilent VEE Pro*. 2008.
174. Ametek Chandler Engineering, *Quizix PumpWorks Software*. 2009.
175. Invensys Eurotherm, *Eurotherm iTools 2012*.
176. Al Ghafri, S.Z., *Operating Manual for HTHP Synthetic Phase Equilibrium Equipment*. QCCSRC Thermophysical Laboratory, 2013.
177. Wagner, W. and A. Pruss, *The IAPWS Formulation 1995 for the Thermodynamic Properties of Ordinary Water Substance for General and Scientific Use*. J. Phys. Chem. Ref. Data, 2002. **31**: p. 387.
178. JCGM 100:2008, *Evaluation of measurement data - guide to the expression of uncertainty in measurement*. 2008.
179. Hoyt, S.L., ed. *ASME Handbook on Metal Properties*. 1956, McGraw-Hill: New York.
180. Span, R. and W. Wagner, *A New Equation of State for Carbon Dioxide Covering the Fluid Region from the Triple-Point Temperature to 1100 K at Pressures up to 800 MPa*. J. Phys. Chem. Ref. Data, 1996. **25**(6): p. 1509-1596.
181. Kunz, O. and W. Wagner, *The GERG-2008 Wide-Range Equation of State for Natural Gases and Other Mixtures: An Expansion of GERG-2004*. J. Chem. Eng. Data, 2012. **57**(11): p. 3032-3091.
182. Span, R. and W. Wagner, *Equations of State for Technical Applications. II. Results for Nonpolar Fluids*. Int. J. Thermophys., 2003. **24**(1): p. 41-109.
183. Kahl, H., T. Wadewitz, and J. Winkelmann, *Surface Tension of Pure Liquids and Binary Liquid Mixtures*. J. Chem. Eng. Data, 2003. **48**(3): p. 580-586.
184. Mutelet, F., et al., *Solubility of CO<sub>2</sub> in branched alkanes in order to extend the PPR78 model (predictive 1978, Peng–Robinson EOS with temperature-dependent  $k_{ij}$  calculated through a group contribution method) to such systems*. Fluid Phase Equilib., 2005. **238**(2): p. 157-168.

185. Kalra, H., et al., *Equilibrium phase properties of the carbon dioxide-n-heptane system*. J. Chem. Eng. Data, 1978. **23**(4): p. 317-321.
186. Inomata, H., K. Arai, and S. Saito, *Measurement of vapor-liquid equilibria at elevated temperatures and pressures using a flow type apparatus*. Fluid Phase Equilib., 1986. **29**(0): p. 225-232.
187. Esther, F., *Measurement and Prediction of the Phase Behaviour of Carbon Dioxide, Alkane and Water Mixtures at Reservoir Conditions*, in *Chemical Engineering*. 2011, Imperial college London: London.
188. Belandria, V., et al., *Compositional Analysis and Hydrate Dissociation Conditions Measurements for Carbon Dioxide + Methane + Water System*. Ind. Eng. Chem. Res., 2011. **50**(9): p. 5783-5794.
189. Ohmura, R., et al., *Clathrate Hydrate Formed with Methane and 2-Propanol: Confirmation of Structure II Hydrate Formation*. Ind. Eng. Chem. Res., 2004. **43**(16): p. 4964-4966.
190. Setzmann, U. and W. Wagner, *A New Equation of State and Tables of Thermodynamic Properties for Methane Covering the Range from the Melting Line to 625 K at Pressures up to 100 MPa*. J. Phys. Chem. Ref. Data, 1991. **20**(6): p. 1061-1155.
191. Schedemann, A., E.C. Ihmels, and J. Gmehling, *Liquid densities of THF and excess volumes for the mixture with water in a wide temperature and pressure range*. Fluid Phase Equilib., 2010. **295**(2): p. 201-207.
192. Ramos-Estrada, M., G.A. Iglesias-Silva, and K.R. Hall, *Experimental measurements and prediction of liquid densities for n-alkane mixtures*. J. Chem. Thermodyn., 2006. **38**(3): p. 337-347.
193. Sako, T., et al., *High pressure vapor-liquid and vapor-liquid-liquid equilibria for systems containing supercritical carbon dioxide, water and furfural*. Fluid Phase Equilib., 1995. **108**(1-2): p. 293-303.
194. King, M.B. and H. Al-Najjar, *The solubilities of carbon dioxide, hydrogen sulphide and propane in some normal alkane solvents—I: Experimental determinations in the range 15–70°C and comparison with ideal solution values*. Chem. Eng. Sci., 1977. **32**(10): p. 1241-1246.
195. Choi, E.-J. and S.-D. Yeo, *Critical Properties for Carbon Dioxide + n-Alkane Mixtures Using a Variable-Volume View Cell*. J. Chem. Eng. Data, 1998. **43**(5): p. 714-716.
196. Fenghour, A., J.P.M. Trusler, and W.A. Wakeham, *Densities and bubble points of binary mixtures of carbon dioxide and n-heptane and ternary mixtures of n-butane, n-heptane and n-hexadecane*. Fluid Phase Equilib., 2001. **185**(1-2): p. 349-358.
197. Lay, E.N., *Measurement and Correlation of Bubble Point Pressure in (CO<sub>2</sub> + C<sub>6</sub>H<sub>6</sub>), (CO<sub>2</sub> + CH<sub>3</sub>C<sub>6</sub>H<sub>5</sub>), (CO<sub>2</sub> + C<sub>6</sub>H<sub>14</sub>), and (CO<sub>2</sub> + C<sub>7</sub>H<sub>16</sub>) at Temperatures from (293.15 to 313.15) K*. J. Chem. Eng. Data, 2009. **55**(1): p. 223-227.



198. Dell'Era, C., et al., *Solubility of carbon dioxide in aqueous solutions of diisopropanolamine and methyldiethanolamine*. Fluid Phase Equilib., 2010. **293**(1): p. 101-109.
199. Stewart, P.B. and P. Munjal, *Solubility of Carbon Dioxide in Pure Water, Synthetic Sea water, and Synthetic Sea Water Concentrates at 5 Degrees to 2 Degrees C And 10-Atm to 45 Atm Pressure*. J. Chem. Eng. Data, 1970. **15**(1): p. 67-&.
200. Campos, C., et al., *Solubility of Carbon Dioxide in Water and Hexadecane: Experimental Measurement and Thermodynamic Modeling*. J. Chem. Eng. Data, 2009. **54**(10): p. 2881-2886.
201. Valtz, A., et al., *Vapour-liquid equilibria in the carbon dioxide-water system, measurement and modelling from 278.2 to 318.2K*. Fluid Phase Equilib., 2004. **226**: p. 333-344.
202. King, M.B., et al., *The mutual solubilities of water with supercritical and liquid carbon dioxide*. J. Supercrit. Fluids, 1992. **5**(4): p. 296-302.
203. Nakayama, T., et al., *High-Pressure Liquid-Liquid Equilibria for the system of Water, Ethanol and 1,1-Difluoroethane at T 323.2 K*. Fluid Phase Equilib., 1987. **38**(1-2): p. 109-127.
204. Hou, S.-X., G.C. Maitland, and J.P.M. Trusler, *Measurement and modeling of the phase behavior of the (carbon dioxide + water) mixture at temperatures from 298.15 to 448.15 K*. J. Supercrit. Fluids, 2013. **73**(0): p. 87-96.
205. Coan, C.R. and A.D. King, *Solubility of Water in Compressed Carbon Dioxide, Nitrous Oxide, and Ethane-Evidence for Hydration of Carbon Dioxide and Nitous Oxide in Gas Phase*. J. Am. Chem. Soc., 1971. **93**(8): p. 1857-&.
206. Lay, E.N., V. Taghikhani, and C. Ghotbi, *Measurement and Correlation of CO<sub>2</sub> Solubility in the Systems of CO<sub>2</sub> + Toluene, CO<sub>2</sub> + Benzene, and CO<sub>2</sub> + n-Hexane at Near-Critical and Supercritical Conditions*. J. Chem. Eng. Data, 2006. **51**(6): p. 2197-2200.
207. Tochigi, K., et al., *Vapor-Liquid Equilibria for the Carbon Dioxide + Pentane and Carbon Dioxide + Toluene Systems*. J. Chem. Eng. Data, 1998. **43**(6): p. 954-956.
208. Wu, W., J. Ke, and M. Poliakoff, *Phase Boundaries of CO<sub>2</sub> + Toluene, CO<sub>2</sub> + Acetone, and CO<sub>2</sub> + Ethanol at High Temperatures and High Pressures*. J. Chem. Eng. Data, 2006. **51**(4): p. 1398-1403.
209. Naidoo, P., D. Ramjugernath, and J.D. Raal, *A new high-pressure vapour-liquid equilibrium apparatus*. Fluid Phase Equilib., 2008. **269**(1-2): p. 104-112.
210. Ng, H.-J. and D.B. Robinson, *Equilibrium-phase properties of the toluene-carbon dioxide system*. J. Chem. Eng. Data, 1978. **23**(4): p. 325-327.
211. Sebastian, H.M., et al., *Gas-liquid equilibrium in mixtures of carbon dioxide + toluene and carbon dioxide + m-xylene*. J. Chem. Eng. Data, 1980. **25**(3): p. 246-248.

212. Morris, W.O. and M.D. Donohue, *Vapor-liquid equilibria in mixtures containing carbon dioxide, toluene, and 1-methylnaphthalene*. J. Chem. Eng. Data, 1985. **30**(3): p. 259-263.
213. Chang, C.J., *The solubility of carbon dioxide in organic solvents at elevated pressures*. Fluid Phase Equilib., 1992. **74**(0): p. 235-242.
214. Chang, C.J., *Volume Expansion Coefficients and Activity Coefficients of High-Pressure Carbon Dioxide Dissolution in Organic Liquids at 298 K*. J. Chem. Eng. Jpn., 1992. **25**(2): p. 164-170.
215. Muhlbauer, A.L. and J.D. Raal, *Measurement and thermodynamic interpretation of high-pressure vapour-liquid equilibria in the toluene + CO<sub>2</sub> system*. Fluid Phase Equilib., 1991. **64**(0): p. 213-236.
216. Kim, C.-H., P. Vimalchand, and M.D. Donohue, *Vapor-liquid equilibria for binary mixtures of carbon dioxide with benzene, toluene and p-xylene*. Fluid Phase Equilib., 1986. **31**(3): p. 299-311.
217. Hayduk, W., E.B. Walter, and P. Simpson, *Solubility of propane and carbon dioxide in heptane, dodecane, and hexadecane*. J. Chem. Eng. Data, 1972. **17**(1): p. 59-61.
218. Galindo, A. and F.J. Blas, *Theoretical Examination of the Global Fluid Phase Behavior and Critical Phenomena in Carbon Dioxide + n-Alkane Binary Mixtures*. J. Phys. Chem. B, 2002. **106**(17): p. 4503-4515.
219. García, J., L. Lugo, and J. Fernández, *Phase equilibria, PVT behavior, and critical phenomena in carbon dioxide + n-alkane mixtures using the perturbed-chain statistical associating fluid theory approach*. Ind. Eng. Chem. Res., 2004. **43**(26): p. 8345-8353.
220. Fu, D., et al., *Investigation of vapor-liquid equilibria for supercritical carbon dioxide and hydrocarbon mixtures by perturbed-chain statistical associating fluid theory*. Ind. Eng. Chem. Res., 2006. **45**(12): p. 4364-4370.
221. Arce, P. and M. Aznar, *Modeling of critical lines and regions for binary and ternary mixtures using non-cubic and cubic equations of state*. J. Supercrit. Fluids, 2007. **42**(1): p. 1-26.
222. Arce, P.F. and M. Aznar, *Computation and modeling of critical phenomena with the perturbed chain-statistical associating fluid theory equation of state*. J. Supercrit. Fluids, 2008. **43**(3): p. 408-420.
223. Llovell, F. and L.F. Vega, *Global fluid phase equilibria and critical phenomena of selected mixtures using the crossover soft-SAFT equation*. J. Phys. Chem. B, 2006. **110**(3): p. 1350-1362.
224. Thi, C.L., et al., *Modeling Phase Equilibrium of H<sub>2</sub> + n-Alkane and CO<sub>2</sub> + n-Alkane Binary Mixtures Using a Group Contribution Statistical Association Fluid Theory Equation of State (GC-SAFT-EOS) with a k<sub>ij</sub> Group Contribution Method*. Ind. Eng. Chem. Res., 2006. **45**(20): p. 6803-6810.

225. Polishuk, I., J. Wisniak, and H. Segura, *Simultaneous prediction of the critical and sub-critical phase behavior in mixtures using equations of state II. Carbon dioxide–heavy n-alkanes*. Chem. Eng. Sci., 2003. **58**(12): p. 2529-2550.
226. Diky, V., et al., *ThermoData Engine (TDE): Software Implementation of the Dynamic Data Evaluation Concept. 2. Equations of State on Demand and Dynamic Updates over the Web*. J. Chem. Inf. Model, 2007. **47**(4): p. 1713-1725.
227. Frenkel, M., et al., *ThermoData Engine (TDE): Software Implementation of the Dynamic Data Evaluation Concept*. J. Chem. Inf. Model, 2005. **45**(4): p. 816-838.
228. Rosenthal, D.J. and A.S. Teja, *The critical properties of n-alkanes using a low-residence time flow apparatus*. AIChE J., 1989. **35**(11): p. 1829-1834.
229. Tsonopoulos, C. and D. Ambrose, *Vapor-Liquid Critical Properties of Elements and Compounds. 3. Aromatic Hydrocarbons*. J. Chem. Eng. Data, 1995. **40**(3): p. 547-558.
230. Diefenbacher, A., M. Crone, and M. Türk, *Critical properties of CO<sub>2</sub>, CHF<sub>3</sub>, SF<sub>6</sub>, (CO<sub>2</sub>+ CHF<sub>3</sub>), and (CHF<sub>3</sub>+ SF<sub>6</sub>)*. J. Chem. Thermodyn., 1998. **30**(4): p. 481-496.
231. Mie G, *Zur kinetischen Theorie der einatomigen Körper*. Annalen der Physik Annalen der Physik 1903. **316.8**: p. 657-697.
232. Kontogeorgis, G.M. and P.M. Vlamos, *An interpretation of the behavior of EoS/GE models for asymmetric systems*. Chem. Eng. Sci., 2000. **55**(13): p. 2351-2358.
233. Brunner, G., C. Saure, and D. Buss, *Phase Equilibrium of Hydrogen, Carbon Dioxide, Squalene, and Squalane*. J. Chem. Eng. Data, 2009. **54**(5): p. 1598-1609.
234. Liphard, K.G. and G.M. Schneider, *Phase equilibria and critical phenomena in fluid mixtures of carbon dioxide + 2,6,10,15,19,23-hexamethyltetracosane up to 423 K and 100 MPa*. J. Chem. Thermodyn., 1975. **7**: p. 805.
235. Sovova, H., J. Jez, and M. Khachatryan, *Solubility of squalane, dinonyl phthalate and glycerol in supercritical CO<sub>2</sub>*. Fluid Phase Equilib., 1997. **137**: p. 3762.
236. Tsai, F.N. and J.S. Yau, *Solubility of carbon dioxide in n-tetracosane and in n-dotriacontane*. J. Chem. Eng. Data, 1990. **35**(1): p. 43-45.
237. Kordikowski, A. and G.M. Schneider, *Fluid phase equilibria of binary and ternary mixtures of supercritical carbon dioxide with low-volatility organic substances up to 100 MPa and 393 K*. Fluid Phase Equilib., 1993. **90**(1): p. 149-162.
238. Sato, Y., et al., *Solubility of carbon dioxide in eicosane, docosane, tetracosane, and octacosane at temperatures from 323 to 473 K and pressures up to 40 MPa*. Fluid Phase Equilib., 1998. **147**(1–2): p. 181-193.
239. Maersk Oil Qatar AS. *Crude Assay Report: AL SHAHEEN CRUDE OIL*. 2006.
240. Aspen Technology, *Aspen Hysys, version 7.3*. 2011.
241. Gupta, D.K., et al., *Fluid Characterization and Modeling of Compositional Variation, Dukhan Field, Qatar*, in *International Petroleum Technology Conference*. 2009, 2009, International Petroleum Technology Conference: Doha, Qatar.

242. Stewart, W.C., *Phase Equilibria for Mixtures of Carbon Dioxide and Several Normal Saturated Hydrocarbons*: Pennsylvania State College.
243. Schneider, G., et al., *Phasengleichgewichte und kritische Erscheinungen in binären Mischsystemen bis 1500 bar, CO<sub>2</sub> mit n-Octan, n-Undecan, n-Tridecan und n-Hexadecan*. Chem. Ing. Tech., 1967. **39**(11): p. 649-656.
244. Henry, R.L. and R.S. Metcalfe, *Multiple-Phase Generation During Carbon Dioxide Flooding*. Soc Petrol Eng J, 1983. **23**(4): p. 595-601.
245. Nikitin, E.D., P.A. Pavlov, and N.V. Bessonova, *Critical constants of n-alkanes with from 17 to 24 carbon atoms*. J. Chem. Thermodyn., 1994. **26**(2): p. 177-182.
246. du Rand, M. and I. Nieuwoudt, *Measurement of phase equilibria of supercritical ethane and paraffins*. J. Supercrit. Fluids, 2001. **21**(3): p. 181-193.
247. Nikitin, E.D., et al., *Vapor-Liquid Critical Properties of n-Alkylbenzenes from Toluene to 1-Phenyltridecane*. J. Chem. Eng. Data, 2002. **47**(4): p. 1012-1016.
248. Starling, K.E., *The properties of gases and liquids*. AIChE J., 1978. **24**(6): p. 1142-1142.
249. Joback, K.G. and R.C. Reid, *Estimation of Pure Component Properties from Group Contributions*. Chem. Eng. Commun., 1987. **57**(1-6): p. 233-243.
250. Constantinou, L. and R. Gani, *New group contribution method for estimating properties of pure compounds*. AIChE J., 1994. **40**(10): p. 1697-1710.
251. Genco, J.M., A.S. Teja, and W.B. Kay, *Study of the critical and azeotropic behavior of binary mixtures. 2. PVT-x data and azeotropic states of perfluoromethylcyclohexane-isomeric hexane systems*. J. Chem. Eng. Data, 1980. **25**(4): p. 355-360.
252. Morton, D.W., et al., *Gas-Liquid Critical Temperatures of Some Alkenes, Amines, and Cyclic Hydrocarbons*. J. Chem. Eng. Data, 2003. **49**(2): p. 283-285.
253. Nikitin, E.D., A.P. Popov, and N.S. Bogatishcheva, *Critical Point Measurements for Five n-Alkylcyclohexanes (C<sub>6</sub> to C<sub>10</sub>) by the Pulse-Heating Method*. J. Chem. Eng. Data, 2003. **48**(5): p. 1137-1140.
254. Gude, M.T.T., A.S., *The Critical Properties of Several n-Alkanals, Tetralin and NMP, Experimental Results for DIPPR 1990-91 Projects on Phase Equilibria and Pure Component Properties*. DIPPR Data Series, 1994. **2**: p. 174-83.
255. Steele, W.V., et al., *Vapor Pressure, Heat Capacity, and Density along the Saturation Line, Measurements for Cyclohexanol, 2-Cyclohexen-1-one, 1,2-Dichloropropane, 1,4-Di-tert-butylbenzene, (±)-2-Ethylhexanoic Acid, 2-(Methylamino)ethanol, Perfluoro-n-heptane, and Sulfolane*. J. Chem. Eng. Data, 1997. **42**(6): p. 1021-1036.
256. Kleinrahm, R. and W. Wagner, *Measurement and correlation of the equilibrium liquid and vapour densities and the vapour pressure along the coexistence curve of methane*. J. Chem. Thermodyn., 1986. **18**(8): p. 739-760.

- 
257. Matschke, D.E. and G. Thodos, *Vapor-Liquid Equilibria for the Ethane-Propane System*. J. Chem. Eng. Data, 1962. **7**(2): p. 232-234.
258. Honda, Y., T. Sato, and M. Uematsu, *Critical parameters for propane determined by the image analysis*. J. Chem. Thermodyn., 2008. **40**(2): p. 208-211.
259. VonNiederhausen, D.M., G.M. Wilson, and N.F. Giles, *Critical Point and Vapor Pressure Measurements at High Temperatures by Means of a New Apparatus with Ultralow Residence Times*. J. Chem. Eng. Data, 2000. **45**(2): p. 157-160.
260. Nikitin, E.D. and A.P. Popov, *Vapor-liquid critical properties of squalane measured by the pulse-heating technique*. Fluid Phase Equilib., 2005. **237**(1-2): p. 16-20.
261. Zhuravlev, N.D. and J. Ilja Siepmann, *Exploration of the vapour-liquid phase equilibria and critical points of triacontane isomers*. Fluid Phase Equilib., 1997. **134**(1-2): p. 55-61.
262. Cui, S.T., P.T. Cummings, and H.D. Cochran, *Configurational bias Gibbs ensemble Monte Carlo simulation of vapor-liquid equilibria of linear and short-branched alkanes*. Fluid Phase Equilib., 1997. **141**(1-2): p. 45-61.
263. Neubauer, B., et al., *Monte Carlo simulations of squalane in the Gibbs ensemble*. Fluid Phase Equilib., 1999. **155**(2): p. 167-176.
264. Zhuravlev, N.D., M.G. Martin, and J. Ilja Siepmann, *Vapor-liquid phase equilibria of triacontane isomers: Deviations from the principle of corresponding states*. Fluid Phase Equilib., 2002. **202**(2): p. 307-324.
265. Marrero, J. and R. Gani, *Group-contribution based estimation of pure component properties*. Fluid Phase Equilib., 2001. **183-184**(0): p. 183-208.
266. Mokbel, I., et al., *Vapor-liquid equilibria of two binary mixtures: benzene+n-tetradecane and benzene+squalane*. Fluid Phase Equilib., 1998. **149**(1-2): p. 287-308.
267. Marteau, P., et al., *High-Pressure Phase Diagrams of Methane + Squalane and Methane + Hexatriacontane Mixtures*. J. Chem. Eng. Data, 1998. **43**(3): p. 362-366.
268. Anderson, G.K., *Solubility of Carbon Dioxide in Water under Incipient Clathrate Formation Conditions*. J. Chem. Eng. Data, 2002. **47**(2): p. 219-222.
269. Bamberger, A., G. Sieder, and G. Maurer, *High-pressure (vapor+liquid) equilibrium in binary mixtures of (carbon dioxide+water or acetic acid) at temperatures from 313 to 353 K*. J. Supercrit. Fluids, 2000. **17**(2): p. 97-110.
270. Bando, S., et al., *Solubility of CO<sub>2</sub> in Aqueous Solutions of NaCl at (30 to 60) °C and (10 to 20) MPa*. J. Chem. Eng. Data, 2003. **48**(3): p. 576-579.
271. Bermejo, M.D., et al., *The influence of Na<sub>2</sub>SO<sub>4</sub> on the CO<sub>2</sub> solubility in water at high pressure*. Fluid Phase Equilib., 2005. **238**(2): p. 220-228.
272. Briones, J.A., et al., *Ternary phase equilibria for acetic acid-water mixtures with supercritical carbon dioxide*. Fluid Phase Equilib., 1987. **36**(0): p. 235-246.

273. Chapoy, A., et al., *Gas solubility measurement and modeling for methane–water and methane–ethane–n-butane–water systems at low temperature conditions*. Fluid Phase Equilib., 2004. **220**(1): p. 111-119.
274. Crovetto, R. and R.H. Wood, *Solubility of CO<sub>2</sub> in water and density of aqueous CO<sub>2</sub> near the solvent critical temperature*. Fluid Phase Equilib., 1992. **74**(0): p. 271-288.
275. Dalmolin, I., et al., *Solubility of carbon dioxide in binary and ternary mixtures with ethanol and water*. Fluid Phase Equilib., 2006. **245**(2): p. 193-200.
276. Dohrn, R., et al., *Experimental measurements of phase equilibria for ternary and quaternary systems of glucose, water, CO<sub>2</sub> and ethanol with a novel apparatus*. Fluid Phase Equilib., 1993. **83**(0): p. 149-158.
277. Fenghour, A., W.A. Wakeham, and J.T.R. Watson, *Densities of (water + methane) in the temperature range 430 K to 699 K and at pressures up to 30 MPa*. J. Chem. Thermodyn., 1996. **28**(4): p. 447-458.
278. Ferrentino, G., et al., *Experimental Measurements and Thermodynamic Modeling of CO<sub>2</sub> Solubility at High Pressure in Model Apple Juices*. Ind. Eng. Chem. Res., 2010. **49**(6): p. 2992-3000.
279. Iwai, Y., et al., *Measurement of solubilities of palmitic acid in supercritical carbon dioxide and entrainer effect of water by FTIR spectroscopy*. J. Supercrit. Fluids, 2004. **28**(2–3): p. 193-200.
280. Jackson, K., L.E. Bowman, and J.L. Fulton, *Water Solubility Measurements In Supercritical Fluids and High-Pressure Liquids Using Near-Infrared Spectroscopy*. Anal. Chem., 1995. **67**(14): p. 2368-2372.
281. Jarne, C., et al., *Dew points of binary carbon dioxide + water and ternary carbon dioxide + water + methanol mixtures: Measurement and modelling*. Fluid Phase Equilib., 2004. **216**(1): p. 85-93.
282. Kiepe, J., et al., *Experimental Determination and Prediction of Gas Solubility Data for CO<sub>2</sub> + H<sub>2</sub>O Mixtures Containing NaCl or KCl at Temperatures between 313 and 393 K and Pressures up to 10 MPa*. Ind. Eng. Chem. Res., 2002. **41**(17): p. 4393-4398.
283. Zawisza, A. and B. Malesinska, *Solubility of carbon dioxide in liquid water and of water in gaseous carbon dioxide in the range 0.2-5 MPa and at temperatures up to 473 K*. J. Chem. Eng. Data, 1981. **26**(4): p. 388-391.
284. Martín, Á., et al., *Phase equilibria of carbon dioxide, poly ethylene glycol and water mixtures at high pressure: Measurements and modelling*. Fluid Phase Equilib., 2009. **286**(2): p. 162-169.
285. Mather, A.E. and E.U. Franck, *Phase equilibria in the system carbon dioxide-water at elevated pressures*. J. Phys. Chem., 1992. **96**(1): p. 6-8.
286. Nighswander, J.A., N. Kalogerakis, and A.K. Mehrotra, *Solubilities of carbon dioxide in water and 1 wt. % sodium chloride solution at pressures up to 10 MPa and temperatures from 80 to 200.degree.C*. J. Chem. Eng. Data, 1989. **34**(3): p. 355-360.

- 
287. Patel, M.R., et al., *Thermophysical properties of gaseous carbon dioxide and water mixtures*. Fluid Phase Equilib., 1987. **36**(0): p. 279-299.
288. Prutton, C.F. and R.L. Savage, *The Solubility of Carbon Dioxide in Calcium Chloride-Water Solutions at 75, 100, 120° and High Pressures*. J. Am. Chem. Soc., 1945. **67**(9): p. 1550-1554.
289. Qin, J., R.J. Rosenbauer, and Z. Duan, *Experimental Measurements of Vapor-Liquid Equilibria of the H<sub>2</sub>O + CO<sub>2</sub> + CH<sub>4</sub> Ternary System*. J. Chem. Eng. Data, 2008. **53**(6): p. 1246-1249.
290. Ruffine, L. and J.P.M. Trusler, *Phase behaviour of mixed-gas hydrate systems containing carbon dioxide*. J. Chem. Thermodyn., 2010. **42**(5): p. 605-611.
291. Servio, P. and P. Englezos, *Effect of temperature and pressure on the solubility of carbon dioxide in water in the presence of gas hydrate*. Fluid Phase Equilib., 2001. **190**(1-2): p. 127-134.
292. Silkenbäumer, D., B. Rumpf, and R.N. Lichtenthaler, *Solubility of Carbon Dioxide in Aqueous Solutions of 2-Amino-2-methyl-1-propanol and N-Methyldiethanolamine and Their Mixtures in the Temperature Range from 313 to 353 K and Pressures up to 2.7 MPa*. Ind. Eng. Chem. Res., 1998. **37**(8): p. 3133-3141.
293. Takahashi, S., K.Y. Song, and R. Kobayashi, *Experimental vapor-liquid equilibria in the carbon dioxide-diethylene glycol-water and carbon dioxide-triethylene glycol-water systems at feasible absorption temperatures and pressures*. J. Chem. Eng. Data, 1984. **29**(1): p. 23-28.
294. Teng, H., et al., *Solubility of liquid CO<sub>2</sub> in water at temperatures from 278 K to 293 K and pressures from 6.44 MPa to 29.49 MPa and densities of the corresponding aqueous solutions*. J. Chem. Thermodyn., 1997. **29**(11): p. 1301-1310.
295. Zheng, D.-Q., T.-M. Guo, and H. Knapp, *Experimental and modeling studies on the solubility of CO<sub>2</sub>, CHC<sub>1</sub>F<sub>2</sub>, CHF<sub>3</sub>, C<sub>2</sub>H<sub>2</sub>F<sub>4</sub> and C<sub>2</sub>H<sub>4</sub>F<sub>2</sub> in water and aqueous NaCl solutions under low pressures*. Fluid Phase Equilib., 1997. **129**(1-2): p. 197-209.
296. Nelson, H.D. and C.L. de Ligny, *The determination of the solubilities of some n-alkanes in water at different temperatures, by means of gas chromatography*. Recl. Trav. Chim. Pays-Bas, 1968. **87**(5): p. 528-544.
297. Donahue, D.J. and F.E. Bartell, *The Boundary Tension at Water-Organic Liquid Interfaces*. J. Phys. Chem., 1952. **56**(4): p. 480-484.
298. Guerrant, R.P., *Hydrocarbon-water Solubilities at High Temperatures Under Vapor-liquid-liquid Equilibrium Conditions*: Pennsylvania State University.
299. Zel'venskii, Y.D., A.A. Efremov, and G.M. Larin, *Investigation of the liquid-vapor equilibrium in hydrocarbon-water systems using the radioactive hydrogen isotope-tritium*. Chem. Technol. Fuels Oils, 1965. **1**(7): p. 506-510.
300. Connolly, J.F., *Solubility of Hydrocarbons in Water Near the Critical Solution Temperatures*. J. Chem. Eng. Data, 1966. **11**(1): p. 13-16.

301. McAuliffe, C., *Solubility in Water of C1-C9 Hydrocarbons*. Nature, 1963. **200**(4911): p. 1092-1093.
302. Galindo, A., P.J. Whitehead, and G. Jackson, *Predicting the High-Pressure Phase Equilibria of Water + n-Alkanes Using a Simplified SAFT Theory with Transferable Intermolecular Interaction Parameters*. J. Phys. Chem., 1996. **100**(16): p. 6781-6792.
303. Yakoumis, I.V., et al., *Prediction of Phase Equilibria in Binary Aqueous Systems Containing Alkanes, Cycloalkanes, and Alkenes with the Cubic-plus-Association Equation of State*. Ind. Eng. Chem. Res., 1998. **37**(10): p. 4175-4182.
304. Patel, B.H., et al., *Prediction of the Salting-Out Effect of Strong Electrolytes on Water + Alkane Solutions*. Ind. Eng. Chem. Res., 2003. **42**(16): p. 3809-3823.
305. Voutsas, E.C., et al., *Water/Hydrocarbon Phase Equilibria Using the Thermodynamic Perturbation Theory*. Ind. Eng. Chem. Res., 2000. **39**(3): p. 797-804.
306. Karakatsani, E.K., G.M. Kontogeorgis, and I.G. Economou, *Evaluation of the Truncated Perturbed Chain-Polar Statistical Associating Fluid Theory for Complex Mixture Fluid Phase Equilibria*. Ind. Eng. Chem. Res., 2006. **45**(17): p. 6063-6074.
307. Li, X.-S. and P. Englezos, *Vapor-liquid equilibrium of systems containing alcohols, water, carbon dioxide and hydrocarbons using SAFT*. Fluid Phase Equilib., 2004. **224**(1): p. 111-118.
308. Oliveira, M.B., J.A.P. Coutinho, and A.J. Queimada, *Mutual solubilities of hydrocarbons and water with the CPA EoS*. Fluid Phase Equilib., 2007. **258**(1): p. 58-66.
309. Vega, L., F. Llovel, and F. Blas, *Capturing the Solubility Minima of n-Alkanes in Water by Soft-SAFT*. J. Phys. Chem. B, 2009. **113**(21): p. 7621-7630.
310. Aparicio-Martínez, S. and K.R. Hall, *Phase equilibria in water containing binary systems from molecular based equations of state*. Fluid Phase Equilib., 2007. **254**(1-2): p. 112-125.
311. Nguyen-Huynh, D., et al., *Modeling Liquid-Liquid and Liquid-Vapor Equilibria of Binary Systems Containing Water with an Alkane, an Aromatic Hydrocarbon, an Alcohol or a Gas (Methane, Ethane, CO<sub>2</sub> or H<sub>2</sub>S), Using Group Contribution Polar Perturbed-Chain Statistical Associating Fluid Theory*. Ind. Eng. Chem. Res., 2011. **50**(12): p. 7467-7483.
312. Pereda, S., et al., *Solubility of hydrocarbons in water: Experimental measurements and modeling using a group contribution with association equation of state (GCA-EoS)*. Fluid Phase Equilib., 2009. **275**(1): p. 52-59.
313. Emborsky, C.P., K.R. Cox, and W.G. Chapman, *Correlation and Prediction of Water Content in Alkanes Using a Molecular Theory*. Ind. Eng. Chem. Res., 2011. **50**(13): p. 7791-7799.
314. Kontogeorgis, G.M., et al., *Ten Years with the CPA (Cubic-Plus-Association) Equation of State. Part 2. Cross-Associating and Multicomponent Systems*. Ind. Eng. Chem. Res., 2006. **45**(14): p. 4869-4878.



- 
315. Kontogeorgis, G.M., et al., *Les théories d'association et le phénomène de la solvation : application aux industries du pétrole et du gaz, et à la pétrochimie*. Oil Gas Sci Technol - Rev. IFP, 2008. **63**(3): p. 305-319.
316. Mac Dowell, N., et al., *Modeling the Fluid Phase Behavior of Carbon Dioxide in Aqueous Solutions of Monoethanolamine Using Transferable Parameters with the SAFT-VR Approach*. Ind. Eng. Chem. Res., 2010. **49**(4): p. 1883-1899.
317. dos Ramos, M.C., F.J. Blas, and A. Galindo, *Modelling the phase equilibria and excess properties of the water+carbon dioxide binary mixture*. Fluid Phase Equilib., 2007. **261**(1-2): p. 359-365.
318. dos Ramos, M.C., F.J. Blas, and A. Galindo, *Phase Equilibria, Excess Properties, and Henry's Constants of the Water + Carbon Dioxide Binary Mixture*. J. Phys. Chem. C, 2007. **111**(43): p. 15924-15934.
319. Clark, G.N.I., et al., *Developing optimal Wertheim-like models of water for use in Statistical Associating Fluid Theory (SAFT) and related approaches*. Mol. Phys., 2006. **104**(22-24): p. 3561-3581.
320. Blas, F.J. and A. Galindo, *Study of the high pressure phase behaviour of CO<sub>2</sub>+n-alkane mixtures using the SAFT-VR approach with transferable parameters*. Fluid Phase Equilib., 2002. **194-197**: p. 501-509.
321. Paricaud, P., A. Galindo, and G. Jackson, *Modeling the Cloud Curves and the Solubility of Gases in Amorphous and Semicrystalline Polyethylene with the SAFT-VR Approach and Flory Theory of Crystallization*. Ind. Eng. Chem. Res., 2004. **43**(21): p. 6871-6889.
322. Lide, D.R., *CRC Handbook of Chemistry and Physics*. 86th ed. ed. 2005: CRC Press / Taylor and Francis: Boca Raton, FL.
323. Buckingham, A.D., *Electric Moments of Molecules*, in *Physical Chemistry*, H. Eyring, D. Henderson, and W. Jost, Editors. 1970, Academic Press: New York / London.
324. Brunner, E., *Fluid mixtures at high pressures IX. Phase separation and critical phenomena in 23 (n-alkane + water) mixtures*. J. Chem. Thermodyn., 1990. **22**(4): p. 335-353.
325. Forte, E., et al., *Application of a renormalization-group treatment to the statistical associating fluid theory for potentials of variable range (SAFT-VR)*. J. Chem. Phys., 2011. **134**(15): p. 154102.
326. Forte, E., et al., *Application of the statistical associating fluid theory for potentials of variable range (SAFT-VR) coupled with renormalisation-group (RG) theory to model the phase equilibria and second-derivative properties of pure fluids*. Fluid Phase Equilib., 2013. **337**(0): p. 274-287.
327. McCabe, C. and S.B. Kiselev, *Application of Crossover Theory to the SAFT-VR Equation of State: SAFT-VR for Pure Fluids*. Ind. Eng. Chem. Res., 2004. **43**(11): p. 2839-2851.
328. Sun, L., et al., *Predicting Mixture Phase Equilibria and Critical Behavior Using the SAFT-VR Approach*. J. Phys. Chem. B, 2005. **109**(18): p. 9047-9058.

329. Zhao, W., et al., *Critical asymmetry in renormalization group theory for fluids*. J. Chem. Phys., 2013. **138**(23): p. 234502-12.
330. Y. He, Z.L., S. Ma, and Y. Hu, *Measuring Phase Equilibria of Carbon Dioxide - n - Heptane System by Stoichiometry*. J. East Chin. Univ. Sci. Technol, 1994. **20**: p. 79.
331. Duan, Z. and R. Sun, *An improved model calculating CO<sub>2</sub> solubility in pure water and aqueous NaCl solutions from 273 to 533 K and from 0 to 2000 bar*. Chem. Geol., 2003. **193**(3-4): p. 257-271.
332. Míguez, J.M., et al., *An Examination of the Ternary Methane + Carbon Dioxide + Water Phase Diagram using the SAFT-VR Approach*. J. Phys. Chem. B, 2011. **115**(31): p. 9604-9617.
333. Uchida, T., et al., *Kinetics and stability of CH<sub>4</sub>-CO<sub>2</sub> mixed gas hydrates during formation and long-term storage*. ChemPhysChem, 2005. **6**(4): p. 646-654.
334. Chapoy, A., et al., *Estimation of Water Content for Methane + Water and Methane + Ethane + n-Butane + Water Systems Using a New Sampling Device*. J. Chem. Eng. Data, 2005. **50**(4): p. 1157-1161.
335. Chapoy, A., C. Coquelet, and D. Richon, *Solubility measurement and modeling of water in the gas phase of the methane/water binary system at temperatures from 283.08 to 318.12 K and pressures up to 34.5 MPa*. Fluid Phase Equilib., 2003. **214**(1): p. 101-117.
336. Folas, G.K., et al., *Data and prediction of water content of high pressure nitrogen, methane and natural gas*. Fluid Phase Equilib., 2007. **252**(1-2): p. 162-174.
337. Mohammadi, A.H., et al., *Experimental Measurement and Thermodynamic Modeling of Water Content in Methane and Ethane Systems*. Ind. Eng. Chem. Res., 2004. **43**(22): p. 7148-7162.
338. Beltrán, J.G. and P. Servio, *Equilibrium Studies for the System Methane + Carbon Dioxide + Neohexane + Water*. J. Chem. Eng. Data, 2008. **53**(8): p. 1745-1749.
339. Seo, Y.-T., H. Lee, and J.-H. Yoon, *Hydrate Phase Equilibria of the Carbon Dioxide, Methane, and Water System*. J. Chem. Eng. Data, 2001. **46**(2): p. 381-384.
340. Ohgaki, K.T., K.; Sangawa, H.; Matsubara, T.; Nakano, S, *Methane exploitation by carbon dioxide from gas hydrates-phase equilibria for CO<sub>2</sub>-CH<sub>4</sub> mixed hydrate system*. J. Chem. Eng. Jpn., 1996. **29**: p. 478.
341. Bruusgaard, H., J.G. Beltrán, and P. Servio, *Solubility measurements for the CH<sub>4</sub> + CO<sub>2</sub> + H<sub>2</sub>O system under hydrate-liquid-vapor equilibrium*. Fluid Phase Equilib., 2010. **296**(2): p. 106-109.
342. Uchida, T., et al., *Kinetics and Stability of CH<sub>4</sub>-CO<sub>2</sub> Mixed Gas Hydrates during Formation and Long-Term Storage*. ChemPhysChem, 2005. **6**(4): p. 646-654.
343. Jarne, C., *Dew Points of Ternary Methane (or Ethane) Carbon Dioxide Water Mixtures: Measurement and Correlation*. Energy, 2004. **18**(2): p. 396-404.

- 
344. Ren, Q.-Y., et al., *Interfacial Tension of (CO<sub>2</sub> + CH<sub>4</sub>) + Water from 298 K to 373 K and Pressures up to 30 MPa*. J. Chem. Eng. Data, 2000. **45**(4): p. 610-612.
345. W Taylor, F., *The greenhouse effect and climate change*. Rep. Prog. Phys., 1991. **54**(6): p. 881.
346. Thomas, S. and R.A. Dawe, *Review of ways to transport natural gas energy from countries which do not need the gas for domestic use*. Energy, 2003. **28**(14): p. 1461-1477.
347. Linga, P., R. Kumar, and P. Englezos, *Gas hydrate formation from hydrogen/carbon dioxide and nitrogen/carbon dioxide gas mixtures*. Chem. Eng. Sci., 2007. **62**(16): p. 4268-4276.
348. Demirbas, A., *Methane hydrates as potential energy resource: Part 2 – Methane production processes from gas hydrates*. Energy Convers. Manage., 2010. **51**(7): p. 1562-1571.
349. Demirbas, A., *Methane hydrates as potential energy resource: Part 1 – Importance, resource and recovery facilities*. Energy Convers. Manage., 2010. **51**(7): p. 1547-1561.
350. Seo, Y.-T. and H. Lee, *Multiple-Phase Hydrate Equilibria of the Ternary Carbon Dioxide, Methane, and Water Mixtures*. J. Phys. Chem. B, 2001. **105**(41): p. 10084-10090.
351. Bi, Y., T. Yang, and K. Guo, *Determination of the upper-quadruple-phase equilibrium region for carbon dioxide and methane mixed gas hydrates*. J.Pet.Sci.Eng., 2013. **101**(0): p. 62-67.
352. Sloan, E.D. and C.A. Koh, *Clathrate Hydrates of Natural Gases*. 2008.
353. Mohammadi, A.H., R. Anderson, and B. Tohidi, *Carbon monoxide clathrate hydrates: Equilibrium data and thermodynamic modeling*. AIChE J., 2005. **51**(10): p. 2825-2833.
354. Dufal, S., et al., *Modelling the effect of methanol, glycol inhibitors and electrolytes on the equilibrium stability of hydrates with the SAFT-VR approach*. Mol. Phys., 2012. **110**(11-12): p. 1223-1240.
355. Waals, J.H.v.d. and J.C. Platteeuw, *Clathrate Solutions*. Adv. Chem. Phys., 1959: p. 1-57.
356. Platteeuw, J.C. and J.H. van der Waals, *Thermodynamic properties of gas hydrates*. Mol. Phys., 1958. **1**(1): p. 91-96.
357. Colorado School of Mine, CSMHYD. 1998.
358. Mraw, S.C., S.-C. Hwang, and R. Kobayashi, *Vapor-liquid equilibrium of the methane-carbon dioxide system at low temperatures*. J. Chem. Eng. Data, 1978. **23**(2): p. 135-139.
359. Al Sahhaf, T., *Liquid vapor equilibriums in the nitrogen carbon dioxide methane system*. Ind. Eng. Chem. Fundam., 1983. **22**(4): p. 372-380.

360. Knapp, H., X. Yang, and Z. Zhang, *Vapor—liquid equilibria in ternary mixtures containing nitrogen, methane, ethane and carbondioxide at low temperatures and high pressures*. Fluid Phase Equilib., 1990. **54**(0): p. 1-18.
361. Davalos, J., *Liquid-vapor equilibria at 250.00.deg.K for systems containing methane, ethane, and carbon dioxide*. J. Chem. Eng. Data, 1976. **21**(1): p. 81-84.
362. Webster, L.A. and A.J. Kidnay, *Vapor-Liquid Equilibria for the Methane-Propane-Carbon Dioxide Systems at 230 K and 270 K*. J. Chem. Eng. Data, 2001. **46**(3): p. 759-764.
363. Somait, *Liquid-vapor equilibriums at 270.00 K for systems containing nitrogen, methane, and carbon dioxide*. J. Chem. Eng. Data, 1978. **23**(4): p. 301-305.
364. Xu, N., et al., *High pressure vapor liquid equilibria at 293 K for systems containing nitrogen, methane and carbon dioxide*. Fluid Phase Equilib., 1992. **81**(0): p. 175-186.
365. Bian, B., et al., *Simultaneous determination of vapor-liquid equilibrium and molar volumes for coexisting phases up to the critical temperature with a static method*. Fluid Phase Equilib., 1993. **90**(1): p. 177-187.
366. Addicks, J., et al., *Solubility of Carbon Dioxide and Methane in Aqueous Methyl-diethanolamine Solutions*. J. Chem. Eng. Data, 2002. **47**(4): p. 855-860.
367. Awan, J.A., et al., *Vapor-Liquid Equilibrium Measurements and Modeling of the Propyl Mercaptan + Methane + Water System*. J. Chem. Eng. Data, 2009. **55**(2): p. 842-846.
368. Crovetto, R., *Solubilities of inert gases and methane in H<sub>2</sub>O and in D<sub>2</sub>O in the temperature range of 300 to 600 K*. J. Chem. Phys., 1982. **76**(2): p. 1077.
369. Duffy, J.R., N.O. Smith, and B. Nagy, *Solubility of natural gases in aqueous salt solutions—I: Liquidus surfaces in the system CH<sub>4</sub>-H<sub>2</sub>O-NaCl<sub>2</sub>-CaCl<sub>2</sub> at room temperatures and at pressures below 1000 psia*. Geochim. Cosmochim. Acta, 1961. **24**(1-2): p. 23-31.
370. Kim, Y.S., et al., *Liquid Water-Hydrate Equilibrium Measurements and Unified Predictions of Hydrate-Containing Phase Equilibria for Methane, Ethane, Propane, and Their Mixtures*. Ind. Eng. Chem. Res., 2003. **42**(11): p. 2409-2414.
371. Lekvam, K. and P.R. Bishnoi, *Dissolution of methane in water at low temperatures and intermediate pressures*. Fluid Phase Equilib., 1997. **131**(1-2): p. 297-309.
372. Yilin, W., et al., *Solubility of CH<sub>4</sub> in the mixed solvent t-butyl alcohol and water*. Thermochim. Acta, 1995. **253**: p. 327-334.
373. Sage, B.H. and W.N. Lacey, *Phase Equilibria in Hydrocarbon Systems I Methods and Apparatus*. Ind. Eng. Chem., 1934. **26**(1): p. 103-106.
374. Siqueira Campos, C.E.P., et al., *Experimental Measurement and Thermodynamic Modeling for the Solubility of Methane in Water and Hexadecane*. J. Chem. Eng. Data, 2010. **55**(7): p. 2576-2580.

375. Rigby, M. and J.M. Prausnitz, *Solubility of water in compressed nitrogen, argon, and methane*. J. Phys. Chem., 1968. **72**(1): p. 330-334.
376. Servio, P. and P. Englezos, *Measurement of Dissolved Methane in Water in Equilibrium with Its Hydrate*. J. Chem. Eng. Data, 2001. **47**(1): p. 87-90.
377. Shmonov, V.M., R.J. Sadus, and E.U. Franck, *High-pressure phase equilibria and supercritical pVT data of the binary water + methane Mixture to 723 K and 200 MPa*. J. Phys. Chem. A, 1993: p. Medium: X; Size: Pages: 9054-9059.
378. Yang, S.O., et al., *Measurement and prediction of phase equilibria for water + methane in hydrate forming conditions*. Fluid Phase Equilib., 2001. **185**(1–2): p. 53-63.
379. Yarrison, M., K.R. Cox, and W.G. Chapman, *Measurement and Modeling of the Solubility of Water in Supercritical Methane and Ethane from 310 to 477 K and Pressures from 3.4 to 110 MPa*. Ind. Eng. Chem. Res., 2006. **45**(20): p. 6770-6777.
380. Duan, Z. and S. Mao, *A thermodynamic model for calculating methane solubility, density and gas phase composition of methane-bearing aqueous fluids from 273 to 523 K and from 1 to 2000 bar*. Geochim. Cosmochim. Acta, 2006. **70**(13): p. 3369-3386.
381. Nakamura, T., et al., *Stability boundaries of gas hydrates helped by methane—structure-H hydrates of methylcyclohexane and cis-1,2-dimethylcyclohexane*. Chem. Eng. Sci., 2003. **58**(2): p. 269-273.
382. Robinson, D.B. and B.R. Metha, *Hydrates In the PropaneCarbon Dioxide- Water System*. J. Can. Pet. Technol., 1971. **10**(1).
383. Takenouchi, S. and G.C. Kennedy, *The binary system H<sub>2</sub>O-CO<sub>2</sub> at high temperatures and pressures*. AM.J.SCI, 1964. **262**(9): p. 1055-1074.
384. Belandria, V., A.H. Mohammadi, and D. Richon, *Phase equilibria of clathrate hydrates of methane and carbon dioxide: New experimental data and predictions*. Fluid Phase Equilib., 2010. **296**(1): p. 60-65.
385. Y. ARAI, G.K., S. SAITO, *The Experimental Determination of the pVTx Relations for the Carbon Dioxide and the Carbon Dioxide-Methane Systems*. J. Chem. Eng. Jpn., 1971. **4**.
386. Donnelly, H.G. and D.L. Katz, *Phase Equilibria in the Carbon Dioxide-Methane System*. Ind. Eng. Chem., 1954. **46**(3): p. 511-517.
387. Al Ghafri, S.Z., G.C. Maitland, and J.P.M. Trusler, *Experimental and Molecular Modeling Study of the Three-Phase Behavior of (n-Heptane + Carbon Dioxide + Water) at Reservoir Conditions*. J. Phys. Chem. B, 2013. **Under Preparation**.
388. Shmulovich, K.I. and C.M. Graham, *Melting of albite and dehydration of brucite in H<sub>2</sub>O–NaCl fluids to 9 kbars and 700–900°C: implications for partial melting and water activities during high pressure metamorphism*. CONTRIB MINERAL PETR, 1996. **124**(3): p. 370-382.

389. Subías, I. and C. Fernández-Nieto, *Hydrothermal events in the Valle de Tena (Spanish Western Pyrenees) as evidenced by fluid inclusions and trace-element distribution from fluorite deposits*. Chem. Geol., 1995. **124**(3-4): p. 267-282.
390. Magueijo, V., V. Semião, and M.N. de Pinho, *Fluid flow and mass transfer modelling in lysozyme ultrafiltration*. Int. J. Heat Mass Transfer, 2005. **48**(9): p. 1716-1726.
391. Huizenga, J.-M., et al., *The Paleoproterozoic carbonate-hosted Poring Zn–Pb deposit, South Africa. II: fluid inclusion, fluid chemistry and stable isotope constraints*. Miner. Deposita, 2006. **40**(6): p. 686-706.
392. Kaszuba, J.P., D.R. Janecky, and M.G. Snow, *Carbon dioxide reaction processes in a model brine aquifer at 200 °C and 200 bars: implications for geologic sequestration of carbon*. Appl. Geochem., 2003. **18**(7): p. 1065-1080.
393. Bachu, S. and J.J. Adams, *Sequestration of CO<sub>2</sub> in geological media in response to climate change: capacity of deep saline aquifers to sequester CO<sub>2</sub> in solution*. Energy Convers. Manage., 2003. **44**(20): p. 3151-3175.
394. Safarov, J.T., et al., *( $p, \rho, T$ ) and ( $p_s, \rho_s, T_s$ ) properties, and apparent molar volumes  $V_\phi$  of CaCl<sub>2</sub> (aq) at  $T=298.15$  to  $398.15$  K and at pressures up to  $p=60$  MPa*. J. Mol. Liq., 2005. **116**(3): p. 165-174.
395. Driesner, T., *The system H<sub>2</sub>O–NaCl. Part II: Correlations for molar volume, enthalpy, and isobaric heat capacity from 0 to 1000 °C, 1 to 5000 bar, and 0 to 1  $X_{\text{NaCl}}$* . Geochim. Cosmochim. Acta, 2007. **71**(20): p. 4902-4919.
396. Al Ghafri, S.Z., G.C. Maitland, and J.P.M. Trusler, *Densities of SrCl<sub>2</sub>(aq), Na<sub>2</sub>SO<sub>4</sub>(aq), NaHCO<sub>3</sub>(aq), and Two Synthetic Reservoir Brines at Temperatures between (298 and 473) K, Pressures up to 68.5 MPa, and Molalities up to 3 mol·kg<sup>-1</sup>*. J. Chem. Eng. Data, 2013. **58**(2): p. 402-412.
397. Al Ghafri, S., G.C. Maitland, and J.P.M. Trusler, *Densities of aqueous MgCl<sub>2</sub>(aq), CaCl<sub>2</sub>(aq), KI(aq), NaCl(aq), KCl(aq), AlCl<sub>3</sub>(aq), and (0.964 NaCl + 0.136 KCl)(aq) at temperatures between (283 and 472) K, pressures up to 68.5 MPa, and molalities up to 6 mol·kg<sup>-1</sup>*. J. Chem. Eng. Data, 2012. **57**(4): p. 1288-1304.
398. Gates, J.A. and R.H. Wood, *Density and apparent molar volume of aqueous calcium chloride at 323-600 K*. J. Chem. Eng. Data, 1989. **34**(1): p. 53-56.
399. Obsil, M., et al., *Volumes of MgCl<sub>2</sub>(aq) at temperatures from 298 K to 623 K and pressures up to 30 MPa*. J. Chem. Thermodyn., 1997. **29**(5): p. 575-593.
400. Swenson, D.M. and E.M. Woolley, *Apparent molar volumes and apparent molar heat capacities of aqueous KI, HIO<sub>3</sub>, NaIO<sub>3</sub>, and KIO<sub>3</sub> at temperatures from 278.15 K to 393.15 K and at the pressure 0.35 MPa*. J. Chem. Thermodyn., 2008. **40**(1): p. 54-66.
401. Corti, H. and J. Simonson, *Densities and apparent molar volumes of NaOH(aq) to the temperature 623 K and pressure to 30 MPa*. J. Solution Chem., 2006. **35**(8): p. 1057-1074.

402. Xiao, C. and P. Trentaine, *Apparent molar volumes of aqueous sodium trifluoromethanesulfonate and trifluoromethanesulfonic acid from 283 K to 600 K and pressures up to 20 MPa*. J. Solution Chem., 1997. **26**(3): p. 277-294.
403. Sharygin, A.V. and R.H. Wood, *Volumes and heat capacities of aqueous solutions of ammonium chloride from the temperatures 298.15 K to 623 K and pressures to 28 MPa*. J. Chem. Thermodyn., 1996. **28**(8): p. 851-872.
404. Crovetto, R., S.N. Lvov, and R.H. Wood, *Vapor pressures and densities of NaCl(aq) and KCl(aq) at the temperature 623 K and CaCl<sub>2</sub>(aq) at the temperatures 623 K and 643 K*. J. Chem. Thermodyn., 1993. **25**(1): p. 127-138.
405. Majer, V., et al., *Volumetric properties of aqueous NaCl solutions from 0.0025 to 5.0 mol·kg<sup>-1</sup>, 323 to 600 K, and 0.1 to 40 MPa*. J. Chem. Thermodyn., 1988. **20**(8): p. 949-968.
406. Majer, V., R. Crovetto, and R.H. Wood, *A new version of vibrating-tube flow densitometer for measurements at temperatures up to 730 K*. J. Chem. Thermodyn., 1991. **23**(4): p. 333-344.
407. Gates, J.A. and R.H. Wood, *Densities of aqueous solutions of sodium chloride, magnesium chloride, potassium chloride, sodium bromide, lithium chloride, and calcium chloride from 0.05 to 5.0 mol·kg<sup>-1</sup> and 0.1013 to 40 MPa at 298.15 K*. J. Chem. Eng. Data, 1985. **30**(1): p. 44-49.
408. Kumar, A., *Densities of aqueous strontium chloride solutions up to 200.degree.C and at 20 bar*. J. Chem. Eng. Data, 1986. **31**(3): p. 347-349.
409. Ellis, A.J., *Partial molal volumes of MgCl<sub>2</sub>, CaCl<sub>2</sub>, SrCl<sub>2</sub>, and BaCl<sub>2</sub> in aqueous solution to 200[degree]*. J. Chem. Soc. A: Ino, Phy, Theo., 1967: p. 660-664.
410. Obšil, M., et al., *Densities and apparent molar volumes of Na<sub>2</sub>SO<sub>4</sub>(aq) and K<sub>2</sub>SO<sub>4</sub>(aq) at temperatures from 298 K to 573 K and at pressures up to 30 MPa*. J. Chem. Eng. Data, 1997. **42**(1): p. 137-142.
411. Phutela, R.C. and K.S. Pitzer, *Densities and apparent molar volumes of aqueous magnesium sulfate and sodium sulfate to 473 K and 100 bar*. J. Chem. Eng. Data, 1986. **31**(3): p. 320-327.
412. Rogers, P.S.Z. and K.S. Pitzer, *High-temperature thermodynamic properties of aqueous sodium sulfate solutions*. J. Phys. Chem., 1981. **85**(20): p. 2886-2895.
413. Sharygin, A.V. and R.H. Wood, *Densities of aqueous solutions of sodium carbonate and sodium bicarbonate at temperatures from (298 to 623) K and pressures to 28 MPa*. J. Chem. Thermodyn., 1998. **30**(12): p. 1555-1570.
414. Mao, S. and Z. Duan, *The P, V, T,x properties of binary aqueous chloride solutions up to T = 573 K and 100 MPa*. J. Chem. Thermodyn., 2008. **40**(7): p. 1046-1063.
415. Safarov, J.T., *The investigation of the (p,p,T) and (p<sub>s</sub>,p<sub>s</sub>,T<sub>s</sub>) properties of {(1-x)CH<sub>3</sub>OH + xLiBr} for the application in absorption refrigeration machines and heat pumps*. J. Chem. Thermodyn., 2003. **35**(12): p. 1929-1937.

416. Francke, H. and M. Thorade, *Density and viscosity of brine: An overview from a process engineers perspective*. Chem. Erde Geochem., 2010. **70**(Supplement 3): p. 23-32.
417. Krumgalz, B.S., et al., *Volumetric interaction parameters for single-solute aqueous electrolyte solutions at various temperatures*. J. Phys. Chem. Ref. Data, 2000. **29**(5): p. 1123-1140.
418. Rowe, A.M. and J.C.S. Chou, *Pressure-volume-temperature-concentration relation of aqueous sodium chloride solutions*. J. Chem. Eng. Data, 1970. **15**(1): p. 61-66.
419. Young, T.F. and M.B. Smith, *Thermodynamic properties of mixtures of electrolytes in aqueous solutions*. J. Phys. Chem., 1954. **58**(9): p. 716-724.
420. Hu, Y.-F., *A new equation for predicting the density of multicomponent aqueous solutions conforming to the linear isopiestic relation*. PCCP, 2000. **2**(10): p. 2379-2382.
421. Patwardhan, V.S. and A. Kumar, *Thermodynamic properties of aqueous solutions of mixed electrolytes: A new mixing rule*. AIChE J., 1993. **39**(4): p. 711-714.
422. Patwardhan, V.S. and A. Kumar, *A unified approach for prediction of thermodynamic properties of aqueous mixed-electrolyte solutions. Part II: Volume, thermal, and other properties*. AIChE J., 1986. **32**(9): p. 1429-1438.
423. Shibue, Y., *A Modified Rackett equation applied to water and aqueous NaCl and KCl solutions*. J. Chem. Eng. Data, 2000. **45**(4): p. 523-529.
424. Yang, J.-Z., et al., *Systematic study of the simple predictive approaches for thermodynamic and transport properties of multicomponent solutions*. Ind. Eng. Chem. Res., 2010. **49**(16): p. 7671-7677.
425. Duan, Z., N. Moller, and J.H. Weare, *A high temperature equation of state for the H<sub>2</sub>O-CaCl<sub>2</sub> and H<sub>2</sub>O-MgCl<sub>2</sub> systems*. Geochim. Cosmochim. Acta, 2006. **70**(15): p. 3765-3777.
426. Liu, Y.-S., et al., *Viscosity and density of the system NaCl + LaCl<sub>3</sub> + H<sub>2</sub>O and its binary subsystems at different temperatures*. J. Chem. Eng. Data, 2009. **54**(3): p. 739-744.
427. Anderko, A. and K.S. Pitzer, *Phase equilibria and volumetric properties of the systems KCl-H<sub>2</sub>O and NaCl-KCl-H<sub>2</sub>O above 573 K: Equation of state representation*. Geochim. Cosmochim. Acta, 1993. **57**(20): p. 4885-4897.
428. Kiepe, J., et al., *Experimental determination and correlation of liquid density data of electrolyte mixtures containing water or methanol*. Ind. Eng. Chem. Res., 2003. **42**(9): p. 2022-2029.
429. Apelblat, A. and E. Manzurola, *Volumetric and thermal properties of some aqueous electrolyte solutions: Part 5. Potassium bromide and potassium iodide 0.1, 0.5, and 1.0 mol·kg<sup>-1</sup> solutions at temperatures from T=278.15 to 338.15 K*. J. Mol. Liq., 2005. **118**(1-3): p. 77-88.



430. Isono, T., *Density, viscosity, and electrolytic conductivity of concentrated aqueous electrolyte solutions at several temperatures. Alkaline-earth chlorides, lanthanum chloride, sodium chloride, sodium nitrate, sodium bromide, potassium nitrate, potassium bromide, and cadmium nitrate.* J. Chem. Eng. Data, 1984. **29**(1): p. 45-52.
431. Wimby, J.M. and T.S. Berntsson, *Viscosity and density of aqueous solutions of lithium bromide, lithium chloride, zinc bromide, calcium chloride and lithium nitrate. 1. Single salt solutions.* J. Chem. Eng. Data, 1994. **39**(1): p. 68-72.
432. Romankiw, L.A. and I.M. Chou, *Densities of aqueous sodium chloride, potassium chloride, magnesium chloride, and calcium chloride binary solutions in the concentration range 0.5-6.1 m at 25, 30, 35, 40, and 45.degree.C.* J. Chem. Eng. Data, 1983. **28**(3): p. 300-305.
433. Dunn, L.A., *Apparent molar volumes of electrolytes. Part 3.-Some 1-1 and 2-1 electrolytes in aqueous solution at 0, 5, 15, 35, 45, 55 and 65 [degree]C.* Transactions of the Faraday Society, 1968. **64**: p. 2951-2961.
434. Pawar, R.R., S.B. Nahire, and M. Hasan, *Solubility and density of potassium iodide in binary ethanol-water solvent mixture at (298.15, 303.15, 308.15, and 313.15) K.* J. Chem. Eng. Data, 2009. **54**(6): p. 1935-1937.
435. Connaughton, L., J. Hershey, and F. Millero, *PVT properties of concentrated aqueous electrolytes: V. Densities and apparent molal volumes of the four major sea salts from dilute solution to saturation and from 0 to 100°C.* J. Solution Chem., 1986. **15**(12): p. 989-1002.
436. Phang, S. and R.H. Stokes, *Density, viscosity, conductance, and transference number of concentrated aqueous magnesium chloride at 25°C.* J. Solution Chem., 1980. **9**(7): p. 497-505.
437. Surdo, A.L., E.M. Alzola, and F.J. Millero, *The (p, V, T) properties of concentrated aqueous electrolytes I. Densities and apparent molar volumes of NaCl, Na<sub>2</sub>SO<sub>4</sub>, MgCl<sub>2</sub>, and MgSO<sub>4</sub> solutions from 0.1 mol·kg<sup>-1</sup> to saturation and from 273.15 to 323.15 K.* J. Chem. Thermodyn., 1982. **14**(7): p. 649-662.
438. Miller, D.G., et al., *Mutual diffusion coefficients and ionic transport coefficients  $I_{ij}$  of magnesium chloride-water at 25.degree.C.* J. Phys. Chem., 1984. **88**(23): p. 5739-5748.
439. Chen, C.-T.A., J.H. Chen, and F.J. Millero, *Densities of sodium chloride, magnesium chloride, sodium sulfate, and magnesium sulfate aqueous solutions at 1 atm from 0 to 50.degree.C and from 0.001 to 1.5 m.* J. Chem. Eng. Data, 1980. **25**(4): p. 307-310.
440. Dedick, E., et al., *The PVT properties of concentrated aqueous electrolytes IX. The volume properties of KCl and K<sub>2</sub>SO<sub>4</sub> and their mixtures with NaCl and Na<sub>2</sub>SO<sub>4</sub> as a function of temperature.* J. Solution Chem., 1990. **19**(4): p. 353-374.
441. Chenlo, F., et al., *Viscosities of aqueous solutions of sucrose and sodium chloride of interest in osmotic dehydration processes.* J. Food Eng., 2002. **54**(4): p. 347-352.

442. Fabuss, B.M., A. Korosi, and A.K.M.S. Hug, *Densities of binary and ternary aqueous solutions of NaCl, Na<sub>2</sub>SO<sub>4</sub> and MgSO<sub>4</sub> of sea waters, and sea water concentrates*. J. Chem. Eng. Data, 1966. **11**(3): p. 325-331.
443. Galleguillos, H.R., et al., *Compositions, densities, and refractive indices of potassium chloride + ethanol + water and sodium chloride + ethanol + water solutions at (298.15 and 313.15) K*. J. Chem. Eng. Data, 2003. **48**(2): p. 405-410.
444. Gucker, F.T., D. Stubley, and D.J. Hill, *The isentropic compressibilities of aqueous solutions of some alkali halides at 298.15 K*. J. Chem. Thermodyn., 1975. **7**(9): p. 865-873.
445. Guetachew, T., et al., *Study of NaCl solutions in a mixed solvent H<sub>2</sub>O-CH<sub>3</sub>OH: Experimental densities and comparison with calculated values obtained with a modified Pitzer's model*. J. Solution Chem., 1996. **25**(9): p. 895-903.
446. Korosi, A. and B.M. Fabuss, *Viscosities of binary aqueous solutions of sodium chloride, potassium chloride, sodium sulfate, and magnesium sulfate at concentrations and temperatures of interest in desalination processes*. J. Chem. Eng. Data, 1968. **13**(4): p. 548-552.
447. Apelblat, A. and E. Manzurola, *Volumetric properties of water, and solutions of sodium chloride and potassium chloride at temperatures from T = 277.15 K to T = 343.15 K at molalities of (0.1, 0.5, and 1.0) mol·kg<sup>-1</sup>*. J. Chem. Thermodyn., 1999. **31**(7): p. 869-893.
448. Kumar, A., *Densities of aqueous strontium chloride solutions up to 200.degree.C and at 20 bar*. J. Chem. Eng. Data, 1986. **31**(3): p. 347-349.
449. Hervello, M.F. and A. Sánchez, *Densities of univalent cation sulfates in ethanol + water solutions*. J. Chem. Eng. Data, 2007. **52**(3): p. 752-756.
450. Hershey, J.P., S. Sotolongo, and F.J. Millero, *Densities and compressibilities of aqueous sodium carbonate and bicarbonate from 0 to 45°C*. J. Solution Chem., 1983. **12**(4): p. 233-254.
451. O. Kratky, H.L., H. Stabinger, *Determination of density of liquids and gases to an accuracy of 10<sup>-6</sup> cm<sup>3</sup>, with a sample volume of only 0,6cm<sup>3</sup>*. Z. Angew. Phys, 1969. **27**: p. 273-277.
452. B Lagourette, C.B., H Saint-Guirons, P Xans and H Zhou, *Densimeter calibration method versus temperature and pressure* Meas. Sci. Technol., 1992. **3**(8): p. 699-703.
453. Sousa, A.T., et al., *Density of HCFC 142b and of its mixture with HCFC 22*. Fluid Phase Equilib., 1992. **80**: p. 213-225.
454. H&D Fitzgerald. *Technical Assessment of the Anton Paar DMA5000 density meter*. 2000 [http://density.co.uk/wp-content/uploads/2012/02/review\\_of\\_5000.pdf](http://density.co.uk/wp-content/uploads/2012/02/review_of_5000.pdf).
455. Eom, H.-C., H. Park, and H.-S. Yoon, *Preparation of anhydrous magnesium chloride from ammonium magnesium chloride hexahydrate*. Adv. Powder Technol., 2010. **21**(2): p. 125-130.

456. Wagner, W. and A. Pruss, *The IAPWS Formulation 1995 for the Thermodynamic Properties of Ordinary Water Substance for General and Scientific Use*. J. Phys. Chem. Ref. Data, 2002. **31**(2): p. 387-535.
457. Bottero, J.Y., et al., *Investigation of the hydrolysis of aqueous solutions of aluminum chloride. 2. Nature and structure by small-angle x-ray scattering*. J. Phys. Chem., 1982. **86**(18): p. 3667-3673.
458. Bottero, J.Y., et al., *Studies of hydrolyzed aluminum chloride solutions. 1. Nature of aluminum species and composition of aqueous solutions*. J. Phys. Chem., 1980. **84**(22): p. 2933-2939.
459. Dymond, J.H. and R. Malhotra, *The Tait equation: 100 years on*. Int. J. Thermophys., 1988. **9**(6): p. 941-951.
460. Miller, D.G., et al., *Effects of different sized concentration differences across free diffusion boundaries and comparison of Gouy and Rayleigh diffusion measurements using NaCl-KCl-H<sub>2</sub>O*. J. Solution Chem., 1996. **25**(12): p. 1185-1211.
461. Zhang and Han, *Viscosity and density of water + sodium chloride + potassium chloride solutions at 298.15 K*. J. Chem. Eng. Data, 1996. **41**(3): p. 516-520.
462. Kumar, A., *Mixture densities of aqueous potassium chloride with sodium chloride up to ionic strength 4.5 mol·kg<sup>-1</sup> and at 298.15 K*. J. Chem. Eng. Data, 1988. **33**(2): p. 198-199.
463. Millero, F.J., et al., *PVT properties of concentrated aqueous electrolytes. III. Volume changes for mixing the major sea salts at I=1.0 and 3.0 at 25°C*. J. Solution Chem., 1985. **14**(12): p. 837-851.
464. Goldsack, D.E. and A.A. Franchetto, *The viscosity of concentrated electrolyte solutions—III. A mixture law*. Electrochim. Acta, 1977. **22**(11): p. 1287-1294.
465. Fabuss, B.M., A. Korosi, and D.F. Othmer, *Viscosities of aqueous solutions of several electrolytes present in sea water*. J. Chem. Eng. Data, 1969. **14**(2): p. 192-197.
466. Millero, F.J. and S. Sotolongo, *PVT properties of concentrated aqueous electrolytes. 7. The volumes of mixing of the reciprocal salt pairs potassium chloride, potassium sulfate, sodium chloride, and sodium sulfate at 25.degree.C and I = 1.5 M*. J. Chem. Eng. Data, 1986. **31**(4): p. 470-472.
467. Sanmamed, Y.A., et al., *An accurate calibration method for high pressure vibrating tube densimeters in the density interval (700 to 1600) kg·m<sup>-3</sup>*. J. Chem. Thermodyn., 2009. **41**(9): p. 1060-1068.
468. Holcomb, C.D. and S.L. Outcalt, *A theoretically-based calibration and evaluation procedure for vibrating-tube densimeters*. Fluid Phase Equilib., 1998. **150-151**: p. 815-827.
469. Lemmon, E.W. and R. Span, *Short Fundamental Equations of State for 20 Industrial Fluids*. J. Chem. Eng. Data, 2006. **51**(3): p. 785-850.

470. Nghiem, L.X., et al., *Asphaltene Precipitation: Phase Behaviour Modelling and Compositional Simulation*, in *SPE Asia Pacific Conference on Integrated Modelling for Asset Management*. 2000, Copyright 2000, Society of Petroleum Engineers Inc.: Yokohama, Japan.
471. Vargas, F.M., et al., *Modeling Asphaltene Phase Behavior in Crude Oil Systems Using the Perturbed Chain Form of the Statistical Associating Fluid Theory (PC-SAFT) Equation of State*. *Energy & Fuels*, 2009. **23**(3): p. 1140-1146.
472. Artola, P.-A., et al., *Understanding the fluid phase behaviour of crude oil: Asphaltene precipitation*. *Fluid Phase Equilib.*, 2011. **306**(1): p. 129-136.
473. Oakes, C.S., J.M. Simonson, and R.J. Bodnar, *Apparent molar volumes of aqueous calcium chloride to 250°C, 400 bars, and from molalities of 0.242 to 6.150*. *J. Solution Chem.*, 1995. **24**(9): p. 897-916.
474. Saluja, P.P.S. and J.C. LeBlanc, *Apparent molar heat capacities and volumes of aqueous solutions of magnesium chloride, calcium chloride, and strontium chloride at elevated temperatures*. *J. Chem. Eng. Data*, 1987. **32**(1): p. 72-76.
475. Saluja, P.P.S., et al., *Apparent molar heat capacities and volumes of mixed electrolytes: [NaCl(aq) + CaCl<sub>2</sub>(aq)], [NaCl(aq) + MgCl<sub>2</sub>(aq)], and [CaCl<sub>2</sub>(aq) + MgCl<sub>2</sub>(aq)]*. *J. Chem. Eng. Data*, 1995. **40**(2): p. 398-406.
476. Zhang, H.-L., G.-H. Chen, and S.-J. Han, *Viscosity and density of H<sub>2</sub>O + NaCl + CaCl<sub>2</sub> and H<sub>2</sub>O + KCl + CaCl<sub>2</sub> at 298.15 K*. *J. Chem. Eng. Data*, 1997. **42**(3): p. 526-530.
477. Oakes, C.S., et al., *CaCl<sub>2</sub>-H<sub>2</sub>O in the supercritical and two-phase ranges* *Int. J. Thermophys.*, 1995. **16**(2): p. 483-492.
478. Kumar, A., G. Atkinson, and R.D. Howell, *Thermodynamics of concentrated electrolyte mixtures. II. Densities and compressibilities of aqueous NaCl-CaCl<sub>2</sub> at 25 °C*. *J. Solution Chem.*, 1982. **11**(12): p. 857-870.
479. Gèrald Perron, A.R., Jacques E. Desnoyers, *Heat capacities and volumes of NaCl, MgCl<sub>2</sub>, CaCl<sub>2</sub>, and NiCl<sub>2</sub> up to 6 molal in water*. *Can. J. Chem.*, 1981. **59**(21): p. 3049-3054.
480. Millero, F.J.W., Gary K.; Chetirkin, Peter V., *Relative sound velocities of sea salts at 25°C*. *J. Acoust. Soc. Am.*, 1977. **61**( 6): p. 1492-1498.
481. Gèrald Perron, J.E.D., Frank J. Millero, *Apparent molal volumes and heat capacities of alkaline earth chlorides in water at 25°C*. *Can. J. Chem.*, 1974. **52**(22): p. 3738-3741.
482. Millero, F.J. and J.H. Knox, *Apparent molal volumes of aqueous sodium fluoride, sodium sulfate, potassium chloride, potassium sulfate, magnesium chloride, and magnesium sulfate solutions at 0.deg. and 50.deg.* *J. Chem. Eng. Data*, 1973. **18**(4): p. 407-411.
483. Ellis, A.J., *Partial molal volumes in high-temperature water. Part III. Halide and oxyanion salts*. *J. Chem. Soc. A: Ino, Phy, Theo.*, 1968: p. 1138-1143.

484. Lemire, R.J., et al., *Heat capacities and densities of electrolyte mixtures in aqueous solution – Application to the determination of apparent molar heat capacities and volumes for potassium triiodide and dioxoneptunium(V) perchlorate*. J. Nucl. Mater., 1993. **201**: p. 165-175.
485. Saluja, P.P.S., R.J. Lemire, and J.C. LeBlanc, *High-temperature thermodynamics of aqueous alkali-metal salts*. J. Chem. Thermodyn., 1992. **24**(2): p. 181-203.
486. Manohar, S., D. Puchalska, and G. Atkinson, *Pressure-volume-temperature properties of aqueous mixed electrolyte solutions: sodium chloride + barium chloride from 25 to 140.degree.C*. J. Chem. Eng. Data, 1994. **39**(1): p. 150-154.
487. Majer, V., et al., *Volumetric properties of aqueous 1-1 electrolyte solutions near and above the critical temperature of water I. Densities and apparent molar volumes of NaCl(aq) from 0.0025 mol·kg<sup>-1</sup> to 3.1 mol·kg<sup>-1</sup>, 604.4 K to 725.5 K, and 18.5 MPa to 38.0 MPa*. J. Chem. Thermodyn., 1991. **23**(3): p. 213-229.
488. Rogers, P.S.Z., D.J. Bradley, and K.S. Pitzer, *Densities of aqueous sodium chloride solutions from 75 to 200.degree.C at 20 bar*. J. Chem. Eng. Data, 1982. **27**(1): p. 47-50.
489. Ellis, A.J., *Partial molal volumes of alkali chlorides in aqueous solution to 200[degree]*. J. Chem. Soc. A: Ino, Phy, Theo., 1966: p. 1579-1584.
490. Sandengen, K. and B. Kaasa, *Estimation of monoethylene Glycol (MEG) content in water + MEG + NaCl + NaHCO<sub>3</sub> solutions*. J. Chem. Eng. Data, 2006. **51**(2): p. 443-447.
491. Mendonça, Â.F.S.S., et al., *Apparent molar volumes of proline-leucine dipeptide in NaCl aqueous solutions at 318.15 K*. J. Solution Chem., 2005. **34**(1): p. 25-32.
492. Comesaña, J.F., et al., *Densities and viscosities of ternary systems of water + glucose + sodium chloride at several temperatures*. J. Chem. Eng. Data, 2003. **48**(2): p. 362-366.
493. Mironenko, M.V., et al., *Experimental determination of the volumetric properties of NaCl solutions to 253 K*. J. Phys. Chem. B, 2001. **105**(41): p. 9909-9912.
494. Patel, S.G. and N. Kishore, *Thermodynamics of nucleic acid bases and nucleosides in water from 25 to 55°C*. J. Solution Chem., 1995. **24**(1): p. 25-38.
495. Oakes, C.S., J.M. Simonson, and R.J. Bodnar, *The system sodium chloride-calcium chloride-water. 2. Densities for ionic strengths 0.1-19.2 mol·kg<sup>-1</sup> at 298.15 and 308.15 and at 0.1 MPa*. J. Chem. Eng. Data, 1990. **35**(3): p. 304-309.
496. Kumar, A. and G. Atkinson, *Thermodynamics of concentrated electrolyte mixtures. 3. Apparent molal volumes, compressibilities, and expansibilities of sodium chloride-calcium chloride mixtures from 5 to 35.degree.C*. J. Phys. Chem., 1983. **87**(26): p. 5504-5507.
497. Perron, G., A. Roux, and J.E. Desnoyers, *Heat capacities and volumes of NaCl, MgCl<sub>2</sub>, CaCl<sub>2</sub>, and NiCl<sub>2</sub> up to 6 molal in water*. Can. J. Chem., 1981. **59**(21): p. 3049-3054.

498. Dessauges, G., N. Miljevic, and W.A. Van Hook, *Isotope effects in aqueous systems. 9. Partial molar volumes of sodium chloride/water and sodium chloride/water-d<sub>2</sub> solutions at 15, 30, and 45.degree.C.* J. Phys. Chem., 1980. **84**(20): p. 2587-2595.
499. Galleguillos, H.R., et al., *Experimental determination of densities of aqueous electrolyte mixtures containing B(OH)<sub>3</sub> or Na<sub>2</sub>B<sub>4</sub>O<sub>7</sub> and their correlation with the Pitzer model.* Ind. Eng. Chem. Res., 2006. **45**(19): p. 6604-6613.
500. Singha, M. and Y.K. Sharma, *Applications of activation energy and transition state theory for nucleos(t)ides and furanose helix puckering interactions in aqueous medium from 288.15 to 298.15K* Phys. Chem. Liq., 2006. **44**(1): p. 1-14.
501. Soto, A., A. Arce, and M.K. Khoshkbarchi, *Thermodynamics of diglycine and triglycine in aqueous NaCl solutions: Apparent molar volume, isentropic compressibility, and refractive index.* J. Solution Chem., 2004. **33**(1): p. 11-21.
502. Zhuo, K., et al., *Volumetric properties for the monosaccharide (d-xylose, d-arabinose, d-glucose, d-galactose)-NaCl-water systems at 298.15 K.* Carbohydr. Res., 2000. **328**(3): p. 383-391.
503. Kawaizumi, F., F. Nakao, and H. Nomura, *Partial molar volumes and compressibilities of 1-1 type chlorides, bromides, tetraphenylphosphonium chloride, and sodium tetraphenylborate in water-acetone mixtures.* J. Chem. Eng. Data, 1988. **33**(2): p. 204-211.
504. Lankford, J.I. and C.M. Criss, *Partial molar heat capacities of selected electrolytes and benzene in methanol and dimethylsulfoxide at 25, 40, and 80°C.* J. Solution Chem., 1987. **16**(11): p. 885-906.
505. Lankford, J.I., W.T. Holladay, and C.M. Criss, *Isentropic compressibilities of univalent electrolytes in methanol at 25°C.* J. Solution Chem., 1984. **13**(10): p. 699-720.
506. Alary, J.F., et al., *Simultaneous flow measurement of specific heats and thermal expansion coefficients of liquids: Aqueous t-BuOH mixtures and neat alkanols and alkanediols at 25°C.* J. Solution Chem., 1982. **11**(11): p. 755-776.
507. Firth, J.G. and H.J.V. Tyrrell, *381. Diffusion coefficients for aqueous silver nitrate solutions at 25[degree], 35[degree], and 45[degree] from diaphragm-cell measurements.* Journal of the Chemical Society (Resumed), 1962: p. 2042-2047.
508. Galleguillos, H.R., E.K. Flores, and C.E. Aguirre, *Density and refractive index for boric acid + potassium chloride + water and disodium tetraborate + potassium chloride + water systems at (20, 25, and 30) °C.* J. Chem. Eng. Data, 2001. **46**(6): p. 1632-1634.
509. Harrison, W.R. and E.P. Perman, *Vapour pressure and heat of dilution of aqueous solutions.* Transactions of the Faraday Society, 1927. **23**: p. 1-22.
510. Sulston, W.J., *The temperature variation of the viscosity of aqueous solutions of strong electrolytes* Proceedings of the Physical Society, 1935. **47**(4): p. 657.
511. Kumar, A., *Densities and apparent molal volumes of aqueous potassium chloride-calcium chloride mixtures at 298.15 K.* J. Chem. Eng. Data, 1986. **31**(1): p. 21-23.

- 
512. MacInnes, D.A. and M.O. Dayhoff, *The partial molal volumes of potassium chloride, potassium and sodium iodides and of iodine in aqueous solution at 25°C.* J. Am. Chem. Soc., 1952. **74**(4): p. 1017-1020.
513. Wirth, H.E., *The partial molal volumes of potassium chloride, potassium bromide and potassium sulfate in sodium chloride solutions.* J. Am. Chem. Soc., 1937. **59**(12): p. 2549-2554.
514. Ostroff, A.G., B.S. Snowden, and D.E. Woessner, *Viscosities of protonated and deuterated water solutions of alkali metal chlorides.* J. Phys. Chem., 1969. **73**(8): p. 2784-2785.
515. Parton, H.N., R.A. Robinson, and A.J. Metson, *Anomalies in aqueous solutions of potassium chloride and lead chloride.* Transactions of the Faraday Society, 1939. **35**: p. 402-412.
516. Jones, G. and W.A. Ray, *The surface tension of solutions of electrolytes as a function of the concentration. I. A differential method for measuring relative surface tension.* J. Am. Chem. Soc., 1937. **59**(1): p. 187-198.
517. Wirth, H.E. and A. LoSurdo, *Temperature dependence of volume changes on mixing electrolyte solutions.* J. Chem. Eng. Data, 1968. **13**(2): p. 226-231.
518. Banipal, P.K., et al., *Effect of sodium sulphate on the volumetric, rheological and refractometric properties of some disaccharides in aqueous solutions at different temperatures.* Z. Phys. Chem., 2008. **222**(1): p. 177-204.
519. Pearce, J.N. and H.C. Eckstrom, *Vapor pressures and partial molal volumes of aqueous solutions of the alkali sulfates at 25°C.* J. Am. Chem. Soc., 1937. **59**(12): p. 2689-2691.
520. Zhuo, K., et al., *Volumetric and viscosity properties of MgSO<sub>4</sub>/CuSO<sub>4</sub> in sucrose + water solutions at 298.15 K.* J. Chem. Eng. Data, 2008. **53**(9): p. 2022-2028.
521. Fleischmann, W. and A. Mersmann, *Solubility, density and viscosity for sodium sulfate-methanol-water systems.* J. Chem. Eng. Data, 1984. **29**(4): p. 452-456.
522. Trimble, H.M., *The solubility of potassium permanganate in solutions of potassium sulfate and of sodium, sulfate.* J. Am. Chem. Soc., 1922. **44**(3): p. 451-460.
523. Sandengen, K. and B. Kaasa, *Estimation of Monoethylene Glycol (MEG) Content in Water + MEG + NaCl + NaHCO<sub>3</sub> Solutions.* J. Chem. Eng. Data, 2006. **51**(2): p. 443-447.
524. Millero, F.J., G.K. Ward, and P.V. Chetirkin, *Relative sound velocities of sea salts at 25[degree]C.* J. Acoust. Soc. Am., 1977. **61**(6): p. 1492-1498.
525. Peña, M.P., E. Vercher, and A. Martínez-Andreu, *Apparent molar volumes of strontium chloride in ethanol + water at 298.15 K.* J. Chem. Eng. Data, 1997. **42**(1): p. 187-189.
526. Shedlovsky, T. and A.S. Brown, *The electrolytic conductivity of alkaline earth chlorides in water at 25°C.* J. Am. Chem. Soc., 1934. **56**(5): p. 1066-1071.

- 
527. Rard, J.A. and D.G. Miller, *Mutual diffusion coefficients of SrCl<sub>2</sub>-H<sub>2</sub>O and CsCl-H<sub>2</sub>O at 25 [degree]C from Rayleigh interferometry*. J. Chem. Soc., Faraday Trans. 1: Phy Chem in Cond Phas, 1982. **78**(3): p. 887-896.
528. Perron, G., J.E. Desnoyers, and F.J. Millero, *Apparent molal volumes and heat capacities of alkaline earth chlorides in water at 25°C*. Can. J. Chem., 1974. **52**(22): p. 3738-3741.
529. Yan, Z., et al., *Effect of temperature on volumetric and viscosity properties of some α-amino acids in aqueous calcium chloride solutions*. Fluid Phase Equilib., 2004. **215**(2): p. 143-150.
530. Ruby, C.E. and J. Kawai, *the densities, equivalent conductances and relative viscosities at 25°C of solutions of hydrochloric acid, potassium chloride and sodium chloride, and the binary and ternary mixtures of constant chloride-ion-constituent content*. J. Am. Chem. Soc., 1926. **48**(5): p. 1119-1128.





## A.2. Technical Specifications of the Servo Motor

### DC - Servo - Motoren

### Moteurs servo DC


### DC - Servo - Motors

### SM - DC

.. 30Nm

.. 5000/min

- Permanent - Erregt
- Für Drehzahl- und Drehmomentregelung
- Integrierter Tachodynamo
- Drehgeberanbau
  
- Aimant permanent
- Pour le réglage de vitesse et couple
- Tachymètre incorporé
- Annexe des encodeurs
  
- Permanent magnet
- Speed and torque control applications
- Integrated tach
- Encoder - annexe



HardmeierControl

**Technische Daten / Données techniques / Characteristics**

Typ Type	Nenn Drehmom. Cp.torq.nominal Cont. stall torque	Nennstrom Courant nominal Cont. stall curr.	Drehzahl Vitesse Speed	Spannung Tension Voltage	Drehmoment Torque Rated torque	Strom Courant Current	Leistung Puissance Rated power
	$M_0$ [Nm]	$I_0$ [A]	$n_n$ [min <sup>-1</sup> ]	$U_n$ [V]	$M_n$ [Nm]	$I_n$ [A]	$P_n$ [kW]
MT22D2-19	0.5	2.8	4000	76	0.34	1.9	0.14
MT22G2-19	0.7	3.9	4000	76	0.50	2.8	0.21
MT22R2-19	1.2	6.7	4000	76	0.96	5.4	0.40
MT30E4-32	1.1	3.8	3200	102	0.94	3.3	0.32
MT30E4-52	1.1	2.3	2200	114	0.65	1.4	0.15
MT30H4-44	2.1	4.9	2500	110	1.60	3.7	0.42
MT30M4-59	3.0	5.6	2000	118	2.04	3.8	0.43
MT30U4-36	4.5	13.3	3200	115	2.79	8.2	0.95
MT30Z4-61	5.0	8.6	1800	110	4.00	7.0	0.74
MT40P4-61	6.0	10.9	2400	146	5.44	9.9	1.42
MT40ZD4-60	11.0	20.0	2400	144	8.50	15.5	2.22

*Weitere Typen auf Anfrage / Autres types sur demande / Further types on request*

**Standardausführung**

- Spitzendrehmomente bis 5 x  $M_0$
- Drehzahlbereich bis 1:10'000
- Thermo-switch (exkl. MT22)
- Schutzart IP44 (IP65), unbelüftet
- DC-Tacho integriert (9.5V/1000min<sup>-1</sup>)
- Klemmenkasten oder Kabelausführung (MT22)
- Montage horizontal oder vertikal
- Leistungsdaten gelten für Formfaktor 1.0 und <40°C Umgebungstemperatur

**Exécution standard**

- Couple de torque max. 5 x  $M_0$
- Gamme de vitesse jusqu'à 1:10'000
- Thermo-rupteur (excl. MT22)
- Protection IP44 (IP65), non ventilé
- Tachymètre DC incorporé (9.5V/1000min<sup>-1</sup>)
- Boîte à bornes ou câble (MT22)
- Montage horizontal ou vertical
- Les données sont valable au facteur de forme 1.0 et temp. ambiante jusqu'à 40°C

**Standard features**

- Peak-torsion up to 5 x  $M_0$
- Speed range up to 1:10'000
- Temperature switch (excl. MT22)
- Protection IP44 (IP65), no cooling
- DC - tach integrated (9.5V/1000min<sup>-1</sup>)
- Terminal box or wires (MT22)
- Horizontal or vertical mounting
- Power - datas with form factor 1.0 and ambient temperature <40°C

**Optionen**

- Wellenende und Adapter für Drehgeber
- Integrierte Stillstandsbremse 24VDC (90V)
- Stecker statt Klemmenkasten
- Öldichtung auf Antriebswelle
- Fussmontage
- Spezialwellen und Flansche nach IEC, NEMA, Sonderspezifikationen
- Fremdlüfter 230V/ac 50/60Hz (für ca. doppeltes Drehmoment)
- Getriebeanbau

**Options**

- Bout d'arbre et adapter pour encodeur
- Frein d'arrêt incorporé 24VDC (90V)
- Fiche au lieu de boîte à bornes
- joint d'arbre
- Montage à pied
- arbres et brides spéciales selon CEI, NEMA, propres spécifications
- Ventilateur auxiliaire 230V/ac 50/60Hz (permet env. double couple)
- Annexe des réducteurs

**Options**

- Shaft-end and adapter for encoder
- Failsafe holding brake 24VDC (90V)
- Plug instead of terminal box
- Oil seal on shaft
- Foot band type
- Special shaft and flange for IEC, NEMA, special specification
- External fan 230V/ac 50/60Hz (for about double torque)
- Gearbox-fitting

*Technische Änderungen vorbehalten*

*Sous réserve de changements techniques.*

*Subject to alteration*

**Hardmeier Control**

DBL\_SMDC\_0417\_DFE.DOC

SM-DC - 1/4

### A.3 Technical Specifications of the Encoder

## Hohlwellen - Encoder

## Encodeur à arbre creux


## Hollow shaft encoder

# E 260

- Speziell geeignet für Einbau in Servomotoren
- Optoelektronisches System mit Infrarot LED
- Flexible Montage mit Hohlwelle 6mm (10mm)
- Speisung 5 bis 24V<sub>DC</sub>

- Spécialement qualifié pour montage aux moteurs servo
- Système optoélectronique avec LED infrarouge
- Montage flexible avec arbre creux 6mm (10mm)
- Alimentation 5 à 24V<sub>DC</sub>

- Ideal for servo-motors applications
- Opto-electronic system with infra-red LED
- Flexible butterfly mounting with hollow shaft 6 (10)mm
- Supply 5 to 24V<sub>DC</sub>



Typ	Type	Type	E 260-6-500-HV	E 260-6-1000-HV
Impulszahl	Nombre d'imp.	Pulses per rev.	500 Imp/U	1000 Imp/U
Anschluss	Alimentation	Supply	5 .. 24V <sub>DC</sub> (+/-5%)	

Weitere Typen auf Anfrage / Autres types sur demande / Further types on request

Umgebungsbedingungen	Conditions d'ambiante	Environmental specifications
Betriebstemperatur	Température de service	Operating temperature
Lagertemperatur	Température de stockage	Storage temperature
Luftfeuchtigkeit	Humidité	Humidity
Vibration	Vibration	Vibration
Shock	Choc	Shock
Schutzart	Protection	Protection

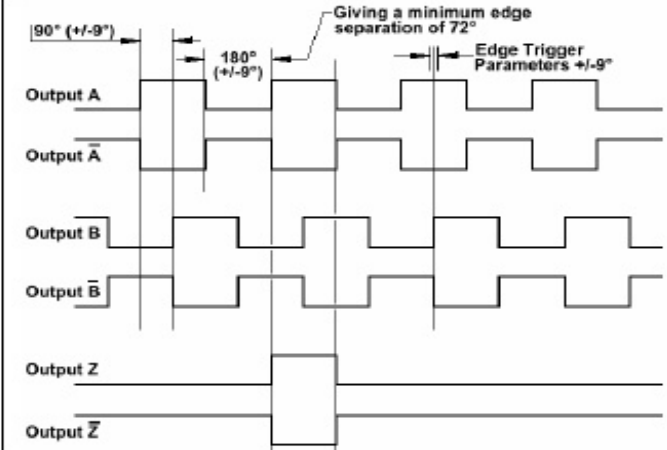
0...+100°C	-25 ... +120°C	95% n.c.
10g @58 ... 500Hz	50g @11ms	IP54

Elektrische Spezifikationen	Données électriques	Electrical specifications
Ausgangssignale	Signaux de sortie	Output signal:
Ausgangsschaltung	Circuit de sortie	Output circuit:
Max. Impulsfrequenz	Fréquence d'impulse max.	Max. frequency response
Stromverbrauch	Consommation de courante	Current consumption

A, B, Z, /A, /B, /Z	5..24V <sub>DC</sub> Line - Driver	200kHz
		50mA (plus output-current)

Optionen	Variantes	Options
- Impulszahlen: 200 .. 2500	- Nombres d'imp	- Pulses per rotation
- Hohlwelle	- Arbre creux	- Hollow shaft
- Schutzart	- Protection	- Protection

250 .. 2500 Imp/U	10, 12mm etc. (E260-10...)	IP64
-------------------	----------------------------	------



Drehrichtung im Uhrzeigersinn

Rotation en sens des aiguilles d'une montre

Clockwise rotation

	Kabel	Câble	Cable
+V	weiss	blanc	white
0V	schwarz	noir	black
A	braun	brun	brown
/A	gelb	jaune	yellow
B	rot	rouge	red
/B	grün	vert	green
Z	orange	orange	orange
/Z	blau	bleu	blue

Technische Änderungen vorbehalten  
 Sous réserve de changements techniques  
 Subject to alteration

**Hardmeier Control**

DBL\_E260\_0601\_DFE.DOC

E260 - 1 / 2



## A.4 Technical Specifications of the Quizix Pumps

Reservoir Analysis

### Quizix™ Q5000

#### **PRECISION METERING PUMPS**

**Pulse-free Pumps For Critical Applications**

Quizix Q5000 Precision Metering Pumps are manufactured by Chandler Engineering and designed for applications that require pulse-free fluid delivery or receiving. These robust pumps are capable of being heated and are ideal for pumping at a constant rate or constant pressure. The Q5000 can also be used to provide a constant differential pressure by using inputs from remote pressure transducers.

These pumps were developed specifically for fluid delivery and fluid pressure control applications in core flow analysis. However, Quizix pumps have satisfied the requirements of many other laboratory and science applications. These pumps are also used production environments where precision pulse-free flow or volume measurements are critical.

The four different models of the Q5000 cover a wide range of pressure capabilities and flow rates. These pumps are supplied as either a single pump cylinder or as systems containing up to eight pump cylinders. Single cylinders deliver or receive a fluid for pressure control or in intermittent flow applications. A dual cylinder pump provides continuous pulse-free pumping.

**Operational Simplicity**

The Q5000 pumps are very easy to operate. PumpWorks™ is a user-friendly software package that provides complete control over any Quizix pump. This easy-to-use interface indicates the detailed status of each pump cylinder including its piston positions and direction, valve positions, flow rate, pressure, cylinder volume and cumulative volume pumped.

**FEATURES**

- ✓ Pulse-free flow at all rates and pressures
- ✓ Deliver, receive or recirculate fluids
- ✓ Control pump based upon time, pressure, rate, fluid volume or sequenced events
- ✓ Operational simplicity via PumpWorks™ software
- ✓ Systems can control up to eight pump cylinders
- ✓ High temperature option to 320°F / 160°C
- ✓ Stainless steel or HASTELLOY® wetted parts

2001 North Indianwood Avenue, Broken Arrow, OK 74012 • Phone: 918-250-7200 • Fax: 918-459-0165

© 2008, by AMETEK, Inc. All rights reserved. e-mail: [chandler.sales@ametek.com](mailto:chandler.sales@ametek.com) • [www.chandlereng.com](http://www.chandlereng.com)

## Quizix™ Q5000

Pumps can be programmed to deliver a specified amount of fluid or operate for a specified period of time and then repeat the cycle as many times as desired. The programming allows for unattended operation of the Quizix pumps. All measured information on the pump can be logged and easily exported for graphing and analysis.

One of the unique features of the Q5000 is the ability to keep the fluid heated when circulating fluids. This high temperature option allows the entire pump barrel to be inserted into an oven assembly where its temperature can be maintained up to 320°F / 160°C.

### Engineering Excellence for Long-term Performance

Chandler Engineering builds durability and reliability into every Quizix pump. The unique design and technology built into each pump eliminates the need for constant maintenance. The long-wearing piston seals are readily accessible and easy to replace if needed. Chandler Engineering also provides worldwide service for maintaining pump performance.

### Specifications

Q5000 Precision Metering Pumps					
Model	Maximum Pressure	Maximum Flow Rate	Cylinder Stroke Volume	Minimum Flow Rate	Options
Q5000-2.5K	2,500 psi 17.2 MPa	60 mL/min 3,600 mL/hr	37 mL	186 nL/min 11,200 nL/hr	SS or HC, HT
Q5000-5K	5,000 psi 34.5 MPa	30 mL/min 1,800 mL/hr	21 mL	105 nL/min 6,300 nL/hr	SS or HC, HT
Q5000-10K	10,000 psi 68.9 MPa	15 mL/min 900 mL/hr	9.3 mL	18 nL/min 1,080 nL/hr	SS or HC, HT
Q5000-20K	20,000 psi 137.9 MPa	7.5 mL/min 450 mL/hr	5.2 mL	10 nL/min 600 nL/hr	HC

**Notes:**  
 SS: Wetted components may be ordered in stainless steel 316  
 HC: Wetted parts may be ordered in HASTELLOY® C-276  
 HT: Available with high temperature option for heating fluid ends up to 320°F / 160°C

Computer required to run PumpWorks™ pump control software.

### Utilities

#### Air

65 - 100 psi / 450 - 690 kPa, clean and dry

#### Power

120/240 VAC, 50/60 Hz

Manufacturer's specifications subject to change without notice

R0109.002



#### CHANDLER ENGINEERING

2001 North Indianwood Avenue, Broken Arrow, OK 74012

Tel: +1 918-250-7200 • Fax: +1 918-459-0165

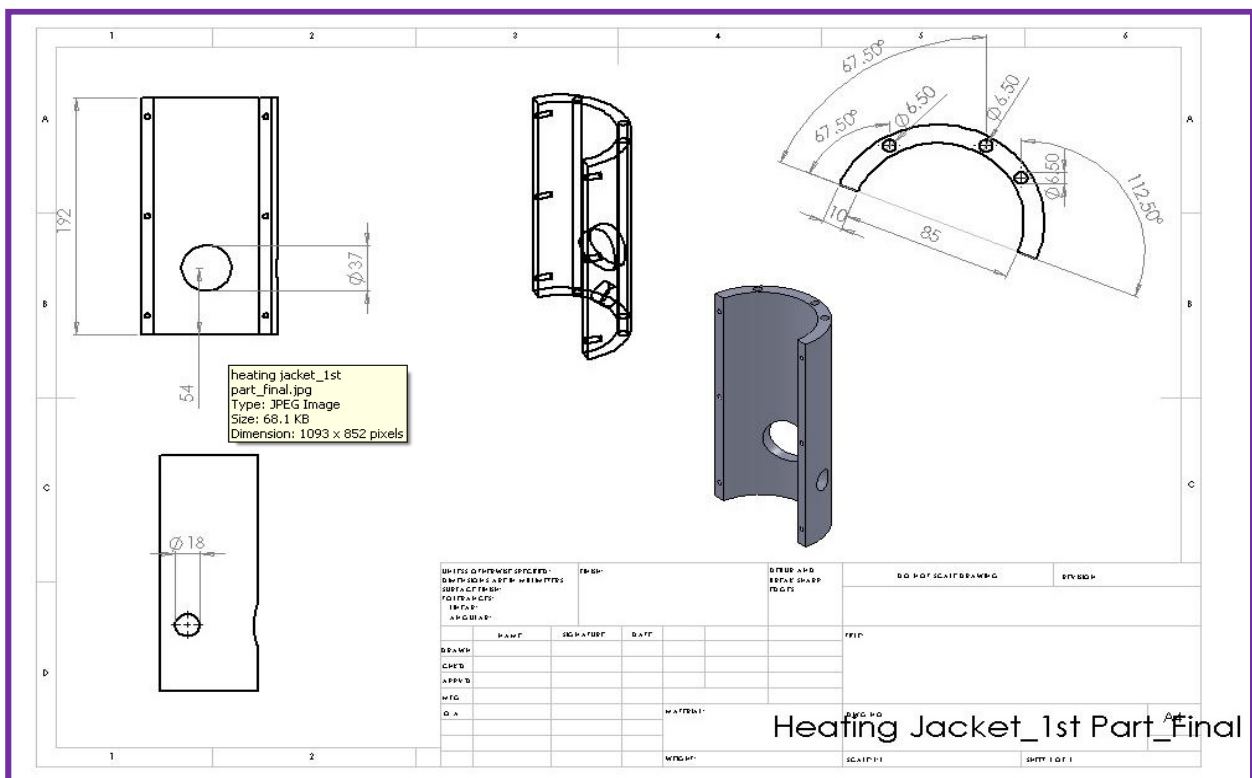
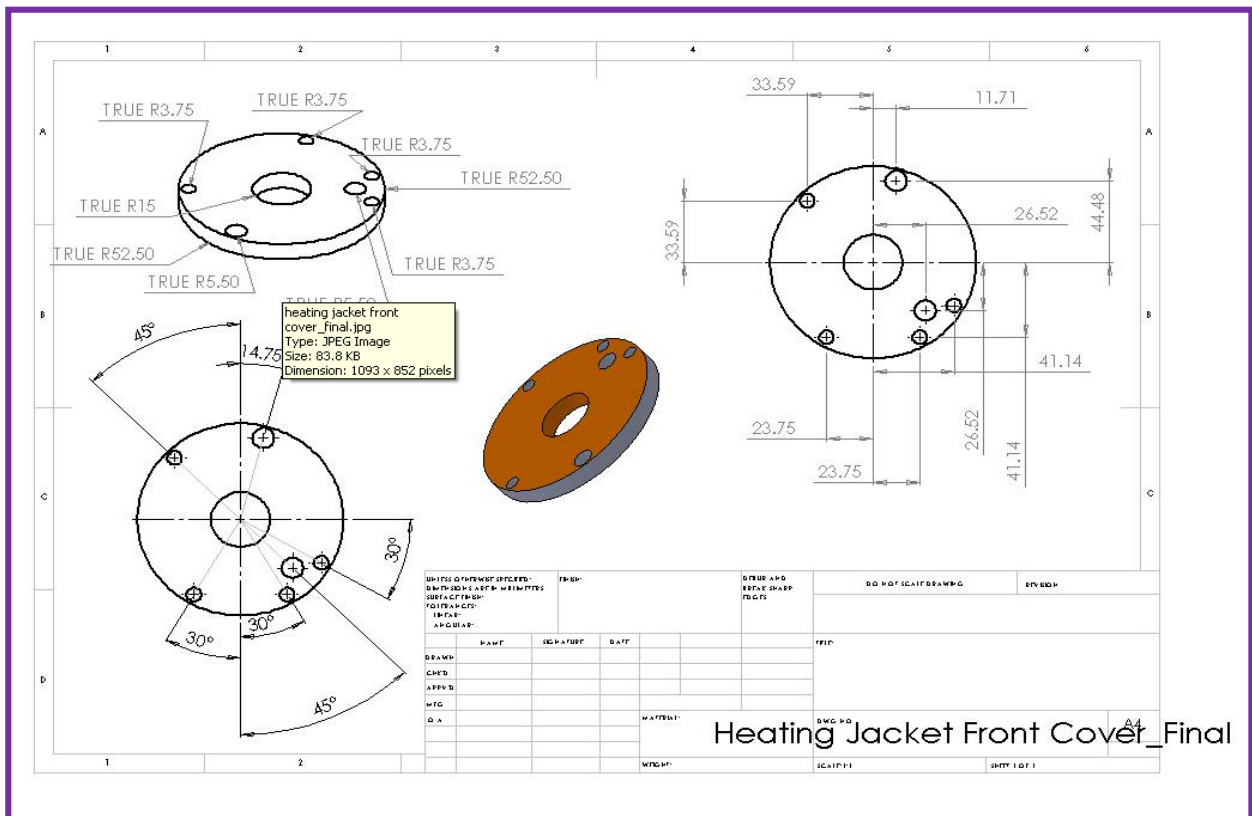
e-mail: [chandler.sales@ametek.com](mailto:chandler.sales@ametek.com) • [www.chandlereng.com](http://www.chandlereng.com)

#### Houston Sales and Services

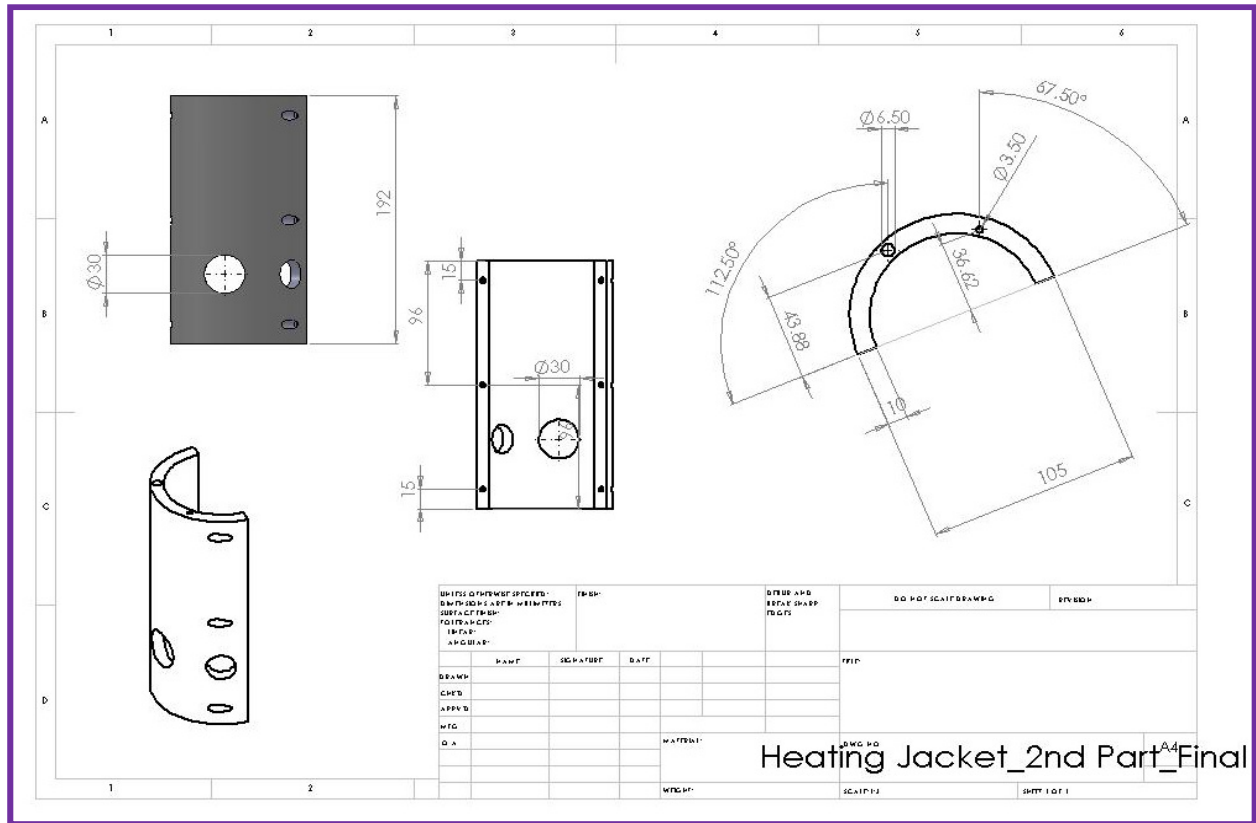
4903 W. Sam Houston Parkway, N., Suite A-400, Houston, TX 77041

Tel: +1 713-466-4900 • Fax: +1 713-649-1924

### A.5 Detailed Drawings of the Heating Jacket







### A.6 Technical Specifications of the Pressure Transducer

## Low Profile *thru-FLO*<sup>TM</sup> Pressure Transducer

## MODEL DF2

Connector pictured is optional

The Model DF2 is well suited for OEM applications that require frequent cleaning and flushing of aggressive fluids. The Model DF2 provides pressure sensing and control in a variety of analytical instruments.

**FEATURES**

- True Zero Internal Dead Volume
- One-Piece Flow-Thru Element
- Pressure Range From 0-1000 Up To 20K psig
- Simple Mounting - Small Footprint
- Accurate And Rugged By Design
- Fine Zero Adjustment
- Choice Of Wetted Materials
- Excellent EMI Protection
- RoHS Compliant (Electronics only)

**TYPICAL APPLICATIONS**

- Chromatography
- Pharmaceutical
- Medical
- Semiconductor

37 Manning Rd, Billerica MA 01821 • phone 1-978-667-5301  
 fax 1-978-667-6804 • www.djstruments.com • straingageexperts@dynisco.com



## LOW PROFILE THRU-FLO™ PRESSURE TRANSDUCER MODEL DF2

### SPECIFICATIONS

#### Performance

Pressure Sensor Type: . . . . . One piece thru-FLO™ Element  
 Pressure ranges . . . . . 0-1000 up to 20,000 psig

#### Linearity and Hysteresis

combined . . . . . Within 0.25% of F.S.(BFSL)  
 Operating temperature range . . -40°F to +140°F (-40°C to +60°C)  
 Compensated temperature range . . . . . 77°F to +140°F (25°C to 60°C)  
 Storage temperature . . . . . -40°F to +176°F (-40°C to +80°C)  
 (cable limited)

#### Temperature compensation

Zero . . . . . 0.02% of Full scale per °C  
 Span . . . . . 0.03% of Full scale per °C  
 Zero Balance AT 25°C . . . . . 0.500 ±0.150 VDC  
 (a zero trim pot is provided)  
 Calibration medium . . . . . Distilled water and IPA

#### Electrical

Electronics . . . . . RoHS Compliant, Splash proof  
 Excitation voltage . . . . . 9.75 to 26 VDC  
 Max. current drain . . . . . 30 mA  
 Output impedance . . . . . 100 Ohms Max.  
 Full scale output change . . . . . 5.000 ±0.050 VDC

#### Electrical connections

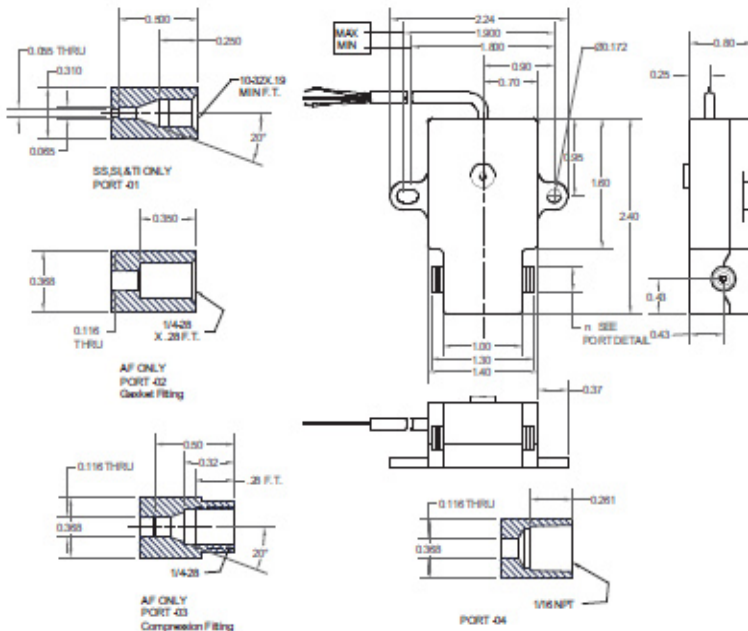
**3 Wire**  
 Pin 1 White +Signal  
 Pin 2 Black -Signal & Common  
 Pin 3 Red +Excitation  
 Yellow Shield  
**4 Wire**  
 Pin 1 Green +Signal  
 Pin 2 White -Signal  
 Pin 3 Red +Excitation  
 Pin 4 Black Common  
 Yellow Shield

#### Mechanical

Proof Pressure . . . . . 2x full scale or 25K psia whichever is less  
 Shock . . . . . 500 G's all axes  
 Wetted materials . . . . . See table  
 Cover and Housing material . . . . . Nickel plated cast zinc  
 Internal volume . . . . . 12 Microliters max. for port -01  
 100 Microliters max. for ports -02,-03,-04  
 Max. installation Torque . . . . . 50 in.lbs. for ports -01 & -04  
 20 in.lbs. for ports -02 & -03  
 Zero shift due to torquing . . . . . 3% of F.S. at 40 in. lbs.  
 Weight . . . . . 150 grams max.

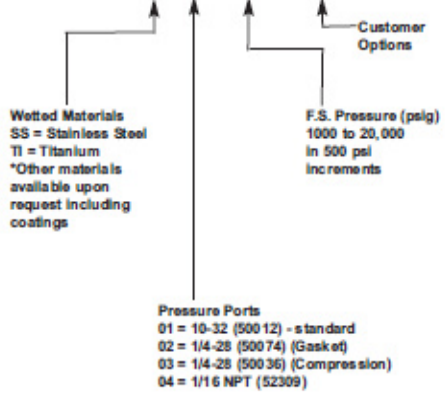
For best EMI immunity, connect cable drain wire at cables end to the analog ground and mount the housing to the chassis.  
 Listed specifications are standard. Specifications may change for certain combinations. Not all combinations are available. Consult factory for further information such as other ranges, materials and options not listed.

#### Model DF2 Dimensions



#### Ordering Information:

DF2-XX-XX-XXXX-XXXX



Example: DF2-SS-01-10000  
 10,000 PSI, stainless steel, 10-32 chromatography pressure port, standard 8 in. of cable.



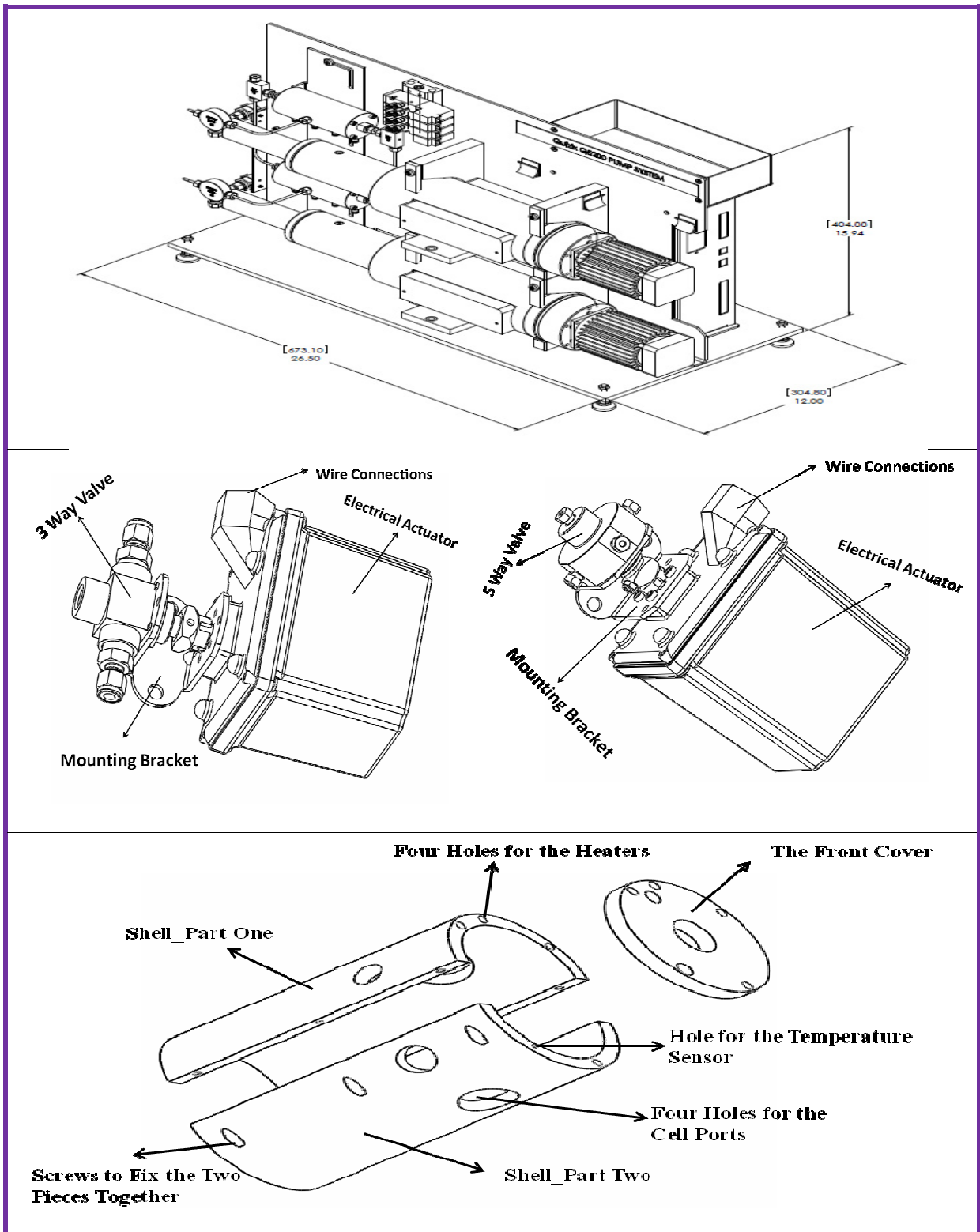
37Manning Road  
 Billerica, MA 01821  
 T: 978-667-5301  
 F: 978-667-6804  
 Email: straingageexperts@dynisco.com  
 Website: www.djstruments.com

This information is accurate to the best of the manufacturer's knowledge. However, we reserve the right to change specifications at any time. Please contact your sales representative for specific order inquiries.

04500-1001-000



**A.7** Schematic drawings representing the Quizix pumps, three and five ways electrical actuated valves, and the heating jacket used in this work.



**A.8** List of the main parts of the synthetic apparatus, together with supplier details and specifications

<b>Part Name</b>	<b>Supplier / Material / Model</b>	<b>Specifications / Notes</b>
Equilibrium Cell	Sitec-Sieber / Hastelloy C-276, Stainless Steel, Sapphire / 759.1061	40 MPa, 473.15 K, 11-67 cm <sup>3</sup>
Servo Motor	Hardmeier Control / MT30U4-36	4.5 Nm, 13.3 A, 950 W, 4000 max rpm
The Encoder	Hardmeier Control / E 260-6-1000 HV	1000 PPM, 5-24 Vdc
Limit Switches	Burgess / V3S	For Safety Precautions
Safety Head	Sitec-Sieber / Hastelloy C-276 / 728.0500-HC276	50 MPa
Motion Controller	Trio Motion Technology / Trio MC302x	For controlling the servo motor
Servo Controller System	Micromech System	Supplied as full servo control package
Quiziz Pumps	Strata Technology / Hastelloy C-276 / Q5000	70 MPa, 15 ml max flow, 9.3 ml stroke volume
Two way air operated valve	Sitec-Sieber / Hastelloy C-276/ 610.3224-HC276	100 MPa
Three way manual valve	Sitec-Sieber / Hastelloy C-276/ 610.3240-HC276	100 MPa
Two way manual valve	Sitec-Sieber / Hastelloy C-276/ 610.3220-HC276	100 MPa
Rupture Disk	Sitec-Sieber / Hastelloy C-276/ 728.0500-HC276	50 MPa
Pressure Transducer	DJ instruments / Ti 6Al4V / DF2	Low dead volume, 5.00 ± 0.050 Vdc, 40 MPa
Temperature Sensors	Sensing Devices / Arnold. Platinum	200 C, 4 wire RTD, different lengths and diameters
Cartridge Heaters	Watlow / stainless steel braid / FIREROD	240V, 200W
PID Controller	Eurotherm / 2216E	Temperature Controller
Supervisory Controller	CAREL	For safety precautions
LE USB Camera (CCD)	Edmund Optics / 54363	Colour, Ultra-Compact, 752 x 480 Pixel
Magnet Stirrer Bar	Fisher Scientific	For stirring
Magnet	Magnet Sales & Service	For stirring
Magnet Servo Motor	RS Components Ltd	Brushless Motor , 50W , 200Vac

<b>Part Name</b>	<b>Supplier / Material / Model</b>	<b>Specifications / Notes</b>
Filter (CO <sub>2</sub> Side)	Swagelok/ stainless steel	Particulate Filter , 1/4", 2 micron
Filter (Gas Side)	Swagelok/ stainless steel	1/8", 2 micron pore size
Filter (Solvents)	Kinesis / Polymer	1/8" OD tubing, 10 micron
Vacuum Pump	Edwards / Teflon heads	Lab Diaphragm Vacuum Pump, 50 Hz
5 way actuator valve	Swagelok / Stainless Steel / SS-43ZFS2-049-42DCZ	17.2 MPa, 24 Vdc
3 way actuator valve	Swagelok / Stainless Steel / SS-H83XPS4-41DCX	70 MPa, 24 Vdc
Chiller	Radleys / HB3006.0015.99	For cooling the Quizix pumps
Solenoid Valve	SMC Pneumatics, model V114A-5LUB-M5)	
Agilent unit	Agilent / 34901A	Acquisition data

## Appendix B. Safety Critical System Analysis (SCSA)

**Table B.1** General experimental procedure steps which are used in SCSA analysis

Step	Procedure
1	Check that all gas supplies for adequate cylinder pressure. Exchange empty cylinders as necessary and leave all cylinder valves closed.
2	Check that there are no leakage and no fault signals/alarms such as high pressure or high temperature alarms.
3	Clean the system and evacuate the entire system. This includes multiple steps of CO <sub>2</sub> and flushing with solvents such as hexane and/or toluene.
4	Charge a desired amount of liquid through valve V-9 to pump E-2 and inject a desired amount of that liquid to the variable volume cell through V-19
5	Charge a desired amount of hydrocarbon gases (if any) through valve V-8 to pump E-1 and inject a desired amount of this gas to the variable volume cell through V-19
6	Clean and vacuum pump E-1 to remove remaining traces of HC gases
7	Charge a desired amount of CO <sub>2</sub> through valve V-8 to Quizix pump E-1 and inject a desired amount of this gas to the variable volume cell through V-19
8	Control temperature using temperature controller to desired value (max. 473 K), control pressure using the servo motor to desired value (max 40 MPa)
9	Carry the measurements and collection of experimental data over a range of operating pressure and temperature as desired.
10	Vent system through V-18 to reduce pressure before opening the valve V-16
11	Dispose fluids when experimental measurements are finished by opening the valve V-16
12	Flush and clean apparatus using solvents such as hexane and/or toluene. Using the same process as in step 3
13	Shutdown. Ensure all gas cylinder outlet valves are closed and adjust pressure to zero pressure. Bring cell pressure and temperature to ambient conditions and shutdown.

**Table B.2** Safety critical system analysis (SCSA) for evaluating the hazards and risks posed by the system and ways to minimize them

<b>Task Step 1.</b>	
Potential Hazards	<ol style="list-style-type: none"> <li>1. Inability to know if the CO<sub>2</sub> cylinder is empty (no regulator and cylinder gauge).</li> <li>2. Failure or inability to follow cylinder exchange procedure. Lifting and transporting of cylinders.</li> </ol>
Potential Consequences	<ol style="list-style-type: none"> <li>1. Possible exposure to gas. Inadvertent overpressure. Possible low O<sub>2</sub> environment in the lab.</li> <li>2. Possible physical injury. Possible release of gas and personnel exposure. Possible low O<sub>2</sub> environment in the lab.</li> </ol>
Recommended Controls	<ol style="list-style-type: none"> <li>1. Ensure that the CO<sub>2</sub> and other cylinders used for the experiments are delivered with pressure gauges.</li> <li>2. Ensure that there are isolation valves between the cylinders and the Quizix pumps.</li> <li>3. Design of facility allowing for removal and replacement of cylinders.</li> <li>4. Consider O<sub>2</sub> detector in the lab</li> </ol>
<b>Task Step 2.</b>	
Potential Hazards	<ol style="list-style-type: none"> <li>1. Possibility that the alarm does not function properly.</li> <li>2. Undetected leak. Not following or inability to follow leak detection procedure.</li> </ol>
Potential Consequences	<ol style="list-style-type: none"> <li>1. Potential for high pressure or high temperature. Possible personnel injury.</li> <li>2. Possible personnel exposure to gas. Possible personnel injury or low O<sub>2</sub> environment</li> </ol>
Recommended Controls	<ol style="list-style-type: none"> <li>1. Conduct routine system checks by setting temperature or pressure below maximum settings and test function by exceeding set points.</li> <li>2. Routine use of snoop test and Helium leak detection process.</li> <li>3. Rate of change of pressure in system. Operator response to rate of change of pressure.</li> <li>4. Routine maintenance of equipment. (e.g. routine replacement of rupture discs and PTFE seals)</li> </ol>
<b>Task Steps 3 and 4.</b>	
Potential Hazards	<ol style="list-style-type: none"> <li>1. Multiple cleaning steps. Potential for excess material to vent systems.</li> <li>2. Possible spill in spill tray due to improper installation of liquid bottle.</li> </ol>
Potential Consequences	<ol style="list-style-type: none"> <li>1. Management of wastes and vents</li> </ol>
Recommended Controls	<ol style="list-style-type: none"> <li>1. Common vent system to lab ventilation system.</li> </ol>
<b>Task Steps 5, 6 and 7</b>	
Potential Hazards	<ol style="list-style-type: none"> <li>1. Human error / misalignment of valves. Leakage in system (already discussed).</li> <li>2. Possibility of backflow through E-2 to liquid bottle.</li> <li>3. Possibility of over pressuring vacuum system. Already addressed through use of relief valve.</li> </ol>

Potential Consequences	<p>4. No new risks introduced by adding CO<sub>2</sub>. Already covered by the addition of HC gas.</p> <p>1. Possible overpressure of VVC if VVC piston is fully extended and Quizix pump is operating.</p> <p>2. Overpressure of bottle.</p>
Recommended Controls	<p>1. Operating and Experimental design procedure.</p> <p>2. Ensure that cylinders are delivered / installed with proper regulators.</p> <p>3. Install check valve at HC cylinder (similar to CO<sub>2</sub> cylinder design).</p> <p>4. Install check valve on outlet of liquid bottle.</p>
<b>Task Steps 8 and 9</b>	
Potential Hazards	<p>1. Possible incorrect set point for Temperature and Pressure controllers.</p> <p>2. Possibility that temperature sensor is removed during maintenance and not replaced when the equipment is reassembled.</p> <p>Possible to overpressure the system when the PVT piston is at end of stroke and system temperature is still increasing.</p>
Potential Consequences	<p>1. Possible equipment failure resulting in release of material and personnel exposure.</p> <p>2. Possible equipment failure resulting in release of material and personnel exposure.</p> <p>3. Possible equipment failure resulting in release of material and personnel exposure.</p>
Recommended Controls	<p>1. Hardware and software limits on maximum inputs for Pressure and Temperature.</p> <p>1. Rupture discs and relieve valves in place to prevent overpressure.</p> <p>2. Procedures for reassembly of equipment. Training and experience of researchers.</p> <p>3. Control logic shuts off temperature controller when PVT piston is fully extended and pressure is at maximum.</p>
<b>Task Steps 10, 11, 12 and 13</b>	
Potential Hazards	<p>1. Human error opening V-16 before system pressure is reduced.</p> <p>2. Cylinder valves not closed.</p>
Potential Consequences	<p>3. Possible high pressure to vacuum and vent system. Possible equipment damage and personnel exposure. No new issues. Already addressed in prior steps.</p> <p>4. System pressurizes to cylinder pressure</p>
Recommended Controls	<p>5. Pressure controllers have electronic readouts. Operator training for working on pressurized system.</p>

## Appendix C. Experimental Data for Mixtures Studied in this Work

Table C.1. Experimentally determined VLE pressures  $p$  for the (CO<sub>2</sub> + *n*-heptane + methylbenzene) mixture at temperatures of  $T$  and mole fractions  $x$ <sup>a</sup>

$p^{\text{exp}}/\text{MPa}$	$x_{\text{heptane}}$	$x_{\text{toluene}}$	$x_{\text{CO}_2}$	$y$	Status	$P^{\text{MIE}}/\text{MPa}$	% AAD
$T = 298.15 \text{ K}$							
0.503	0.1149	0.8319	0.0532	0.1214	bubble	0.434	13.7 2
1.052	0.1066	0.7719	0.1215	0.1214	bubble	0.994	5.51
1.755	0.0961	0.6956	0.2083	0.1214	bubble	1.704	2.91
3.313	0.0708	0.5129	0.4163	0.1214	bubble	3.271	1.27
4.352	0.0489	0.3543	0.5968	0.1214	bubble	4.299	1.22
4.774	0.0351	0.2541	0.7108	0.1214	bubble	4.766	0.17
5.104	0.0227	0.1646	0.8127	0.1214	bubble	5.132	-0.5 5
5.531	0.0125	0.0903	0.8972	0.1214	bubble	5.502	0.52
5.892	0.0060	0.0436	0.9504	0.1214	bubble	5.853	0.66
5.968	0.0050	0.0361	0.9589	0.1214	bubble	5.925	0.72
6.062	0.0032	0.0234	0.9734	0.1214	bubble	6.066	-0.0 7
6.085	0.0028	0.0202	0.9770	0.1214	bubble	6.105	-0.3 3
6.126	0.0022	0.0162	0.9816	0.1214	bubble	6.158	-0.5 2
6.21	0.0013	0.0097	0.9889	0.1214	bubble	6.249	-0.63
6.223	0.0011	0.0082	0.9906	0.1214	bubble	6.272	-0.7 9
6.186	0.0011	0.0080	0.9909	0.1214	bubble	6.276	-1.4 5
6.256	0.0006	0.0041	0.9954	0.1214	bubble	6.340	-1.3 4
0.695	0.2508	0.6761	0.0731	0.2706	bubble	0.574	17.4 1
1.425	0.2245	0.6050	0.1705	0.2706	bubble	1.345	5.61
2.901	0.1739	0.4689	0.3572	0.2706	bubble	2.773	4.41
4.206	0.1183	0.3190	0.5627	0.2706	bubble	4.059	3.50
5.250	0.0523	0.1409	0.8068	0.2706	bubble	5.087	3.10
5.475	0.0362	0.0977	0.8661	0.2706	bubble	5.335	2.56
5.625	0.0277	0.0746	0.8978	0.2706	bubble	5.495	2.31
5.725	0.0224	0.0605	0.9171	0.2706	bubble	5.608	2.04
5.792	0.0196	0.0529	0.9274	0.2706	bubble	5.676	2.00
0.473	0.4586	0.4931	0.0483	0.4819	bubble	0.364	23.0 4
1.241	0.4093	0.4400	0.1507	0.4819	bubble	1.142	7.98
2.205	0.3486	0.3747	0.2767	0.4819	bubble	2.101	4.72
3.825	0.2410	0.2591	0.5000	0.4819	bubble	3.634	4.99
4.501	0.1810	0.1945	0.6245	0.4819	bubble	4.307	4.31
4.850	0.1373	0.1476	0.7152	0.4819	bubble	4.707	2.95
5.355	0.0742	0.0798	0.8459	0.4819	bubble	5.233	2.28
5.525	0.0566	0.0609	0.8825	0.4819	bubble	5.406	2.15
5.712	0.0406	0.0437	0.9157	0.4819	bubble	5.594	2.07
5.805	0.0341	0.0367	0.9292	0.4819	bubble	5.683	2.10
6.135	0.0124	0.0133	0.9743	0.4819	bubble	6.073	1.01
6.230	0.0076	0.0082	0.9841	0.4819	bubble	6.187	0.69
6.255	0.0064	0.0068	0.9868	0.4819	bubble	6.222	0.53
0.882	0.6793	0.2261	0.0946	0.7503	bubble	0.689	21.8 8
1.565	0.6117	0.2036	0.1847	0.7503	bubble	1.359	13.1 6
2.419	0.5263	0.1751	0.2986	0.7503	bubble	2.205	8.85

*Appendix C. Experimental Data for Mixtures Studied in this Work*

$p^{exp}/\text{MPa}$	$x_{\text{heptane}}$	$x_{\text{toluene}}$	$x_{\text{CO}_2}$	$y$	Status	$P^{MIE}/\text{MPa}$	% AAD
2.937	0.4763	0.1585	0.3652	0.7503	bubble	2.686	8.55
3.625	0.4037	0.1343	0.4620	0.7503	bubble	3.343	7.78
4.221	0.3241	0.1079	0.5680	0.7503	bubble	3.983	5.64
4.762	0.2355	0.0784	0.6861	0.7503	bubble	4.572	3.99
4.930	0.2008	0.0668	0.7324	0.7503	bubble	4.771	3.23
5.012	0.1807	0.0601	0.7592	0.7503	bubble	4.881	2.61
5.101	0.1634	0.0544	0.7823	0.7503	bubble	4.974	2.49
5.152	0.1473	0.0490	0.8036	0.7503	bubble	5.060	1.79
5.455	0.1065	0.0354	0.8581	0.7503	bubble	5.291	3.01
5.625	0.0788	0.0262	0.8950	0.7503	bubble	5.474	2.68
5.736	0.0628	0.0209	0.9163	0.7503	bubble	5.598	2.41
5.975	0.0412	0.0137	0.9450	0.7503	bubble	5.801	2.91
6.053	0.0305	0.0102	0.9593	0.7503	bubble	5.923	2.15
6.145	0.0229	0.0076	0.9694	0.7503	bubble	6.021	2.02
6.172	0.0203	0.0067	0.9730	0.7503	bubble	6.059	1.83
6.223	0.0190	0.0063	0.9747	0.7503	bubble	6.078	2.33
<b>T = 323.15 K</b>							
1.245	0.1096	0.7928	0.0976	0.1214	bubble	1.135	8.84
2.400	0.0987	0.7146	0.1867	0.1214	bubble	2.180	9.17
2.65	0.0961	0.6957	0.2082	0.1214	bubble	2.433	8.19
3.742	0.0840	0.6079	0.3081	0.1214	bubble	3.590	4.06
4.815	0.0709	0.5130	0.4161	0.1214	bubble	4.777	0.79
6.381	0.0491	0.3553	0.5956	0.1214	bubble	6.478	-1.5 2
7.197	0.0352	0.2550	0.7098	0.1214	bubble	7.344	-2.0 4
7.84	0.0228	0.1650	0.8123	0.1214	bubble	8.033	-2.46
8.775	0.0113	0.0817	0.9071	0.1214	bubble	8.733	0.48
8.852	0.0085	0.0618	0.9297	0.1214	bubble	8.914	-0.7 0
8.965	0.0056	0.0407	0.9537	0.1214	bubble	9.035	-0.7 8
8.925	0.0040	0.0291	0.9669	0.1214	Dew	8.996	-0.80
8.824	0.0025	0.0182	0.9793	0.1214	Dew	8.728	1.09
8.756	0.0022	0.0162	0.9816	0.1214	Dew	8.599	1.79
0.676	0.2576	0.6942	0.0482	0.2706	bubble	0.541	19.9 7
1.678	0.2335	0.6293	0.1373	0.2706	bubble	1.536	8.46
4.175	0.1786	0.4813	0.3401	0.2706	bubble	3.812	8.69
6.015	0.1236	0.3331	0.5434	0.2706	bubble	5.872	2.38
7.295	0.0773	0.2084	0.7142	0.2706	bubble	7.259	0.49
8.142	0.0484	0.1306	0.8210	0.2706	bubble	8.009	1.63
8.423	0.0360	0.0971	0.8669	0.2706	bubble	8.347	0.90
8.625	0.0278	0.0750	0.8972	0.2706	bubble	8.586	0.45
8.865	0.0201	0.0543	0.9256	0.2706	bubble	8.815	0.56
9.016	0.0142	0.0382	0.9476	0.2706	bubble	8.949	0.74



*Appendix C. Experimental Data for Mixtures Studied in this Work*

$p^{EXP}/\text{MPa}$	$x_{\text{heptane}}$	$x_{\text{toluene}}$	$x_{\text{CO}_2}$	$y$	Status	$P^{MIE}/\text{MPa}$	% AAD
8.995	0.0092	0.0248	0.9660	0.2706	Dew	8.924	0.79
8.752	0.0053	0.0144	0.9803	0.2706	Dew	8.573	2.05
1.385	0.4324	0.4648	0.1028	0.4819	bubble	1.097	20.7 9
2.885	0.3717	0.3995	0.2288	0.4819	bubble	2.463	14.6 3
4.215	0.3100	0.3333	0.3566	0.4819	bubble	3.845	8.78
5.650	0.2412	0.2593	0.4996	0.4819	bubble	5.302	6.16
6.302	0.1917	0.2061	0.6022	0.4819	bubble	6.242	0.95
7.075	0.1429	0.1536	0.7035	0.4819	bubble	7.062	0.18
7.550	0.1147	0.1233	0.7620	0.4819	bubble	7.495	0.73
8.415	0.0616	0.0662	0.8722	0.4819	bubble	8.308	1.27
8.645	0.0486	0.0522	0.8992	0.4819	bubble	8.524	1.40
8.767	0.0408	0.0438	0.9154	0.4819	bubble	8.653	1.30
8.952	0.0208	0.0224	0.9569	0.4819	bubble	8.857	1.06
8.785	0.0137	0.0147	0.9716	0.4819	Dew	8.744	0.47
8.675	0.0124	0.0133	0.9743	0.4819	Dew	8.685	-0.12
0.550	0.7101	0.2364	0.0536	0.7503	bubble	0.552	-0.3 6
2.000	0.6232	0.2074	0.1694	0.7503	bubble	1.745	12.7 5
3.305	0.5419	0.1804	0.2777	0.7503	bubble	2.890	12.5 6
4.110	0.4933	0.1642	0.3425	0.7503	bubble	3.575	13.0 2
5.000	0.4190	0.1394	0.4416	0.7503	bubble	4.600	8.00
5.950	0.3397	0.1131	0.5472	0.7503	bubble	5.631	5.36
6.827	0.2374	0.0790	0.6836	0.7503	bubble	6.819	0.12
7.436	0.1814	0.0604	0.7583	0.7503	bubble	7.395	0.55
8.015	0.1321	0.0440	0.8240	0.7503	bubble	7.878	1.71
8.395	0.0926	0.0308	0.8766	0.7503	bubble	8.273	1.45
8.635	0.0699	0.0233	0.9068	0.7503	bubble	8.506	1.49
8.796	0.0562	0.0187	0.9251	0.7503	bubble	8.636	1.82
8.865	0.0545	0.0181	0.9274	0.7503	bubble	8.651	2.41
8.895	0.0371	0.0123	0.9506	0.7503	bubble	8.737	1.78
<b>T = 373.15 K</b>							
1.025	0.1161	0.8402	0.0437	0.1214	bubble	0.882	13.9 5
2.441	0.1076	0.7786	0.1138	0.1214	bubble	2.191	10.2 4
3.765	0.0987	0.7149	0.1864	0.1214	bubble	3.576	5.02
3.885	0.0979	0.7084	0.1937	0.1214	bubble	3.716	4.35
4.115	0.0961	0.6960	0.2079	0.1214	bubble	3.990	3.04
6.017	0.0839	0.6070	0.3091	0.1214	bubble	5.950	1.11
7.768	0.0712	0.5152	0.4136	0.1214	bubble	7.967	-2.5 6
7.875	0.0704	0.5097	0.4199	0.1214	bubble	8.087	-2.6 9
10.162	0.0546	0.3952	0.5502	0.1214	bubble	10.528	-3. 60
10.751	0.0491	0.3554	0.5955	0.1214	bubble	11.349	-5. 56
12.547	0.0352	0.2551	0.7096	0.1214	bubble	13.315	-6. 12

*Appendix C. Experimental Data for Mixtures Studied in this Work*

$p^{exp}/\text{MPa}$	$x_{\text{heptane}}$	$x_{\text{toluene}}$	$x_{\text{CO}_2}$	$y$	Status	$P^{MIE}/\text{MPa}$	% AAD
13.547	0.0228	0.1650	0.8122	0.1214	bubble	14.497	-7.01
1.922	0.2456	0.6619	0.0925	0.2706	bubble	1.713	10.87
3.786	0.2174	0.5860	0.1966	0.2706	bubble	3.603	4.83
7.175	0.1664	0.4486	0.3850	0.2706	bubble	7.103	1.00
10.435	0.1146	0.3090	0.5763	0.2706	bubble	10.584	-1.43
11.694	0.0913	0.2460	0.6627	0.2706	bubble	12.076	-3.27
13.256	0.0606	0.1634	0.7760	0.2706	bubble	13.741	-3.66
13.562	0.0450	0.1213	0.8337	0.2706	bubble	14.013	-3.33
13.532	0.0356	0.0961	0.8683	0.2706	Dew	13.700	-1.24
13.256	0.0240	0.0648	0.9112	0.2706	Dew	12.573	5.15
12.752	0.0180	0.0486	0.9334	0.2706	Dew	11.551	9.42
11.653	0.0136	0.0366	0.9498	0.2706	Dew	10.221	12.29
0.110	0.4819	0.5181	0.0000	0.4819	bubble		
0.650	0.4638	0.4986	0.0376	0.4819	bubble	0.712	-9.54
3.501	0.3914	0.4208	0.1879	0.4819	bubble	3.264	6.77
5.432	0.3399	0.3654	0.2947	0.4819	bubble	5.146	5.27
8.080	0.2664	0.2863	0.4473	0.4819	bubble	7.868	2.62
10.880	0.1841	0.1979	0.6180	0.4819	bubble	10.832	0.44
11.950	0.1485	0.1596	0.6919	0.4819	bubble	12.038	-0.74
13.040	0.1077	0.1158	0.7765	0.4819	bubble	13.179	-1.07
13.170	0.0718	0.0772	0.8509	0.4819	Dew	13.294	-0.94
13.100	0.0612	0.0658	0.8729	0.4819	Dew	12.986	0.87
12.250	0.0339	0.0364	0.9297	0.4819	Dew	11.184	8.70
0.853	0.7102	0.2364	0.0535	0.7503	bubble	0.930	-9.03
2.256	0.6529	0.2173	0.1298	0.7503	bubble	2.145	4.92
6.825	0.4511	0.1502	0.3987	0.7503	bubble	6.673	2.23
9.351	0.3378	0.1125	0.5497	0.7503	bubble	9.258	0.99
11.250	0.2443	0.0813	0.6744	0.7503	bubble	11.290	-0.36
12.160	0.1914	0.0637	0.7449	0.7503	bubble	12.295	-1.11
12.653	0.1547	0.0515	0.7938	0.7503	bubble	12.758	-0.83
12.812	0.1123	0.0374	0.8503	0.7503	bubble	12.678	1.05
12.702	0.0887	0.0295	0.8818	0.7503	Dew	12.189	4.04
12.431	0.0665	0.0221	0.9114	0.7503	Dew	11.404	8.26
12.152	0.0581	0.0193	0.9225	0.7503	Dew	10.968	9.74
11.735	0.0513	0.0171	0.9316	0.7503	Dew	10.486	10.64
<b>T = 423.15 K</b>							
1.258	0.1173	0.8492	0.0335	0.1214	bubble	1.080	14.15
3.454	0.1061	0.7682	0.1257	0.1214	bubble	3.371	2.40
4.905	0.0988	0.7152	0.1860	0.1214	bubble	4.880	0.51
5.415	0.0962	0.6963	0.2075	0.1214	bubble	5.421	-0.11
7.946	0.0839	0.6069	0.3092	0.1214	bubble	7.994	-0.60

*Appendix C. Experimental Data for Mixtures Studied in this Work*

$p^{EXP}/\text{MPa}$	$x_{\text{heptane}}$	$x_{\text{toluene}}$	$x_{\text{CO}_2}$	$y$	Status	$P^{MIE}/\text{MPa}$	% AAD
10.164	0.0712	0.5154	0.4134	0.1214	bubble	10.611	-4.40
12.526	0.0580	0.4199	0.5221	0.1214	bubble	13.230	-5.62
14.087	0.0491	0.3555	0.5954	0.1214	bubble	14.828	-5.26
15.857	0.0352	0.2552	0.7096	0.1214	bubble	16.382	-3.31
16.065	0.0279	0.2022	0.7698	0.1214	bubble	16.103	-0.24
16.021	0.0243	0.1761	0.7996	0.1214	Dew	15.534	3.04
15.775	0.0203	0.1469	0.8328	0.1214	Dew	14.555	7.73
15.372	0.0179	0.1294	0.8527	0.1214	Dew	13.761	10.48
15.276	0.0170	0.1234	0.8596	0.1214	Dew	13.437	12.04
1.425	0.2576	0.6942	0.0482	0.2706	bubble	1.420	0.35
4.323	0.2254	0.6074	0.1672	0.2706	bubble	4.200	2.85
6.153	0.2032	0.5477	0.2491	0.2706	bubble	6.155	-0.03
9.956	0.1578	0.4255	0.4167	0.2706	bubble	10.161	-2.06
11.813	0.1352	0.3645	0.5003	0.2706	bubble	12.084	-2.29
14.225	0.1024	0.2761	0.6215	0.2706	bubble	14.533	-2.17
15.536	0.0601	0.1620	0.7780	0.2706	bubble	15.009	3.39
15.375	0.0523	0.1410	0.8067	0.2706	Dew	14.411	6.27
15.052	0.0430	0.1159	0.8412	0.2706	Dew	13.345	11.34
14.832	0.0412	0.1110	0.8478	0.2706	Dew	13.082	11.80
14.432	0.0361	0.0972	0.8668	0.2706	Dew	12.137	15.90
0.405	0.4819	0.5181	0.0000	0.4819	bubble		
1.256	0.4637	0.4985	0.0379	0.4819	bubble	1.147	8.68
2.962	0.4255	0.4575	0.1170	0.4819	bubble	2.855	3.61
4.545	0.3916	0.4209	0.1875	0.4819	bubble	4.411	2.95
6.625	0.3437	0.3695	0.2868	0.4819	bubble	6.640	-0.23
10.320	0.2645	0.2843	0.4512	0.4819	bubble	10.306	0.14
13.250	0.1919	0.2063	0.6019	0.4819	bubble	13.287	-0.28
14.595	0.1405	0.1510	0.7086	0.4819	bubble	14.341	1.74
14.755	0.1107	0.1191	0.7702	0.4819	bubble	13.969	5.33
14.550	0.0865	0.0929	0.8206	0.4819	Dew	12.919	11.21
14.200	0.0747	0.0803	0.8449	0.4819	Dew	12.097	14.81
2.150	0.6846	0.2278	0.0876	0.7503	bubble	2.099	2.37
4.421	0.6017	0.2003	0.1980	0.7503	bubble	4.363	1.31
7.615	0.4884	0.1626	0.3490	0.7503	bubble	7.540	0.98
11.532	0.3436	0.1144	0.5420	0.7503	bubble	11.412	1.04
13.625	0.2376	0.0791	0.6833	0.7503	bubble	13.225	2.94
13.853	0.2102	0.0700	0.7199	0.7503	bubble	13.253	4.33
13.792	0.1692	0.0563	0.7745	0.7503	Dew	12.775	7.37
13.650	0.1514	0.0504	0.7982	0.7503	Dew	12.367	9.40
13.375	0.1269	0.0422	0.8309	0.7503	Dew	11.517	13.89

Appendix C. Experimental Data for Mixtures Studied in this Work

$p^{EXP}/\text{MPa}$	$x_{\text{heptane}}$	$x_{\text{toluene}}$	$x_{\text{CO}_2}$	$y$	Status	$P^{MIE}/\text{MPa}$	% AAD
<b><math>T = 473.15 \text{ K}</math></b>							
3.425	0.1099	0.7951	0.0950	0.1214	bubble	3.460	-1.0 2
5.915	0.0989	0.7157	0.1855	0.1214	bubble	6.002	-1.4 7
6.423	0.0967	0.7000	0.2033	0.1214	bubble	6.499	-1.1 8
9.540	0.0819	0.5930	0.3251	0.1214	bubble	9.822	-2.9 6
11.575	0.0712	0.5154	0.4134	0.1214	bubble	12.031	-3. 94
13.762	0.0577	0.4173	0.5250	0.1214	bubble	14.222	-3. 34
15.012	0.0473	0.3420	0.6107	0.1214	bubble	14.850	1. 08
15.979	0.0352	0.2552	0.7096	0.1214	bubble	13.679	14. 39
16.125	0.0331	0.2395	0.7275	0.1214	bubble	13.189	18. 21
0.955	0.2706	0.7294	0.0000	0.2706	bubble		
2.705	0.2513	0.6773	0.0714	0.2706	bubble	2.716	-0.4 1
5.975	0.2159	0.5821	0.2020	0.2706	bubble	6.140	-2.7 6
8.525	0.1884	0.5079	0.3037	0.2706	bubble	8.742	-2.5 5
10.875	0.1634	0.4404	0.3963	0.2706	bubble	10.933	-0. 53
13.520	0.1320	0.3559	0.5121	0.2706	bubble	13.073	3. 31
14.580	0.1116	0.3009	0.5875	0.2706	bubble	13.658	6. 32
15.285	0.0909	0.2449	0.6642	0.2706	bubble	13.222	13. 50
15.350	0.0829	0.2235	0.6935	0.2706	Dew	12.725	17.10
15.325	0.0752	0.2028	0.7220	0.2706	Dew	11.995	21.73
14.850	0.0675	0.1818	0.7507	0.2706	Dew	10.764	27.52
13.850	0.0622	0.1676	0.7702	0.2706	Dew	8.650	37.55
1.010	0.4819	0.5181	0.0000	0.4819	bubble		
2.610	0.4476	0.4812	0.0712	0.4819	bubble	2.608	0.08
4.950	0.4000	0.4300	0.1700	0.4819	bubble	4.988	-0.7 7
7.825	0.3398	0.3653	0.2949	0.4819	bubble	7.932	-1.3 7
9.875	0.2979	0.3203	0.3818	0.4819	bubble	9.813	0.63
12.610	0.2404	0.2584	0.5012	0.4819	bubble	11.785	6. 54
14.175	0.1731	0.1861	0.6409	0.4819	bubble	11.959	15. 63
14.350	0.1645	0.1768	0.6587	0.4819	bubble	11.743	18. 17
14.425	0.1503	0.1616	0.6881	0.4819	Dew	11.223	22.20
14.380	0.1362	0.1464	0.7174	0.4819	Dew	10.356	27.98
13.575	0.1250	0.1344	0.7406	0.4819	Dew	8.913	34.34
0.957	0.7503	0.2497	0.0000	0.7503	bubble		
1.975	0.7177	0.2389	0.0434	0.7503	bubble	1.892	4.20
4.456	0.6354	0.2115	0.1531	0.7503	bubble	4.293	3.66
7.513	0.5307	0.1766	0.2927	0.7503	bubble	7.281	3.09
9.452	0.4648	0.1547	0.3804	0.7503	bubble	8.971	5.09
12.515	0.3380	0.1125	0.5494	0.7503	bubble	10.858	13. 24
13.276	0.2687	0.0894	0.6419	0.7503	bubble	10.422	21. 50
13.424	0.2390	0.0796	0.6814	0.7503	bubble	9.687	27. 84

$p^{\text{EXP}}/\text{MPa}$	$x_{\text{heptane}}$	$x_{\text{toluene}}$	$x_{\text{CO}_2}$	$y$	Status	$P^{\text{MIE}}/\text{MPa}$	% AAD
13.352	0.2284	0.0760	0.6956	0.7503	Dew	9.218	30.96
13.019	0.2151	0.0716	0.7133	0.7503	Dew	8.112	37.69
12.596	0.2058	0.0685	0.7257	0.7503	Dew		
12.125	0.1988	0.0662	0.7350	0.7503	Dew		

<sup>a</sup> Expanded uncertainties are  $U(T) = 0.08 \text{ K}$ ,  $U(p_b) = 0.2 \text{ MPa}$ ,  $U(p_d) = 0.3 \text{ MPa}$  for  $T \leq 373.15 \text{ MPa}$  and  $0.4 \text{ MPa}$  for  $T > 373.15 \text{ K}$ , and  $U(x_{\text{CO}_2}) = 0.0042x_{\text{CO}_2}(1 - x_{\text{CO}_2})$ , with coverage factor  $k = 2$ .

**Table C.2.** Experimentally determined VLE, LLE, VLLE pressures  $p$  and densities  $\rho$  for the ( $\text{CO}_2$  + synthetic dead oil) mixture at temperatures of  $T$  and  $\text{CO}_2$  mole fractions  $x_{\text{CO}_2}$  <sup>a</sup>

$p$ (MPa)	$x_{\text{CO}_2}$	Status	$\rho$ ( $\text{kg}\cdot\text{m}^{-3}$ )	$p$ (MPa)	$x_{\text{CO}_2}$	Status	$\rho$ ( $\text{kg}\cdot\text{m}^{-3}$ )
<b><math>T = 298.15 \text{ K}</math></b>				25.350	0.9393	Critical	870
0.011	0.0000	L <sub>1</sub> -V	801	25.850	0.9473	dew	874
0.465	0.0662	L <sub>1</sub> -V	795	25.750	0.9601	dew	863
1.450	0.1843	L <sub>1</sub> -V	798	24.650	0.9678	dew	858
2.740	0.3266	L <sub>1</sub> -V	802	23.950	0.9732	dew	853
4.050	0.4954	L <sub>1</sub> -V	807	23.050	0.9798	dew	845
5.450	0.6458	L <sub>1</sub> -V	818	<b><math>T = 373.15 \text{ K}</math></b>			
5.950	0.6749	L <sub>1</sub> -V	825	0.205	0.0000	bubble	735
8.030	0.7332	L <sub>1</sub> -L <sub>2</sub>	836	3.550	0.2211	bubble	741
11.150	0.7791	L <sub>1</sub> -L <sub>2</sub>	850	5.850	0.3517	bubble	742
13.150	0.7929	L <sub>1</sub> -L <sub>2</sub>	856	8.150	0.4560	bubble	750
17.850	0.8158	L <sub>1</sub> -L <sub>2</sub>	870	11.150	0.5745	bubble	753
24.950	0.8438	L <sub>1</sub> -L <sub>2</sub>	890	13.860	0.6413	bubble	753
36.052	0.8632	L <sub>1</sub> -L <sub>2</sub>	901	16.050	0.7011	bubble	757
6.060	0.7332	L <sub>1</sub> -L <sub>2</sub> -V	N/A	20.980	0.7927	bubble	760
6.060	0.7793	L <sub>1</sub> -L <sub>2</sub> -V	N/A	23.050	0.8315	bubble	761
6.060	0.7929	L <sub>1</sub> -L <sub>2</sub> -V	N/A	24.250	0.8588	bubble	755
6.060	0.8161	L <sub>1</sub> -L <sub>2</sub> -V	N/A	25.480	0.8844	bubble	751
6.060	0.8440	L <sub>1</sub> -L <sub>2</sub> -V	N/A	27.850	0.9261	bubble	741
6.060	0.8738	L <sub>1</sub> -L <sub>2</sub> -V	N/A	28.350	0.9469	critical	738
6.060	0.9024	L <sub>1</sub> -L <sub>2</sub> -V	N/A	28.650	0.9601	dew	731
6.060	0.9500	L <sub>1</sub> -L <sub>2</sub> -V	N/A	28.450	0.9689	dew	716
6.060	0.9800	L <sub>1</sub> -L <sub>2</sub> -V	N/A	27.820	0.9762	dew	715
6.060	0.9911	L <sub>1</sub> -L <sub>2</sub> -V	N/A	27.350	0.9798	dew	705
<b><math>T = 323.15 \text{ K}</math></b>				26.350	0.9845	dew	679
0.175	0.0019	bubble	788	<b><math>T = 423.15 \text{ K}</math></b>			
1.010	0.0948	bubble	786	0.340	0.0000	bubble	721
3.075	0.2897	bubble	796	0.796	0.0295	bubble	723
4.780	0.4113	bubble	798	3.250	0.1522	bubble	726

$p$ (MPa)	$x_{\text{CO}_2}$	Status	$\rho$ (kg·m <sup>-3</sup> )	$p$ (MPa)	$x_{\text{CO}_2}$	Status	$\rho$ (kg·m <sup>-3</sup> )
6.820	0.5558	bubble	806	5.350	0.2783	bubble	726
8.350	0.6578	bubble	815	9.250	0.4178	bubble	726
11.750	0.7796	bubble	825	14.850	0.5742	bubble	729
13.230	0.8000	bubble	828	20.620	0.7010	bubble	729
16.150	0.8358	bubble	836	25.850	0.7948	bubble	721
18.650	0.8694	bubble	843	29.250	0.8588	bubble	710
19.100	0.8736	bubble	843	31.950	0.9261	bubble	659
19.850	0.8844	bubble	848	32.700	0.9469	critical	645
19.980	0.8866	bubble	847	32.250	0.9689	dew	612
21.480	0.9023	bubble	851	31.850	0.9725	dew	602
21.950	0.9073	bubble	850	31.400	0.9774	dew	590
23.650	0.9265	bubble	861	30.050	0.9845	dew	578

<sup>a</sup> Expanded uncertainties are  $U(T) = 0.08$  K,  $U(p_b) = 0.2$  MPa for  $p_b \leq 25$  MPa and 0.3 MPa for  $p_b > 25$  MPa,  $U(p_d) = 0.3$  MPa for  $T \leq 373.15$  MPa and 0.4 MPa for  $T > 373.15$  K, and  $U(x_{\text{CO}_2}) = 0.0042x_{\text{CO}_2}(1 - x_{\text{CO}_2})$ , with coverage factor  $k = 2$ .

**Table C.3.** Experimentally determined VLE, LLE, VLLE pressures  $p$  and densities  $\rho$  for the (CO<sub>2</sub> + synthetic live oil) mixture with the low GOR at temperatures of  $T$  and CO<sub>2</sub> mole fractions  $x_{\text{CO}_2}$ <sup>a</sup>

$p$ (MPa)	$x_{\text{CO}_2}$	Status	$\rho$ (kg·m <sup>-3</sup> )	$p$ (MPa)	$x_{\text{CO}_2}$	Status	$\rho$ (kg·m <sup>-3</sup> )
<b><math>T = 298.15</math> K</b>				26.450	0.9323	dew	840
8.710	0.0000	L <sub>1</sub> -V	744	25.850	0.9453	dew	834
9.800	0.0659	L <sub>1</sub> -V	754	25.550	0.9493	dew	826
10.520	0.2208	L <sub>1</sub> -V	765	24.500	0.9583	dew	814
11.150	0.3543	L <sub>1</sub> -V	764	24.000	0.9618	dew	812
11.640	0.4211	L <sub>1</sub> -V	781	22.150	0.9717	dew	810
12.630	0.6000	L <sub>1</sub> -V	796	20.220	0.9788	dew	806
14.820	0.6481	L <sub>1</sub> -L <sub>2</sub>	800	16.650	0.9846	dew	801
17.550	0.7053	L <sub>1</sub> -L <sub>2</sub>	818	16.230	0.9868	dew	788
19.230	0.7288	L <sub>1</sub> -L <sub>2</sub>	836	14.920	0.9915	dew	763
23.460	0.7831	L <sub>1</sub> -L <sub>2</sub>	848	<b><math>T = 373.15</math> K</b>			
29.350	0.8296	L <sub>1</sub> -L <sub>2</sub>	876	12.250	0.0000	bubble	696
9.300	0.6483	L <sub>1</sub> -L <sub>2</sub> -V	N/A	13.060	0.0648	bubble	703
8.500	0.7053	L <sub>1</sub> -L <sub>2</sub> -V	N/A	15.460	0.2200	bubble	711
7.725	0.7831	L <sub>1</sub> -L <sub>2</sub> -V	N/A	16.450	0.2739	bubble	716
7.050	0.8296	L <sub>1</sub> -L <sub>2</sub> -V	N/A	19.550	0.4205	bubble	722
6.710	0.9164	L <sub>1</sub> -L <sub>2</sub> -V	N/A	20.050	0.4433	bubble	727
6.560	0.9725	L <sub>1</sub> -L <sub>2</sub> -V	N/A	23.560	0.5996	bubble	732
6.507	0.9803	L <sub>1</sub> -L <sub>2</sub> -V	N/A	24.370	0.6320	bubble	738
6.440	0.9850	L <sub>1</sub> -L <sub>2</sub> -V	N/A	26.750	0.7286	bubble	742
6.440	0.9880	L <sub>1</sub> -L <sub>2</sub> -V	N/A	27.340	0.7595	bubble	743
6.440	0.9890	L <sub>1</sub> -L <sub>2</sub> -V	N/A	27.920	0.7957	bubble	741
6.500	0.9910	L <sub>1</sub> -L <sub>2</sub> -V	N/A	28.280	0.8157	bubble	747
9.300	0.6483	L <sub>1</sub> -L <sub>2</sub> -V	N/A	28.750	0.8450	bubble	744

$p$ (MPa)	$x_{\text{CO}_2}$	Status	$\rho$ (kg·m <sup>-3</sup> )	$p$ (MPa)	$x_{\text{CO}_2}$	Status	$\rho$ (kg·m <sup>-3</sup> )
8.650	0.7053	L <sub>1</sub> -L <sub>2</sub> -V	N/A	29.060	0.8724	critical	728
8.010	0.7831	L <sub>1</sub> -L <sub>2</sub> -V	N/A	29.500	0.9164	dew	721
7.850	0.8296	L <sub>1</sub> -L <sub>2</sub> -V	N/A	28.950	0.9503	dew	709
7.010	0.9164	L <sub>1</sub> -L <sub>2</sub> -V	N/A	28.000	0.9613	dew	702
28.250	0.9851	L <sub>1</sub> -L <sub>2</sub>	802	27.500	0.9678	dew	700
20.550	0.9853	L <sub>1</sub> -L <sub>2</sub>	862	26.950	0.9725	dew	699
7.400	0.9860	L <sub>1</sub> -L <sub>2</sub>	832	25.920	0.9788	dew	697
6.850	0.9880	L <sub>1</sub> -L <sub>2</sub>	778	25.030	0.9827	dew	681
6.730	0.9890	L <sub>1</sub> -L <sub>2</sub>	770	24.450	0.9846	dew	677
6.500	0.9910	L <sub>1</sub> -L <sub>2</sub>	762	<b>T = 423.15 K</b>			
<b>T = 323.15 K</b>				13.200	0.0000	bubble	666
10.210	0.0000	bubble	728	14.470	0.0643	bubble	666
11.040	0.0654	bubble	737	17.450	0.2197	bubble	674
12.480	0.2205	bubble	747	22.460	0.4203	bubble	681
14.620	0.4208	bubble	762	27.510	0.5995	bubble	683
16.710	0.5998	bubble	778	30.870	0.7285	bubble	684
20.240	0.7287	bubble	800	31.960	0.7956	bubble	675
22.150	0.7957	bubble	811	33.120	0.8724	Critical	648
23.250	0.8297	bubble	826	33.380	0.9164	dew	628
24.050	0.8494	bubble	842	32.750	0.9503	dew	607
25.050	0.8724	bubble	846	31.500	0.9613	dew	598
24.930	0.8750	bubble	848	31.030	0.9678	dew	593
26.420	0.9041	bubble	849	30.020	0.9725	dew	586
27.050	0.9164	dew	849				

<sup>a</sup> Expanded uncertainties are  $U(T) = 0.08$  K,  $U(p_b) = 0.2$  MPa for  $p_b \leq 25$  MPa and 0.3 MPa for  $p_b > 25$  MPa,  $U(p_d) = 0.3$  MPa for  $T \leq 373.15$  MPa and 0.4 MPa for  $T > 373.15$  K, and  $U(x_{\text{CO}_2}) = 0.0042x_{\text{CO}_2}(1 - x_{\text{CO}_2})$ , with coverage factor  $k = 2$ .

**Table C.4.** Experimentally determined VLE, LLE, VLLE pressures  $p$  and densities  $\rho$  for the (CO<sub>2</sub> + synthetic live oil) mixture with the high GOR at temperatures of  $T$  and CO<sub>2</sub> mole fractions  $x_{\text{CO}_2}$ <sup>a</sup>

$p$ (MPa)	$x_{\text{CO}_2}$	Status	$\rho$ (kg·m <sup>-3</sup> )	$p$ (MPa)	$x_{\text{CO}_2}$	Status	$\rho$ (kg·m <sup>-3</sup> )
<b>T = 298.15 K</b>				26.000	0.8835	dew	802
22.250	0.0000	L <sub>1</sub> -V	689	25.350	0.9226	dew	799
23.780	0.1404	L <sub>1</sub> -V	698	23.620	0.9412	dew	797
24.150	0.3428	L <sub>1</sub> -V	724	22.050	0.9526	dew	792
24.420	0.5122	L <sub>1</sub> -V	749	21.130	0.9594	dew	789
24.750	0.6291	L <sub>1</sub> -V	782	19.940	0.9653	dew	783
25.920	0.7078	L <sub>1</sub> -L <sub>2</sub>	809	18.400	0.9773	dew	778
27.750	0.7605	L <sub>1</sub> -L <sub>2</sub>	835	16.900	0.9855	dew	762
33.900	0.8432	L <sub>1</sub> -L <sub>2</sub>	890	15.020	0.9933	dew	726
36.000	0.8600	L <sub>1</sub> -L <sub>2</sub>	916	14.130	0.9944	dew	708
6.620	0.9774	L <sub>1</sub> -L <sub>2</sub> -V	N/A	<b>T = 373.15 K</b>			
6.550	0.9824	L <sub>1</sub> -L <sub>2</sub> -V	N/A	26.280	0.0000	bubble	637
6.540	0.9855	L <sub>1</sub> -L <sub>2</sub> -V	N/A	28.015	0.1401	bubble	642
6.410	0.9933	L <sub>1</sub> -L <sub>2</sub> -V	N/A	29.520	0.3425	bubble	657

$p$ (MPa)	$x_{CO_2}$	Status	$\rho$ (kg·m <sup>-3</sup> )	$p$ (MPa)	$x_{CO_2}$	Status	$\rho$ (kg·m <sup>-3</sup> )	
6.407	0.9944	L <sub>1</sub> -L <sub>2</sub> -V	N/A	31.380	0.5121	bubble	676	
6.780	0.9309	L <sub>1</sub> -L <sub>2</sub> -V	N/A	32.140	0.6290	bubble	686	
7.000	0.8845	L <sub>1</sub> -L <sub>2</sub> -V	N/A	32.692	0.7078	bubble	698	
7.363	0.8261	L <sub>1</sub> -L <sub>2</sub> -V	N/A	32.450	0.7588	dew	704	
8.630	0.7539	L <sub>1</sub> -L <sub>2</sub> -V	N/A	31.750	0.8114	dew	705.	
11.230	0.6857	L <sub>1</sub> -L <sub>2</sub> -V	N/A	31.100	0.8432	dew	706	
6.650	0.9774	L <sub>1</sub> -L <sub>2</sub> -V	N/A	29.815	0.8923	dew	698	
6.550	0.9824	L <sub>1</sub> -L <sub>2</sub> -V	N/A	28.645	0.9225	dew	688	
6.540	0.9855	L <sub>1</sub> -L <sub>2</sub> -V	N/A	26.215	0.9565	dew	666	
6.410	0.9933	L <sub>1</sub> -L <sub>2</sub> -V	N/A	25.620	0.9624	dew	660	
6.407	0.9944	L <sub>1</sub> -L <sub>2</sub> -V	N/A	24.050	0.9753	dew	648	
7.250	0.9309	L <sub>1</sub> -L <sub>2</sub> -V	N/A	23.220	0.9788	dew	647	
7.750	0.8845	L <sub>1</sub> -L <sub>2</sub> -V	N/A	22.130	0.9859	dew	631	
8.270	0.8261	L <sub>1</sub> -L <sub>2</sub> -V	N/A	21.070	0.9922	dew	580	
8.890	0.7539	L <sub>1</sub> -L <sub>2</sub> -V	N/A	20.250	0.9933	dew	567	
11.230	0.6857	L <sub>1</sub> -L <sub>2</sub> -V	N/A	<b>T = 423.15 K</b>				
14.820	0.9653	L <sub>1</sub> -L <sub>2</sub>	852	27.500	0.0000	bubble	605	
13.460	0.9692	L <sub>1</sub> -L <sub>2</sub>	845	29.580	0.1269	bubble	606	
11.400	0.9774	L <sub>1</sub> -L <sub>2</sub>	826	32.450	0.3348	bubble	615	
9.350	0.9824	L <sub>1</sub> -L <sub>2</sub>	807	34.280	0.5076	bubble	622	
8.620	0.9855	L <sub>1</sub> -L <sub>2</sub>	797	35.100	0.6262	bubble	623	
7.380	0.9933	L <sub>1</sub> -L <sub>2</sub>	766	35.300	0.6711	bubble	624	
7.300	0.9944	L <sub>1</sub> -L <sub>2</sub>	744	35.200	0.7535	Critical	613	
<b>T = 323.15 K</b>				35.100	0.8230	dew	610	
23.730	0.0000	bubble	672	34.700	0.8608	dew	598	
25.030	0.1403	bubble	679	34.250	0.8837	dew	583	
25.830	0.3426	bubble	703	33.500	0.9010	dew	573	
26.770	0.5122	bubble	726	32.800	0.9220	dew	552	
27.120	0.6291	bubble	746	31.120	0.9503	dew	520	
26.950	0.7078	bubble	767	29.010	0.9695	dew	502	
26.750	0.7605	bubble	784	25.370	0.9902	dew	464	
26.400	0.8432	bubble	804					

<sup>a</sup> Expanded uncertainties are  $U(T) = 0.08$  K,  $U(p_b) = 0.2$  MPa for  $p_b \leq 25$  MPa and 0.3 MPa for  $p_b > 25$  MPa,  $U(p_a) = 0.3$  MPa for  $T \leq 373.15$  MPa and 0.4 MPa for  $T > 373.15$  K, and  $U(x_{CO_2}) = 0.0042x_{CO_2}(1 - x_{CO_2})$ , with coverage factor  $k = 2$ .

**Table C.5.** Experimental VLLE data and SAFT-VR calculations for (water (1) + *n*-heptane (2) + carbon dioxide (3)) where I, II and III denote the heptane liquid rich phase, carbon dioxide gas phase and water-rich phase respectively.

Phase	$p$ /MPa	$x_1^{exp}$	$x_2^{exp}$	$x_3^{exp}$	$x_1^{pre}$	$x_2^{pre}$	$x_3^{pre}$
<b>T = 323.15 K</b>							
I	2.04	0.0045	0.8159	0.1797	0.0018	0.7676	0.2306
II	2.04	0.0064	0.0153	0.9783	0.0071	0.0109	0.9820
III	2.04	0.9934	1.90E-04	0.0065	0.9944	1.00E-08	0.0056
I	3.31	0.0048	0.6947	0.3005	0.0020	0.6450	0.3530



*Appendix C. Experimental Data for Mixtures Studied in this Work*

Phase	$p/\text{MPa}$	$x_1^{\text{exp}}$	$x_2^{\text{exp}}$	$x_3^{\text{exp}}$	$x_1^{\text{pre}}$	$x_2^{\text{pre}}$	$x_3^{\text{pre}}$
II	3.31	0.0054	0.0127	0.9818	0.0049	0.0078	0.9873
III	3.31	0.9898	1.37E-04	0.0101	0.9912	3.69E-14	0.0088
I	4.40	0.0058	0.5890	0.4052	0.0022	0.5481	0.4496
II	4.40	0.0033	0.0101	0.9866	0.0041	0.0068	0.9891
III	4.40	0.9869	2.32E-04	0.0128	0.9886	3.71E-14	0.0114
I	5.57	0.0066	0.4679	0.5255	0.0026	0.4484	0.5490
II	5.57	0.0019	0.0094	0.9887	0.0036	0.0063	0.9901
III	5.57	0.9840	2.20E-04	0.0157	0.9860	3.65E-14	0.0140
I	6.94	0.0077	0.3093	0.6830	0.0033	0.3307	0.6660
II	6.94	0.0021	0.0100	0.9878	0.0034	0.0061	0.9904
III	6.94	0.9822	1.21E-04	0.0177	0.9833	3.44E-14	0.0167
<b><math>T = 343.15 \text{ K}</math></b>							
I	2.05	0.0082	0.8426	0.1492	0.0037	0.8132	0.1832
II	2.05	0.0135	0.0273	0.9593	0.0173	0.0233	0.9594
III	2.05	0.9948	5.80E-05	0.0052	0.9955	2.54E-13	0.0045
I	4.11	0.0092	0.6822	0.3086	0.0041	0.6544	0.3414
II	4.11	0.0088	0.0179	0.9733	0.0102	0.0147	0.9752
III	4.11	0.9903	1.02E-04	0.0096	0.9911	2.65E-13	0.0089
I	6.00	0.0100	0.5356	0.4544	0.0047	0.5262	0.4690
II	6.00	0.0064	0.0171	0.9765	0.0082	0.0127	0.9791
III	6.00	0.9868	1.22E-04	0.0131	0.9876	2.67E-13	0.0124
I	8.00	0.0115	0.3727	0.6159	0.0057	0.3999	0.5944
II	8.00	0.0047	0.0214	0.9739	0.0074	0.0126	0.9800
III	8.00	0.9836	7.86E-05	0.0163	0.9843	2.61E-13	0.0157
I	10.00	0.0126	0.2012	0.7862	0.0075	0.2729	0.7197
II	10.00	0.0051	0.0309	0.9640	0.0074	0.0138	0.9788
III	10.00	0.9816	4.35E-05	0.0184	0.9815	2.41E-13	0.0185
<b><math>T = 363.15 \text{ K}</math></b>							
I	1.85	0.0303	0.8030	0.1666	0.0070	0.8601	0.1329
II	1.85	0.0347	0.0536	0.9117	0.0417	0.0490	0.9093
III	1.85	0.9965	4.67E-05	0.0035	0.9966	1.54E-12	0.0034
I	3.16	0.0212	0.7786	0.3000	0.0074	0.7700	0.2227
II	3.16	0.0253	0.0371	0.9376	0.0267	0.0327	0.9406
III	3.16	0.9931	6.24E-05	0.0069	0.9941	1.59E-12	0.0059
I	4.93	0.0219	0.6612	0.3168	0.0079	0.6606	0.3315
II	4.93	0.0178	0.0295	0.9527	0.0194	0.0253	0.9553
III	4.93	0.9896	6.31E-05	0.0104	0.9910	1.65E-12	0.0090
I	7.00	0.0237	0.5275	0.4488	0.0088	0.5459	0.4453
II	7.00	0.0132	0.0265	0.9603	0.0159	0.0226	0.9615
III	7.00	0.9871	4.97E-05	0.0129	0.9877	1.68E-12	0.0123
I	9.00	0.0238	0.3984	0.5778	0.0100	0.4437	0.5464
II	9.00	0.0110	0.0292	0.9598	0.0146	0.0225	0.9630
III	9.00	0.9856	4.60E-05	0.0143	0.9848	1.67E-12	0.0152
I	11.00	0.0249	0.2599	0.7152	0.0117	0.3454	0.6430
II	11.00	0.0103	0.0432	0.9465	0.0142	0.0243	0.9615

Phase	$p/\text{MPa}$	$x_1^{\text{exp}}$	$x_2^{\text{exp}}$	$x_3^{\text{exp}}$	$x_1^{\text{pre}}$	$x_2^{\text{pre}}$	$x_3^{\text{pre}}$
III	11.00	0.9843	3.69E-05	0.0157	0.9823	1.62E-12	0.0177
<b><math>T = 388.15 \text{ K}</math></b>							
I	2.16	0.0281	0.8654	0.1065	0.0147	0.8678	0.1175
II	2.16	0.1003	0.0920	0.8077	0.0860	0.0883	0.8257
III	2.16	0.9969	7.91E-05	0.0030	0.9968	1.26E-11	0.0032
I	5.00	0.0284	0.7026	0.2690	0.0158	0.7113	0.2728
II	5.00	0.0402	0.0561	0.9037	0.0439	0.0495	0.9066
III	5.00	0.9916	1.08E-04	0.0083	0.9922	1.35E-11	0.0078
I	7.50	0.0336	0.5627	0.4037	0.0172	0.5921	0.3907
II	7.50	0.0292	0.0489	0.9219	0.0342	0.0421	0.9237
III	7.50	0.9881	1.19E-04	0.0118	0.9885	1.40E-11	0.0115
I	10.00	0.0373	0.4242	0.5385	0.0191	0.4843	0.4967
II	10.00	0.0240	0.0559	0.9200	0.0302	0.0411	0.9287
III	10.00	0.9870	1.49E-04	0.0129	0.9852	1.43E-11	0.0148
I	12.10	0.0408	0.2997	0.6595	0.0210	0.4024	0.5766
II	12.10	0.0217	0.0766	0.9018	0.0290	0.0433	0.9277
III	12.10	0.9854	7.31E-05	0.0145	0.9828	1.43E-11	0.0172
<b><math>T = 413.15 \text{ K}</math></b>							
I	1.87	0.0428	0.8961	0.0611	0.0280	0.9044	0.0675
II	1.87	0.1674	0.1847	0.6479	0.2038	0.1841	0.6121
III	1.87	0.9982	1.28E-04	0.0017	0.9980	8.64E-11	0.0020
I	5.00	0.0476	0.7291	0.2233	0.0296	0.7486	0.2218
II	5.00	0.0794	0.0926	0.8280	0.0895	0.0891	0.8214
III	5.00	0.9939	1.12E-04	0.0060	0.9932	9.36E-11	0.0068
I	8.00	0.0643	0.5685	0.3672	0.0317	0.6197	0.3486
II	8.00	0.0571	0.0841	0.8588	0.0655	0.0720	0.8625
III	8.00	0.9903	1.29E-04	0.0095	0.9890	9.93E-11	0.0110
I	11.00	0.0764	0.4139	0.5096	0.0347	0.5037	0.4616
II	11.00	0.0458	0.1174	0.8368	0.0563	0.0691	0.8746
III	11.00	0.9874	1.43E-04	0.0124	0.9852	1.03E-10	0.0148
I	13.00	0.0846	0.2814	0.6340	0.0372	0.4306	0.5322
II	13.00	0.0402	0.1688	0.7910	0.0535	0.0716	0.8748
III	13.00	0.9857	2.07E-04	0.0141	0.9828	1.05E-10	0.0172

**Table C.6.** Experimental VLLE data and SAFT-VR calculations for (Methane (1) + Carbon Dioxide (2) + Water (3))<sup>a</sup>

phase	$p/\text{MPa}$	$x_1^{\text{exp}}$	$x_2^{\text{exp}}$	$x_3^{\text{exp}}$	$p/\text{MPa}$	$x_1^{\text{pred}}$	$x_2^{\text{pred}}$	$x_3^{\text{pred}}$
<b><math>T=285.15 \text{ K}</math></b>								
I	4.9631	0.0187	0.9809	0.0004	4.963	0.0199	0.9783	0.0018
II	4.9611	0.0061	0.9899	0.0040	4.961	0.0069	0.9878	0.0053
III	4.9570	4.50E-05	0.0283	0.9717	4.957	3.23E-06	0.0054	0.9946
I	5.5382	0.0917	0.9080	0.0003	5.538	0.0887	0.9096	0.0018

Appendix C. Experimental Data for Mixtures Studied in this Work

phase	$p/\text{MPa}$	$x_1^{\text{exp}}$	$x_2^{\text{exp}}$	$x_3^{\text{exp}}$	$p/\text{MPa}$	$x_1^{\text{pred}}$	$x_2^{\text{pred}}$	$x_3^{\text{pred}}$
II	5.5293	0.0275	0.9699	0.0026	5.529	0.0352	0.9598	0.0050
III	5.5246	2.16E-04	0.0280	0.9718	5.525	1.62E-05	0.0053	0.9947
I	6.3810	0.1692	0.8306	0.0002	6.381	0.1643	0.8339	0.0018
II	6.3836	0.0631	0.9347	0.0022	6.384	0.0806	0.9149	0.0045
III	6.3792	5.27E-04	0.0274	0.9720	6.379	3.44E-05	0.0051	0.9948
I	7.0770	0.2122	0.7877	0.0002	7.077	0.2091	0.7890	0.0019
II	7.0750	0.0964	0.9018	0.0018	7.075	0.1207	0.8752	0.0041
III	7.0700	6.28E-04	0.0269	0.9725	7.070	4.834E-05	0.0050	0.9950
<b>T=287.65 K</b>								
I	5.2893	0.0242	0.9754	0.0004	5.289	0.0230	0.9750	0.0020
II	5.2874	0.0074	0.9895	0.0031	5.287	0.0087	0.9857	0.0056
III	5.2832	5.09E-05	0.0277	0.9722	5.283	4.16E-06	0.0055	0.9945
I	5.5573	0.0495	0.9502	0.0003	5.557	0.0540	0.9439	0.0020
II	5.5550	0.0177	0.9797	0.0026	5.555	0.0219	0.9726	0.0055
III	5.5545	1.27E-04	0.0276	0.9723	5.555	1.05E-05	0.0055	0.9945
I	6.4053	0.1283	0.8715	0.0002	6.405	0.1329	0.8650	0.0021
II	6.3968	0.0515	0.9463	0.0022	6.397	0.0657	0.9294	0.0050
III	6.3929	3.94E-04	0.0270	0.9726	6.393	2.92E-05	0.0053	0.9947
I	7.0828	0.1769	0.8230	0.0002	7.083	0.1785	0.8193	0.0022
II	7.0922	0.0834	0.9147	0.0019	7.092	0.1052	0.8903	0.0045
III	7.0851	5.57E-04	0.0265	0.9730	7.085	4.36E-05	0.0052	0.9948
I	7.9238	0.2158	0.7841	0.0001	7.924	0.2142	0.7833	0.0025
II	7.9174	0.1318	0.8664	0.0018	7.917	0.1608	0.8354	0.0038
III	7.9141	7.55E-04	0.0256	0.9736	7.914	5.99E-05	0.0050	0.9949
<b>T=290.15 K</b>								
I	5.6930	0.0328	0.9669	0.0004	5.693	0.0326	0.9651	0.0023
II	5.6902	0.0108	0.9856	0.0036	5.691	0.0138	0.9803	0.0059
III	5.6865	7.61E-05	0.0272	0.9727	5.686	6.65E-06	0.0056	0.9944
I	5.7251	0.0345	0.9651	0.0004	5.726	0.0361	0.9615	0.0023
II	5.7251	0.0116	0.9851	0.0033	5.726	0.0155	0.9786	0.0059
III	5.7251	8.52E-05	0.0272	0.9727	5.726	7.60E-06	0.0056	0.9944
I	6.1171	0.0699	0.9298	0.0003	6.117	0.0748	0.9228	0.0024
II	6.1142	0.0275	0.9696	0.0029	6.114	0.0351	0.9593	0.0056
III	6.1107	1.94E-04	0.0269	0.9729	6.111	1.66E-05	0.0055	0.9945
I	6.5550	0.1146	0.8852	0.0003	6.555	0.1116	0.8860	0.0024
II	6.5480	0.0455	0.9520	0.0025	6.548	0.0579	0.9368	0.0053
III	6.5510	2.93E-04	0.0266	0.9731	6.551	2.65E-05	0.0054	0.9945
I	7.1763	0.1557	0.8441	0.0002	7.176	0.1530	0.8445	0.0025
II	7.1770	0.0745	0.9233	0.0022	7.177	0.0936	0.9016	0.0048
III	7.1785	4.31E-04	0.0262	0.9734	7.177	4.00E-05	0.0053	0.9947
I	7.2746	0.1628	0.8371	0.0002	7.275	0.1585	0.8390	0.0026
II	7.2648	0.0784	0.9195	0.0021	7.265	0.0989	0.8963	0.0048
III	7.2691	4.75E-04	0.0261	0.9735	7.269	4.19E-05	0.0053	0.9947

Appendix C. Experimental Data for Mixtures Studied in this Work

phase	$p/\text{MPa}$	$x_1^{\text{exp}}$	$x_2^{\text{exp}}$	$x_3^{\text{exp}}$	$p/\text{MPa}$	$x_1^{\text{pred}}$	$x_2^{\text{pred}}$	$x_3^{\text{pred}}$
I	7.9265	0.1840	0.8159	0.0001	7.927	0.1852	0.8119	0.0029
II	7.9296	0.1186	0.8793	0.0021	7.929	0.1444	0.8515	0.0041
III	7.926	5.98E-0	0.0255	0.9740	7.926	5.53E-05	0.0052	0.9948
<b>T=292.65 K</b>								
I	5.9540	0.0225	0.9771	0.0004	5.954	0.0247	0.9726	0.0027
II	5.9520	0.0083	0.9884	0.0034	5.952	0.0112	0.9825	0.0063
III	5.9540	5.48E-05	0.0266	0.9733	5.954	5.66E-06	0.0057	0.9943
I	6.1510	0.0392	0.9605	0.0003	6.151	0.0440	0.9533	0.0027
II	6.1430	0.0159	0.9810	0.0031	6.143	0.0208	0.9731	0.0061
III	6.1410	1.01E-04	0.0265	0.9734	6.141	1.01E-05	0.0057	0.9943
I	6.5613	0.0760	0.9237	0.0003	6.561	0.0796	0.9177	0.0028
II	6.5544	0.0341	0.9630	0.0029	6.554	0.0420	0.9522	0.0058
III	6.5510	2.05E-04	0.0262	0.9736	6.551	1.98E-05	0.0056	0.9944
I	7.1432	0.1214	0.8784	0.0002	7.143	0.1205	0.8766	0.0029
II	7.1364	0.0579	0.9396	0.0025	7.136	0.0742	0.9205	0.0053
III	7.1355	3.45E-04	0.0257	0.9739	7.136	3.30E-05	0.0055	0.9945
I	7.8025	0.1540	0.8458	0.0002	7.803	0.1525	0.8443	0.0032
II	7.7872	0.1023	0.8955	0.0022	7.787	0.1161	0.8793	0.0046
III	7.7871	4.81E-04	0.0250	0.9746	7.787	4.69E-05	0.0054	0.9946
<b>T=295.15 K</b>								
I	6.2782	0.0207	0.9790	0.0004	6.278	0.0224	0.9745	0.0031
II	6.2720	0.0080	0.9878	0.0042	6.272	0.0111	0.9824	0.0066
III	6.2680	4.58E-05	0.0257	0.9742	6.268	5.45E-06	0.0058	0.9942
I	6.7870	0.0632	0.9365	0.0003	6.787	0.0653	0.9315	0.0032
II	6.7700	0.0284	0.9682	0.0034	6.770	0.0367	0.9572	0.0061
III	6.7780	1.60E-04	0.0254	0.9744	6.778	1.77E-05	0.0057	0.9943
I	7.1620	0.0920	0.9077	0.0002	7.162	0.0913	0.9053	0.0033
II	7.1610	0.0452	0.9516	0.0032	7.161	0.0583	0.9359	0.0058
III	7.1595	2.39E-04	0.0251	0.9747	7.160	2.66E-05	0.0057	0.9943
I	7.7265	0.1192	0.8806	0.0002	7.727	0.1208	0.8756	0.0037
II	7.7200	0.0745	0.9225	0.0030	7.720	0.0935	0.9014	0.0051
III	7.7170	3.66E-04	0.0246	0.9751	7.717	3.91E-05	0.0055	0.9944
<b>T=297.65 K</b>								
I	6.6750	0.0220	0.9776	0.0004	6.700	0.0273	0.9690	0.0036
II	6.6750	0.0100	0.9854	0.0046	6.700	0.0158	0.9775	0.0067
III	6.6632	5.56E-05	0.0249	0.9750	6.700	7.85E-06	0.0059	0.9941
I	7.1773	0.0584	0.9413	0.0003	7.177	0.0625	0.9337	0.0038
II	7.1773	0.0305	0.9656	0.0040	7.177	0.0415	0.9523	0.0062
III	7.1595	1.68E-04	0.0246	0.9753	7.160	1.90E-05	0.0058	0.9941
I	7.7097	0.0856	0.9142	0.0002	7.710	0.0913	0.9044	0.0042
II	7.7019	0.0576	0.9387	0.0036	7.702	0.0743	0.9203	0.0054
III	7.6978	2.73E-04	0.0241	0.9757	7.698	3.16E-05	0.0057	0.9942
<b>T=300.15 K</b>								

phase	$p/\text{MPa}$	$x_1^{\text{exp}}$	$x_2^{\text{exp}}$	$x_3^{\text{exp}}$	$p/\text{MPa}$	$x_1^{\text{pred}}$	$x_2^{\text{pred}}$	$x_3^{\text{pred}}$
I	7.1605	0.0275	0.9722	0.0003	6.940	0.0174	0.9784	0.0042
II	7.1528	0.0151	0.9797	0.0052	6.940	0.0111	0.9820	0.0070
III	7.1530	7.25E-05	0.0239	0.9760	6.940	5.50E-06	0.0061	0.9939
I	7.612	0.0533	0.9465	0.0002				
II	7.603	0.0365	0.9587	0.0048				
III	7.602	1.63E-04	0.0235	0.9764				
<b><math>T=303.5 \text{ K}</math></b>								
I	7.5240	0.0136	0.9861	0.0003				
II	7.5170	0.0093	0.9850	0.0056				
III	7.5140	3.78E-05	0.0231	0.9769				

<sup>a</sup> The phases are labelled as I, II and III for the gas rich, CO<sub>2</sub> rich and water-rich phases respectively.

**Table C.7.** Experimental VLE Data for (water (1) + methane (2) + carbon dioxide (3)) at different temperatures. <sup>a</sup>

$p/\text{MPa}$	phase II			phase III		
	$x_1$	$x_2$	$x_3$	$x_1$	$x_2$	$x_3$
<b><math>T = 323.15 \text{ K}</math></b>						
1.911	0.0127	0.4971	0.4902	0.9964	0.0005	0.0031
6.035	0.0038	0.4868	0.5094	0.9908	0.0007	0.0085
10.011	0.0042	0.4913	0.5046	0.9874	0.0010	0.0116
14.021	0.0048	0.5018	0.4933	0.9855	0.0014	0.0131
17.986	0.0056	0.4961	0.4983	0.9843	0.0015	0.0142
<b><math>T = 373.15 \text{ K}</math></b>						
2.009	0.0658	0.4727	0.4615	0.9980	0.0002	0.0018
6.059	0.0103	0.4864	0.5033	0.9939	0.0008	0.0053
10.207	0.0107	0.4915	0.4978	0.9900	0.0015	0.0084
14.051	0.0113	0.4814	0.5073	0.9888	0.0014	0.0098
17.912	0.0121	0.4835	0.5044	0.9862	0.0020	0.0118
<b><math>T = 423.15 \text{ K}</math></b>						
2.102	0.3445	0.3269	0.3286	0.9985	0.0003	0.0013
4.201	0.2181	0.3838	0.3981	0.9970	0.0006	0.0024
5.956	0.1145	0.4427	0.4428	0.9946	0.0010	0.0043
9.982	0.0689	0.4770	0.4541	0.9912	0.0016	0.0072
14.061	0.0489	0.4792	0.4719	0.9897	0.0015	0.0088
18.001	0.0470	0.4868	0.4662	0.9878	0.0019	0.0103

<sup>a</sup> The phases are labelled as II and III for the CO<sub>2</sub> rich and water-rich phases respectively

## Appendix D. Experimental Density Data for Aqueous Solutions

Table D.1. Densities  $\rho$  of brines at temperatures  $T$ , pressures  $p$  and molalities  $b$ .<sup>(a)</sup>

$p/\text{MPa}$	$\rho/\text{kg}\cdot\text{m}^{-3}$	$\rho/\text{kg}\cdot\text{m}^{-3}$	$\rho/\text{kg}\cdot\text{m}^{-3}$	$\rho/\text{kg}\cdot\text{m}^{-3}$	$\rho/\text{kg}\cdot\text{m}^{-3}$	$\rho/\text{kg}\cdot\text{m}^{-3}$	$\rho/\text{kg}\cdot\text{m}^{-3}$	$\rho/\text{kg}\cdot\text{m}^{-3}$
	298.12 K	323.07 K	348.04 K	372.99 K	397.97 K	422.94 K	447.94 K	472.96 K
<b>CaCl<sub>2</sub>(aq): <math>b = 1.00 \text{ mol}\cdot\text{kg}^{-1}</math></b>								
1.05	1082.37	1072.02	1058.99	1043.73	1026.22	1006.80	985.31	
10.02	1085.93	1075.48	1062.51	1047.42	1030.11	1011.09	989.96	966.77
19.97	1089.70	1079.27	1066.31	1051.39	1034.38	1015.62	995.04	972.43
29.90	1093.48	1082.99	1070.05	1055.27	1038.38	1020.00	999.90	977.79
39.83	1097.27	1086.62	1073.75	1059.05	1042.42	1024.30	1004.57	983.04
49.76	1100.95	1090.10	1077.29	1062.77	1046.36	1028.53	1009.07	988.08
59.68	1104.52	1093.62	1080.87	1066.34	1050.19	1032.62	1013.53	992.91
68.12	1107.46	1096.56	1083.78	1069.39	1053.29	1036.00	1017.15	996.86
<b>CaCl<sub>2</sub>(aq): <math>b = 3.00 \text{ mol}\cdot\text{kg}^{-1}</math></b>								
1.05	1225.07	1212.47	1198.77	1184.12	1167.99	1150.79	1132.22	
10.02	1228.17	1215.47	1201.83	1187.20	1171.26	1154.33	1135.97	1116.32
19.97	1231.30	1218.73	1205.15	1190.58	1174.82	1158.03	1139.99	1120.67
29.90	1234.60	1221.98	1208.41	1193.94	1178.23	1161.68	1143.88	1124.82
39.83	1237.81	1225.08	1211.58	1197.14	1181.65	1165.21	1147.62	1129.01
49.76	1240.96	1228.11	1214.64	1200.38	1184.96	1168.72	1151.30	1132.99
59.68	1244.00	1231.21	1217.80	1203.46	1188.20	1172.12	1154.99	1136.86
68.12	1246.57	1233.72	1220.39	1206.10	1190.88	1174.94	1157.94	1140.04
<b>CaCl<sub>2</sub>(aq): <math>b = 6.00 \text{ mol}\cdot\text{kg}^{-1}</math></b>								
1.05	1388.00	1372.06	1356.18	1340.35	1324.03	1307.39	1290.23	
10.02	1390.67	1374.67	1358.90	1343.09	1326.81	1310.40	1293.23	1275.65
19.97	1393.43	1377.58	1361.82	1346.07	1329.91	1313.54	1296.61	1279.19
29.90	1396.28	1380.48	1364.67	1349.03	1332.86	1316.63	1299.83	1282.53
39.83	1399.14	1383.27	1367.55	1351.92	1335.87	1319.70	1303.02	1285.96
49.76	1401.93	1385.94	1370.29	1354.76	1338.78	1322.71	1306.09	1289.19
59.68	1404.61	1388.68	1373.09	1357.57	1341.67	1325.64	1309.22	1292.45
68.12	1406.89	1390.90	1375.40	1359.88	1344.00	1328.12	1311.73	1295.04
<b>MgCl<sub>2</sub>(aq): <math>b = 1.00 \text{ mol}\cdot\text{kg}^{-1}</math></b>								
1.05	1070.86	1061.56	1049.32	1034.76	1017.83	999.03		
10.02	1074.43	1065.03	1052.80	1038.36	1021.72	1003.28	982.73	960.31
19.97	1078.17	1068.73	1056.56	1042.33	1025.91	1007.77	987.82	965.92
29.90	1081.96	1072.46	1060.31	1046.17	1029.97	1012.16	992.59	971.25
39.83	1085.70	1076.00	1063.92	1049.91	1033.96	1016.47	997.27	976.50
49.76	1089.34	1079.49	1067.47	1053.59	1037.86	1020.62	1001.73	981.41
59.68	1092.83	1082.98	1070.97	1057.17	1041.60	1024.61	1006.15	986.20
68.12	1095.78	1085.82	1073.88	1060.13	1044.71	1027.95	1009.73	990.10
<b>MgCl<sub>2</sub>(aq): <math>b = 3.00 \text{ mol}\cdot\text{kg}^{-1}</math></b>								
1.10	1194.98	1185.53	1174.63	1162.60	1149.22	1134.62	1118.93	
10.10	1197.76	1188.36	1177.48	1165.51	1152.27	1137.91	1122.27	1105.72
20.10	1200.84	1191.36	1180.55	1168.64	1155.47	1141.36	1126.00	1109.63
30.10	1203.93	1194.33	1183.56	1171.77	1158.76	1144.67	1129.62	1113.50

Appendix D. Experimental Density Data for Aqueous Solutions

$p/\text{MPa}$	$\rho/\text{kg}\cdot\text{m}^{-3}$	$\rho/\text{kg}\cdot\text{m}^{-3}$	$\rho/\text{kg}\cdot\text{m}^{-3}$	$\rho/\text{kg}\cdot\text{m}^{-3}$	$\rho/\text{kg}\cdot\text{m}^{-3}$	$\rho/\text{kg}\cdot\text{m}^{-3}$	$\rho/\text{kg}\cdot\text{m}^{-3}$	$\rho/\text{kg}\cdot\text{m}^{-3}$
40.10	1206.91	1197.32	1186.60	1174.82	1162.02	1147.96	1133.07	1117.27
50.10	1209.79	1200.25	1189.47	1177.87	1165.10	1151.23	1136.51	1120.96
60.10	1212.66	1203.13	1192.42	1180.77	1168.09	1154.39	1139.92	1124.60
68.60	1215.18	1205.42	1194.89	1183.21	1170.63	1157.07	1142.62	1127.48
<b>MgCl<sub>2</sub>(aq): <math>b = 5.00 \text{ mol}\cdot\text{kg}^{-1}</math></b>								
1.05	1298.01	1288.53	1278.25	1267.42	1255.66	1243.30	1230.19	
10.02	1300.39	1290.86	1280.63	1269.83	1258.16	1245.98	1232.81	1219.23
19.97	1302.84	1293.39	1283.18	1272.48	1260.88	1248.69	1235.76	1222.30
29.90	1305.37	1295.97	1285.71	1275.12	1263.46	1251.46	1238.61	1225.27
39.83	1307.91	1298.44	1288.26	1277.64	1266.15	1254.16	1241.42	1228.28
49.76	1310.34	1300.80	1290.69	1280.15	1268.74	1256.84	1244.17	1231.18
59.68	1312.81	1303.27	1293.17	1282.60	1271.25	1259.41	1246.88	1234.02
68.12	1314.82	1305.22	1295.26	1284.68	1273.36	1261.60	1249.11	1236.38
<b>KI(aq): <math>b = 0.669 \text{ mol}\cdot\text{kg}^{-1}</math></b>								
1.05	1074.75	1064.04	1049.72	1032.60	1012.71	990.31	965.35	944.19
10.02	1078.81	1067.95	1053.73	1036.79	1017.19	995.34	970.94	950.96
19.97	1083.04	1072.19	1057.99	1041.30	1022.06	1000.61	976.95	957.40
29.90	1087.37	1076.42	1062.23	1045.73	1026.71	1005.73	982.65	963.57
39.83	1091.56	1080.45	1066.38	1050.01	1031.29	1010.72	988.10	969.44
49.76	1095.69	1084.42	1070.32	1054.18	1035.78	1015.55	993.34	975.11
59.68	1099.67	1088.30	1074.35	1058.24	1040.10	1020.17	998.49	979.68
68.12	1103.00	1091.53	1077.66	1061.64	1043.65	1024.00	1002.64	944.19
<b>KI(aq): <math>b = 0.900 \text{ mol}\cdot\text{kg}^{-1}</math></b>								
1.05	1100.27	1088.99	1074.24	1056.80	1036.96	1014.85	990.56	
10.02	1104.27	1092.94	1078.29	1061.02	1041.47	1019.62	996.18	
19.97	1108.67	1097.21	1082.62	1065.55	1046.32	1024.97	1002.22	
29.90	1112.93	1101.41	1086.89	1070.01	1050.95	1030.16	1007.94	
39.83	1117.15	1105.46	1091.06	1074.32	1055.56	1035.28	1013.36	
49.76	1121.30	1109.41	1095.03	1078.51	1060.02	1040.03	1018.68	
59.68	1125.31	1113.37	1099.04	1082.50	1064.32	1044.78	1023.80	
68.12	1128.62	1116.58	1102.03	1085.89	1067.94	1048.68	1027.98	
<b>KI(aq): <math>b = 1.063 \text{ mol}\cdot\text{kg}^{-1}</math></b>								
1.05	1117.90	1106.19	1091.20	1073.46	1053.24	1030.64	1005.63	
10.02	1121.98	1110.17	1095.23	1077.72	1057.79	1035.74	1011.23	984.84
19.97	1126.32	1114.52	1099.65	1082.29	1062.77	1041.07	1017.26	991.38
29.90	1130.67	1118.76	1103.95	1086.83	1067.47	1046.25	1022.96	997.97
39.83	1134.96	1122.89	1108.16	1091.17	1072.16	1051.30	1028.47	1004.20
49.76	1139.11	1126.88	1112.21	1095.44	1076.71	1056.19	1033.81	1010.14
59.68	1143.14	1130.86	1116.30	1099.61	1081.09	1060.87	1038.97	1015.81
68.12	1146.49	1134.11	1119.62	1103.03	1084.70	1064.81	1043.19	1020.40
<b>0.864 NaCl + 0.136KCl(aq): <math>b = 1.05 \text{ mol}\cdot\text{kg}^{-1}</math></b>								
1.05	1039.58	1029.20	1015.69	999.54	981.06	960.34	937.36	
10.02	1043.32	1032.84	1019.39	1003.46	985.22	964.96	942.49	917.64
19.97	1047.29	1036.81	1023.43	1007.66	989.73	969.88	948.00	923.91
29.90	1051.20	1040.67	1027.31	1011.73	994.12	974.59	953.24	929.85
39.83	1055.12	1044.44	1031.24	1015.75	998.35	979.23	958.29	935.62
49.76	1058.94	1048.10	1034.88	1019.66	1002.52	983.70	963.22	941.09

*Appendix D. Experimental Density Data for Aqueous Solutions*

$p/\text{MPa}$	$\rho/\text{kg}\cdot\text{m}^{-3}$	$\rho/\text{kg}\cdot\text{m}^{-3}$	$\rho/\text{kg}\cdot\text{m}^{-3}$	$\rho/\text{kg}\cdot\text{m}^{-3}$	$\rho/\text{kg}\cdot\text{m}^{-3}$	$\rho/\text{kg}\cdot\text{m}^{-3}$	$\rho/\text{kg}\cdot\text{m}^{-3}$	$\rho/\text{kg}\cdot\text{m}^{-3}$
59.68	1062.65	1051.77	1038.60	1023.46	1006.54	988.02	967.97	946.40
68.12	1065.77	1054.74	1041.64	1026.61	1009.83	991.58	971.82	950.72
<b>0.864 NaCl + 0.136KCl(aq): <math>b = 1.98 \text{ mol}\cdot\text{kg}^{-1}</math></b>								
0.92	1073.46	1062.21	1048.37	1032.50	1014.52	994.44	972.49	
9.92	1076.94	1065.64	1051.92	1036.21	1018.48	998.81	977.23	953.84
19.92	1080.78	1069.40	1055.75	1040.20	1022.74	1003.42	982.40	959.59
29.92	1084.52	1073.08	1059.53	1044.24	1026.84	1007.90	987.31	965.06
39.92	1088.21	1076.77	1063.22	1048.05	1030.96	1012.29	992.12	970.41
49.92	1091.80	1080.31	1066.81	1051.76	1034.94	1016.57	996.72	975.50
59.92	1095.29	1083.80	1070.37	1055.37	1038.81	1020.69	1001.24	980.43
68.42	1098.34	1086.65	1073.33	1058.46	1042.00	1024.12	1004.93	984.46
<b>0.864 NaCl + 0.136KCl(aq): <math>b = 3.15 \text{ mol}\cdot\text{kg}^{-1}</math></b>								
0.92	1113.08	1100.94	1086.80	1070.97	1053.46	1034.07	1013.19	
9.92	1116.33	1104.19	1090.12	1074.45	1057.19	1038.17	1017.60	994.68
19.92	1119.88	1107.71	1093.72	1078.26	1061.17	1042.46	1022.35	999.91
29.92	1123.39	1111.16	1097.30	1082.01	1065.09	1046.70	1026.97	1005.05
39.92	1126.85	1114.67	1100.82	1085.59	1068.93	1050.91	1031.42	1009.93
49.92	1130.25	1118.08	1104.22	1089.17	1072.73	1054.81	1035.74	1014.65
59.92	1133.50	1121.33	1107.60	1092.70	1076.36	1058.75	1039.97	1019.26
68.42	1136.42	1124.04	1110.43	1095.56	1079.37	1062.00	1043.40	1022.96
<b>0.864 NaCl + 0.136KCl(aq): <math>b = 4.95 \text{ mol}\cdot\text{kg}^{-1}</math></b>								
0.92	1168.01	1154.75	1140.17	1124.41	1107.25	1088.67	1068.86	
9.92	1170.96	1157.75	1143.25	1127.60	1110.73	1092.44	1072.83	1052.13
19.92	1174.22	1161.03	1146.65	1131.16	1114.41	1096.37	1077.20	1056.87
29.92	1177.43	1164.27	1149.94	1134.67	1118.04	1100.22	1081.38	1061.38
39.92	1180.64	1167.54	1153.21	1138.06	1121.63	1104.04	1085.48	1065.92
49.92	1183.74	1170.65	1156.41	1141.34	1125.14	1107.79	1089.45	1070.19
59.92	1186.74	1173.70	1159.59	1144.61	1128.57	1111.39	1093.35	1074.41
68.42	1189.37	1176.22	1162.24	1147.28	1131.38	1114.39	1096.53	1077.83
<b>NaCl(aq): <math>b = 1.06 \text{ mol}\cdot\text{kg}^{-1}</math></b>								
0.90	1038.78	1028.45	1014.93	998.89	980.42	959.71	936.49	
9.90	1042.49	1032.10	1018.61	1002.77	984.60	964.31	941.64	916.86
19.90	1046.61	1036.09	1022.67	1007.00	989.13	969.29	947.14	923.12
29.90	1050.58	1039.95	1026.61	1011.16	993.51	974.04	952.41	929.00
39.90	1054.45	1043.77	1030.49	1015.15	997.76	978.60	957.55	934.76
49.90	1058.27	1047.49	1034.25	1019.09	1002.02	983.20	962.42	940.22
59.90	1061.93	1051.10	1037.94	1022.88	1006.01	987.46	967.35	945.52
68.40	1065.11	1054.12	1041.08	1026.09	1009.32	991.15	971.22	949.91
<b>NaCl(aq): <math>b = 3.16 \text{ mol}\cdot\text{kg}^{-1}</math></b>								
0.90	1111.08	1098.80	1084.57	1068.60	1051.16	1031.93	1010.87	
9.90	1114.33	1102.10	1087.94	1072.14	1054.84	1036.08	1015.28	993.19
19.90	1117.89	1105.63	1091.54	1075.95	1058.92	1040.37	1020.13	998.47
29.90	1121.40	1109.07	1095.09	1079.61	1062.79	1044.51	1024.61	1003.47
39.90	1124.91	1112.54	1098.65	1083.24	1066.63	1048.68	1029.15	1008.45
49.90	1128.21	1115.90	1101.95	1086.77	1070.44	1052.68	1033.43	1013.17
59.90	1131.46	1119.20	1105.34	1090.25	1074.07	1056.58	1037.71	1017.78
68.40	1134.29	1121.87	1108.22	1093.16	1077.08	1059.82	1041.14	1021.53



Appendix D. Experimental Density Data for Aqueous Solutions

$p/\text{MPa}$	$\rho/\text{kg}\cdot\text{m}^{-3}$	$\rho/\text{kg}\cdot\text{m}^{-3}$	$\rho/\text{kg}\cdot\text{m}^{-3}$	$\rho/\text{kg}\cdot\text{m}^{-3}$	$\rho/\text{kg}\cdot\text{m}^{-3}$	$\rho/\text{kg}\cdot\text{m}^{-3}$	$\rho/\text{kg}\cdot\text{m}^{-3}$	$\rho/\text{kg}\cdot\text{m}^{-3}$
<b>NaCl(aq): <math>b = 6.00 \text{ mol}\cdot\text{kg}^{-1}</math></b>								
0.90	1194.53	1180.58	1165.53	1149.58	1132.48	1114.20	1094.62	
9.90	1197.36	1183.46	1168.53	1152.70	1135.74	1117.84	1098.38	1078.20
19.90	1200.44	1186.57	1171.76	1156.09	1139.35	1121.56	1102.62	1082.67
29.90	1203.47	1189.69	1174.98	1159.48	1142.80	1125.33	1106.53	1087.01
39.90	1206.51	1192.73	1178.07	1162.74	1146.27	1128.98	1110.46	1091.28
49.90	1209.49	1195.77	1181.15	1165.95	1149.66	1132.56	1114.27	1095.39
59.90	1212.31	1198.70	1184.21	1169.00	1152.86	1136.03	1118.04	1099.39
68.40	1214.78	1201.09	1186.78	1171.60	1155.61	1138.92	1121.10	1102.68
<b>KCl(aq): <math>b = 1.06 \text{ mol}\cdot\text{kg}^{-1}</math></b>								
0.90	1044.20	1034.14	1020.74	1004.76	986.31	965.57	942.89	
9.90	1047.96	1037.83	1024.46	1008.64	990.53	970.25	948.08	923.68
19.90	1052.02	1041.82	1028.51	1012.91	995.11	975.13	953.62	929.93
29.90	1056.08	1045.67	1032.50	1017.11	999.53	979.97	958.88	935.86
39.90	1060.00	1049.58	1036.42	1021.10	1003.82	984.63	963.97	941.62
49.90	1063.86	1053.35	1040.18	1025.08	1008.02	989.18	968.88	947.07
59.90	1067.62	1057.01	1043.91	1028.91	1012.10	993.52	973.66	952.36
68.40	1070.84	1060.07	1047.14	1032.17	1015.46	997.11	977.57	956.79
<b>KCl(aq): <math>b = 3.015 \text{ mol}\cdot\text{kg}^{-1}</math></b>								
0.90	1124.07	1112.58	1098.82	1083.32	1065.90	1046.73	1025.62	
9.90	1127.47	1115.91	1102.28	1086.89	1069.71	1050.87	1030.11	1007.94
19.90	1131.16	1119.53	1105.97	1090.74	1073.82	1055.23	1034.96	1013.25
29.90	1134.81	1123.11	1109.59	1094.53	1077.73	1059.51	1039.57	1018.38
39.90	1138.35	1126.71	1113.24	1098.25	1081.65	1063.66	1044.09	1023.39
49.90	1141.90	1130.16	1116.68	1101.91	1085.49	1067.79	1048.45	1028.19
59.90	1145.28	1133.60	1120.15	1105.38	1089.26	1071.77	1052.77	1032.84
68.40	1148.20	1136.35	1123.07	1108.37	1092.30	1075.00	1056.27	1036.57
<b>KCl(aq): <math>b = 4.49 \text{ mol}\cdot\text{kg}^{-1}</math></b>								
0.90	1168.21	1156.09	1142.21	1126.88	1109.90	1091.46	1071.39	
9.90	1171.42	1159.30	1145.43	1130.26	1113.48	1095.41	1075.50	1054.54
19.90	1174.92	1162.77	1148.98	1133.92	1117.40	1099.54	1080.06	1059.47
29.90	1178.38	1166.16	1152.52	1137.58	1121.12	1103.53	1084.38	1064.17
39.90	1181.79	1169.63	1155.93	1141.11	1124.86	1107.49	1088.62	1068.85
49.90	1185.09	1172.93	1159.38	1144.58	1128.56	1111.34	1092.74	1073.32
59.90	1188.28	1176.14	1162.56	1147.95	1132.08	1115.08	1096.73	1077.68
68.40	1191.12	1178.80	1165.39	1150.77	1135.00	1118.18	1100.10	1081.18
	<b>298.12 K</b>	<b>323.07 K</b>	<b>348.04 K</b>	<b>372.99 K</b>	<b>298.12 K</b>	<b>323.07 K</b>	<b>348.04 K</b>	<b>372.99 K</b>
<b><math>\text{AlCl}_3(\text{aq}): b = 1.00 \text{ mol}\cdot\text{kg}^{-1}</math></b>				<b><math>\text{AlCl}_3(\text{aq}): b = 2.00 \text{ mol}\cdot\text{kg}^{-1}</math></b>				
0.90	1105.53	1096.76	1085.66	1072.64	1212.19	1203.26	1192.82	1181.64
9.90	1108.79	1099.96	1088.98	1075.97	1214.96	1206.02	1196.00	1184.73
19.90	1112.30	1103.44	1092.48	1079.63	1217.92	1209.01	1199.11	1187.90
29.90	1115.82	1106.84	1096.02	1083.19	1220.94	1211.90	1202.10	1191.11
39.90	1119.28	1110.31	1099.44	1086.72	1223.85	1214.88	1205.07	1194.19
49.90	1122.69	1113.67	1102.74	1090.20	1226.72	1217.80	1207.92	1197.22
59.90	1125.95	1116.93	1106.07	1093.58	1229.57	1220.60	1210.85	1200.14
68.40	1128.83	1119.60	1108.86	1096.34	1232.02	1222.88	1213.26	1202.66

Appendix D. Experimental Density Data for Aqueous Solutions

$p/\text{MPa}$	$\rho/\text{kg}\cdot\text{m}^{-3}$	$\rho/\text{kg}\cdot\text{m}^{-3}$	$\rho/\text{kg}\cdot\text{m}^{-3}$	$\rho/\text{kg}\cdot\text{m}^{-3}$	$\rho/\text{kg}\cdot\text{m}^{-3}$	$\rho/\text{kg}\cdot\text{m}^{-3}$	$\rho/\text{kg}\cdot\text{m}^{-3}$	$\rho/\text{kg}\cdot\text{m}^{-3}$
	298.11 K	323.13 K	348.12 K	373.12 K	398.08 K	423.07 K	448.03 K	473.02 K
<b>Na<sub>2</sub>SO<sub>4</sub>(aq): <math>b = 0.783 \text{ mol}\cdot\text{kg}^{-1}</math></b>								
1.10	1089.58	1077.81	1063.59	1047.00	1028.03	1006.98	983.81	
10.10	1092.97	1081.15	1067.05	1050.62	1032.04	1011.36	988.74	963.68
20.10	1096.83	1084.87	1070.84	1054.57	1036.41	1016.13	994.07	969.72
30.10	1100.47	1088.46	1074.53	1058.52	1040.58	1020.77	998.93	975.48
40.10	1104.07	1092.02	1078.24	1062.40	1044.61	1025.11	1004.10	981.03
50.10	1107.68	1095.52	1081.79	1066.07	1048.55	1029.51	1008.75	986.37
60.10	1111.07	1098.98	1085.27	1069.75	1052.44	1033.66	1013.33	991.46
68.60	1113.99	1101.80	1088.20	1072.82	1055.65	1037.10	1017.15	995.65
<b>Na<sub>2</sub>SO<sub>4</sub>(aq): <math>b = 1.502 \text{ mol}\cdot\text{kg}^{-1}</math></b>								
1.10	1164.61	1151.30	1136.41	1119.57	1100.73	1080.12	1057.71	
10.10	1167.61	1154.41	1139.53	1122.86	1104.32	1084.06	1062.06	1038.23
20.10	1170.98	1157.75	1143.04	1126.48	1108.32	1088.31	1067.00	1043.59
30.10	1174.24	1161.00	1146.45	1130.05	1112.10	1092.62	1071.61	1048.78
40.10	1177.46	1164.24	1149.78	1133.55	1115.80	1096.64	1076.11	1053.91
50.10	1180.69	1167.41	1153.06	1136.94	1119.47	1100.57	1080.33	1058.64
60.10	1183.64	1170.49	1156.20	1140.35	1123.02	1104.44	1084.59	1063.34
68.60	1186.24	1173.08	1158.87	1143.15	1125.97	1107.66	1088.14	1067.18
<b>SrCl<sub>2</sub>(aq): <math>b = 1.022 \text{ mol}\cdot\text{kg}^{-1}</math></b>								
1.10	1130.15	1118.47	1104.60	1088.34	1069.78	1049.35	1026.97	
10.10	1133.60	1121.92	1108.06	1092.02	1073.81	1053.57	1031.70	1007.66
20.10	1137.52	1125.75	1111.92	1095.98	1078.08	1058.30	1037.05	1013.50
30.10	1141.28	1129.44	1115.71	1100.03	1082.31	1062.95	1042.00	1019.02
40.10	1145.04	1133.12	1119.42	1103.81	1086.33	1067.24	1046.83	1024.58
50.10	1148.76	1136.68	1123.04	1107.65	1090.29	1071.70	1051.49	1029.72
60.10	1152.26	1140.25	1126.67	1111.38	1094.27	1075.85	1056.12	1034.76
68.60	1155.30	1143.18	1129.67	1114.46	1097.55	1079.30	1059.85	1038.86
<b>SrCl<sub>2</sub>(aq): <math>b = 2.024 \text{ mol}\cdot\text{kg}^{-1}</math></b>								
1.10	1247.60	1234.10	1219.34	1202.92	1184.72	1165.03	1143.84	
10.10	1250.68	1237.28	1222.48	1206.28	1188.28	1168.83	1147.95	1125.38
20.10	1254.27	1240.69	1226.06	1209.96	1192.23	1173.04	1152.74	1130.50
30.10	1257.65	1244.10	1229.57	1213.53	1196.08	1177.32	1157.21	1135.33
40.10	1260.99	1247.56	1233.02	1217.20	1199.73	1181.23	1161.52	1140.28
50.10	1264.44	1250.90	1236.41	1220.60	1203.40	1185.23	1165.80	1144.86
60.10	1267.55	1254.09	1239.66	1224.07	1207.02	1189.05	1169.91	1149.32
68.60	1270.33	1256.76	1242.52	1226.94	1210.03	1192.19	1173.33	1153.07
<b>SrCl<sub>2</sub>(aq): <math>b = 3.031 \text{ mol}\cdot\text{kg}^{-1}</math></b>								
1.10	1354.92	1340.16	1324.81	1308.43	1290.36	1271.02	1250.51	
10.10	1357.74	1343.03	1327.78	1311.58	1293.65	1274.46	1254.24	1232.68
20.10	1360.96	1346.27	1331.14	1315.04	1297.24	1278.29	1258.62	1237.28
30.10	1364.07	1349.35	1334.39	1318.40	1300.87	1282.22	1262.72	1241.64
40.10	1367.19	1352.55	1337.62	1321.75	1304.29	1285.90	1266.77	1246.19
50.10	1370.34	1355.63	1340.81	1324.88	1307.65	1289.64	1270.62	1250.44
60.10	1373.16	1358.71	1343.89	1328.14	1311.10	1293.25	1274.47	1254.53
68.60	1375.70	1361.18	1346.54	1330.91	1313.86	1296.08	1277.59	1257.93

Appendix D. Experimental Density Data for Aqueous Solutions

$p/\text{MPa}$	$\rho/\text{kg}\cdot\text{m}^{-3}$	$\rho/\text{kg}\cdot\text{m}^{-3}$	$\rho/\text{kg}\cdot\text{m}^{-3}$	$\rho/\text{kg}\cdot\text{m}^{-3}$	$\rho/\text{kg}\cdot\text{m}^{-3}$	$\rho/\text{kg}\cdot\text{m}^{-3}$	$\rho/\text{kg}\cdot\text{m}^{-3}$	$\rho/\text{kg}\cdot\text{m}^{-3}$
<b>NaHCO<sub>3</sub>(aq): <math>b = 0.507 \text{ mol}\cdot\text{kg}^{-1}</math></b>								
1.10	1026.64	1016.27	1002.67	986.45	967.23	945.60	921.60	
10.10	1030.34	1019.92	1006.34	990.43	971.50	950.33	926.98	900.80
20.10	1034.56	1023.96	1010.50	994.75	976.19	955.52	932.57	907.44
30.10	1038.58	1027.87	1014.50	998.96	980.67	960.51	938.23	913.71
40.10	1042.55	1031.74	1018.42	1003.05	985.06	965.22	943.62	919.81
50.10	1046.47	1035.56	1022.29	1007.05	989.37	969.93	948.68	925.55
60.10	1050.19	1039.28	1026.03	1010.74	993.56	974.48	953.67	931.00
68.60	1053.46	1042.41	1029.22	1014.16	996.98	978.13	957.69	935.54
<b>NaHCO<sub>3</sub>(aq): <math>b = 1.00 \text{ mol}\cdot\text{kg}^{-1}</math></b>								
1.10	1053.32	1042.10	1028.17	1011.61	992.49	971.16	947.75	
10.10	1056.90	1045.63	1031.76	1015.42	996.59	975.62	952.76	927.94
20.10	1060.94	1049.49	1035.74	1019.51	1001.10	980.58	958.38	934.21
30.10	1064.78	1053.27	1039.62	1023.49	1005.36	985.40	963.67	940.30
40.10	1068.62	1057.11	1043.26	1027.56	1009.57	989.89	968.83	946.08
50.10	1072.42	1060.81	1047.06	1031.43	1013.71	994.52	973.77	951.65
60.10	1075.95	1064.40	1050.67	1035.29	1017.88	998.85	978.58	956.83
68.60	1079.05	1067.35	1053.84	1038.44	1021.02	1002.43	982.48	961.25
<b>Synthetic reservoir brines: <math>b = 0.359 \text{ mol}\cdot\text{kg}^{-1}</math></b>								
1.10	1016.39	1006.38	993.08	977.02	957.95	936.03	912.28	
10.10	1020.21	1010.15	996.91	981.11	962.34	940.92	917.73	891.65
20.10	1024.54	1014.30	1001.04	985.49	967.18	946.22	923.62	898.30
30.10	1028.62	1018.22	1005.10	989.76	971.72	951.37	929.29	904.58
40.10	1032.70	1022.25	1009.03	993.91	976.12	956.19	934.74	910.69
50.10	1036.79	1026.08	1013.01	997.97	980.44	961.00	939.81	916.44
60.10	1040.56	1029.86	1016.86	1001.92	984.64	965.61	944.95	922.05
68.60	1043.85	1033.00	1020.06	1005.19	988.12	969.32	949.08	926.59
<b>Synthetic reservoir brines: <math>b = 1.900 \text{ mol}\cdot\text{kg}^{-1}</math></b>								
1.10	1085.33	1073.58	1060.00	1044.22	1026.32	1006.68	985.20	
10.10	1088.68	1076.98	1063.40	1047.85	1030.24	1010.91	989.82	966.93
20.10	1092.43	1080.70	1067.20	1051.85	1034.56	1015.53	995.06	972.67
30.10	1096.13	1084.24	1070.89	1055.70	1038.63	1020.02	999.86	978.08
40.10	1099.74	1087.91	1074.55	1059.49	1042.56	1024.12	1004.45	983.38
50.10	1103.30	1091.42	1078.12	1063.11	1046.46	1028.52	1009.15	988.23
60.10	1106.65	1094.88	1081.59	1066.80	1050.29	1032.52	1013.58	992.97
68.60	1109.62	1097.65	1084.53	1069.77	1053.41	1035.86	1017.25	997.06
<sup>a</sup> Expanded relative uncertainties are expressed as $U_r(\rho) \leq 0.01 \left[ b/(\text{mol}\cdot\text{kg}^{-1}) \right] + 0.03$								

## Appendix E. Relative Deviations of Densities from the Correlation Model

Table E.1. Deviations of literature data for densities  $\rho$  of  $\text{CaCl}_2(\text{aq})$ ,  $\text{MgCl}_2(\text{aq})$ ,  $\text{NaCl}(\text{aq})$ ,  $\text{KCl}(\text{aq})$ ,  $\text{KI}(\text{aq})$ ,  $\text{Na}_2\text{SO}_4(\text{aq})$ ,  $\text{NaHCO}_3(\text{aq})$  and  $\text{SrCl}_2(\text{aq})$  from the correlation model developed in this work.

Ref	$T_{\min}$ K	$T_{\max}$ K	$\rho_{\min}$ MPa	$\rho_{\max}$ MPa	$b_{\min}$ ( $\text{mol}\cdot\text{kg}^{-1}$ )	$b_{\max}$ ( $\text{mol}\cdot\text{kg}^{-1}$ )	$10^2\Delta_{\text{AAD}}$	$10^2\Delta_{\text{Bias}}$	$10^2\Delta_{\text{MAD}}$	$N$
<b>CaCl<sub>2</sub>(aq)</b>										
[394]	323.15	398.15	3.78	60	0.184	6.007	0.063	0.042	0.327	168
[473]	323.18	472.95	≈7.0	40.0	0.242	6.150	0.056	0.042	0.224	86
[398]	323.16	450.13	1.00	40.71	0.0497	6.424	0.066	-0.063	0.267	176
[474]	321.90	371.96	0.60	0.60	0.030	0.985	0.053	-0.053	0.216	25
[409]	348.15	473.15	2.03	2.03	0.05	1.00	0.009	0.004	0.040	30
[394]	298.15	298.15	5.03	59.94	0.184	6.007	0.068	0.038	0.273	41
[473]	≈298.15	≈298.15	≈7.0	40.0	0.242	6.150	0.039	0.029	0.100	24
[398]	298.15	298.15	1.00	40.71	0.050	4.980	0.020	-0.004	0.090	31
[394]	323.15	398.15	0.10	0.10	0.184	6.007	0.120	0.114	0.369	21
[475]	321.97	371.82	0.10	0.10	1.456	5.541	0.052	-0.052	0.112	17
[431]	303.07	343.06	0.10	0.10	0.987	5.902	0.051	0.042	0.124	54
[398]	323.16	323.16	0.10	0.10	0.050	6.424	0.041	0.000	0.102	17
[430]	288.15	328.15	0.10	0.10	0.05	6.00	0.042	-0.005	0.159	48
[394]	298.15	298.15	0.10	0.10	0.184	6.007	0.103	0.102	0.340	6
[476]	298.15	298.15	0.10	0.10	0.022	7.878	0.069	0.066	0.216	97
[477]	298.15	298.15	0.10	0.10	0.300	2.000	0.103	-0.003	0.202	4
[431]	298.15	298.15	0.10	0.10	3.821	5.902	0.080	0.080	0.107	5
[407]	298.15	298.15	0.10	0.10	0.101	4.980	0.055	0.051	0.213	7
[430]	298.15	298.15	0.10	0.10	0.050	6.000	0.040	-0.007	0.157	8
[478]	298.15	298.15	0.10	0.10	0.033	6.286	0.081	0.069	0.253	17
[479]	298.15	298.15	0.10	0.10	0.050	6.464	0.095	0.092	0.210	14
[480]	298.15	298.15	0.10	0.10	0.010	0.984	0.007	-0.003	0.011	12
[481]	298.15	298.15	0.10	0.10	0.013	0.328	0.007	-0.007	0.013	8
<b>MgCl<sub>2</sub>(aq)</b>										
[399]	369.36	450.07	10.17	30.58	0.031	1.153	0.027	0.024	0.118	52
[475]	297.05	371.82	0.6	0.6	0.442	5.189	0.088	0.084	0.204	25
[474]	297.19	371.82	0.6	0.6	0.108	0.528	0.013	-0.013	0.021	20
[409]	348.15	473.15	2.03	2.03	0.1	1.00	0.039	-0.032	0.112	24
[407]	298.15	298.15	10.38	40.55	0.0312	2.952	0.033	-0.033	0.059	26
[435]	308.15	368.15	0.10	0.10	0.695	4.608	0.013	-0.006	0.053	59
[430]	288.15	328.15	0.10	0.10	0.50	5.000	0.157	-0.157	0.350	36
[432]	303.15	318.15	0.10	0.10	0.54	3.31	0.021	0.011	0.051	24
[437]	278.15	318.15	0.10	0.10	0.491	5.272	0.011	0.001	0.032	65
[439]	273.15	308.15	0.10	0.10	0.005	0.974	0.010	-0.009	0.025	54
[482]	273.15	323.15	0.10	0.10	0.009	1.018	0.007	-0.002	0.028	41
[407]	298.15	298.15	0.10	0.10	0.031	2.952	0.015	-0.010	0.022	7
[438]	298.15	298.15	0.10	0.10	0.303	5.781	0.019	-0.018	0.041	19
[479]	298.15	298.15	0.10	0.10	0.482	5.028	0.015	0.013	0.041	11
[436]	298.15	298.15	0.10	0.10	0.656	5.674	0.018	0.012	0.049	10
[439]	298.15	298.15	0.10	0.10	0.005	1.475	0.011	-0.008	0.020	27
[480]	298.15	298.15	0.10	0.10	0.048	0.971	0.017	-0.017	0.021	10
[481]	298.15	298.15	0.10	0.10	0.004	0.341	0.011	-0.011	0.024	9
<b>KI(aq)</b>										
[400]	278.15	368.15	0.35	0.35	0.015	1.001	0.018	-0.012	0.075	77
[483]	348.15	423.15	2.03	2.03	0.100	1.000	0.064	0.015	0.256	18
[429]	278.15	338.15	0.10	0.10	0.100	0.999	0.017	0.005	0.063	183
[484]	296.02	321.1	0.10	0.10	0.050	0.100	0.006	0.005	0.021	7
[485]	297.19	373.17	0.6	0.6	0.010	1.040	0.009	0.004	0.026	28
[480]	298.15	298.15	0.1	0.1	0.049	0.999	0.007	0.007	0.012	10
[433]	278.15	338.15	0.1	0.1	0.221	0.845	0.021	-0.001	0.091	15
<b>NaCl(aq)</b>										
[401]	373.56	473.40	6.96	30.20	5.972	5.972	0.146	-0.133	0.327	6
[402]	373.15	475.94	0.50	10.22	0.115	2.329	0.021	-0.016	0.036	8

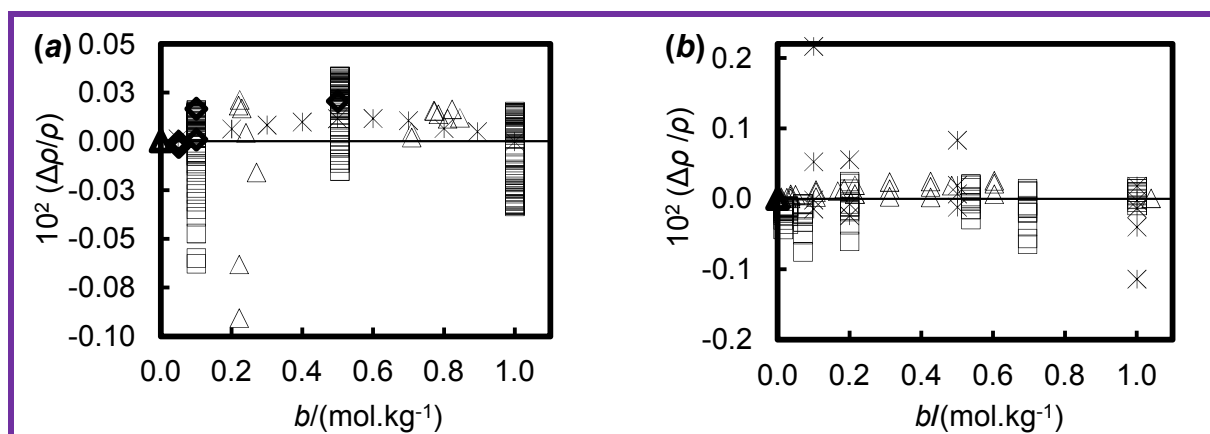
*Appendix E. Relative Deviations of Densities from the Correlation Model*

[403]	298.15	448.57	10.00	28.25	3.001	3.001	0.021	0.005	0.056	12
[486]	298.15	413.15	2.00	2.00	0.500	4.500	0.016	-0.006	0.041	32
[487]	393.40	393.40	1.00	37.40	0.051	3.090	0.022	-0.021	0.039	8
[405]	321.57	498.90	0.10	40.16	0.003	5.046	0.022	-0.008	0.114	326
[407]	298.15	298.15	10.38	40.78	0.058	4.991	0.013	-0.004	0.039	32
[488]	348.15	473.15	2.03	2.03	0.053	4.393	0.014	-0.009	0.073	48
[489]	348.15	473.15	2.03	2.03	0.100	1.000	0.018	-0.016	0.039	24
[490]	288.15	323.15	0.10	0.10	0.050	6.000	0.023	0.000	0.093	29
[491]	318.15	318.15	0.10	0.10	0.101	1.027	0.003	0.001	0.008	5
[492]	293.15	313.15	0.10	0.10	0.000	4.000	0.008	-0.004	0.025	27
[428]	283.15	353.15	0.10	0.10	0.501	4.999	0.120	0.056	0.395	25
[493]	263.00	293.00	0.10	0.10	0.009	6.014	0.018	0.007	0.137	123
[447]	277.15	343.15	0.10	0.10	0.100	1.000	0.006	-0.004	0.060	201
[494]	298.15	328.15	0.10	0.10	0.089	0.346	0.005	-0.005	0.009	12
[475]	297.05	371.82	0.10	0.10	0.108	5.948	0.020	0.009	0.052	36
[495]	308.12	308.12	0.10	0.10	0.084	5.134	0.004	0.000	0.008	10
[405]	323.16	323.16	0.10	0.10	0.056	5.046	0.013	0.008	0.030	17
[435]	308.15	368.15	0.10	0.10	0.217	6.198	0.008	-0.003	0.022	140
[496]	278.15	308.15	0.10	0.10	0.400	6.200	0.013	0.001	0.051	33
[432]	303.15	318.15	0.10	0.10	0.000	6.100	0.009	-0.007	0.021	36
[437]	278.15	318.15	0.10	0.10	0.371	5.997	0.014	0.003	0.055	25
[497]	278.15	318.15	0.10	0.10	0.787	5.952	0.010	-0.006	0.033	36
[498]	288.15	318.15	0.10	0.10	0.062	5.924	0.005	-0.003	0.016	57
[446]	298.15	423.15	0.10	0.10	0.100	3.602	0.033	0.023	0.150	28
[442]	318.15	448.15	0.10	0.10	0.100	2.500	0.048	0.040	0.196	28
[439]	273.15	308.15	0.10	0.10	0.010	1.500	0.050	-0.050	0.535	32
[499]	293.15	303.15	0.10	0.10	0.100	4.000	0.009	-0.009	0.018	15
[500]	298.15	298.15	0.10	0.10	0.050	1.250	0.038	0.038	0.093	7
[501]	298.15	298.15	0.10	0.10	0.000	1.000	0.008	-0.008	0.012	6
[441]	298.15	298.15	0.10	0.10	0.000	4.500	0.068	-0.019	0.138	10
[502]	298.15	298.15	0.10	0.10	0.000	1.000	0.009	-0.009	0.013	6
[495]	298.15	298.15	0.10	0.10	0.504	6.040	0.005	0.004	0.012	13
[503]	298.15	298.15	0.10	0.10	0.295	1.001	0.060	-0.060	0.205	4
[462]	298.15	298.15	0.10	0.10	0.500	4.000	0.041	0.020	0.154	5
[504]	298.15	298.15	0.10	0.10	0.020	3.265	0.010	0.001	0.090	33
[407]	298.15	298.15	0.10	0.10	0.058	4.991	0.009	-0.001	0.022	8
[505]	298.15	298.15	0.10	0.10	0.012	1.844	0.005	-0.004	0.011	17
[432]	298.15	298.15	0.10	0.10	0.000	6.100	0.020	-0.020	0.030	9
[506]	298.15	298.15	0.10	0.10	0.279	5.105	0.010	-0.010	0.032	10
[437]	298.15	298.15	0.10	0.10	0.378	5.993	0.006	-0.005	0.012	21
[497]	298.15	298.15	0.10	0.10	0.995	5.952	0.014	-0.014	0.032	17
[480]	298.15	298.15	0.10	0.10	0.010	1.000	0.008	-0.008	0.011	12
[439]	298.15	298.15	0.10	0.10	0.010	1.500	0.006	-0.006	0.011	25
[461]	298.15	298.15	0.10	0.10	0.022	6.024	0.008	-0.001	0.026	54
<b>KCl(aq)</b>										
[489]	348.15	473.15	2.03	2.03	0.100	1.000	0.020	-0.006	0.105	23
[407]	298.15	298.15	10.38	40.64	0.059	3.012	0.014	-0.013	0.048	28
[485]	297.19	371.97	0.60	0.60	0.010	2.013	0.003	0.003	0.014	29
[507]	308.15	318.15	0.10	0.10	0.045	4.632	0.032	-0.010	0.077	16
[482]	323.15	323.15	0.10	0.10	0.029	1.003	0.009	0.009	0.018	7
[432]	303.15	318.15	0.10	0.10	0.500	4.500	0.010	0.009	0.023	36
[446]	313.15	423.15	0.10	0.10	0.100	3.608	0.036	0.035	0.151	24
[447]	277.15	343.15	0.10	0.10	0.100	1.000	0.009	0.009	0.027	201
[433]	273.20	338.15	0.10	0.10	0.190	0.828	0.011	0.011	0.022	16
[508]	303.15	303.15	0.10	0.10	0.050	4.000	0.099	0.099	0.106	8
[440]	278.15	368.15	0.10	0.10	0.005	4.501	0.010	-0.003	0.058	97
[509]	313.15	353.15	0.10	0.10	0.443	5.229	0.094	-0.003	0.270	37
[510]	291.15	358.15	0.10	0.10	0.100	0.100	0.010	0.010	0.011	14
[511]	298.15	298.15	0.10	0.10	0.500	4.500	0.007	-0.006	0.015	4
[503]	298.15	298.15	0.10	0.10	0.131	0.477	0.001	0.000	0.002	4
[512]	298.15	298.15	0.10	0.10	0.009	0.600	0.006	0.006	0.012	12
[462]	298.15	298.15	0.10	0.10	0.500	4.500	0.007	-0.006	0.016	5
[513]	298.15	298.15	0.10	0.10	0.040	0.997	0.051	0.051	0.148	10
[407]	298.15	298.15	0.10	0.10	0.059	3.012	0.037	0.033	0.148	10
[461]	298.15	298.15	0.10	0.10	0.021	4.818	0.013	0.013	0.033	24
[480]	298.15	298.15	0.10	0.10	0.100	1.005	0.010	0.010	0.017	10
[432]	298.15	298.15	0.10	0.10	0.000	4.500	0.009	-0.008	0.017	10
[514]	298.15	298.15	0.10	0.10	0.498	3.993	0.024	0.015	0.053	8
[440]	298.15	298.15	0.10	0.10	0.051	4.400	0.030	-0.029	0.066	21
[515]	298.15	298.15	0.10	0.10	0.412	1.025	0.015	0.015	0.022	24

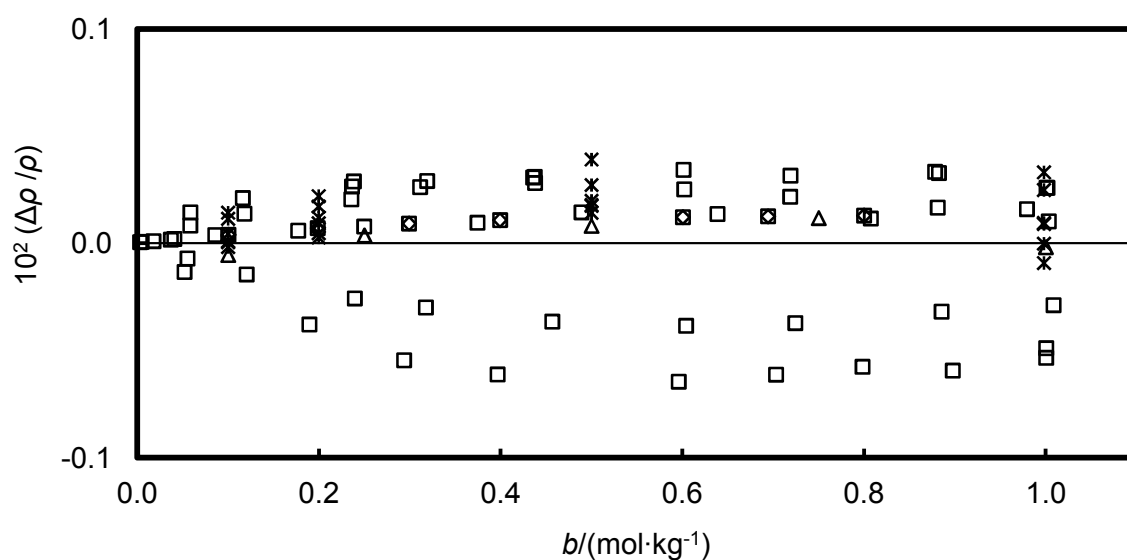
*Appendix E. Relative Deviations of Densities from the Correlation Model*

[516]	298.15	298.15	0.10	0.10	0.000	3.308	0.005	0.005	0.017	15
					<b>Na<sub>2</sub>SO<sub>4</sub> (aq)</b>					
[442]	298.20	448.20	0.1	0.1	0.010	0.150	0.066	0.054	0.239	32
[517]	278.27	318.41	0.1	0.1	1.333	1.333	0.023	-0.019	0.051	10
[435]	308.20	368.20	0.1	0.1	0.101	2.068	0.027	0.018	0.114	67
[430]	288.20	328.20	0.1	0.1	0.050	1.500	0.034	-0.026	0.193	44
[437]	288.15	318.15	0.1	0.1	0.052	1.625	0.015	0.006	0.044	65
[439]	273.20	308.20	0.1	0.1	0.003	0.720	0.017	-0.016	0.054	81
[518]	288.15	318.15	0.1	0.1	0.499	0.997	0.126	0.126	0.170	8
[519]	298.20	298.20	0.1	0.1	0.100	1.964	0.035	-0.035	0.133	8
[482]	273.20	323.20	0.1	0.1	0.002	1.005	0.020	-0.011	0.056	52
[428]	283.16	343.14	0.1	0.1	0.500	1.751	0.026	0.016	0.065	13
[446]	298.20	423.20	0.1	0.1	0.033	1.203	0.071	0.068	0.212	28
[480]	298.20	298.20	0.1	0.1	0.100	1.000	0.013	-0.005	0.022	10
[449]	283.20	298.20	0.1	0.1	0.100	1.848	0.022	-0.019	0.066	24
[520]	298.20	298.20	0.1	0.1	0.092	0.500	0.012	-0.012	0.017	5
[521]	313.20	313.20	0.1	0.1	0.035	1.408	0.019	0.003	0.049	9
[522]	298.20	298.20	0.1	0.1	0.063	1.555	0.078	0.078	0.276	7
[485]	297.19	371.82	0.60	0.60	0.010	1.532	0.013	0.005	0.047	43
[410]	298.18	450.10	9.87	30.70	0.010	1.003	0.026	0.017	0.137	76
[483]	348.20	473.20	2.03	2.03	0.050	1.000	0.018	0.015	0.059	30
[411]	293.99	475.81	2.00	10.25	0.058	0.330	0.016	-0.004	0.073	216
					<b>NaHCO<sub>3</sub> (aq)</b>					
[523]	293.15	293.15	0.10	0.10	0.100	1.000	0.006	0.003	0.012	5
[413]	298.13	448.50	9.80	28.20	0.100	0.998	0.014	0.013	0.039	24
[450]	278.15	318.15	0.10	0.10	0.003	1.008	0.024	-0.001	0.064	61
[524]	298.15	298.15	0.10	0.10	0.100	0.800	0.010	0.010	0.013	7
					<b>SrCl<sub>2</sub> (aq)</b>					
[524]	298.15	298.15	0.1	0.1	0.200	0.996	0.006	-0.005	0.018	9
[525]	298.15	298.15	0.1	0.1	0.100	3.629	0.017	-0.011	0.054	13
[526]	298.15	298.15	0.1	0.1	0.050	0.264	0.002	0.002	0.004	5
[527]	298.15	298.15	0.1	0.1	0.250	3.421	0.009	0.008	0.020	13
[528]	298.15	298.15	0.1	0.1	0.004	0.329	0.001	0.000	0.002	9
[430]	288.20	328.20	0.10	0.10	0.050	2.500	0.329	-0.227	1.237	49
[408]	323.15	473.15	2.03	2.03	0.303	2.718	0.347	0.347	1.681	56
[409]	348.20	473.20	2.03	2.03	0.100	1.000	0.087	0.087	0.217	24

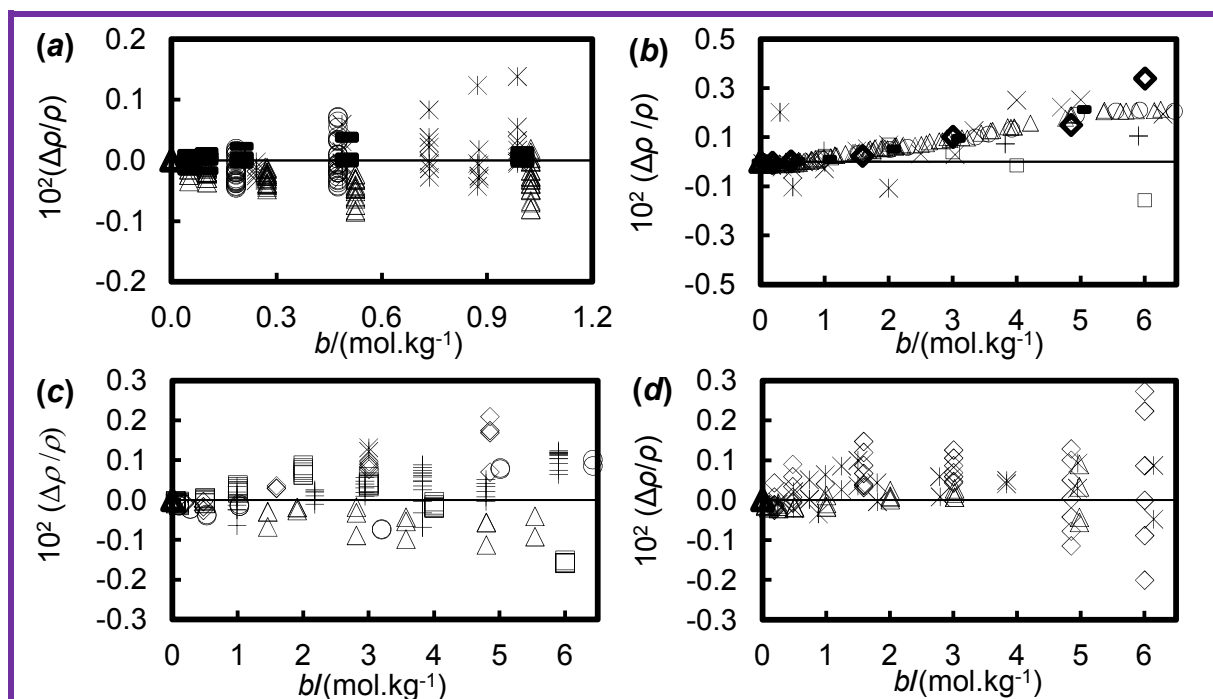
**Figures E-1 to E-8.** Relative deviations  $\Delta\rho/\rho$  of densities  $\rho$  from the present correlation model for the brines studied in this work as a function of molality  $b$



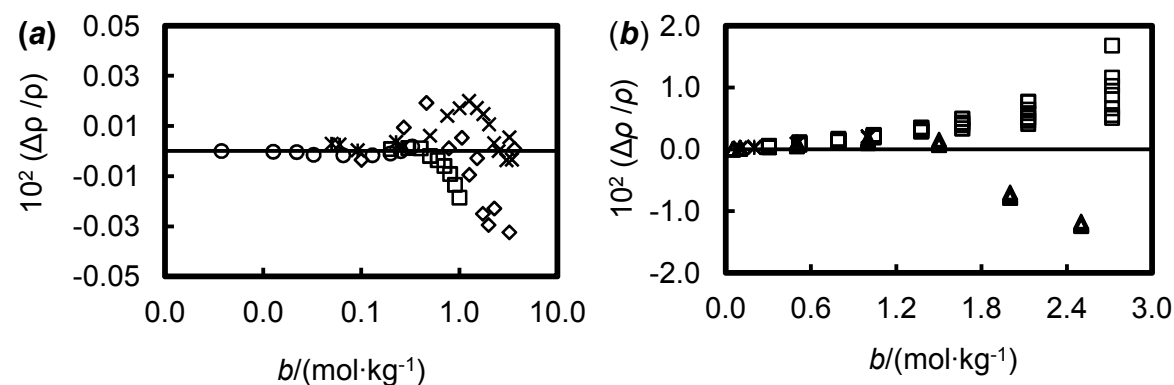
**Figure E-1.** Relative deviations  $\Delta\rho/\rho$  of densities  $\rho$  from the present model for KI (aq) as a function of molality  $b$ . (a):  $p = 0.1$  MPa, ( $\square$ ) Apelblat and Manzurola,[429]  $T = 278$  K to 338 K, ( $\diamond$ ) Lemire et al.,[484]  $T = 296$  K and 321 K, ( $*$ ) Millero et al.,[480]  $T = 298.15$  K, ( $\triangle$ ) Dunn,[433]  $T = 278$  K to 338 K. (b): ( $\square$ ) Swenson and Woolley.,[400]  $T = 278$  K to 368 K,  $p = 0.35$  MPa, ( $*$ ) Ellis,[409]  $T = 348$  K to 423 K,  $p = 2.0$  MPa, ( $\triangle$ ) Saluja et al.,[485]  $T = 297$  K to 373 K,  $p = 0.6$  MPa



**Figure E-2.** Relative deviations  $\Delta\rho/\rho$  of densities  $\rho$  from the present model for  $\text{NaHCO}_3(\text{aq})$  as a function of molality  $b$  at different pressure and temperature values:  $\triangle$ , Sandengen and Kaasa; [523] (293.15 to 293.15) K and (0.1 to 0.1) MPa,  $*$ , Sharygin and Wood, [413] (293.13 to 448.50) K and (9.8 to 28.20) MPa,  $\square$ , Hershey et al.; [450] (278.15 to 318.15) K and (0.1 to 0.1) MPa,  $\diamond$ , Millero et al.; [524] (298.15 to 298.15) K and (0.1 to 0.1) MPa.

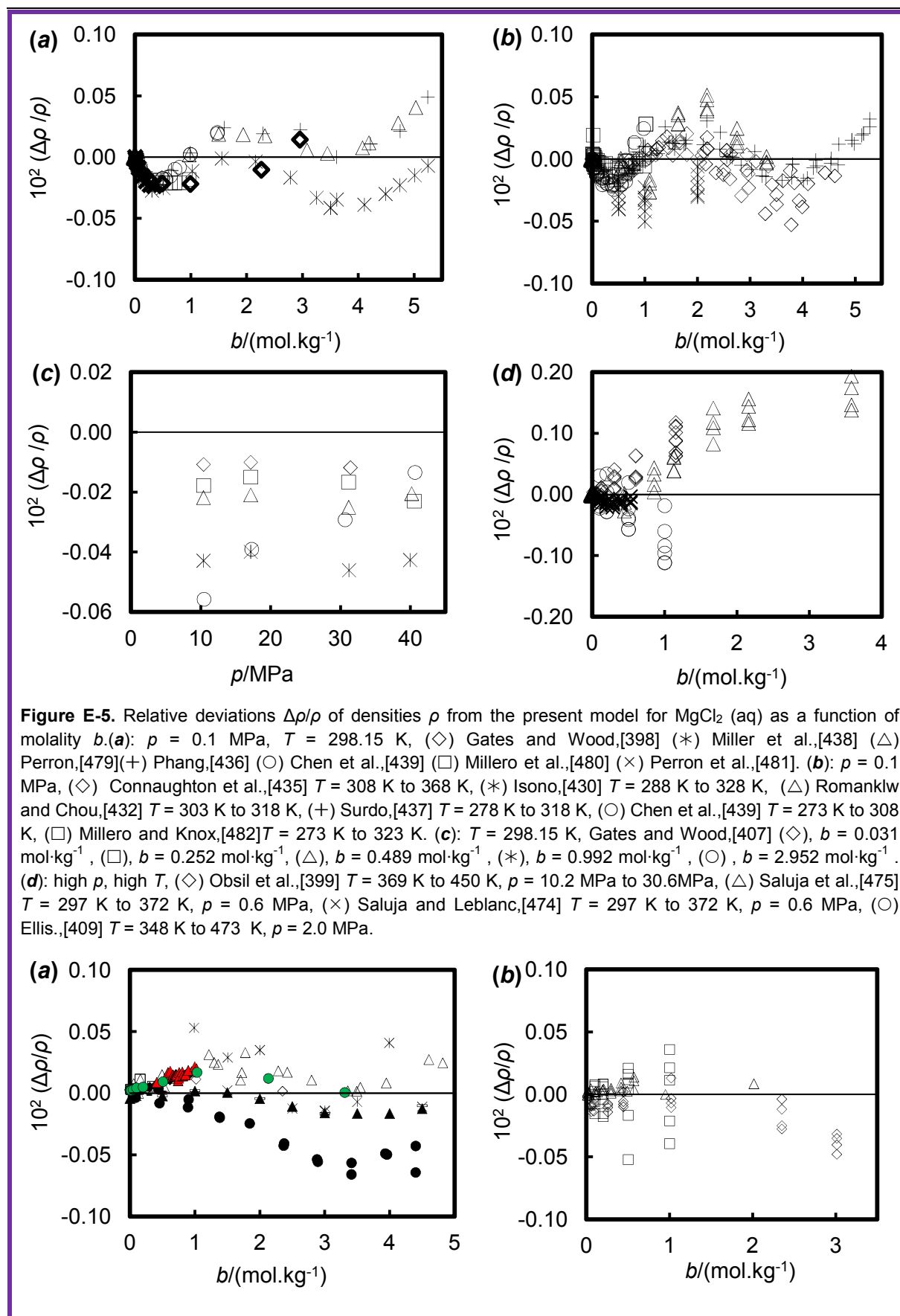


**Figure E-3.** Relative deviations  $\Delta\rho/\rho$  of densities  $\rho$  from the present model for  $\text{CaCl}_2(\text{aq})$  as a function of molality  $b$ . (a): high  $p$ , high  $T$ , ( $\circ$ ) Safarov et al.,[394]  $T = 323 \text{ K}$  to  $398 \text{ K}$ ,  $p = 5.7 \text{ MPa}$  to  $59.9 \text{ MPa}$ . ( $*$ ) Oakes et al.,[473]  $T = 323 \text{ K}$  to  $473 \text{ K}$ ,  $p = 7.1 \text{ MPa}$  to  $41.5 \text{ MPa}$ . ( $\triangle$ ) Gates and Wood,[398]  $T = 323 \text{ K}$  to  $450 \text{ K}$ ,  $p = 1 \text{ MPa}$  to  $40.7 \text{ MPa}$ . ( $\bullet$ ) Ellis,[409]  $T = 348 \text{ K}$  to  $473 \text{ K}$ ,  $p = 2.0 \text{ MPa}$ . (b):  $0.1 \text{ MPa}$ ,  $298.15 \text{ K}$ , ( $\triangle$ ) Zhang et al.,[476] ( $*$ ) Oakes et al.,[473] ( $+$ ) Wimby and Berntsson,[431] ( $\bullet$ ) Gates and Wood,[407] ( $\square$ ) Isono,[430] ( $\times$ ) Kumar et al.,[478] ( $\circ$ ) Perron et al.,[479] ( $\diamond$ ) Millero et al.,[480] (c):  $0.1 \text{ MPa}$ , ( $\diamond$ ) Safarov et al.,[394]  $T = 323 \text{ K}$  to  $398 \text{ K}$ , ( $*$ ) Yan et al.,[529]  $T = 288 \text{ K}$  to  $308 \text{ K}$ , ( $\triangle$ ) Saluja et al.,[475]  $T = 322 \text{ K}$  to  $372 \text{ K}$ , ( $+$ ) Wimby and Berntsson,[431]  $T = 292 \text{ K}$  to  $352 \text{ K}$ , ( $\circ$ ) Gates and Wood,[398]  $T = 323 \text{ K}$ , ( $\square$ ) Isono,[430]  $T = 288 \text{ K}$  to  $323 \text{ K}$ . (d):  $298.15 \text{ K}$ , ( $\diamond$ ) Safarov et al.,[394]  $p = 5.4 \text{ MPa}$  to  $59.9 \text{ MPa}$ , ( $*$ ) Oakes et al.,[473]  $p = 7.3 \text{ MPa}$  and  $42 \text{ MPa}$ , ( $\triangle$ ) Gates and Wood,[407]  $p = 10.4 \text{ MPa}$  to  $40.6 \text{ MPa}$ .



**Figure E-4.** Relative deviations  $\Delta\rho/\rho$  of densities  $\rho$  from the present model for  $\text{SrCl}_2(\text{aq})$  as a function of molality  $b$ . (a)  $T = 298.15 \text{ K}$  and  $p = 0.1 \text{ MPa}$ : ( $\square$ ), Millero et al.,[524], ( $\diamond$ ), Peña et al., [525], ( $\times$ ), Rard and Miller; [527], ( $*$ ), Shedlovsky and Brown; [526], ( $\circ$ ), Perron et al.,[528] (b): high  $T$  and high  $p$ : ( $\square$ ), Kumar; [408] ( $323.15$  to  $473.15$ )  $\text{K}$  and ( $2.03$  to  $2.03$ )  $\text{MPa}$ , ( $\triangle$ ), Isono; [430] ( $288.20$  to  $328.20$ )  $\text{K}$  and ( $0.1$  to  $0.1$ )  $\text{MPa}$ , ( $*$ ), Ellis; [409] ( $348.20$  to  $473.20$ )  $\text{K}$  and ( $2.03$  to  $2.03$ )  $\text{MPa}$ .





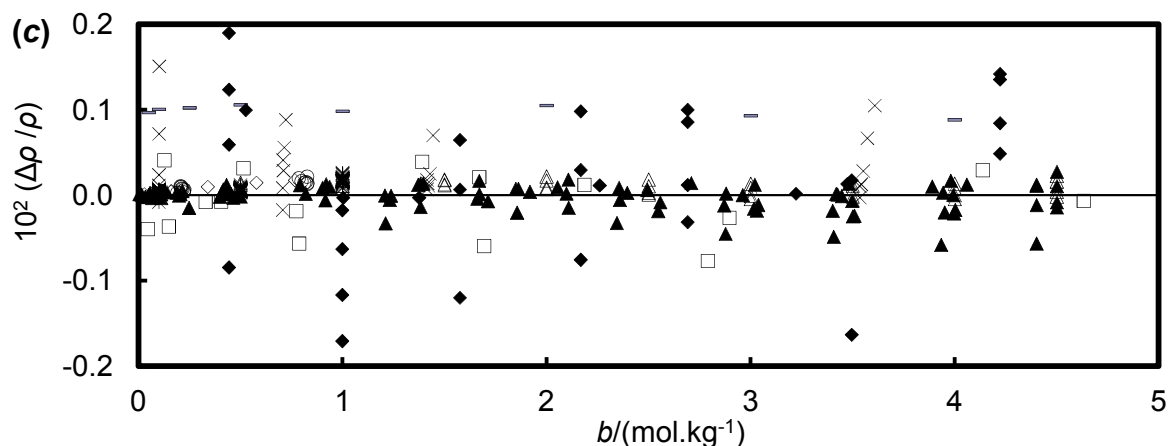


**Figure E-6.** Relative deviations  $\Delta\rho/\rho$  of densities  $\rho$  from the present model for KCl(aq) as a function of molality  $b$ . (a): 298.15 K, 0.1 MPa, ( $\times$ ) Kumar,[408] ( $\square$ ) MacInnes and Dayhoff,[512] ( $-$ ) Kawaizumi et al.,[503] ( $\blacktriangleright$ ) Kumar,[462] ( $\diamond$ ) Gates and Wood,[407] ( $\triangle$ ) Zhang and Han,[461] ( $\blacksquare$ ) Ruby and Kawai,[530] ( $\blacklozenge$ ) Millero et al.,[480] ( $\blacktriangle$ ) Romankiw and Chou.,[432] ( $*$ ) Ostroff et al.,[514] ( $\bullet$ ) Dedick et al.,[440] ( $\triangleleft$ ) Parton et al.,[515] ( $\circ$ ) Jones and Ray.[516] (b): high P, High T, ( $\square$ ) Ellis,[489] (348.15 to 473.15) K and (2.03) MPa, ( $\diamond$ ) Gates and Wood,[407] (298.15) K and (10.38 to 40.64) MPa, ( $\triangle$ ) Saluja et al.,[485] (297.19 to 371.97) K and (0.6) MPa. (c): 0.1 MPa, T, ( $\square$ ) Firth and Tyrrell,[507] (308.15 to 318.15) K, ( $\diamond$ ) Millero and Knox,[482] (323.15) K, ( $\triangle$ ) Romankiw and Chou,[432] (303.15 to 318.15) K, ( $\times$ ) Korosi and Fabuss,[446] (313.14 to 423.15) K, ( $*$ ) Apelblat and Manzurola,[447] (277.15 to 343.15) K, ( $\circ$ ) Dunn,[433] (278.15 to 338.15) K, ( $\bullet$ ) Galleguillos et al.,[508] (303.15) K, ( $\blacktriangle$ ) Dedick et al.,[440] (278.15 to 368.15) K, ( $\blacklozenge$ ) Harrison and Perman.,[509] (313.15 to 353.15), ( $-$ ) Sulston,[510] (291.15 to 358.15) K.

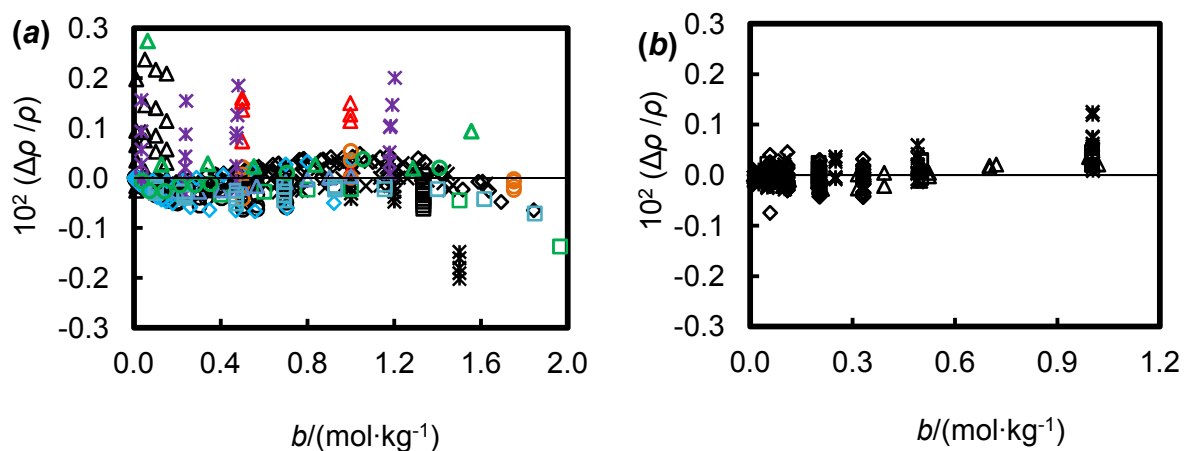
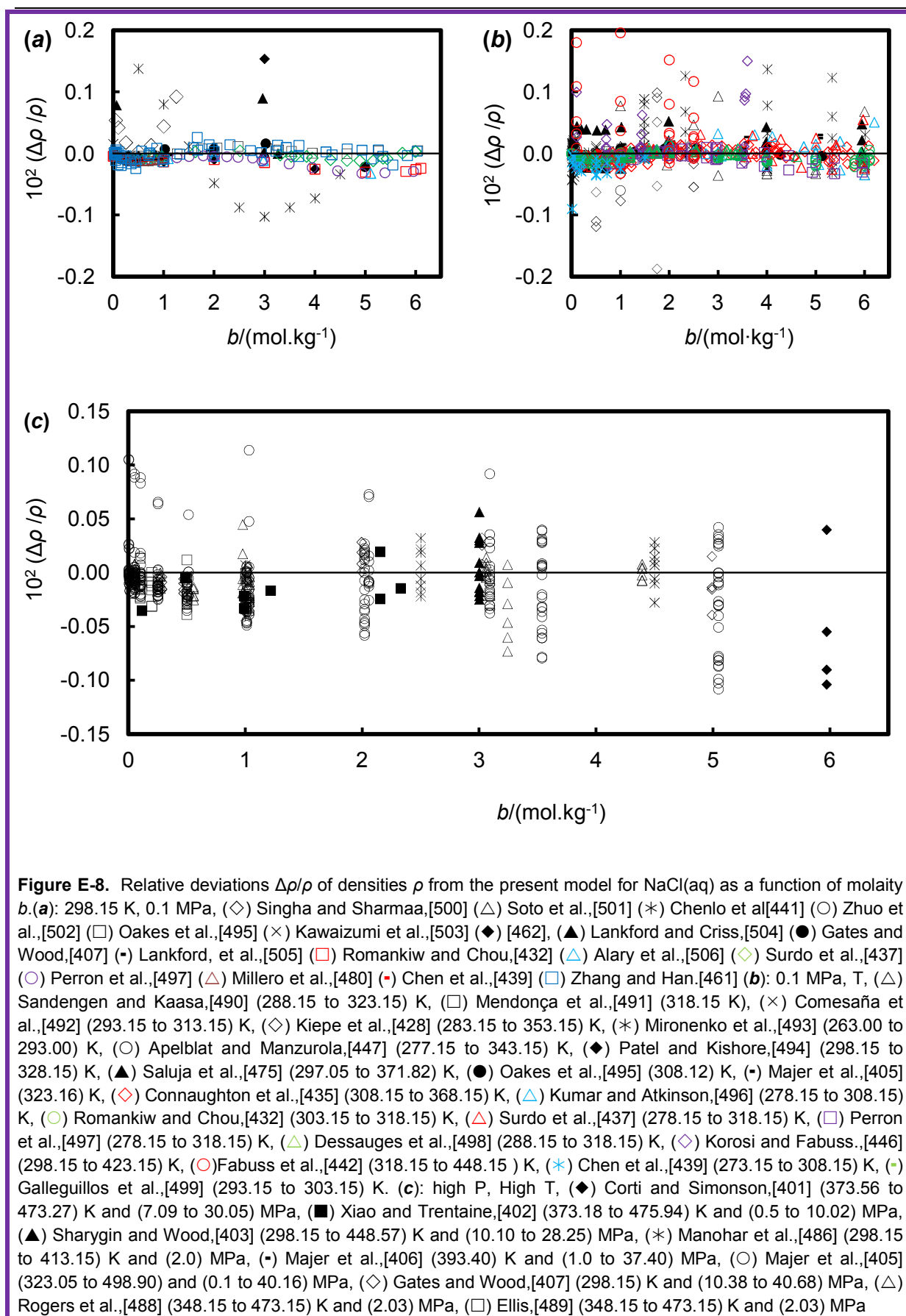


**Figure E-7.** Relative deviations  $\Delta\rho/\rho$  of densities  $\rho$  from the present model for Na<sub>2</sub>SO<sub>4</sub>(aq) as a function of molality  $b$ . (a): 0.1 MPa and different temperatures:  $\triangle$ , Fabuss et al.; [442] (298.20 to 448.20) K,  $\square$ , Wirth and Losurdo; [517] (278.27 to 318.41) K,  $\diamond$ , Connaughton et al.;[435] (308.20 to 368.20) K,  $*$ , Isono;[430] (288.20 to 328.20) K,  $\times$ , Surdo et al.;[437] (288.15 to 318.15) K,  $\circ$ , Chen et al.;[439] (273.20 to 308.20) K,  $\triangleleft$ , Banipal et al.;[518] (288.15 to 318.15) K,  $\square$ , Pearce and Eckstrom;[519] (298.20 to 298.20) K,  $\diamond$ , Millero and Knox;[482] (273.20 to 323.20) K,  $\circ$ , Kiepe et al.;[428] (283.16 to 343.14) K,  $*$ , Korosi and Fabuss;[446] (298.20 to 423.20) K,  $\triangleleft$ , Millero et al.;[480] (298.20 to 298.20) K,  $\square$ , Hervello and Sánchez;[449] (283.20 to 298.20) K,  $-$ , Zhuo et al.;[520] (298.20 to 298.20) K,  $\circ$ , Fleischmann and Mersmann;[521] (313.20 to 313.20) K,  $\triangleleft$ , Trimble;[522] (298.20 to 298.20) K. (b): high  $p$ , high  $T$ :  $\triangle$ , Saluja et al.;[485] (297.19 to 371.82) K and (0.60 to 0.60) MPa  $*$ , Obšil et al.;[410] (298.18 to 450.10) K and (9.87 to 30.70) MPa,  $\square$ , Ellis;[483] (348.20 to 473.20) K and (2.03 to 2.03) MPa  $\diamond$ , Phutela and Pitzer;[411] (293.99 to 475.81) K and (2.00 to 10.25) MPa.



## Appendix F. An Analytical Expression for the Determination of Density Error

Consider isothermal calibration with water and vacuum over a range of pressures. In this case the exact working equation can be expressed as following:

$$\rho = A_0(1 + \alpha p)\tau^2 - B_0(1 + \beta p), \quad (\text{F1})$$

where  $\alpha$  and  $\beta$  are coefficients, which are determined by regression during calibration. Let the parameter  $r$  be defined such that

$$r = \frac{\alpha}{\beta}, \quad (\text{F2})$$

The value of  $r$  depends on the calibration method used. It reflects the isothermal dependence of  $\alpha$  and  $\beta$  upon pressure.

If we calibrate with vacuum and with water at  $p \rightarrow 0$ ,  $A_0$  and  $B_0$  can be expressed by:

$$A_0 = \frac{\rho_{w,0}}{\tau_{w,0}^2 - \tau_0^2} \text{ and } B_0 = \frac{\rho_{w,0}\tau_0^2}{\tau_{w,0}^2 - \tau_0^2} \quad (\text{F3})$$

If we then calibrate at pressure  $p$  assuming a value of  $r = r'$  that is incorrect, we will obtain a value of the remaining parameter  $\beta = \beta'$  that is also incorrect. Therefore, there will be a density error given by<sup>19</sup>

$$\Delta\rho = A_0(r'\beta' - r\beta)p\tau^2 - B_0(\beta' - \beta)p \quad (\text{F4})$$

Since this will vanish at the density of water (because that was a calibration point), it follows that

$$\Delta\rho = A_0(r'\beta' - r\beta)p(\tau^2 - \tau_w^2), \quad (\text{F5})$$

This suggests that the error is in fact proportional to the product of pressure and  $(\rho - \rho_w)$ . In order to determine the relationship between  $\beta$  and  $\beta'$ , appearing in Equation F5. We make use of the following Equations

---

<sup>19</sup> Note that from Equation F4, when  $\tau = \tau_w$ ,  $0 = A_0(r'\beta' - r\beta)p\tau_w^2 - B_0(\beta' - \beta)p$

For water calibration at pressure  $p$ :

$$\begin{cases} \rho_w = A_0(1 + r' \beta' p) \tau_w^2 - B_0(1 + \beta' p), & \text{with assumed } r' \\ \rho_w = A_0(1 + r \beta p) \tau_w^2 - B_0(1 + \beta p), & \text{with real } r \end{cases}, \quad (\text{F6})$$

This results in the following expression:

$$0 = A_0(r' \beta' - r \beta) p \tau_w^2 - B_0(\beta' - \beta) p, \quad (\text{F7})$$

Since  $B_0/A_0 = \tau_0^2$ , we find

$$\beta' = \left( \frac{r \tau_w^2 - \tau_0^2}{r' \tau_w^2 - \tau_0^2} \right) \beta, \quad (\text{F8})$$

Therefore, using Equation F7 and Equation F5, we find that

$$\begin{cases} \Delta \rho = B_0(\beta' - \beta) \left[ \frac{\tau^2}{\tau_w^2} - 1 \right] p \\ = \frac{B_0(r - r') \tau_w^2}{r' \tau_w^2 - \tau_0^2} \left[ \frac{\tau^2}{\tau_w^2} - 1 \right] \beta p \\ = B_0(r - r') \beta p \left( \frac{\tau^2 - \tau_w^2}{r' \tau_w^2 - \tau_0^2} \right) \\ = B_0(r - r') \beta' p \left( \frac{\tau^2 - \tau_w^2}{r \tau_w^2 - \tau_0^2} \right) \end{cases}, \quad (\text{F9})$$

Equation F9 can then be used to evaluate the density error knowing  $r^{20}$  and  $\beta$  from the original calibration and the correct value of  $r$ . All of these values can be obtained by regression during the calibration. The correct value of  $r$  will, however, require the use of two (or more fluids) at given pressure and temperature during calibration.

---

<sup>20</sup> Note that in the case of using vacuum and water,  $r' = 1$ . Because both  $\alpha$  and  $\beta$  assumed to vary with the pressure in the same way, hence  $\alpha = \beta$  in this case.